

# **The Characterisation, Photocatalytic Performance, and Theoretical Investigation of Small Gold Clusters Supported on Titanium Dioxide Nanoparticles**

---

**Jason Frankie Alvino**

B.Sc. (Nanoscience and Materials) (Hons), MRACI

A thesis submitted in total fulfilment of the requirements for the  
degree of Doctor of Philosophy



THE UNIVERSITY  
*of* ADELAIDE

July 2015

School of Physical Sciences

Department of Chemistry

The University of Adelaide

## **Declaration**

I certify that this work contains no material which has been accepted for the award of any other degree or diploma in any university or other tertiary institution and, to the best of my knowledge and belief, contains no material previously published or written by another person, except where due reference has been made in the text. In addition, I certify that no part of this work will, in the future, be used in a submission for any other degree or diploma in any university or other tertiary institution without the prior approval of the University of Adelaide and where applicable, any partner institution responsible for the joint-award of this degree.

I give consent to this copy of my thesis when deposited in the University Library, being made available for loan and photocopying, subject to the provisions of the Copyright Act 1968.

The author acknowledges that copyright of published works contained within this thesis resides with the copyright holder(s) of those works.

I also give permission for the digital version of my thesis to be made available on the web, via the University's digital research repository, the Library catalogue and also through web search engines, unless permission has been granted by the University to restrict access for a period of time.

## Abstract

Renewable photocatalytic systems that can use solar radiation to produce chemical fuels are appealing technologies that have garnered much interest over the last few decades. The development of novel gold-based heterogeneous photocatalysts has the potential to drive this new form of green chemistry. In this thesis, ligand-protected, atomically precise gold clusters supported on titanium dioxide nanoparticles are characterised by various surface science techniques and their photocatalytic potential for water photolysis is investigated. Given the difficulty associated with acquiring experimental data in the incredibly small size regime of clusters, complementary density functional theory calculations are also performed to match with experimental data and to help elucidate the interactions occurring between gold atoms and the titanium dioxide surface.

The characterisation of these gold clusters begins with the far infra-red absorption spectra of isolated  $\text{Au}_6(\text{Ph}_2\text{P}(\text{CH}_2)_3\text{PPh}_2)_4(\text{NO}_3)_2$ ,  $\text{Au}_8(\text{PPh}_3)_8(\text{NO}_3)$ ,  $\text{Au}_9(\text{PPh}_3)_8(\text{NO}_3)_3$ ,  $\text{Au}_{11}(\text{PPh}_3)_8\text{Cl}_3$ ,  $\text{Pd}(\text{PPh}_3)\text{Au}_6(\text{PPh}_3)_6(\text{NO}_3)_2$ , and  $\text{Pt}(\text{H})(\text{PPh}_3)(\text{AuPPh}_3)_7(\text{NO}_3)_2$  recorded using synchrotron light. These experiments reveal a series of unique peaks between 50 and  $475\text{ cm}^{-1}$  that are assigned to specific vibrational modes by comparison with density functional theory calculations. The distinct peaks for each cluster can be assigned to the calculated cluster core vibrations:  $80.4$  and  $84.1\text{ cm}^{-1}$  for  $\text{Au}_6$ ;  $165.1$  and  $166.4\text{ cm}^{-1}$  for  $\text{Au}_8$ ;  $170.1$  and  $185.2\text{ cm}^{-1}$  for  $\text{Au}_9$ ;  $173.7$  and  $182.2\text{ cm}^{-1}$  for  $\text{Au}_{11}$ ;  $158.9$ ,  $195.2$ , and  $206.7\text{ cm}^{-1}$  for  $\text{Au}_6\text{Pd}$ ; and  $156.3$ ,  $171.8$ , and  $173.5\text{ cm}^{-1}$  for  $\text{Au}_7\text{Pt}$ . There is also a strong absorption for all clusters near  $420\text{ cm}^{-1}$  that are assigned to P- $\text{Ph}_3$  vibrations.

Characterisation is continued with the use of Synchrotron X-ray and TEM techniques to investigate the full effect of treatments that are undertaken to remove the organic protective ligands after the gold clusters are supported upon titanium dioxide. These experiments show an increase in particle size and loss of ligands with successively harsher post-treatments. Acidic pre-treatment and the form of the titanium dioxide support are shown to have a strong impact on the severity of agglomeration and ligand loss. These results are also supported by X-ray absorption near edge structure and extended X-ray absorption near edge structure analysis of complementary X-ray absorption experiments.

The photocatalytic potential for water photolysis by these catalysts is also investigated using a new experimental apparatus designed and built during the project. It consists of a heterogeneous gas-phase reactor operating near ambient conditions that can deliver constant and controlled samples of gas to a residual gas mass spectrometer for analysis of the gas composition over time. Using this apparatus,  $\text{Au}_8(\text{PPh}_3)_8(\text{NO}_3)_2$ ,  $\text{Au}_9(\text{PPh}_3)_8(\text{NO}_3)_3$ , and  $\text{Au}_{101}[\text{P}(\text{C}_6\text{H}_5)_3]_{21}\text{Cl}_5$  supported on anatase or P25  $\text{TiO}_2$  nanoparticles are investigated for their activity towards water photolysis and their peak  $\text{H}_2$  production rates are quantified. Anatase-supported samples are found to increase in activity with successively harsher post-treatment conditions, suggesting that increasing the size of the gold particles is beneficial for photocatalytic activity. In contrast, samples prepared on acid-washed P25 or acid-washed anatase show evidence of an ideal gold particle size and ligand coverage after relatively gentle post-treatment conditions.

Finally, density functional theory investigations are undertaken of  $\text{Au}_1$ ,  $\text{Au}_2$ ,  $\text{Au}_3$ , and  $\text{Au}_4$  clusters bound to the stoichiometric and oxygen-deficient titanium dioxide anatase(101) surface using an atomic-centred basis set approach. Numerous isomers are found within 0.5 eV of the lowest energy structure for  $\text{Au}_2$ ,  $\text{Au}_3$ , and  $\text{Au}_4$ . The structural parameters, binding energies, infrared spectra, charge transfer, and density of states for each isomer are described in detail. Key findings include: increased binding energy as the number of Au atoms are increased; strong Au-Au stretching and cluster breathing modes that shift considerably between isomers; charge transfer from the Au clusters to the titanium dioxide surface; and the introduction of numerous occupied gold states at the valence band edge that extend into the band gap. This work provides the foundation for future studies that will use these anatase models to investigate the properties of small Au clusters with photocatalytically relevant molecules and their reaction pathways.

## Acknowledgements

First and foremost, the successful completion of this project would never have been possible without the guidance and support of my primary supervisor Prof. Greg Metha. Greg has provided me with a great deal of knowledge, advice, and encouragement throughout the entire project, without which the last few years would have been far less enjoyable. He has also given me many opportunities to perform experiments at the synchrotron and attend conferences to discover new science while meeting new people, for which I am grateful. I'd also like to thank my co-supervisors Dr. Tak Kee and Dr. David Huang for their support throughout the years and constructive critique of my work.

Thanks to Dr. Matt Addicoat, Dr. Rika Kobayashi, and Dr. Alexander Gentleman for all their guidance with theoretical calculations over the years. They were always willing to lend a hand and guide me in the right direction when I was lost in a sea of papers and technical manuals. Dr. Alexander Gentleman has also been an inspiring and knowledgeable mentor ever since he first taught me during undergraduate laboratory sessions. His passion for physical chemistry and dedication to his work has certainly motivated many of us in the laser lab to aspire for greatness.

Big thankyou to Peter Apoefis for building various parts of the experimental apparatus throughout the course of my project, as well as his patience when teaching me about vacuum system design and technical systems. Also thanks to Matthew Bull for helping me with many of the electronics and designing our pulsed nozzle driver. Without their help, construction of the new apparatus simply would not have been possible.

I would like to thank the Australian Synchrotron and their wonderful staff, especially Dr. Dominique Appadoo, who was always willing to come into the lab and help us even in the most ridiculous hours of the night. His hospitality while we were at the synchrotron with the 'Rastonites' was certainly more than one could ever ask for. In addition, Assoc. Prof. Hugh Harris and Dr. Claire Weekley were very helpful back in Adelaide for the analysis and interpretation of our XAS data.

Thanks to all the people in the department that I have become friends with throughout my studies. There are some people I have known since our undergraduate days and there have certainly been some experiences I won't soon forget. Special shout-outs go to all the members of the laser lab, including characters such as Robert Hardy, Aidan Karayilan,

and Trystan Bennett, whom have made the many years spent in the lab and at conferences so much more entertaining. Special mention to Trystan, with whom I have worked closely throughout the various aspects of this project, including the continued development of the experimental apparatus. We have been friends since the start of undergrad and I am not sure either of us ever thought we would make it this far and be working together on a PhD project.

Last but certainly not least, I would like to thank my family for their love and support throughout my university studies, especially for being patient with what I am sure was a fairly grouchy and difficult Jason after many long hours spent in the lab or while writing my thesis. If it were not for my family encouraging me to head to university when I finished school, I would never have reached this stage of my studies.

## Publications

The publications listed below contain some of the work presented in this thesis:

### **Far-Infrared Absorption Spectra of Synthetically-Prepared, Ligated Metal Clusters with Au<sub>6</sub>, Au<sub>8</sub>, Au<sub>9</sub> and Au<sub>6</sub>Pd Metal Cores**

Jason F. Alvino, Trystan Bennett, David Anderson, Baira Donoeva, Daniil Ovoshchnikov, Rohul H. Adnan, Dominique Appadoo, Vladimir Golovko, Gunther Andersson, Gregory F. Metha, RSC Advances, 3, 22140–22149 (2013).

### **Chemically-Synthesised, Atomically-Precise Gold Clusters Deposited and Activated on Titania**

David P. Anderson, Jason F. Alvino, Alexander Gentleman, Hassan Al Qahtani, Lars Thomsen, Matthew I.J. Polson, Gregory F. Metha, Vladimir B. Golovko, Gunther G. Andersson, Physical Chemistry Chemical Physics, 15, 3917–3929 (2013).

### **Chemically Synthesised Atomically Precise Gold Clusters Deposited and Activated on Titania. Part II**

David P. Anderson, Rohul H. Adnan, Jason F. Alvino, Oliver Shipper, Baira Donoeva, Jan-Yves Ruzicka, Hassan Al Qahtani, Hugh H. Harris, Bruce Cowie, Jade B. Atkin, Vladimir B. Golovko, Gregory F. Metha, Gunther G. Andersson, Physical Chemistry Chemical Physics, 15, 14806–14813 (2013).

The publications listed below are currently in preparation and will contain some of the work presented in this thesis:

### **DFT Studies of Au<sub>1-4</sub> on the Stoichiometric and Oxygen-deficient TiO<sub>2</sub> Anatase(101) Surface**

Jason F. Alvino, Trystan Bennett, Gregory F. Metha.

## Abbreviations

ADF-STEM	Angular Dark Field Scanning Transmission Electron Microscopy
AO	Atomic Orbital
AuNP	Au Nanoparticle
CEM	Channel Electron Multiplier
CSD	Cambridge Structural Database
DFT	Density Functional Theory
DOS	Density of States
ECP	Effective Core Potential
eV	Electron Volt
EXAFS	Extended X-ray Absorption Fine Structure
FC	Faraday Cup
FCC	Face Centred Cubic
FWHM	Full Width at Half Maximum
GGA	Generalised Gradient Approximation
GTO	Gaussian Type Orbital
HBP	High Binding Peak
HOMO	Highest Occupied Molecular Orbital
HRTEM	High-resolution Transmission Electron Microscopy
LBP	Low Binding Peak
LDA	Local Density Approximation
LSPR	Localised Surface Plasmon Resonance
LUMO	Lowest Unoccupied Molecular Orbital
MO	Molecular Orbital
NBO	Natural Bond Orbital
O <sub>2c</sub>	2 Coordinated Oxygen Atom
O <sub>3c</sub>	3 Coordinated Oxygen Atom
PBC	Periodic Boundary Conditions
PID	Proportional-Integral-Derivative
RGA	Residual Gas Analyser
SCF	Self-Consistent Field
SOMO	Singly Occupied Molecular Orbital
STM	Scanning Tunnelling Microscopy
STO	Slater Type Orbital

TEM	Transmission Electron Microscopy
Ti <sub>4c</sub>	4 Coordinated Ti Atom
Ti <sub>5c</sub>	5 Coordinated Ti Atom
UHV	Ultra High Vacuum
XANES	X-ray Absorption Near Edge Structure
XAS	X-ray Absorption Spectroscopy
XPS	X-ray Photoelectron Spectroscopy
ZPE	Zero-point Energy

# Table of Contents

<b>Declaration</b>	I
<b>Abstract</b>	II
<b>Acknowledgements</b>	IV
<b>Publications</b>	VI
<b>Abbreviations</b>	VII
<b>Chapter 1. Introduction</b>	
1.1 Background	2
1.2 Photocatalysis	4
1.2.1 Semiconductor Electrodes and Supports	5
1.2.2 Mechanisms of Photocatalysis	7
1.2.3 Semiconductor Nanoparticles as Supports	9
1.3 TiO <sub>2</sub> Photocatalysis	12
1.3.1 The Structure of TiO <sub>2</sub> Surfaces and Nanoparticles	13
1.3.2 TiO <sub>2</sub> Defects	15
1.3.3 Co-catalysts, Lattice Doping, and Dye Sensitisation	16
1.4 The Catalytic Capacity of Gold Nanoparticles	19
1.4.1 Gold Nanoparticles Supported on TiO <sub>2</sub>	20
1.4.2 Growth and Morphology of Gold Nanoparticles Supported Upon TiO <sub>2</sub>	20
1.5 Particle Size Effects	24
1.5.1 Clusters versus Nanoparticles	24
1.5.2 Optical and Electronic Properties of Gold Nanoparticles	24
1.5.3 Size Effects on Catalytic Activity	26
1.5.4 Atomically Precise, Ligand Stabilised, Small Gold Clusters	28
1.6 Gas-Phase Photocatalysis	32
1.7 The Scope of this Thesis	33
<b>Chapter 2. Experimental Techniques, Apparatus, and Method</b>	
2.1 Catalyst Synthesis and Preparation	37
2.1.1 Preparation of Ligated Gold Clusters	37

2.1.2	Preparation of TiO <sub>2</sub> -Supported Gold Clusters	38
2.1.3	Activation Post-Treatment of Supported Gold Clusters	38
2.1.4	Preparation of Platinised TiO <sub>2</sub> Nanoparticles	39
2.2	Far-IR Spectroscopy	41
2.2.1	Sample Preparation and Apparatus	42
2.3	X-ray Photoelectron Spectroscopy	43
2.3.1	Sample Preparation and Apparatus	44
2.3.2	Peak Fitting	45
2.4	X-ray Absorption Spectroscopy	46
2.4.1	Sample Preparation and Apparatus	48
2.4.2	Data Analysis	49
2.5	Transmission Electron Microscopy Studies	51
2.6	Photocatalysis Investigations	52
2.6.1	Description of the Photocatalysis Experimental Apparatus	52
2.6.2	Sample Preparation	57
2.6.3	Experimental Procedure	57
2.6.4	Residual Gas Analyser and Quadrupole Ion Filter	58
2.6.5	Data Acquisition	59
2.6.6	Post-Experiment Data Analysis	60
2.6.7	Calibration	63
2.6.7.1	Gas Fractionation	64
2.6.7.2	Linear Detector Response	65
<b>Chapter 3. Computational Theory and Method</b>		
3.1	Introduction to Density Functional Theory	68
3.1.1	The Schrödinger Equation	68
3.1.2	The Variational Principle	69
3.1.3	Electron Density Functionals	70
3.2	Basis Sets	73
3.3	Computational Methods	76
3.3.1	Calculation of Ligated Gold Clusters	76
3.3.2	Calculation of the Anatase(101) Surface and Au <sub>1-4</sub> Clusters	77

## **Chapter 4. DFT Assisted Characterisation of the Far-Infrared Spectra of Au<sub>6</sub>, Au<sub>8</sub>, Au<sub>9</sub>, Au<sub>11</sub>, Au<sub>6</sub>Pd, and Au<sub>7</sub>Pt Clusters**

4.1	Optimised Ligated Metal Cluster Geometries	80
4.2	Far-IR Results and DFT Assignment	81
4.2.1	AuPPh <sub>3</sub> Cl	81
4.2.2	Au <sub>6</sub>	84
4.2.3	Au <sub>8</sub>	88
4.2.4	Au <sub>9</sub>	90
4.2.5	Au <sub>11</sub>	94
4.2.6	Au <sub>6</sub> Pd	99
4.2.7	Au <sub>7</sub> Pt	102
4.3	Charge Population Analysis	106
4.4	Conclusions	108

## **Chapter 5. X-ray and TEM Characterisation of Au<sub>8</sub>, Au<sub>9</sub>, Au<sub>11</sub>, and Au<sub>101</sub> Clusters**

5.1	X-ray Photoelectron Spectroscopy Studies of TiO <sub>2</sub> -Supported Gold Clusters	110
5.1.1	Au <sub>8</sub> , Au <sub>9</sub> , Au <sub>11</sub> , and Au <sub>101</sub> Supported on Acid-washed P25 Nanoparticles	114
5.1.1.1	Untreated	114
5.1.1.2	Washed at 100 °C	114
5.1.1.3	Heated Under Vacuum at 200 °C	116
5.1.2	Au <sub>8</sub> , Au <sub>9</sub> , and Au <sub>101</sub> Supported on Pure Anatase Nanoparticles	117
5.1.2.1	Untreated	117
5.1.2.2	Calcined under O <sub>2</sub> at 200 °C	118
5.1.2.3	Calcined under O <sub>2</sub> followed by H <sub>2</sub> at 200 °C	118
5.1.3	Comparison Between Supports	119
5.2	X-ray Absorption Near Edge Structure of Supported Gold Clusters	120
5.2.1	Anatase-Supported Au <sub>9</sub> clusters	120
5.2.2	Silica-Supported Au <sub>9</sub> clusters	124
5.3	Extended X-ray Absorption Fine Structure Analysis	128
5.3.1	Unsupported Au <sub>8</sub> and Au <sub>9</sub>	128
5.3.2	Anatase- and Silica-Supported Au <sub>9</sub> Clusters	131
5.4	Transmission Electron Microscopy Studies of TiO <sub>2</sub> -Supported Gold Clusters	136
5.4.1	Angular Dark Field Scanning Transmission Electron Microscopy	136

5.4.2	High Resolution Electron Microscopy Studies	137
5.6	Conclusions	140

## **Chapter 6. Photocatalytic Studies of Au<sub>8</sub>, Au<sub>9</sub>, and Au<sub>101</sub> Supported on TiO<sub>2</sub> Nanoparticles**

6.1	Experimental Benchmarks and Preliminary Evaluations	145
6.1.1	Photocatalytic Performance of Pt-TiO <sub>2</sub> for Water-Splitting	145
6.1.2	Degradation of Samples and Observed Colour Changes	147
6.1.3	Effects of Sample Exposure to Vacuum	150
6.1.4	Production of CO <sub>2</sub> and Consumption of O <sub>2</sub>	151
6.1.4.1	The Behaviour of Atomic and Gaseous Oxygen Species	154
6.1.4.2	Sources of Carbon Contamination	157
6.2	Photocatalytic Performance of Au Clusters on TiO <sub>2</sub> for Water-Splitting	159
6.2.1	Photocatalytic Performance of the Au <sub>8</sub> cluster	161
6.2.2	Photocatalytic Performance of the Au <sub>9</sub> cluster	162
6.2.3	Photocatalytic Performance of the Au <sub>101</sub> cluster	164
6.2.4	Overall Comparisons of the Photocatalytic Performance Between Clusters	166
6.2.5	Photocatalytic Performance of Au <sub>8</sub> , Au <sub>9</sub> , and Au <sub>101</sub> Compared to Pt-TiO <sub>2</sub>	169
6.3	Conclusions	171

## **Chapter 7. DFT Studies of Au<sub>1-4</sub> on the Stoichiometric and Oxygen-Deficient TiO<sub>2</sub> Anatase(101) Surface**

7.1	Optimisation of the Anatase(101) Model	175
7.1.1	Anatase(101) Model Size Considerations	178
7.2	Structural Parameters and Binding Energies	180
7.2.1	Stoichiometric TiO <sub>2</sub> Anatase(101)	180
7.2.1.1	Discussion	186
7.2.2	Oxygen-Deficient TiO <sub>2</sub> Anatase(101)	190
7.2.2.1	Discussion	196
7.3	Predicted Vibrational Spectra	199
7.3.1	Au <sub>1</sub> on the Stoichiometric and Oxygen-Deficient Anatase(101) Surfaces	199
7.3.2	Au <sub>2</sub> on the Stoichiometric and Oxygen-Deficient Anatase(101) Surfaces	201
7.3.3	Au <sub>3</sub> on the Stoichiometric and Oxygen-Deficient Anatase(101) Surfaces	205

7.3.4	Au <sub>4</sub> on the Stoichiometric and Oxygen-Deficient Anatase(101) Surfaces	213
7.3.5	Discussion	221
7.4	Charge Analysis of Au <sub>1-4</sub> on Anatase(101) Surfaces	223
7.4.1	Stoichiometric and Oxygen-Deficient Anatase(101) Surfaces	223
7.4.2	Au <sub>1-4</sub> on the Stoichiometric Anatase(101) Surface	224
7.4.3	Au <sub>1-4</sub> on the Oxygen-Deficient Anatase(101) Surface	227
7.4.4	Discussion	230
7.5	Predicted Molecular Orbital Properties of Au <sub>1-4</sub> on Anatase(101) Surfaces	233
7.5.1	Stoichiometric and Oxygen-Deficient Anatase(101)	233
7.5.2	Au <sub>1-4</sub> on the Stoichiometric Anatase(101) Surface	237
7.5.2.1	Au <sub>1</sub> and Au <sub>2</sub>	238
7.5.2.2	Au <sub>3</sub>	243
7.5.2.3	Au <sub>4</sub>	247
7.5.3	Au <sub>1-4</sub> on the Oxygen-Deficient Anatase(101) Surface	251
7.5.3.1	Au <sub>1</sub> and Au <sub>2</sub>	252
7.5.3.2	Au <sub>3</sub>	257
7.5.3.3	Au <sub>4</sub>	260
7.5.4	Discussion	263
7.6	Conclusions	265
<b>Chapter 8. Conclusions and Future Work</b>		268
<b>References</b>		276
<b>Appendix A.</b> Cartesian Coordinates and Additional Information of the Refined EXAFS Models		296
<b>Appendix B.</b> Additional Calculated Parameters of Gas-phase Au <sub>1-4</sub> Clusters and the Anatase(101) Surface Model		298
<b>Appendix C.</b> Cartesian Coordinates and Electronic Parameters of Ligated Gas-phase Gold Clusters		305
<b>Appendix D.</b> Cartesian Coordinates and Electronic Parameters of Au <sub>1-4</sub> on the Stoichiometric and Oxygen-Deficient Anatase(101) Surface		313



# Chapter One

Introduction

## 1 Introduction

### 1.1 Background

The renewable and efficient production of environmentally clean energy has been the focus of a great deal of research over the last few decades. This has been driven by the well-established effects of anthropogenic climate change,<sup>1</sup> increasing demand for energy worldwide<sup>2,3</sup> (Figure 1), and the finite nature of fossil fuel reserves. This has resulted in a strong push towards the use of carbon-free or carbon-neutral renewable energy that has led to the development of a great deal of new technologies and alternative energy paradigms, one of which is the idea of using hydrogen as a renewable fuel source.

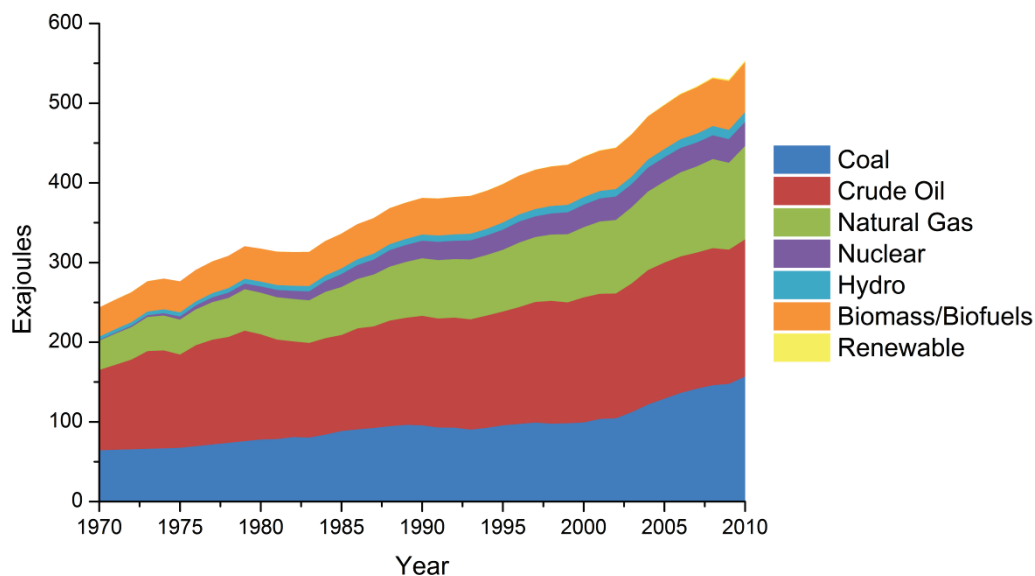


Figure 1.1: Breakdown of global primary energy consumption between 1970–2010, showing the increasing demand for energy over time. Data obtained from the BP Statistical Review of World Energy.<sup>2,3</sup>

Hydrogen is an excellent renewable energy carrier that burns cleanly in a typical combustion system with water as the only product, and can be used in fuel cells. Hydrogen is also a valuable chemical commodity used in a range of industrial processes, such as the production of industrial ammonia via the Haber-Bosch process to feed the world's growing population, which uses over 1% of the world's energy supply.<sup>4,5</sup> Currently, hydrogen is produced primarily from fossil fuel sources via steam reforming to yield  $\text{CO}_2$  and  $\text{H}_2$ , clearly not an ideal solution for an environmentally friendly future. The quest for alternative methods for hydrogen production has led to many approaches including biomass reduction and water electrolysis driven by photovoltaic cells; however,

## Chapter 1. Introduction

there are problems with alternatives such as these, for biomass competes with crop production, and water electrolysis has high losses and large capital costs for photovoltaic cells.

Solar-driven renewable hydrogen production is seen as having great potential for an environmentally friendly future. The Earth receives  $3 \times 10^{24}$  joules of solar energy per year,<sup>6</sup> which is  $\sim 5000$  times more than the current consumption of energy worldwide. Despite this large source of available energy, solar based sources contribute less than 2% of energy production worldwide.<sup>2</sup> The seasonal and daily variability of sunlight requires the energy to be stored efficiently, so as to be used during times of peak load or on demand.<sup>7</sup> This adds complexity and additional infrastructure costs to solar-based energy production systems. The ability to store this energy as a chemical fuel is ideal, as it allows for the long-term storage and transport of solar energy, making it useful in a wide range of applications. Therefore, using solar energy to drive chemical reactions to yield energy-rich molecules such as hydrogen is an attractive concept. However, the low energy density of hydrogen when in the gaseous form has proven to be an issue for some applications. Despite this, photoelectrochemical systems that can directly drive the processes required for water-splitting to produce hydrogen, with minimal losses and low capital costs, are clearly an appealing technology that has garnered much interest over the last few decades.

## 1.2 Photocatalysis

The capability for direct photoelectrochemical water-splitting was first shown by Fujishima and Honda<sup>8</sup> in 1972. Their system involved a TiO<sub>2</sub> photo-anode and Pt cathode, whereby photogenerated electrons carried through the circuit reduce H<sup>+</sup> ions at the Pt cathode to produce H<sub>2</sub>, and the positive electron-holes left behind at the TiO<sub>2</sub> photoanode oxidise the water to produce O<sub>2</sub> and H<sup>+</sup>. The schematic of this system is illustrated in Figure 1.2.

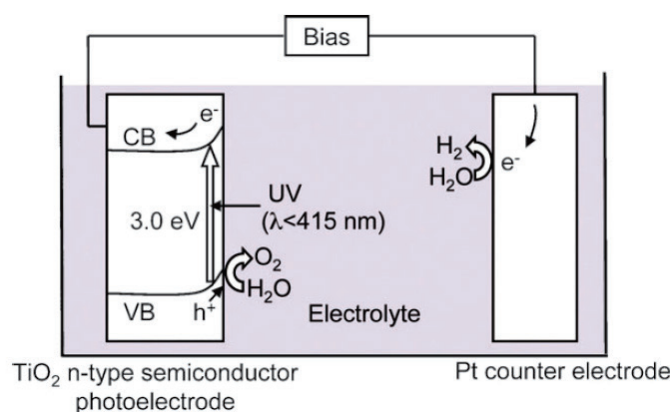
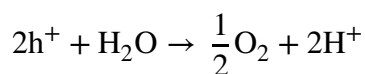
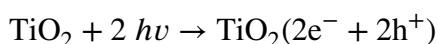
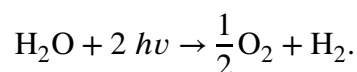


Figure 1.2: Photoelectrochemical water electrolysis using a semiconductor photoanode such as TiO<sub>2</sub> and a Pt cathode.<sup>8,9</sup> Incident light with energy greater than the band gap of the semiconductor excites electrons from the valence band to the conduction band where they can drive chemical reactions.<sup>i</sup>

The reactions of this photocatalytic system are outlined below:



Here,  $h^+$  represents an electron-hole (hereafter referred to as hole) delocalised within the TiO<sub>2</sub> semiconductor. The overall reaction for this photon driven water-splitting process is



Through this photocatalytic process, the incoming photon energy is essentially converted into readily storable chemical energy, involving an increase in the Gibbs free energy ( $\Delta G$ )

<sup>i</sup> Reproduced from Ref. 9 with permission of The Royal Society of Chemistry.

of the system. The free energy change for the reaction of one molecule of  $\text{H}_2\text{O}$  to  $\text{H}_2$  and  $\frac{1}{2} \text{O}_2$  under standard conditions is  $+237.2 \text{ kJ mol}^{-1}$ . This differs greatly from a traditional catalyst, which typically reduces the activation energy of a chemical reaction by influencing transition states. Thermodynamically, splitting water using a conventional electrolysis cell requires a potential difference of 1.23 V between the electrodes, equivalent to a 1000 nm photon. Experimentally however, an electrolysis cell requires additional voltage to overcome various losses throughout the cell that occur in a practical device. This difference between the thermodynamic voltage and the experimentally observed redox event is defined as the overpotential.

The work by Fujishima and Honda has been followed by decades of intense research into photocatalytic water-splitting systems involving a range of semiconductor supports and other materials.<sup>9-28</sup> These water-splitting cells typically remain cheaper than the significant fabrication costs involved for electrolyzers combined with p-n junction photovoltaic cells.<sup>29</sup> There are also a number solar water-splitting systems that have been developed with high solar to hydrogen conversion efficiencies, but which use expensive or difficult to scale systems.<sup>30-32</sup> One such study was able to achieve a 13.3% solar conversion efficiency to  $\text{H}_2$  using a p-InP semiconductor covered with small Pt islands dispersed across its surface.<sup>33</sup> While there have been many studies that have undertaken extensive work to improve the catalytic efficiency of these photocatalytic systems, there are still numerous challenges that must be overcome in order for these systems to become industrially viable. Some of these challenges include their response range to light, electron-hole recombination, back-reactions, and many others that will be reviewed in the following sections.

### 1.2.1 Semiconductor Electrodes and Supports

Photocatalytic systems often make use of semiconductor materials that have separated valence and conduction bands, creating a band gap. When light is incident upon a semiconductor with an energy greater than that of the band gap, photoexcitation occurs, whereby an electron is excited from the valence band to the conduction band, leaving behind a hole in the valence band. Note that there is virtually no initial spatial change in the position of an electron, merely its energetic state. This particle and virtual particle pair are initially in a bound-state (sometimes referred to as an exciton) and can migrate

through the semiconductor. They can also dissociate into electrons and holes, which can migrate through various trapping sites in the crystal lattice towards the surface of a semiconductor, whereby they can drive redox reactions. There are numerous semiconductors that have well-positioned bands for water-splitting, as shown in Figure 1.3. Those semiconductors that have large band gaps or that have bands close to the edge of the redox potentials for water-splitting are often modified by various methods to improve their effectiveness.

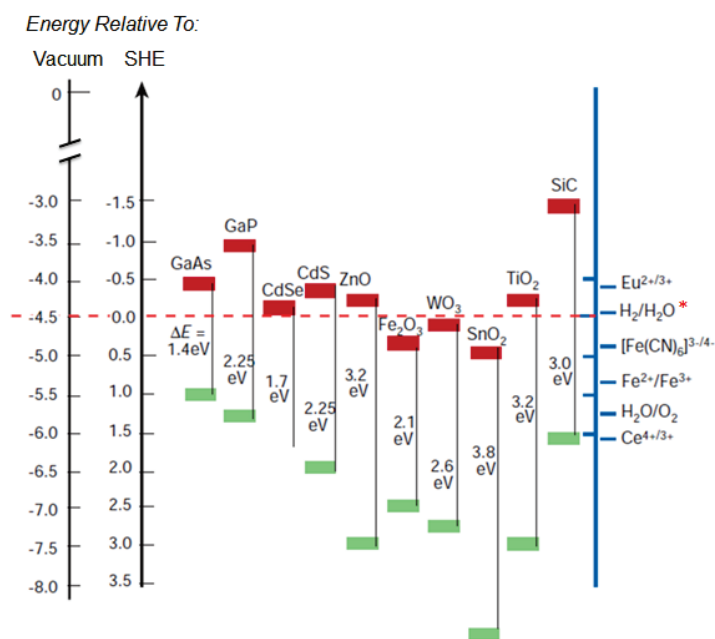


Figure 1.3: Valence (green) and conduction (red) band levels for a number of commonly used semiconductors for photocatalysis relative to the standard hydrogen electrode (SHE) and vacuum energy. The dashed red line indicates the reduction potential of  $H^+$ . Other common redox couples are also listed on the right side of the figure for comparison. <sup>ii</sup>

The relative position of both the valence and conduction bands will determine if a semiconductor has the capability to drive a redox reaction of interest. In the case of water-splitting for the production of  $H_2$  and  $O_2$ , the bottom of the conduction band must be more negative than the redox potential of  $H^+/H_2$ . This is defined as 0 eV for the Standard Hydrogen Electrode (SHE), which is assigned to the potential of a Pt electrode in a theoretical 1 M solution of  $H^+$ . It is also equivalent to  $-4.44 \pm 0.02$  eV relative to an absolute electrode potential under standard conditions (pH 7)<sup>34</sup> or relative to the solid-

<sup>ii</sup> Reprinted by permission from Macmillan Publishers Ltd: Nature,<sup>6</sup> copyright (2001)

state vacuum energy. Conversely, the top of the valence band must be more positive than the redox potential of  $O_2/H_2O$ , which is 1.23 eV relative to the SHE.<sup>9</sup>

Some materials that can drive water-splitting redox reactions cannot absorb an adequate amount of sunlight due to a large band gap, while other materials that can readily absorb a wide range of the solar spectrum degrade over time under extended solar exposure.<sup>35</sup> This limits the number of applicable semiconductors available for water-splitting, and often requires the photocatalysts to undergo significant modification to perform effectively. For practical devices, an additional potential driving force is sometimes required to help drive the reaction if the valence or conduction bands are very close to the redox potentials. This is often achieved by using a small voltage bias across the photoelectrochemical cell, or by adjusting the pH of the solution. There are many other characteristics of a material that play a role in the complex processes occurring during photoexcitation that can have a large impact on the effectiveness for a photocatalytic system. These processes and characteristics will be briefly outlined in the following sections.

### 1.2.2 Mechanisms of Photocatalysis

Photocatalysts are inherently different from regular catalysts in their points of interest. While a regular catalyst has an active site, a photocatalyst may not necessarily have a specific site of catalysis, but instead has a region of photoexcited charge carriers near the surface that drive the redox chemistry. Since the rate of a photocatalytic reaction is strongly influenced by the number or density of photogenerated charge carriers at the surface, photocatalytic performance depends on the intensity of irradiated light.<sup>36</sup> Sometimes the term active site is used in the literature to refer to a dispersed chemical species on the surface of a photocatalyst, such as a metal complex or atomically adsorbed species, but even for these photocatalysts, the reaction will only proceed when the semiconductor support is being irradiated with light. The photogenerated charges can, however, migrate to the dispersed chemical species to create stable "reaction sites".<sup>36</sup>

There are a number of different mechanisms that can have a significant effect on the performance of a photocatalytic system, which is a result of a complex combination of charge separation and heterogeneous redox chemistry.<sup>37</sup> One of the primary processes that can affect this photocatalytic performance is considered to be electron-hole

recombination. This process has a chance to occur after photoexcitation, whereby an excited electron and positive hole may recombine, generating heat, and wasting energy, before they can be used to drive a reaction. Electron-hole recombination is most likely to occur when the photoexcited charge carriers become trapped at defect sites, decreasing the overall catalytic efficiency of the system. The density and position of these defect sites can be influenced by the crystal structure of the semiconductor material, as well as its level of uniform crystallinity.<sup>36</sup> The defect structure of photocatalytic materials can therefore play a major role in their performance.

There are a number of methods available to help reduce the rate of electron-hole recombination. Calcination at elevated temperatures is one such method that has been used to decrease the density of defect sites that act as recombination centres, increasing the performance of photocatalysts.<sup>37,38</sup> Calcination under specific gaseous environments can also be used to control the number and form of defect sites, as well as to influence the morphology and crystallinity of a semiconductor.<sup>20</sup> Loewe *et al.*<sup>39</sup> have shown that light-harvesting rods of semiconductor material can be used to increase the efficiency of charge migration to the surface by having the electron and hole move in opposite directions along the length of a semiconducting nano-scale rod. This is possible as the physical migration processes of the electron and hole are fundamentally different. Since holes are virtual particles, they "travel" through the lattice via the absence of electrons spread over many unit cells of a crystal and not via the same process that an electron travels through a lattice. Many modern photocatalysts also use a metal co-catalyst to help trap the photo-excited electrons and separate them from the photogeneration site to reduce electron-hole recombination. The use of co-catalysts will be reviewed in detail in the coming sections.

The electron-hole recombination rate can also be affected by the number of photo-excited charge carriers generated over a defined period, which in turn depends upon the irradiation intensity of incident light. The kinetics of charge recombination have been shown to be first order for low-intensity irradiation, and second order for high-intensity irradiation.<sup>20</sup> It is also possible to have multiple electron-hole pair excitation that may be useful for some multi-step photocatalysts that involve multi-electron processes.<sup>7</sup> They have been shown to increase the efficiency of dye-sensitised solar cells, for example.<sup>40,41</sup> In relation to multi-exciton production, transient absorption experiments undertaken by Tamaki *et al.*<sup>42,43</sup> have shown that low-intensity 355 nm excitation of TiO<sub>2</sub> resulted in charge carrier density, and therefore second-order electron-hole recombination processes

could be ignored. It was also shown that 355 nm excitation resulted in electrons and holes generated in the conduction and valence bands without excess energy that are trapped very rapidly at surface trap states within 100 fs.

Quantitative kinetic analysis of photocatalytic reactions is difficult, given that the overall photocatalytic reaction rate depends on electron-hole recombination and migration rates. Photocatalytic reactions can also be limited by other processes that do not depend on electron-hole recombination or migration, such as the rate of reactant adsorption to the surface of the photocatalyst, the rate of charge carrier reaction with adsorbed reactants, or the efficiency of exciton production by light. There are also some dependencies on mass transport and kinetics at the interface of the semiconductor to the gas/liquid phase. In the case of water-splitting, semiconductor oxides are typically covered with chemically or physically adsorbed water; therefore, any charge carrier originating from the semiconductor lattice must reach the surface and pass through the water layer into the solution or gas phase as a hydroxyl radical or its protonated/deprotonated species.<sup>36</sup> It is unknown whether there is a difference in the photocatalytic oxidation mechanisms for direct hole transfer and surface-adsorbed hydroxyl radical/hydroxide ion reactions.

Due to these complex processes, a valence band which is not sufficiently positive for water oxidation, or a conduction band which is not sufficiently negative for proton reduction, can lead to slow or negligible water-splitting.<sup>44</sup> These processes and their full effects are too complex to cover here in detail but have been the subject of a number of comprehensive reviews available in the literature.<sup>6,9,22,36,45-49</sup>

### 1.2.3 Semiconductor Nanoparticles as Supports

For typical photocatalysts, the more distance a charge carrier must migrate through the semiconductor, the higher its likelihood of encountering defect sites within the lattice that act as non-radiative recombination centres. Due to this effect, using a semiconductor particle of very small size is beneficial, as the migration length for the charge carriers to the surface becomes shorter, decreasing the chance of charge recombination. This makes nanoparticles an ideal size regime for the application of photocatalytic systems. An example of such a photocatalytic system is shown in Figure 1.4, whereby a small amount of co-catalyst is deposited onto a semiconductor nanoparticle, creating a small

photoelectrochemical cell.<sup>50</sup> The redox reactions can then proceed at the interfacial region between the nanoparticle/co-catalyst and the liquid or gas it is in contact with. The extremely high surface area to volume ratio of nanoparticles decreases the number of sub-surface lattice boundaries and defects relative to the surface defects. These nanoparticulate systems have the advantage of being relatively simple and cheaper to construct compared with a photoelectrochemical cell; although the charge carriers are not as spatially separated and back reactions can be more likely to occur.<sup>51</sup>

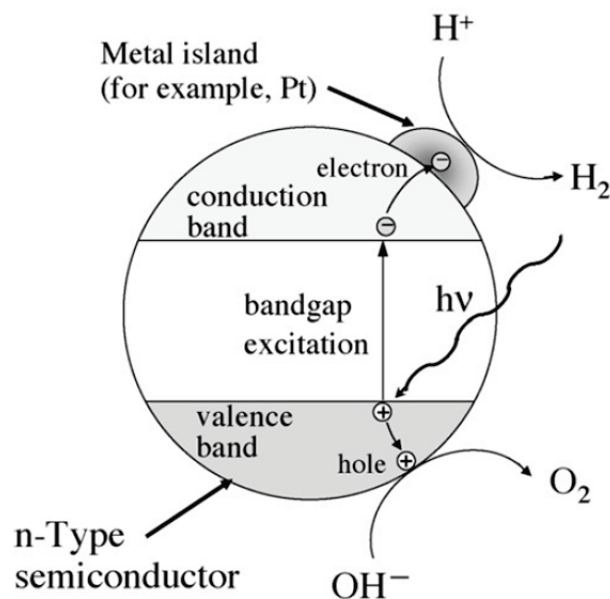


Figure 1.4: Simplified illustration of a semiconductor nanoparticle with a surface co-catalyst used as a complete photocatalytic system. The small size increases the likelihood for photogenerated charge carriers to reach the surface of the semiconductor where they can drive redox reactions.<sup>iii</sup>

There are also Z-scheme photocatalysts that take advantage of the well-positioned bands of two separate semiconductors to use multiple visible light photons to drive water-splitting beyond what each individual photon could achieve. Such a photocatalyst is illustrated in Figure 1.5. These devices however, have numerous problems, such as shortened device lifespans due to the added complexity of a combined system, additional electron-hole recombination resulting from the added defects at the multiple semiconductor interfaces, and higher fabrication costs.<sup>36,52-55</sup>

<sup>iii</sup> Reprinted from Catalysis Today, 122, Matsuoka, M.; Kitano, M.; Takeuchi, M.; Tsujimaru, K.; Anpo, M.; Thomas, J. M., "Photocatalysis for new energy production Recent advances in photocatalytic water-splitting reactions for hydrogen production", 51-61, Copyright (2007), with permission from Elsevier.

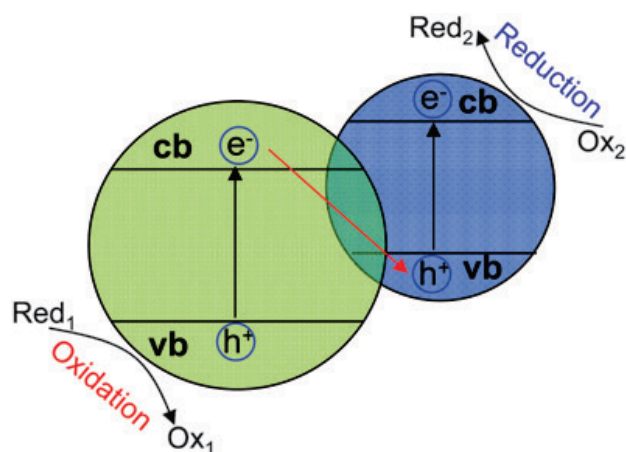


Figure 1.5: Direct Z-scheme photocatalytic system that transfer electrons between the two semiconductors to take advantage of greater band separation while using two lower energy photons.<sup>56</sup> The conduction and valence bands are indicated by "cb" and "vb", respectively.<sup>iv</sup>

While there are many semiconducting materials and devices being continually developed in the literature, they often have many properties that remain poorly understood. However, TiO<sub>2</sub> is one particular semiconductor that has been studied extensively over the past few decades, becoming one of the most well characterised, photocatalytically active semiconductors to date.

<sup>iv</sup> Reproduced from Ref. 56 with permission of The Royal Society of Chemistry.

### 1.3 TiO<sub>2</sub> Photocatalysis

TiO<sub>2</sub> has attracted a great amount of attention in the heterogeneous photochemistry field; it was recently mentioned that of the ~2400 papers published in 2008 in this field, 80% involved TiO<sub>2</sub>-based materials.<sup>45</sup> It is currently one of the most promising semiconductor materials available for photocatalysis. TiO<sub>2</sub> is relatively cheap, abundant, photo-stable, non-toxic, and highly oxidising. It has been shown to have applications in a number of useful areas, including solar cells,<sup>41,57</sup> photocatalysis,<sup>58-64</sup> gas sensors,<sup>65</sup> contaminant photo-decomposition,<sup>66-73</sup> bactericide,<sup>74-77</sup> and self-cleaning glass.<sup>78</sup> In terms of photocatalysis, TiO<sub>2</sub> has been shown to be active towards a number of reactions including CO<sub>2</sub> fixation,<sup>63,79,80</sup> the reduction of NO<sub>3</sub><sup>-</sup>,<sup>81,82</sup> photo-oxidation of organic compounds using lattice or gaseous oxygen,<sup>83</sup> decomposition of cyanide in water,<sup>84-86</sup> and many others. The use of TiO<sub>2</sub> thin films is common for photocatalytic systems in the literature.<sup>58,59,72,73,83,87-92</sup> There have also been a number of particulate and nano-particulate TiO<sub>2</sub> systems designed for photocatalytic water-splitting.<sup>93-104</sup>

TiO<sub>2</sub> has just enough reducing capacity to reduce H<sub>2</sub> from H<sup>+</sup> due to the redox potential of the conduction band electrons (~-0.52 eV vs SHE), while the valence band holes easily have enough potential to oxidise O<sub>2</sub> from H<sub>2</sub>O (~2.53 eV vs SHE).<sup>83</sup> These half-reactions are critical for the photocatalytic splitting of water into H<sub>2</sub> and O<sub>2</sub>. In addition to these properties, the conduction band electrons can react with gaseous O<sub>2</sub> to produce the superoxide radical anion (O<sub>2</sub><sup>•-</sup>).<sup>105</sup> These OH<sup>•</sup> and O<sub>2</sub><sup>•-</sup> molecules are thought to play a significant role in photo-oxidation and photo-decomposition reactions by TiO<sub>2</sub>.

It is well established that the conduction and valence bands mainly consist of Ti 3*d* orbitals and O 2*p* orbitals, respectively. The large difference between the conduction and valence band positions result in a wide band gap for unmodified TiO<sub>2</sub> of 3.03 and 3.20 eV for rutile and anatase, respectively, the two most common polymorphs of TiO<sub>2</sub>.<sup>106</sup> This equates to photons with a wavelength of 409.2 nm for rutile and 387.5 nm for anatase. The direct band gap for rutile at 3.03 eV is forbidden however, and the nearly degenerate, indirect transition at 3.05 eV is the one that usually occurs.<sup>107</sup>

There have been many experimental and theoretical studies undertaken of the photocatalytic TiO<sub>2</sub> system for its application in water-splitting that are far too numerous to review comprehensively in this thesis. There are a large number of reviews for TiO<sub>2</sub>

photocatalysis available in the literature that provide additional detail of this well-studied system.<sup>6,7,9,12,36,45-47,51,60,61,64,83,105,108-113</sup>

### 1.3.1 The Structure of TiO<sub>2</sub> Surfaces and Nanoparticles

The unit cells of rutile and anatase, the two most well-studied polymorphs of TiO<sub>2</sub>, are illustrated in Figure 1.6. For each of these polymorphs, there are a number of possible surfaces defined by their Miller indices that are the most stable or reactive surfaces. Only the most stable surface for each polymorph will be briefly discussed here. For further information about the various surfaces of TiO<sub>2</sub>, see the comprehensive review by Diebold.<sup>114</sup>

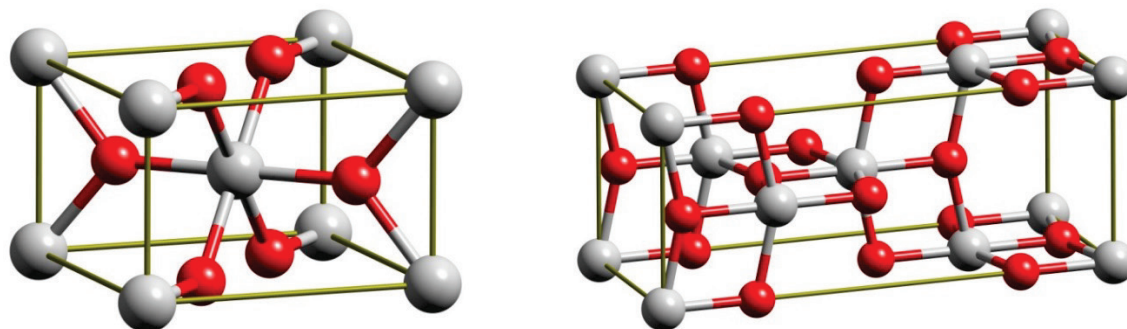


Figure 1.6: The unit cells of rutile (left) and anatase (right); the two most common and well-studied polymorphs of TiO<sub>2</sub>. The oxygen and titanium atoms are coloured red and grey, respectively.<sup>115</sup>

The most stable and common surface of the rutile polymorph is the (110) surface. This surface is often reduced by ion sputtering and annealing, resulting in bridging O vacancies and interstitial Ti species.<sup>114,116,117</sup> Hole-mediated reactions on TiO<sub>2</sub> rutile(110) are not restricted by issues related to the creation, transport, or surface stabilisation of holes,<sup>45</sup> but are instead heavily influenced by the degree of surface oxidation of the surface.<sup>118</sup>

The anatase(101) surface is the most stable well-studied anatase surface. It is thought to have a lower electron-hole recombination rate compared with rutile,<sup>119</sup> which is highly desirable for photocatalysis. The TiO<sub>2</sub> anatase surface been shown to be more active towards the photo-reduction of O<sub>2</sub>,<sup>120,121</sup> which is useful for oxidative decomposition of organic compounds but also results in an undesirable back-reaction during the water-

splitting reaction.<sup>96</sup> In fact, water-splitting by anatase TiO<sub>2</sub> typically shows a lack of O<sub>2</sub> evolution during reaction, due to the photo-reduction of O<sub>2</sub> being favoured over H<sup>+</sup> reduction for H<sub>2</sub> formation, often requiring methanol as a sacrificial reagent that is irreversibly oxidised by holes to produce a significant H<sub>2</sub> yield.<sup>9,47,97,122</sup> The study by Daskalaki *et al.*<sup>97</sup> also suggested that molecular oxygen can be adsorbed too strongly to the surface of P25 nanoparticles (composed mainly of anatase) in the form of adsorbed oxygenated species, and does not desorb into the gas phase.

No clear advantage in photocatalytic performance for rutile vs anatase has been established,<sup>123</sup> although it has been the subject of a number of studies.<sup>106,124,125</sup> There have also been numerous density functional theory (DFT) studies of TiO<sub>2</sub> surfaces,<sup>106,126-133</sup> including investigations into small molecule adsorption on anatase(101)<sup>134,135</sup> and rutile(110),<sup>135-137</sup> as well as their effects on catalytic processes.<sup>62,138-142</sup>

P25 nanoparticles are some of the most widely used TiO<sub>2</sub> nanoparticles for photocatalysis, as they often have high levels of photocatalytic activity. P25 TiO<sub>2</sub> nanoparticles are 21 nm in diameter on average, and have recently been quantified to contain a mixture of anatase, rutile, and amorphous TiO<sub>2</sub> at a ratio of 76:11:13;<sup>143</sup> although the authors note that there may be some variability in this ratio between manufactured batches. One of the reasons for the high photocatalytic activity of these nanoparticles is thought to be the combined anatase and rutile phases enhancing charge separation via the transfer of photo-generated electrons between them, decreasing electron-hole recombination by spatially separating the charge carriers. Recently, a study using pure, porous thin films of TiO<sub>2</sub> for the photocatalytic oxidation of methylene blue showed that a film with ~60% anatase and ~40% rutile exhibited an optimal performance 50% greater than that of pure anatase alone, due to a synergistic effect.<sup>144</sup> The results of this study suggest a similar effect may be taking place for P25 nanoparticles. However, further study of this effect may be necessary, as it has been shown that methylene blue is not an ideal probe molecule for semiconductor photocatalysis. This is because the photo-induced reaction of methylene blue itself can lead to misleading photocatalytic results for TiO<sub>2</sub>, as it can be difficult to disentangle the two processes.<sup>145</sup> A review by Ohtani has also discussed the lack of direct evidence for inter-particle photo-electron charge migration in P25 that would support such a hypothesis for the increased photocatalytic activity.<sup>146</sup>

### 1.3.2 TiO<sub>2</sub> Defects

TiO<sub>2</sub> surfaces typically have a number of common defects, including oxygen vacancies, step edges, line defects, and lattice boundaries.<sup>114</sup> These surface defects can have a significant influence on the interaction between TiO<sub>2</sub> and dispersed metals on its surface or during the adsorption of reactant species, and therefore influence its catalytic ability.<sup>147</sup> The type and distribution of these surface defects depend on the polymorph of TiO<sub>2</sub> in question, as well as the type of exposed surface.

Surface oxygen vacancies can act as chemisorption sites for small, photocatalytically relevant molecules such as H<sub>2</sub>, CO, O<sub>2</sub>, and H<sub>2</sub>O,<sup>147,148</sup> even under ambient temperature conditions.<sup>149,150</sup> Surface oxygen vacancies have also been suggested to promote the separation of electrons and holes while under irradiation.<sup>124</sup> In addition, the defect structure of TiO<sub>2</sub> surfaces can also be strongly influenced by the sub-surface defect structure. In the bulk phase of TiO<sub>2</sub> it is known that lattice defects, including oxygen vacancies and interstitial defects, can have high diffusion rates at elevated temperatures.<sup>117,124,147,151</sup> This high diffusion rate allows for sub-surface oxygen defects to readily replace surface oxygen vacancies that may be quenched during reactions at the surface of the TiO<sub>2</sub>, such as during photo-adsorption of O<sub>2</sub>, or through the annealing of gas-phase O<sub>2</sub> when above the maximum temperature for thermal desorption. Research by Besenbacher and co-workers<sup>152</sup> has shown that oxygen vacancies can diffuse along the surface upon the adsorption of O<sub>2</sub>, even at temperatures as low as 180–250 K. The opposite process can also occur when reactions such as the oxidation of CO are performed,<sup>147</sup> whereby bridging oxygen atoms on the surface are removed from TiO<sub>2</sub> and incorporated into the CO<sub>2</sub> product.

It is currently well-established by multiple experiments ranging from ultraviolet photoelectron spectroscopy to scanning tunnelling<sup>153-156</sup> and atomic force microscopy<sup>157</sup> that these bridging oxygen vacancies are also the cause of Ti 3*d* defect states within the band gap of TiO<sub>2</sub>, where two excess electrons per bridging oxygen vacancy are transferred to neighbouring Ti atoms.<sup>64,114,158-161</sup> This band gap state is found ~1 eV below the Fermi level via ultraviolet photoemission spectroscopy<sup>148,159</sup> and as a 1 eV loss in electron energy loss spectroscopy.<sup>162,163</sup> Recently however, two publications have shown that Ti interstitial defects in the lattice near the surface may instead be responsible for the defect states observed within the band gap, at least for the rutile(110) surface.<sup>164,165</sup> They

propose that quenching of Ti 3*d* defect states can be attributed to the withdrawal of electronic charge from the near-surface region via the accumulation of electronegative adsorbates. This was recently refuted in the study by Yim *et al.*<sup>163</sup> that showed the bridging oxygen vacancies to be the dominant contribution to the defect state in the band gap, while a very minor proportion arises from other defects such as interstitial Ti or subsurface oxygen vacancies. Kido and co-workers<sup>166</sup> have also showed that Ti interstitials condensed near the surface region can contribute to the Ti 3*d* defect state under certain conditions.

### 1.3.3 Co-catalysts, Lattice Doping, and Dye Sensitisation

Co-catalysts are often necessary for photocatalytic systems, as the charge carriers that reach the semiconductor surface are highly likely to recombine if they do not have a thermodynamically favourable pathway for a redox reaction.<sup>9,167</sup> Pt is an example of a commonly used co-catalyst in a number of photocatalytic systems<sup>59,95-99,103,141,168-178</sup> that reduces the overpotential for H<sub>2</sub> evolution and readily accepts the photogenerated electrons due to the low barrier at the semiconductor-metal junction.<sup>83,169,170</sup> Without a Pt co-catalyst, pure TiO<sub>2</sub> is unable to split water effectively, producing only trace amounts of H<sub>2</sub>.<sup>168</sup> Photocatalytic hydrogen production using Pt co-catalysts dispersed over TiO<sub>2</sub> has been shown in a number of studies.<sup>59,96,97,99,168,169,176-178</sup> Au is another common co-catalyst used for water-splitting that is also able to reduce the back-reaction from H<sub>2</sub> and O<sub>2</sub> to H<sub>2</sub>O from occurring.<sup>173,179</sup> Au co-catalysts will be discussed in further detail in the following sections. There are also many other co-catalysts such as Rh,<sup>177</sup> NiO,<sup>180</sup> and RuO<sub>2</sub><sup>17</sup> that have appropriate characteristics for water-splitting photocatalysts.

As mentioned earlier for nanoparticle systems, the junction between the semiconductor support and the co-catalyst acts as a type of photoelectrochemical cell.<sup>50</sup> For example, when using small Pt island co-catalysts dispersed over a TiO<sub>2</sub> nanoparticle, the Pt and the TiO<sub>2</sub> act as the cathode and anode, respectively. These small Pt islands, due to the well-positioned Fermi level of Pt, can act as reduction sites that are spatially separated from the site of charge carrier photogeneration. It is thought that this allows photoexcited electrons to migrate from the TiO<sub>2</sub> support to the Pt co-catalysts through an Ohmic junction between the TiO<sub>2</sub> and Pt,<sup>36</sup> decreasing the chance of electron-hole recombination. Investigating this charge transfer process is difficult and there is currently

no established technique to directly observe this process. There is, however, a study that has provided indirect evidence by observing the isotope distribution of H<sub>2</sub> molecules produced during photocatalytic water-splitting.<sup>98</sup> By using Pt/TiO<sub>2</sub> with both water and heavy water, it was shown that the experimentally determined isotope distribution matched that of the calculated isotope distribution based upon hydrogen being generated at the surface of the Pt co-catalyst.

Nevertheless, using Pt as a co-catalyst is also known to increase the rate of back-reaction of H<sub>2</sub> and O<sub>2</sub> to gas-phase water.<sup>169</sup> This occurs because splitting water is an uphill reaction with a positive Gibbs free energy change, while the back-reaction is downhill. Prevention of this back reaction from H<sub>2</sub> and O<sub>2</sub> to H<sub>2</sub>O is essential to maintain high photocatalytic efficiency. The use of Na<sub>2</sub>CO<sub>3</sub> promoters in addition to Pt co-catalysts has been shown to suppress the back-reaction on Pt by covering the Pt with titanium hydroxide, possibly aiding the desorption of O<sub>2</sub> from the TiO<sub>2</sub> surface.<sup>96</sup> NaOH-coating and alkali carbonates have also been shown to behave as effective promoters for water-splitting using Pt/TiO<sub>2</sub> photocatalysts.<sup>177,181</sup> Na<sub>2</sub>CO<sub>3</sub> promoters have made previously unusable catalysts such as RuO<sub>2</sub>-Ta<sub>2</sub>O<sub>5</sub> and NiO<sub>x</sub>-Ta<sub>2</sub>O<sub>5</sub> systems able to decompose liquid water into H<sub>2</sub> and O<sub>2</sub> in an effective manner.<sup>170</sup> It has also been shown that the weight % loading of the co-catalyst on TiO<sub>2</sub> can play an important part in their catalytic efficiency, with most studies showing the optimum ratios to be between 0.3 and 2.0% by weight co-catalyst relative to TiO<sub>2</sub>.<sup>173</sup> Using higher loadings of co-catalyst decreases the photocatalytic efficiency of the system, as the positive benefits of the co-catalyst begin to be outweighed by the increased charge recombination at co-catalyst sites and increased rate of back-reactions.

Another key issue for the use of TiO<sub>2</sub> in solar-driven photocatalytic water-splitting is the large band gap of TiO<sub>2</sub> (409.2 nm for rutile and 387.5 nm for anatase) that only allows high energy UV radiation to be absorbed. Based upon the AM1.5 spectral standard for solar irradiation at ground level in a temperature zone, the accumulated solar intensity below 380, 390, 400, and 410 nm equates to only 3.23, 3.87, 4.63, and 5.81%, respectively, of the total solar energy available from 280 to 4000 nm.<sup>36</sup> Therefore, TiO<sub>2</sub> is only able to absorb a small fraction of incident solar radiation. Lattice doping and visible light sensitive dyes are two common approaches that have are used to extend the absorption of TiO<sub>2</sub> into the visible range to address this issue.

## Chapter 1. Introduction

Lattice doping involves impregnating the TiO<sub>2</sub> lattice with metals such as Fe,<sup>182</sup> Cr,<sup>183</sup> and Y,<sup>184</sup> as well as non-metallic elements such as N,<sup>185-191</sup> S,<sup>145,192-194</sup> F,<sup>195</sup> C,<sup>196,197</sup> and B.<sup>198</sup> These atoms tend to occupy substitutional or interstitial sites within the lattice of TiO<sub>2</sub>. This doping method introduces localised and discrete valence levels or electron donor levels within the TiO<sub>2</sub> band gap. This results in an "effective" band gap that is considerably smaller, enabling the absorption of longer wavelengths of light.<sup>9</sup> Note that these new energy levels are not typically considered bands, as there are not enough dopant atoms to form a complete band. In practical applications, new levels are not usually introduced near the TiO<sub>2</sub> conduction band, as this may hinder the ability for TiO<sub>2</sub> to reduce H<sup>+</sup> ions. Instead, the focus is placed on the region near the valence band, which is already far more oxidising than necessary for water-splitting.<sup>9</sup> Lattice doping, however, can result in decreases in the photocatalytic activity, as the impregnated impurities increase the number of recombination centres available.<sup>9</sup> It has been shown that this problem can be alleviated to some extent through the use of paired co-doping materials, such as Cr<sup>3+</sup>/Sb<sup>5+</sup>, Rh<sup>3+</sup>/Sb<sup>5+</sup>, or Ni<sup>2+</sup>/Nb<sup>5+</sup>, as the secondary co-dopant is able to balance the charge of having a multiple Ti<sup>4+</sup> centres replaced by a Cr<sup>3+</sup>, for example.<sup>9</sup>

Visible light photo-response can also be achieved by using metal complexes or organic dyes that respond to visible light. In these systems, incident visible light with less energy than the TiO<sub>2</sub> band gap is instead absorbed by the sensitiser, exciting an electron from the HOMO to the LUMO for the metal complex or dye, which is then injected into the conduction band of the photocatalyst.<sup>9,135,199</sup> The shortcoming of such an approach, is that the photosensitisers are typically unstable and readily degrade when exposed to light for extended periods of time.<sup>200</sup> The extension of TiO<sub>2</sub> absorption into the visible range by these methods is beyond the scope of this thesis; for further information about TiO<sub>2</sub> visible light sensitisation, there are a number of extensive reviews available in the literature.<sup>61,200-203</sup>

## 1.4 The Catalytic Capacity of Gold Nanoparticles

The discovery by Haruta *et al.* of the remarkable catalytic capacity of oxide-supported Au nanoparticles (AuNPs) for low-temperature CO<sup>204</sup> and H<sub>2</sub><sup>205</sup> oxidation has led to extensive research into their use for catalysis.<sup>205-224</sup> AuNPs have been shown to be catalytically active towards many reactions including, but not limited to, NO reduction,<sup>225,226</sup> CO<sub>2</sub> hydrogenation,<sup>227</sup> the water-gas shift reaction,<sup>228-238</sup> low-temperature catalytic combustion of methanol,<sup>239</sup> electro-catalytic reduction of CO<sub>2</sub> to CO,<sup>240</sup> hydrogenation reactions,<sup>240,241</sup> selective oxidation reactions,<sup>207,242-245</sup> and many others.<sup>58,205,206,209,246-253</sup> AuNPs have been shown to be effective as both heterogeneous<sup>241,254</sup> and homogenous catalysts.<sup>64,255-258</sup>

One of the most widely studied reactions catalysed by AuNPs has been the oxidation of CO at low temperatures on both reducible and non-reducible oxides; some of these studies on reducible oxides include supports such as Fe<sub>x</sub>O<sub>y</sub>,<sup>223,244,245,259-268</sup> CeO<sub>2</sub>,<sup>269,270</sup> NiO<sub>2</sub>,<sup>271</sup> ZnO,<sup>272,273</sup> and TiO<sub>2</sub>.<sup>138,206,264,274-298</sup> Studies of this reaction have been used to help understand the catalytic processes behind AuNP catalysis. Some studies have attributed the high catalytic activity of these oxide supported AuNPs to the formation of an active Au nanoparticle/support interface along the perimeter of the AuNPs.<sup>208,268,279,296,299,300</sup> This interface results in a synergistic mechanism that incorporates the oxide as part of the catalytic process, whereby CO can adsorb to the AuNP and migrate to the perimeter of the AuNP/support, while O<sub>2</sub> adsorbs adjacent to the AuNP on the support itself. Bond and Thompson have suggested that the Au atoms at this perimeter could be cationic Au, and may be responsible for the activation of O<sub>2</sub> during the catalytic reaction.<sup>279</sup> It has also been suggested that the overall reaction would proceed through a bidentate carbonate intermediate species before being converted to CO<sub>2</sub> and desorbed from the catalyst.<sup>264</sup> Defects on the AuNPs themselves after being supported has also been claimed to be the active site for CO oxidation.<sup>278,284,285,301,302</sup>

Photocatalytic water-splitting by supported AuNPs co-catalysts has been shown for a range of different supports ranging from metal-titanites,<sup>303</sup> to oxides such as TiO<sub>2</sub>,<sup>304-309</sup> and many others.<sup>58,179,246,253,310-312</sup> The remainder of this introduction will focus on the catalytic properties of AuNPs supported on TiO<sub>2</sub>. For further information on supported AuNPs as catalytic systems, there are a number of excellent reviews available.<sup>208,255,313-315</sup>

### 1.4.1 Gold Nanoparticles Supported on TiO<sub>2</sub>

TiO<sub>2</sub>-supported AuNPs have been shown to be active for a number of important reactions including the water gas shift reaction,<sup>230,232,233,236,237,316</sup> reduction of NO,<sup>225</sup> hydrogenation of CO<sub>2</sub> and CO,<sup>227,317</sup> CO oxidation,<sup>275-278,280-283,294-298,318,319</sup> selective oxidation of propylene,<sup>207,320</sup> oxidation of ethylene glycol to glycolate,<sup>321</sup> vapour-phase epoxidation of propylene over AuNPs/TiO<sub>2</sub>,<sup>207</sup> and many others.<sup>212,294,322</sup> In relation to H<sub>2</sub> production, there are numerous studies of photocatalytically active AuNPs/TiO<sub>2</sub> showing production from water/ethanol solutions,<sup>173</sup> water/methanol solutions,<sup>304,305,307,323</sup> and from ethanol solutions using 3–30 nm AuNPs.<sup>167</sup> The study by Murdoch *et al.*<sup>167</sup> also found a strong polymorph-dependent activity, whereby AuNPs/anatase was ~100 times more active than AuNPs/rutile towards H<sub>2</sub> production.

TiO<sub>2</sub>-supported AuNPs often show a number of interesting features that differ from their bulk counterparts. For example, CO can adsorb reversibly on AuNPs/TiO<sub>2</sub>,<sup>288,324</sup> and atomic oxygen has also been shown to adsorb to small gold islands 1 to 6 atomic layers thick on TiO<sub>2</sub> rutile(110) surfaces.<sup>284</sup>

The mechanisms by which AuNPs supported on TiO<sub>2</sub> make for active catalysts is an area of intense research and there is still a lack of agreement on the catalytic processes, as highlighted by a number of reviews<sup>36,47,247</sup> It has been suggested by Ohtani that the lack of agreement in photocatalytic results has also been the result of non-standard preparation procedures and inconsistent characterisation methods used between many labs in the literature, often making it difficult to compare publications directly.<sup>36</sup> The interaction between AuNPs and their TiO<sub>2</sub> support can have a large influence on their adsorption geometries, dispersion across the surface, electronic properties, and their propensity to agglomerate. The Au/TiO<sub>2</sub> system has also been the focus of numerous theoretical studies investigating these properties in detail (*vide infra*), many of which are difficult to investigate experimentally. These parameters can play a significant role in the catalytic performance and have therefore had a large impact on the design of catalytic systems.

### 1.4.2 Growth and Morphology of Gold Nanoparticles Supported Upon TiO<sub>2</sub>

The methods used for the preparation, treatment, and annealing of Au particles on TiO<sub>2</sub> surfaces have been shown to have a significant effect on the catalytic performance for a

variety of systems. One of the primary reasons for this is the variation in Au particle size and morphology.<sup>324</sup> Given that the field of Au/TiO<sub>2</sub> catalysis is so large, numerous studies have shown a great number of different preparation methods for Au/TiO<sub>2</sub>.<sup>276,278,325,326</sup> CO oxidation is one of the most well studied processes where the effects of particle size and morphology have been shown to occur.<sup>206,283,292,324,327-329</sup> It is thought that the bilayer Au structure between two and three nm in diameter correlates with optimal catalytic activity, and the strong structure sensitivity is thought to arise from quantum size effects. Haruta *et al.* have also shown that higher calcination temperatures can provide higher catalytic activity, even if the AuNPs grew in size, due to increased contact with the support.<sup>208</sup> The following sections will discuss some of the primary factors that can influence the growth and morphology of Au nanoparticles during their deposition onto TiO<sub>2</sub>.

The distribution and dynamics of oxygen vacancies on the surface of TiO<sub>2</sub> is another factor that has been shown to have a significant influence on the growth process of AuNPs.<sup>301</sup> During deposition, Au particles have been shown to bind above and nucleate at oxygen vacancies via scanning tunnelling microscopy (STM) measurements on the TiO<sub>2</sub> rutile(110) surface.<sup>330</sup> It was shown that increased temperatures tend to result in greater coverage of oxygen vacancies by AuNPs, with the possibility of trapping multiple oxygen vacancies beneath a AuNP as its size increases. This is supported by the DFT calculations provided concurrently with the study, as well as the DFT calculations of other groups, which have shown that gold atoms prefer to bind above oxygen vacancy sites.<sup>331-333</sup> There is a great deal of DFT investigations of AuNPs on the TiO<sub>2</sub> rutile(110) surface. One such study showed that the density of nucleation saturates faster at terraces, while the average height of the particles grows faster at step edges for TiO<sub>2</sub> rutile(110) surfaces.<sup>334</sup> Lopez and Nørskov<sup>335</sup> found that for the non-defective rutile(110) surface, the interaction between TiO<sub>2</sub> and Au was small, leading to 3D growth being thermodynamically favoured, with little effect on the electronic structure of the AuNP. In comparison, Goodman and co-workers have also shown that nucleation occurs readily over highly reduced TiO<sub>x</sub> surfaces, with reduced Ti sites acting as nucleation centres.<sup>336</sup> DFT and STM investigations have also shown similar results when investigating the binding of Au to TiO<sub>2</sub> anatase(101) surfaces.<sup>127,337</sup>

Be that as it may, there are numerous DFT studies in the literature that disagree on the precise location for the binding of Au to the various forms of TiO<sub>2</sub> surfaces,<sup>127,332,333,335,337-344</sup> since the energy differences between the adsorption sites are

often quite small. Overall, these studies have shown that gold binds rather weakly to TiO<sub>2</sub> when compared with other metals such as copper or silver, regardless of the adsorption site under investigation.<sup>247,338</sup>

Wang and Hwang<sup>333</sup> have suggested that investigations using periodic boundary conditions (PBC) must be careful with regards to the size of the unit cells used. This is to ensure that the Au-TiO<sub>2</sub> interaction is adequately modelled over the Au-Au interactions along the surface, which would otherwise effect the prediction of nucleation sites. This is of particular note, since many investigations in the literature make use of PBC. Their study also showed that neighbouring oxygen vacancies increased the level of interaction between the Au atom and its defect site.

High temperature treatments used to adhere Au particles to TiO<sub>2</sub> surfaces have been shown to have a significant impact on their final size and structure. AuNPs/TiO<sub>2</sub> are generally unstable and also tend to agglomerate under gaseous environments during heat treatment.<sup>333</sup> For example, annealing Au particles on TiO<sub>2</sub> at elevated temperatures has been shown to result in small, two-dimensional Au particles transforming irreversibly into three-dimensional morphologies, depending upon surface defects and temperature.<sup>324</sup> For the TiO<sub>2</sub> rutile(110) surface, agglomeration of AuNPs tends to occur at relatively high temperatures, such as 700,<sup>345</sup> 750,<sup>346</sup> or 775 K,<sup>347</sup> showing a large increase in average AuNP size and corresponding decrease in total particle numbers. Boccuzzi *et al.* have showed that calcination at 473, 573, and 873 K led to 2.4, 2.5, and 10.6 nm particles, respectively.<sup>293</sup> Buffat and Borel showed that gold particles less than 22 nm in size are susceptible to having a low melting temperature, showing that there is a strong size effect on the melting temperature of AuNPs.<sup>348</sup> The particle size distribution after the annealing of Au on TiO<sub>2</sub> has also been found to depend heavily on the defect structure of the TiO<sub>2</sub> surface.<sup>349</sup> It has even been shown that agglomeration at relatively low temperature (300 K) can occur when simply increasing the Au coverage on TiO<sub>2</sub>(001) thin films under UHV conditions.<sup>350</sup>

Agglomeration of Au particles has also been observed to occur via Ostwald ripening for some high temperature annealing studies of Au/TiO<sub>2</sub>. Ostwald ripening is a process by which large particles grow at the expense of smaller particles, typically resulting in a bimodal particle size distribution.<sup>346,351,352</sup> In the work by Egdell and co-workers, for example, they observed a bimodal AuNP size distribution with peaks at ~2.2 and 4 nm

after heat treatment at 750 K for 36 hours.<sup>346</sup> They suggested that this process may occur via migration of gold atoms from the edges of smaller Au particles or from "gas-like" lone Au adatoms not already incorporated into particles. Their hypothesis is supported by another study showing the decrease of free Pd adatoms on the surface as their Pd particle size increases.<sup>353</sup> Ostwald ripening has also been shown to occur for Au/TiO<sub>2</sub> under reactive conditions involving O<sub>2</sub> at ambient temperature,<sup>354</sup> O<sub>2</sub> and CO at 450 K,<sup>355,356</sup> and under a standard atmosphere at 363 K.<sup>247,357</sup>

Pre-treatment of TiO<sub>2</sub> surfaces before the annealing of AuNPs has been shown to influence their dispersion and agglomeration properties. The presence of hydroxyl groups on the surface of TiO<sub>2</sub> has been demonstrated to be useful in controlling the growth and morphology of small metal particles, helping to prevent agglomeration.<sup>291,358,359</sup> In another study, UV irradiation of a TiO<sub>2</sub> single crystal surface before deposition of Au was shown to reduce the size of the AuNPs after calcination via the formation of hydroxyl groups on the surface of the TiO<sub>2</sub>.<sup>357</sup> Pre-treatment of TiO<sub>2</sub> via acid-washing has also been demonstrated to increase the performance and selectivity of the subsequent AuNPs/TiO<sub>2</sub> catalysts for the production of H<sub>2</sub>O<sub>2</sub> from H<sub>2</sub> and O<sub>2</sub>.<sup>360</sup> Additionally, the relative loading of Au on TiO<sub>2</sub> can affect the growth and morphology of AuNPs.<sup>334,347,361-365</sup> For example, for coverages of Au resulting in less than 0.15 monolayers (where one monolayer is  $\sim 1.39 \times 10^{15}$  Au atoms per cm<sup>2</sup>), two-dimensional particles are formed, but beyond this, growth changes to three-dimensional particles.

While the structure and growth of AuNPs on TiO<sub>2</sub> have been well studied and is the subject of a number of reviews, there are only a handful of studies that have explored the interaction between ligand-protected, small gold clusters and the TiO<sub>2</sub> surface.<sup>357,366-369</sup> Two of these publications are early work from our group, some of which is included in this thesis. It is assumed that the clusters presented herein may bind to TiO<sub>2</sub> in a similar way to those prepared using Au vapour deposition or Au colloids, but given that they are pre-synthesised and ligand-protected, they may not grow and nucleate in the same way. They are also too small to form crystallographic or epitaxial structures on the surface. Nonetheless, it is clear that there are many factors, both of the TiO<sub>2</sub> support and during preparation that have a significant impact upon the properties of Au particles, which may also influence the properties of the ligand-protected clusters used in this project.

## 1.5 Particle Size Effects

### 1.5.1 Clusters versus Nanoparticles

Clusters are typically small aggregates of atoms with precisely defined stoichiometries and structures that are usually less than 1 nm in size. These properties tend to result in unique geometric and chemical configurations that are not observed for their bulk counterparts. The very high surface area to volume ratio of clusters also creates a unique chemical environment. For clusters, the majority of atoms are exposed and heavily undercoordinated. Therefore, the addition or modification of a single atom in a cluster can often have a dramatic impact upon its shape and reactivity (*vide infra*).<sup>370-376</sup>

In comparison, nanoparticles are larger and typically have a distribution of particle sizes, while remaining in the nano size regime (< 100 nm). Nanoparticles can still exhibit unique chemical properties that depend on their size or shape and protective shell, but are less sensitive to changes to the number of atoms when compared with clusters. They can also have crystalline faces that resemble those of their bulk counterparts with defined edge transitions to other faces. For nanoparticles, the high surface area to volume ratio can result in the atoms on the surface of the nanoparticle perceiving a unique chemical environment compared with those contained within the centre of the nanoparticle. Note that there is currently no widely accepted definition of a "nanoparticle" or "cluster" in published literature,<sup>377</sup> but these are some broad features that can be used to describe the two species.

### 1.5.2 Optical and Electronic Properties of Gold Nanoparticles

AuNPs exhibit a number of interesting effects related to their electronic and optical properties. They are known to show size-induced semiconductor properties when the particle size becomes sufficiently small, giving rise to a valence and a conduction band in remarkable contrast to bulk gold, which behaves as a conductor. This effect is due to the loss of numerous overlapping electronic bands normally seen in a bulk metal, instead giving rise to discrete electronic energy levels.<sup>377</sup> A number of studies indicate that the transition from conducting to semi-conducting behaviour should occur when AuNPs become smaller than 1.5 to 4 nm in size, dependent upon the support and surface coverage.<sup>247,286</sup> Okazaki *et al.* have showed that when the particle height becomes less

than 0.4 nm on a TiO<sub>2</sub> rutile(110) surface, semi-conductor behaviour begins to occur, also showing substantial changes to the adsorption energies and charge transfer based on the stoichiometry of the surface.<sup>378</sup>

AuNPs can also display a characteristic localised surface plasmon resonance (LSPR), which appears near 530nm for AuNPs less than 20 nm in diameter.<sup>315</sup> This phenomenon occurs when the electromagnetic field of incident light causes the collective oscillation of conduction electrons at the surface of the gold nanoparticles (the surface plasmon) resulting in a strong absorption and scattering cross-section for the nanoparticles at the resonant frequency.<sup>379</sup> The LSPR can change significantly with the size and shape of a AuNP, as well as with the adsorption of molecules to the surface or interaction with a support. This has been useful for the design of a number of visible light sensitised plasmonic Au applications,<sup>308,379-382</sup> including biomedical applications,<sup>383-386</sup> gas sensors,<sup>65,381</sup> and photocatalytic water-splitting.<sup>304-309,316,387-389</sup> The water-splitting applications that use AuNP LSPR to sensitise TiO<sub>2</sub> to visible light also have the advantage of promoting conduction band electron transfer from Au to TiO<sub>2</sub>, whereby they can reduce H<sup>+</sup> to H<sub>2</sub>.<sup>304</sup> Unfortunately, LSPR is not seen for AuNPs once they become too small, whereby they lose their conducting properties (*vide supra*). Further information on the physics behind LSPR and its effect on photocatalysis are available in comprehensive reviews by Mayer and Hafner,<sup>381</sup> and Zhang *et al.*<sup>390</sup>

The benefits of increased charge separation are not limited only to AuNPs with LSPR; the study by Qian *et al.* showed that AuNPs can also facilitate charge separation at the Au-TiO<sub>2</sub> interface when irradiated with light > 400 nm, but less than the LSPR.<sup>304</sup> This promoted the transfer of photoexcited electrons from the conduction band of TiO<sub>2</sub> to the AuNPs, spatially separating the photoexcited charges. They also indicated that many other studies ignore the fact that the absorption edge of TiO<sub>2</sub> extends beyond 400 nm for rutile.

Au particles supported on TiO<sub>2</sub> also exhibit initial and final state effects that can influence the binding energies as well as the full-width-half-maximum (FWHM) of peaks in experimental X-ray photoelectron spectroscopy (XPS) spectra. Initial state effects arise from changes in the valence band structure of a nanoparticle and due to interaction with the support. In comparison, final state effects arise from post-excitation of the nanoparticle, whereby it can remain in an excited state for a period of time that depends

on its size and support.<sup>391</sup> The combination of these two effects can substantially influence experimental XPS spectra.

XPS studies of Au particles on TiO<sub>2</sub> have shown that the Au 4*f* peak shifts to higher binding energy as particle size decreases.<sup>361</sup> In this study, there were no changes to the oxidation state of Ti, and therefore the shift can be attributed primarily to Au particle size. Chusuei *et al.*<sup>392</sup> have shown large differences in binding energy shifts for AuNPs/TiO<sub>2</sub> compared with AuNPs/SiO<sub>2</sub> of 0.8 eV and 1.6 eV respectively, indicating there are unique interactions between the support and the nanoparticles that affect their electronic structure. They suggest that these strong interactions lead to a shift in the binding energy of the *d*-band to higher energy relative to a gas-phase gold cluster. DFT calculations have also shown that the positive binding energy shifts for Au/TiO<sub>2</sub> can be attributed to the interaction of gold with oxygen vacancies.<sup>393</sup> Another XPS study of AuNPs on TiO<sub>2</sub> rutile(110) surfaces concluded that the decrease in peak intensity was a result of the strong interaction between the Ti 3*d* defect states caused by oxygen vacancies and the AuNPs.<sup>394</sup> The DFT study by Lopez and Nørskov has also showed that as the number and size of AuNPs on the TiO<sub>2</sub> surface increased, more Au–Au bonds are formed due to the increased average Au coordination number of larger particles. This results in electron density being taken away from the interface between the gold cluster and the TiO<sub>2</sub> support, influencing the core level shifts seen in XPS.<sup>331</sup> These studies have shown that XPS is sensitive to the electronic structure and size of small AuNPs supported on TiO<sub>2</sub>, which is typically difficult to investigate. Further information is available in the review by Meyer *et al.*,<sup>247</sup> which goes into extensive detail about initial and final state effects observed for XPS of Au on various supports.

### 1.5.3 Size Effects on Catalytic Activity

The catalytic activity of supported AuNPs has been shown to be strongly size and shape dependent for a range of different supports in the literature.<sup>167,222,238,240,278,395,396</sup> Some reactions have even shown remarkable size-dependent selectivity; for example, for the catalytic reaction of propylene over AuNPs/TiO<sub>2</sub> in the presence of O<sub>2</sub> and H<sub>2</sub>, AuNPs smaller than 2 nm cause hydrogenation of the reactants to produce propane, while those larger than 2 nm cause partial oxidation to form propylene oxide.<sup>207,320,397</sup> The latter reaction to form propylene oxide can only occur for the combined AuNP/TiO<sub>2</sub> anatase

system and not for isolated Au or TiO<sub>2</sub>. This study also showed that there was no activity for the rutile polymorph. This may be related to the findings that AuNPs supported on anatase are smaller than those supported on rutile using identical preparation methods.<sup>167</sup> Okazaki *et al.*<sup>378</sup> have shown, based on STM observations and DFT calculations, that the activity of AuNPs supported on TiO<sub>2</sub> rutile(110) increases below 5 nm, followed by a further increase below 2 nm. Another study has observed a change in selective hydrogenation as Au particle size decreased below 2 nm.<sup>222</sup> The adsorption of styrene to AuNPs/TiO<sub>2</sub> has been shown to be more likely for smaller AuNPs, changing the desorption temperature from 350 to 410 K.<sup>354</sup> For the photocatalytic reforming of methanol over Au/TiO<sub>2</sub>, the smaller Au particles are known to produce H<sub>2</sub> and CO<sub>2</sub>, while suppressing CO and H<sub>2</sub>O products.<sup>323</sup> Further examples that show a strong size dependency for Au are also available in the literature.<sup>295,304,321</sup>

There have been a number of suggestions as to the cause of the strong size effects that arise for small AuNPs. Haruta and co-workers<sup>282</sup> have shown that hemispherical Au particles with flat planes in good contact with the TiO<sub>2</sub>, which yield long perimeter interfaces around the Au, are more catalytically active for the oxidation of CO. This is because there are a greater number of edge atoms in contact with the support as the nanoparticle size decreases. In a study of CO<sub>2</sub> production from a CO:O<sub>2</sub> mixture at 40 Torr at standard temperature over a Au/TiO<sub>2</sub> catalyst, optimal catalytic performance is found with 3 nm Au clusters.<sup>286</sup> In contrast to the study by Haruta and co-workers, the authors attributed this to the transition between conducting and semi-conducting AuNPs and not to a geometric effect due to changing Au/TiO<sub>2</sub> perimeter ratios. In the study by Okazaki *et al.*<sup>378</sup> mentioned earlier, the increase in activity as size decreased was attributed to an increase in the averaged electrostatic potential and electron transfer from the Au nanoparticles to the TiO<sub>2</sub> support. Small AuNPs have also been shown to induce a greater negative shift in the Fermi level than large AuNPs, resulting in better charge separation.<sup>398</sup> The size of AuNPs can also influence their internal crystalline structure; for example, it was shown that AuNPs on Mg(OH)<sub>2</sub> had icosahedral symmetry when below 1 nm, while above 1 nm, they had face-centred cubic (FCC) cuboctahedral symmetry, playing an important part in their catalytic activity.<sup>329</sup>

There have also been studies that have shown strong size-dependent effects for small Au clusters consisting of only a few atoms. Landman and co-workers have shown that Au clusters between 8 and 20 atoms supported on MgO thin films have a strong size-

dependent activity for CO oxidation.<sup>372</sup> Below 8 atoms there was no activity, but between 8 and 20 atoms catalytic activity increased in an oscillatory pattern with the addition of each Au atom. The temperature for CO<sub>2</sub> desorption was also found to depend on the number of atoms in the cluster for temperature programmed desorption. Chrétien and Metiu<sup>373</sup> have showed via DFT calculations that the charge transfer for small Au clusters ranging from one to seven atoms on oxygen-deficient TiO<sub>2</sub> rutile(110) varied dramatically from negative to positively charged species, depending upon the number of Au atoms in the cluster. A DFT study by Lopez and Nørskov<sup>331</sup> showed that gas-phase Au<sub>10</sub> clusters should be active towards the low temperature oxidation of CO due to the enhanced ability for under-coordinated gold atoms to react with adsorbates, which has been shown experimentally on FeO<sub>x</sub> supports.<sup>267</sup> These studies showed that the reactivity of Au can vary dramatically with the addition or subtraction of only a single atom.

The precise number of atoms and morphology of gas-phase Au clusters have also been shown to have an influence on their reactivity, highlighting the sensitivity of Au clusters in regards to catalysis. This work was started by a publication by Huber *et al.*, who showed that a single gold atom can catalyse the oxidation of CO at 10 K.<sup>399</sup> Since then, many groups have looked at the catalytic properties of gas-phase Au clusters and great deal of work has been performed, finding a number of cluster size dependencies for both the cationic and anionic gold clusters.<sup>247</sup> For example, Ervin and co-workers showed that that odd clusters up to Au<sub>7</sub> were more active towards oxygen, whereas large clusters were more active towards reactions with CO.<sup>370</sup> Cox *et al.* have examined the adsorption of small reactants such as O<sub>2</sub>, D<sub>2</sub>, and CH<sub>4</sub> on various gas-phase clusters up to ~28 Au atoms and found strong dependencies on cluster size and charge state.<sup>371</sup> Other studies that have been performed include photoelectron spectroscopy,<sup>400,401</sup> flow reactor experiments, and DFT investigations.<sup>247,402</sup> Despite this great deal of work that has been performed on gas-phase Au clusters, there is very little work performed on the interaction between small gold clusters and TiO<sub>2</sub> supports.

### 1.5.4 Atomically Precise, Ligand Stabilised, Small Gold Clusters

Investigations into the catalytic performance of AuNPs/TiO<sub>2</sub> are often difficult to achieve without precise control of the size distribution of deposited Au particles, which depends heavily on the preparation method used. The fabrication of catalytic systems using TiO<sub>2</sub>-

supported Au particles can be achieved by numerous methods that have been covered in detail by a number of reviews available in the literature.<sup>315,403</sup> Briefly, there are two general approaches used: ultra-high vacuum (UHV) techniques and chemical synthetic techniques. UHV techniques typically employ gas-phase delivery of metal atoms by vaporisation of a metal target followed by size-selection of the gas-phase cluster before deposition via the use of quadrupole or ion-traps,<sup>404-408</sup> as well as support-assisted self-assembly techniques.<sup>409</sup> Chemical synthetic techniques involve a wider range of approaches, such as the reduction and decomposition of simple precursors or metal ion templates that result in the growth of nanoparticles,<sup>410,411</sup> to the immobilisation of Au colloids with narrow or specific size distributions that are typically stabilised with protective ligand groups.<sup>278,281,292,366,412,413</sup> The use of ligand-stabilised Au clusters typically yields better particle size control compared with top-down approaches that use mechanical, thermal, or laser based methods to break down the structure of a bulk material. The synthesis of phosphine ligand stabilised Au clusters was first developed in the early 1970s,<sup>414</sup> allowing for precise control over the number of metal atoms present in the cluster core.

These atomically precise, chemically synthesised clusters have been shown to be catalytically active in a number of studies; the  $\text{Au}_9(\text{PPh}_3)_8(\text{NO}_3)_3$  cluster used in this thesis, for example, has been shown to oxidise CO at temperatures as low as 203 K when impregnated into various metal hydroxides.<sup>224</sup>  $\text{Au}_{11}(\text{PPh}_3)_8\text{Cl}_3$  has been used to fabricate mesoporous silicon supported Au clusters that are active towards the oxidation of various alcohols by  $\text{H}_2\text{O}_2$  under microwave irradiation.<sup>415</sup> XPS studies have shown that  $\text{Au}_{55}(\text{PPh}_3)_{12}\text{Cl}_6$  supported on silicon wafers have excellent oxidation resistance and have suggested that  $\text{Au}_{55}$  clusters may make for effective CO oxidation catalysts.<sup>416</sup> Ligand-protected Au clusters have also been used as effective precursors for the synthesis of small AuNPs for low-temperature CO oxidation on various supports.<sup>417</sup> The metal cores of many of these Au clusters are charged, which may be beneficial for catalysis, as there are studies that have shown that the  $\text{Au}^+$  or  $\text{Au}^{\delta+}$  species are more active than the  $\text{Au}^0$  species.<sup>226,262,418</sup> However, it is unknown what charge state these clusters are in after they are deposited onto  $\text{TiO}_2$  surfaces. Examples of the atomically precise, ligand-stabilised clusters that are used in this project are illustrated in Figure 1.7.

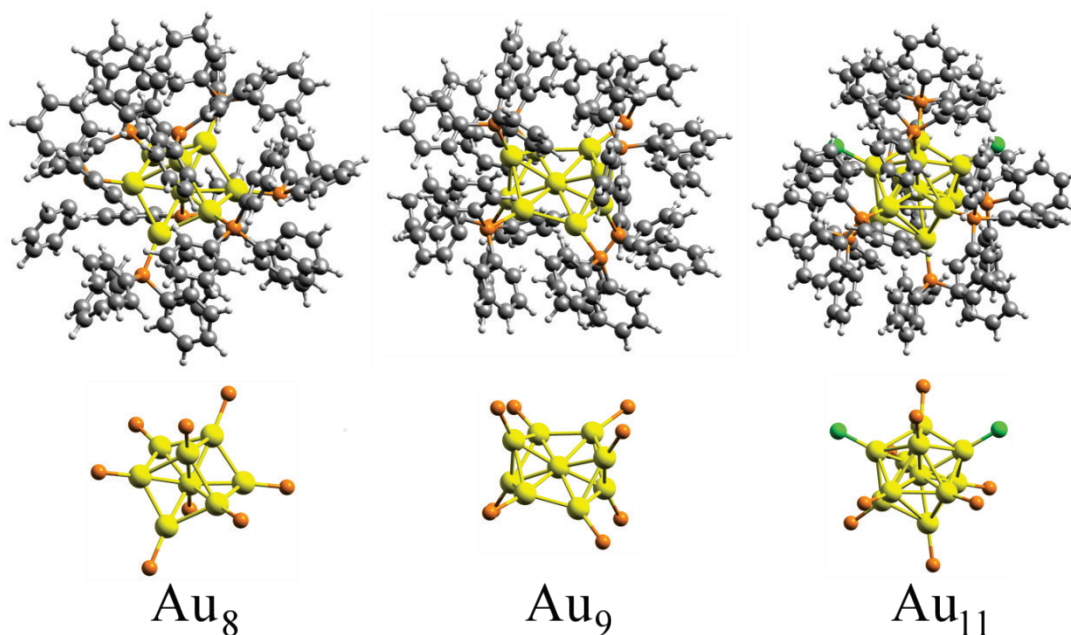


Figure 1.7: The crystal structures of  $Au_8(PPh_3)_8(NO_3)$ ,  $Au_9(PPh_3)_8(NO_3)_3$ , and  $Au_{11}(PPh_3)_8Cl_3$  with and without ligands. Au, P, Cl, C, and H are coloured yellow, orange, green, dark grey, and light grey, respectively. The  $NO_3$  and one of the Cl counterions have been omitted for clarity.

These types of Au clusters are often "activated" after deposition onto the support surface by annealing or other treatments in order to remove the protective ligand groups and adhere them to the support.<sup>243,414,419-422</sup> The ligands are necessary during synthesis to stabilise the clusters due to their high surface energy,<sup>423</sup> but once synthesised, their presence can potentially be detrimental for catalysis, blocking access to light and reactants.<sup>367</sup> However, given the likelihood for unprotected Au atoms to sinter and agglomerate on  $TiO_2$  surfaces under elevated temperatures or gaseous environments (*vide supra*), the final Au particle size may be different to that of the ligand-protected cluster if the treatments are too harsh. Removal of ligands can also cause cluster condensation via the formation of M-M bonds between adjacent clusters.<sup>424</sup> Reducing the chances of agglomeration during ligand removal can be achieved via the reduction of cluster density at low loadings, using high surface area nanoparticle supports, and homogenous absorption to the support surface by tuning of solvent parameters.<sup>414</sup>

Delicate control of the annealing and immobilisation procedures used to fabricate catalytic materials using ligand-stabilised clusters can allow for a great deal of control in the final particle size. The recent study by Tsukuda and co-workers showed that clusters

can even be deposited intact under ideal treatment conditions, whereby Au<sub>11</sub> clusters were deposited on mesoporous silica via the calcination of Au<sub>11</sub>(PPh<sub>3</sub>)<sub>8</sub>Cl<sub>3</sub>, yielding particle sizes of  $0.8 \pm 0.3$  nm, which is the approximate size of the precursor.<sup>415</sup> Au<sub>6</sub>(PPh<sub>3</sub>)<sub>6</sub>(BF<sub>4</sub>)<sub>2</sub> is a derivative of one of the clusters used in this thesis and has also been used as a precursor to produce highly dispersed Au<sub>6</sub> clusters on a planar TiO<sub>2</sub> (110) crystal after electron stimulated desorption of the ligands.<sup>425</sup> In addition, the use of ozone exposure to limit the agglomeration of Au<sub>13</sub>[PPh<sub>3</sub>]<sub>4</sub>[S(CH<sub>2</sub>)<sub>11</sub>CH<sub>3</sub>]<sub>4</sub> clusters has been found to be an effective method to control particle size, with final particles being smaller than those annealed under 400 K treatment under atmosphere.<sup>366</sup> The removal of ligands using solvent extraction has also been shown to help reduce the amount of agglomeration for Au clusters, without the need for subsequent thermal treatments.<sup>367</sup> UV irradiation of the TiO<sub>2</sub> rutile(110) surface before calcination can also dramatically reduce the amount of agglomeration for subsequent deposition of Au(PPh<sub>3</sub>)(NO<sub>3</sub>) complexes.<sup>357</sup>

The ability to control the growth and morphology of Au particles with high precision enables investigators to readily draw correlations with the reactivity of a system. Many of these isolated clusters have already been characterised extensively by crystallography, NMR and EXAFS techniques, but few studies have investigated their interactions with the TiO<sub>2</sub> support, or their photocatalytic potential.

## 1.6 Gas-Phase Photocatalysis

Almost all of the previous work using TiO<sub>2</sub> in the field of photocatalytic water-splitting has involved the use of aqueous solutions of suspended TiO<sub>2</sub> particles. Nevertheless, gas-phase photocatalysis over catalytic surfaces is a valuable avenue to explore, as it can be used to eliminate aqueous parameters such as pH, in order to focus on the interaction between AuNPs and TiO<sub>2</sub>. Photocatalytic studies over solid catalysts can also be directly compared to surface sensitive experimental techniques for characterisation. Despite this, there has been very little work performed on heterogeneous gas-phase water-splitting with TiO<sub>2</sub>.

Inoue *et al.*<sup>59</sup> have shown that 100 nm films of TiO<sub>2</sub> co-doped with Pt can photocatalytically split water vapour when illuminated under a 500-W Xe lamp with a cut-off filter > 410 nm, yielding an initial production rate of 0.16  $\mu\text{mol h}^{-1} \text{cm}^{-2}$  of H<sub>2</sub>. Yamaguti and Sato<sup>177</sup> found that Rh, Pd, and Pt/TiO<sub>2</sub> powders coated with various loadings of NaOH were able to photocatalytically split water vapour, with maximum hydrogen production rates of 449, 30, and 284  $\mu\text{mol h}^{-1} \text{g}^{-1} \text{cm}^{-2}$ , respectively, under a 500 W high-pressure Hg lamp with a 250–400 nm band-pass filter. They found the maximum hydrogen production rate to vary dramatically between the TiO<sub>2</sub> manufacturers. They also found a strong catalytic activity dependence of the water-vapour partial pressure for NaOH coated Rh/TiO<sub>2</sub> catalysts, with higher water-vapour pressures producing more hydrogen for higher loadings of NaOH. In similar work, Grimes and co-workers have shown the production of methane and other hydrocarbons from CO<sub>2</sub> and H<sub>2</sub>O over N-doped TiO<sub>2</sub> nanotube arrays. All other systems found in the literature using TiO<sub>2</sub> make use of aqueous solutions for photocatalytic water-splitting.

### 1.7 The Scope of this Thesis

This thesis will aim to characterise the interaction between ligand-protected, atomically precise Au clusters and their TiO<sub>2</sub> support, in addition to investigating their photocatalytic potential as co-catalysts for gas-phase photocatalytic water-splitting. Research into the fabrication and activation of heterogeneous photocatalysts using ligand-protected, small gold clusters on TiO<sub>2</sub> for water-splitting has not been undertaken previously in the literature to the best of this author's knowledge. Understanding the structural and electronic properties of these clusters and correlation of this information with observed catalytic activity will provide useful insights into future heterogeneous photocatalytic system design. These investigations form part of a multi-faceted, collaborative approach to understanding the Au cluster/TiO<sub>2</sub> system. Given the difficulty associated with acquiring experimental data in the incredibly small size regime of clusters, complementary density functional theory calculations are also performed to match with experimental data and to help elucidate the interactions occurring between gold atoms and the titanium dioxide surface. While there are a number of theoretical studies published on the Au/TiO<sub>2</sub> system using plane-wave basis sets and periodic boundary conditions, there are no studies of this system using atom-centred basis sets similar to those used in this thesis.

Chapter two provides an overview of the experimental techniques, apparatus, and methods used throughout the project. It also provides a detailed description of the design and operation for the heterogeneous photocatalytic reactor. This description includes the procedures used for the quantitative analysis of the gas mixture in the reaction cell.

Chapter three briefly covers the relevant theoretical background to DFT and basis sets. In addition, the selection of basis set and functional used in this study is justified, and their parameters are outlined. Details about the computational method employed are included at the end of this chapter.

Chapter four investigates the far infra-red absorption spectra of Au<sub>6</sub>(Ph<sub>2</sub>P(CH<sub>2</sub>)<sub>3</sub>PPh<sub>2</sub>)<sub>4</sub>(NO<sub>3</sub>)<sub>2</sub>, Au<sub>8</sub>(PPh<sub>3</sub>)<sub>8</sub>(NO<sub>3</sub>), Au<sub>9</sub>(PPh<sub>3</sub>)<sub>8</sub>(NO<sub>3</sub>)<sub>3</sub>, Au<sub>11</sub>(PPh<sub>3</sub>)<sub>8</sub>Cl<sub>3</sub>, Pd(PPh<sub>3</sub>)Au<sub>6</sub>(PPh<sub>3</sub>)<sub>6</sub>(NO<sub>3</sub>)<sub>2</sub>, and Pt(H)(PPh<sub>3</sub>)(AuPPh<sub>3</sub>)<sub>7</sub>(NO<sub>3</sub>)<sub>2</sub> recorded using synchrotron light. These experiments reveal a series of unique peaks between 50 and 475 cm<sup>-1</sup> that are assigned to specific vibrational modes by comparison to density functional theory calculations. The distinct peaks for each cluster can be assigned to the calculated

## Chapter 1. Introduction

cluster core vibrations: 80.4 and 84.1  $\text{cm}^{-1}$  for  $\text{Au}_6$ ; 165.1 and 166.4  $\text{cm}^{-1}$  for  $\text{Au}_8$ ; 170.1 and 185.2  $\text{cm}^{-1}$  for  $\text{Au}_9$ ; 173.7 and 182.2  $\text{cm}^{-1}$  for  $\text{Au}_{11}$ ; 158.9, 195.2, and 206.7  $\text{cm}^{-1}$  for  $\text{Au}_6\text{Pd}$ ; and 156.3, 171.8, and 173.5  $\text{cm}^{-1}$  for  $\text{Au}_7\text{Pt}$ . There is also a strong absorption for all clusters near 420  $\text{cm}^{-1}$  that are assigned to P- $\text{Ph}_3$  vibrations.

Chapter five continues the characterisation with the use of synchrotron X-ray and TEM techniques to investigate the full effect of treatments that are undertaken to remove the organic protective ligands after the gold clusters are supported upon titanium dioxide. X-ray photoelectron spectroscopy shows an increase in particle size and loss of ligands with successively harsher post-treatments. The increases in particle size are supported by complementary TEM results. Acidic pre-treatment and the form of the titanium dioxide support are shown to have a strong impact on the severity of agglomeration and ligand loss. These results are also supported by X-ray absorption near edge structure and extended X-ray absorption near edge structure analysis of complementary X-ray absorption experiments.

In Chapter six, the photocatalytic potential for water photolysis of these catalysts is investigated using a new experimental apparatus designed and built during the project. It consists of a heterogeneous gas-phase reactor operating near ambient conditions that can deliver constant and controlled samples of gas to a residual gas mass spectrometer for analysis of the gas composition over time. Using this apparatus,  $\text{Au}_8(\text{PPh}_3)_8(\text{NO}_3)_2$ ,  $\text{Au}_9(\text{PPh}_3)_8(\text{NO}_3)_3$ , and  $\text{Au}_{101}[\text{P}(\text{C}_6\text{H}_5)_3]_{21}\text{Cl}_5$  supported on anatase or P25  $\text{TiO}_2$  nanoparticles are investigated for their activity towards water photolysis and their peak  $\text{H}_2$  production rates are quantified. Anatase-supported samples are found to increase in activity with successively harsher post-treatment conditions, with data suggesting that increasing the size of the gold particles to be beneficial for photocatalytic activity. In contrast, samples prepared upon acid-washed P25 or acid-washed anatase show evidence for an ideal gold particle size and ligand coverage after relatively gentle post-treatment conditions.

Chapter seven contains the density functional theory investigations of  $\text{Au}_1$ ,  $\text{Au}_2$ ,  $\text{Au}_3$ , and  $\text{Au}_4$  clusters bound to the stoichiometric and oxygen-deficient titanium dioxide anatase(101) surface using an atomic centred basis set approach. Numerous isomers are found within 0.5 eV of the lowest energy isomer for  $\text{Au}_2$ ,  $\text{Au}_3$ , and  $\text{Au}_4$ . The structural parameters, binding energies, infrared spectra, charge transfer, and density of states for

## Chapter 1. Introduction

each isomer are described in detail. Key findings include: increasing binding energy as the number of Au atoms are increased; strong Au-Au stretching and cluster breathing modes that shift considerably between isomers or with additional Au atoms; the general trend of charge transfer from the Au clusters to the titanium dioxide surface; and the introduction of numerous occupied gold states at the valence band edge that extend into the band gap, as well as isolated states also introduced in the middle of the band gap.

These four result chapters bring together a variety of techniques to investigate the Au cluster/TiO<sub>2</sub> system. Correlations between the different data reveal a series of trends that would otherwise be difficult to understand on their own. Knowledge of the interaction between gold clusters and semiconductor supports is vital to the development of novel gold-based heterogeneous photocatalysts for a wide range of green chemistry. Renewable photocatalytic systems that can use solar radiation to produce chemical fuels are appealing technologies that have garnered much interest over the last few decades. In this thesis, ligand-protected, atomically precise gold clusters supported on titanium dioxide nanoparticles are characterised and their photocatalytic potential for water photolysis is investigated. Given the difficulty associated with acquiring experimental data in the incredibly small size regime of clusters, complementary density functional theory calculations are also performed to match with experimental data and to help elucidate the interactions occurring between gold atoms and the titanium dioxide surface.

# **Chapter Two**

Experimental Techniques, Apparatus, and Method

## 2 Experimental Techniques, Apparatus, and Method

### 2.1 Catalyst Synthesis and Preparation

The ligand-protected, small gold clusters used throughout this thesis were prepared by the group of Vladimir Golovko (University of Canterbury) according to the procedures outlined in the following sections and are the same as those used in collaborative publications between our groups.<sup>368,369,426,427</sup> Samples were delivered in small batches to the University of Adelaide or directly to the synchrotron where experiments were undertaken. Not all samples were available for all experiments due to material and time constraints.

#### 2.1.1 Preparation of Ligated Gold Clusters

The  $\text{Au}_6(\text{Ph}_2\text{P}(\text{CH}_2)_3\text{PPh}_2)_4(\text{NO}_3)_2$  cluster (CSD<sup>428</sup> reference code BOTSOS) was synthesised according to the procedure described by Van der Velden *et al.*<sup>429</sup> The  $\text{Au}_8(\text{PPh}_3)_8(\text{NO}_3)_2$  cluster (CSD reference code OPAUPF) was synthesised according to the protocol described by Van der Velden *et al.*<sup>430</sup> The  $\text{Au}_9(\text{PPh}_3)_8(\text{NO}_3)_3$  cluster (CSD reference code MIVPOX) was synthesised according to the protocol described by Wen *et al.*<sup>431</sup> The  $\text{Au}_{11}(\text{PPh}_3)_8\text{Cl}_3$  cluster (CSD reference code PESJAA) was synthesised according to the protocol described by Hutchison *et al.*<sup>432</sup> The  $\text{Au}_{101}[\text{P}(\text{C}_6\text{H}_5)_3]_{21}\text{Cl}_5$  cluster was prepared following the method described by Hutchison *et al.*<sup>433</sup> Note that the authors estimate this formula based on the particle size and the method used by Whetten *et al.*<sup>434</sup> The  $\text{Pd}(\text{PPh}_3)\text{Au}_6(\text{PPh}_3)_6(\text{NO}_3)_2$  cluster (CSD reference code UHIPEG) was synthesised according to the protocol described by Takata *et al.*<sup>435</sup> Note that the crystal structure available in CSD for this cluster has  $\text{PF}_6^-$  counter-ions instead of  $\text{NO}_3^-$ . The  $\text{Pt}(\text{H})(\text{PPh}_3)(\text{AuPPH}_3)_7(\text{NO}_3)_2$  cluster (CSD reference code JAPBEH) was synthesised according to the protocol described by Kanters *et al.*<sup>436</sup> Synthesis of  $\text{AuPPH}_3\text{Cl}$  used as a benchmark for far-IR studies was prepared following the method described by Malatesta *et al.*<sup>437</sup> These clusters will hereafter be referred to by their metal cores; i.e.  $\text{Au}_6$ ,  $\text{Au}_8$ ,  $\text{Au}_9$ ,  $\text{Au}_{11}$ ,  $\text{Au}_{101}$ ,  $\text{PdAu}_6$ , and  $\text{PtAu}_7$ .

### 2.1.2 Preparation of TiO<sub>2</sub>-Supported Gold Clusters

There were two forms of nanoparticle TiO<sub>2</sub> used for sample preparation: i) Aeroxide P25 TiO<sub>2</sub> (Evonik), which is a mixture of 76:11:13 anatase:rutile:amorphous TiO<sub>2</sub><sup>143</sup> with 21 nm average nanoparticle size and  $50 \pm 15 \text{ m}^2 \text{ g}^{-1}$  surface area or ii) pure anatase TiO<sub>2</sub> (Sigma-Aldrich) with 25 nm average particle size and  $35\text{--}65 \text{ m}^2 \text{ g}^{-1}$  surface area. Some TiO<sub>2</sub> was acid-washed with sulphuric acid before being used as supports,<sup>367</sup> and these have been denoted as their own sample sets in the results.

Deposition of clusters on Aeroxide P25 was achieved by mixing a solution of dissolved Au cluster with a magnetically stirred (1000 rpm) suspension of P25 in methanol in a Schlenk Tube at calculated concentrations to yield solutions with 0.17% w/w Au cluster/TiO<sub>2</sub>. The suspension was then left stirring overnight (12 hr) and the resultant mixture was dried under vacuum at room temperature, which was then stored in a refrigerator away from light.

Deposition of clusters onto anatase nanoparticles was achieved following the method outlined by Zhu *et al.*<sup>438</sup> The support was dried in a Schlenk tube under vacuum at 200 °C with magnetic stirring (1000 rpm) overnight (12 hr). The support was then allowed to cool to room temperature, before being suspended in dichloromethane with magnetic stirring (750 rpm). A solution with the calculated amount of cluster dissolved in dichloromethane was then added to the suspension of anatase at calculated concentrations to yield solutions with 0.17% w/w Au cluster/TiO<sub>2</sub>. The solution was then left stirring (1000 rpm) at room temperature overnight (12 hr). The mixture was then dried under vacuum at room temperature and stored in a refrigerator away from light.

This 0.17% loading was chosen as it allows for a reasonable amount of active material to be present on the support for study, whilst minimising agglomeration. This yields a surface coverage of ~4% for an average P25 nanoparticle surface when using ligated Au<sub>9</sub> as an example, resulting in ~14 ligated Au<sub>9</sub> clusters per P25 nanoparticle.

### 2.1.3 Activation Post-Treatment of Supported Gold Clusters

Some samples underwent various activation procedures to probe the effects of these treatments on the photocatalytic performance of the final catalyst. As discussed in the

introduction, these sample treatments have been proposed to help improve catalytic performance by removing some or all of the organic stabilising ligands that remain present during the synthesis of these clusters.

Solvent washing was undertaken following a similar protocol as that described by Lopez-Sanchez *et al.*<sup>367</sup> whereby a magnetically stirred (1000 rpm) suspension of the supported gold cluster on TiO<sub>2</sub> (~500 mg) in toluene (50 mL) was heated to 100 °C for 2 hours. Centrifugation (10 min, 5000 rpm) was used to recover the solid, which was then suspended and washed three times with toluene (50 mL) using a Vortex agitator followed by further centrifugation to recover the solid, which was dried under a vacuum of  $7.5 \times 10^{-2}$  Torr. The samples were then stored in a refrigerated Schlenk tube under a N<sub>2</sub> atmosphere in the absence of light.

Heat treatments were undertaken according to the procedure outlined by M. Turner *et al.*<sup>243</sup> The supported gold cluster on TiO<sub>2</sub> (~ 500 mg) in a Schlenk tube was magnetically stirred (1000 rpm) and heated to 200 °C under a vacuum of  $7.5 \times 10^{-2}$  Torr for 2 hours. The sample was then allowed to cool to ambient temperature while under the same vacuum. The samples were then stored in a refrigerated Schlenk tube under a N<sub>2</sub> atmosphere in the absence of light.

Calcination treatments were undertaken according to the procedure outlined above, except the Schlenk tube was not evacuated to a low vacuum, and was instead filled with pure O<sub>2</sub> (1 atm) at 200 °C for 2 hours. For O<sub>2</sub>/H<sub>2</sub> calcination treatments, the samples were calcined in the Schlenk tube with pure O<sub>2</sub> (1 atm) at 200 °C for 2 hours, followed by calcination under pure H<sub>2</sub> (1 atm) at 200 °C for 2 hours.

### 2.1.4 Preparation of Platinised TiO<sub>2</sub> Nanoparticles

Platinised P25 and platinised anatase nanoparticles were prepared at the University of Adelaide by our group. Synthesis of Pt-TiO<sub>2</sub> nanoparticles was undertaken following the protocol outlined by T. Peng *et al.*<sup>199</sup> H<sub>2</sub>PtCl<sub>6</sub>H<sub>2</sub>O (0.01 g) and Aeroxide P25 (0.38 g, Evonik) were added to a solution of Na<sub>2</sub>CO<sub>3</sub> (2.0 M, 175 mL) and exposed to an unfiltered sun lamp for 5 hours while being magnetically stirred. The solution was then allowed to settle, and the solvent was decanted. The sample was then washed with water (50 mL) and decanted two times, before being dried at 120 °C for an hour to obtain 1.0%

## Chapter 2. Experimental Techniques, Apparatus, and Method

w/w Pt/P25. This same procedure was used for the preparation of Pt/anatase, using pure anatase nanoparticles (0.38 g, Sigma-Aldrich).

## 2.2 Far-IR Spectroscopy

Infrared (IR) spectroscopy is a well-known spectroscopic technique commonly employed by many laboratories. It is typically quick and easy to use, while providing a wealth of information about the structure and symmetry of a molecule. IR spectra are recorded by measuring the IR photon transmission as a function of frequency. The photon energy at which molecules absorb IR radiation corresponds to the energy of a quantised transition between two vibrational states of a molecule. In order for a vibrational mode to be IR active there must be a change in the molecular dipole moment as the vibration occurs during incident photon absorption, as shown in Figure 2.1; the larger this change, more intense the absorption.

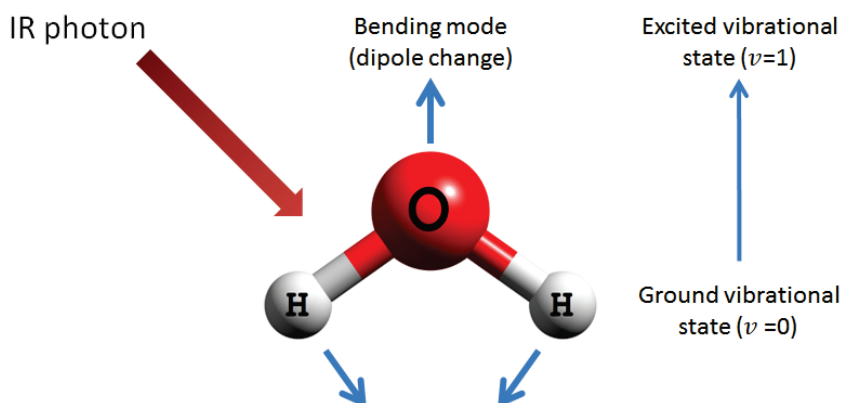


Figure 2.1: Illustration of the excitation from a ground-state to the first excited state vibrational mode after the absorption of a  $1595\text{ cm}^{-1}$  IR photon by the  $\text{H}_2\text{O}$  molecule.

Fundamental IR modes arise from the excitation of molecules from the ground-state to the first excited state, and these are most commonly observed, as molecules tend to be in their ground vibrational state at room temperature. Excitation from the ground-state to the second or higher excited states is referred to as overtone or combination bands.

In the context of far-IR spectroscopy at the Australian Synchrotron, this technique has the capability to probe modes as low as  $\sim 5\text{ cm}^{-1}$ , which is much lower than the typical capability range of most IR spectrometers. Based upon previous work by Fielicke and co-workers<sup>439</sup> of gas-phase small Au clusters, as well as DFT calculations undertaken during the course of this project, it was known that the core metal-metal vibrational modes of Au clusters would be found in the far-IR region, while very few ligand vibrations would be found here that would otherwise interfere with spectral assignment.

### 2.2.1 Sample Preparation and Apparatus

Samples were prepared by manual grinding of approximately 50 mg of pure dried cluster to yield a fine homogenous powder, which was then pressed into a pellet 10 mm in diameter using a hydraulic pellet press. For samples where the transmission through the pellet was too low, it was not possible to press pellets with less cluster material, as this resulted in structurally weak pellets that would easily break. Therefore, clusters were mixed with polyethylene to make up a total mass of 50 mg before being manually ground into a fine homogenous powder and then pressed into a pellet. Pellets were then mounted onto a cryostat sample holder and fastened gently to ensure the fragile pellets did not break under the pressure of the mounting cap. Three loading slots were available, with one of the three loading slots left blank or loaded with polyethylene for use as a reference. During some experiments, the cryostat was cooled using liquid nitrogen to 77 K. After experiments were performed at 77 K, the cryostat was allowed to equilibrate slowly to room temperature and condensation was removed before unfastening samples to prevent water contamination.

The far-IR absorption spectra of samples were recorded using the IFS125 (Bruker) Fourier transform spectrometer at the high-resolution THz/Far-IR beamline of the Australian Synchrotron. The transmission spectrum for each sample was recorded from 50 to 650  $\text{cm}^{-1}$  at 1  $\text{cm}^{-1}$  resolution using a 6 micron thick multilayer Mylar beamsplitter in combination with a Si bolometer detector; the bolometer was equipped with a 800  $\text{cm}^{-1}$  far-IR cut-on cold-filter consisting of a 13 micron polyethylene film overlaid with a 6 micron diamond scatter layer. 200 mA of synchrotron light operating in top-up mode was used as the light source. The samples were recorded both at room temperature and at 77 K. All sample spectra were divided by the relevant background spectra and baseline corrected.

### 2.3 X-ray Photoelectron Spectroscopy

X-ray Photoelectron Spectroscopy (XPS) is a surface sensitive technique that can probe the chemical and electronic state of elements within a sample. Experiments are undertaken by irradiating a sample with monochromatic, low energy X-rays, while measuring the kinetic energy and flux of the emitted photoelectrons that escape from within 10 to 100 Å of the sample surface. The technique is surface sensitive as photoelectrons emitted from deep within the sample undergo numerous attenuating interactions with the sample itself, thus exponentially reducing the number of photoelectrons that can escape into the vacuum the deeper they come from within the sample.

Photoelectrons are emitted if the binding energy of an electronic orbital is lower than the energy of the incident X-ray photon; when this occurs, the photoelectron kinetic energy corresponds to the incident X-ray energy minus the binding energy of the electronic orbital, as shown in Figure 2.2. These emitted photoelectrons are then typically filtered using a dispersive electron energy analyser, which can separate the emitted photoelectrons according to their kinetic energy. This allows for the measurement of the number of photoelectrons reaching the detector at a range of energies, producing an XPS spectrum as shown in Figure 2.3. The XPS spectrum consists of a series of peaks that correspond to the binding energies of the electronic orbitals for all elements present within a sample, which have binding energies less than the incident X-ray energy.

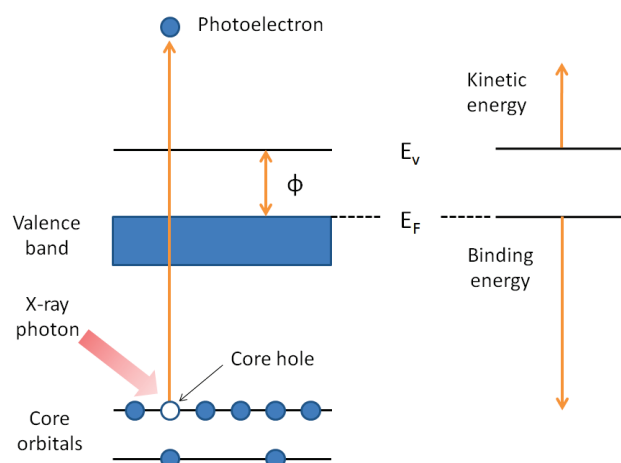


Figure 2.2: Emission of a photoelectron due to incident X-ray absorption. The photoelectron kinetic energy corresponds to the incident X-ray energy minus the binding energy of the electronic orbital.  $\Phi$  represents the work function for a solid sample. Figure adapted from an online resource.<sup>440</sup>

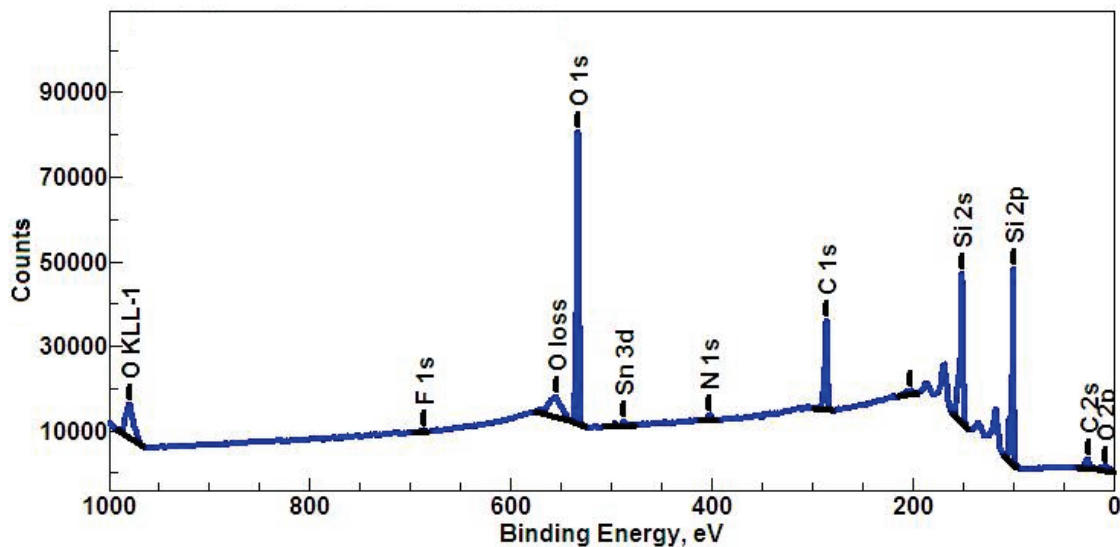


Figure 2.3: Survey XPS spectrum of showing the major contributing orbitals from various elemental species.<sup>441</sup>

Each element has a characteristic set of XPS peaks based upon the binding energy of its electronic orbitals. Even so, shifts in binding energies can arise due to changes in the initial (absorption and ionisation) and final (relaxation) states of the element, which depend on the local chemical environment. These binding energy shifts, relative peak intensities, and FWHM of peaks can provide important chemical information about the sample, including the type of bonding, element of nearby atoms, oxidation states, and more.

### 2.3.1 Sample Preparation and Apparatus

Samples were suspended in dichloromethane at concentrations of  $\sim 1 \text{ mg mL}^{-1}$ , and a  $10 \mu\text{L}$  drop of each solution was deposited onto clean  $6 \times 6 \text{ mm}$  silicon wafers then dried in air. Each sample was then fixed by double-side copper tape onto a gold-plated mount, which had space for six samples at a time. For a number of representative samples, various spots across the surface were investigated to ensure there was no significant variation between the XPS signals.

XPS data was recorded at the Soft X-ray Beamline at the Australian Synchrotron using a SPECS Phoibos 150 hemispherical electron analyser with the photon energy set to  $650 \text{ eV}$ . The beam was adjusted to yield an irradiation spot size of  $\sim 600 \times 600 \mu\text{m}$ , yielding an

X-ray photon flux of  $\sim 10^{12}$  photons  $\text{mm}^{-2} \text{s}^{-1}$ , conditions that have been shown not to induce thermal damage to samples of NaAuCl<sub>4</sub>.<sup>442</sup> High resolution XPS spectra of C, O, Si, P, Ti and Au were recorded at a pass energy of 10 eV, yielding an instrumental resolution of 295 meV.<sup>443</sup> Scans were repeated several times to ensure that no photon-induced changes occurred in the samples. The stability of the energy of the X-ray was also monitored using a bulk gold reference.

### 2.3.2 Peak Fitting

All XPS spectra were fitted by first applying a Shirley background to remove the electron-scattering background and to maintain the intrinsic line shape of the raw data.<sup>444,445</sup> The peaks were then fit with a pseudo-Voigt function composed of the sum of Gaussian (70%) and Lorentzian (30%) functions via nonlinear least-squares minimisation.<sup>446</sup> For the Au 4*f* doublet, the peak splitting was fixed at 3.67 eV, while for the P 2*p* doublet, a splitting of 0.84 eV was used.<sup>447</sup> All spectra were fit with the minimum number of peaks, allowing for variation in the FWHM; however, the FWHM for a single contributing species was kept constant. For example, for a Au spectrum fit with two sets of doublets, the FWHM within a single doublet was kept constant, yet allowed to differ between the two doublets.

## 2.4 X-ray Absorption Spectroscopy

X-ray Absorption Spectroscopy (XAS) considers the probability by which X-rays are absorbed by an atom of interest due to core level electron binding energies. The modulation of an atom's X-ray absorption probability due to its chemical and physical state allows for this technique to be sensitive to the oxidation state, coordination chemistry, structural properties, and the composition of other atoms immediately surrounding selected element.<sup>448</sup> X-ray absorption of an atom occurs when the incident X-ray energy is greater than the binding energy of a core electron, with the excess photon energy transferred to the ejected photoelectron. Given that the binding energy of core level electrons are unique and well defined for each element, there is a large difference in the binding energies between each element, allowing for good contrast between elements, even if the sample consists of a complex mixture.

This X-ray absorption process results in an excited state consisting of the ejected photoelectron and the core hole, which can decay either via X-ray fluorescence, where a higher core-level electron fills the core hole, ejecting an X-ray photon; or via the Auger effect, where an electron drops from a higher electronic shell and the energy is released in the form of an electron emitted into the continuum.<sup>448</sup> Experimentally, the X-ray absorption spectrum can be acquired by measuring either the transmission of incident X-rays through a sample, or via the observation of the X-ray fluorescence or Auger electrons, as the incident X-ray energy is systematically increased. This yields the energy dependence for the absorption coefficient ( $\mu$ ) as Equation 2.1 for transmission, or Equation 2.2 for fluorescence and Auger emission:

$$\mu(E) = \log(I_0/I) , \quad \text{Eq. 2.1}$$

$$\mu(E) \propto I_f/I_0 , \quad \text{Eq. 2.2}$$

where  $I_0$  is the intensity of the incident X-ray radiation,  $I$  is the intensity of the transmitted radiation, and  $I_f$  is the measured fluorescence intensity or Auger emission intensity. Interpretation of the X-ray absorption spectra is usually divided into two analysis regions; the X-ray absorption near-edge spectroscopy (XANES) region, which considers energies within  $\sim 30$  eV of the absorption edge, and extended X-ray absorption fine structure spectroscopy (EXAFS) region, as shown in Figure 2.4.

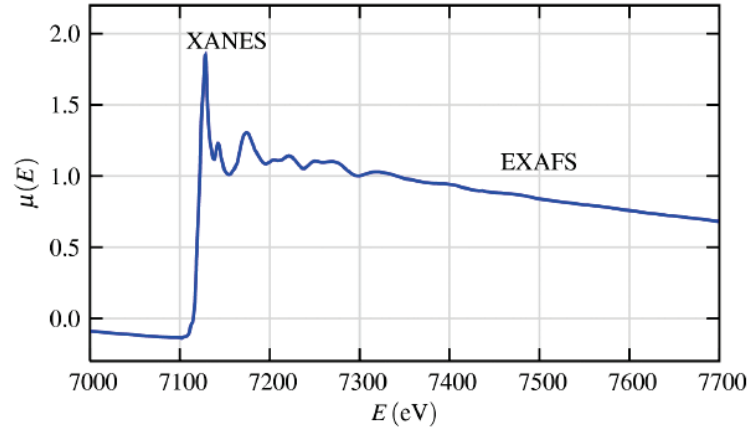


Figure 2.4: Typical X-ray absorption spectra of FeO showing the oscillatory behaviour arising from backscattering between the absorbing and neighbouring atoms.<sup>448</sup>

The excited photo-electrons created during the absorption process portray wave-like behaviour due to their inherent de Broglie wavelength, and can interact with neighbouring atoms, causing oscillatory behaviour in the post-edge region due to constructive and destructive wave interactions. This occurs when the photo-electrons scatter from nearby atoms before returning to the absorbing atom, which modulates the X-ray absorption, since the absorption coefficient depends on the available electronic states of the absorbing atom. These oscillations originate from the interference between outgoing and incoming photo-electron waves as illustrated in Figure 2.5. These oscillations depend on the chemical state of the surrounding atoms and allow for the extraction of useful information from X-ray absorption spectra via comparison to known chemical standards, or via modelling using the EXAFS function

$$\chi(k) = \sum_j \frac{N_j f_j(k) e^{-2k^2 \sigma_j^2}}{k R_j^2} \sin[2k R_j + \delta_j(k)] , \quad \text{Eq. 2.3}$$

where  $k$  is the photo-electron wavenumber,  $N$  is the coordination to nearby atoms,  $f(k)$  and  $\delta(k)$  are the scattering properties of nearby atoms,  $R$  is the distance to the neighbouring atom, and  $\sigma^2$  is the disorder in this distance. Modelling and data fitting of XANES and EXAFS is an extensive process that will not be covered here; for further information on the fundamentals of EXAFS, see the publication by Newville.<sup>448</sup>

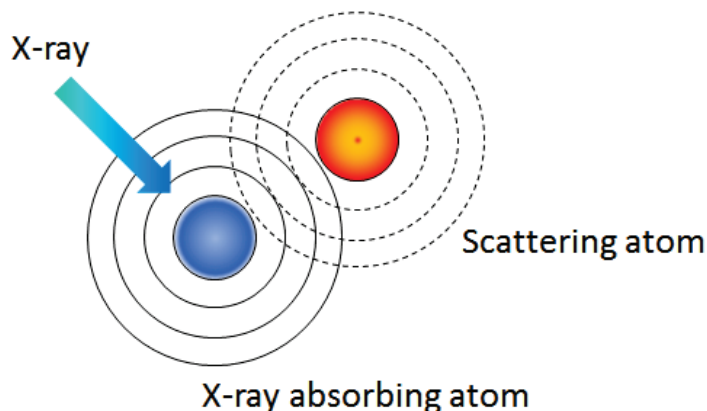


Figure 2.5: Illustration of X-ray absorption and wave overlap of the photo-electron with a nearby atom, resulting in backscatter and modulation of the X-ray absorption signal.

#### 2.4.1 Sample Preparation and Apparatus

Au-L<sub>III</sub>-edge X-ray absorption spectra were recorded at the Australian National Beamline Facility (ANBF, beamline 20B) at the Photon Factory, Tsukuba, Japan. Unsupported clusters were recorded in transmission mode as pressed pellets with a 1:5 dilution in cellulose that were ground into a fine homogenous powder. Supported cluster samples were recorded neat in fluorescence mode with the sample suspended in a 1×5 mm aluminium sample holder secured between Kapton tape and measured using a 36-pixel Ge-monolith fluorescence detector (Canberra/Unisys) at 90° to the incident beam. Harmonic rejection was achieved by detuning a channel-cut Si[111] monochromator by 50%. All data was collected at ~15 K using a closed-cycle He cryostat. The following energy ranges were used for data collection: pre-edge region from 11700 to 11900 eV (10 eV steps), XANES region from 11900 to 11960 eV (0.5 eV steps), and post-edge EXAFS region from 11960 to 13145 eV (0.05 Å<sup>-1</sup> steps in *k*-space). The Au(s) foil standard was used to calibrate the energy scale to the first peak of the first derivative of the Au-L<sub>III</sub> edge, assumed to be 11919 eV.

### 2.4.2 Data Analysis

Averaging of all collected data was performed in Average 2.0.<sup>449</sup> For XANES analysis, calibration, background subtraction, and linear regression analysis was performed in Athena.<sup>450</sup> The threshold energy was determined as the maximum of the first derivative of each spectrum in the near-edge region. Samples were calibrated to  $11919 \pm 0.05$  eV and linear combination fits between 11880 to 11980 eV were performed using the Au foil and the unsupported Au<sub>9</sub> cluster as components.  $E_0$  was fixed during the fitting procedure.

For the 3D multiple scattering models used for the unsupported Au<sub>8</sub> and Au<sub>9</sub> clusters, EXAFS analysis, including calibration and background subtraction, was performed using the XFIT 1.1 suite of programs<sup>449</sup> with FEFF6.<sup>451-453</sup> The Cartesian coordinates of the crystal structures for Au<sub>8</sub><sup>430</sup> and Au<sub>9</sub><sup>431</sup> were used to create a starting model. Model refinement was undertaken in R-space between 1-4 Å with sharp cosine cut-offs, a k-window of 2–18 Å<sup>-1</sup> with soft cosine cut-offs, a maximum effective path length of 4 Å, and 4 maximum legs in a multiple-scattering path. Each Au atom was modelled as an absorbing atom, with the  $E_0$  and  $S_0^2$  coefficients of all absorbing atoms constrained to two variables (i.e one  $E_0$  variable and one  $S_0^2$  variable for all Au atoms). Restraints were imposed for the Debye-Waller factors (0.02–0.001) to ensure physically realistic values, and the Debye-Waller factors for all P atoms were constrained to a single variable. The Debye-Waller parameter is modelled using the isotropic uncorrelated vibration model as implemented in XFIT.

For the bulk gold multiple scattering model used for the supported Au<sub>9</sub> clusters, EXAFS analysis, including calibration and background subtraction, was performed using Athena and Artemis.<sup>450</sup> The bulk gold model was created using a FCC (space group F m 3 m) bulk gold lattice<sup>454</sup> with a cluster size of 8 Å and longest path length of 7 Å, resulting in a 134 atom model used as FEFF6L<sup>451-453</sup> input in Artemis with 4 maximum legs in a multiple scattering path, generating 53 unique scattering paths. Model refinement was undertaken using all 53 paths in R-space between 1–7 Å with sharp linear cut-offs and a k-window of 3–16 Å<sup>-1</sup>.  $\Delta R$  was modelled using the volumetric expansion coefficient for a cubic crystal lattice

$$\Delta R = \alpha R_{\text{eff}} , \quad \text{Eq. 2.4}$$

where  $\alpha$  is the volumetric expansion coefficient and  $R_{\text{eff}}$  is the effective path-length of each scattering path. The correlated-Debye model was used for modelling disorder as implemented in Artemis.<sup>455</sup>  $E_0$ ,  $\alpha$ , and the Debye-temperature ( $\Theta_D$ ) are the three variables that were refined during the fitting process.  $\Theta_D$  was restrained between 0 to 1000 and  $S_0^2$  was fixed at 0.9.

## 2.5 Transmission Electron Microscopy Studies

High-resolution transmission electron microscope (HRTEM) experiments were performed by David P. Anderson using a 200 kV Philips CM200 at the University of Canterbury, New Zealand. Approximately 0.5 mg of TiO<sub>2</sub>-supported cluster samples were dissolved in 2 mL of diethyl ether, of which 20  $\mu$ L was then micro-pipetted onto an amorphous carbon coated copper TEM grid. Samples were then dried under a gentle flow of N<sub>2</sub>, followed by drying under vacuum for 1 hr before being loaded into the sample holder of the TEM. Au<sub>101</sub> cluster samples were placed into the sample holder immediately after pipetting, as the cluster can rapidly agglomerate in solution due to the lability of the PPh<sub>3</sub> ligands for this sample. Particle size resolution was limited to approximately 1 nm due to the level of contrast between the nanoparticles and the carbon film of the copper TEM grids, in addition to poor electron beam quality.

Angular dark field scanning transmission electron microscope (ADF-STEM) experiments were performed by Shery Chang using a double-corrected FEI Titan<sup>3</sup> 80–300 FEGTEM at Monash University, Australia. Two samples concentrations were used: The first sample had approximately 1 mg of the Au<sub>9</sub>(PPh<sub>3</sub>)<sub>8</sub>(NO<sub>3</sub>)<sub>3</sub> cluster suspended in 10 mL of high purity methanol; the second sample had 1 grain of Au<sub>9</sub>(PPh<sub>3</sub>)<sub>8</sub>(NO<sub>3</sub>)<sub>3</sub> suspended in 6 mL of high purity methanol. For each of these samples, a small droplet was deposited onto an agar holey carbon film and dried under pure N<sub>2</sub> gas.

## 2.6 Photocatalysis Investigations

In order to investigate the gas-phase photocatalytic capability of small Au clusters supported on TiO<sub>2</sub> nanoparticles under ambient conditions, a new experimental apparatus was designed as part of this project that would enable the accurate measurement of a range of reaction products simultaneously, as the reaction proceeds in real-time. The experimental procedure and apparatus went through multiple revisions, testing, and development during the project, with the final revision at the time of writing for this thesis presented below.

### 2.6.1 Description of the Photocatalysis Experimental Apparatus

The experimental apparatus consists of two main sections, the vacuum system, and the reaction cell, as shown in the schematics of the experimental apparatus in Figure 2.6 and Figure 2.7. Where possible, 316 stainless steel and metal gaskets have been used in all construction to minimise contamination.

The reaction cell itself consists of a custom-built 316 stainless steel chamber machined in the school workshop. It consists of an internal chamber for samples to reside in with ~6.15 mL of volume including ports. This is covered by a fused silica window (Esco Optics, S1-UV, P110188) and sealed using a nitrile O-ring that sits in a recess. The window is held in place against the O-ring via a removable mounting cap above the sample chamber, which is held in place via six bolts. This allows for quick and easy sample changeover and convenient access to the inside of the chamber for cleaning purposes. The six inlet and outlet ports are connected to the internal chamber via 2 mm boreholes leading to a tapped 1/8" NPT thread, whereby the external Swagelok is connected and sealed using yellow PTFE gas-rated thread sealing tape.

The reaction cell is isolated from the vacuum line and two liquid vessels via plug valves (Swagelok P4T series). The two liquid vessels are used for introducing volatile liquids into the reaction cell. Dissolved gases are removed from the liquid in these cells by freezing with liquid N<sub>2</sub>, evacuating the liquid cell for five minutes to remove any evolved gas, and then thawing the liquid. This process is repeated two more times, to ensure the removal of all dissolved gases. The pressure in the reaction cell is monitored by a gas independent piezo silicon diaphragm gauge (TerraNova Model 808 vacuum sensor) and

associated controller (TerraNova Model 809 diaphragm gauge controller) providing a 2% accuracy and range of 1-1000 Torr. The pressure can be roughly monitored below 1 Torr via the thermocouple gauge attached to the vacuum line during pumping. The primary pulsed nozzle (Parker, Series 9 Pulse Valve) is used to pulse controlled amounts of gas from the reaction cell into the vacuum system, which has a residual gas analyser (RGA) for sampling of the gas mixture (*vide infra*). The pulsed nozzles are driven by a custom-built pulsed nozzle driver that interfaces to the acquisition computer via an RS232 port and is controlled by LabVIEW software written during the course of the project. Typical pulse rates range from 0.9 to 10 Hz with a pulse width of 26 or 27 ms and is controlled in real-time via a proportional-integral-derivative (PID) software controller in the LabVIEW code. This allows full control of the amount of gas being delivered and the rate at which it is delivered, while maintaining an appropriate pressure level in the vacuum system for safe operation of the RGA at calibrated pressures.

The reaction cell is in direct thermal contact with a hollow 316 stainless steel water conduit, which is connected to a water bath (Thermoline scientific, LWB-311DS). This allows for stable and accurate temperature control of the reaction cell ( $\pm 0.1$  °C) via the heater controller of the water bath, and acts as a thermal reservoir due to any heat released via catalysis or added to the system via the UV light. The temperature of the reaction cell is also independently monitored by a thermistor (Jaycar, NTC 100 $\Omega$ ) lab-wired and attached directly to the side of the reaction cell, which is measured via a DAQ card (Measurement Computing, USB-1608FS-Plus). The DAQ card is connected to the acquisition computer, and interfaces via USB to the LabVIEW control software to record thermistor temperature readings, vacuum system pressure (from the Agilent Technologies XGS-600), reaction cell pressure (Silicon diaphragm gauge), and can also control the vacuum system gate valve.

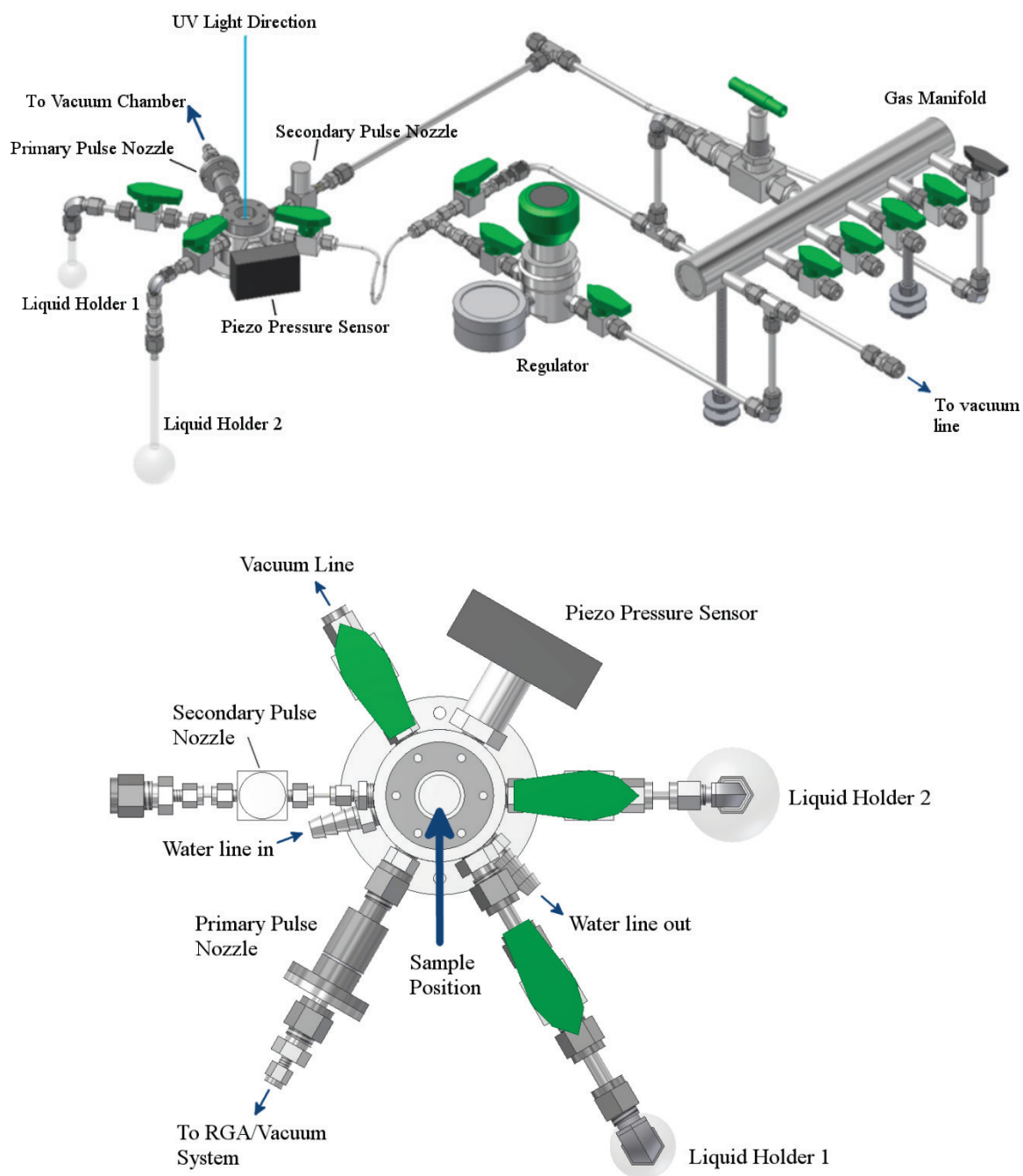


Figure 2.6: Isometric view of the ambient pressure segment of the apparatus (top) and overhead view of the custom-built reaction cell (bottom). The thermistor that is typically attached directly to the side of the reaction cell walls has been omitted for clarity. See the text for detail of individual components.

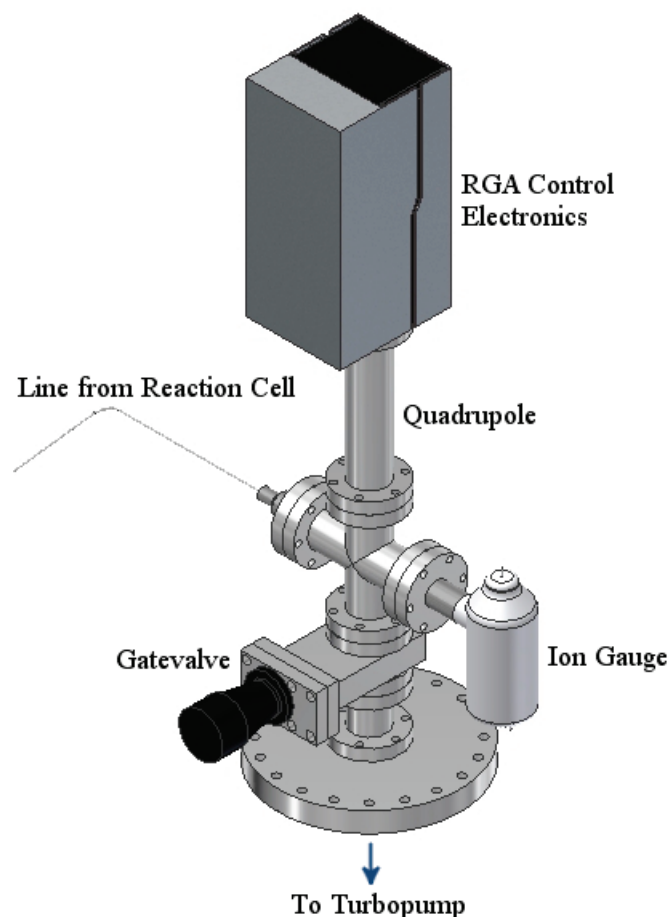


Figure 2.7: Isometric view of the vacuum system. See the text for detail of individual components.

The gas manifold is attached to a series of gas bottles including  $N_2$ ,  $O_2$ ,  $CO_2$ ,  $CO$ , and  $Ar$  that can be mixed at various partial pressures within the gas manifold if necessary by utilising the pressure gauge attached to the regulator (Swagelok KPR Regulator, KPR1DFM411A20000). Gas can then be delivered to the reaction cell either via the regulator, or for more precise pressure control, via the secondary pulsed nozzle (Parker, Series 9 Pulse Valve). The manifold and reaction cell can be evacuated via a sealed rotary vane pump (Edwards, E2M0.7) with an oil trap (Edwards, FL20K) to prevent oil back-streaming into the system. The vacuum pressure is monitored via a thermocouple tube (Duniway, DST-531) controlled via a combined ion and thermocouple gauge controller (Agilent Technologies, XGS-600).

The ultraviolet light is provided by a small LED lamp (Shenzhen UVET, UV50-S) that produces 368 nm light with a FWHM of 11.98 nm, as shown in Figure 2.8. It is controlled

by a custom-wired power supply with adjustable current to control the intensity of the light; the maximum power setting results in a power output of  $58.1 \text{ mW}\cdot\text{cm}^{-2}$  at 17 cm distance from the light source.

The 1/16" line from the primary pulsed nozzle to the vacuum chamber is connected via an ultra-Torr connection (Swagelok, SS-1-UT-A-4) welded into a 2.75 ConFlat flange. The vacuum chamber consists of an RGA (Stanford Research Systems, RGA200) with a channel electron multiplier (CEM), controlled via Stanford Research Systems RGA software for data collection. Pressure is measured by a Bayard-Alpert ionisation gauge with a tungsten filament (Duniway, T-CFF-275) monitored via a combined ionisation gauge and thermocouple controller (Agilent Technologies, XGS-600). The gate-valve (Kurt K. Lesker, SG0150PCCF) is controlled via a VAC Digital Output Module (Opto 22, SNAP-OAC5) which is triggered by the DAQ card for vacuum system isolation and control. In order to reduce contamination of the vacuum system to ensure analytical results, the system is pumped via an oil-free turbo-pump (Varian, Turbo-V 550) controlled via the corresponding turbo-pump controller (Varian, Turbo-V 550 controller), backed by a rotary vane pump (Edwards, E2M8) with mesh oil trap (Duniway AFT-NW25-4) to minimise oil back-streaming from the pump, and is monitored via another thermocouple tube (Duniway, DST-531). It should be noted the turbo-pump is of far greater size than necessary and was used due to its availability as surplus equipment.

The configuration of the RGA Electronic Control Unit for all experiments are as follows: firmware revision 0.24; Ioniser electron energy is 70 eV, emission current is 1.00 mA, ion energy is high, and focus plate voltage is 90 eV; CEM high voltage is 1523 V, CEM gain is 308, and bias voltage is 1525 V. The partial pressure sensitivity calibration factor used for converting current into units of Torr is  $5.78 \times 10^{-5}$  Amps/Torr.

Typical operating pressures of the vacuum system range from  $2 \times 10^{-9}$  Torr when idle, to  $2 \times 10^{-6}$  during experimental conditions when gas is being pulsed from the reaction cell to the vacuum system. During experiments, the reaction cell typically contains 300 Torr of gas, but can be operated at ambient pressure and beyond. The maximum pressure rating of the reaction cell has not been tested beyond 2000 Torr.

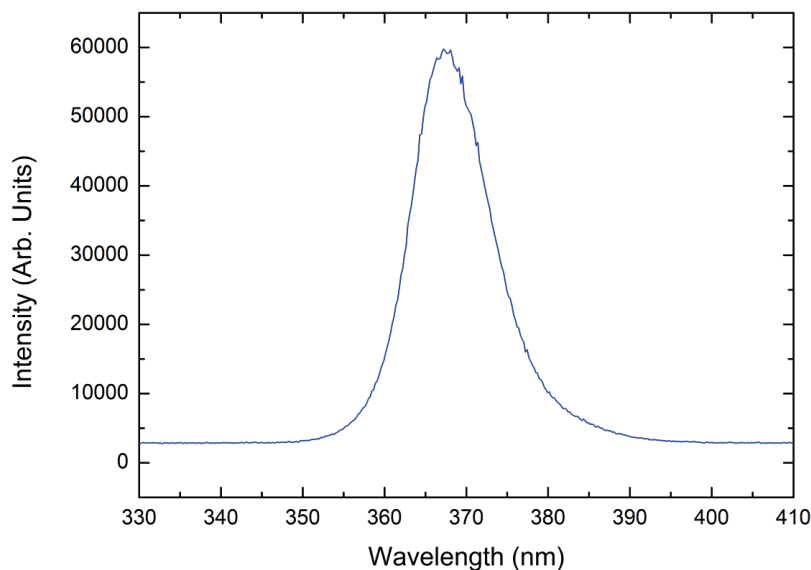


Figure 2.8: UV LED spectral bandwidth showing a  $\lambda_{\text{max}}$  of 368 nm and FWHM of ~12 nm.

### 2.6.2 Sample Preparation

For photocatalysis experiments, a small amount of  $\text{TiO}_2$ -supported sample (~12 mg) was suspended in methanol (~3 mL) and drop coated onto multiple glass microfiber discs (PALL Glass Fiber Filter, 61628) of 13 mm diameter, allowing the solvent to evaporate between each drop of suspension, leaving the  $\text{TiO}_2$ -supported sample behind and adhered to the surface of the microfiber disc. This yielded microfiber discs with 3–5 mg of supported sample adhered to the surface, which were then stored in airtight glass vials. Heating of samples was avoided at all steps of the preparation to prevent agglomeration of the clusters and maintain post-treatment consistency. After preparation, samples were typically used in the experiment within five days.

### 2.6.3 Experimental Procedure

When running experiments, the reaction cell faceplate and silica window are removed by unscrewing the six threaded bolts that hold the faceplate to the reaction cell chamber. A sample adhered to a glass microfiber disc is placed in the reaction cell cavity, and the silica window and faceplate are then re-secured. The sample cell is then evacuated to  $3 \times 10^{-2}$  Torr for 10 minutes to 12 hours depending upon the nature of the experiment. The

vacuum line is then closed, and the reactant gases of interest are added to the cell from either the gas manifold or from the vapour pressure of a liquid contained within a liquid holder. After the gases of interest are added the reaction cell, Ar is added as a bath gas to raise the pressure to 300 Torr. The gases are given time to equilibrate to the reaction cell temperature which is typically at 28° C, a couple degrees lower than the water flowing through the lines due to thermal losses through the stainless steel connections.

Once the reaction cell has been prepared, the LabVIEW program is executed, which begins pulsing gas from the reaction cell into the vacuum system, whilst simultaneously starting the data collection of the RGA control software to begin recording partial pressures of reactants by scanning through a defined mass range in histogram mode. The PID controller within the LabVIEW software controls the pulse rate and pulse width of the pulsed nozzle to ensure a stable flow of gas from the reaction cell to the vacuum system and maintains the vacuum system pressure within 2% of the  $2 \times 10^{-6}$  Torr target pressure. This is the same pressure that all calibrations are performed at, as shall be discussed in the calibration section. After pulsing for 30 to 60 minutes to obtain a suitable background, the UV LED is switched on and the sample is irradiated with 27.4 mW of light, which equates to  $20.7 \text{ mW cm}^{-2}$  over the sample disc. The gas mixture is continually monitored by the RGA as the reaction proceeds, until the reaction is deemed complete or an appropriate amount of time has elapsed for quantitative data analysis.

### 2.6.4 Residual Gas Analyser and Quadrupole Ion Filter

The RGA is a quadrupole mass spectrometer specifically designed for the detection of partial pressures of gases inside a vacuum system. The basic operational components of an RGA consist of an electron impact ioniser, followed by a quadrupole ion filter, and finally a type of ion detector, as shown in the RGA schematic of Figure 2.9. In operation, a small fraction of gas molecules in the vacuum system are ionised to become positive ions, separated according to mass via the quadrupole mass filter, and the current of the remaining ions are detected at the ion detector. In this way, the quadrupole mass filter can be cycled through all the masses of interest, and the ion current can be measured at each mass and converted to partial pressures to produce a mass spectrum. The operation of the instrument is controlled automatically via software supplied by the manufacturer.

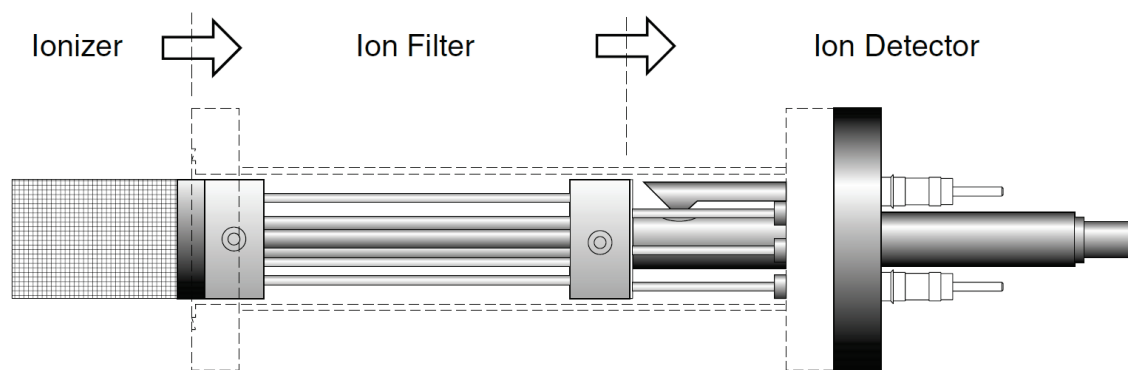


Figure 2.9: Schematic cross-section of the RGA probe used in the experimental apparatus, showing the key areas of operation.<sup>456</sup>

### 2.6.5 Data Acquisition

During the procedure outlined previously for running an experiment, the RGA software is operated in histogram mode between masses 1 to 65, which takes seven measurements per amu, with a range of 0.6 amu centred at each mass. The RGA then sends the maximum current detected of those seven points to the RGA acquisition program for storage. This eliminates any spurious results due to a drift in the mass-axis calibration of the RGA when running a histogram scan. The scan is run at the slowest possible scan speed to decrease the noise floor and increase the signal to noise ratio. This mode results in a single datum per mass measured as current. This current is automatically converted to units of pressure (Torr) via the calibrated partial sensitivity factor stored in the RGA Electronic Control Unit. This results in a typical histogram mass spectrum, where the x-axis is mass, and the y-axis is partial pressure. Each histogram scan data is then converted to ASCII text files and saved in a specified folder for further analysis.

While the RGA software is acquiring data, the LabVIEW program is also acquiring data while it controls the pulsed nozzle parameters. Every second, the program logs the vacuum pressure measured by the ion gauge, the pressure in the reaction cell measured by the silicon diaphragm gauge, the reaction cell temperature measured by the thermistor attached to the side of the reaction cell, and the water bath temperature measured by a thermistor in the water bath. This data is automatically saved to an excel spreadsheet in the same folder as the related ASCII text files produced by the RGA software for further analysis.

### 2.6.6 Post-Experiment Data Analysis

After the experiment has been completed, post-processing of the collected data is necessary to obtain the quantitative gas composition of the reaction cell over the course of the experiment. The partial pressure data collected by the RGA and the reaction cell sensor data is parsed using a post-experimental LabVIEW program coded by our group. In order to correlate the partial pressures measured by the RGA in the detection chamber to the partial pressures in the reaction cell, there are a number of steps that must be undertaken. First, the time taken per histogram scan is calculated (typically 132 seconds for a scan from 1 to 65 amu at the slowest scan speed), and the acquisition start time is aligned with the reaction cell sensor data, which has a polling rate of 1 Hz. The reaction cell sensor data then has a moving average applied over 25 seconds for the pressure and temperature to smooth out the electrical noise, and is inspected to ensure that there was no abnormal temperature fluctuations during the course of the experiment. The absolute partial pressures measured by the RGA are then converted to % contributions for each histogram scan by the equation

$$\%P_g = \left( \frac{P_g C_g}{P_{\text{Total}}} \right) 100, \quad \text{Eq. 2.5}$$

where  $P_g$  is the sum of partial pressures of gas  $g$  based upon known fragmentation patterns,  $C_g$  is the calibration factor applied based on calibration experiments, and  $P_{\text{Total}}$  is the total pressure inside the vacuum system as measured by the RGA.

Typically, gases used in experiments are designed to prevent the daughter ions of one gas to overlap the parent ion of another. However, if this cannot be avoided, looking at the parent ions only and their fragmentation ratio, or multiple non-linear regression fitting using a set of expected gas fragmentation patterns can be used to determine the ratio of gases present in the system.

The % contributions of each gas in the vacuum system are assumed to be representative of the % contribution in the reaction cell. This is possible since the background pressure of the vacuum system at idle is  $\sim 2 \times 10^{-9}$  Torr or lower. It can therefore be assumed that by pulsing gas into the vacuum system at  $2 \times 10^{-6}$  Torr (1000 times greater than background) that the gas composition the RGA measures consists of 99.9% gas from the reaction cell, with only 0.01% contribution from background gases present in the vacuum system. Hence, the gas composition that the RGA measures inside the vacuum system is an

accurate representation of the gas composition present in the reaction cell at any point in time while gas is being delivered from the reaction cell into the vacuum system.

Since the volume of the reaction cell is known, the % contributions within the reaction cell for each histogram scan can be converted to moles via the ideal gas law  $PV=nRT$ , which can be written as

$$n_g = \frac{P_{rc} V_{rc}}{RT_{rc}} \frac{\%P_g}{100}, \quad \text{Eq. 2.6}$$

where  $P_{rc}$  is the pressure of the reaction cell at the time of each histogram scan as measured by the silicon diaphragm gauge attached to the reaction cell,  $V_{rc}$  is the volume of the reaction cell,  $R$  is the ideal gas constant in units of L Torr K<sup>-1</sup> mol<sup>-1</sup>,  $T_{rc}$  is the temperature of the reaction cell at the time of each histogram scan as measured by the thermistor attached to the reaction cell, and  $\%P_g$  is the % contribution of gas  $g$  as determined by Equation 2.5. It should be noted that the ideal gas law is appropriate given the ambient pressure and temperature conditions that the experiment is operated under. Given that the time taken for each histogram scan is known, the data can be plotted in the form of time(s) on the x-axis, and number of moles of gas  $g$  on the y-axis as shown in Figure 2.10. The data then undergoes a fitting procedure to determine production rates as outlined in the following text.

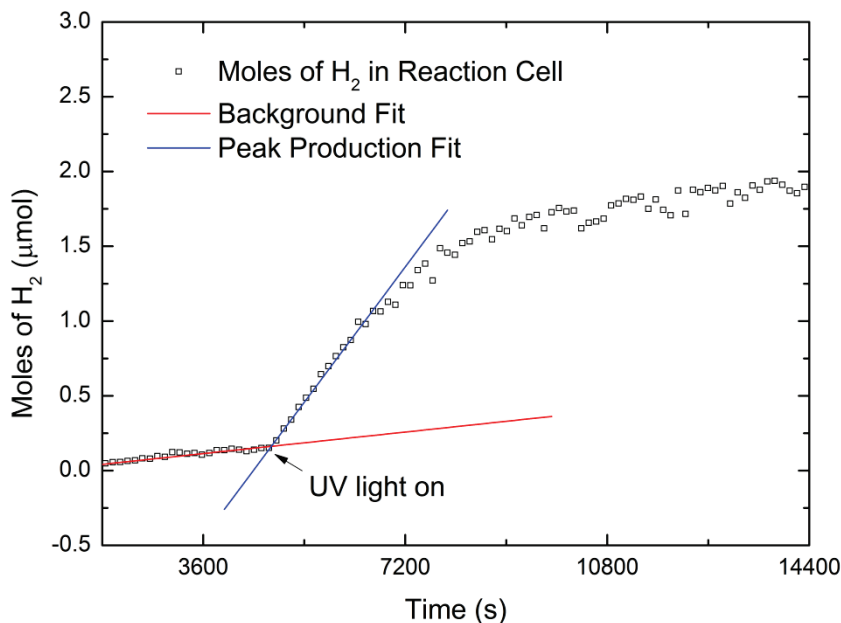


Figure 2.10: Typical increase of H<sub>2</sub> gas observed in the reaction cell during photocatalytic experiments.

In order to determine peak production rate for a given gas, a linear or logarithmic background is fit to the first 30–60 minutes of data, which is then used to background subtract the data. A linear line of best fit is then applied to the first 20 minutes of data after the UV light is switched on, which yields a peak production rate in units of  $\mu\text{mol s}^{-1}$ . Given that the mass of each sample is measured before experiment, and the surface area of the microfiber discs is also known, peak production rates are typically presented in units of  $\mu\text{mol hr}^{-1} \text{g}^{-1} \text{cm}^{-2}$ , which are often used in the related literature. The mass weighting uses the total Au/TiO<sub>2</sub> catalyst mass. Two to three experiments are typically performed for a given sample, with fresh catalyst used each time. From these multiple experiments of the same sample, the results are combined to yield a average peak production rate and standard error of the mean for each gas of interest. For those samples where only a single experiment was performed successfully, the error is estimated to be approximately 10% based upon the typical standard error of the mean observed for other samples. The overall procedure is summarised in the flowchart of Figure 2.11.

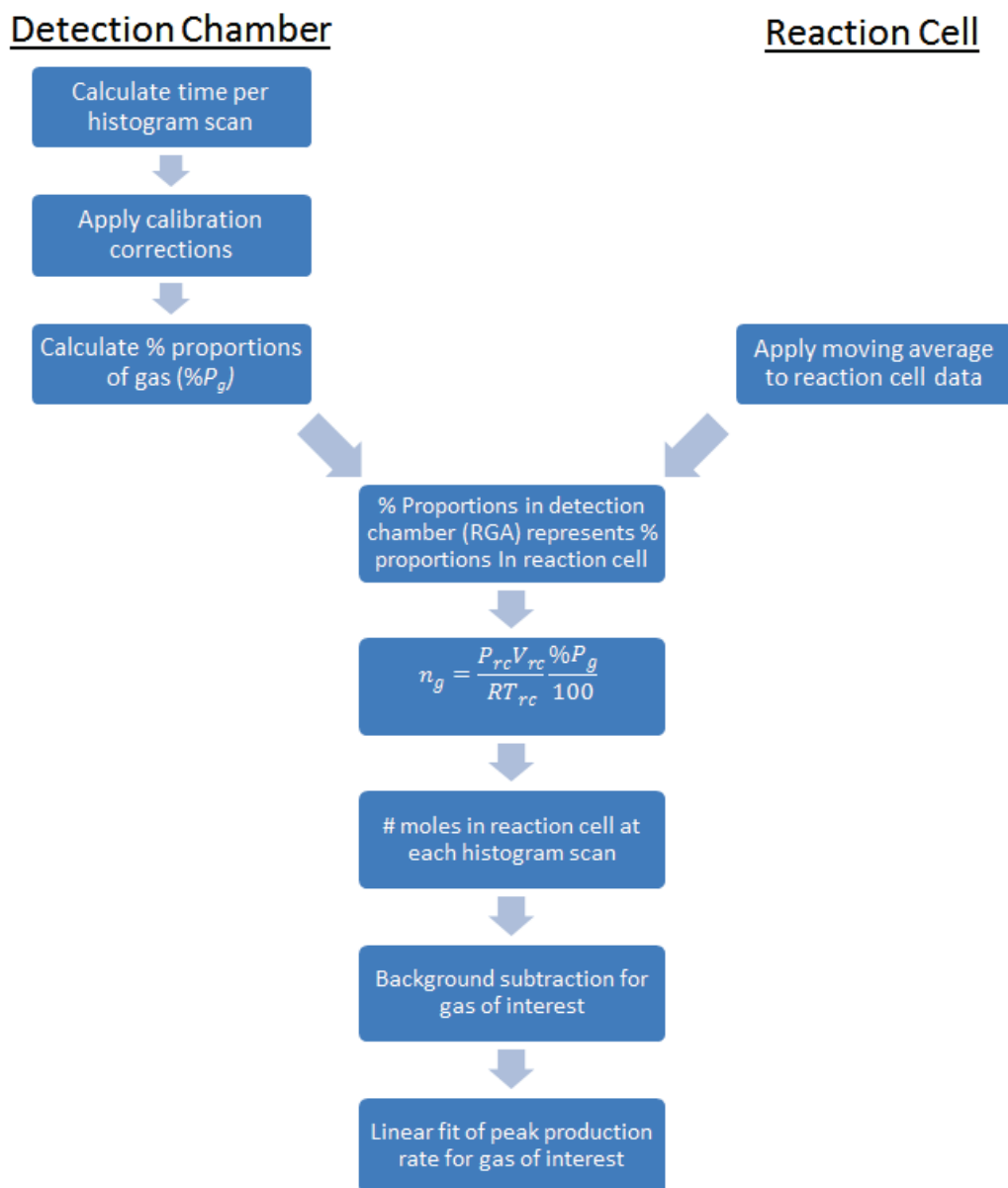


Figure 2.11: Flowchart of the post-experimental data processing steps undertaken to achieve quantitative analysis of the reaction cell gas composition over the course of the experiment and resultant production rate.

### 2.6.7 Calibrations

The RGA itself has two inbuilt calibration functions for peak tuning and partial pressure sensitivity factors that are carried out following the protocols outlined by Stanford Research Systems for this instrument.<sup>456</sup> The former is conducted to ensure that the peak positions are accurate in terms of mass position, and that the peak widths are sufficiently narrow to minimise spill-over of one mass peak into the adjacent peak. The latter

calibration is required to convert the current measured by the Faraday cup (FC) or CEM into partial pressures, and is undertaken using pure N<sub>2</sub> at a vacuum pressure of  $2 \times 10^{-6}$  Torr.

In order to ensure quantitative results for gas composition analysis, calibration gas (Matheson TriGas, Micro Mat 14) is introduced to the reaction cell consisting of a mixture of CO<sub>2</sub> (5.004%), CO (5.001%), N<sub>2</sub>(5.000%), O<sub>2</sub> (4.003%), CH<sub>4</sub> (3.997%), H<sub>2</sub> (3.999%), and He (72.996%), with a mixture accuracy of  $\pm 2\%$ . As the gas mixture is pulsed into the vacuum system at  $2 \times 10^{-6}$  Torr, histogram scans are collected over an hour and the data for each mass is averaged. These calibration experiments are performed multiple times, and all data combined to yield an averaged histogram plot. The fragmentation pattern of each gas known to be present in the gas mixture is then fit using multiple non-linear regression to determine the % contribution of each gas species as measured by the RGA. The difference between the % contribution as determined by the RGA and that specified by the manufacturer of the calibration gas bottle provides a calculated calibration factor, which can then be used to quantitatively measure the gas composition of the vacuum system during photocatalysis experiments as discussed earlier. These differences are due to the variation in ionisation cross-section and ionisation efficiency of different molecules depending upon the ionisation source, and varying mass sensitivity for the CEM. Concerns about gas fractionation and non-linear detector response are addressed in the following two subsections.

### 2.6.7.1 Gas Fractionation

Gas fractionation is the effect of lighter gas species flowing through an aperture at a faster rate than heavier species. This effect can be reduced by ensuring that a small molecular leak is used, along with a large gas source relative to the gas flow.<sup>457</sup> In order to ensure quantitative results, experiments were undertaken to investigate if the primary pulsed nozzle was affected by gas fractionation under typical experimental conditions by tracking the partial pressures of a mixture of He and Ar gas. If fractionation were occurring, then the relative ratio of He/Ar would change over time as more of one gas was pulsed out of the reaction cell compared to the other. Figure 2.12 shows that the relative ratio of He/Ar stayed practically constant over the course of the experiment, indicating that there is no notable level of gas fractionation occurring over five hours.

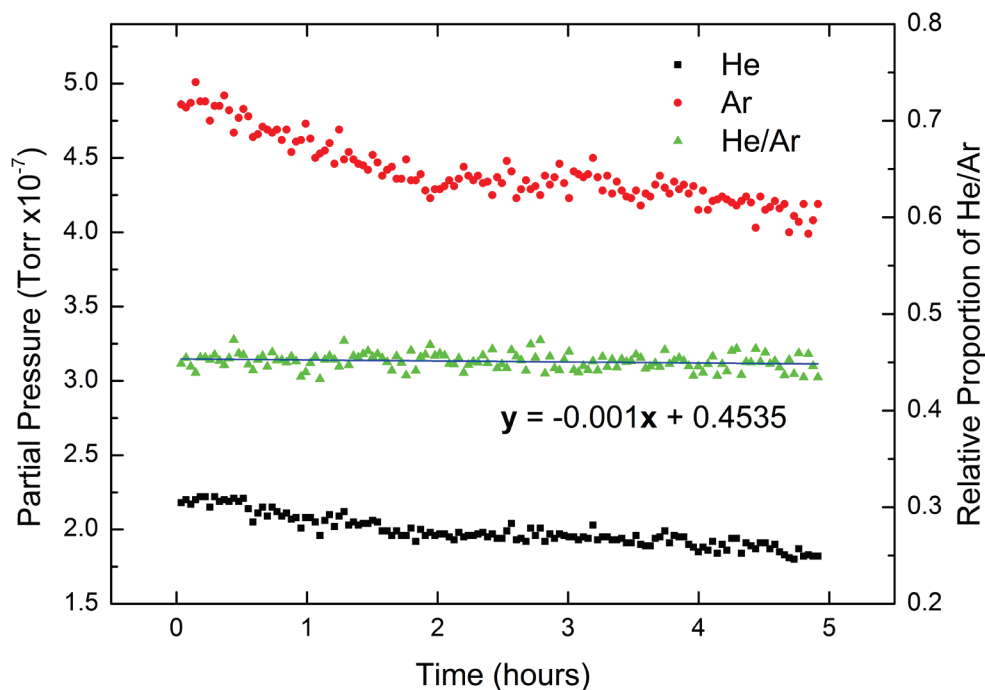


Figure 2.12: Uncorrected partial pressure of He and Ar in the reaction cell, showing both species decreasing at the same rate. The ratio of He/Ar has been fit with an almost flat linear line, with the equation of the line shown beneath.

### 2.6.7.2 Linear Detector Response

One of the key assumptions made during measurements is that the response of the RGA detector to the partial pressure of gas is linear up to the operating pressure of  $2 \times 10^{-6}$  Torr. Linear operation of the RGA should be expected up to  $10^{-4}$  Torr according to the RGA manual.<sup>456</sup> Operation of the RGA well below this pressure helps reduce the number of collisions between ions and neutral gas molecules by maximising the mean free path of the ions, as well as reducing the chance of charge exchange reactions ( $X + Y^+ \rightarrow X^+ + Y$ ) from occurring, both of which would bias the mixture analysis.<sup>457</sup> Keeping the pressure under this limit would also help to reduce the effect of fractionation by ensuring that gas flow is maintained in the molecular flow regime. Pure  $N_2$  gas was introduced to the vacuum system and the partial pressure measured by the RGA was compared to that measured by Bayard-Alpert ionisation gauge attached to the vacuum system. Both the RGA CEM and FC response were found to be linear as shown in Figure 2.13.

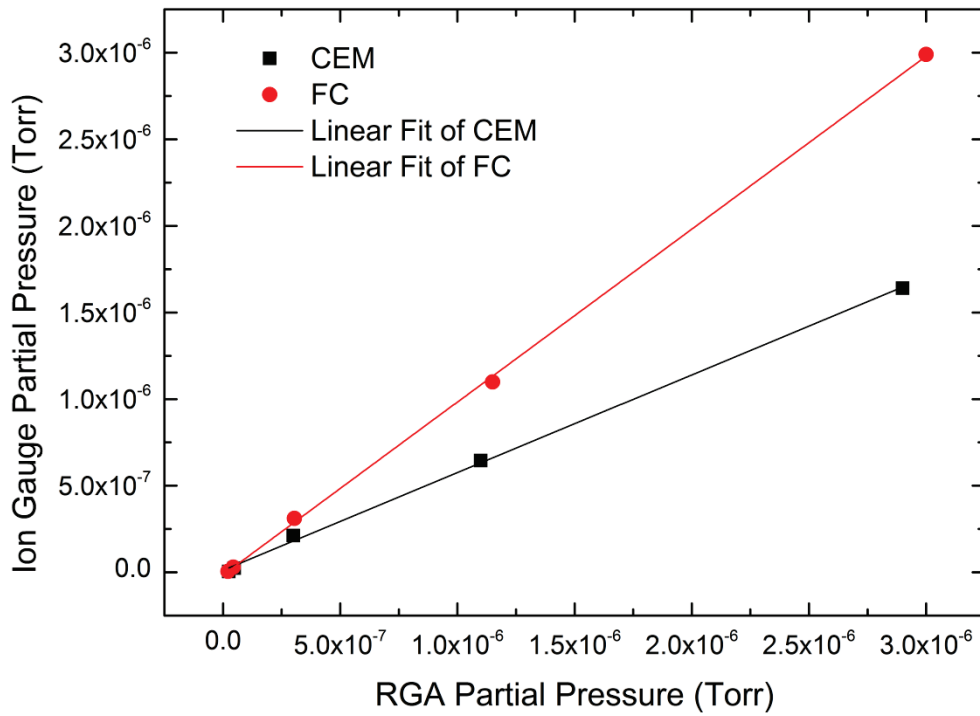


Figure 2.13: Comparison between the partial pressures measured by the Bayard-Alpert ionisation gauge and the two detectors of the RGA, showing a linear response for a range of pressures from  $4 \times 10^{-9}$  to  $3 \times 10^{-6}$ .

# Chapter Three

Computational Theory and Method

### 3 Computational Theory and Method

#### 3.1 Introduction to Density Functional Theory

Density functional theory (DFT) can predict the molecular properties of a chemical system directly from theoretical calculation. It has become a very popular and widespread theoretical tool for both quantum chemistry and condensed-matter physics due to its accuracy and computational efficiency. It is also the only approach viable when considering the heavy metals and very large size of the systems to be calculated in this work.<sup>458</sup> The theoretical framework behind DFT is intricate and only a brief summary of the key principles will be described in the following sections.

##### 3.1.1 The Schrödinger Equation

The aim of most modern quantum chemical calculations is to find an approximate solution to the time-independent Schrödinger equation to obtain the total ground-state energy for a molecular system,

$$\hat{H}\Psi_0(\vec{r}_N, \vec{R}_M) = E_0^{\text{tot}}\Psi_0(\vec{r}_N, \vec{R}_M), \quad \text{Eq. 3.1}$$

where  $E_0^{\text{tot}}$  is the total energy of the ground-state,  $\Psi_0$  is the ground-state wavefunction, and  $\hat{H}$  is the Hamilton operator for a molecular system of  $N$  electrons and  $M$  nuclei (expressed as position vectors) in the absence of magnetic or electric fields, which returns the system energy. The Hamilton operator typically takes the form

$$\hat{H} = \hat{T}_e + \hat{T}_N + \hat{V}_{eN} + \hat{V}_{NN} + \hat{V}_{ee}, \quad \text{Eq. 3.2}$$

where  $\hat{T}_e$  and  $\hat{T}_N$  represent the kinetic energy contribution of the electrons and nuclei respectively, while  $\hat{V}_{eN}$ ,  $\hat{V}_{NN}$ , and  $\hat{V}_{ee}$  represent the potential energy contribution from the electron-nucleus, nucleus-nucleus, and electron-electron interactions, respectively. Exact solutions to the total Hamilton operator are impossible for anything other than single electron cases however, due to the difficulties of solving a many-body problem of correlated particles. Therefore, a number of approximations are made to solve the Hamiltonian for more complex systems.

The Born–Oppenheimer approximation can simplify the Hamiltonian by considering that nuclei move far slower than electrons due to their significant difference in mass. This

allows for the approximation that the electrons are moving in a fixed field of nuclei; therefore, the kinetic energy contribution from the nuclei becomes zero ( $\hat{T}_N = 0$ ), the potential energy due to nuclei-nuclei interactions becomes fixed for given nuclear positions, and correlation in the electron-nuclear potential energy is eliminated. These approximations allow for the total energy of the system to be expressed as

$$E_0^{\text{tot}} \approx E_{\text{NN}} + E_0^{\text{elec}}, \quad \text{Eq. 3.3}$$

where  $E_{\text{NN}}$  is the fixed potential energy of the nuclei-nuclei interactions and  $E_0^{\text{elec}}$  is the ground state electronic energy contribution to  $E_0^{\text{tot}}$ .  $E_0^{\text{elec}}$  can then be obtained by solving the electronic Schrödinger equation

$$\hat{H}_{\text{elec}} = \hat{T}_e + \hat{V}_{eN} + \hat{V}_{ee}. \quad \text{Eq. 3.4}$$

This simplifies the solution to the Schrödinger equation, as the electronic coordinates are independent variables with the nuclear coordinates entering as a parameter to the final solution.

$$\hat{H}_{\text{elec}} \Psi_0^{\text{elec}}(\vec{r}_N; \vec{R}_M) = E_0^{\text{elec}} \Psi_0^{\text{elec}}(\vec{r}_N; \vec{R}_M). \quad \text{Eq. 3.5}$$

### 3.1.2 The Variational Principle

In order to find a solution for the Schrödinger equation for a given system, the correct wavefunction from the subset of all possible  $N$ -electron wavefunctions ( $\Psi_{\text{trial}}$ ) must be selected.<sup>459</sup> This is not trivial, however, as there is a computationally unfeasible number of possible solutions. The variational principle states that the energy computed by the Hamiltonian for any estimated  $\Psi_{\text{trial}}$  will be an upper bound to the true energy of the ground-state,  $E_0^{\text{elec}}$ . In practice, this enables the optimisation of the wavefunction parameters to reduce the energy of a system, to iteratively reach a close approximation of the true wavefunction, and therefore the true energy, of the molecular system.

Given the Born–Oppenheimer approximation, it is assumed that the electronic wavefunction instantaneously adjusts to changes in nuclear position. Therefore, nuclei travel on a single electronic potential energy surface associated with a single electronic state, which is obtained by solving the time-independent Schrödinger equation for a series of fixed nuclear geometries. In practice, this means that the lowest potential energy of a

molecular system can be found by iteratively adjusting the nuclear coordinates to find the minimum on the potential energy surface, where the gradient of the energy is equal to zero for all atoms. This will equal the approximate ground-state energy for the system. However, the many-body problem still exists between the correlated motion of electrons interacting with one another due to Coulombic repulsion and the Pauli Exclusion Principle. To account for this, a number of approaches can be undertaken, which form the fundamental differences between the various theoretical chemistry methods. An electron density-based approach such as DFT is one such method that can be used to solve the electronic Schrödinger equation.

### 3.1.3 Electron Density Functionals

The Hohenberg–Kohn theorem<sup>460</sup> states that the energy and all other electronic properties of a ground-state molecular system can be uniquely determined by the ground-state electron density  $\rho_0(\vec{r}_N)$ . This electron density can be used to describe a many-electron system by reducing the many-body problem of  $N$  electrons and their respective  $3N$  spatial coordinates to only three spatial coordinates by using functionals of the electron density:

$$E_0^{\text{elec}}[\rho_0(\vec{r}_N)] = E_{T_e}[\rho_0(\vec{r}_N)] + E_{eN}[\rho_0(\vec{r}_N)] + E_{ee}[\rho_0(\vec{r}_N)] . \quad \text{Eq. 3.6}$$

This allows DFT to scale with  $N^3$  and tolerate calculations of large systems with a low computational cost. This is far more scalable than correlated methods such as Møller–Plesset ( $N^4$  or  $N^5$  scaling) or coupled cluster ( $N^6$ ), making DFT more appropriate for the study of large systems. The second Hohenberg–Kohn theorem states that the density which minimises the total energy of the system is the exact ground-state electron density. In essence, this implies that the energy calculated from any trial electron density will always be greater than the exact ground-state electron density.<sup>460</sup> This is similar to the variational principle of a wavefunction, and enables the same iterative approach to minimising the energy of the system in order to find the exact ground-state electron density.

The difficulty in solving Eq. 3.6 arises from the electron kinetic energy and electron–electron interaction terms, which remain self-interacting due to their correlated nature. Further work by Kohn and Sham<sup>461</sup> showed that this equation could be separated by

treating all electrons in the molecule as a fictitious system of non-interacting electrons with the same electron density as the correct many-body function,<sup>458</sup> according to

$$E_0^{\text{elec}}[\rho_0(\vec{r}_N)] = E_{T_e}^{\text{NI}}[\rho_0(\vec{r}_N)] + E_{eN}[\rho_0(\vec{r}_N)] + E_{ee}^{\text{CL}}[\rho_0(\vec{r}_N)] + \Delta E_{T_e}^{\text{I}}[\rho_0(\vec{r}_N)] + \Delta E_{ee}^{\text{QM}}[\rho_0(\vec{r}_N)], \quad \text{Eq. 3.7}$$

where  $E_{T_e}^{\text{NI}}[\rho_0(\vec{r}_N)]$  represents the kinetic energy of the non-interacting electrons,  $E_{ee}^{\text{CL}}[\rho_0(\vec{r}_N)]$  and  $\Delta E_{ee}^{\text{QM}}[\rho_0(\vec{r}_N)]$  represent the classical and quantum mechanical electron-electron interactions (correlation), and  $\Delta E_{T_e}^{\text{I}}[\rho_0(\vec{r}_N)]$  represents corrections to the kinetic energy due to the fictitious non-interacting electron system (exchange). These Kohn–Sham equations allow computational methods to solve the Schrödinger equation as a series of single-electron equations with single-electron basis functions (*vide infra*).

Note that the first three terms of Eq. 3.7 are known exactly, while the exact form of the last two terms are unknown. These last two terms are often combined into a single term, referred to as the exchange-correlation energy  $E_{\text{XC}}[\rho_0(\vec{r}_N)]$ . This exchange-correlation energy is one of the major differences between the various functionals available in the literature, as each functional uses its own approximation of these interactions that result in the best description of molecular systems for a given set of empirical data.

The development of functionals is under constant research in the literature, resulting in a number of approximations that have been developed over the years. The local density approximation (LDA) is one of the simplest approximations for the exchange-correlation energy used in the first generation of functionals, and is based entirely upon the electron density. Second generation functionals make use of both the electron density and the gradient of the electron density to account for the non-homogenous nature of a true electron density, termed the generalised gradient approximation (GGA). The most recent and widely used functionals are the hybrid functionals, which are the most accurate and computationally expensive. These modern functionals define the exchange functional using a linear combination of exact exchange and kinetic density from Hartree-Fock theory with exchange and correlation from LDA and GGA DFT functionals.

The M06 functional chosen for use in this work is a hybrid meta-GGA functional that has been well parameterised for both transition metals and main group elements, and has been recommended as one of the best functionals for organometallic and inorganometallic chemistry.<sup>458</sup> The hybrid exchange-correlation energy for M06 can be written as

$$E_{\text{XC}}^{\text{M06}} = \frac{27}{100} E_{\text{X}}^{\text{HF}} + \left(1 - \frac{27}{100}\right) E_{\text{X}}^{\text{DFT}} + E_{\text{C}}^{\text{DFT}}, \quad \text{Eq. 3.8}$$

where  $E_{\text{X}}^{\text{HF}}$  is the hybrid Hartree-Fock exchange component,  $E_{\text{X}}^{\text{DFT}}$  is the DFT exchange component, and  $E_{\text{C}}^{\text{DFT}}$  is the DFT correlation component. The exact form of these terms is too large to go into detail here, and the reader is referred to the relevant literature for further information.<sup>462</sup>

### 3.2 Basis Sets

Basis sets typically consist of basis functions used to describe the shape and behaviour of single electron atomic orbitals (AOs) centred about an atom. Early basis functions consisted of Slater Type Orbitals (STOs) due to their accuracy and similarity to the atomic orbitals of a hydrogen atom, but these basis functions are computationally expensive to calculate. Therefore, Gaussian Type Orbitals (GTOs), sometimes referred to as gaussian primitives, are typically used to approximate the shape of a STO function while being cheaper to calculate. GTOs have the general form

$$\eta^{\text{GTO}} = N e^{-\alpha r^2} x^l y^m z^n, \quad \text{Eq. 3.9}$$

where  $N$  is a normalisation constant,  $\alpha$  is the exponent that controls the width of the GTO, and  $l$ ,  $m$ , and  $n$  are positive integers that determine the shell shape of the orbital (s, p, d, etc.).

Modern basis functions do not necessarily resemble orbitals of isolated atoms, however, and are often constructed or refined based upon benchmark studies. To achieve this, a linear combination of GTOs with varied exponents and coefficients are used to construct a more accurate basis function, termed Contracted Gaussian Functions (CGF):

$$\eta_{\tau}^{\text{CGF}} = \sum_a^A d_{a\tau} \eta_a^{\text{GTO}}, \quad \text{Eq. 3.10}$$

where  $d_{a\tau}$  are the contraction coefficients for each GTO. When using basis functions to model molecular systems, further improvement is often necessary. One such method involves using two GTO functions for each AO of an atom, termed a double zeta basis set, and this can be extended to even more functions to create a higher zeta basis sets. Another class, called split-valence basis sets, takes advantage of the notion that it is typically only the valence electrons involved in binding. Therefore, a single basis function may be used for the core orbitals, but numerous basis functions are used to describe the valence electrons with more accuracy and flexibility. The goal of these improvements is to describe the AOs as accurately as possible to thoroughly model the system, while minimising the computational expense.

For transition metals and heavy atoms, where the core electrons of an atom play only a minor role in their chemistry, effective core potentials (ECPs) are used to approximate the core electrons as a potential energy term of electron charge that shields the nucleus. This allows the valence electrons to be modelled with high accuracy, without the large

computational expense of calculating the energy of all core electrons that will have little effect on the molecular system. There are typically specific basis sets optimised for use with specific ECPs available in the literature. These ECPs often include relativistic corrections that become important for heavier atoms, where the speed of electrons begin to approach the speed of light, resulting in contraction of the core electronic orbitals. By including the effects of relativistic core contraction in the ECP, a non-relativistic approach to calculating the energy of a system can be undertaken, therefore increasing computational efficiency further.

Linear combinations of the aforementioned basis sets can then be used to approximate the molecular orbitals (MOs) of a given system, according to

$$\phi_i = \sum_{\mu=1}^L c_{i\mu} \chi_{\mu}, \quad \text{Eq. 3.11}$$

where  $\phi_i$  is the  $i$ th MO,  $\chi_{\mu}$  is the set of  $L$  basis functions that represent each AO, and  $c_{i\mu}$  are the expansion coefficients for each individual basis set.<sup>463</sup> The expansion coefficients are optimised via the self-consistent field (SCF) procedure to iteratively yield the orbitals with the lowest energy configuration. In DFT, these MOs are Kohn–Sham orbitals, which are used to establish the approximate electron density,

$$\rho(\vec{r}_N) = \sum_i^N |\phi_i(\vec{r}_N)|^2, \quad \text{Eq. 3.12}$$

from which the approximate energy of the molecular system can be solved. By extension, the actual geometry of a molecular system can then be optimised by iteratively adjusting the nuclear coordinates and calculating the approximate electron density for each nuclear coordinate system, until the electron density that yields the lowest energy is found. This is the key procedure by which DFT can optimise the geometry of a molecular system to yield the ground-state electron density at the minimum of the potential energy surface. Once this has been achieved, numerous other useful properties of the molecular system can be predicted from the ground-state electron density.

The LanL2DZ basis set was chosen for use in this work as it affords good accuracy with reasonable computational cost and converges readily for the large systems under investigation. These were important considerations when modelling such large systems, which were too computationally expensive to calculate with larger basis sets. The LanL2DZ basis set uses the D95V all-electron double zeta basis set for all elements up to

Ne, with Los Alamos ECPs and the D95 double-zeta basis sets for the valence electrons of elements beyond Ne.<sup>464-467</sup> These ECPs also incorporate relativistic effects for the heavier elements Rb to Bi. The basis set form and number of core electrons included in the ECP for each element are summarised in Table 3.1.

Table 3.1: Summary of the basis sets and corresponding Los Alamos ECPs used for each element included in calculations within this thesis.

Element	Contracted Basis Set	Core Electrons in ECP
H	(4s)/[2s]	None
O	(10s,5p)/[3s,2p]	None
Ti	(5s,5p,5d)/[3s,3p,2d]	10
Pd	(5s,6p,4d)/[3s,3p,2d]	28
Pt	(5s,6p,3d)/[3s,3p,2d]	60
Au	(5s,6p,3d)/[3s,3p,2d]	60

### 3.3 Computational Methods

DFT geometry optimisations were performed using the M06<sup>462</sup> functional in combination with the LanL2DZ basis set and corresponding ECPs<sup>464-467</sup> as implemented in the Gaussian 09 suite of programs.<sup>468</sup> All optimisations were performed without symmetry constraints using an ultrafine integration grid. The Cartesian coordinates and absolute energies of all optimised structures are provided in Appendix C and D for future reference. To obtain the predicted IR and Raman spectra, each calculated transition was convoluted using a Gaussian line shape function with a FWHM of 8 cm<sup>-1</sup> using the GaussView 5 program.<sup>469</sup> Note that all spectra show only the calculated fundamental vibrations, and therefore do not include overtones or combination bands. The GaussView 5 and Chemcraft<sup>470</sup> software packages were used to analyse and visualise calculation results.

Population analysis was undertaken using natural bond orbital (NBO), Löwdin, and Hirshfeld charge analysis methods. Although the NBO method is one of the most popular in the literature, multiple analysis methods are included for comparison with the wide range of methods presented in some studies in the literature. NBO and Löwdin use basis set based partitioning in Hilbert space, while Hirshfeld uses the separation of the electron density in real space.<sup>471</sup> It has been argued that since methods such as Hirshfeld charge analysis are based directly on the calculated electron density as a function of space, that they may be a more chemically realistic form of charge analysis.<sup>472</sup> Note that the method of Hirshfeld analysis used sums the charge of hydrogen atoms into the heavy atoms to simplify analysis.

#### 3.3.1 Calculation of Ligated Gold Clusters

Initial geometries, including all ligands, were obtained from the crystal structures reported by our collaborators or other groups in the literature that were available in the Cambridge Crystallographic Database.<sup>428</sup> Counter-ions were removed from the structures and the equivalent numbers of electrons were then removed from the calculations to ensure the total charge of the cluster was conserved. Structures of isolated PPh<sub>3</sub> and AuPPh<sub>3</sub> were created in GaussView 5 by chemical intuition and optimised using the same level of theory.

All structures underwent vibrational frequency calculations to ensure that they were true minima with no imaginary frequencies. There are two exceptions to this: the Au<sub>8</sub> and Au<sub>11</sub> structures were optimised to a stationary point that contained three imaginary frequencies of 42.6*i*, 30.8*i*, and 26.1*i* cm<sup>-1</sup> for Au<sub>8</sub> and one imaginary frequency of 1.5*i* cm<sup>-1</sup> for Au<sub>11</sub>. Close inspection of these imaginary modes revealed that they correspond to small rotations of ligand phenyl groups. Despite numerous attempts to re-optimize the structure using finer integration grid sizes and alternative minimisation algorithms, the imaginary frequencies remained present. Attempts to optimize the structures using PH<sub>3</sub> ligands as an alternative to P-Ph<sub>3</sub> ligands yielded unrealistic geometries. Given the small intensity and localised nature of these imaginary vibrations within the ligands, it was assumed that they would not adversely affect the identification and characterisation of the gold core cluster vibrations, which were of primary concern. Calculated frequencies have not been scaled to match the experimental data in any way.

### 3.3.2 Calculation of the Anatase(101) Surface and Au<sub>1-4</sub> Clusters

The model of the anatase surface is represented by a cluster of Ti<sub>14</sub>O<sub>45</sub>H<sub>34</sub> atoms cleaved from the 101 terminated surface of an anatase lattice,<sup>115</sup> adapted from a previous study by Zapol and co-workers who used a smaller (Ti<sub>7</sub>O<sub>27</sub>H<sub>26</sub>) model.<sup>134</sup> The larger model was developed to reduce edge effects resulting from the gold clusters binding too close to the periphery of the surface. Hydrogen atoms were added along the terminating lattice coordinates to saturate dangling oxygen bonds and the resultant OH groups were kept fixed in position during geometry optimisations. The lowest energy multiplicity of the surface was found to be a singlet. Oxygen-deficient anatase was modelled by removing a single doubly-coordinated bridging oxygen from the surface and re-optimising the structure. The lowest energy multiplicity was found to be a triplet, lower than the singlet state by 0.40 eV. Vibrational frequency calculations were performed on both surfaces and no imaginary frequencies were found.

Au<sub>1-4</sub> clusters were added to the TiO<sub>2</sub> model and their structures optimised from multiple unique starting positions. Each of the optimised geometries was then re-optimised as doublets, quartets, and sextets for Au<sub>1</sub> and Au<sub>3</sub>, or as triplets, quintets, and septets for Au<sub>2</sub> and Au<sub>4</sub>. All structures underwent vibrational frequency calculations to ensure that they were true minima with no imaginary frequencies. Only isomers within 0.5 eV of the

lowest energy isomer are considered significant and are presented in this thesis. Binding energies of Au<sub>1-4</sub> to the model surface were calculated by

$$E_a = E_{\text{Au}_x/\text{Anatase}} - (E_{\text{Anatase}} + E_{\text{Au}_x}),$$

where  $(E_{\text{Anatase}} + E_{\text{Au}_x})$  is the energy of a single point calculation of the anatase surface with the Au<sub>x</sub> molecule located 20 Å away. Counterpoise correction was not used in the calculations as the study by Mentel and Baerends<sup>473</sup> showed that the procedure was not justified for use with standard basis sets in quantum chemistry.

The density of states (DOS) graphs were created using GaussSum<sup>474</sup> by convoluting the molecular orbital energy levels using a Gaussian line shape function with a full width half maximum of 0.3 eV. For open shell calculations, the alpha (up) and beta (down) spin DOS were summed together and then divided by 2 to produce the total DOS plots. The density of state atomic contributions, also known as partial density of states (PDOS), were calculated using GaussSum based on the overlap matrix, molecular orbital coefficients, and Mulliken population analysis.<sup>474</sup> Illustrations of the MOs were created using Chemcraft, with 10.46 map points per Å and a map size expansion of 1.50. AO contributions to MOs were also determined using Chemcraft and by visual inspection of the MO illustrations.

# Chapter Four

## DFT Assisted Characterisation of the Far-Infrared Spectra of Au<sub>6</sub>, Au<sub>8</sub>, Au<sub>9</sub>, Au<sub>11</sub>, Au<sub>6</sub>Pd, and Au<sub>7</sub>Pt Clusters

In this Chapter, the far-infrared spectra of Au<sub>6</sub>, Au<sub>8</sub>, Au<sub>9</sub>, Au<sub>11</sub>, Au<sub>6</sub>Pd, and Au<sub>7</sub>Pt are assigned to specific vibrational modes by comparison to DFT calculations. Valuable information about the metal core structure of these atomically precise clusters is obtained by careful study of the calculated transitions. The distinct peaks for each cluster can be assigned to the calculated cluster core vibrations: 80.4 and 84.1 cm<sup>-1</sup> for Au<sub>6</sub>; 165.1 and 166.4 cm<sup>-1</sup> for Au<sub>8</sub>; 170.1 and 185.2 cm<sup>-1</sup> for Au<sub>9</sub>; 173.7 and 182.2 cm<sup>-1</sup> for Au<sub>11</sub>; 158.9, 195.2, and 206.7 cm<sup>-1</sup> for Au<sub>6</sub>Pd; and 156.3, 171.8, and 173.5 cm<sup>-1</sup> for Au<sub>7</sub>Pt. There are also strong absorptions beyond 200 cm<sup>-1</sup> and near 420 cm<sup>-1</sup> that are assigned to metal-P and P-Ph<sub>3</sub> vibrations, respectively. Charge population analysis is also presented to show the charge transfer between the metal core and the surrounding ligands.

## 4 DFT Assisted Characterisation of the Far-Infrared Spectra of Au<sub>6</sub>, Au<sub>8</sub>, Au<sub>9</sub>, Au<sub>11</sub>, Au<sub>6</sub>Pd, and Au<sub>7</sub>Pt Clusters

### 4.1 Optimised Ligated Metal Cluster Geometries

The optimised cluster geometries superimposed upon their crystal structures are shown in Figure 4.1, with ligand groups and counter-ions removed for clarity. These superimposed structures show the close match between the gas-phase optimised DFT structures and the solid-state X-ray crystal structure of the starting geometry. Upon optimisation, there is typically a small increase in the bond lengths of the clusters as the molecules are optimised to their gas-phase energetic minima. This is to be expected, as the gas-phase calculations do not account for crystal-packing effects since there is only a single molecule being optimised. All of these clusters were optimised to their lowest geometric minima and harmonic frequency calculations were performed to predict the infrared and Raman spectra for comparison to experiment.

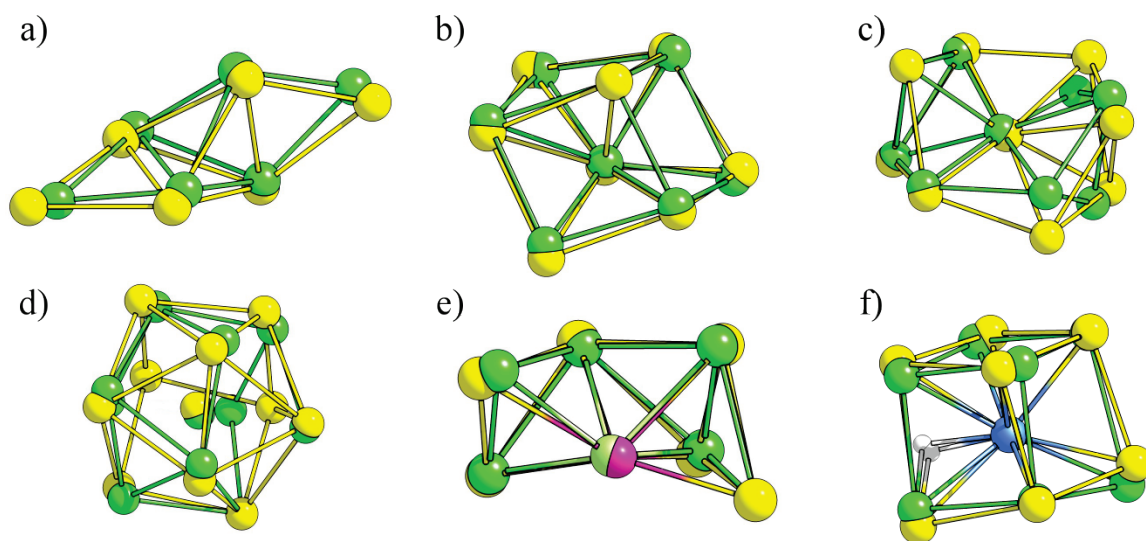


Figure 4.1: Comparison between X-ray crystal structures (green) and DFT optimised structures (yellow) for the a) Au<sub>6</sub>, b) Au<sub>8</sub>, c) Au<sub>9</sub>, d) Au<sub>11</sub>, e) Au<sub>6</sub>Pd, and f) Au<sub>7</sub>Pt clusters. The purple and blue atoms are Pd and Pt respectively, while the small white atom in f) is a H atom. Ligand groups and counter-ions have been omitted for clarity.

## 4.2 Far-IR Results and DFT Assignment

### 4.2.1 AuPPh<sub>3</sub>Cl

The far-IR spectrum of AuPPh<sub>3</sub>Cl shown in Figure 4.2 was measured to test the sample preparation method and to ensure that the apparatus was performing adequately in this spectral region. Initial experiments using polyethylene pressed clusters resulted in poor signal and inconsistent backgrounds. The ratio between cluster sample and polyethylene binding agent was then adjusted to obtain increased absorption signal from the clusters. However, the slight variations in the thickness of each pellet after being pressed with various amounts of polyethylene resulted in an inconsistent background. There were also issues with the polyethylene absorbing ambient moisture during sample preparation that was observed in the experimental spectra. Therefore, some samples were prepared as pressed pellets of pure cluster without any polyethylene, which provided higher quality spectra at the cost of some transmission loss for the ligand peaks due to their high absorption, as shown in Figure 4.2; however, these peaks were of less interest than the low intensity metal vibrational modes. Comparison of the spectral features observed in these experiments with previously recorded data<sup>475</sup> of AuPPh<sub>3</sub>Cl confirmed that the experimental setup and pure sample pellet preparation methods were adequate for the study of small metal clusters.

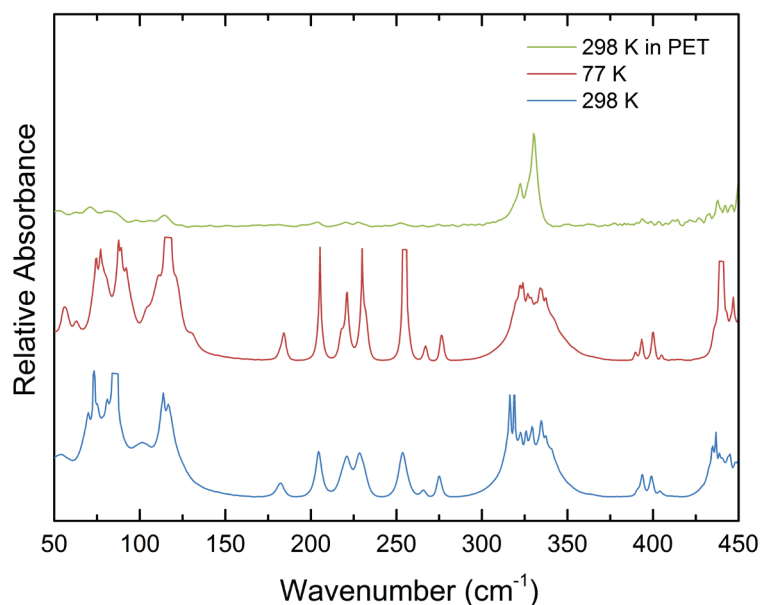


Figure 4.2: Absorption spectra of pure AuPPh<sub>3</sub>Cl sample pellets at 298 K (blue line) and 77 K (red line) showing increased signal and line narrowing for peaks below 300 cm<sup>-1</sup>. The third sample is mixed with polyethylene and performed at 298 K (green line).

Due to unavoidable vibrational interference in the experimental apparatus below  $50\text{ cm}^{-1}$  and low sensitivity above  $450\text{ cm}^{-1}$  due to detector limitations, experimental data in this Chapter is presented between  $50$  and  $450\text{ cm}^{-1}$ . Within this region there are typically more than 150 transitions predicted by DFT calculations for all cluster structures. Consequently, to obtain the predicted IR spectra, each calculated transition is convoluted using a Gaussian line shape function with a FWHM of  $8\text{ cm}^{-1}$ . Given the very large number of transitions that could be considered, only those that pass one of two selection criteria have been presented in Tables 4.1–4.6. Firstly, in order to distinguish vibrations involving the metal core atoms, only the vibrational modes that have  $> 0.5\%$  contribution from Au, Pt, Pd, or P atoms are included in the tabulated data as a percentage of the total non-mass-weighted atomic motion. Secondly, the presented data also includes vibrations that have  $> 1\text{ km mol}^{-1}$  IR intensity contributing to a peak of interest. The transitions are listed as groups that contribute to a convoluted peak in the predicted infrared spectrum and are numbered sequentially from low to high wavenumbers. Each group of transitions is labelled with a number that matches the convoluted peaks shown in the predicted infrared spectra and those with asterisks indicate significant core vibrations. Many of these key vibrations are also presented in the vector displacement diagrams throughout this Chapter. Furthermore, the assignment of predicted peaks to the experimental spectra is provided in the Tables, along with a qualitative description of the type of motion involved in the vibrational mode. It should be noted that the predicted spectral data only includes the fundamental vibrations and therefore does not include any overtone or combination bands. Even so, all observed peaks seem to be accounted for by the fundamental vibrations.

The experimental spectra for all clusters investigated in this study are presented together in Figure 4.3 for comparison. As can be clearly seen, all clusters exhibit an intense set of absorption bands near  $430\text{ cm}^{-1}$  and a broad, mostly featureless absorption below  $130\text{ cm}^{-1}$  except for  $\text{Au}_6$  and  $\text{Au}_{11}$ , which have small peaks at  $90$  and  $117\text{ cm}^{-1}$ , respectively. All clusters except  $\text{Au}_6$  display several distinct peaks between  $150$  and  $270\text{ cm}^{-1}$ , although the peaks of  $\text{Au}_{11}$  are not as well defined as other clusters in this region. The spectra for  $\text{Au}_8$  and  $\text{Au}_7\text{Pt}$  are very alike due to their similar geometries as shown in Figure 4.1, with the Pt of  $\text{Au}_7\text{Pt}$  replacing the central Au atom of  $\text{Au}_8$ ; this will be discussed in detail later.

The intense set of absorption bands near  $430\text{ cm}^{-1}$  are due to the  $\text{P-Ph}_3$  ligand vibrations as previously assigned in the literature<sup>476</sup> and confirmed by our DFT calculations. The one exception to this is  $\text{Au}_6$ , where the absorption bands are assigned to its  $\text{P}_2\text{Ph}_4\text{-(CH}_3\text{)}_3$  ligands. Some of the intense features for samples between  $420$  and  $450\text{ cm}^{-1}$  display 100% absorption during experiments, but given limited beamtime and the low significance of this spectral region, few attempts were made to reduce sample concentrations.

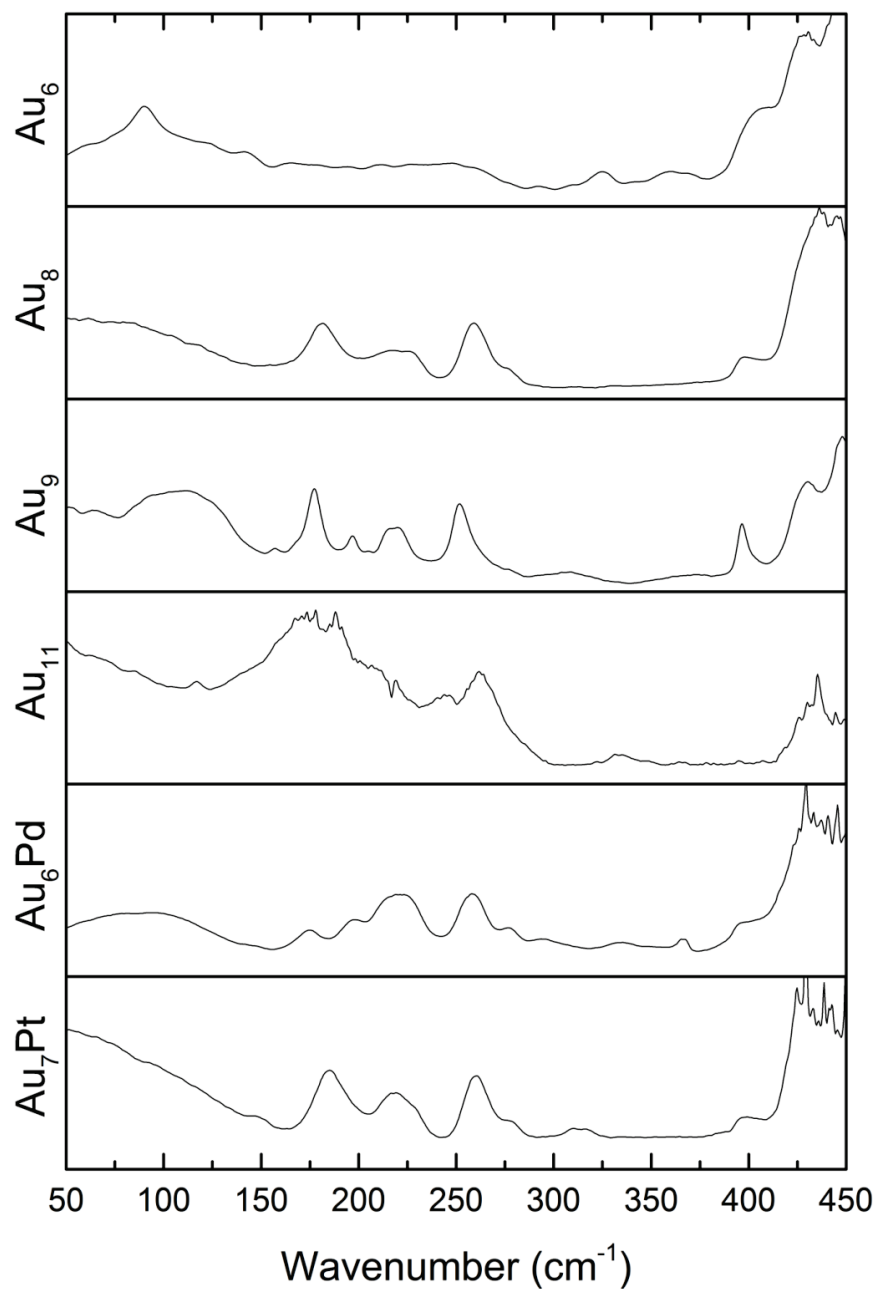


Figure 4.3: Comparison of the experimental far-IR absorption spectra for the  $\text{Au}_6$ ,  $\text{Au}_8$ ,  $\text{Au}_9$ ,  $\text{Au}_{11}$ ,  $\text{Au}_6\text{Pd}$ , and  $\text{Au}_7\text{Pt}$  clusters.

Given that there are small peaks observed for Au<sub>6</sub> and Au<sub>11</sub> in the region below 130 cm<sup>-1</sup>, along with clear peaks observed for AuPPh<sub>3</sub>Cl in this region, it can be concluded that the broad absorption below 130 cm<sup>-1</sup> is real and not due to experimental error. To determine if this broad absorption is due to phonon modes arising from a crystalline lattice, all samples are measured at both 298 K and 77 K. However, there is very little difference in any peak when comparing the spectra, indicating that there are no phonon bands present that could be confused with molecular vibrations for spectral assignment. AuPPh<sub>3</sub>Cl did show a small degree of narrowing of the vibrational bands as shown in Figure 4.2, however, this was not observed for the cluster samples. It seems plausible that the broad features below 130 cm<sup>-1</sup> arise from dampening of the low frequency vibrations due to the condensed phase nature of the samples used during experiments compared with the predicted spectrum, which is calculated for a single molecule under gas-phase conditions.

#### 4.2.2 Au<sub>6</sub>

The experimental and predicted spectra between 50 and 450 cm<sup>-1</sup> for Au<sub>6</sub> are shown in Figure 4.4, along with a summary of the predicted transitions and spectral assignment in Table 4.1. The experimental spectrum displays a broad peak at 90 cm<sup>-1</sup>, two small peaks at 325 and 359 cm<sup>-1</sup>, and three large peaks at 410, 432, and 448 cm<sup>-1</sup>.

The broad experimentally observed peak at 90 cm<sup>-1</sup> is assigned to the calculated peak at 81 cm<sup>-1</sup> labelled in Figure 4.4 (#2\*), which consists of multiple metal core transitions. All of these transitions have large %Au motions of 8.6–17.1%, and the two most IR active modes of these at 80.4 and 87.9 cm<sup>-1</sup> are represented in the vector displacement diagrams shown in Figure 4.5. This peak is of note as it is the only cluster that has a resolved peak in the experimental spectrum below 100 cm<sup>-1</sup>. The predicted spectrum also shows two strong peaks at 131 and 138 cm<sup>-1</sup>, which both consist of several transitions with moderate %Au motion ranging from 3.4–6.7% and significant IR intensities between 3.6 and 9.6 km mol<sup>-1</sup>. These predicted peaks could match the two small shoulders present in the experimental spectrum near 120 and 148 cm<sup>-1</sup>.

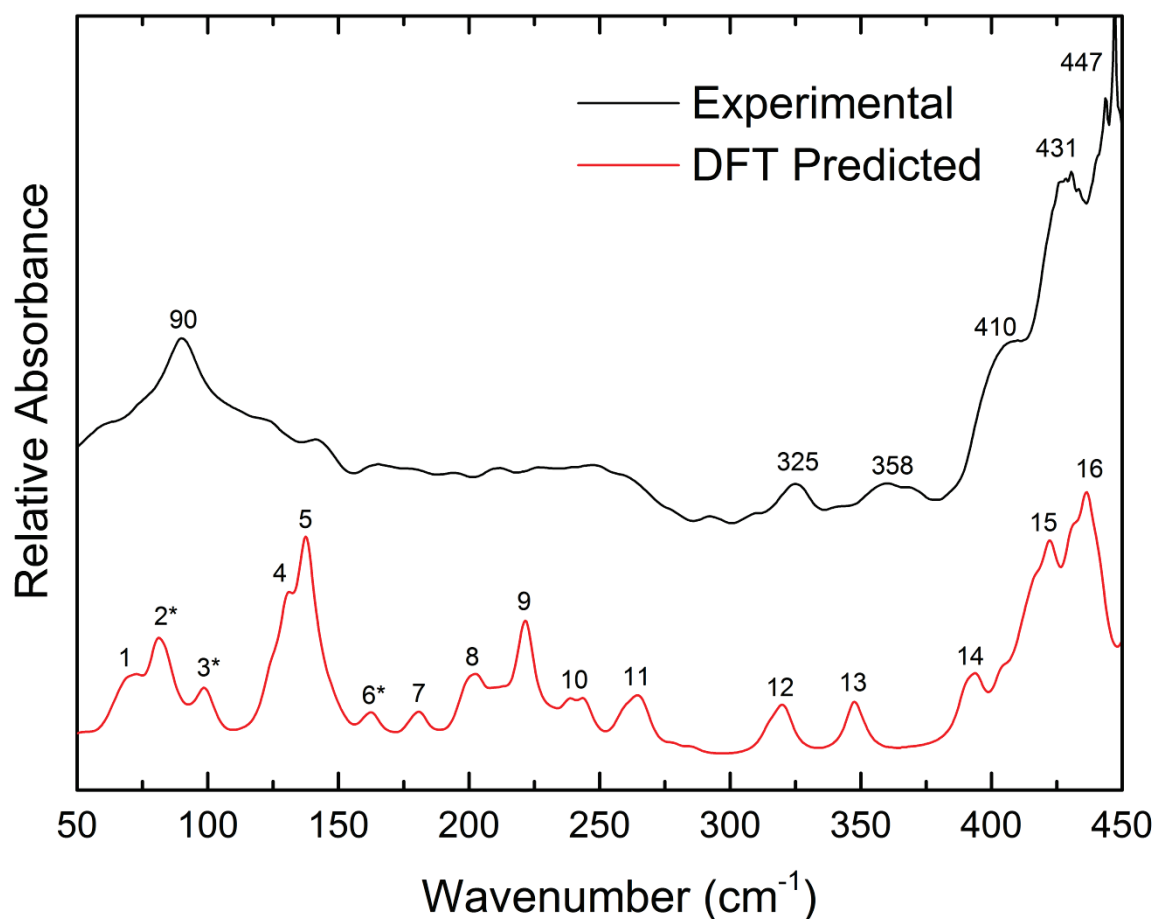


Figure 4.4: Experimental (black line) and simulated (red line) absorption spectra of the  $\text{Au}_6$  cluster.

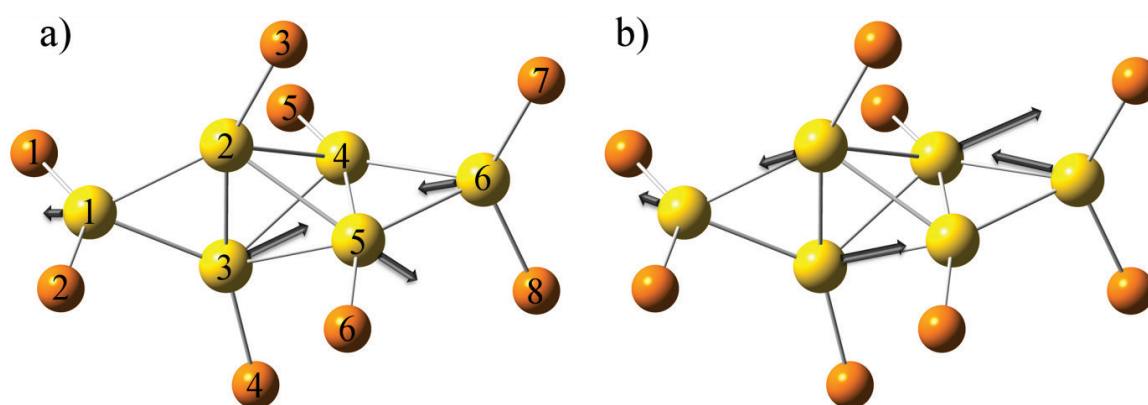


Figure 4.5: Predicted normal mode displacements of the cluster core vibrations for  $\text{Au}_6$  at a)  $80.4 \text{ cm}^{-1}$  and b)  $84.1 \text{ cm}^{-1}$ . Phenyl groups have been omitted for clarity.

The two small peaks at  $325$  and  $358 \text{ cm}^{-1}$  in the experimental spectrum are assigned to the peaks in the calculated spectrum at  $320 \text{ cm}^{-1}$  (#12) and  $348 \text{ cm}^{-1}$  (#13) respectively. These calculated peaks consist of transitions that correspond to distortions of the chelated

P-(CH<sub>2</sub>)<sub>3</sub>-P part of the ligands. These transitions have virtually no %Au motion, but have significant %P motion ranging from 7.3–11.4%. Finally, the three large peaks at 410, 432, and 448 cm<sup>-1</sup> in the experimental spectrum match well to the three predicted peaks at 394, 422, and 436 cm<sup>-1</sup> in the simulated spectrum. These three predicted peaks contain transitions with large amounts of %P motion ranging from 11.1–15.7%, with the transitions at 394 cm<sup>-1</sup> consisting of P-C-C-P bending motions, while the transitions at 422 and 436 cm<sup>-1</sup> primarily consist of Au-P and P-Ph stretches.

The predicted vibrational spectrum also shows a number of peaks between 160 and 265 cm<sup>-1</sup> (#6–11) that are not clearly resolved in the experimental spectrum. The transitions that form these peaks mainly correspond to distortions in the chelating P-(CH<sub>2</sub>)<sub>3</sub>-P ligands, with only one transition at 163.9 cm<sup>-1</sup> containing a significant %Au motion of 13.3%. There are also a number of predicted transitions below 150 cm<sup>-1</sup> that involve large motions spanning multiple ligand groups, as well as metal core distortions that are predicted to have significant %Au motion and moderate IR intensities, which are not clearly resolved in the experimental spectrum.

## Chapter 4. DFT Assisted Characterisation of the Far-Infrared Spectra of Au Clusters

 Table 4.1: Summary of significant calculated transitions for the Au<sub>6</sub> cluster, their assignment to the experimental far-IR spectrum, and brief descriptions of the assigned transition modes.

#	Peak (cm <sup>-1</sup> )	Contributing vibrations (cm <sup>-1</sup> )	IR intensity (km mol <sup>-1</sup> )	%Au motion	%P motion	Assigned (cm <sup>-1</sup> )	Mode description
1	73	69.6 72.9	1.3 1.4	6.1% 8.7%	4.8% 4.6%		
2*	81	80.4* 81.1 84.1* 87.9*	4.7 1.1 4.3 0.8	17.1% 8.6% 16.4% 16.8%	5.1% 6.3% 6.6% 5.0%	90.2	Au core distortion
3*	99	98.8 104.9*	3.7 0.1	5.6% 14.5%	5.4% 5.7%		Ph wag Au core distortion
4	131	129.9 130.5	3.6 6.1	3.4% 4.9%	7.3% 6.6%		
5	138	137.2 137.9 139.0 142.8	5.3 9.6 1.8 2.9	4.8% 6.7% 4.3% 6.1%	5.9% 7.0% 7.4% 6.9%		
6*	163	162.6 163.9*	1.3 1.1	1.9% 13.3%	4.0% 4.6%		P <sub>2</sub> Ph <sub>4</sub> -(CH <sub>3</sub> ) <sub>3</sub> wag Au-P stretch
7	180	179.8 181.8	1.1 2.0	2.2% 1.3%	3.3% 3.0%		
8	203	198.3 200.1 203.5	1.9 2.3 3.7	0.0% 0.8% 0.7%	2.8% 1.8% 2.1%		
9	222	219.3 220.9 222.0	1.5 1.3 7.8	0.0% 0.0% 0.0%	1.4% 1.2% 1.4%		
10	244	238.5 244.2	2.9 3.6	0.0% 0.0%	1.4% 1.6%		
11	265	263.3 264.2 265.3	1.0 1.1 1.1	0.0% 0.0% 0.0%	1.5% 2.0% 1.9%		
12	320	314.8 318.9 319.9 321.7	1.7 1.5 1.4 1.9	0.0% 0.0% 0.7% 0.0%	7.3% 8.0% 9.4% 8.2%	325.4	P <sub>2</sub> Ph <sub>4</sub> -(CH <sub>3</sub> ) <sub>3</sub> wag - ligand 1 P <sub>2</sub> Ph <sub>4</sub> -(CH <sub>3</sub> ) <sub>3</sub> wag - ligand 2 P <sub>2</sub> Ph <sub>4</sub> -(CH <sub>3</sub> ) <sub>3</sub> wag - ligand 3 P <sub>2</sub> Ph <sub>4</sub> -(CH <sub>3</sub> ) <sub>3</sub> wag - ligand 4
13	348	347.2 347.8	3.4 1.3	0.0% 0.0%	10.7% 11.4%	357.7	P-(CH <sub>2</sub> ) <sub>3</sub> -P distortion
14	394	390.0 394.3	3.6 4.2	0.9% 0.8%	15.1% 15.1%	410.3	P-C-C-C-P bend
15	422	421.7 422.3	4.9 4.6	0.5% 0.0%	13.2% 11.1%	430.5	Au-P stretch P-Ph stretch
16	436	429.8 431.3 436.4 441.0	5.2 6.3 14.6 7.7	1.2% 1.2% 0.0% 0.8%	16.3% 16.5% 16.6% 17.0%	446.9	Au-P stretch Au-P stretch P-Ph stretch P-Ph stretch

### 4.2.3 Au<sub>8</sub>

The experimental and predicted spectra between 50 and 450 cm<sup>-1</sup> for Au<sub>8</sub> are shown in Figure 4.6, along with a summary of the predicted transitions and spectral assignments in Table 4.2. The experimental spectrum displays a large peak at 182 cm<sup>-1</sup>, a broad doublet at 218 cm<sup>-1</sup>, a peak at 259 cm<sup>-1</sup> with shoulders, and large peaks at 398 and 436 cm<sup>-1</sup>. The large experimentally observed peak at 182 cm<sup>-1</sup> is assigned to the Au core distortion modes predicted near 166 cm<sup>-1</sup> (#4\*). Two of these transitions involve significant Au core distortions, with %Au motion of up to 20.3% and IR intensities of 23.9 km mol<sup>-1</sup>. The vector displacement diagrams for these two modes are shown in Figure 4.7.

The two peaks at 218 and 259 cm<sup>-1</sup> are assigned to the phenyl rocking modes predicted near 216 and 250 cm<sup>-1</sup> (#5 and #6). These modes have essentially no %Au motion and only a small amount of %P motion ranging from 0.8–1.5%. The large experimental peaks at 398 and 436 cm<sup>-1</sup> are assigned to a phenyl twisting mode at 411 cm<sup>-1</sup> (#7) and a PPh<sub>3</sub> distortion mode at 441 cm<sup>-1</sup> (#8) in the predicted spectrum. Neither of these two sets of transitions have any %Au motion, while the PPh<sub>3</sub> distortion modes have significant %P motion averaging 13%, with IR intensities of 3.9 km mol<sup>-1</sup> on average. The high intensity of the latter peak arises from the large number of similar bonds, as there are eight PPh<sub>3</sub> ligands per cluster core, each of which give rise to three P-Ph vibrations.

Furthermore, below 150 cm<sup>-1</sup> there are a number of predicted peaks that do not match the experimental data. These transitions do not involve core cluster vibrations but instead involve a collection of modes comprising large-amplitude motion of the P-Ph<sub>3</sub> ligand groups that may be suppressed by the solid-state nature of the sample.

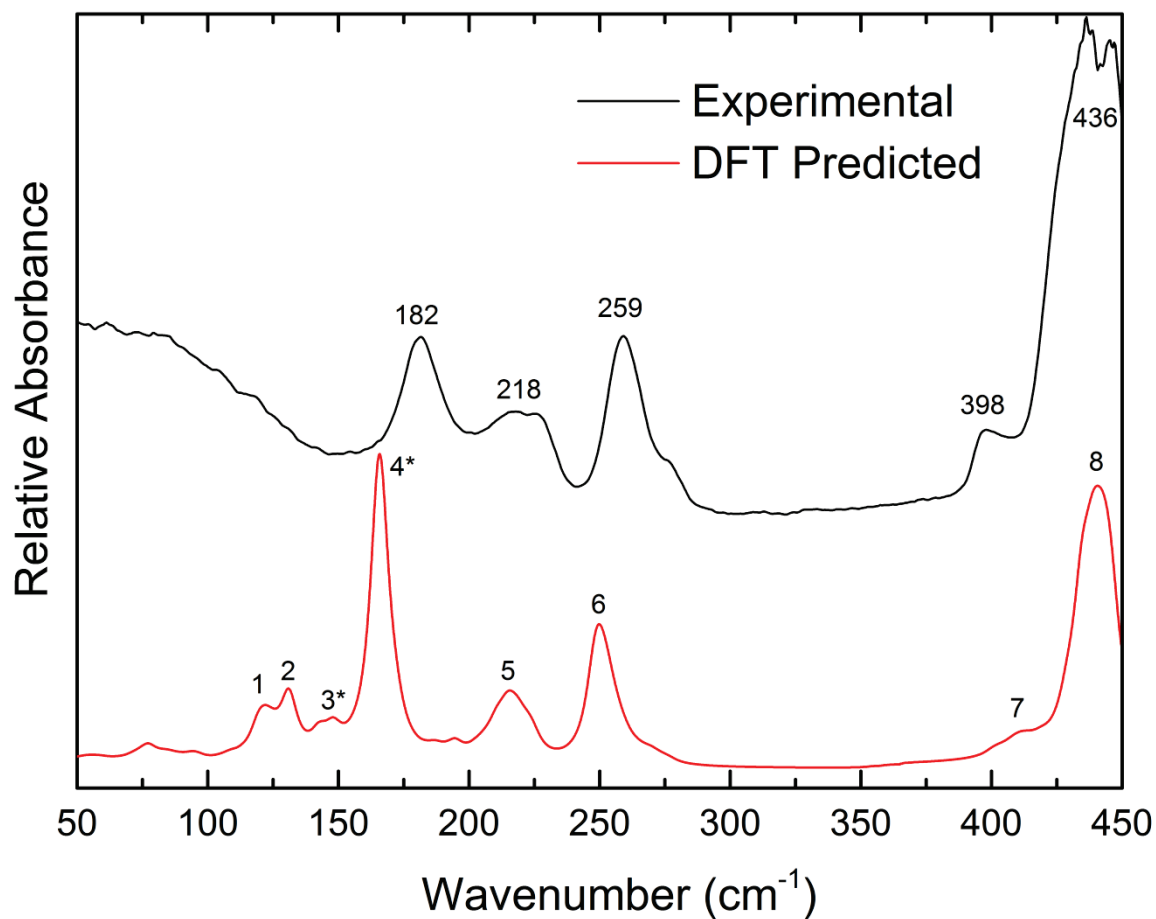


Figure 4.6: Experimental (black line) and simulated (red line) absorption spectra of the  $\text{Au}_8$  cluster.

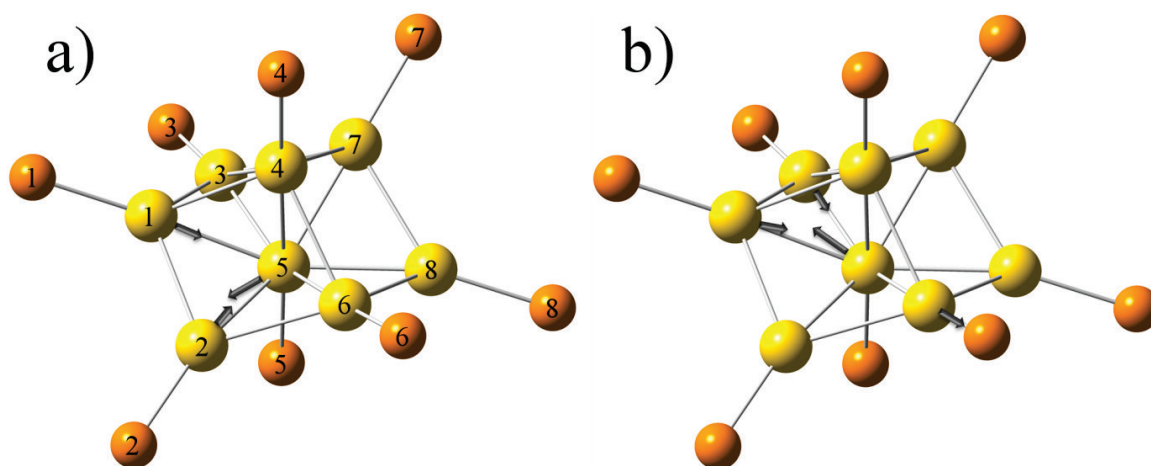


Figure 4.7: Predicted normal mode displacements of the cluster core vibrations for  $\text{Au}_8$  at a)  $165.1 \text{ cm}^{-1}$  and b)  $166.4 \text{ cm}^{-1}$ . Phenyl groups have been omitted for clarity.

Table 4.2: Summary of significant calculated transitions for the Au<sub>8</sub> cluster, their assignment to the experimental far-IR spectrum, and brief descriptions of the assigned transition modes.

#	Peak (cm <sup>-1</sup> )	Contributing vibrations (cm <sup>-1</sup> )	IR intensity (km mol <sup>-1</sup> )	%Au motion	%P motion	Assigned (cm <sup>-1</sup> )	Mode description
1	122	119.1	3.4	5.2%	4.6%		
		121.1	1.7	3.8%	3.9%		
		122.2	2.0	3.2%	3.5%		
		124.4	1.9	4.8%	4.3%		
2	131	131.1	9.3	7.5%	5.6%		
3*	148	142.6*	2.9	10.7%	5.2%		Au-P stretches
		147.4*	1.7	12.7%	5.0%		
		148.7*	1.9	12.6%	4.8%		
4*	166	165.1*	23.9	20.3%	2.7%	181.8	Au core distortion
		166.4*	23.9	20.2%	2.9%		
		171.6*	3.2	16.7%	1.6%		
5	216	210.3	1.5	0.0%	0.8%	217.9	Ph rock
		210.9	1.7	0.0%	1.4%		
		214.5	2.8	0.0%	1.2%		
		215.8	1.2	0.0%	1.3%		
		217.0	1.6	0.5%	1.5%		
		219.1	1.8	0.0%	1.3%		
6	250	247.4	4.1	0.0%	1.1%	258.9	Ph rock
		248.3	3.8	0.0%	0.9%		
		249.4	4.1	0.0%	1.2%		
		249.9	3.3	0.0%	1.3%		
		250.2	1.7	0.0%	1.4%		
		251.7	3.1	0.0%	1.0%		
		253.1	3.9	0.0%	1.3%		
7	411 (shoulder)	410.5	0.5	0.0%	1.9%	398.2	Ph twist
		411.5	0.4	0.0%	0.7%		
8	441	428.9–445.8	Avg. 3.9	Avg. 0%	Avg. 13%	436.3	PPh <sub>3</sub> distortion

#### 4.2.4 Au<sub>9</sub>

The experimental and predicted spectra between 50 and 450 cm<sup>-1</sup> for Au<sub>9</sub> are shown in Figure 4.8, along with a summary of the predicted transitions and spectral assignment in Table 4.3. Au<sub>9</sub> has similar set of spectra to that of Au<sub>8</sub>, with the same intense peak in the experimental spectrum at 177 cm<sup>-1</sup>, along with the broad doublet near 218 cm<sup>-1</sup>, and a large peak at 252 cm<sup>-1</sup>. The large peaks at 397, 430, and 448 cm<sup>-1</sup> are also similar to Au<sub>8</sub>, but the latter two are better resolved for Au<sub>9</sub>. The major differences between the experimental spectra of the two clusters are the two peaks at 182 and 218 cm<sup>-1</sup> for Au<sub>8</sub>, which shift to 157 and 197 cm<sup>-1</sup> for Au<sub>9</sub>.

The calculated peaks at 141, 170, and 185  $\text{cm}^{-1}$  (#2\*, #3\*, and #4\*) are assigned to 157, 177, and 197  $\text{cm}^{-1}$  in the experimental spectrum. These three sets of calculated transitions are Au core distortion modes, with the two transitions at 170.1 and 185.2  $\text{cm}^{-1}$  having significant %Au motions of 17.7%, along with IR intensities of 28.0 and 11.1  $\text{km mol}^{-1}$ , respectively. The vector displacement diagrams for these two intense modes are displayed in Figure 4.9. The calculated transition at 140.9  $\text{cm}^{-1}$  arises primarily from vibration of the central Au atom (8.3% Au) relative to the surrounding ring of eight Au atoms and is calculated to have a much lower IR intensity of 7.2  $\text{km mol}^{-1}$ . This transition is assigned to the peak at 141  $\text{cm}^{-1}$  in the experimental spectrum.

The broad doublet at 218  $\text{cm}^{-1}$  in the experimental spectrum is assigned to the two sets of predicted transitions at 211 and 224  $\text{cm}^{-1}$ . These are phenyl rocking modes with no %Au motion and only a marginal contribution of %P motion ranging from 0.7–1.4%. The large, experimentally observed peak at 252  $\text{cm}^{-1}$  is assigned to PPh<sub>3</sub> distortions predicted at 253  $\text{cm}^{-1}$ , with up to 1% P atom motion, but no Au motion. Similar to the Au<sub>8</sub> cluster, the large peaks at 397 and 430  $\text{cm}^{-1}$  in the experimental spectrum correspond to phenyl twisting modes, while the experimentally observed peak at 448  $\text{cm}^{-1}$  is assigned to PPh<sub>3</sub> distortion modes, with an average 13% P atom motion. As expected, none of these ligand vibrational modes involve any Au motion. Below 150  $\text{cm}^{-1}$  there are a number of predicted peaks that do not match the experimental data, similar to that shown for Au<sub>8</sub>, and may be due to the solid-state nature of the samples as discussed previously.

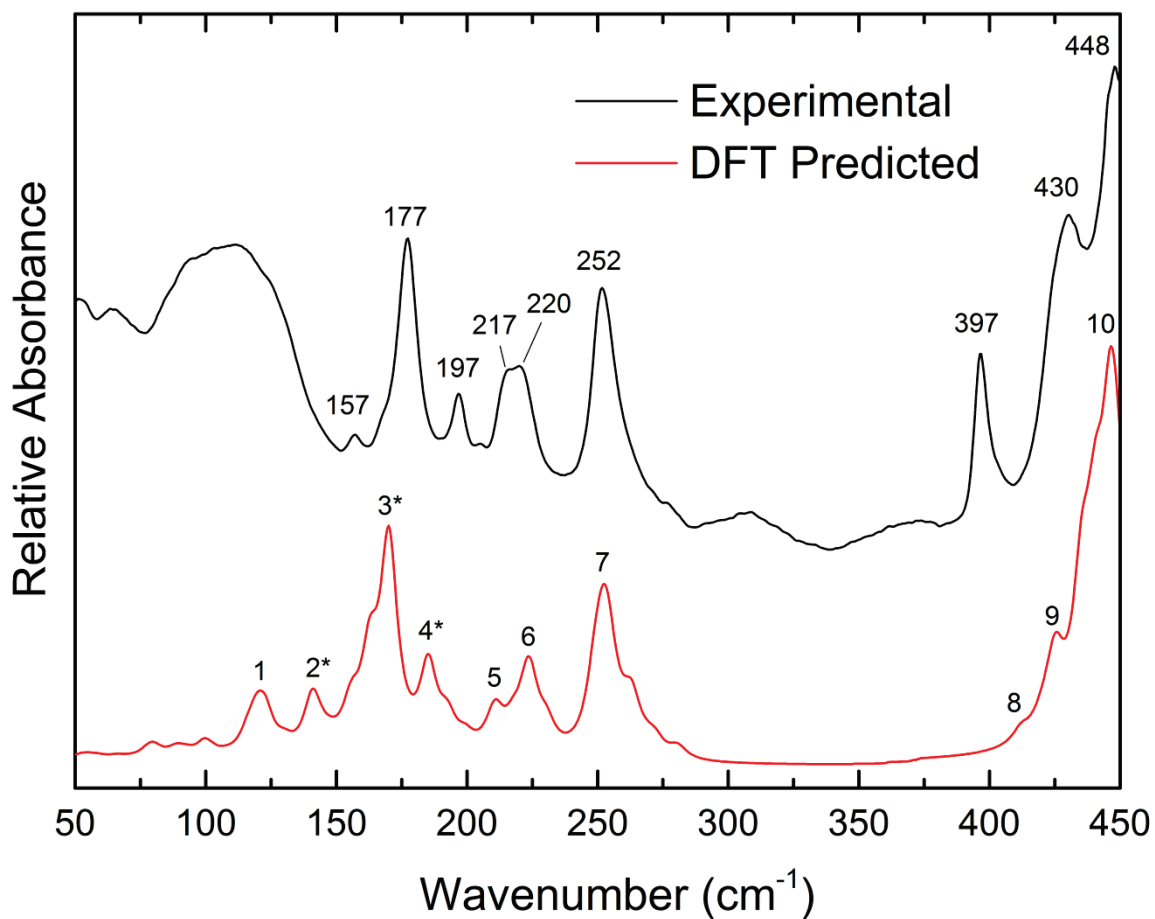


Figure 4.8: Experimental (black line) and simulated (red line) absorption spectra of the Au<sub>9</sub> cluster.

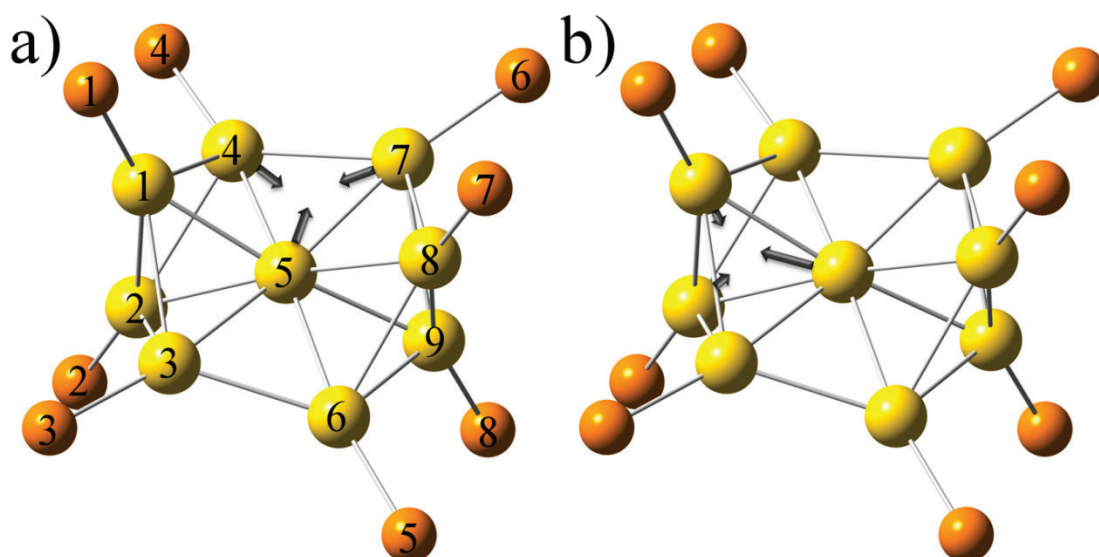


Figure 4.9: Predicted normal mode displacements of the cluster core vibrations for Au<sub>9</sub> at a) 170.1 cm<sup>-1</sup> and b) 185.2 cm<sup>-1</sup>. Phenyl groups have been omitted for clarity.

As described above, Au<sub>8</sub> and Au<sub>9</sub> have two intense predicted transitions that involve the largest combined motion of Au atoms at 165.1 and 166.4 cm<sup>-1</sup> for Au<sub>8</sub>, and 170.1 and 185.2 cm<sup>-1</sup> for Au<sub>9</sub> (~18% for Au<sub>8</sub> and ~20% for Au<sub>9</sub>). These calculated transitions are similar to those observed for gas-phase IR studies of the Au<sub>7</sub>-Kr cluster reported by Fielicke and co-workers.<sup>439</sup> By using IR-depletion spectroscopy, these authors observed three peaks at 165, 186, and 201 cm<sup>-1</sup> that correlate very well with their DFT-predicted IR spectrum. The three prominent vibrational peaks were assigned to various delocalised motions of the Au atoms. Note that the addition of the Kr atom used for IR depletion spectroscopy has very little effect on the vibrational frequencies of the Au<sub>7</sub> cluster core. In this case, the predicted structure of the Au<sub>7</sub>-Kr cluster core has five equilateral triangles and C<sub>s</sub>-planar symmetry, with or without the Kr atom attached. This results in a gas-phase Au<sub>7</sub> cluster that has a 2D shape as opposed to the 3D shape of the ligand-protected solid-phase clusters reported in this thesis. Despite this geometric difference, the core Au vibrational frequencies are very similar. Given that the two types of clusters are of similar size, this would indicate that the bond strengths within the metal cores are comparable for both types of cluster.

Table 4.3: Summary of significant calculated transitions for the Au<sub>9</sub> cluster, their assignment to the experimental far-IR spectrum, and brief descriptions of the assigned transition modes.

#	Peak (cm <sup>-1</sup> )	Contributing vibrations (cm <sup>-1</sup> )	IR intensity (km mol <sup>-1</sup> )	%Au motion	%P motion	Assigned (cm <sup>-1</sup> )	Mode description
1	121	116.0	2.1	1.9%	1.7%		
		119.3	2.7	6.0%	2.4%		
		120.0	2.0	5.6%	2.3%		
		122.9	4.6	3.6%	1.7%		
2*	141	140.9*	7.2	8.3%	5.8%	157.2	Au core distortion
3*	170	162.8*	11.2	8.1%	4.6%	177.4	Au core distortion
		170.1*	28.0	17.7%	3.3%		
4*	185	185.2*	11.2	17.7%	1.7%	196.7	Au core distortion
5	211	210.7	2.0	0.0%	1.1%	216.5	Ph rock
		211.0	3.2	0.0%	0.8%		
6	224	217.6	2.7	0.0%	1.2%	219.8	Ph rock
		222.2	2.3	0.0%	0.7%		
		223.7	5.6	0.0%	0.7%		
		224.2	3.1	0.0%	1.4%		
7	253	248.9	6.6	0.0%	1.0%	251.7	PPh <sub>3</sub> distortion
		251.6	6.2	0.0%	0.8%		
		252.2	3.2	0.0%	0.6%		
		253.9	9.9	0.0%	0.9%		
8	411 (shoulder)	411.8	0.9	0.0%	1.0%	396.8	Ph twist
		412.2	0.7	0.0%	1.0%		
9	426	424.5	1.5	0.0%	3.2%	430.0	Ph twist
		424.6	1.9	0.0%	3.0%		
		425.4	3.6	0.0%	4.7%		
		425.5	1.9	0.0%	2.5%		
10	447	435.2–448.8	Avg. 8.1	Avg. 0%	Avg. 13%	447.9	PPh <sub>3</sub> distortion

#### 4.2.5 Au<sub>11</sub>

The experimental and predicted spectra between 50 and 450 cm<sup>-1</sup> for Au<sub>11</sub> are shown in Figure 4.10, along with a summary of the predicted transitions and spectral assignment in Table 4.4. The experimental spectrum displays a number of small, difficult to resolve peaks between 117 and 219 cm<sup>-1</sup>, followed by two large peaks at 245 and 262 cm<sup>-1</sup>, and a broad peak at 333 cm<sup>-1</sup>. There are also a group of peaks near 426 cm<sup>-1</sup> assigned to PPh<sub>3</sub> that are of lower intensity than other pure Au clusters.

The experimentally observed peak at 117 cm<sup>-1</sup> is assigned to a series of predicted transitions that compose peak #1\* at 98 cm<sup>-1</sup>. For this predicted peak, there are two transitions at 96.1 and 97.6 cm<sup>-1</sup> that are composed of Au core distortions with Cl atom wags, while the remaining transitions are primarily composed of Cl wags with phenyl

twisting motions, although they still retain reasonably high Au contribution  $> 5\%$ . This peak at  $117\text{ cm}^{-1}$  is of note, as it is the only experimentally observed peak below  $150\text{ cm}^{-1}$  with multiple transitions that have significant Au contribution (up to  $15.8\%$ ) for the pure Au clusters presented in this chapter. The experimentally observed shoulder at  $141\text{ cm}^{-1}$  can tentatively be assigned to peak #2\* at  $135\text{ cm}^{-1}$  in the predicted spectrum, which consists primarily of Au core ( $\sim 6\%$ ) + P atom ( $\sim 4\%$ ) distortions of varying degree, in addition to a Cl atom wag transition at  $123.5\text{ cm}^{-1}$  with less than  $2\%$  Au atom motion. The two broad experimentally observed features at  $173$  and  $188\text{ cm}^{-1}$  are assigned to peaks #3\* and #4\* in the predicted spectrum, which primarily contain large Au core distortion modes. The two predicted transitions at  $173.7$  and  $182.2\text{ cm}^{-1}$  have  $23.5$  and  $22.3\%$  Au motion with large IR intensities of  $13.0$  and  $21.1\text{ km mol}^{-1}$ , respectively. These two key transitions are visualised in the vector displacement diagrams of Figure 4.11.

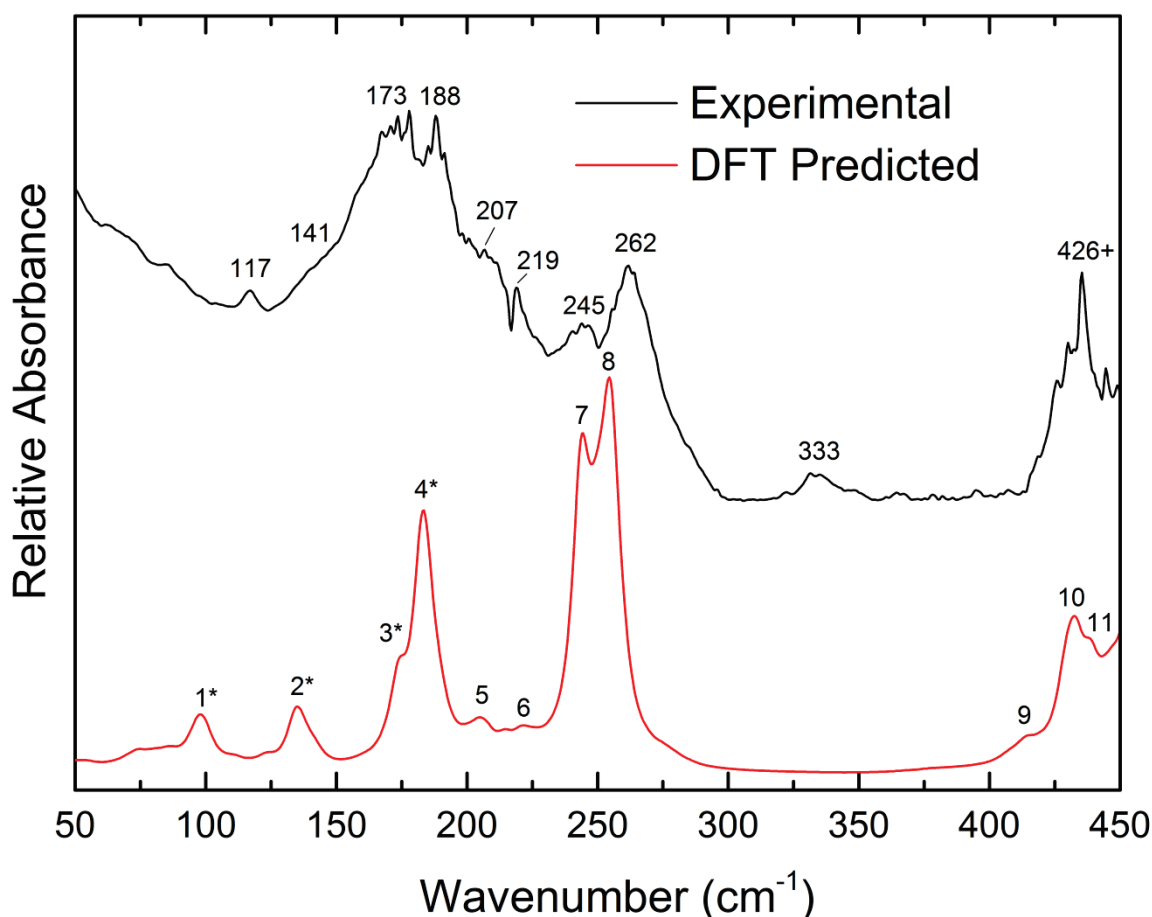


Figure 4.10: Experimental (black line) and simulated (red line) absorption spectra of the  $\text{Au}_{11}$  cluster.

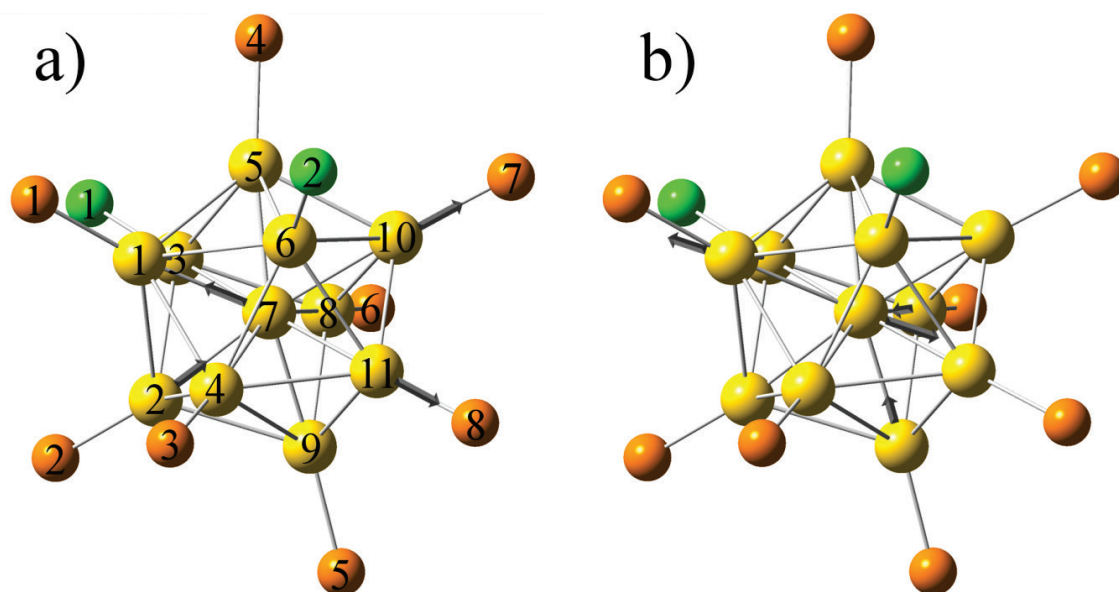


Figure 4.11: Predicted normal mode displacements of the cluster core vibrations for  $\text{Au}_{11}$  at a)  $173.7 \text{ cm}^{-1}$  and b)  $182.2 \text{ cm}^{-1}$ . Phenyl groups have been omitted for clarity.

There is a small shoulder  $207 \text{ cm}^{-1}$  and a peak at  $219 \text{ cm}^{-1}$  assigned to peaks #5 and #6, which correspond to phenyl rocking modes, the former of which has a small amount (up to 2.0%) of Au motion. The two broad peaks at  $245$  and  $262 \text{ cm}^{-1}$  in the experimental spectrum are assigned to peaks #7 and #8 in the predicted spectrum. Peak #7 contains a transition with 9.9% Au motion and is a Au-Cl stretching mode with a large IR intensity of  $47.1 \text{ km mol}^{-1}$ . Peak #8 consists of a number of phenyl rocking modes, along with two more intense Au-Cl stretching modes with large IR intensities of  $25.7$  and  $20.8 \text{ km mol}^{-1}$ , although they only have  $\sim 2.9\%$  Au motion. The last two transitions of peak #8 are primarily  $\text{PPh}_3$  distortion modes with a very small Au-Cl stretching component.

Compared with other pure Au clusters presented thus far, the predicted spectrum of  $\text{Au}_{11}$  has the weakest correlation with the experimental data in terms of peak intensity, although the peak positions are reasonably matched. The broad peak observed at  $333 \text{ cm}^{-1}$  in the experimental spectrum is not reproduced in the calculated spectrum, nor is it present in any other pure Au cluster experimental spectrum. This broad peak may be the result of a third Cl counter-ion that is not included in the calculation as its position in the crystal structure is far removed from the molecule. This peak and the broad nature of the entire experimental spectrum could also be due to the presence of a  $\text{Au}_{11}$  by-product during synthesis. There are studies in the literature<sup>477,478</sup> that show a number of similar polymorphs, such as  $\text{Au}_{11}(\text{PPh}_3)_7\text{Cl}_2$ , which may be difficult to distinguish from the

intended cluster. Our collaborators had followed the synthetic procedure outlined by Hutchison *et al.*,<sup>432</sup> however, who showed monodispersity of the compound via a number of different techniques.<sup>479</sup> Our collaborators had also confirmed the purity of their Au<sub>11</sub>(PPh<sub>3</sub>)<sub>8</sub>Cl<sub>3</sub> cluster during preparation via NMR techniques; therefore it is unlikely that there are any significant levels of by-products present in the sample.

It is also interesting that the broad, featureless absorption observed for Au<sub>11</sub> below ~110 cm<sup>-1</sup> does not extend as far as that seen for Au<sub>6</sub>, Au<sub>8</sub>, and Au<sub>9</sub>, for which the absorption extends to ~150 cm<sup>-1</sup>. This allows for the assignment of the two predicted peaks of #1 and #2\* for Au<sub>11</sub> to experimental peaks at 114 and 141 cm<sup>-1</sup>, which indicates that the predicted peaks in this range are correct and would most likely be observed for the other clusters if it were not for the broad featureless absorption present in their experimental spectra.

## Chapter 4. DFT Assisted Characterisation of the Far-Infrared Spectra of Au Clusters

 Table 4.4: Summary of significant calculated transitions for the Au<sub>11</sub> cluster, their assignment to the experimental far-IR spectrum, and brief descriptions of the assigned transition modes.

#	Peak (cm <sup>-1</sup> )	Contributing vibrations (cm <sup>-1</sup> )	IR intensity (km mol <sup>-1</sup> )	%Au motion	%P motion	Assigned (cm <sup>-1</sup> )	Mode description
1*	98	96.1*	1.7	15.8%	4.3%	117	Au core distortion + Cl wag
		97.1	2.4	6.0%	2.8%		Cl wag + Ph twist
		97.6*	1.2	8.1%	3.5%		Au core distortion + Cl wag
		99.2	4.1	6.7%	2.9%		Cl wag + Ph twist
		101.0	1.2	6.0%	3.0%		
2*	135	123.5	1.3	1.7%	1.4%	141	Cl wag + Ph twist
		133.5*	1.5	6.4%	4.0%		Au core + P distortions
		134.3*	3.7	6.3%	3.7%		
		134.8*	3.7	6.2%	4.5%		
3*	174 (shoulder)	173.7*	13.0	23.5%	2.7%	173	Au core distortion focused on central Au
4*	183	182.2*	21.1	22.3%	1.3%	188	Au core distortion focused on central Au
		183.9*	21.9	13.2%	1.1%		Au core distortion + PPh <sub>3</sub> rock
		185.5*	6.1	11.4%	1.6%		
		189.3	4.2	8.1%	1.4%		
5	205	204.2	2.7	2.0%	1.7%	207	Ph rock
		206.4	1.4	0.6%	1.7%		
		207.7	2.3	0.8%	1.6%		
6	222	221.2	1.2	0.8%	0.8%	219	Ph rock
7	244	243.6	47.1	9.9%	0.3%	245	Au-Cl stretch
		244.5	1.1	0.0%	0.7%		Ph rock
		247.5	4.7	0.0%	0.7%		
8	255	249.4	8.7	0.5%	0.9%	262	Ph rock
		250.7	7.5	0.8%	1.1%		
		252.0	1.2	0.8%	1.0%		
		252.8	5.5	0.8%	1.3%		
		253.7	2.7	0.0%	1.4%		
		254.7	25.7	2.8%	0.8%		
		255.3	20.8	3.0%	1.4%		
		256.9	6.8	1.4%	1.4%		PPh <sub>3</sub> distortion + small Au-Cl stretch
		258.7	1.1	1.1%	1.5%		PPh <sub>3</sub> distortion + small Au-Cl stretch
9	414 (shoulder)	414.3	1.6	0.0%	1.4%	426+	Ph twist
10	433	428.3	6.0	0.0%	13.2%	426+	PPh <sub>3</sub> distortion
		430.1	4.7	0.9%	13.3%		
		431.2	2.3	0.0%	13.1%		
		431.5	3.3	0.5%	12.5%		
		433.2	5.5	1.2%	13.7%		
		433.4	6.1	0.0%	13.7%		
11	439 (shoulder)	438.0	1.5	0.7%	11.5%	426+	PPh <sub>3</sub> distortion
		438.5	6.2	0.0%	13.6%		
		439.5	4.0	0.0%	13.9%		

#### 4.2.6 Au<sub>6</sub>Pd

The experimental and predicted spectra between 50 and 450  $\text{cm}^{-1}$  for Au<sub>6</sub>Pd are shown in Figure 4.12, along with a summary of the predicted transitions and spectral assignment in Table 4.5. This cluster displays a series of well-resolved peaks between 175 and 277  $\text{cm}^{-1}$ , followed by unresolved features between 300 and 375  $\text{cm}^{-1}$ , with intense absorption beyond 400  $\text{cm}^{-1}$  due to large PPh<sub>3</sub> distortions as observed for other clusters. The experimental and predicted spectra of Au<sub>6</sub>Pd are significantly distinct from those of the pure Au series of clusters due to the addition of the Pd heteroatom; nevertheless, it is simulated quite well.

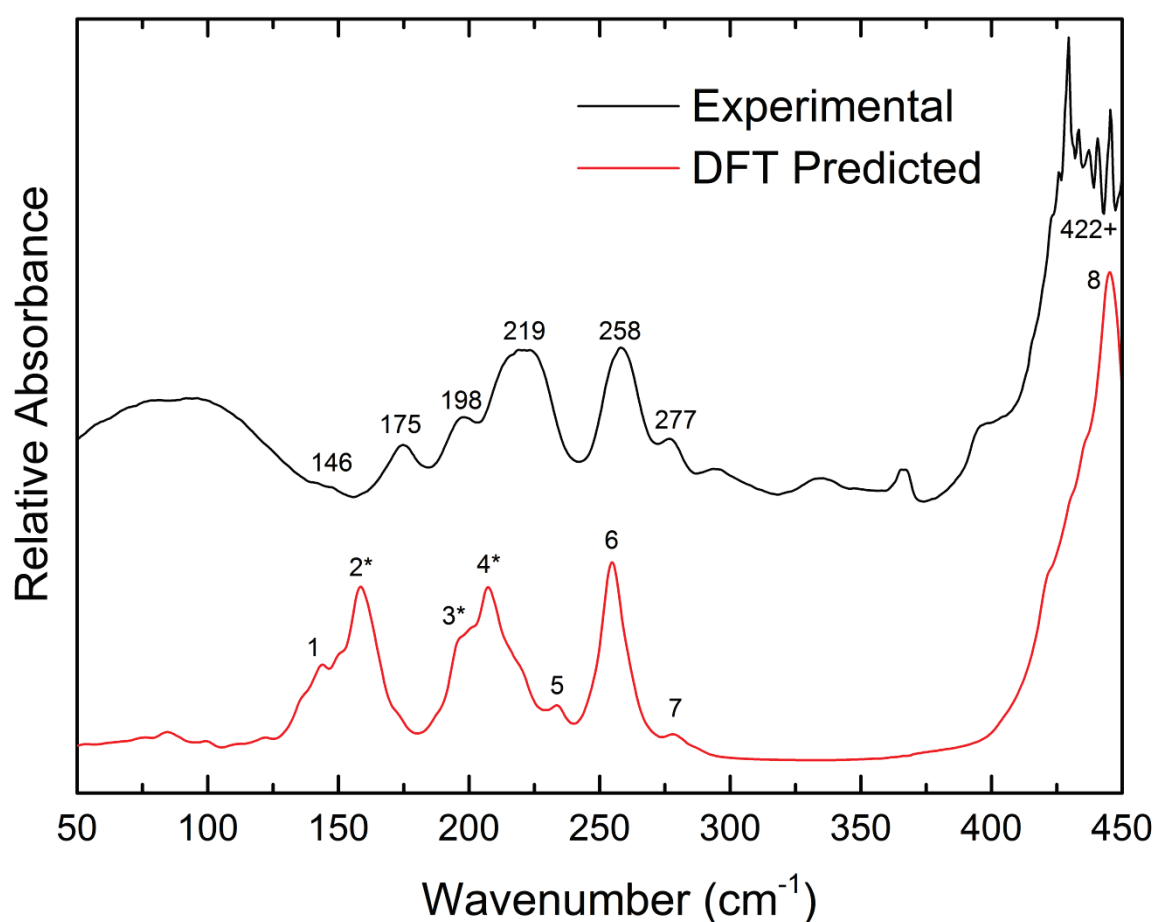


Figure 4.12: Experimental (black line) and simulated (red line) absorption spectra of the Au<sub>6</sub>Pd cluster.

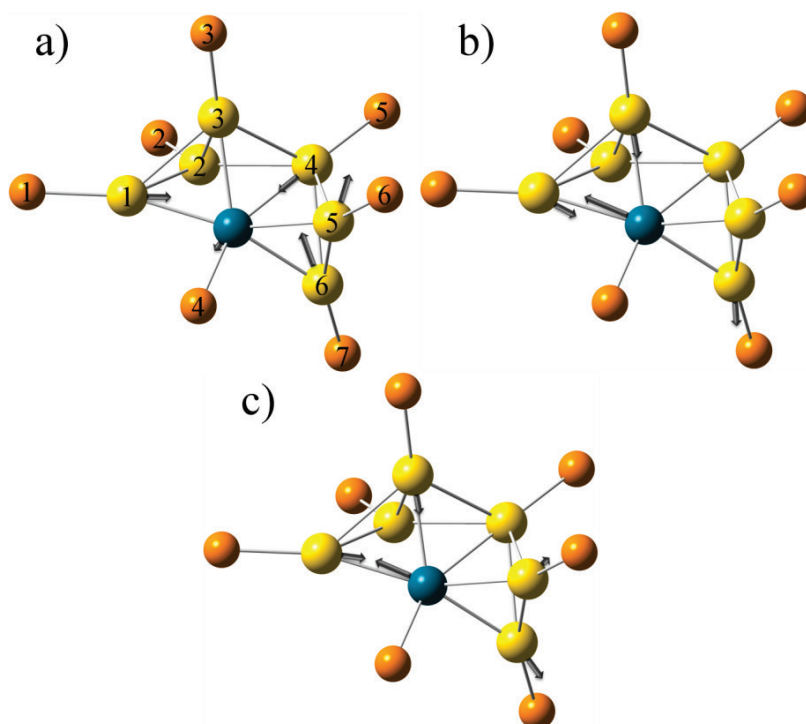


Figure 4.13: Predicted normal mode displacements of the cluster core vibrations for  $\text{Au}_6\text{Pd}$  at a)  $158.9\text{ cm}^{-1}$ , b)  $195.2\text{ cm}^{-1}$ , and c)  $206.7\text{ cm}^{-1}$ . Phenyl groups have been omitted for clarity.

$\text{Au}_6\text{Pd}$  displays the same large featureless absorption below  $\sim 145\text{ cm}^{-1}$  as observed for other clusters presented thus far. The small shoulder in the predicted spectrum at peak #1 could potentially be assigned to the small shoulder near  $146\text{ cm}^{-1}$  in the experimental spectrum, but this cannot be assigned with certainty. The experimentally observed peaks at  $175$ ,  $198$ , and  $219\text{ cm}^{-1}$  are assigned to the predicted peaks #2\*, #3\*, and #4\* at  $159$ ,  $195$ , and  $207\text{ cm}^{-1}$  in the simulated spectrum. These three sets of transitions involve a combination of Au and Pd motion, with predicted transitions at  $158.9$ ,  $195.2$ , and  $206.7\text{ cm}^{-1}$  having a total metal atom motion of over 7%. The contribution from the Pd heteroatom for these transitions ranges from 1–5%. The vector displacement diagrams for these key modes are shown in Figure 4.13 and can be described as the main metal core distortion modes. The other transitions of peak #2\* consist of Pd-Au-P and Pd-Au-Au-P stretches, while the remaining transitions for peaks #3\* and #4\* are Pd-P stretches, along with  $\text{PPh}_3$  rotational and phenyl rocking modes.

The predicted peaks at  $234\text{ cm}^{-1}$  (#5) and  $255\text{ cm}^{-1}$  (#6) are due to phenyl rocking modes, the former of which is not observed in the experimental spectrum, but the latter is assigned to the experimental peak at  $258\text{ cm}^{-1}$ . The predicted peak at  $278\text{ cm}^{-1}$  (#7) is due

to phenyl rotational modes and is assigned to the small shoulder at  $277\text{ cm}^{-1}$  in the experimental spectrum. None of the experimentally observed features in the region between  $300$  and  $375\text{ cm}^{-1}$  are present in the predicted spectrum.

The large shifts in key metal core vibrational modes for  $\text{Au}_6\text{Pd}$  can be attributed to the addition of a metal atom of significantly different mass to Au ( $106.42\text{ amu}$  for Pd compared with  $196.96\text{ amu}$  for Au) and the large change in geometry compared with the  $\text{Au}_6$  or  $\text{Au}_8$  structures.

There is previously published FELIX IR data for the neutral<sup>480,481</sup> and cationic<sup>482</sup> gas-phase  $\text{Au}_6\text{Y}$  cluster that is similar to the  $\text{Au}_6\text{Pd}$  cluster spectral data presented here. These studies show that the neutral structure is distorted from planarity and this yields an IR spectrum with broad peaks ranging from  $75$ – $220\text{ cm}^{-1}$ , while the cationic structure has  $\text{C}_{3v}$  symmetry and sharp peaks at  $121$  and  $181\text{ cm}^{-1}$ . The connectivity of the gas-phase structure is different to that of the ligand-protected  $\text{Au}_6\text{Pd}$  presented here. As stated earlier in the discussion for  $\text{Au}_8$  and  $\text{Au}_9$ , given the difference in cluster geometry, charge, and the solid phase nature of the ligand-protected  $\text{Au}_6\text{Pd}$  cluster, it is surprising that the IR spectrum is comparable to gas-phase  $\text{Au}_6\text{Y}$ .

Table 4.5: Summary of significant calculated transitions for the Au<sub>6</sub>Pd cluster, their assignment to the experimental far-IR spectrum, and brief descriptions of the assigned transition modes.

#	Peak (cm <sup>-1</sup> )	Contributing vibrations (cm <sup>-1</sup> )	IR intensity (km mol <sup>-1</sup> )	%Au motion	%Pd motion	%P motion	Assigned (cm <sup>-1</sup> )	Mode description
1	144	135.7 139.7 142.3 143.9	2.6 1.6 1.4 3.9	2.8% 2.7% 3.3% 3.8%	2.6% 1.5% 0.7% 2.4%	4.1% 2.1% 2.1% 2.4%		
2*	159	149.7* 150.9* 156.0*  157.1* 158.9*  162.2*	3.4 1.5 2.2  4.1 6.5  5.2	5.3% 5.6% 5.8%  6.8% 7.7%  8.3%	2.7% 0.7% 0.8%  0.7% 1.1%  1.9%	3.9% 3.2% 2.6%  4.0% 3.8%  3.7%	174.5	Pd-Au-P stretch P-Au-Au-P stretch Metal core distortion Pd-Au-P stretch Metal core distortion P-Au-Au-P stretch
3*	195 (shoulder)	195.2*  198.9 200.8*	6.0  1.5 1.8	4.7%  1.3% 4.8%	2.5%  1.4% 2.0%	1.8%  2.2% 1.9%	197.7	Metal core distortion PPh <sub>3</sub> rotation Pd-P stretch
4*	207	201.1 206.7*  210.1 211.2 214.5	2.6 9.0  3.7 1.7 1.5	1.9% 8.0%  0.5% 2.6% 8.4%	1.6% 4.9%  1.0% 1.4% 8.5%	1.8% 1.0%  1.5% 1.1% 1.8%	218.9	PPh <sub>3</sub> rotation Metal core distortion Ph rock PPh <sub>3</sub> rotation Pd-P stretch
5	234	233.8	2.1	0.0%	0.0%	0.9%		Ph rock
6	255	252.1 253.5 254.3 254.9 255.7 256.8 260.6	3.1 3.2 4.2 1.4 3.3 3.8 2.5	0.0% 0.0% 0.0% 0.4% 0.0% 0.0% 0.0%	0.0% 0.0% 0.0% 0.3% 0.4% 0.0% 0.0%	1.0% 1.1% 1.1% 1.7% 1.9% 1.3% 0.6%	257.9	Ph rock
7	278	277.6 279.6	0.7 0.4	0.0% 0.0%	0.0% 0.0%	1.0% 1.3%	276.7	Ph rotation
8	445	421.1–449.2	Avg. 4.6	Avg. 0%	Avg. 0%	Avg. 11%	400 - 450+	PPh <sub>3</sub> distortion

#### 4.2.7 Au<sub>7</sub>Pt

The experimental and predicted spectra between 50 and 450 cm<sup>-1</sup> for Au<sub>7</sub>Pt are shown in Figure 4.14, along with a summary of the predicted transitions and spectral assignment in Table 4.6. There are a series of well-resolved peaks between 185 and 279 cm<sup>-1</sup>, along with a shoulder at 398 cm<sup>-1</sup>, and intense absorption from 425 cm<sup>-1</sup> onwards due to PPh<sub>3</sub> ligands. There is also a small shoulder at 149 cm<sup>-1</sup> at the edge of the broad absorption peak, as well as a small doublet at 314 cm<sup>-1</sup>, which is not seen for other clusters.

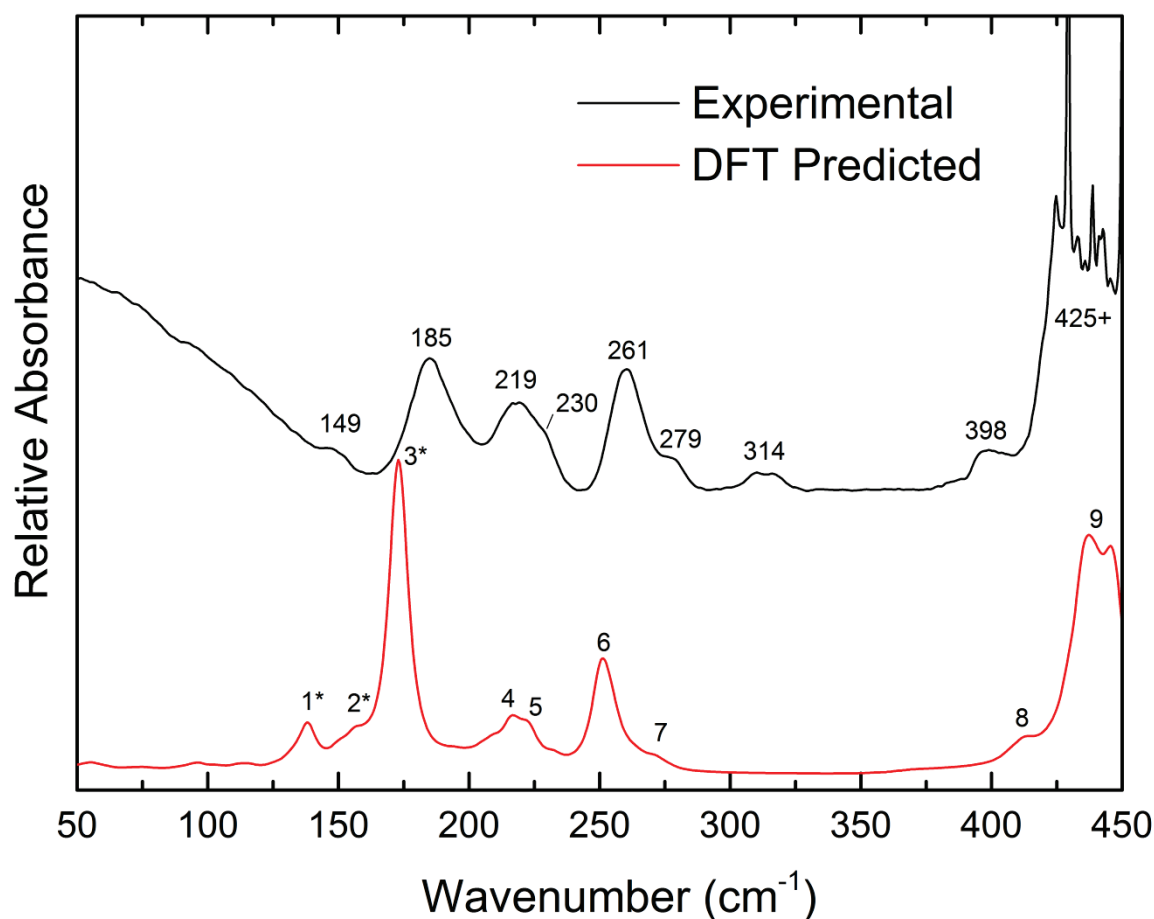


Figure 4.14: Experimental (black line) and simulated (red line) absorption spectra of the  $\text{Au}_7\text{Pt}$  cluster.

The intense calculated peak #3\* at  $173\text{ cm}^{-1}$  is assigned to the large peak at  $185\text{ cm}^{-1}$  in the experimental spectrum and consists of P-Au-Pt-P stretches, P-Au-Pt stretches, and metal core distortion modes. These three transitions have the most combined metal motion out of all the calculated transitions for this cluster, with up to 14.7% Au motion and up to 5.2% Pt motion, along with high IR intensity. The calculated peak #2\* at  $157\text{ cm}^{-1}$  also has large metal atom contributions involving metal core distortion modes and a Pt-H-Au-P distortion, but has lower IR intensity compared with peak #3. Due to the low intensity of this peak as a small shoulder, it is not observed in the experimental spectrum, nor is it likely to be assigned to the peak at  $149\text{ cm}^{-1}$ , given that the position of calculated transitions are typically lower in energy than the experimental peaks for all clusters investigated. Instead, peak #1\* at  $138\text{ cm}^{-1}$  is assigned to peak  $149\text{ cm}^{-1}$  in the experimental spectrum as a P-Au-Pt-P stretching mode contributing a single transition with IR intensity of  $7.9\text{ km mol}^{-1}$ . The vector displacement diagram for the three intense

stretching mode transitions with high %Au motion at  $156.3$ ,  $171.8$ , and  $173.5$   $\text{cm}^{-1}$  are presented in Figure 4.15.

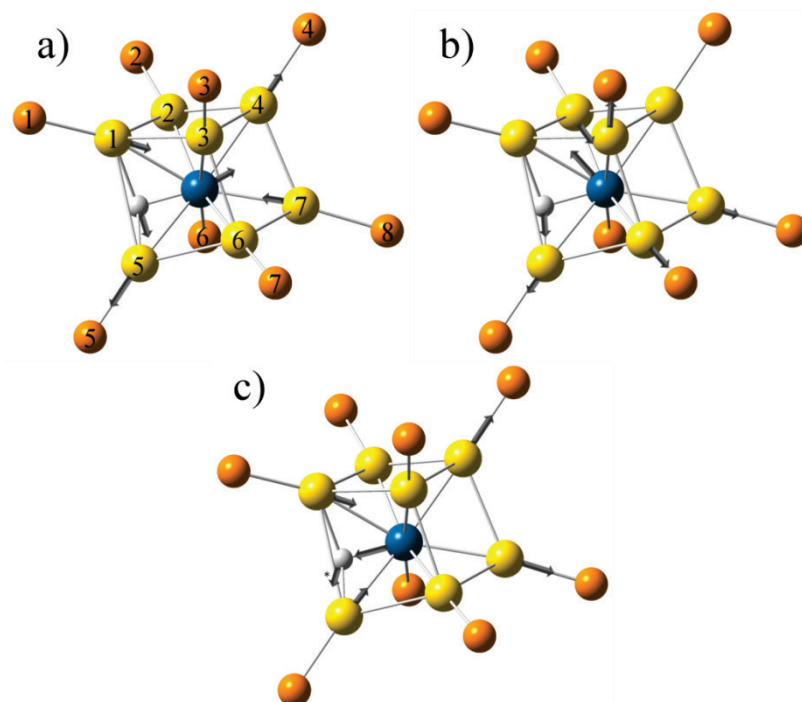


Figure 4.15: Predicted normal mode displacements of the cluster core vibrations for  $\text{Au}_7\text{Pt}$  at a)  $156.3$   $\text{cm}^{-1}$ , b)  $171.8$   $\text{cm}^{-1}$ , and c)  $173.5$   $\text{cm}^{-1}$ . The H atom denoted with an asterisk in c) indicates the atom moves behind the plane of the image. Phenyl groups have been omitted for clarity.

The calculated peaks #4 and #5 at  $217$  and  $223$   $\text{cm}^{-1}$  are assigned to the experimentally observed peaks at  $219$  and  $230$   $\text{cm}^{-1}$ , and consist of multiple low intensity phenyl rocking modes with no significant metal atom motion. The calculated peaks #6 and #7 at  $251$  and  $272$   $\text{cm}^{-1}$  correspond to the experimentally observed peaks at  $261$  and  $279$   $\text{cm}^{-1}$ , and consist of multiple low intensity  $\text{PPh}_3$  breathing and  $\text{PPh}_3$  distortion modes, with no significant metal motion. The small, unassigned doublet at  $314$   $\text{cm}^{-1}$  may be the result of a counter-ion that is not included in the DFT calculation, as proposed earlier for  $\text{Au}_{11}$ .

The experimental and calculated spectra of this sample are similar to that of the  $\text{Au}_8$  cluster spectra, with the differences arising only as a small shift in the peak positions by  $\sim 5\text{--}10$   $\text{cm}^{-1}$ , along with changes to the intensity of various peaks. The similarity of the two spectra is most likely because the two clusters contain the same total number of atoms, they have similar geometry, and the atomic weight of Pt is only  $1.883$  amu lighter than Au. The similar vibrational modes indicate that the differences in bond strength

within the cluster core may be minimal. One of the few key differences is the small doublet at  $314\text{ cm}^{-1}$  observed in the experimental spectrum for  $\text{Au}_7\text{Pt}$ , which is not seen for  $\text{Au}_8$ . Both of these clusters have  $\text{NO}_3$  counter-ions in the crystal structure that are not included in the calculation, yet this peak is only observed for  $\text{Au}_7\text{Pt}$ . This decreases the likelihood that this peak arises from counter-ions, or indicates that such a peak may be difficult to resolve for the  $\text{Au}_8$  cluster. Our collaborators have suggested that their synthesis of this compound may have left some small amount of  $\text{Au}_8\text{Pt}$  impurity present; although this does not appear to have affected the peak assignment in any significant way.

Table 4.6: Summary of significant calculated transitions for the  $\text{Au}_7\text{Pt}$  cluster, their assignment to the experimental far-IR spectrum, and brief descriptions of the assigned transition modes.

#	Peak ( $\text{cm}^{-1}$ )	Contributing vibrations ( $\text{cm}^{-1}$ )	IR intensity ( $\text{km mol}^{-1}$ )	%Au motion	%Pt motion	%P motion	Assigned ( $\text{cm}^{-1}$ )	Mode description
1*	138	138.2	7.9	5.7%	2.9%	5.3%	149	P-Au-Pt-P stretch
2*	157	149.7*	1.7	10.0%	1.2%	5.3%	219	Metal core distortion
		152.4*	1.0	11.0%	1.1%	4.5%		
		156.3*	3.4	10.8%	1.3%	4.6%		
		160.5*	1.4	11.1%	2.5%	4.2%		
3*	173	171.8*	24.5	14.7%	5.2%	2.6%	185	P-Au-Pt-P stretch P-Au-Pt stretch Metal core distortion
		173.5*	28.6	14.8%	5.2%	2.3%		
		174.9*	10.6	12.1%	4.6%	1.9%		
4	217	215.1	1.0	0.0%	0.0%	0.8%	219	Ph rock
		215.8	1.4	0.5%	0.0%	1.0%		
		216.1	1.7	0.0%	0.0%	1.0%		
		217.3	2.1	0.0%	0.0%	0.9%		
5	223 (shoulder)	219.7	1.4	0.0%	0.0%	1.0%	230	Ph rock
		222.1	1.5	0.0%	0.0%	0.8%		
		222.9	2.4	0.0%	0.0%	1.0%		
		223.7	1.6	0.0%	0.8%	1.3%		
6	251	249.5	6.6	0.0%	0.0%	1.2%	261	PPh <sub>3</sub> breathing
		250.0	2.4	0.0%	0.0%	0.8%		
		250.5	1.9	0.0%	0.0%	1.3%		
		251.3	3.2	0.0%	0.0%	1.1%		
		252.1	4.3	0.0%	0.0%	1.7%		
		252.6	0.1	0.5%	0.0%	1.6%		
		253.5	3.4	0.0%	0.0%	1.4%		
		255.1	2.0	0.0%	0.0%	1.1%		
		255.9	1.3	0.0%	0.0%	0.8%		
7	272	271.3	0.4	0.0%	0.0%	1.1%	279	PPh <sub>3</sub> distortion
		271.7	0.2	0.0%	0.0%	1.2%		
8	412 (shoulder)	410.6–417.0	Avg. 0.3	Avg. 0.0%	Avg. 0.0%	Avg. 1.2%	398	Ph twist
9	441	429.1–447.2	Avg. 3.8	Avg. 0.2%	Avg. 0.0%	Avg. 12.8%	425+	PPh <sub>3</sub> wag + H wag

### 4.3 Charge Population Analysis

Charge population calculations were performed for all clusters using Mulliken,<sup>483</sup> NBO,<sup>484</sup> Löwdin,<sup>485</sup> and Hirshfeld<sup>486</sup> charge analysis methods. These values are presented in Table 4.7, with atom labels that correspond to the numbering scheme used in previous Figures. The general trend observed across all clusters and methods is that the metal core atoms have neutral to negative charge, while the P atoms of the ligands have strong positive charge. The metal heteroatoms of Au<sub>6</sub>Pd and Au<sub>7</sub>Pt develop greater negative charge than their surrounding Au atoms, although the Hirshfeld method predicts a positive charge for Pd in Au<sub>6</sub>Pd. The H atom for Au<sub>7</sub>Pt is also predicted to be neutral by all methods except Löwdin, which indicates a small positive charge for the atom. The Hirshfeld prediction of 0 charge for H is due to this method summing hydrogen atom charges into the heavy atoms.

The general trend of positive P atoms holds true for all clusters, however, the Au charges vary somewhat between clusters. For the Au<sub>8</sub> and Au<sub>9</sub> clusters, all methods except Hirshfeld predict the central Au(5) atom to have a stronger negative charge compared with the surrounding Au atoms of the cluster core. For Au<sub>11</sub>, the NBO, and to a greater extent, Mulliken methods, predict many of the surrounding Au atoms to have a positive charge, with the central Au(7) developing a large negative charge. The two Cl atoms of Au<sub>11</sub> also have a reasonable negative charge in all charge analysis methods used. Overall, having a highly coordinated central atom within a cluster, or the presence of any heteroatoms within a cluster, appears to have a strong electron withdrawal effect on the surrounding metal atoms for the Mulliken and NBO methods, while for the Löwdin and Hirshfeld methods, they are simply the most negatively charged of the metal atoms. The large negative charge of these central Au atoms or heteroatoms does not appear to have much effect on the ligand P atoms under any analysis method used.

Comparison of the different methods shows that Mulliken and NBO tend to vary between slightly positive to slightly negative charges for the core metals atoms, while Löwdin and Hirshfeld tend to predict a much larger negative charge for the core metal atoms overall. Hirshfeld analysis does not predict any strong negative bias towards core Au atoms, while Löwdin predicts strong bias for Au(5) and Au(7) atoms in Au<sub>8</sub> and Au<sub>11</sub> respectively, but not for Au<sub>9</sub>. Hirshfeld also predicts much less positive charge for the P atoms compared with all the other methods.

Table 4.7: Predicted atomic charge distributions for the cluster core and ligated atoms. Negatively charged atoms are highlighted in a green gradient, while positively charged atoms are highlighted with a red gradient.

Cluster & Atom #	Core atoms				P atoms			
	Mulliken	NBO	Löwdin	Hirshfeld	Mulliken	NBO	Löwdin	Hirshfeld
<b>Au<sub>6</sub></b>								
1	-0.158	0.094	-0.734	-0.147	0.620	0.854	1.026	0.337
2	-0.236	-0.202	-0.583	-0.118	0.630	0.864	1.042	0.328
3	-0.221	-0.243	-0.586	-0.103	0.527	0.866	1.049	0.341
4	-0.148	-0.179	-0.551	-0.111	0.618	0.888	1.055	0.353
5	-0.113	-0.217	-0.575	-0.108	0.693	0.884	1.054	0.337
6	-0.180	0.102	-0.687	-0.145	0.612	0.877	1.053	0.349
7	-	-	-	-	0.608	0.872	1.037	0.348
8	-	-	-	-	0.626	0.890	1.048	0.346
<b>Au<sub>8</sub></b>								
1	-0.119	0.050	-0.495	-0.114	0.615	0.888	1.075	0.353
2	0.307	0.085	-0.416	-0.114	0.615	0.889	1.075	0.353
3	0.178	0.083	-0.418	-0.113	0.619	0.887	1.074	0.351
4	-0.091	0.061	-0.441	-0.089	0.625	0.942	1.104	0.367
5	-0.928	-1.392	-0.771	-0.096	0.742	1.062	1.149	0.327
6	-0.220	0.043	-0.493	-0.116	0.611	0.887	1.075	0.352
7	-0.126	0.058	-0.485	-0.114	0.614	0.888	1.076	0.353
8	0.285	0.092	-0.406	-0.111	0.614	0.887	1.074	0.354
<b>Au<sub>9</sub></b>								
1	0.010	0.091	-0.399	-0.065	0.585	0.920	1.089	0.375
2	0.010	0.091	-0.399	-0.065	0.585	0.920	1.089	0.375
3	-0.022	0.087	-0.408	-0.100	0.613	0.894	1.077	0.357
4	-0.022	0.087	-0.408	-0.100	0.613	0.894	1.077	0.357
5	-0.688	-1.113	-0.442	-0.033	0.613	0.894	1.077	0.357
6	-0.022	0.087	-0.408	-0.010	0.613	0.894	1.077	0.357
7	-0.022	0.087	-0.408	-0.010	0.585	0.920	1.089	0.375
8	0.010	0.091	-0.399	-0.065	0.585	0.920	1.089	0.375
9	0.010	0.091	-0.399	-0.065	-	-	-	-
<b>Au<sub>11</sub></b>								
1	0.375	0.107	-0.389	-0.080	0.616	0.922	1.094	0.368
2	0.044	0.090	-0.421	-0.105	0.619	0.904	1.086	0.359
3	0.595	0.166	-0.409	-0.027	0.603	0.903	1.086	0.357
4	0.236	0.093	-0.406	-0.102	0.594	0.927	1.096	0.372
5	0.394	0.100	-0.392	-0.085	0.625	0.898	1.083	0.353
6	-0.610	0.130	-0.428	-0.028	0.627	0.903	1.079	0.355
7	-1.299	-2.118	-0.603	-0.024	0.621	0.914	1.091	0.363
8	-0.143	0.170	-0.358	-0.118	0.649	0.922	1.095	0.362
9	-0.022	0.138	-0.388	-0.118	-	-	-	-
10	0.142	0.116	-0.398	-0.095	-	-	-	-
11	0.178	0.130	-0.394	-0.094	-	-	-	-
Cl 1	-0.244	-0.549	-0.136	-0.358	-	-	-	-
Cl 2	-0.250	-0.569	-0.158	-0.354	-	-	-	-
<b>Au<sub>6</sub>Pd</b>								
1	-0.049	0.093	-0.426	-0.139	0.605	0.892	1.075	0.362
2	-0.069	0.018	-0.453	-0.126	0.604	0.886	1.078	0.360
3	-0.078	0.061	-0.404	-0.132	0.596	0.904	1.087	0.365
4	-0.108	-0.029	-0.482	-0.142	0.671	1.003	1.148	0.269
5	0.010	0.090	-0.368	-0.137	0.599	0.896	1.088	0.355
6	-0.113	0.076	-0.398	-0.132	0.590	0.889	1.075	0.362
Pd	-0.126	-0.901	-0.869	0.172	0.614	0.886	1.073	0.363
<b>Au<sub>7</sub>Pt</b>								
1	-0.275	0.143	-0.506	-0.113	0.579	0.900	1.076	0.364
2	0.153	0.123	-0.429	-0.117	0.618	0.892	1.076	0.354
3	0.022	0.109	-0.409	-0.110	0.641	0.920	1.093	0.353
4	-0.256	0.081	-0.485	-0.122	0.612	0.902	1.081	0.355
5	0.047	0.159	-0.452	-0.108	0.579	0.899	1.072	0.364
6	-0.232	0.066	-0.487	-0.125	0.708	1.150	1.206	0.341
7	0.246	0.130	-0.430	-0.116	0.622	0.892	1.074	0.348
Pt	-0.440	-1.900	-1.081	-0.084	0.615	0.905	1.081	0.359
H	0.062	-0.006	0.269	0.000	-	-	-	-



#### 4.4 Conclusions

Synchrotron-based far-IR spectroscopy was used to elucidate the solid-phase vibrational characteristics of Au<sub>6</sub>, Au<sub>8</sub>, Au<sub>9</sub>, Au<sub>11</sub>, Au<sub>6</sub>Pd, and Au<sub>7</sub>Pt clusters in the far-IR region between 50 and 450 cm<sup>-1</sup>. Gas-phase DFT calculations were used to provide verification and detailed analysis of the vibrational modes of each cluster. Characteristic metal-core distortion modes were observed for all clusters between 80 and 185 cm<sup>-1</sup> that shift depending upon the cluster geometry and composition. The most significant of such shifts was observed for Au<sub>6</sub>Pd, which was attributed to the addition of a metal atom of significantly different mass compared to a Au atom. Conversely, the addition of a Pt atom to Au<sub>7</sub>Pt had only marginal affect upon its vibrational spectrum, which was closely related to that of the Au<sub>8</sub> cluster, due to their similar geometry. The Au<sub>6</sub> cluster also has a metal core transition resolved at 90 cm<sup>-1</sup> that was the lowest in energy of all clusters studied in this Chapter. Additionally, strong absorptions in all spectra from 400 cm<sup>-1</sup> and higher were attributed to PPh<sub>3</sub> ligand modes. Au-P stretches were only observed experimentally for Au<sub>6</sub> and Au<sub>6</sub>Pd, near 420 and 180 cm<sup>-1</sup> respectively. The positions of metal core vibrations were observed at similar energies to those reported for gas-phase Au<sub>7</sub> and Au<sub>6</sub>Y clusters reported in FELIX IR studies in the literature.

Charge population analysis showed a general negative to neutral charge for the majority of cluster metal atoms, with the P atoms of the ligands developing a strong positive charge. The central atoms of Au<sub>8</sub>, Au<sub>9</sub>, and Au<sub>11</sub>, as well as the heteroatoms of Au<sub>6</sub>Pd and Au<sub>7</sub>Pt were also predicted to have a larger negative charge than their surrounding metal atoms. While all methods presented agreed on the strong positive charges of the P atoms, there was some discrepancy between the methods for the core metal atoms.

This work has provided valuable information about the metal core structure of ligated gold clusters, and will provide a foundation for future experimental and computational studies of their TiO<sub>2</sub>-supported counterparts.

# Chapter Five

## X-ray and TEM Characterisation of Au<sub>8</sub>, Au<sub>9</sub>, Au<sub>11</sub>, and Au<sub>101</sub> Clusters

In this Chapter, XPS, XANES, EXAFS, and TEM techniques are used to determine the size and chemical state of these gold clusters after they are supported upon acid-washed P25 or pure anatase nanoparticles. In addition, the effects of the following post-treatments designed to remove ligands to activate the catalysts are investigated: 100 °C washing, 200 °C heating under vacuum, 200 °C calcination under an O<sub>2</sub> atmosphere, and 200 °C calcination under an O<sub>2</sub> followed by a H<sub>2</sub> atmosphere. This work allows correlations to be drawn between the photocatalysis results presented in Chapter 6 and the changes to cluster size and chemical state due to these post-treatments.

## 5 X-ray and TEM Characterisation of Au<sub>8</sub>, Au<sub>9</sub>, Au<sub>11</sub>, and Au<sub>101</sub> Clusters

### 5.1 X-ray Photoelectron Spectroscopy Studies of TiO<sub>2</sub>-Supported Gold Clusters

The XPS experiments presented in this section have been performed and analysed as a collaborative effort with the research group of Gunther Anderson and Vladimir Golovko over multiple synchrotron trips. As part of this effort, I undertook data processing and subsequent peak fitting for data acquired from the first soft X-ray beamtime at the Australian Synchrotron, in addition to helping perform experiments during the second soft X-ray beamtime. This work has been included in two recent publications<sup>368,369</sup> and only key results relevant to the discussion of the photocatalytic results in this thesis will be summarised. For further details of the peak intensities and phosphorous spectra that complement the conclusions presented in this section, please see the two publications available in the literature.

XPS spectra were recorded in the Au 4*f*, P 2*p*, Si 2*p*, Ti 2*p*, C 1*s*, and O 1*s* regions for Au<sub>8</sub>, Au<sub>9</sub>, Au<sub>11</sub>, and Au<sub>101</sub> on acid-washed P25 nanoparticles, as well as for Au<sub>8</sub>, Au<sub>9</sub>, and Au<sub>101</sub> on pure anatase nanoparticles. The gold 4*f* region was also measured for a bulk gold reference sample. The energy range of each element were as follows: gold due to the presence of Au<sub>n</sub> clusters was found between 83.7 and 86.1 eV; phosphorous from the PPh<sub>3</sub> ligands was found at 131.8 ± 0.1 and 133.0 ± 0.2 eV; silicon from the silicon wafer used as a sample substrate was found at 99.2 ± 0.1 eV; titanium due to the acid-washed P25 or anatase nanoparticles was found at 459.0 ± 0.1 eV; carbon from the PPh<sub>3</sub> ligands and adventitious hydrocarbons was found at 285 eV; and oxygen from the titanium dioxide was found at 530.3 ± 0.1 eV. The peak fitting procedure used for all elements is described in Section 2.4.2 of Chapter 2.

The C 1*s* peak was used for calibration of the peak positions for all other elements as it is known that adventitious hydrocarbons show a very reproducible C 1*s* peak position and is typically observed in any samples that have been previously exposed to the air during preparation.<sup>487</sup> Adventitious hydrocarbons are usually a thin layer of carbonaceous molecules that are found on the surface of any material or vacuum system exposed to the atmosphere. It consists primarily of short chain hydrocarbons and small amounts of single and double bonded, functionalised groups.<sup>488</sup> The bulk Au 4*f*<sub>7/2</sub> peak is used for comparison to the Au cluster samples as it is known to be found at a binding energy of 84 eV within a range of ~0.2 eV.<sup>489-492</sup> It was determined that there was no charging effects

occurring for the samples, as the invariance between the titanium and silicon signals relative to the gold reference sample was less than 0.05 eV.

Note that the Au 4*f* region consists of a doublet, with the Au 4*f*<sub>7/2</sub> peak having 25% greater intensity than the Au 4*f*<sub>5/2</sub> peak, separated by 3.67 eV. However, for clarity during discussion, it is only the position of the Au 4*f*<sub>7/2</sub> peak that is reported. For some samples, a second set of Au 4*f* peaks is required to fit the data due to the presence of multiple species; an example of such a fit is presented in Figure 5.1. The set of peaks with low binding energy are hereafter referred to as the Au low binding peak (LBP), while the set of peaks with higher binding energy are referred to as the Au high binding peak (HBP). As described in the introduction Chapter, the shifts to higher binding energy for the Au 4*f* peaks relative to bulk Au are indicative of decreasing cluster size,<sup>361,392</sup> while the change in FWHM of peaks is influenced by both initial and final state effects, which depend on the cluster size and their interaction with the support.<sup>391</sup> The fitted peak positions of the Au 4*f* region for all samples presented throughout this section are summarised in Table 5.1 and illustrated in Figure 5.2 for easy comparison of the trends that will be discussed in the following sections.

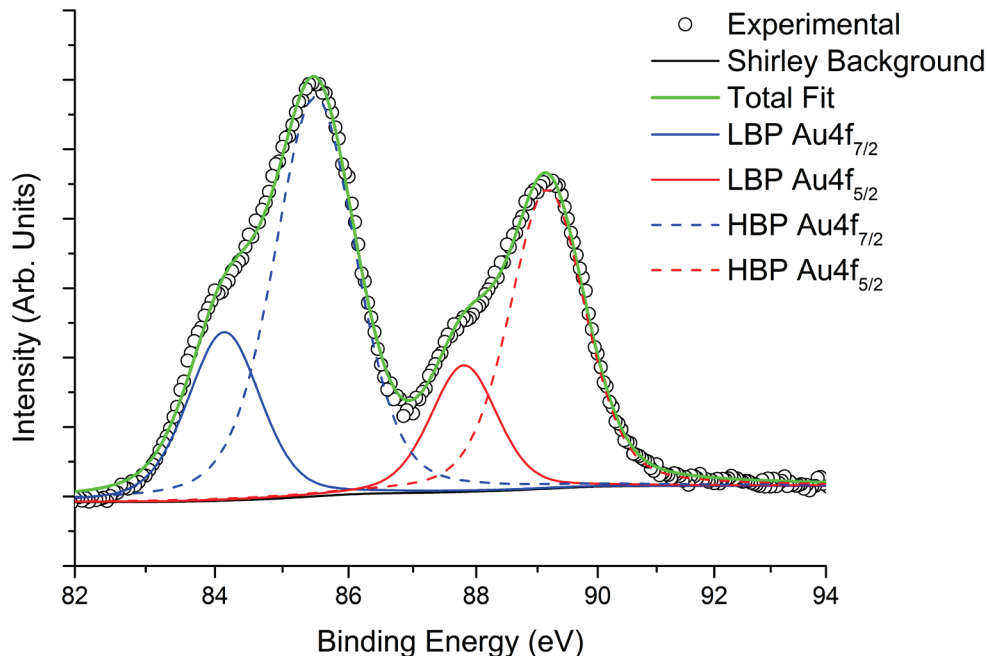


Figure 5.1: Fit of the Au<sub>9</sub>/P25 sample heated under vacuum at 200 °C, requiring both a low and high binding energy set of peaks to adequately model the data.

Table 5.1: The position and FWHM of the Au-LBP and Au-HBP peaks for each cluster and their respective treatments. These results show the decreasing binding energies and FWHMs with succesivley harsher treatments.

	Untreated		Washed 100 °C		Heated under Vac. 200 °C		Calcined O <sub>2</sub> 200 °C		Calcined O <sub>2</sub> /H <sub>2</sub> 200 °C	
	Energy (eV)	FWHM (eV)	Energy (eV)	FWHM (eV)	Energy (eV)	FWHM (eV)	Energy (eV)	FWHM (eV)	Energy (eV)	FWHM (eV)
<b>Acid-washed P25 Nanoparticle Support</b>										
Au <sub>8</sub> LBP	85.1 ± 0.1	1.6 ± 0.2	84.8 ± 0.1	1.5 ± 0.2	84.0 ± 0.1	1.2 ± 0.2	-	-	-	-
Au <sub>8</sub> HBP	-	-	85.6 ± 0.1	1.5 ± 0.2	85.4 ± 0.1	1.6 ± 0.1	-	-	-	-
Au <sub>9</sub> LBP	85.1 ± 0.1	1.6 ± 0.2	84.8 ± 0.1	1.7 ± 0.2	84.2 ± 0.1	1.3 ± 0.2	-	-	-	-
Au <sub>9</sub> HBP	-	-	85.9 ± 0.1	1.2 ± 0.2	85.5 ± 0.1	1.5 ± 0.1	-	-	-	-
Au <sub>11</sub> LBP	84.7 ± 0.1	1.6 ± 0.2	85.0 ± 0.2	1.9 ± 0.2	84.2 ± 0.1	1.1 ± 0.2	-	-	-	-
Au <sub>11</sub> HBP	-	-	86.1 ± 0.1	1.3 ± 0.2	85.5 ± 0.1	1.5 ± 0.1	-	-	-	-
Au <sub>101</sub> LBP	83.9 ± 0.1	1.0 ± 0.2	83.9 ± 0.1	1.0 ± 0.2	83.9 ± 0.1	0.9 ± 0.2	-	-	-	-
Au <sub>101</sub> HBP	-	-	-	-	84.8 ± 0.1	2.3 ± 0.2	-	-	-	-
<b>Pure Anatase Nanoparticle Support</b>										
Au <sub>8</sub> LBP	83.7 ± 0.1	1.1 ± 0.2	-	-	-	-	83.7 ± 0.1	1.0 ± 0.2	83.7 ± 0.1	1.0 ± 0.2
Au <sub>8</sub> HBP	85.3 ± 0.2	1.5 ± 0.2	-	-	-	-	85.4 ± 0.2	2.2 ± 0.1	-	-
Au <sub>9</sub> LBP	83.7 ± 0.1	1.1 ± 0.2	-	-	-	-	83.7 ± 0.1	1.0 ± 0.2	83.7 ± 0.1	1.0 ± 0.2
Au <sub>9</sub> HBP	85.3 ± 0.2	1.9 ± 0.2	-	-	-	-	-	-	-	-
Au <sub>101</sub> LBP	83.7 ± 0.1	1.0 ± 0.2	-	-	-	-	83.8 ± 0.1	1.0 ± 0.2	84.0 ± 0.1	1.0 ± 0.2
Au <sub>101</sub> HBP	-	-	-	-	-	-	-	-	-	-

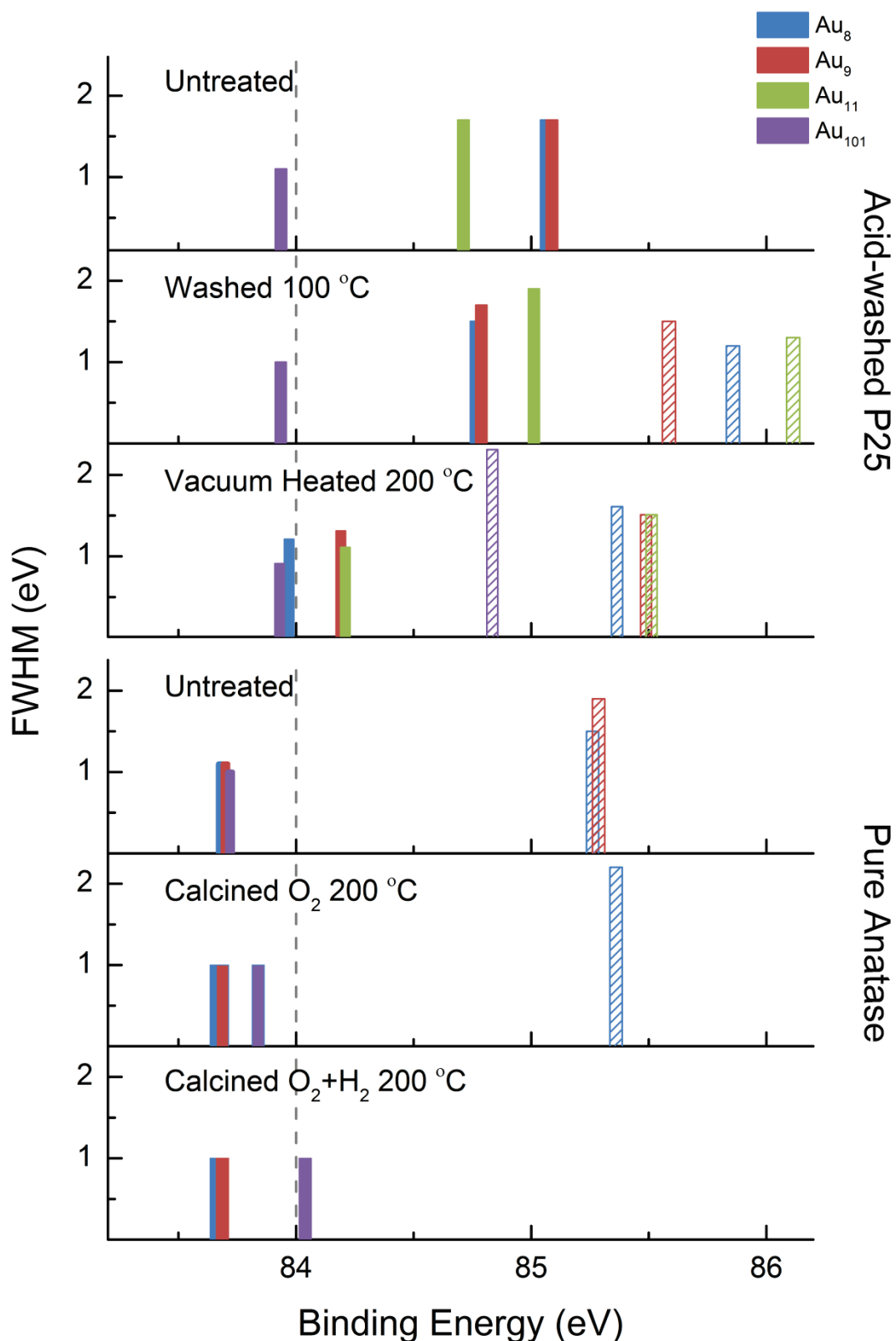


Figure 5.2: Comparison of the fitted XPS peak positions and FWHM between the different cluster treatments and supports. The solid bars represent the Au 4f<sub>7/2</sub> LBP and the dashed bars represent the Au 4f<sub>7/2</sub> HBP. The vertical dashed line is the binding energy of metallic bulk gold.

### 5.1.1 Au<sub>8</sub>, Au<sub>9</sub>, Au<sub>11</sub>, and Au<sub>101</sub> Supported on Acid-washed P25 Nanoparticles

#### 5.1.1.1 Untreated

For the untreated samples, all gold spectra can be fit with a single peak for the Au 4f<sub>7/2</sub> and 4f<sub>5/2</sub> doublet. Au<sub>101</sub> has a binding energy and FWHM within experimental error of the metallic bulk gold reference (84 eV). In comparison, the peak positions of the Au<sub>8</sub>, Au<sub>9</sub>, and Au<sub>11</sub> clusters are shifted to a higher binding energy, and the FWHM of these clusters are also greater ( $1.6 \pm 0.2$  eV) than that of the bulk gold reference (1 eV).

These shifts represent a clear trend, with the untreated Au<sub>8</sub> and Au<sub>9</sub> samples having a greater binding energy than Au<sub>11</sub>, which in turn has a greater binding energy and FWHM than Au<sub>101</sub> or the metallic gold reference sample. Essentially, as the number of gold atoms is increased, the binding energy of the cluster decreases, accompanied by a decrease in the FWHM of the peak. These shifts in peak position and FWHM have previously been attributed to finite size effects that depend upon the elemental composition and type of support<sup>405,493</sup> due to changes in initial and final state effects.<sup>391</sup> Therefore, these shifts can be attributed to the finite nature of the clusters and decreases in cluster size. These binding energies shifts are similar to that observed by other reports of nano-sized gold clusters.<sup>404,409,494</sup> These untreated samples also have the same peak positions and FWHM as the reference Au<sub>n</sub> samples deposited onto atomic layer deposited (ALD) TiO<sub>2</sub>. These results indicate that the precise cluster sizes are unaffected by being supported on acid-washed P25 nanoparticles, maintaining their small size. By comparison, Au<sub>101</sub> is so large that it cannot be differentiated from bulk gold, as it has a binding energy and FWHM within experimental error of the reference.

#### 5.1.1.2 Washed at 100 °C

For the samples washed at 100 °C in toluene, a second peak is required to fit the data for the Au<sub>8</sub>, Au<sub>9</sub>, and Au<sub>11</sub> samples (Au-HBP). The Au<sub>101</sub> sample does not require a second peak to adequately fit the experimental data and instead has a peak at a similar binding energy and FWHM to that of its untreated counterpart. The Au-LBP for Au<sub>8</sub>, Au<sub>9</sub>, and Au<sub>11</sub> is found at similar positions and with a comparable FWHM to the untreated samples. This indicates that this portion of the clusters is not significantly altered after washing. In comparison, the Au-HBP is attributed to the formation of Au-O bonds with

the surface, as the binding energy shifts are much greater than those of the untreated samples. It is not attributed to the formation of fully oxidised gold clusters, as the binding energy shifts relative to the untreated samples is only +0.8 and +1.1 eV, which is significantly less than the +2 eV shifts that have been reported previously in the literature.<sup>495,496</sup> Given the relatively gentle washing treatment in toluene used here, compared with the strong oxidising agents used in the literature previously,<sup>497-499</sup> oxidation of the gold clusters with the ambient air is less likely than the formation of Au-O bonds to the surface. The formation of Au-O indicates that some ligands have been removed from the cluster and that the gold core is now in direct contact with the TiO<sub>2</sub>.

The formation of the Au-HBP could also be attributed to the possibility of a portion of the gold clusters agglomerating to form bulk gold oxide with the applied treatment. However, this is unlikely given the relatively mild conditions of washing at 100 °C discussed previously. There is no Au-HBP observed for Au<sub>101</sub>, and therefore no evidence of the formation of Au-O bonds.

The ratio of the normalised total Au signal intensity of the washed samples relative to the untreated samples shown in Table 5.2 indicates a large decrease in the total signal intensity after washing. This indicates that the washings remove a fraction of the clusters from the support, with Au<sub>11</sub> and Au<sub>101</sub> losing greater amount of clusters compared to others. The associated publication shows that there is too much experimental uncertainty in the intensity of the phosphorous signal for it to be used to determine if there is a loss of ligands to support the argument for the formation of Au-O bonds above.<sup>368</sup>

Table 5.2: Total intensity of the Au 4*f* peaks relative to the untreated samples.

	Washed at 100 °C (%)	Heat under vac. at 200 °C (%)
Au <sub>8</sub> LBP	37 ± 10	7 ± 10
Au <sub>8</sub> HBP	16 ± 20	19 ± 10
Au <sub>9</sub> LBP	47 ± 10	12 ± 10
Au <sub>9</sub> HBP	17 ± 10	33 ± 10
Au <sub>11</sub> LBP	13 ± 10	15 ± 10
Au <sub>11</sub> HBP	18 ± 10	40 ± 10
Au <sub>101</sub> LBP	5 ± 5	28 ± 10
Au <sub>101</sub> HBP	-	14 ± 10

### 5.1.1.3 Heated Under Vacuum at 200 °C

For the samples heated under vacuum at 200 °C, the Au-LBPs for Au<sub>8</sub>, Au<sub>9</sub>, and Au<sub>11</sub> have all shifted close to that of bulk gold. The FWHM of these peaks have also decreased substantially. Given the large shift in binding energies and FWHM towards that of bulk gold, these calcined clusters have almost certainly undergone significant agglomeration. Since the binding energies and the FWHM of these clusters remain slightly larger than that of Au<sub>101</sub>, these clusters would be only marginally smaller than those of untreated Au<sub>101</sub>.

The Au-HBPs for these clusters are found at much higher binding energies relative to bulk, but are less than that observed for the samples washed at 100 °C. The FWHM of these peaks are also close to those of the untreated samples. In addition, this treatment results in the appearance of a Au-HBP for the Au<sub>101</sub> cluster. Therefore, as discussed previously for the washed samples, this is attributed to the formation of Au-O bonds for this portion of the clusters. However, given that the binding energy of these peaks are closer to that of bulk gold than for the washed samples, it is difficult to assign with certainty whether these peaks are due to fully oxidised gold clusters or oxidised bulk gold. The formation of these Au-O bonds are again most likely to involve the TiO<sub>2</sub> surface oxygen atoms, as heating at 200 °C under a vacuum is not considered a harsh enough treatment for the gold to react with gas-phase oxygen. Note that of this portion of

clusters that lose their ligands to form Au-O bonds, there may be agglomeration, since the Au-HBP shift has reduced compared to the washed samples.

The total intensity of Au 4*f* peaks for the samples heated at 200 °C shown in Table 5.2 is also significantly reduced compared to the untreated samples, and the Au-HBP of Au<sub>8</sub>, Au<sub>9</sub>, and Au<sub>11</sub> show more intensity than their Au-LBP. Given that calcination does not result in the removal of any clusters from the support surface, the decrease in intensity would be the result of signal attenuation from cluster agglomeration. This is because signal from gold at the side of the cluster close to the support would be attenuated due to the limited mean free path of the photoelectrons. Further information and supporting arguments using P 2*p* spectra are available in the associated publication.<sup>368</sup> The conclusions of this were that the removal of ligands from the cluster and their concurrent oxidation is less efficient for Au<sub>9</sub> when compared with Au<sub>8</sub> or Au<sub>11</sub>. In addition, the phosphorous of the ligands are oxidised during heat treatment for all clusters, but remain on the surface.

## 5.1.2 Au<sub>8</sub>, Au<sub>9</sub>, and Au<sub>101</sub> Supported on Pure Anatase Nanoparticles

### 5.1.2.1 Untreated

For the untreated Au<sub>8</sub> and Au<sub>9</sub> clusters supported on pure anatase nanoparticles, a second peak at higher binding energies (~85.3 eV) is required to fit the data adequately. Given the high binding energies and large FWHM of these Au-HBP peaks, they are attributed to clusters that maintain their size and chemical nature due to the large shift from bulk gold, and are at similar positions to the peaks observed for these untreated clusters on acid-washed P25 nanoparticles. There is no Au-HBP present for the Au<sub>101</sub> sample. Note that for discussion of this support, the Au-HBP is attributed to non-agglomerated clusters in a similar fashion to the Au-LBP of the P25 supported clusters.

The Au-LBP peak of the Au<sub>8</sub> and Au<sub>9</sub> clusters are at the same binding energy as that of Au<sub>101</sub>, at 83.7 eV. These binding energies are close to the 84 eV binding energy of bulk gold and are therefore attributed to agglomerated clusters. The small Au/total P intensity shown in the publication<sup>369</sup> supports the argument that the gold clusters are agglomerating. The P 2*p* spectra also indicate the removal of some PPh<sub>3</sub> ligands.

The intensity ratio of the Au-HBP:LBP presented in the associated publication<sup>369</sup> for Au<sub>8</sub> and Au<sub>9</sub> are close to 1:1, indicating that there is an approximately equal amount of pristine and agglomerated clusters present in the sample. It is unknown if there is any agglomeration occurring for Au<sub>101</sub>, as the peak position and FWHM of the Au-LBP is already near that of bulk Au. It is surprising that such a large portion of the clusters have agglomerated on the pure anatase nanoparticles without any post-treatment, compared with the same clusters supported on acid-washed P25 nanoparticles.

### 5.1.2.2 Calcined under O<sub>2</sub> at 200 °C

For the samples calcined under O<sub>2</sub> at 200 °C, it is only the Au<sub>8</sub> cluster that displays a Au-HBP with a large FWHM. The signal intensity of the Au-HBP relative to the Au-LBP for Au<sub>8</sub> is close to 1:1. Given the high binding energy and large FWHM of the Au<sub>8</sub> Au-HBP, it is likely that this portion of the Au<sub>8</sub> clusters maintain their size on the pure anatase surface. The position of this peak is also remarkably similar to the Au-HBP of acid-washed P25 supported Au<sub>8</sub> clusters heat treated at 200 °C under vacuum, although with a much larger FWHM (2.2 vs 1.6 eV).

The low binding energy and small FWHM of the Au-LBP for all clusters are similar to that of the untreated samples, being close to that of bulk gold, indicating that this portion of the clusters have agglomerated. The P 2*p* data shown in the associated publication<sup>369</sup> indicates that ligands are removed from the clusters and become bound to the anatase surface, providing further evidence for the agglomeration of the gold clusters. This effect is more pronounced for the calcined under O<sub>2</sub> samples compared to the untreated samples, indicating that the removal of ligands and agglomeration has progressed to a greater extent.

### 5.1.2.3 Calcined under O<sub>2</sub> followed by H<sub>2</sub> at 200 °C

For the samples calcined under O<sub>2</sub> + H<sub>2</sub> at 200 °C, there are no Au-HBPs required for fitting, with all three clusters having only a Au-LBP near that of bulk gold. Analysis of the P 2*p* peaks in the associated publication,<sup>369</sup> which demonstrates that the intensity ratio between Au/P peaks is less than the stoichiometric ratio of Au/P in pristine clusters,

indicates that the PPh<sub>3</sub> ligands have been completely removed from the clusters and are now deposited onto the TiO<sub>2</sub> surface. Given this information, it can be concluded that calcination under O<sub>2</sub> + H<sub>2</sub> at 200 °C results in complete removal of ligands from the gold clusters and significant agglomeration, to a greater extent than calcination under O<sub>2</sub> at 200 °C. This is expected for these samples, due to the harsh environment of extended calcination for 2 hours under O<sub>2</sub> followed by 2 hours under H<sub>2</sub>, compared with the 2-hour calcination under O<sub>2</sub> alone for the previous set of samples. There is no change to the binding energy or FWHM for the Au<sub>101</sub>, so although ligands are certainly removed, it is unknown from this data if there is any agglomeration for this cluster.

### 5.1.3 Comparison Between Supports

Comparison of the binding energy and FWHM between the P25 and anatase supports for the untreated Au<sub>8</sub> and Au<sub>9</sub> clusters shows the most pronounced differences. For the acid-washed P25 nanoparticles, the untreated clusters remain small and pristine, while for the same clusters supported pure anatase nanoparticles, there is partial removal of ligands, with a portion of clusters maintaining their size, while the others undergo partial agglomeration. This shows the strong influence that acidic pre-treatment of TiO<sub>2</sub> can have on its interaction with supported clusters, as well as the effect of a pure anatase polymorph compared with the 76:11:13 anatase:rutile:amorphous<sup>143</sup> mix of P25. Acidic pre-treatment of TiO<sub>2</sub> has been shown previously to enhance the dispersion of small metal particles, helping to prevent agglomeration.<sup>360</sup> This would likely be due to the presence of hydroxyl groups on the surface of TiO<sub>2</sub> after acidic pre-treatment, as this has been demonstrated to influence the growth and morphology of small metal clusters.<sup>291,358,359</sup>

Subsequent heat treatments at 200 °C results in ligand removal and agglomeration for clusters on both supports but this effect is far more pronounced on the pure anatase nanoparticles. The harsher heat treatments under O<sub>2</sub> and O<sub>2</sub>/H<sub>2</sub> used for the pure anatase-supported clusters also result in a greater extent of agglomeration and full ligand loss when compared to those on the acid-washed P25 support. In addition to this, the lack of gentle washing at 100 °C post-treatment for the pure anatase samples prevents the observation of an intermediate shift in the peak position and FWHM for the Au region as seen for the acid-washed P25 supported samples.

## 5.2 X-ray Absorption Near Edge Structure of Supported Gold Clusters

Unsupported and supported Au<sub>8</sub> and Au<sub>9</sub> clusters were investigated using XAS at the Australian National Beamline Facility at the Photon Factory, Tsukuba, Japan. Part of the XANES data presented in this section was also included in the publication mentioned previously.<sup>369</sup> The sample loadings and post-treatments used for these experiments are identical to those used for the XPS and photocatalysis experiments presented in the previous section and Chapter 6. In order to test the susceptibility of the Au<sub>9</sub> cluster to photo-induced ligand desorption, one sample was kept in the dark leading up to the XAS experiments. Additionally, Au<sub>9</sub> clusters were also supported on fumed silica for comparison of support effects. For further information about the sample preparation methods used at the XAS beamline, please see Chapter 2.

### 5.2.1 Anatase-Supported Au<sub>9</sub> clusters

The Au L<sub>III</sub>-edge XANES spectra for unsupported Au<sub>9</sub> and anatase-supported Au<sub>9</sub> clusters, as well as that of the bulk gold reference foil, are shown in Figure 5.3. Features indicated by arrows at 11925, 11947, 11969, and 11977 eV change substantially between the various treatments of samples. The spectrum of the unsupported Au<sub>9</sub> cluster has been confirmed by EXAFS analysis in the next section to match that of the crystal structure reported by Wen *et al.*<sup>431</sup> and can therefore be used as a baseline for the XANES spectrum of atomically precise, non-agglomerated Au<sub>9</sub>. The unsupported Au<sub>9</sub> cluster has a unique spectrum, showing a distinct peak at 11925 eV. In comparison, the supported Au<sub>9</sub> clusters approach the features of bulk gold with successively harsher treatments.

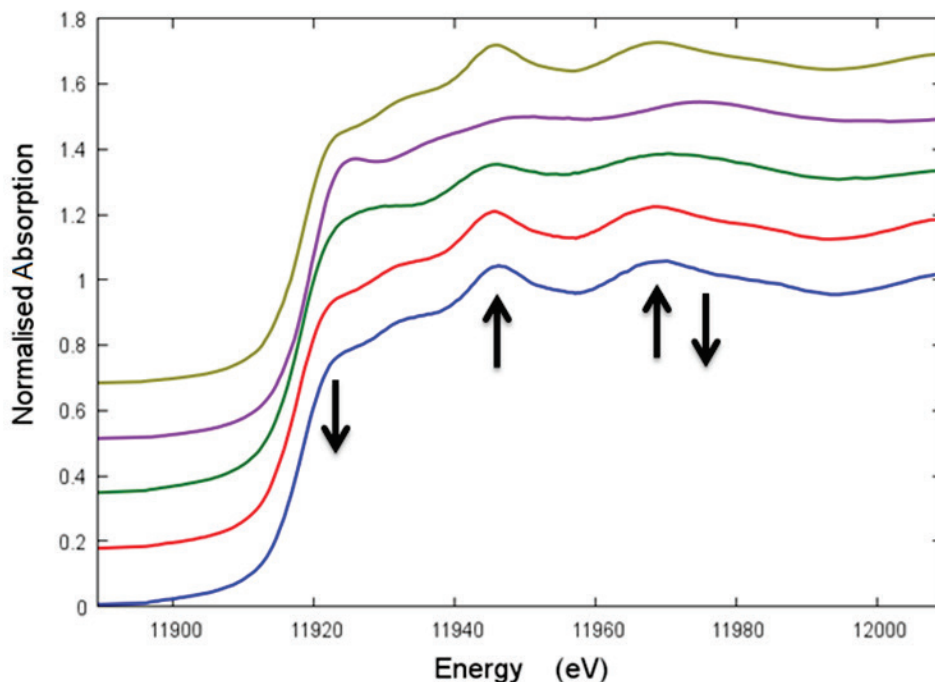


Figure 5.3: Au L<sub>III</sub>-edge XANES spectra of unsupported Au<sub>9</sub> clusters (purple line), untreated Au<sub>9</sub>/anatase (green line), Au<sub>9</sub>/anatase calcined under O<sub>2</sub> at 200 °C (red line), Au<sub>9</sub>/anatase calcined under O<sub>2</sub> + H<sub>2</sub> at 200 °C (blue line), and the bulk Au reference foil (gold line). The arrows indicate regions of significant change with successively harsher treatments.

It can be assumed that the clusters are agglomerating and losing ligands upon being supported on the anatase nanoparticles and after successively harsher treatments in a similar fashion to that observed during XPS investigations. Therefore, it is possible to distinguish the changes to the XANES spectra of the supported Au<sub>9</sub> clusters using multiple linear regression with a linear combination fit of the pure, unsupported Au<sub>9</sub> cluster and the bulk Au reference foil. A summary of the refined fitting parameters for the linear combination fitting procedure are presented in Table 5.3. The R-factor reported in the table is defined as  $\sum(data - fit)^2 / \sum data^2$  and is an indicator of how well the linear combination fit matches the experimental data.

Table 5.3: Summary of linear combination fitting parameters for XANES analysis of Au<sub>9</sub> supported on pure anatase. The R-factor is defined as  $\sum(data - fit)^2 / \sum data^2$ .

Treatment	Unsupported Au <sub>9</sub> contribution (%)	Bulk Au reference contribution (%)	R-factor
Untreated	61.9 ± 5.9	38.1 ± 4.9	0.0018942
Calcined O <sub>2</sub> 200 °C	0.0 ± 3.2	100.0 ± 0.00	0.0006479
Calcined O <sub>2</sub> + H <sub>2</sub> 200 °C	0.0 ± 6.8	100.0 ± 0.00	0.0007426
Untreated and kept away from ambient light	100.0 ± 5.5	0.0 ± 4.5	0.0015041

The results from Table 5.3 are shown pictorially in Figure 5.4 for each sample. The best fit for untreated Au<sub>9</sub> supported on anatase contains 61.9 ± 5.9 % contribution from pure Au<sub>9</sub> and 38.1 ± 4.9 % contribution from bulk Au, with a small difference in the residual visible just after the edge. In the context of XANES analysis, the bulk Au signal is characteristic of agglomerated Au nanoparticles that have begun to show an internal lattice structure as their size increases. These results indicate that the Au<sub>9</sub> cluster has agglomerated significantly after being supported on the anatase surface. This analysis is in agreement with the XPS data, which showed that support of Au<sub>9</sub> upon anatase resulted in loss of ligands and partial agglomeration of a fraction of the clusters. The small discrepancy in the fit just after the edge is expected, since the sample would consist of a complex mixture of intact clusters with a portion of agglomerated clusters that are still smaller than that of bulk gold. Hence, the exact chemical nature of this mixture would be difficult to model precisely using a simple linear combination of the pristine Au<sub>9</sub> cluster and bulk Au foil.

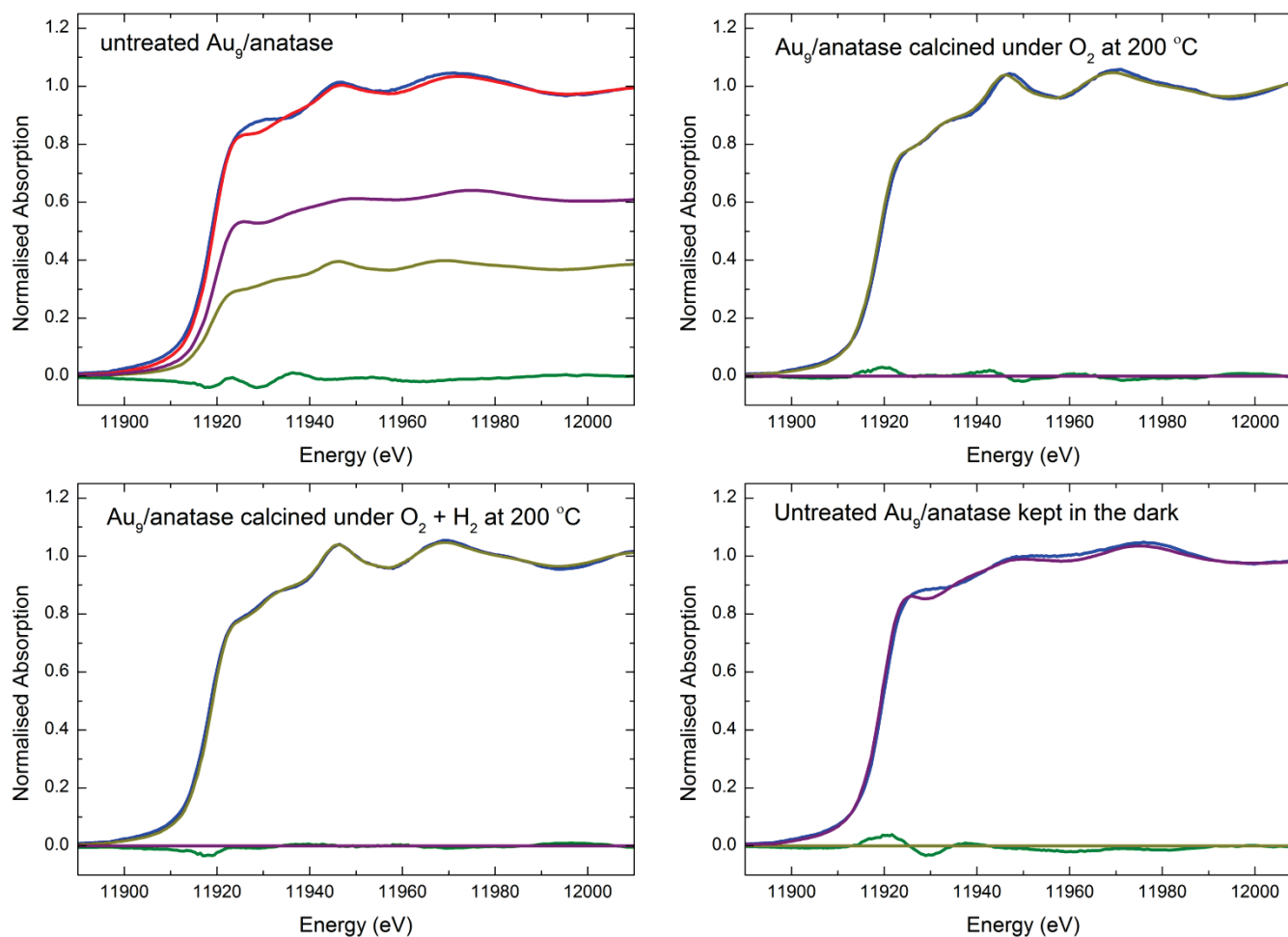


Figure 5.4: Linear combination fits of the Au L<sub>III</sub>-edge XANES spectra (blue) for the various anatase-supported Au<sub>9</sub> clusters. The fit components are unsupported Au<sub>9</sub> (violet line) and bulk Au (gold line). The residual difference between the fit and the experimental spectrum is shown as the green line. The total linear combination fit (ref) is only shown for untreated Au<sub>9</sub>/anatase for clarity.

The linear combination fit for the Au<sub>9</sub>/anatase calcined under O<sub>2</sub> at 200 °C sample is shown in Figure 5.4. The best fit of 100% bulk Au signal is clearly a near exact match for this sample, with the residual showing very little difference between the two spectra. The XANES spectrum of Au<sub>9</sub>/anatase calcined under O<sub>2</sub> + H<sub>2</sub> 200 °C also has a best fit comprising entirely of bulk Au signal that is a near exact match. The linear combination fitting of these XANES spectra are in agreement with the XPS results, which showed that calcination under O<sub>2</sub> for Au<sub>9</sub>/anatase resulted in close to complete removal of ligands and a large degree of agglomeration for the Au<sub>9</sub> clusters, while calcination under O<sub>2</sub> and H<sub>2</sub> resulted in complete removal of ligands in addition to further agglomeration of clusters. The samples calcined under O<sub>2</sub> should also have some small amount of ligands remaining according to XPS, but they do not appear to affect the XANES signal by any detectable amount.

In order to test the susceptibility of the Au<sub>9</sub> cluster to photo-induced ligand desorption, one sample was kept away from ambient light leading up to the XAS experiments; Figure 5.4 shows a linear combination fit of the untreated Au<sub>9</sub>/anatase Au-L<sub>III</sub>-edge XANES spectrum kept in the dark. The best fit for this spectrum contains  $100.0 \pm 5.5$  % unsupported Au<sub>9</sub> and  $0.0 \pm 4.5$  % bulk Au signal, with some small difference in the residual seen above the edge at 11930 eV. This result indicates that the vast majority of the untreated Au<sub>9</sub> cluster remains intact upon the anatase surface when the sample is kept away from ambient light, compared with the light exposed sample that had  $35.1 \pm 3.0$  % of the clusters agglomerated. Unfortunately, this effect was not investigated for other clusters, nor was it investigated during XPS experiments. It is an observation that should be investigated more thoroughly in the future as it may have an effect on the outcome of related experiments.

### 5.2.2 Silica-Supported Au<sub>9</sub> clusters

Au<sub>9</sub> clusters were supported on fumed silica to determine if there were any significant changes to the Au<sub>9</sub> clusters when supported on a different oxide support. The Au L<sub>III</sub>-edge XANES spectra for unsupported Au<sub>9</sub> and silica-supported Au<sub>9</sub> clusters, as well as that of the bulk gold reference foil, are shown in Figure 5.5. Similar to the anatase-supported XANES spectra, there are strong features indicated by arrows at 11925, 11947, 11969, and 11977 eV that change substantially after the clusters undergo harsher treatments,

approaching the signal shown for bulk Au. Note that there are no XPS data available for these samples. A summary of all the refined fitting parameters discussed in this section are presented in Table 5.4. The results of the fitting procedure are also shown pictorially in Figure 5.6.

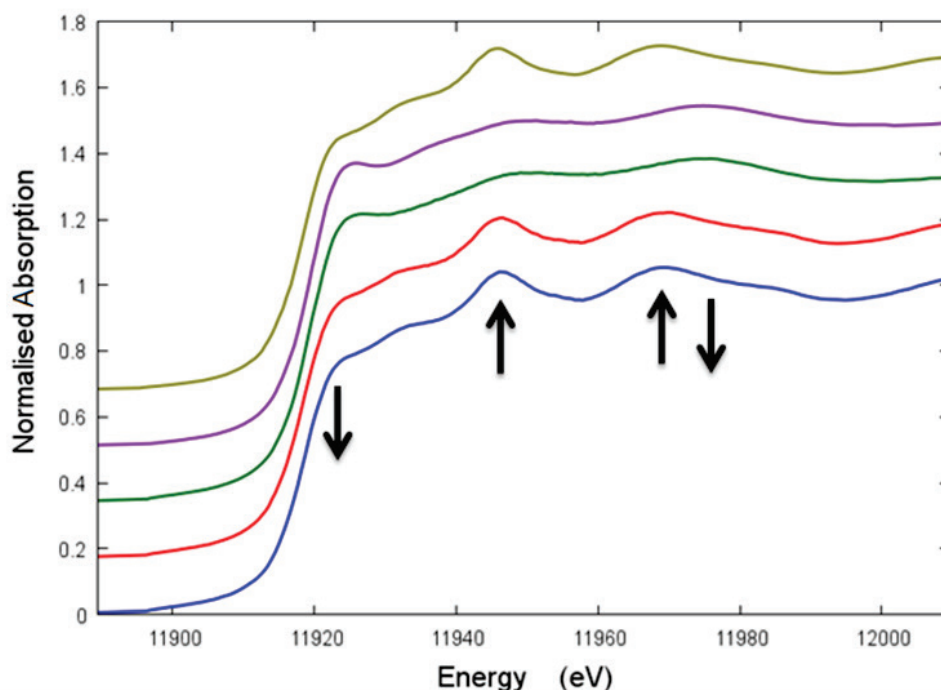


Figure 5.5: Au L<sub>III</sub>-edge XANES spectra of unsupported Au<sub>9</sub> clusters (purple line), untreated Au<sub>9</sub>/silica (green line), Au<sub>9</sub>/silica calcined under O<sub>2</sub> at 200 °C (red line), Au<sub>9</sub>/silica calcined under O<sub>2</sub> + H<sub>2</sub> at 200 °C (blue line), and the bulk Au reference foil (gold line). The arrows indicate regions of significant change with successively harsher treatments.

Table 5.4: Summary of linear combination fitting parameters for XANES analysis of Au<sub>9</sub> supported on fumed silica. The R-factor is defined as  $\sum(data - fit)^2 / \sum data^2$ .

Treatment	Unsupported Au <sub>9</sub> contribution (%)	Bulk Au reference contribution (%)	R-factor
Untreated	100.0 ± 5.4	0.0 ± 4.3	0.0013929
Calcined O <sub>2</sub> 200 °C	15.5 ± 4.8	84.5 ± 3.6	0.0010360
Calcined O <sub>2</sub> + H <sub>2</sub> 200 °C	1.3 ± 3.9	98.7 ± 2.2	0.0003811

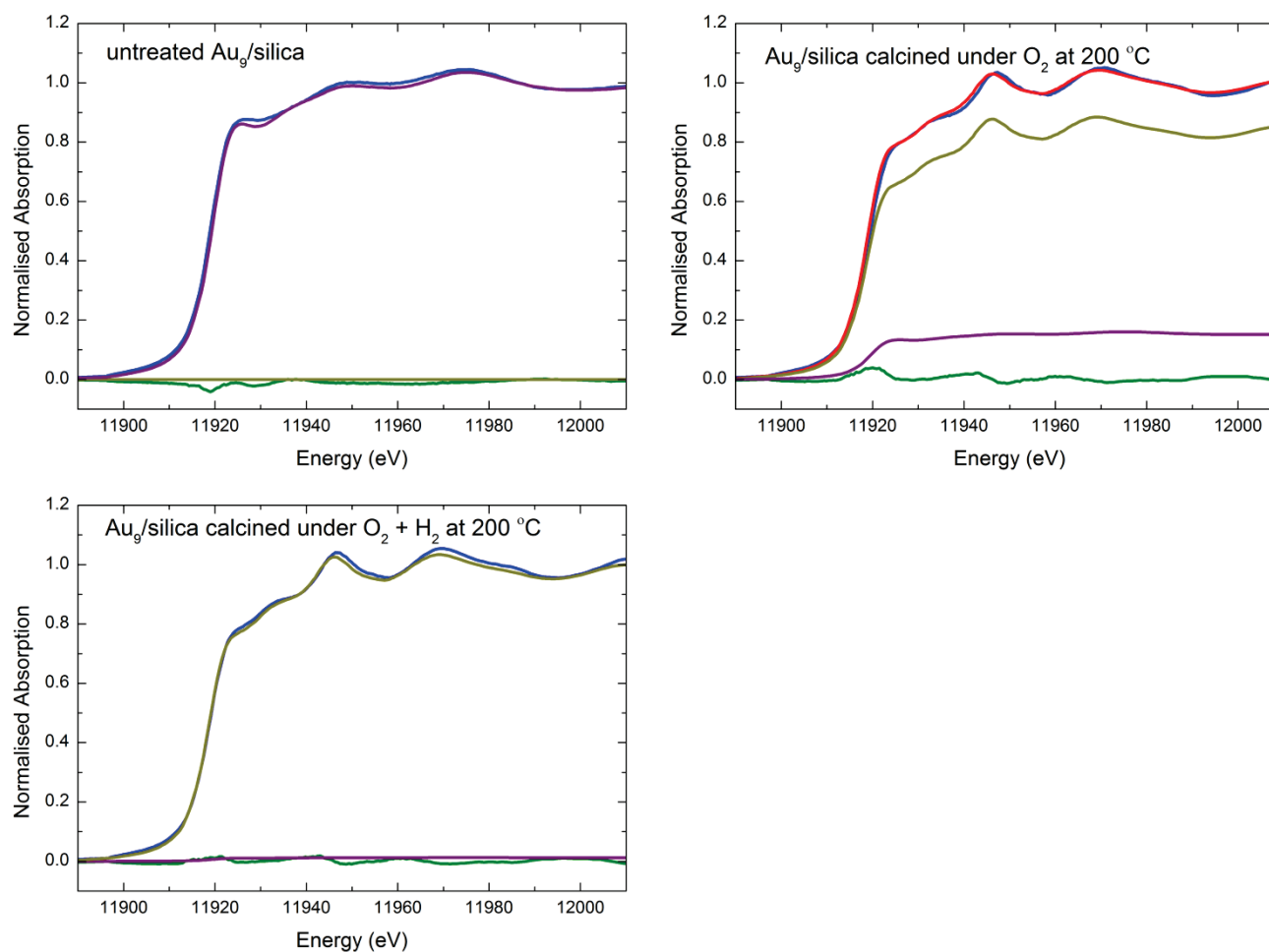


Figure 5.6: Linear combination fits of the Au L<sub>III</sub>-edge XANES spectra (blue) for the various silica-supported Au<sub>9</sub> clusters. The fit components are unsupported Au<sub>9</sub> (violet line) and bulk Au (gold line). The residual difference between the fit and the experimental spectrum is shown as the green line. The total linear combination fit (ref) is only shown for Au<sub>9</sub>/silica calcined under O<sub>2</sub> at 200 °C for clarity.

The best fit for the untreated Au<sub>9</sub>/silica sample contains  $100 \pm 5.4$  % unsupported Au<sub>9</sub> signal, with no contribution from bulk Au, and only a small difference in the residual observed above the edge at 11930 eV. This indicates that the untreated Au<sub>9</sub> cluster remains intact when supported on silica surfaces, with no agglomeration occurring. This is in remarkable contrast to the large amount of agglomeration observed for untreated Au<sub>9</sub>/anatase in Figure 5.4.

For the Au<sub>9</sub>/silica sample calcined under O<sub>2</sub> at 200 °C, the best fit contains  $15.5 \pm 4.8$  % contribution from an unsupported Au<sub>9</sub> XANES spectrum, and  $84.5 \pm 3.6$  % contribution from a bulk Au XANES spectrum. The best fit for the calcined under O<sub>2</sub> and H<sub>2</sub> Au<sub>9</sub>/silica sample contains  $1.3 \pm 3.9$  % contribution from an unsupported Au<sub>9</sub> XANES spectrum and  $98.7 \pm 2.2$  % from a bulk Au XANES spectrum. Both of these fits show good agreement with the experimental data. Calcination under O<sub>2</sub> for silica-supported Au<sub>9</sub> clearly results in significant agglomeration of the clusters, with only a small fraction remaining intact; however, the agglomeration is not as complete as it was for Au<sub>9</sub>/anatase when calcined under O<sub>2</sub>. It is only after extended calcination under an O<sub>2</sub> and H<sub>2</sub> atmosphere that the silica-supported samples reach almost complete agglomeration, evidenced by the bulk Au signal contributing the majority of the signal. When compared with the anatase-supported samples, it becomes clear that the support plays an important role in the properties of the supported clusters.

### 5.3 Extended X-ray Absorption Fine Structure Analysis

#### 5.3.1 Unsupported Au<sub>8</sub> and Au<sub>9</sub>

EXAFS modelling was undertaken on the unsupported Au<sub>8</sub> and Au<sub>9</sub> samples to confirm the atomically precise nature of the clusters and to support the conclusions drawn from XANES analysis. 3D multiple scattering models were created in the XFIT program based upon the Cartesian coordinates available in the literature for the X-ray crystal structures of pure Au<sub>8</sub> and Au<sub>9</sub>. Only the Au and P atoms are included in the model to reduce the number of fitting parameters as the contribution from the phenyl rings to the EXAFS signal are expected to be negligible.

Table 5.5 summarises the refined fitting parameters for the Au<sub>8</sub> and Au<sub>9</sub> models, as well as the R-factor values, which indicate how well the calculated model fits the experimental data. The experimental EXAFS spectra for the unsupported Au<sub>8</sub> and Au<sub>9</sub> clusters, as well as the calculated best-fits, are presented in Figure 5.7 and Figure 5.8, respectively. Each Au atom is modelled as an absorbing atom with unique potential, with one  $E_0$  and one  $S_0^2$  variable shared between all Au atoms. All P atoms share one variable for their Debye-Waller factor to reduce the number of fitting parameters. The  $k$  space window is 2–18 Å<sup>-1</sup> with a Fourier window between 1 and 4 Å for the fit refinement. Two types of models are used for each cluster; one with the  $S_0^2$  scaling factor fixed at 1.00, and another where  $S_0^2$  is refined as a variable. The second model allows  $S_0^2$  to be refined during the fitting procedure and matches the experimental data more closely for both clusters; however, a  $S_0^2$  greater than 1 is not typically used during the refinement process in the literature. Allowing the  $S_0^2$  variable to be refined is necessary in order to match the large magnitude of the experimental data without using unphysically small Debye-Waller factors.

Table 5.5: EXAFS fitting parameters for the 3D multiple scattering models refined using XFIT. The  $k$  space window is 2–18 Å<sup>-1</sup> with a Fourier window between 1 and 4 Å for the fit refinement. The numbers in parenthesis indicate the precision of the last digit.

Sample	Model #	$S_0^2$	Au Average $\sigma^2$ (Å <sup>2</sup> )	P $\sigma^2$ (Å <sup>2</sup> )	$\Delta E_0$ (eV)	R-factor
Au <sub>8</sub>	1	1.00 (fixed)	0.0074	0.00012	5 (2)	28.6 %
Au <sub>8</sub>	2	1.3 (1)	0.0094	0.00096	6 (2)	26.7 %
Au <sub>9</sub>	1	1.00 (fixed)	0.0003	0.000008	-24(2)	31.0 %
Au <sub>9</sub>	2	2.0 (4)	0.0011	0.00096	-25(2)	29.8 %
Au <sub>9</sub>	3	4 (3)	0.0015	0.00096	-15.2 (9)	26.7 %

$S_0^2$  is the scale factor,  $\sigma^2$  is the multiple scattering Debye-Waller factor,  $\Delta E_0$  is the difference between the start of the calculated EXAFS and the threshold energy for the absorbing atoms defined as 11935 eV in the XFIT program, and the R-factor represents the residual between the calculated and experimental data. R-factor is defined as  $R = \sqrt{X^2/X_{calculated=0^2}}$  where  $X^2$  is the quantity minimised during refinement and  $X_{calculated=0^2}$  is the value of  $X^2$  when the calculated EXAFS is uniformly zero.

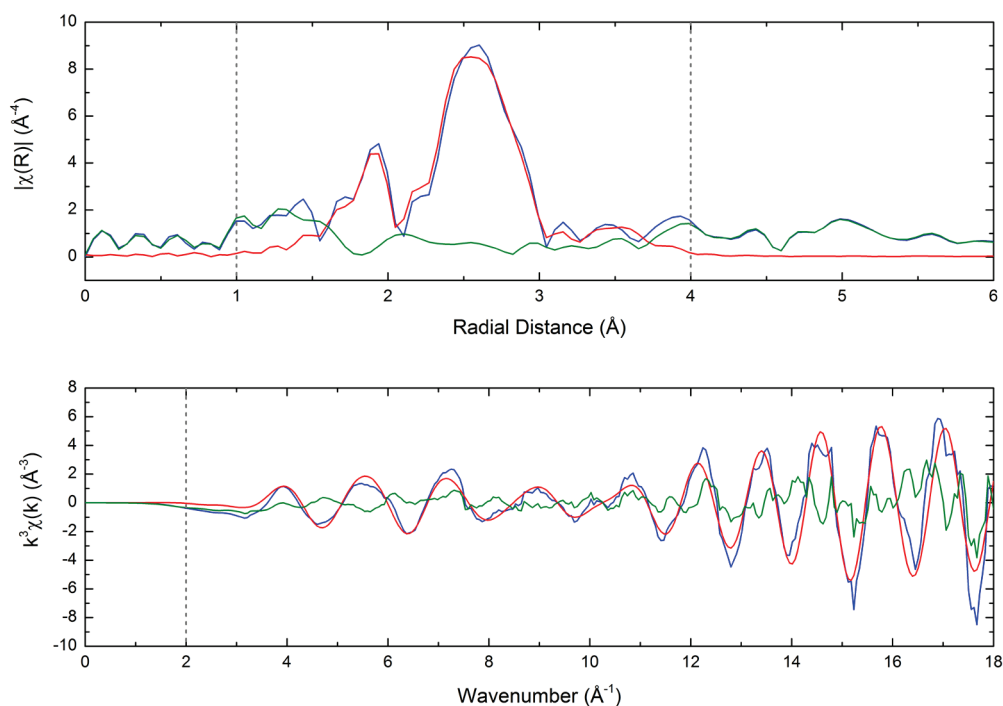


Figure 5.7: Multiple scattering 3D model #2 of the unsupported Au<sub>8</sub> cluster EXAFS in  $k^3$  weighted  $k$  space (bottom) and the associated Fourier transform of the EXAFS fit (top). The blue line is the experimental EXAFS, the red line is the calculated EXAFS, and the green line is the residual of the fit. The dashed lines indicate the window of the fit.

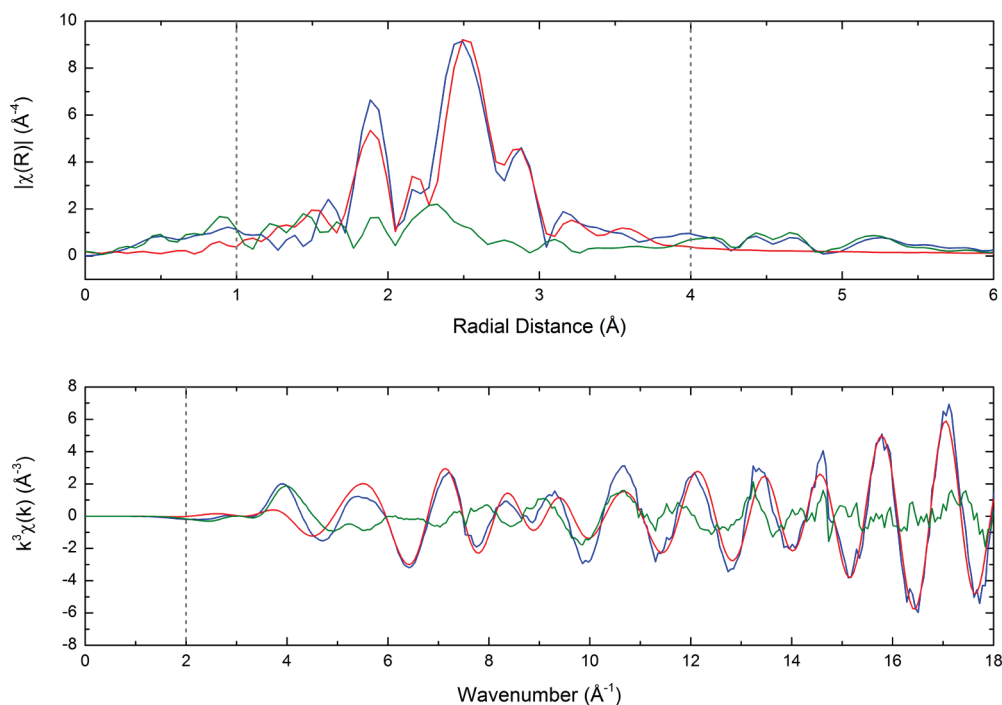


Figure 5.8: Multiple scattering 3D model #2 of the unsupported Au<sub>9</sub> cluster EXAFS in  $k^3$  weighted  $k$  space (bottom) and the associated Fourier transform of the EXAFS fit (top). The blue line is the experimental EXAFS, the red line is the calculated EXAFS, and the green line is the residual of the fit. The dashed lines indicate the window of the fit.

Both Au<sub>8</sub> and Au<sub>9</sub> show a good match between the calculated model and the experimental EXAFS between the fitting space of 1 and 4 Å in the Fourier transform. The Fourier transform of the EXAFS clearly shows strong Au-Au paths between 2.2 and 3 Å, and Au-P paths due to the PPh<sub>3</sub> ligands between 1.6 and 2 Å. There is some discrepancy in the  $k^3$  weighted  $k$  space for Au<sub>9</sub> at 4 Å<sup>-1</sup>, although this is typical of EXAFS data close to the edge, as this region is very sensitive to spline fitting during data processing. Model #2 is considered the most appropriate, as model #3 for Au<sub>9</sub>, while having a lower R-factor, has a very large  $S_0^2$  that may be considered unreasonable.

The refined geometries of model #2 for both Au<sub>8</sub> and Au<sub>9</sub> are presented in Figure 5.9, as well as the starting geometries obtained from crystal structures in the literature.<sup>430,431</sup> The full Cartesian coordinates of these models are available in Appendix A. This figure shows how closely the geometry of the EXAFS model matches that of the crystal structure. Both the Au<sub>8</sub> and Au<sub>9</sub> crystal structures have C<sub>s</sub> and D<sub>2</sub> symmetry respectively, and attempts made to constrain the 3D models to these forms of symmetry to reduce the number of

fitting parameters resulted in poor fits, with R-factors over 50 %. It is only by removing the symmetry constraints that acceptable fits are found.

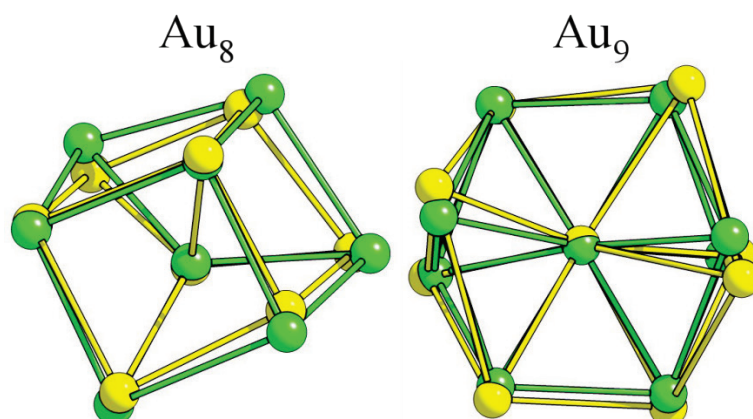


Figure 5.9: Au atom positions for the Au<sub>8</sub> and Au<sub>9</sub> clusters used for the calculated EXAFS model (yellow) superimposed upon the respective X-ray crystal structure geometries (green), showing the close match in atomic positions.

This EXAFS analysis confirms the atomically precise structure of the unsupported Au<sub>8</sub> and Au<sub>9</sub> cluster. This supports the XANES linear combination fitting presented in the previous section, as the unsupported Au<sub>9</sub> experimental XANES signal used as a model of non-agglomerated cluster is the same experimental data used for the EXAFS fitting of the Au<sub>9</sub> model.

### 5.3.2 Anatase- and Silica-Supported Au<sub>9</sub> Clusters

Attempts were made to analyse the EXAFS of anatase-supported Au<sub>9</sub> clusters using the same models used for the pure unsupported Au<sub>9</sub> cluster. However, the presence of agglomerated clusters evidenced by XANES and XPS makes for a complex EXAFS signal. Therefore, it was not possible to fit this EXAFS data with the same 3D models used for unsupported Au<sub>9</sub>. Multiple attempts were made to model the supported Au<sub>9</sub> clusters with large nanoparticle-like 3D models, or models involving Ti and O atoms of surface TiO<sub>2</sub>, but none of these models yielded physically realistic fitting parameters. Since the XANES indicated that the treated samples are fit remarkably well with bulk Au foil, multiple scattering crystalline bulk Au models were created and fit to the experimental data to determine if it was possible to distinguish the agglomerated clusters from the Au reference foil and to confirm the XANES analysis.

The experimental and calculated EXAFS for the Au foil and Au<sub>9</sub>/anatase samples are presented in Figure 5.10, with the corresponding refined parameters for the multiple scattering bulk Au model shown in Table 5.6. The EXAFS spectra of silica-supported Au<sub>9</sub> samples are visually similar to that of Au<sub>9</sub>/anatase and are available in Appendix A. The fitting  $k$ -range is 1–14 Å<sup>-1</sup> and a fixed  $S_0^2$  of 0.9 is used for all fits.  $\Delta E_0$ ,  $\alpha$ , and  $\Theta_D$  are the only parameters refined during the fitting process.  $\alpha$  is the isotropic thermal expansion coefficient a crystal lattice, expressed in the form  $\alpha \cdot R_{eff}$ , where  $R_{eff}$  is the effective path length of the various multiple scattering paths in the model.  $\Theta_D$  is the temperature coefficient for the correlated Debye model where  $\sigma^2 = Debye(Temp \cdot \Theta_D)$  and is a measure of disorder in the system. The untreated samples are unable to be fit using this metallic bulk Au model and are not presented here, since they are primarily composed of pristine Au<sub>9</sub> clusters according to XPS and XANES.

Table 5.6: Refined EXAFS fitting parameters for the multiple-scattering bulk Au model. The  $k$ -range is 1–14 Å<sup>-1</sup> and a fixed  $S_0^2$  of 0.9 is used for all fits.  $\Delta E_0$ ,  $\alpha$ , and  $\Theta_D$  are the three variables refined during the fitting process. The numbers in parenthesis indicate the precision of the last digit.

Sample	$\Delta E_0$ (eV)	$\alpha$	$\Theta_D$	Temp (K)	R-factor (%)
Au foil	3.9 (3)	-0.0144 (9)	177 (2)	300	4.57
Au <sub>9</sub> /anatase calc. O <sub>2</sub>	6.9 (5)	-0.0085 (5)	142 (5)	15	4.01
Au <sub>9</sub> /anatase calc. O <sub>2</sub> +H <sub>2</sub>	7.7 (5)	-0.0085 (5)	154 (5)	15	3.48
Au <sub>9</sub> /silica calc. O <sub>2</sub>	7.7 (5)	-0.0082 (5)	140 (5)	15	3.65
Au <sub>9</sub> /silica calc. O <sub>2</sub> +H <sub>2</sub>	6.5 (5)	-0.0084 (4)	154 (5)	15	3.08

$S_0^2$  is the scale factor,  $\Delta E_0 = E_0 - 11919$  eV where  $\Delta E_0$  is the difference between the start of the calculated EXAFS and the threshold energy for the absorbing atoms defined as 11919 eV in the Athena program;  $\alpha$  is the isotropic thermal expansion coefficient expressed in the form  $\alpha \cdot R_{eff}$ , where  $R_{eff}$  is the effective path length of the various multiple scattering paths;  $\Theta_D$  is the temperature coefficient for the correlated Debye model where  $\sigma^2 = Debye(Temp \cdot \Theta_D)$ ; and the R-factor is defined as  $\sum(data - fit)^2 / \sum data^2$ .

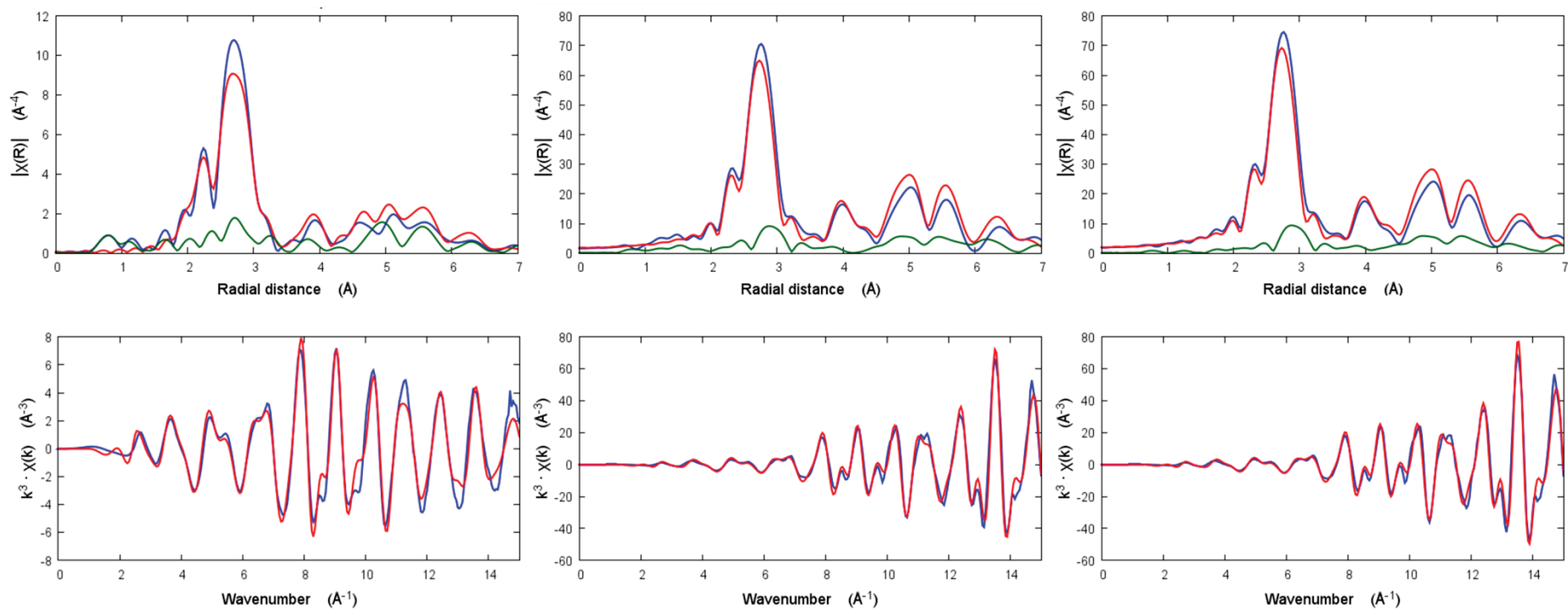


Figure 5.10: Multiple scattering bulk Au EXAFS fits in  $k^3$  weighted  $k$  space (bottom) and the associated Fourier transform (top) for the Au reference foil (left), Au<sub>9</sub>/anatase calcined under O<sub>2</sub> at 200 °C (centre), and Au<sub>9</sub>/anatase calcined under O<sub>2</sub> + H<sub>2</sub> 200 °C (right). The experimental EXAFS data is represented as the blue line, the calculated EXAFS is the red line, and the residual is the green line. The data is fit between 1 and 7 Å in  $R$  space, with all 53 multiple scattering paths up to 7 Å included in the model.

All the models fit the data very well (R-factor <5 %) with only three parameters used in the fitting process. Note that the Au<sub>9</sub> samples were cooled to 15 K, while the Au reference foil that resides outside the sample chamber was unable to be cooled due to the experimental setup. Low temperature measurements provide high intensity EXAFS spectra by decreasing the disorder; hence, the quality of supported Au<sub>9</sub> samples far exceeds that of the Au reference foil, which is typically only used for edge calibration. The large amplitude in  $k^3$ -weighted space and  $R$  space for the supported Au<sub>9</sub> samples are also the result of the low temperature measurement and have been observed previously for low-temperature studies of AuNPs.<sup>500</sup>

Visual inspection of the calculated models shows no Au-P scattering at 1.6–2 Å and a large amount of long-range multiple scattering paths appearing from 3.9 Å and beyond. This is consistent with a loss of PPh<sub>3</sub> ligands and agglomeration of the cluster. It is due to this agglomeration that the clusters can be modelled using a bulk Au lattice, as the particles develop an internal lattice structure. The loss of the Au-P bonds in the EXAFS and the appearance of metallic gold properties for the Au<sub>9</sub>/anatase samples has also been observed in an EXAFS study by Yuan *et al.*,<sup>501</sup> which showed decomposition of the Au<sub>9</sub> cluster and the formation of metallic gold particles on their TiO<sub>2</sub> surfaces when heat treated at 300 °C under vacuum. The fact that the agglomerated clusters can be fit well with a FCC bulk gold model has been shown previously for Au clusters as small as 11 Å,<sup>502</sup> although deviation from the octahedral closed shell structure of bulk gold has been shown for particles 25 Å in size.<sup>503</sup> Pinto *et al.* has also shown that gold clusters deposited by evaporation can show truncated octahedral structures.<sup>504</sup> It is therefore unsurprising that the FCC bulk Au model fits the agglomerated clusters so well.

Inspection of the fitted parameters shows that all of the supported Au<sub>9</sub> samples are fit with a negative thermal expansion coefficient ( $-\alpha$ ); however, it is unknown why the Au foil also shows lattice contraction ( $-\alpha$ ), given that it is measured at 300 K. It would be expected that the Au foil would show positive lattice contraction at this temperature. Attempts to fit the Au foil with a fixed thermal expansion coefficient resulted in poor fits to the experimental data. This could be attributed to the lack of experimental repeats for the Au reference foil, in addition to the high temperature measurement, both of which would increase the noise of the spectrum and increase disorder in the photoelectron scattering, resulting in poor quality data. For the Au<sub>9</sub> clusters, some lattice contraction would be expected due to their low temperature measurement. In addition to this, size-

dependent Au particle lattice contraction can occur, whereby the smaller the Au particle, the greater the amount of lattice contraction observed.<sup>500,502-506</sup> This effect can be quite significant, for example, the negative expansion coefficient for the Au<sub>9</sub>/anatase clusters result in bond length contraction for the first Au-Au scattering path of  $\sim 0.02 \text{ \AA}$  ( $\alpha \cdot R_{eff}$ ). Surface stress has been proposed as the cause of this lattice contraction for finite-size metallic systems.<sup>500</sup> It is difficult, however, to disentangle the size-dependent lattice contraction from that of thermal contraction in the results presented herein, without a more detailed study using a variety of temperatures.

Similarly, the calculated Debye temperature can be used to ascertain the approximate size of a Au nanoparticle. The study by Yang and Li showed that the Debye temperature decreases with decreasing particle size for metallic nanocrystals  $> 1 \text{ nm}$  in size, and have also developed a model that can be used to predict this size-dependency.<sup>507</sup> However, this model was developed for measurements taken at room temperature, so it cannot be directly applied here. The general trend of decreasing Debye temperature with decreasing particle size can instead be used to provide a general explanation of the calculated trends for the supported Au<sub>9</sub> samples. Both Au<sub>9</sub>/anatase and Au<sub>9</sub>/silica are calculated to have smaller Debye temperatures than the Au foil. In addition to this, the samples calcined for an extended period under O<sub>2</sub> + H<sub>2</sub> have larger Debye temperatures than those samples calcined only under O<sub>2</sub>. Clearly, the Debye temperature is increasing and approaching that of the bulk Au reference foil with successively harsher calcination treatments. No clear difference in size can be distinguished here between the two supports, due to the precision of the refined parameters. Given the information already known about the agglomeration of Au<sub>9</sub>/anatase samples from XPS and XANES, these results show that extended calcination under O<sub>2</sub> + H<sub>2</sub> results in larger particle sizes, but that they are still nanoparticulate in nature and do not match that of the bulk Au.

#### 5.4 Transmission Electron Microscopy Studies of TiO<sub>2</sub>-Supported Gold Clusters

The data presented in this section is a summary of a combination of TEM work from our collaborators that is relevant to the results presented in this thesis. Initial experiments using ADF-STEM were performed by Shery Chang at Monash University, Australia. HRTEM experiments were performed by David P. Anderson at the University of Canterbury, New Zealand. These images and data also appear in David Anderson's thesis, but some have been included here as they form an important part of the discussion for the post-treatment of supported gold clusters.

##### 5.4.1 Angular Dark Field Scanning Transmission Electron Microscopy

ADF-STEM images of pure, unsupported Au<sub>9</sub> deposited on agar holey carbon films are shown in Figure 5.11. These samples were deposited at a concentration of 1 mg of clusters per 10 mL of methanol. The ADF-STEM images show two sets of particle sizes, with the small set of particles typically ~0.85 nm in size, while the larger set of particles vary greatly, with the largest measuring ~2 nm. The 0.85 nm particles are close to the expected size of the Au<sub>9</sub> core according to the X-ray crystal structure and are therefore attributed to intact cluster. The large particles are most likely Au<sub>9</sub> clusters that have agglomerated due to ligand desorption under vacuum or due to the 300 keV electron beam. <sup>31</sup>P NMR confirmed that there is only one P peak present in the sample, which corresponds to the P peak of the cluster ligands and not from any other species.

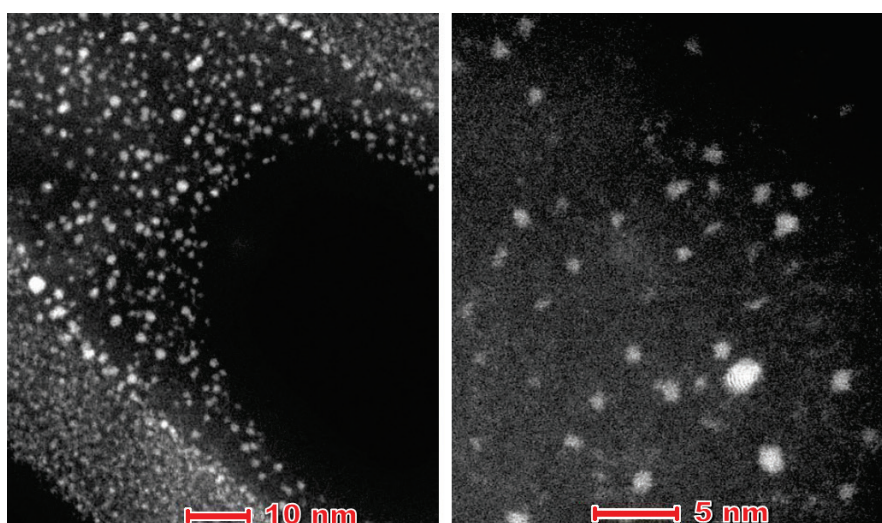


Figure 5.11: ADF-STEM images of pure Au<sub>9</sub> clusters deposited on an agar holey carbon film at concentrations of 1 mg of cluster per 10 mL of methanol.

ADF-STEM images of low concentration samples of unsupported Au<sub>9</sub> and are shown in Figure 5.12. The concentration of these samples was 1 grain (<0.1 mg) per 6 mL of methanol. These low concentration samples resulted in uniform particles ~0.8 nm in size. However, there are also a small number of single gold atoms present in the images. In the case of the low concentration samples, the single gold atoms could be the result of beam damage and fragmentation, compared to the high concentration samples whereby it is more likely for the clusters to agglomerate due to beam exposure. The likelihood of these single gold atoms arising from AuPPh<sub>3</sub>Cl precursor is low, given that <sup>31</sup>P NMR does not show any evidence of another species being present, as discussed earlier. These images confirm that the majority of clusters remain intact after synthesis and during TEM studies if an appropriate sample loading is used, while a small amount may undergo unintended beam damage.

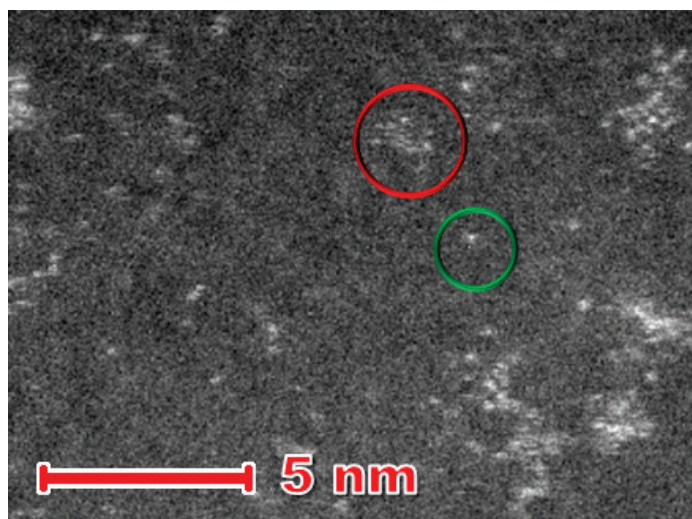


Figure 5.12: ADF-STEM of Au<sub>9</sub> clusters at low concentrations on agar holey carbon film showing a Au<sub>9</sub> cluster (red circle) as well as a single Au atom (green circle).

#### 5.4.2 High Resolution Electron Microscopy Studies

Following the preliminary ADF-STEM investigations, HRTEM was used to sample the size distribution of supported clusters and examine any changes to particle size after post-treatment. A tabulated summary of the average size of acid-washed P25 and fumed silica-supported Au<sub>8</sub>, Au<sub>9</sub>, Au<sub>11</sub>, and Au<sub>101</sub> clusters with various post-treatments are shown in Table 5.7. Note that the acid-washed P25 nanoparticles are different from the pure anatase nanoparticles presented in the previous section.

Untreated samples of Au<sub>8</sub>, Au<sub>9</sub>, and Au<sub>11</sub> are unable to be resolved using the HRTEM. These HRTEM results show that for all of supported gold clusters investigated, there is a general trend towards increased particle size and increased size distribution as successively harsher treatments are applied. Note that these studies are preliminary, as the size distributions presented here are skewed towards larger particles, since the HRTEM is unable to conclusively observe particles smaller than ~1.5 nm when supported on TiO<sub>2</sub>. The smaller particles may be difficult to observe when supported by a crystalline substrate, compared to unsupported clusters on an amorphous carbon film, which provides better contrast. It was also observed that Au<sub>101</sub> clusters undergo significant agglomeration after prolonged exposure to ambient light; therefore, samples of Au<sub>101</sub> were prepared with the least amount of exposure to ambient light possible and were loaded into the sample chamber as quickly as possible.

Table 5.7: Summary of the mean size and standard deviation of Au clusters supported on acid-washed P25 TiO<sub>2</sub> and fumed SiO<sub>2</sub> as measured by HRTEM, showing the trend of increasing agglomeration with harsher treatment.

Cluster	Treatment Method	P25 TiO <sub>2</sub> -Supported		SiO <sub>2</sub> -Supported	
		Mean Size (nm)	Std. deviation (nm)	Mean size (nm)	Std. deviation (nm)
Au <sub>8</sub>	Untreated	-	-	-	-
	Heated 200 °C	2.2	1.4	1.9	0.9
	Calcined O <sub>2</sub> 200 °C	3.6	2.7	2.7	1.9
	Calcined O <sub>2</sub> 400 °C	5.2	3.4	4.1	2.1
Au <sub>9</sub>	Untreated	-	-	-	-
	Heated 200 °C	2.4	1.7	1.8	1.0
	Calcined O <sub>2</sub> 200 °C	3.1	2.1	2.6	1.6
	Calcined O <sub>2</sub> 400 °C	4.8	2.8	3.5	2.2
Au <sub>11</sub>	Untreated	-	-	-	-
	Heated 200 °C	2.7	1.4	2.1	0.8
	Calcined O <sub>2</sub> 200 °C	-	-	-	-
	Calcined O <sub>2</sub> 400 °C	-	-	-	-
Au <sub>101</sub>	Untreated	2.3	0.8	1.8	0.8
	Heated 200 °C	3.2	1.7	2.3	1.3
	Calcined O <sub>2</sub> 200 °C	3.8	2.3	3.4	1.5
	Calcined O <sub>2</sub> 400 °C	5.3	3.5	4.7	2.6

## 5.5 Conclusions

For the Au<sub>8</sub>, Au<sub>9</sub>, and Au<sub>11</sub> clusters supported upon acid-washed P25 nanoparticles, the untreated samples remain intact according to XPS, and are too small to be seen under HRTEM. Subsequent washing at 100 °C in toluene results in the removal of some ligands for a portion of the clusters, in addition to the formation of Au-O bonds. Another portion of the clusters remain intact upon the surface, while a significant fraction of the clusters have clearly been removed from the surface during treatment when comparing the total signal intensity to those of the untreated samples. Further treatment by heating to 200 °C under vacuum results in the agglomeration of a portion of the clusters, while still being protected by ligands (these remain smaller than Au<sub>101</sub>), while another portion of the clusters lose ligands to form Au-O bonds and agglomerate into larger particles. Of the portion that loses ligands to form Au-O bonds, some clusters may remain intact. The removal of ligands is also less effective for the Au<sub>9</sub> cluster. The agglomeration of a portion of the clusters is supported by HRTEM as the particles become large enough to be resolvable. Calcination under an O<sub>2</sub> atmosphere at 200 °C results in a further increase in particle size as observed by HRTEM for all clusters, but it is unknown as to the state of the ligands without further complementary experimental studies.

For the Au<sub>8</sub> and Au<sub>9</sub> clusters supported upon pure anatase nanoparticles, the untreated samples undergo partial ligand removal, with approximately half of the clusters remaining intact, while the other half undergo agglomeration, according to XPS. This effect of immediate agglomeration upon being supported on anatase is supported by XANES analysis, which showed that 38% of the Au<sub>9</sub> clusters had agglomerated. Interestingly, untreated Au<sub>9</sub> samples supported on anatase that were kept in the dark showed no agglomeration according to XANES, and is an observation that will have to be explored further in future studies. Treatment of Au<sub>8</sub> by calcination under O<sub>2</sub> at 200 °C results in further removal of ligands and increased agglomeration for half of the clusters, while the remaining portion of clusters maintain their size. In comparison, Au<sub>9</sub> calcined under O<sub>2</sub> at 200 °C also results in further removal of ligands and increased agglomeration for the entire sample, with no Au<sub>9</sub> clusters remaining intact. EXAFS analysis showed that these supported Au<sub>9</sub> clusters had agglomerated to such an extent that they could be modelled using a FCC bulk gold structure, and exhibited lattice contraction and small Debye temperatures indicative of nanoparticulate gold. Further calcination of Au<sub>8</sub> and Au<sub>9</sub> under O<sub>2</sub> + H<sub>2</sub> at 200 °C results in complete ligand removal and further progression of

agglomeration, with no evidence of either cluster remaining intact upon the anatase surface. An increase in Debye temperature is calculated by EXAFS modelling for Au<sub>9</sub>, indicating a further increase in particle size.

In comparison, untreated Au<sub>9</sub> samples supported on fumed silica showed no signs of agglomeration. XANES indicated that calcination under O<sub>2</sub> at 200 °C leaves 15.5% intact Au<sub>9</sub> clusters, although EXAFS analysis showed that the remaining portion of agglomerated clusters could still be fit well with a bulk gold lattice model, showing similar lattice contraction and small Debye temperatures, similar to that calculated for the same treatment on anatase. Further treatment under O<sub>2</sub> + H<sub>2</sub> at 200 °C for silica-supported Au<sub>9</sub> results in negligible intact cluster remaining according to XANES, while EXAFS analysis calculated an increase in Debye temperature indicative of increased agglomeration.

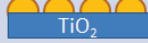
For the Au<sub>101</sub> series, the untreated sample supported upon acid-washed P25 nanoparticles showed a small increase in particle size according to HRTEM. During HRTEM studies it was also observed that Au<sub>101</sub> is prone to agglomeration under ambient light, and this should be investigated further in future studies. Washing at 100 °C in toluene results in a loss of a significant amount of clusters from the surface according to XPS, however, there is no indication of Au-O bond formation or an increase in particle size. Samples heated at 200 °C under vacuum result in further agglomeration of the particles according to HRTEM, the removal of some ligands, and the formation of Au-O bonds. By comparison, Au<sub>101</sub> supported on pure anatase nanoparticles show a similar progression of ligand removal, but to a far greater extent, with complete ligand removal for those samples calcined under O<sub>2</sub> + H<sub>2</sub> at 200 °C. It is unknown, however, if these anatase-supported Au<sub>101</sub> particles undergo agglomeration.

This work has shown that harsher treatments result in the removal of a greater number of ligands and increased agglomeration of the clusters. The effect of acidic pre-treatment of the surface, and the strong influence of supports, are also remarkably clear, with ligand loss and agglomeration more severe on untreated anatase nanoparticles. EXAFS analysis and ADF-STEM images confirm the atomically precise nature of the clusters before being supported upon TiO<sub>2</sub> nanoparticles. Table 5.8 summarises these conclusions for samples that are used in the following photocatalysis Chapter for easy comparison with photocatalytic results.

Table 5.8: Summary of the key trends in ligand loss and agglomeration observed for Au<sub>8</sub>, Au<sub>9</sub>, Au<sub>11</sub> and Au<sub>101</sub> on acid-washed P25 and pure anatase supports under the various post-treatment conditions. These have been determined by XPS, XANES, EXAFS, and TEM investigations.

Treatment	Acid washed P25 Nanoparticle Supported				Pure Anatase Nanoparticle Supported		
	Au <sub>8</sub>	Au <sub>9</sub>	Au <sub>11</sub>	Au <sub>101</sub>	Au <sub>8</sub>	Au <sub>9</sub>	Au <sub>101</sub>
Untreated	•Virtually Unchanged			•Small increase in particle size	•Partial ligand removal •Half of clusters remain intact, while the other half undergo partial agglomeration		•Partial ligand removal •Unknown if agglomeration occurs, but likely
Washed at 100 °C	•Removal of a fraction of clusters from the surface •A portion of clusters remain virtually unchanged •Some removal of ligands •No significant agglomeration •Formation of Au-O bonds, to a greater extent for Au <sub>11</sub>			•Unknown changes to size •Loss of a significant amount of clusters from the surface •No Au-O formation		N/A	
Heated at 200 °C	•Agglomeration of a portion of clusters while still ligand-protected (these are still smaller than Au <sub>101</sub> ) •Other portion of clusters lose some ligands and form Au-O and agglomerate to larger particles •Of the portion that loses ligands, some clusters may not agglomerate •Removal of ligands is less effective for Au <sub>9</sub>			•Further agglomeration of clusters, but still nanoparticulate in nature •Removal of some ligands and formation of Au-O bonds		N/A	
Calcined O <sub>2</sub> at 200 °C			Increased agglomeration and size distribution		•Removal of ligands and agglomeration has progressed further •Half of clusters maintain their size	•Removal of ligands and agglomeration has progressed further •No fraction of clusters maintain their size	•Removal of ligands has progressed further •Unknown if agglomeration occurs, but likely
Calcined O <sub>2</sub> /H <sub>2</sub> at 200 °C			N/A		•Complete ligand removal •Agglomeration has progressed further, no evidence of any clusters remaining intact.		•Complete ligand removal •Unknown if agglomeration progresses further, but likely.

Table 5.9: Schematic illustration of the key trends in ligand loss and agglomeration observed for Au<sub>8</sub>, Au<sub>9</sub>, Au<sub>11</sub> and Au<sub>101</sub> on acid-washed P25 and pure anatase supports under the various post-treatment conditions. The gold semi-circles represent the clusters, while the outer brown semi-circle represents the ligand coverage.

Treatment	Acid-washed P25 Nanoparticle Supported				Pure Anatase Nanoparticle Supported		
	Au <sub>8</sub>	Au <sub>9</sub>	Au <sub>11</sub>	Au <sub>101</sub>	Au <sub>8</sub>	Au <sub>9</sub>	Au <sub>101</sub>
Untreated							
Washed at 100 °C					N/A		
Heated at 200 °C					N/A		
Calcined O <sub>2</sub> at 200 °C	*Ligand status unknown						
Calcined O <sub>2</sub> /H <sub>2</sub> at 200 °C			N/A				

# Chapter Six

## Photocatalytic Studies of Au<sub>8</sub>, Au<sub>9</sub>, and Au<sub>101</sub> Supported on TiO<sub>2</sub> Nanoparticles

In this Chapter, the photocatalytic capacity for water photolysis by Au/TiO<sub>2</sub> catalysts is investigated using the new experimental apparatus designed and built throughout the project that was presented in Chapter 2. It consists of a heterogeneous gas-phase reactor operating near ambient conditions that can deliver constant and controlled samples of gas to a residual gas mass spectrometer for analysis of the gas composition over time. Using this apparatus, Au<sub>8</sub>(PPh<sub>3</sub>)<sub>8</sub>(NO<sub>3</sub>)<sub>2</sub>, Au<sub>9</sub>(PPh<sub>3</sub>)<sub>8</sub>(NO<sub>3</sub>)<sub>3</sub>, and Au<sub>101</sub>[P(C<sub>6</sub>H<sub>5</sub>)<sub>3</sub>]<sub>21</sub>Cl<sub>5</sub> supported on anatase or P25 TiO<sub>2</sub> nanoparticles are investigated for their activity towards water photolysis and their peak H<sub>2</sub> production rates are quantified. Anatase-supported samples are found to increase in activity with successively harsher post-treatment conditions, with data suggesting that increasing the size of the gold particles to be beneficial for photocatalytic activity. In contrast, samples prepared upon acid-washed P25 or acid-washed anatase show evidence for an ideal gold particle size and ligand coverage after relatively gentle post-treatment conditions.

## 6 Photocatalytic Studies of Au<sub>8</sub>, Au<sub>9</sub>, and Au<sub>101</sub> Supported on TiO<sub>2</sub> Nanoparticles

### 6.1 Experimental Benchmarks and Preliminary Evaluations

#### 6.1.1 Photocatalytic Performance of Pt-TiO<sub>2</sub> for Water-Splitting

In order to establish a benchmark for photocatalytic experiments of Au/TiO<sub>2</sub>, photocatalytic water-splitting experiments were undertaken using platinised P25 nanoparticles (1.0% w/w Pt/TiO<sub>2</sub>) and platinised anatase nanoparticles (1.0% w/w Pt/anatase) prepared using the same synthetic procedure outlined by Peng *et al.*<sup>199</sup> In addition, various control experiments were also performed to ensure that the water vapour was the source of H<sub>2</sub> production. Experiments were performed at 28 °C with 20 Torr of H<sub>2</sub>O vapour and 280 Torr of Ar in the reaction cell at the start of the experiment, with 20.7 mW cm<sup>-2</sup> of UV light irradiating the sample disc, equivalent to ~4.5 suns worth of UV intensity (assuming UV <400 nm). Selected results of these experiments are presented in Figure 6.1.

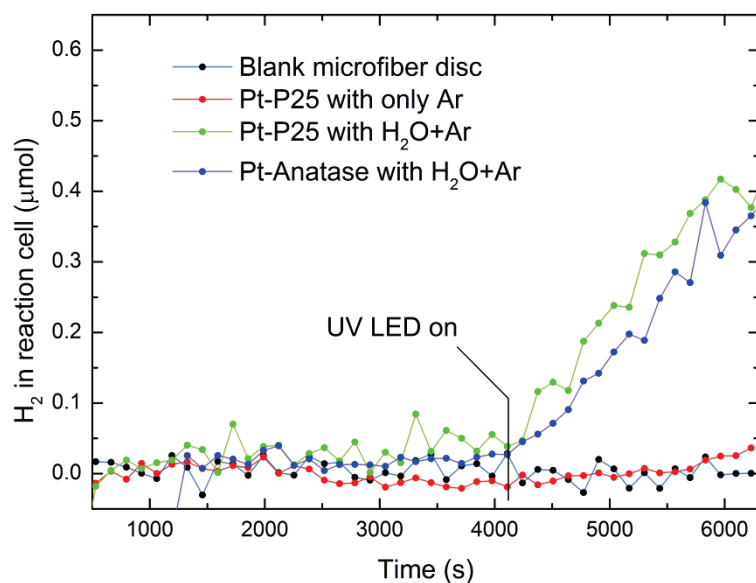


Figure 6.1: H<sub>2</sub> gas yield for benchmark Pt-TiO<sub>2</sub> photocatalysts and control experiments, the latter of which showed no H<sub>2</sub> production.

Both Pt-P25 and Pt-anatase begin to produce H<sub>2</sub> gas after the reaction cell is irradiated with UV light. The blank microfiber disc and Pt-P25 without water vapour show no production of H<sub>2</sub> after irradiation with UV light, indicating that there is only H<sub>2</sub> production when Pt is present on TiO<sub>2</sub> or when Pt-TiO<sub>2</sub> has access to water vapour. Non-

platinised P25 and anatase do not show any measurable levels of H<sub>2</sub> production, but are not included in the figure for clarity.

For all TiO<sub>2</sub> samples, there is also production of CO<sub>2</sub>, but no measurable levels of O<sub>2</sub> production. This is most likely a consequence of the well-known capacity for TiO<sub>2</sub> to photo-degrade carbonaceous species in the presence of O<sub>2</sub>,<sup>66-73</sup> which will be discussed in detail in the following sections. In order to make comparisons to Au/TiO<sub>2</sub> catalytic data presented later in the Chapter, the peak H<sub>2</sub> production rates averaged over three experiments for Pt-P25 and Pt-anatase, respectively, are presented in Figure 6.2.

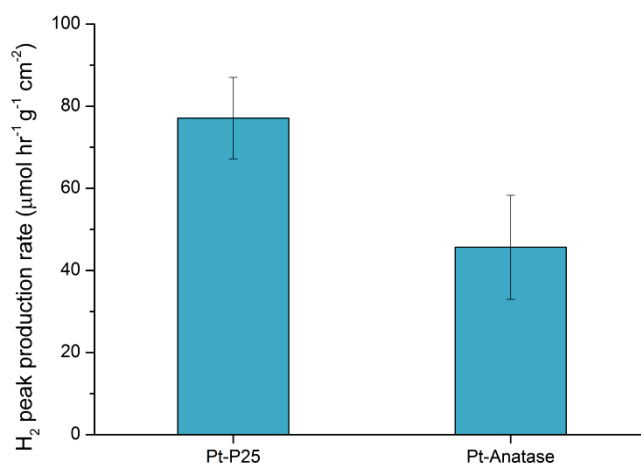


Figure 6.2: Average H<sub>2</sub> peak production rate for Pt-P25 and Pt-Anatase across three experiments. The error bars represent the standard error of the mean.

Pt-P25 and Pt-anatase have average production rates of  $77.1 \pm 9.9$  and  $45.6 \pm 12.7$   $\mu\text{mol hr}^{-1} \text{g}^{-1} \text{cm}^{-2}$  respectively. These results show the well-known effectiveness of Pt co-catalysts in enabling TiO<sub>2</sub> to photocatalytically split water. It has been widely accepted for some time that this is due to decreased electron-hole recombination by allowing for greater charge separation via migration of the photo-excited electron to Pt.<sup>36</sup> The unplatinised samples do not produce any notable amounts of H<sub>2</sub> as the rate of electron-hole recombination is too high to afford any detectable levels of H<sub>2</sub>, as it is known that TiO<sub>2</sub> cannot split water photocatalytically without co-catalysts.<sup>61,508</sup> The increased performance observed for Pt-P25 compared with Pt-anatase could be due to the mixed polymorphs of anatase, rutile, and amorphous TiO<sub>2</sub> present in these nanoparticles, which has been demonstrated to provide a greater degree of charge separation during photo-excitation,<sup>106</sup> as well as possible synergistic effects between anatase and rutile.<sup>120,144</sup>

There are a number of studies in the literature using similar Pt-TiO<sub>2</sub> photocatalyst systems for water-splitting, but there are few which are in the gas phase. It is difficult to find experimental conditions that closely match those presented here due to the vast variety of experimental systems in the literature. Yamaguti and Sato<sup>177,509</sup> have shown a production rate of 947  $\mu\text{mol of H}_2 \text{ hr}^{-1} \text{ g}^{-1}$  using 2% Pt/TiO<sub>2</sub> with 10% NaOH coatings in the gas-phase, while the study by Sato and White<sup>99</sup> showed a production rate of 1.4  $\mu\text{mol of H}_2 \text{ hr}^{-1} \text{ g}^{-1}$  when using 2% Pt/TiO<sub>2</sub> without any NaOH coating, in the gas-phase. There are also two similar liquid phase studies; Daskalaki *et al.*<sup>97</sup> showed a peak H<sub>2</sub> production of 42.75  $\mu\text{mol hr}^{-1} \text{ g}^{-1}$  using 0.5% Pt/TiO<sub>2</sub> photocatalysts, which decreased to 13.5  $\text{hr}^{-1} \text{ g}^{-1}$  after 65 hours of illumination, while Moon *et al.*<sup>104</sup> showed 253  $\mu\text{mol of H}_2 \text{ hr}^{-1} \text{ g}^{-1}$  using 0.1% Pt/TiO<sub>2</sub>. The large difference between the various studies are not simply due to the use of NaOH coatings in some studies, but because each study uses vastly different experimental setups, ranging from varying irradiation power, diverse light filters, different catalyst surface areas, and many other factors. This makes it difficult to directly compare or normalise the results between various studies, however, it is still possible to conclude that the production rates observed for the 1% Pt-TiO<sub>2</sub> samples presented herein to be within the appropriate range that would be expected of such catalysts. This helps to validate the experimental apparatus and analysis procedures used for quantifying the performance of Pt/TiO<sub>2</sub>, and allows some comparisons to be made to Au/TiO<sub>2</sub> presented later in this Chapter.

### 6.1.2 Degradation of Samples and Observed Colour Changes

Catalyst degradation under during photocatalysis was investigated by repeating experiments with previously irradiated samples under identical experimental conditions to that of the first experiment. In all cases, the reaction cell was completely evacuated and replaced with fresh reactant gas. Four total experiments were performed on one catalyst, one consisting of the fresh sample, and then three repeats of the same sample. The investigation was undertaken for three different samples of Pt-P25, and the H<sub>2</sub> production rate was averaged at each stage of the procedure (12 total experiments over 3 catalyst samples). This investigation shows a decrease in the H<sub>2</sub> production rate over the course of multiple experiments when using the same catalyst material, as shown in Figure 6.3. The second experiment on the same Pt-P25 sample results in H<sub>2</sub> production rate decreasing to

$57.7 \pm 25.0 \mu\text{mol hr}^{-1} \text{g}^{-1} \text{cm}^{-2}$  on average, followed by further reduction for the 3<sup>rd</sup> and 4<sup>th</sup> experiments to  $17.4 \pm 8.27$  and  $16.0 \pm 4.65 \mu\text{mol hr}^{-1} \text{g}^{-1} \text{cm}^{-2}$  respectively. The large error for the 1<sup>st</sup> repeat is due to the large variation in the production rate between the three samples at this stage; however, comparison to the 3<sup>rd</sup> and 4<sup>th</sup> experiments show a clear decrease in H<sub>2</sub> production.

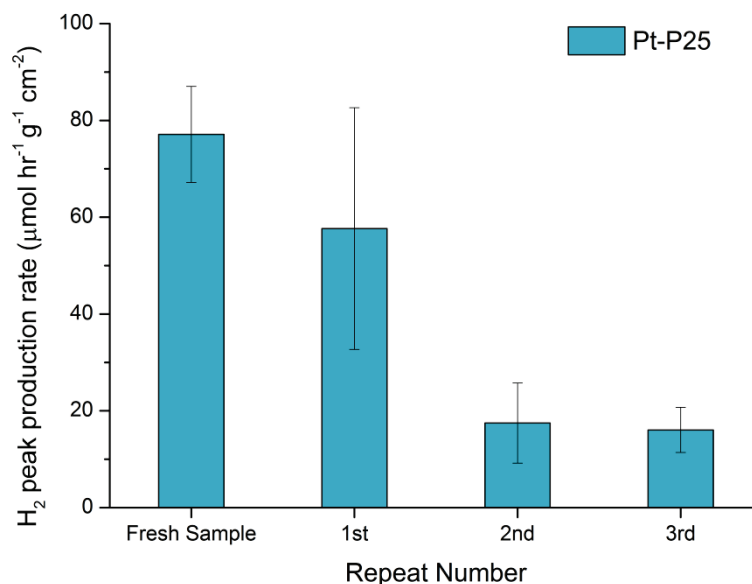


Figure 6.3: Average H<sub>2</sub> peak production rate for Pt-P25 over four experiments showing the decrease in H<sub>2</sub> production rate when re-using the same catalytic material. This procedure was repeated with three different samples and the results have been averaged.

In addition to the decrease in H<sub>2</sub> production, the samples also begin to develop a darkened, metallic hue. Given that TiO<sub>2</sub> is extremely photo-stable under UV light for extended periods, it seems most likely that the Pt co-catalyst is degrading. Daskalaki *et al.*<sup>97</sup> have also reported the degradation of their Pt-TiO<sub>2</sub> samples over extended periods of UV irradiation.

Both the Pt-TiO<sub>2</sub> and Au/TiO<sub>2</sub> samples discussed later in this Chapter show a change in colour after being subjected to repeated photocatalysis experiments under UV irradiation. Pt-P25 and Pt-anatase samples change from a very light grey to a dark grey colour over the course of a single experiment as shown in Figure 6.4. Repeated experiments using the same samples results in a slight darkening of the catalyst that ceases to be noticeable after three to four experiments, although none of these subsequent colour changes are as significant as the initial exposure.

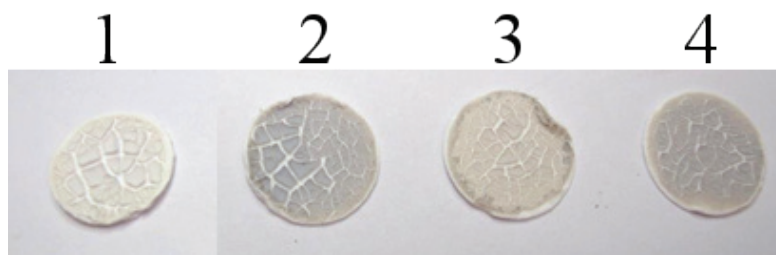


Figure 6.4: Microfiber discs coated with Pt/P25 used in photocatalytic water-splitting experiments. Disc 1 is a freshly prepared sample that has not been exposed to UV, while discs 2–4 have been exposed to UV light over numerous experiments.

Au/TiO<sub>2</sub> samples also show a marginal degree of colour change over repeated experiments. An example is shown Figure 6.5 for Au<sub>101</sub>/anatase calcined under O<sub>2</sub>, which was repeatedly exposed to UV light over the course of four experiments, resulting in a small change in colour. The changes varied slightly between other Au/TiO<sub>2</sub> samples, due to each cluster having a unique colour.



Figure 6.5: Microfiber discs coated with Au<sub>101</sub>/anatase calcined under O<sub>2</sub> before (left) and after (right) four photocatalytic water-splitting experiments.

Given that these changes in colour for both Pt-TiO<sub>2</sub> and Au/TiO<sub>2</sub> samples are correlated with decreased production of H<sub>2</sub> after each repeated experiment, there is clearly some form of degradation occurring during photocatalytic experiments. The metallic hue of the Pt-TiO<sub>2</sub> samples may be the result of aggregation of Pt as it becomes unbound from the TiO<sub>2</sub> surface, through some unknown degradation process. It is also known from XANES and HRTEM (see Chapter 5) for Au<sub>9</sub> and Au<sub>101</sub>, respectively, that these clusters can agglomerate under the irradiation of ambient light. Therefore, the UV light used during photocatalytic experiments would likely have a similar effect on these clusters. Other studies have also suggested that the degradation of TiO<sub>2</sub> over time could be due to the accumulation of carbon deposits during the oxidation of organic compounds, which can manifest as visible deposits of "brownish carbonaceous matter".<sup>68,510</sup> This may also be

contributing to the colour change observed for the Pt-TiO<sub>2</sub> and Au/TiO<sub>2</sub> samples. Because of this unknown degradation process, only the production rates from fresh samples have been included in the remainder of this Chapter.

### 6.1.3 Effects of Sample Exposure to Vacuum

Over the course of running control and benchmark experiments, it was discovered that the photocatalytic performance of the catalysts were improved when they were prepared under vacuum for an extended period. Examples of the difference in peak H<sub>2</sub> production rates for samples exposed to vacuum for 10 minutes, compared to those exposed to vacuum for 12 hours, are shown in Figure 6.6. This effect is most pronounced for the Au/TiO<sub>2</sub> samples, such as Au<sub>9</sub>/acid-washed P25, which has a H<sub>2</sub> production rate of  $166.9 \pm 42.3 \mu\text{mol hr}^{-1} \text{g}^{-1} \text{cm}^{-2}$  for those samples that were exposed to vacuum for 10 minutes, compared with  $511.4 \pm 51.1 \mu\text{mol hr}^{-1} \text{g}^{-1} \text{cm}^{-2}$  for those that were exposed for 12 hours.

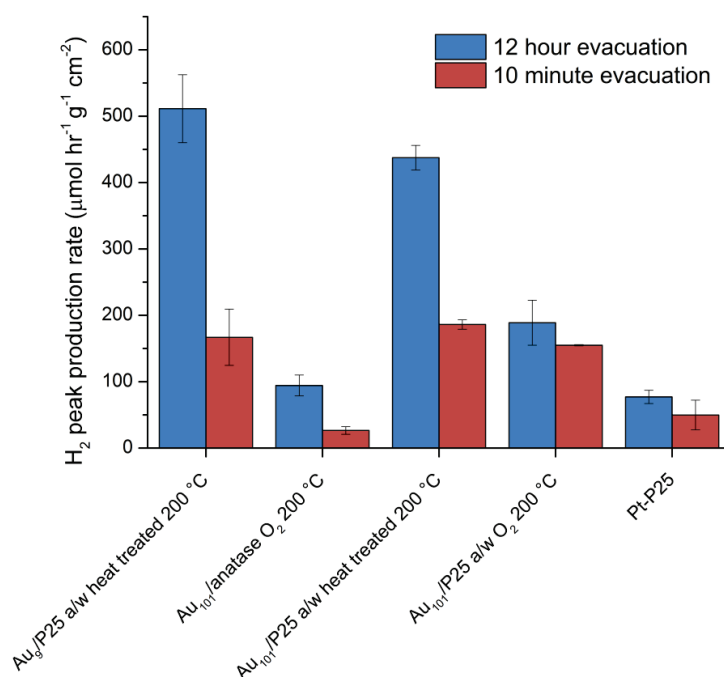


Figure 6.6: Comparison of mean H<sub>2</sub> peak production rates for samples that were exposed to vacuum in the reaction cell for 10 minutes, compared with those that were evacuated for 12 hours. Acid-washed supports are denoted with the a/w abbreviation.

Given that exposing a sample in the reaction cell to vacuum for 12 hours prevented the use of the experiment for other samples, attempts were made to prepare samples under

vacuum in a secondary stainless steel cell preparation cell, evacuated overnight, using the same vacuum line as the reaction cell. This secondary cell did not have the features of the primary reaction cell and was only used for the preparation of samples under vacuum. The samples would then be transferred from the secondary cell and into the main reaction cell as rapidly as possible, taking approximately 5 minutes for sample changeover. However, this still resulted in decreased catalytic performance due to the brief exposure to the atmosphere during sample transfer. There must therefore be some effect on the catalysts after exposure to an oxidising environment, even for a short period, compared with those samples that were evacuated within the reaction cell overnight. After this discovery was made apparent for a number of samples, all future samples were prepared for photocatalysis experiments by placing them in the reaction cell and evacuating the cell overnight, then performing experiments without exposing the sample to the atmosphere. Only those samples that have been prepared in this way have been included in the results presented in the remainder of this Chapter. This is similar to most literature studies that undergo rigorous sample preparation procedures, such as extended flushing of reaction cells with Ar or baking samples under UHV for prolonged periods.

#### **6.1.4 Production of CO<sub>2</sub> and Consumption of O<sub>2</sub>**

During all water-splitting photocatalysis experiments, the increase in H<sub>2</sub> present in the reaction cell upon UV irradiation is accompanied by an increase in CO<sub>2</sub>, and a decrease in O<sub>2</sub>, as shown in Figure 6.7. It should also be noted that the increased catalytic performance observed between different samples manifest as both an increase in the H<sub>2</sub> production rate and an increase in the CO<sub>2</sub> production rate.

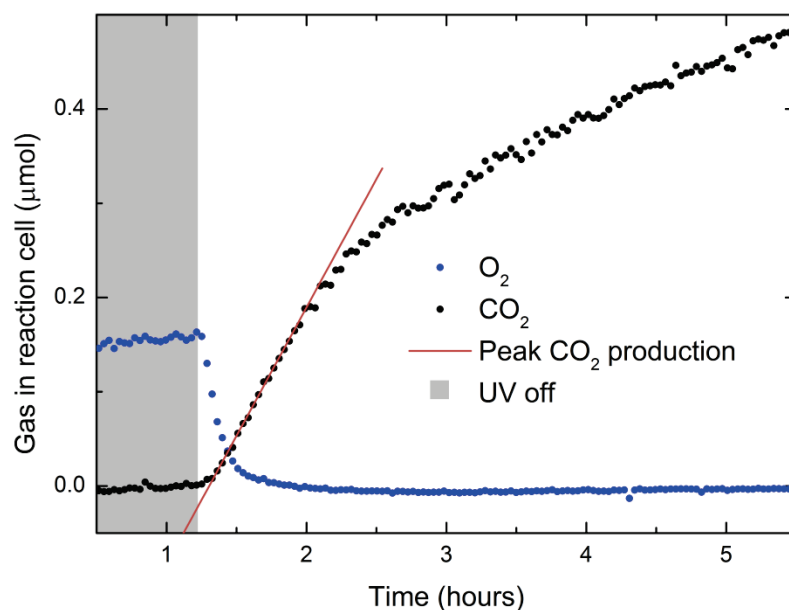


Figure 6.7: The number of moles of O<sub>2</sub> and CO<sub>2</sub> in the reaction cell throughout the course of an extended experiment, showing the consumption of O<sub>2</sub> and peak CO<sub>2</sub> production.

Studies that deal with the photo-oxidation of organic contaminants present on the TiO<sub>2</sub> surface have shown the production of CO<sub>2</sub>, and this has been suggested to be due to photo-activated oxygen.<sup>66-73,511</sup> These studies have shown that even after rigorous steps were taken to clean the TiO<sub>2</sub> surface, that even under UHV conditions, there are still carbon contaminants present, which react with oxygen in the system when irradiated with UV light to produce CO<sub>2</sub> (*vide infra*). There are a number of similar studies in the literature using TiO<sub>2</sub> photocatalysts for water-splitting that do not see the stoichiometric production of O<sub>2</sub>.<sup>46,97,102</sup> It has been postulated that the photo-oxidation occurs through the formation of superoxide ions (O<sub>2</sub><sup>•-</sup>, *vide infra*). Other groups have reported the photo-reduction of CO<sub>2</sub> and H<sub>2</sub>O into formic acid, formaldehyde, and methanol.<sup>512</sup> However, these studies were performed in the liquid phase, and no other carbon-based species are observed in the results presented here.

The initial presence of O<sub>2</sub> inside the reaction cell is leftover from evacuation of atmospheric gases during sample preparation. The vacuum achieved in the reaction cell reaches 10<sup>-3</sup> Torr, which is most likely insufficient to remove all of the adsorbed O<sub>2</sub> from the walls of the reaction cell. This could also include those O<sub>2</sub> molecules adsorbed to the TiO<sub>2</sub> surface at ambient temperature.<sup>149,150</sup> Despite repeated procedures to remove dissolved O<sub>2</sub> from the water vapour used in experiments, it is also possible that there is a

small amount remaining in the water vapour when it is introduced to the reaction cell at the start of an experiment.

This initial consumption of O<sub>2</sub> coincides with a steady rise in both H<sub>2</sub> and CO<sub>2</sub> immediately after the reaction cell is irradiated with UV light until approximately 2 hours into the experiment, whereby all of the latent O<sub>2</sub> available from the start of the reaction has been consumed, as shown in Figure 6.8. At this point, the production rate of both H<sub>2</sub> and CO<sub>2</sub> decrease substantially, while O<sub>2</sub> remains near the detection limit for the remainder of the experiment. Typically, experiments are completed within 2 hours, and it is the production rate during the peak period that is presented throughout the remainder of this Chapter. The source of O<sub>2</sub> used for the production of CO<sub>2</sub> from 2 hours and beyond is likely from the stoichiometric O<sub>2</sub> that should be evolved from the water-splitting reaction. Note that this O<sub>2</sub> may not necessarily be molecular or gaseous O<sub>2</sub>, as its form is unknown and could be reacting directly with carbon.

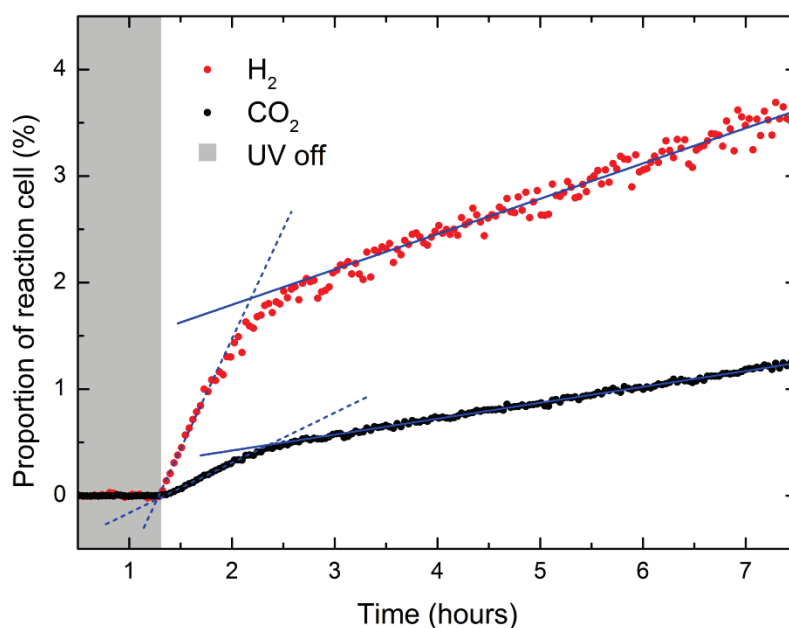


Figure 6.8: The % contribution of H<sub>2</sub> and CO<sub>2</sub> to the total gas mixture in the reaction cell throughout the course of an extended experiment, showing a significant change in productivity at ~2 hours.

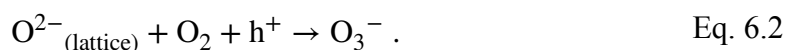
For this experiment, the peak production between 1 and 2 hours results in a production ratio of ~4:1 H<sub>2</sub>:CO<sub>2</sub>, while the production ratio beyond 3 hours is ~2:1 H<sub>2</sub>:CO<sub>2</sub>; the latter is consistent with the CO<sub>2</sub> being produced from the stoichiometric production of H<sub>2</sub> and O<sub>2</sub> from H<sub>2</sub>O, but the initial 4:1 ratio cannot be explained by this. This initial 4:1 ratio for

the peak production appears to vary substantially between different experiments. It could be that the residual carbonaceous species (*vide infra*) being used to produce CO<sub>2</sub> are acting as some form of sacrificial electron donor.<sup>104</sup> Alternatively, the photo-adsorption of O<sub>2</sub> (*vide infra*) may also be having an effect on the photocatalytic performance.

Concerns that the carbon, or even the hydrogen, may arise from decomposition of the PPh<sub>3</sub> ligands of a Au cluster is unlikely for two reasons; first, the Au<sub>101</sub> cluster shown in Figure 6.7 and Figure 6.8 has been calcined under O<sub>2</sub> and H<sub>2</sub> at 200 °C, which has been shown by the characterisation work summarised in Table 5.8 to result in almost complete removal of ligands. Second, calculation of the number of moles of carbon or hydrogen available from the ligands, assuming all ligands have been retained throughout the treatment process (which is unlikely), amounts to only  $2.874 \times 10^{-7}$  moles of carbon and  $2.40 \times 10^{-7}$  moles of hydrogen for a 8.9 mg sample of 0.17% Au<sub>101</sub>/TiO<sub>2</sub>. In comparison, the total number of moles produced over the course of the experiment shown in Figure 6.7 and Figure 6.8 equates to  $6.00 \times 10^{-7}$  and  $3.70 \times 10^{-6}$  moles of carbon and hydrogen respectively; this is far more than the amount that could be provided by ligand decomposition. The 18 Torr of H<sub>2</sub>O typically included at the start of photocatalysis experiments yields  $5.92 \times 10^{-6}$  moles of H<sub>2</sub> gas for comparison. This indicates that over the course of ~6 hours shown in this extended experiment, 62.5% of the H<sub>2</sub>O present in the reaction cell has been converted to H<sub>2</sub> and O<sub>2</sub>.

#### 6.1.4.1 The Behaviour of Atomic and Gaseous Oxygen Species

There are additional reactions that could involve O<sub>2</sub> in the reaction cell that can explain the behaviour of O<sub>2</sub> during the early stages of the experiment. The photo-adsorption of oxygen to TiO<sub>2</sub> could be one method by which the rapid decrease in O<sub>2</sub> gas occurs. For example, the presence of water on the surface of rutile(110) surface has been shown<sup>513-515</sup> to enhance the photo-adsorption of oxygen by helping to trap the photo-generated holes at the OH<sup>-</sup> sites that are formed when water is available. It has been suggested that this leads to the formation of surface HO<sub>2</sub><sup>-</sup> by electron trapping and surface O<sub>3</sub><sup>-</sup> by hole trapping reactions (Eq. 6.1 and 6.2) as the primary means of O<sub>2</sub> photo-adsorption;



In fact, water-splitting by anatase TiO<sub>2</sub> typically shows a lack of O<sub>2</sub> evolution during reaction, due to the photo-reduction of O<sub>2</sub> to O<sub>2</sub><sup>-</sup> being favoured over H<sup>+</sup> reduction for H<sub>2</sub> formation, often requiring methanol as a sacrificial reagent that is irreversibly oxidised by holes to produce a significant H<sub>2</sub> yield.<sup>9,47,97,122</sup> However, there is no clear difference in O<sub>2</sub> consumption or CO<sub>2</sub> production between P25 or anatase nanoparticles used in the experiments presented herein. The presence of O<sub>2</sub>, and the subsequent production of surface O<sub>2</sub><sup>-</sup> have, nevertheless, been shown to improve the photocatalytic efficiency of catalysts by helping to trap photogenerated electrons.<sup>516-518</sup>

The study by Lu *et al.*<sup>519</sup> revealed that the oxygen atom left over during water-splitting can be extracted by TiO<sub>2</sub> to quench the oxygen vacancies on the surface. These oxygen vacancies and interstitial defects are known to have high diffusion rates, allowing sub-surface oxygen vacancies to migrate and replace surface oxygen vacancies that may be quenched during reactions at the surface of TiO<sub>2</sub>.<sup>117,124,147,151</sup> The possibility of reducing O<sub>2</sub> to H<sub>2</sub>O<sub>2</sub> has also been reported previously;<sup>83,97</sup> however, this is not observed in the mass spectra of experiments presented in this Chapter. These processes could allow for a significant amount of oxygen species to be consumed by reactions other than CO<sub>2</sub> production.

It has also been shown by Göpel *et al.*<sup>520</sup> that chemisorption of CO<sub>2</sub> in equilibrium upon the TiO<sub>2</sub> surface does not kinetically hinder the reaction between chemisorbed O<sub>2</sub> and oxygen vacancies on the TiO<sub>2</sub> surface, nor is the chemisorption equilibria of CO<sub>2</sub> influenced by oxygen vacancies. Therefore, the production of CO<sub>2</sub> during the reaction should not have any retarding effects on the quenching of oxygen vacancies as the reaction progresses.

Investigation of the total number of moles present in the reaction cell over a given period for the experiment presented in Figure 6.8 shows that 0.152 μmol of O<sub>2</sub> is consumed within the first hour of UV exposure, while 0.0095 μmol of CO<sub>2</sub> is produced over this same period. Over the course of the total experiment, 0.6 μmol of CO<sub>2</sub> is produced, requiring 0.6 μmol of O<sub>2</sub>, while 1.85 μmol of O<sub>2</sub> should be produced given the 3.70 μmol of H<sub>2</sub> evolved from the water-splitting reaction. This leaves 1.4 μmol of O<sub>2</sub> that is consumed but cannot be accounted for by CO<sub>2</sub> production, yet there are no other products

observed in the mass range between 1 and 100 amu. Using the number determined by Ikeda *et al.*<sup>521</sup> of 50  $\mu\text{mol}$  of defect sites per gram of P25, then for 8.9 mg of Au/TiO<sub>2</sub>, there would be  $\sim 0.445$   $\mu\text{mol}$  of oxygen vacancies present in the TiO<sub>2</sub>, which could explain  $\sim 0.2235$   $\mu\text{mol}$  of unaccounted O<sub>2</sub> gas, leaving  $\sim 1.1765$   $\mu\text{mol}$  of O<sub>2</sub>. Calculation of the prospective surface coverage of the  $\sim 1.1765$   $\mu\text{mol}$  of O<sub>2</sub> over the 0.4984 m<sup>2</sup> of surface area available in the P25 of the sample results in a reasonable surface coverage of 8.45%, assuming a reasonably sparse, small gas molecule adsorption area of 10<sup>19</sup> molecules per m<sup>2</sup>.

The control experiments shown in Figure 6.9 show that the Pt-TiO<sub>2</sub> samples will consume the available oxygen more rapidly than bare TiO<sub>2</sub> samples. Pt-TiO<sub>2</sub> without a supply of water vapour also rapidly consumes O<sub>2</sub>, but at a slightly slower rate, perhaps due to the enhanced photo-adsorption of O<sub>2</sub> when water is present, as discussed earlier. Based on these experiments, the rate of O<sub>2</sub> consumption is primarily affected by the photocatalytic capacity of the catalyst in question.

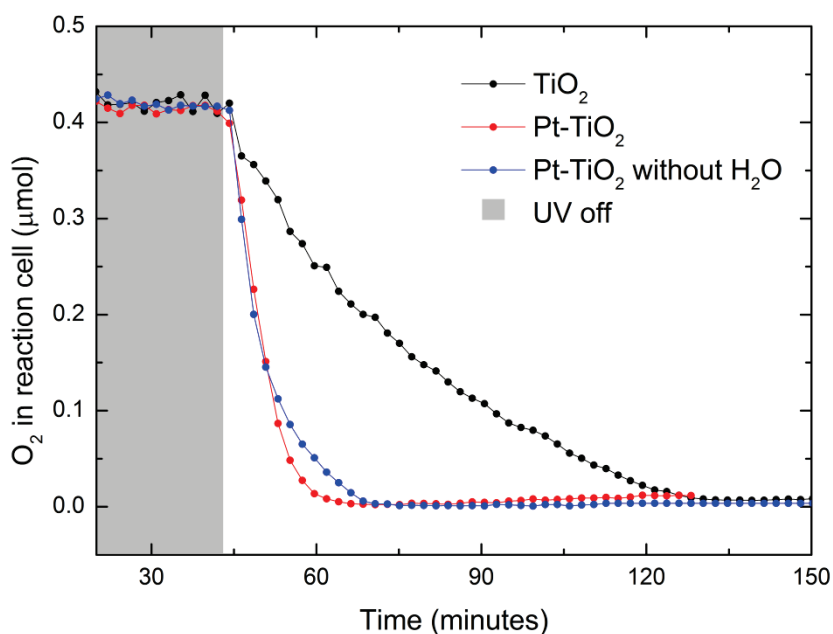


Figure 6.9: Comparison of the rate of O<sub>2</sub> consumption between Pt/P25 with water vapour, bare P25 with water vapour, and Pt/P25 without water vapour.

#### 6.1.4.2 Sources of Carbon Contamination

One of the most likely sources of carbon in the reaction cell is that of adventitious carbon. This is usually a thin layer of carbonaceous molecules that are found on the surface of any material or vacuum system exposed to the atmosphere. It consists primarily of short chain hydrocarbons and small amounts of single and double bonded, functionalised groups.<sup>488</sup> The origin of these hydrocarbons is still debated and they remain unavoidable in virtually all vacuum systems. It is also easier for carbon contaminants to reach the surface of TiO<sub>2</sub> when in a gas-phase reactor compared to a liquid phase reactor. There are numerous methods available to remove adventitious carbon, including acid treatments, xenon excimer lamps, and plasma cleaners. However, these treatments are harsh, and it is currently unknown what type of effect these treatments would have on the Au clusters or their ligands while they are in the reaction cell, so these techniques have been avoided.

By basic calculation, a typical adventitious carbon layer of  $\sim 1.66 \times 10^{-6}$  moles of carbon per m<sup>2</sup> equates to  $3.13 \times 10^{-9}$  moles of carbon adhered to  $\sim 18.85$  cm<sup>2</sup> of reaction cell surface area. Calculating the number of moles adhered to the 0.4984 m<sup>2</sup> of surface area of 8.9 mg of Au/TiO<sub>2</sub> yields  $8.28 \times 10^{-7}$  moles of carbon. This would be sufficient to account for the carbon in the  $6.00 \times 10^{-7}$  moles of CO<sub>2</sub> produced in the experiment shown in Figure 6.7 previously. This amount of adventitious carbon may be unreasonably large, however, as the entire surface area of P25 may not be covered with such a uniform thickness of adventitious carbon in comparison to the stainless steel walls of the reaction cell.

Another possible source of carbon that may contribute to adventitious carbon could be from oil-backstreaming from the rotary pump into the reaction cell. While there is an oil trap between the rotary pump and the reaction cell, these traps are not guaranteed to collect all of the oil vapour from the pump and a small amount may get through the vacuum line and into the reaction cell during overnight evacuations. The use of a liquid nitrogen trap in place of a standard mesh trap was not possible during an overnight evacuation due to equipment constraints. A cost-effective and improved alternative that could be used in the future would be a reusable zeolite trap.

Carbon based thread sealant tape used on the NPT connections in the reaction cell, the rubber O-ring used to seal the silica window, and nylon lines used to deliver gases to the manifold may contribute to carbon contamination via outgassing. Replacement of the rubber O-ring with a silicon based O-ring was found to decrease the amount of the

extended CO<sub>2</sub> production observed after 3 hours. The outgassing of the O-ring may have been exacerbated by the UV light during reactions as well, which would photo-degrade the O-ring. Extended evacuation of the nylon gas lines and gas manifold was found to lead to a small decrease in CO<sub>2</sub> observed during experiments. The nylon lines have since been replaced with stainless steel to reduce this effect.

Given that CO is present in the atmosphere and is difficult to remove from a typical vacuum system, it is likely that there is a small amount of CO adsorbed to the surface of the TiO<sub>2</sub> and to the walls of the reaction cell during preparation of samples. It has also been shown that surface oxygen vacancies can act as chemisorption sites for H<sub>2</sub>, CO and O<sub>2</sub>.<sup>520</sup> During this adsorption process, additional oxygen vacancies are formed when adsorbed CO reacts with nearby lattice oxygen atoms to form CO<sub>2</sub>, which is released in gaseous form. The close proximity of these point defects can cause them to diffuse further into the lattice, therefore regenerating the surface oxygen atoms and allowing the reaction of CO with surface oxygen atoms to continue. Anpo *et al.*<sup>522</sup> have shown that gas-phase oxygen can also be incorporated into the CO<sub>2</sub> product formed from CO *without* any lattice oxygen by using isotopically labelled reactants, and their calculations suggest that the oxygen is photo-activated by formation of the O<sub>3</sub><sup>-</sup> species formed on the TiO<sub>2</sub> surface.

It is also well-known that Au nanoparticles supported on TiO<sub>2</sub> show remarkable catalytic activity for CO oxidation.<sup>138,206,264,274-298</sup> Stiehl *et al.*<sup>523</sup> have shown Au/TiO<sub>2</sub> populated with atomic oxygen and molecular oxygen produces 41% more CO<sub>2</sub> than one with only atomic oxygen. This reaction pathway may also contribute to the production of CO<sub>2</sub> if there is any significant levels of CO present in the reaction cell.

## 6.2 Photocatalytic Performance of Au Clusters on TiO<sub>2</sub> for Water-Splitting

Au<sub>8</sub>, Au<sub>9</sub>, and Au<sub>101</sub> clusters were supported on P25 and anatase nanoparticles with various treatments as summarised in Table 6.1. All samples in this table were tested for their capacity for photocatalytic water-splitting. It should be noted that the sample matrix is limited by the samples that were available from collaborators and synchrotron visits at the time of experimentation, but still covers a large range of treatments and supports. Table 5.8 summarises the key changes to the physical properties of these catalysts due to the various treatments (see Chapter 5), to readily draw correlations with the photocatalytic production rates of these samples in the coming sections.

Table 6.1: Sample matrix summarising the different pre- and post-treatments applied to the various supported Au clusters used in photocatalytic experiments.

Cluster Type	Support	Pre-Treatment	Post-Treatments	Clusters Per Nanoparticle	Approximate Coverage (%)
Au <sub>8</sub>	Anatase	None	Untreated	25.56	5.21
			O <sub>2</sub> 200 °C		
			O <sub>2</sub> + H <sub>2</sub> 200 °C		
Au <sub>9</sub>	Anatase	None	Untreated	22.71	4.62
			O <sub>2</sub> 200 °C		
	P25	Acid washed	Untreated	14.31	4.13
			Heat treated 200 °C O <sub>2</sub> 200 °C		
Au <sub>101</sub>	Anatase	none	Untreated	2.02	0.81
			O <sub>2</sub> 200 °C		
			O <sub>2</sub> + H <sub>2</sub> 200 °C		
	Anatase	Acid washed	Untreated	2.02	0.81
			O <sub>2</sub> 200 °C		
			O <sub>2</sub> + H <sub>2</sub> 200 °C		
P25	Acid washed	Untreated	1.28	0.72	
		Heat treated 200 °C			
		O <sub>2</sub> + H <sub>2</sub> 200 °C			

Table 6.2: Summary of the key trends in ligand loss and agglomeration observed for Au<sub>8</sub>, Au<sub>9</sub>, Au<sub>11</sub> and Au<sub>101</sub> on acid-washed P25 and pure anatase supports under the various post-treatment conditions. This Table has been reproduced from the conclusion of Chapter 5.

Treatment	Acid washed P25 Nanoparticle Supported				Pure Anatase Nanoparticle Supported		
	Au <sub>8</sub>	Au <sub>9</sub>	Au <sub>11</sub>	Au <sub>101</sub>	Au <sub>8</sub>	Au <sub>9</sub>	Au <sub>101</sub>
Untreated	•Virtually Unchanged			•Small increase in particle size	•Partial ligand removal •Half of clusters remain intact, while the other half undergo partial agglomeration		•Partial ligand removal •Unknown if agglomeration occurs, but likely
Washed at 100 °C	•Removal of a fraction of clusters from the surface •A portion of clusters remain virtually unchanged •Some removal of ligands •No significant agglomeration •Formation of Au-O bonds, to a greater extent for Au <sub>11</sub>			•Unknown changes to size •Loss of a significant amount of clusters from the surface •No Au-O formation		N/A	
Heated at 200 °C	•Agglomeration of a portion of clusters while still ligand-protected (these are still smaller than Au <sub>101</sub> ) •Other portion of clusters lose some ligands and form Au-O and agglomerate to larger particles •Of the portion that loses ligands, some clusters may not agglomerate •Removal of ligands is less effective for Au <sub>9</sub>			•Further agglomeration of clusters, but still nanoparticulate in nature •Removal of some ligands and formation of Au-O bonds		N/A	
Calcined O <sub>2</sub> at 200 °C		Increased agglomeration and size distribution			•Removal of ligands and agglomeration has progressed further •Half of clusters maintain their size	•Removal of ligands and agglomeration has progressed further •No fraction of clusters maintain their size	•Removal of ligands has progressed further •Unknown if agglomeration occurs, but likely
Calcined O <sub>2</sub> /H <sub>2</sub> at 200 °C			N/A		•Complete ligand removal •Agglomeration has progressed further, no evidence of any clusters remaining intact.		•Complete ligand removal •Unknown if agglomeration progresses further, but likely.

In general, there is a trend of ligand loss and agglomeration with successively harsher post-treatment conditions. This effect is far more pronounced for clusters supported on pure anatase nanoparticles than on the acid-washed P25 nanoparticles, showing the strong effect of acidic pre-treatment on the interaction between the TiO<sub>2</sub> surface and Au clusters. For samples on either support, there is general evidence for two cluster states after post-treatment, with one portion remaining unchanged, while the other undergoes some level of agglomeration. For further discussion about how these physical properties were determined, see Chapter 5. Given that the exact number of particles present after agglomeration is unknown, it is not possible to calculate turnover frequencies for most samples, and these numbers have therefore not been included in the discussion.

### 6.2.1 Photocatalytic Performance of the Au<sub>8</sub> cluster

The peak H<sub>2</sub> production rates for Au<sub>8</sub>/anatase with various treatments are shown in Figure 6.10. The Au<sub>8</sub>/anatase samples have peak H<sub>2</sub> production rates of  $17.92 \pm 3.22$ ,  $51.74 \pm 5.17$ , and  $71.12 \pm 7.11 \mu\text{mol hr}^{-1} \text{g}^{-1} \text{cm}^{-2}$  for the untreated, calcined at 200 °C under O<sub>2</sub>, and calcined at 200 °C under O<sub>2</sub>+H<sub>2</sub> treatments, respectively. There is a clear improvement in H<sub>2</sub> gas production as the clusters are treated under successively harsher conditions.

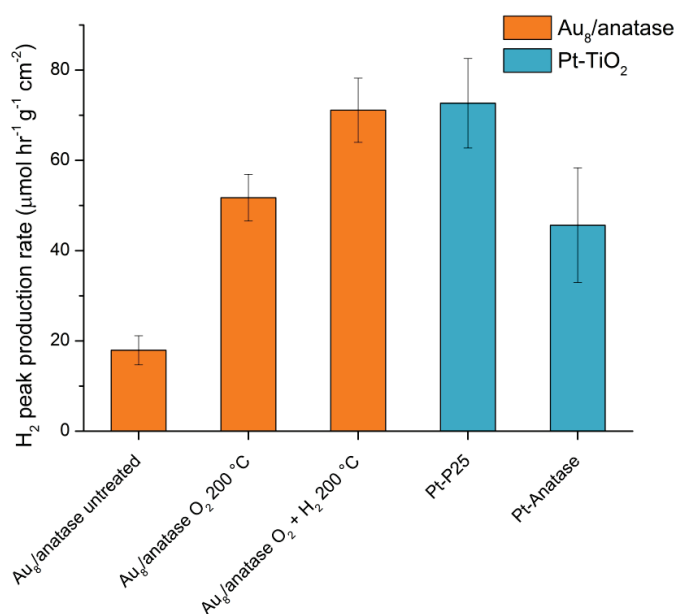


Figure 6.10: Average H<sub>2</sub> peak production rate for Au<sub>8</sub> clusters supported on pure anatase nanoparticles with various treatments.

200 °C calcination under O<sub>2</sub> for Au<sub>8</sub>/anatase results in almost complete removal of ligands and agglomeration (See Table 5.8), while harsher calcination under O<sub>2</sub> followed by H<sub>2</sub> results in complete removal of ligands. Given this information, it is the exposed Au<sub>8</sub> clusters that are more effective catalysts for photocatalytic water-splitting, compared to untreated Au<sub>8</sub>/anatase, of which there is only partial removal of ligands. However, the loss of ligands may not be the primary cause of increased catalytic activity, given that these calcination treatments bring about agglomerated clusters, which do not maintain their Au<sub>8</sub> size. It could therefore be argued that the small size of the Au<sub>8</sub> clusters are not beneficial for photocatalytic water-splitting, with larger Au nanoparticles on the anatase surface yielding the best catalytic environment. This is further supported by the deposition of Au<sub>8</sub> on anatase without any treatment, which also results in some loss of ligands, and a small fraction of Au<sub>8</sub> clusters agglomerating. Given the low, but still present catalytic activity of these untreated samples, this is further evidence that the agglomerated Au<sub>8</sub> clusters are the catalytically active sites.

### 6.2.2 Photocatalytic Performance of the Au<sub>9</sub> cluster

The average H<sub>2</sub> production rates for Au<sub>9</sub> supported on anatase and acid-washed P25 nanoparticles with various treatments are shown in Figure 6.11. The Au<sub>9</sub>/anatase samples have H<sub>2</sub> production rates of  $33.5 \pm 3.35$  and  $112.9 \pm 12.3 \mu\text{mol hr}^{-1} \text{g}^{-1} \text{cm}^{-2}$  for untreated and calcined under O<sub>2</sub> samples, respectively. The acid-washed P25 supported samples yield H<sub>2</sub> production rates of  $82.7 \pm 8.27$ ,  $511.4 \pm 51.1$ , and  $75.3 \pm 7.53 \mu\text{mol hr}^{-1} \text{g}^{-1} \text{cm}^{-2}$  for the untreated, heat treated under vacuum, and calcined under O<sub>2</sub> samples respectively. There is a clear improvement in productivity for the Au<sub>9</sub>/anatase clusters after calcination under an O<sub>2</sub> atmosphere, whereas for the Au<sub>9</sub>/acid-washed P25 clusters, there is a large increase in performance after heat-treatment at 200 °C under vacuum, followed by a decrease in performance after further calcination at 200 °C under an O<sub>2</sub> atmosphere.

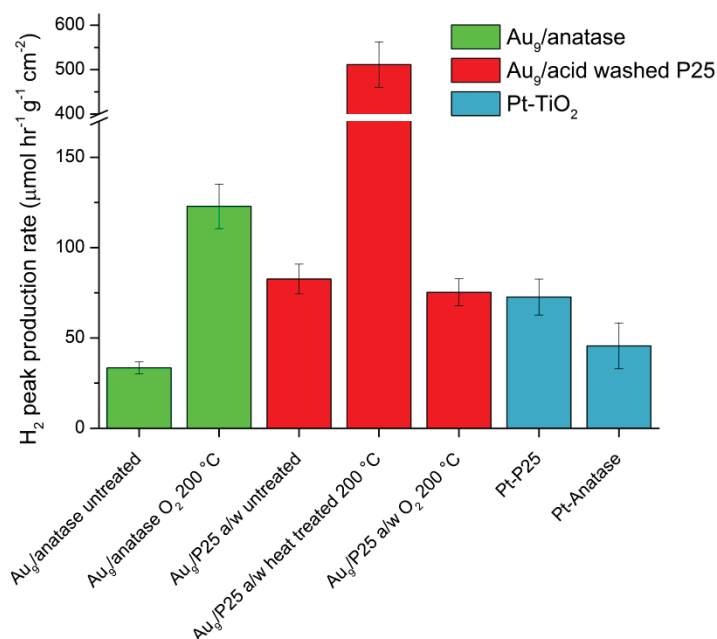


Figure 6.11: Average H<sub>2</sub> peak production rate for Au<sub>9</sub> clusters supported on pure anatase and acid-washed P25 nanoparticles with various treatments.

200 °C calcination under O<sub>2</sub> for Au<sub>9</sub>/anatase results in a large degree of ligand removal and agglomeration, with only a fraction of the clusters maintaining their size. Given that this support is not acid-washed, this effect is likely more severe than the same treatment on the acid-washed P25 nanoparticles. This treatment for the anatase-supported Au<sub>9</sub> clusters yields a higher production rate than the untreated or calcined under O<sub>2</sub> at 200 °C treated, acid-washed P25 supported Au<sub>9</sub> clusters, possibly due to the increased size and removal of ligands.

It is therefore interesting that the untreated Au<sub>9</sub>/acid-washed P25 has a greater performance than untreated Au<sub>9</sub>/anatase, as the former results in virtually no change in the size or ligand coverage of the Au<sub>9</sub> clusters after they are supported. Heat treatment at 200 °C results in agglomeration of a portion of the Au<sub>9</sub> clusters while still ligand-protected, while the other portion lose some ligands, forming Au-O bonds, and begin to agglomerate. There is also evidence that of the portion that loses ligands, some may not agglomerate. Further calcination at 200 °C under O<sub>2</sub> for Au<sub>9</sub>/acid-washed P25 results in increased agglomeration according to HRTEM, but there is no XPS data to provide details about ligand removal or bond formation between the cluster and the surface. The decrease in performance observed for this treatment could imply that there is an ideal size for the Au particles when supported on acid-washed P25, whereby a small amount of Au<sub>9</sub>

agglomeration and ligand loss is necessary for ideal performance. Alternatively, it could be the small portion of Au<sub>9</sub> clusters that have lost ligands without agglomerating that are the most effective, as these are most likely lost with further calcination at 200 °C under O<sub>2</sub>. It is difficult to determine if the large differences in performance between the anatase and P25 series is due to the pure vs mixed polymorph nature of the support, or if it is due to the acid-wash pre-treatment, without further characterisation studies.

### 6.2.3 Photocatalytic Performance of the Au<sub>101</sub> cluster

The average H<sub>2</sub> production rates for Au<sub>101</sub> supported on anatase and P25 nanoparticles with various treatments are summarised in Figure 6.12. For the Au<sub>101</sub>/untreated anatase series, the production rates are  $50.93 \pm 13.3$ ,  $94.3 \pm 15.7$ , and  $190.4 \pm 29.6 \mu\text{mol hr}^{-1} \text{g}^{-1} \text{cm}^{-2}$  for the untreated, calcined under O<sub>2</sub>, and calcined under O<sub>2</sub> and H<sub>2</sub> samples respectively. For the Au<sub>101</sub>/acid-washed anatase series, the production rates are  $534.8 \pm 53.5$ ,  $112.2 \pm 11.2$ , and  $122.7 \pm 11.2 \mu\text{mol hr}^{-1} \text{g}^{-1} \text{cm}^{-2}$  for the untreated, calcined under O<sub>2</sub>, and calcined under O<sub>2</sub> and H<sub>2</sub> samples respectively. For the Au<sub>101</sub>/acid-washed P25 series, the production rates are  $238.3 \pm 16.5$ ,  $437.5 \pm 43.7$ , and  $188.8 \pm 34.0 \mu\text{mol hr}^{-1} \text{g}^{-1} \text{cm}^{-2}$  for the untreated, heat treated, and calcined under O<sub>2</sub> samples respectively.

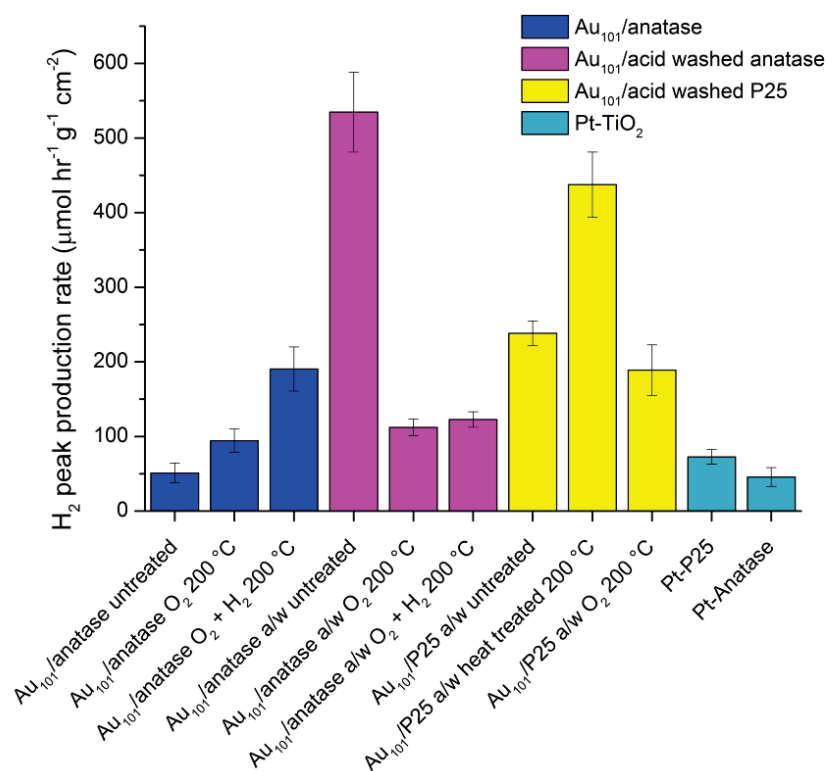


Figure 6.12: Average H<sub>2</sub> peak production rate for Au<sub>101</sub> clusters supported on acid-washed P25, acid-washed anatase, and pure anatase nanoparticles with various treatments.

The trend of increasing H<sub>2</sub> production for Au<sub>101</sub>/untreated anatase can be attributed to the increased amount of ligand removal and possible agglomeration under successively harsher calcination conditions. This effect is the same as that discussed previously for both Au<sub>8</sub> and Au<sub>9</sub>, supporting the hypothesis that removal of ligands and an increase in particle size improves the catalytic performance of anatase-supported Au clusters.

For the Au<sub>101</sub>/acid-washed P25 series, there is a clear maximum in performance for the heat-treated sample, followed by a decrease with harsher calcination under O<sub>2</sub>, similar to the trend observed for Au<sub>9</sub> previously. Nevertheless, there is no evidence for a bimodal distribution of clusters; instead, all clusters have ligands removed and agglomerate, while forming Au-O bonds to the surface. Further calcination under O<sub>2</sub> results in a decrease in H<sub>2</sub> production, with an increase in particle size evidenced by HRTEM. Also of note is that the untreated samples are more effective than those supported on pure anatase, but less effective than those supported on acid-washed anatase. There is evidence to suggest that support of untreated Au<sub>101</sub> on acid-washed P25 results in virtually no change to the size or ligand coverage of the clusters.

For the Au<sub>101</sub> clusters supported on acid-washed anatase, the highest H<sub>2</sub> production rate is observed for the untreated Au<sub>101</sub> sample, which is the highest of all samples in this series. The H<sub>2</sub> production rate drops significantly after harsher calcination treatments. There is no characterisation data available for this series of clusters, therefore it is unknown if the untreated Au<sub>101</sub> clusters are maintaining their size after deposition on acid-washed anatase, similar to what occurs for untreated Au<sub>101</sub> on acid-washed P25, or if there is partial removal of ligands as seen for untreated anatase supports. Given that pre-treatment of the TiO<sub>2</sub> surface with acid should help to reduce agglomeration, the former seems more likely. If this is the case, then there is a clear performance advantage to keeping the Au<sub>101</sub> cluster intact on the acid-washed anatase surface. Nonetheless, there is the possibility of a small amount of ligand removal (given the likelihood of this occurring on anatase) comparable to that observed for heat-treated Au<sub>101</sub> on acid-washed P25, resulting in the similar production rate observed for clusters that maintain size, but have partial ligand removal. This will need to be confirmed with further characterisation experiments in the near future.

These results suggest that for the acid-washed supports, there may be an ideal particle size regime that provides the most performance, compared with the unwashed anatase supports, which favour increasingly larger particles and ligand removal.

### 6.2.4 Overall Comparisons of the Photocatalytic Performance Between Clusters

Figure 6.13 shows a comparison between Au<sub>8</sub>, Au<sub>9</sub>, and Au<sub>101</sub> clusters supported on anatase nanoparticles. Similar trends are observed for all three clusters as successively harsher post-treatments are applied. When samples are calcined under an O<sub>2</sub> atmosphere, their H<sub>2</sub> production rate increases compared to their untreated counterparts. When samples are calcined under O<sub>2</sub> and H<sub>2</sub>, a harsher and prolonged calcination, their H<sub>2</sub> production rate is increased beyond that of samples calcined under O<sub>2</sub> alone. There is no data available for Au<sub>9</sub> calcined under O<sub>2</sub> and H<sub>2</sub>, although it can be assumed that it would follow the same trend as the other clusters, given that Au<sub>9</sub> calcined under O<sub>2</sub> has a production rate within experimental error of the production rate for Au<sub>101</sub> calcined under O<sub>2</sub>.

As shown in Table 5.8, these successively harsher treatments result in increasing ligand removal and agglomeration for all clusters on the anatase surface. It is clear that it is the large, unligated Au particles that have lost their defined size, which are the most effective photocatalysts on the unwashed anatase nanoparticles. Since the overall performance also increases when comparing the set of Au<sub>8</sub> to Au<sub>9</sub> to Au<sub>101</sub> samples, this is further evidence that it is the largest Au particles that are the most effective photocatalysts on this support.

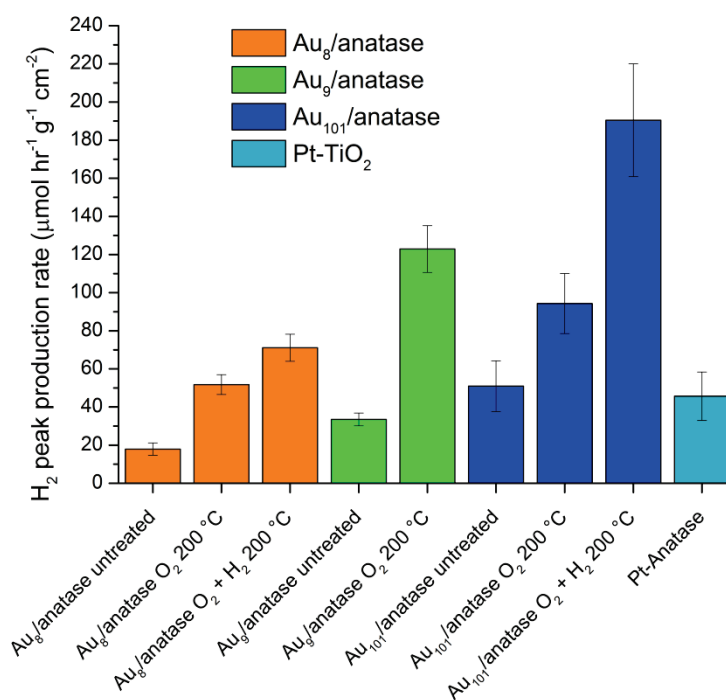


Figure 6.13: Comparison of H<sub>2</sub> peak production rate for Au<sub>8</sub>, Au<sub>9</sub>, and Au<sub>101</sub> clusters supported on anatase nanoparticles with various treatments.

Figure 6.14 shows a comparison between Au<sub>9</sub> and Au<sub>101</sub> clusters supported on acid-washed P25 nanoparticles. This figure shows the similar trends in H<sub>2</sub> production rates for both clusters after treatment, whereby 200 °C heat treatment of the clusters results in a large increase in performance compared to the untreated samples, followed by a decrease in performance for the calcined under O<sub>2</sub> samples.

For the untreated samples, it is known that the clusters remain virtually unchanged after being supported on acid-washed P25; therefore, the intact Au<sub>101</sub> clusters are more effective photocatalysts for water photolysis than Au<sub>9</sub>. This could be due to their larger particle size, similar to the effect observed for Au<sub>101</sub> supported on pure anatase nanoparticles. Comparison between these two clusters also reveals that the untreated

Au<sub>101</sub> clusters do not form any Au-O bonds with the surface according to XPS, while untreated Au<sub>9</sub> has a portion of clusters forming Au-O bonds.

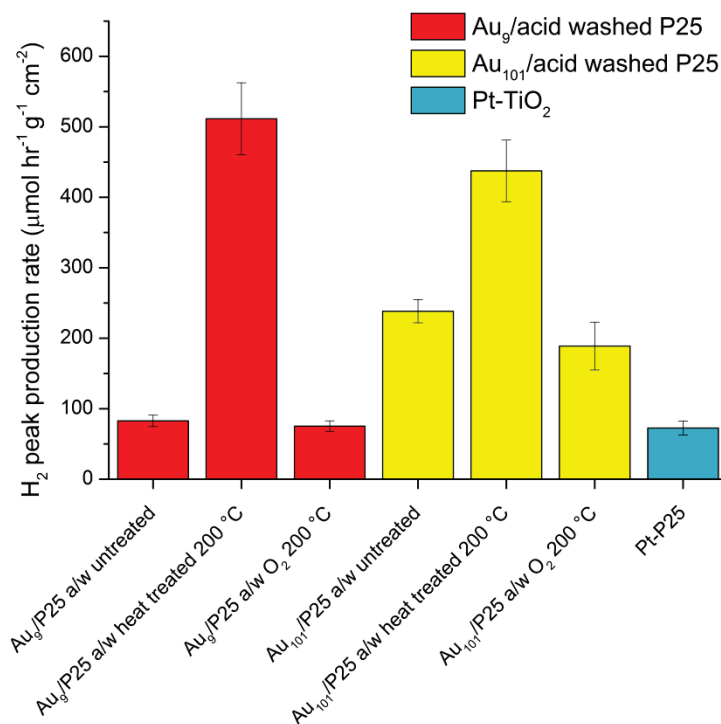


Figure 6.14: Comparison of H<sub>2</sub> peak production rate for Au<sub>55</sub> and Au<sub>9</sub> clusters supported on acid-washed P25 nanoparticles with various treatments.

The production rate of the heat treated samples are within the experimental error of each other, and the size measurement by the HRTEM are also within sampling error of each other ( $2.4 \pm 1.7$  vs  $3.2 \pm 1.7$  nm for Au<sub>9</sub> and Au<sub>101</sub> respectively). Therefore, the similar production rate measured for these two clusters on acid-washed P25 with the same treatment could be because the two samples are of similar size after agglomeration, while still being protected by a comparable number of ligands.

The large drop in production rate for Au<sub>9</sub> calcined under O<sub>2</sub> is surprising given that the size of the nanoparticle is now the same as that of heat-treated Au<sub>101</sub> according to HRTEM ( $3.1 \pm 2.1$  vs  $3.2 \pm 1.7$  nm for Au<sub>9</sub> and Au<sub>101</sub> respectively). There is no XPS data for this treatment, but it could be assumed that the extent of Au-O bond formation has increased, following the increase observed for the heat-treated samples. Since untreated Au<sub>101</sub> has no Au-O bonds and performs better than untreated Au<sub>9</sub> with Au-O bonds, and that Au<sub>101</sub> calcined under O<sub>2</sub> may have an increased amount of Au-O bond formation, it is feasible that high levels of Au-O bond formation is detrimental to the photocatalytic

performance. This is further evidenced by Au<sub>101</sub> calcined under O<sub>2</sub> performing worse than the untreated Au<sub>101</sub> samples.

### 6.2.5 Photocatalytic Performance of Au<sub>8</sub>, Au<sub>9</sub>, and Au<sub>101</sub> Compared to Pt-TiO<sub>2</sub>

Given that TiO<sub>2</sub> is cheap and relatively abundant, while both Au and Pt are expensive elements in the current marketplace, it is fair to assume that the major cost of these catalysts would come from the procurement of these two rare elements. Comparison between the production rates for 1.0% Pt-P25 and 1.0% Pt-anatase to that of the 0.17% Au supported on P25 or anatase nanoparticles can be made by normalising for the amount of precious metal present in the catalyst instead of by the total mass of the catalyst; these H<sub>2</sub> production rates normalised by precious metal mass are shown in Figure 6.15.

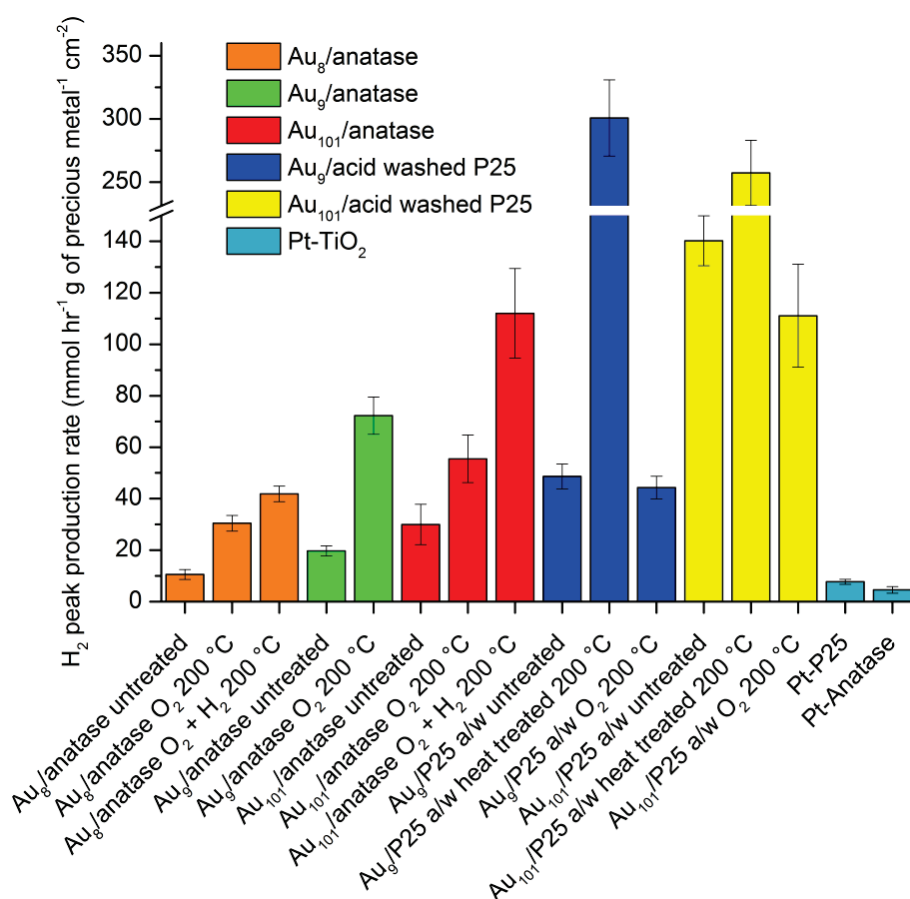


Figure 6.15: Comparison of H<sub>2</sub> peak production rate for 0.17% w/w Au<sub>101</sub>, Au<sub>9</sub>, and Au<sub>8</sub> clusters supported on TiO<sub>2</sub> against 1.0% w/w Pt-P25 and 1.0% w/w Pt-anatase. The H<sub>2</sub> production rate is weighted per gram of precious metal instead of per gram of total catalyst.

This comparison shows the increased efficacy of Au/TiO<sub>2</sub> compared to typical Pt-TiO<sub>2</sub> photocatalysts. For the anatase-supported series, Au<sub>101</sub> calcined under O<sub>2</sub> and H<sub>2</sub> is ~20 times more effective than Pt-anatase for the same amount of precious metal present in the catalyst, while for the P25 series, heat-treated Au<sub>9</sub> is ~66 times more effective than Pt-P25 for the same amount of precious metal present in the catalyst. Even the least effective Au catalyst in the series, untreated Au<sub>8</sub> on pure anatase, is more effective than both Pt-P25 and Pt-anatase when compared using this normalisation scheme.

### 6.3 Conclusions

Benchmark photocatalytic water-splitting experiments were undertaken using Pt-P25 and Pt-Anatase nanoparticles to ensure the newly designed experimental apparatus was performing adequately. During these studies, it was discovered that there is a decrease in the photocatalytic performance of samples when repeating experiments using the same catalyst material. Further preliminary studies of Au/TiO<sub>2</sub> found a similar effect of performance degradation. This degradation in the performance of samples was accompanied by a colour change in the samples. The degradation and colour change of samples was attributed to accumulation of carbon deposits during the oxidation of organic compounds, and may be related to the known photo-induced agglomeration effects of ambient light on the Au<sub>9</sub> and Au<sub>101</sub> clusters evidenced by XANES and HRTEM data from Chapter 5. Improved performance was also observed for all samples prepared in the reaction cell with 12 hours of exposure to vacuum, compared to relatively short vacuum exposure times of 10 minutes.

The production of H<sub>2</sub> from photocatalytic water-splitting experiments was accompanied by the production of CO<sub>2</sub> and consumption of O<sub>2</sub>. The CO<sub>2</sub> by-product arises from the well-known capacity for TiO<sub>2</sub> to photo-oxidise organic contaminants, and consumes the stoichiometrically evolved O<sub>2</sub> from the water-splitting reaction throughout the experiment. The source of carbon in the reaction cell is most likely from unavoidable adventitious carbon that is present in all vacuum systems and samples exposed to atmosphere, in addition to the possible contribution from oil backstreaming from the rotary pump. Various carbon based sealant material used in the reaction cell and adsorbed CO that is difficult to evacuate during sample preparation may also contribute to the source of carbon.

O<sub>2</sub> present in the reaction cell at the beginning of the experiment due to low vacuum is likely rapidly consumed by quenching defect states within the TiO<sub>2</sub> nanoparticles and by photo-adsorption of O<sub>2</sub> to the TiO<sub>2</sub> surface over the initial hour of experiments. This initial O<sub>2</sub> presence could also include O<sub>2</sub> molecules adsorbed to the TiO<sub>2</sub> surface at ambient temperature, or those adsorbed to the walls of the reaction cell. The formation of surface O<sub>2</sub><sup>-</sup> and O<sub>3</sub><sup>-</sup> species during this period by molecular O<sub>2</sub> likely behaves as electron traps or hole scavengers after photo-excitation, increasing electron-hole separation, which

could explain the decrease in both H<sub>2</sub> and CO<sub>2</sub> production after the excess O<sub>2</sub> in the reaction cell is consumed.

Following this work, photocatalytic water-splitting experiments were successfully undertaken with a wide range of chemically synthesised Au<sub>8</sub>, Au<sub>9</sub>, and Au<sub>101</sub> clusters supported on P25 and pure anatase nanoparticles with various pre- and post-treatments. All samples were found to be active towards photocatalytic water-splitting. For the anatase-supported samples, successively harsher treatments led to higher catalytic performance for all clusters, with calcination under an O<sub>2</sub> and H<sub>2</sub> atmosphere resulting in the highest performance. It was found that it is the unligated, large Au particles that have lost their atomically precise nature, which are the most effective photocatalysts on the unwashed anatase nanoparticles. The overall performance also increased as the initial size of the cluster increased, providing further evidence that it is the largest Au particles that are the most effective photocatalysts on this support. Changes in Au particle size are known to have a dramatic effect on their catalytic capacity due to a number of reasons outlined in detail in the introduction Chapter. Au<sub>101</sub>/anatase calcined under O<sub>2</sub> and H<sub>2</sub> at 200 °C was found to be the most effective photocatalyst, with a H<sub>2</sub> production rate of  $190.4 \pm 29.6 \mu\text{mol hr}^{-1} \text{g}^{-1} \text{cm}^{-2}$ . It is also known that anatase is more active towards the photo-reduction of O<sub>2</sub> that contributes to the unwanted backward reaction between H<sub>2</sub> and O<sub>2</sub>, which may contribute to the overall lower performance of the anatase-supported samples compared to the P25 supported samples.<sup>103,120,524</sup>

For the acid-washed P25 supported samples, heat treatment under vacuum at 200 °C was found to be the most effective for Au<sub>101</sub> and Au<sub>9</sub> for maximum H<sub>2</sub> production, while further treatment via calcination under an O<sub>2</sub> atmosphere resulted in decreased performance. The H<sub>2</sub> production rate for these heat treated samples was found to be  $511.4 \pm 51.1$  and  $437.5 \pm 43.7 \mu\text{mol hr}^{-1} \text{g}^{-1} \text{cm}^{-2}$  for Au<sub>9</sub> and Au<sub>101</sub> respectively. The comparable production rate was attributed to the heat treatment yielding Au particles of similar size after agglomeration. Untreated Au<sub>101</sub> on acid-washed anatase nanoparticles were also found to be very effective, with a production rate of  $534.8 \pm 53.5 \mu\text{mol hr}^{-1} \text{g}^{-1} \text{cm}^{-2}$ . These clusters may be of similar size and with a comparable number of ligands to the heat-treated samples on acid-washed P25, hence the similar production rates. These results suggest that for the acid-washed nanoparticle supports, there may be an ideal Au particle size and ligand coverage that provides the most performance, compared to the unwashed anatase supports, which favour increasingly larger particles and major ligand

removal. When weighted by grams of precious metal present in the catalyst, it was also shown that small Au particles supported on TiO<sub>2</sub> vastly outperform platinised TiO<sub>2</sub>.

This work has demonstrated the capability of TiO<sub>2</sub>-supported gold clusters for photocatalytic water-splitting. Future directions will look at the possibly of supporting samples on silicon wafer chips, so that after samples undergo photocatalytic experiments, they may then be investigated via XPS, MIES, or UPS techniques to determine if any significant changes have occurred. Further characterisation experiments on acid-washed anatase will be necessary to understand the probable differences between the anatase and P25 nanoparticle support, in addition to the full effects of acidic pre-treatment. Future studies will also begin to explore alternative photocatalytic reactions that can be driven by these catalysts, as well as investigating the effects of various irradiation wavelengths, irradiation intensity, pressure, and temperature.

# Chapter Seven

## DFT Studies of Au<sub>1-4</sub> on the Stoichiometric and Oxygen-deficient TiO<sub>2</sub> Anatase(101) Surface

In this Chapter, the theoretical insight gained from DFT calculations of Au<sub>1</sub>, Au<sub>2</sub>, Au<sub>3</sub>, and Au<sub>4</sub> clusters bound to the stoichiometric and oxygen-deficient titanium dioxide anatase(101) surface using an atomic centred basis set are presented. Numerous isomers are found within 0.5 eV of the lowest energy structure for Au<sub>2</sub>, Au<sub>3</sub>, and Au<sub>4</sub>. The structural parameters, binding energies, infrared spectra, charge transfer, and density of states for each isomer are described in detail. Key findings include: increasing binding energy as the number of Au atoms are increased; strong Au-Au stretching and cluster breathing modes that shift considerably between isomers or with additional Au atoms; the general trend of charge transfer from the Au clusters to the titanium dioxide surface; and the introduction of numerous occupied gold states at the valence band edge that extend into the band gap, as well as isolated states introduced in the middle of the band gap.

## 7 DFT Studies of Au<sub>1-4</sub> on the Stoichiometric and Oxygen-deficient TiO<sub>2</sub> Anatase(101) Surface

### 7.1 Optimisation of the Anatase(101) Model

The structure of the stoichiometric TiO<sub>2</sub> anatase(101) model used in the following calculations is shown in Figure 7.1, displaying the common Miller index planes that will be used in the discussion. This Ti<sub>14</sub>O<sub>45</sub>H<sub>34</sub> model surface of anatase has C<sub>s</sub> symmetry and exposes two main types of undercoordinated atoms; the 5 coordinated titanium atom (Ti<sub>5c</sub>), and the 2 coordinated bridging oxygen atom (O<sub>2c</sub>). These two sites account for the majority of cluster binding positions as shall be discussed in the coming sections. Previous studies by Vittadini and Selloni have shown that these sites can behave as Lewis acid and Lewis base sites respectively.<sup>342</sup> The publications that are compared with throughout this thesis use the same type of stoichiometric and oxygen-deficient anatase(101) surface. The anatase(101) surface was chosen as the focus of this computational study, since this surface is used in a number of photocatalytic experiments and anatase is also the major polymorph component of P25 nanoparticles.<sup>143</sup>

After geometric optimisation of the model, the surface atoms relax away from the unit cell derived lattice positions, although the model maintains C<sub>s</sub> symmetry during optimisation. Relaxation of the surface away from the unit cell positions is expected and has been observed in other theoretical studies.<sup>127,128,132</sup> The magnitude and direction of these relaxations are summarised in Table 7.1, with Figure 7.1 showing the corresponding atom labels; the Ti(3) and Ti(7) atoms correspond to undercoordinated Ti<sub>5c</sub>, while the O(4) and O(8) atoms correspond to undercoordinated O<sub>2c</sub>. The most significant atomic displacements are those of the two fully coordinated titanium atoms, Ti(1) and Ti(5), which both rise above the surface along the [101] axis by 0.16 and 0.15 Å respectively, and those of O(1), O(6), and O(5), which also displace along the [101] axis by 0.29, 0.23 and 0.19 Å respectively. Ti(7) and Ti(8) relax away from the centre of the model, along the [10 $\bar{1}$ ] and [010] lateral axes. The bridging O<sub>2c</sub> atoms, O(4) and O(8), sink into the surface along the [101] axis by 0.09 and 0.07 Å respectively, while moving laterally along the [10 $\bar{1}$ ] axis by 0.04 and 0.11 Å. The direction and magnitude of relaxations for Ti(1), Ti(3), Ti(5), O(1), O(3), O(4), O(6), and O(8) are similar to other computational studies of the anatase surface.<sup>128,132</sup> The remaining atomic relaxations differ from these studies, which includes the peripheral Ti(7), Ti(8), and O(8) atoms. The general trend of

relaxations are expected, given the isolated and finite model of the surface atoms, which are no longer being constrained within an infinite lattice framework as they would have been when the unit cell was determined from a crystal structure.<sup>115</sup> Given that other studies that have been used as comparison were performed using periodic boundary conditions with plane-wave basis sets, while these calculations have been performed on a finite model with atomic-centred basis sets, differences in predicted relaxations are to be expected.

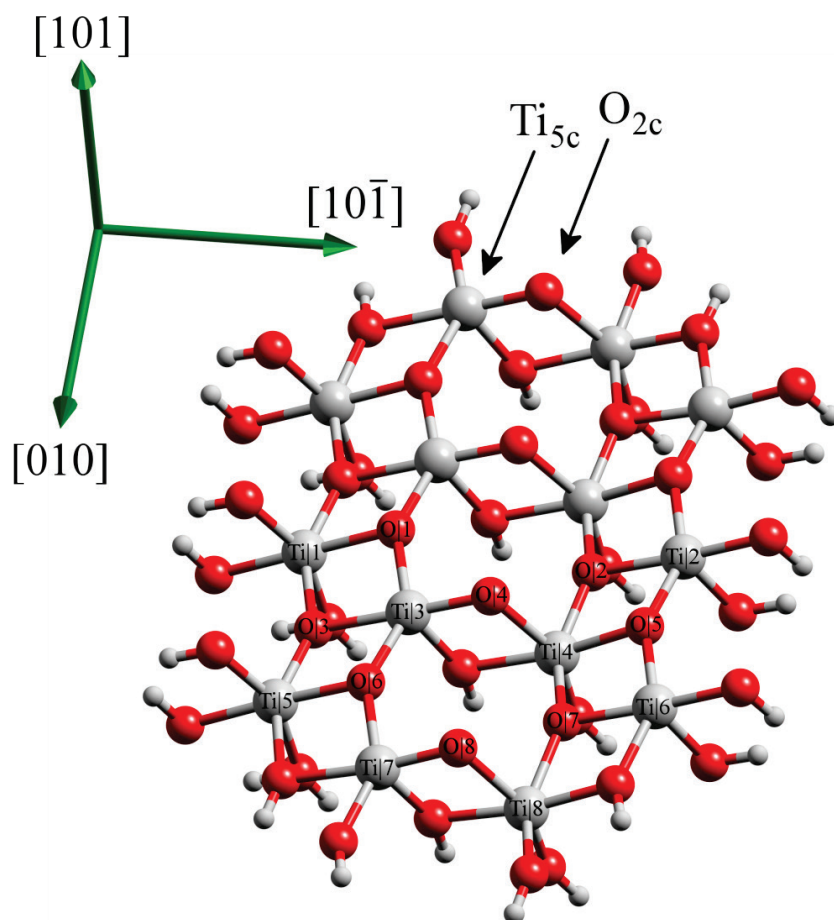


Figure 7.1: Stoichiometric anatase(101) surface with corresponding Miller index axes and key titanium and oxygen atoms numbered sequentially. This structure has  $C_s$  symmetry with a mirror plane along the  $[101]$  and  $[10\bar{1}]$  axes, therefore the atoms in the top half of the image are identical to those in the bottom half and have not been labelled.

Table 7.1: Relaxations of the anatase(101) model after optimisation. The displacement of each atom is separated into a vector along each of the Miller index axes.

Atom No.	Ti Atom Relaxations (Å)			O Atom Relaxations (Å)		
	[10 $\bar{1}$ ]	[101]	[010]	[10 $\bar{1}$ ]	[101]	[010]
1	-0.01	0.16	0.00	0.02	0.29	0.00
2	0.11	-0.06	0.00	0.10	0.01	0.00
3	0.15	0.00	0.02	0.06	-0.01	-0.01
4	0.09	-0.05	0.02	-0.04	-0.09	0.01
5	-0.01	0.15	-0.04	0.03	0.19	0.00
6	0.10	-0.08	-0.04	-0.01	0.23	0.01
7	0.12	-0.04	0.10	0.09	0.03	0.00
8	0.06	-0.07	0.11	-0.11	-0.07	0.05

Oxygen vacancies in the anatase(101) surface can have a strong influence on its reactivity, and is therefore an important facet to investigate, in addition to the stoichiometric surface. In order to model an oxygen-deficient anatase(101) surface, an O<sub>2c</sub> atom is removed from the calculation, resulting in the unrelaxed geometry being lower in energy for the triplet rather than the singlet state by 0.13 eV. However, once the geometry is optimised, the relaxed energy of the triplet is lower by 0.40 eV.

This result disagrees with a previous study,<sup>342</sup> which found that when the oxygen-deficient surface is relaxed, the singlet state is favoured, with the excess electrons delocalised over all the surface cations. Instead, the results presented here show the two unpaired electrons to be delocalised over the newly formed 4 and 5 under-coordinated titanium atoms (Ti<sub>4c</sub> and Ti<sub>5c</sub>, as a result of the removal of the bridging O<sub>2c</sub>) and other nearby atoms. This will be discussed in further detail within the molecular orbital properties section.

In the following sections, the lowest energy optimised geometries of Au<sub>1-4</sub> on the stoichiometric and oxygen-deficient anatase(101) surfaces will be presented. Only structures within 0.5 eV of the lowest energy isomer have been presented. These structures were found via the optimisation of multiple unique starting positions on the surface using isolated Au<sub>1-4</sub> clusters that had previously been optimised at the same level

of theory in the gas-phase. The positions chosen were based upon similar studies and chemical intuition. Each of the optimised geometries were then re-optimised as doublets, quartets, and sextets for Au<sub>1</sub> and Au<sub>3</sub>, or as triplets, quintets, and septets for Au<sub>2</sub> and Au<sub>4</sub>, to check for higher spin isomers that may have been within 0.5 eV of the lowest energy isomer. No higher spin isomers within 0.5 eV were found for the Au<sub>1-4</sub> clusters and they have therefore not been included in the following discussion.

### 7.1.1 Anatase(101) Model Size Considerations

The Ti<sub>14</sub>O<sub>45</sub>H<sub>34</sub> stoichiometric anatase(101) surface model used in this Chapter was created based upon a smaller Ti<sub>7</sub>O<sub>27</sub>H<sub>26</sub> anatase(101) surface model used in the work by Zapol and co-workers<sup>134</sup> The increased size of the model was considered to be necessary to adequately encompass the interactions between the surface model and the larger molecules under investigation. The Ti<sub>14</sub>O<sub>45</sub>H<sub>34</sub> model is of the same structure as that created by Zapol and co-workers, with OH terminating groups, and has been extended in the [010] and [10 $\bar{1}$ ] directions, but not in the [101] direction. Zapol and co-workers have also reported a deeper model that was extended along the [101] direction, but found very little change in their results when using this model.

As part of an endeavour to benchmark the Ti<sub>14</sub>O<sub>45</sub>H<sub>34</sub> model in its feasibility for the study of Au<sub>1-4</sub> clusters on the anatase(101) surface, an even larger anatase(101) surface model of the formula Ti<sub>28</sub>O<sub>86</sub>H<sub>60</sub> was created. The stoichiometric polymorph of this Ti<sub>28</sub>O<sub>86</sub>H<sub>60</sub> model was optimised, and the singlet was found to be the lowest in energy. Preliminary investigations of gas-phase optimised Au<sub>1-3</sub> isomers were then added to the surface in similar configurations to those found for the smaller Ti<sub>14</sub>O<sub>45</sub>H<sub>34</sub> model. The binding energies for these clusters bound to the Ti<sub>14</sub>O<sub>45</sub>H<sub>34</sub> and Ti<sub>28</sub>O<sub>86</sub>H<sub>60</sub> models are presented in Figure 7.2, showing the close match between the two models.

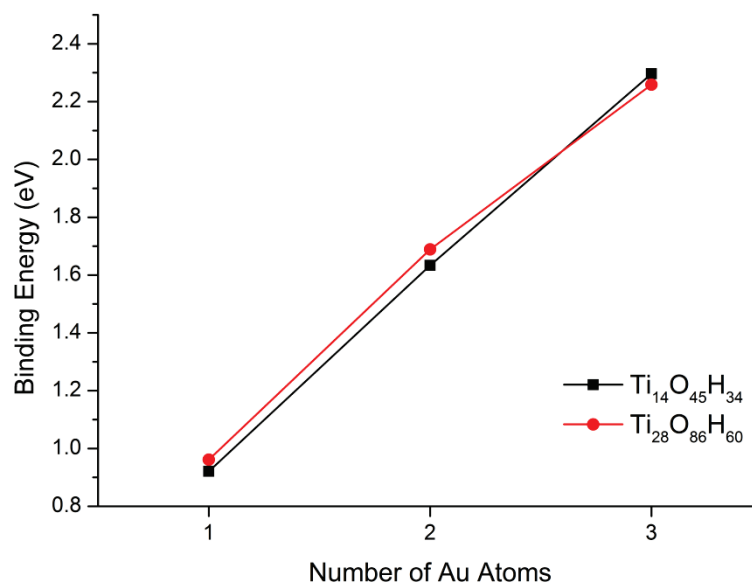


Figure 7.2: The binding energy of the Au<sub>1-3</sub> clusters on the Ti<sub>14</sub>O<sub>45</sub>H<sub>34</sub> and Ti<sub>28</sub>O<sub>86</sub>H<sub>60</sub> anatase(101) surface models, showing a close match between the two models.

The geometries of Au<sub>1-3</sub> on the Ti<sub>28</sub>O<sub>86</sub>H<sub>60</sub> model match those on the smaller Ti<sub>14</sub>O<sub>45</sub>H<sub>34</sub> model, although the ordering for the lowest energy Au<sub>3</sub> isomers have changed slightly, with the Au<sub>3</sub>-B geometry being favoured by 0.22 eV over Au<sub>3</sub>-A. Au<sub>4</sub> was not included in this preliminary study and only a small number of Au<sub>1-3</sub> isomers were investigated on this surface due to the computational expense of this large model and limited timeframes. Given that this Ti<sub>28</sub>O<sub>86</sub>H<sub>60</sub> model has significantly more atoms (174 vs 93), while providing similar results to that of the Ti<sub>14</sub>O<sub>45</sub>H<sub>34</sub> model, along with the fact that DFT scales with N<sup>3</sup> number of atoms, it was decided to run all future calculations using the Ti<sub>14</sub>O<sub>45</sub>H<sub>34</sub> model to make the most efficient use of computational time available. There were also many convergence issues faced with the Ti<sub>28</sub>O<sub>86</sub>H<sub>60</sub> model due to the large number of TiO<sub>2</sub> states with almost degenerate energy levels.

## 7.2 Structural Parameters and Binding Energies

### 7.2.1 Stoichiometric TiO<sub>2</sub> Anatase(101)

The calculated parameters for the lowest energy optimised geometries of Au<sub>1-4</sub> on the stoichiometric anatase(101) surface are summarised in Table 7.2. For clusters that have multiple isomers within 0.5 eV, the isomers are labelled alphabetically, with the A isomer being the lowest in energy. The doublet state is found to be the lowest in energy for Au<sub>1</sub> and Au<sub>3</sub>, while the singlet state is found to be the lowest in energy for Au<sub>2</sub> and Au<sub>4</sub>. The lowest energy optimised geometries of the Au<sub>1-4</sub> clusters adsorbed to the stoichiometric TiO<sub>2</sub> anatase(101) surface are displayed in Figure 7.3-7.5.

Table 7.2: Calculated structural parameters and binding energies ( $E_a$ ) of Au<sub>1-4</sub> on the stoichiometric anatase(101) surface.

Cluster	Vittadini & Selloni <sup>342</sup>	$E_a$ (eV)		Bond Lengths (Å)		
		Gong <sup>337</sup>	This work	Au-O <sub>2c</sub>	Au-O <sub>3c</sub>	Au-Ti <sub>5c</sub>
Au <sub>1</sub>	0.39	0.25	0.92	2.822	2.959	2.993
Au <sub>2</sub> -A	0.80	1.68	1.63	2.240	3.039	2.886
Au <sub>2</sub> -B			1.29	2.322	2.833	2.848
Au <sub>3</sub> -A	1.87	1.63	2.30	2.175	3.212	2.809
Au <sub>3</sub> -B			2.28	2.193	3.067	2.902
Au <sub>3</sub> -C			2.23	2.177	3.157	2.805
Au <sub>3</sub> -D			1.87	2.197	3.047	2.813
Au <sub>4</sub> -A	N/A	N/A	2.59	2.231	3.018	2.883
Au <sub>4</sub> -B			2.54	2.242	3.033	2.862
Au <sub>4</sub> -C			2.38	2.183	3.411	2.779
Au <sub>4</sub> -D			2.11	2.304	3.005	2.939

Au<sub>1</sub> adsorbs directly above the 3 coordinated oxygen atom (O<sub>3c</sub>) with a bond length of 2.959 Å, and is equidistant from the O<sub>2c</sub> atom, with bond lengths of 2.822 Å. The bond length of the Au to the Ti<sub>5c</sub> atom beneath is 2.993 Å.

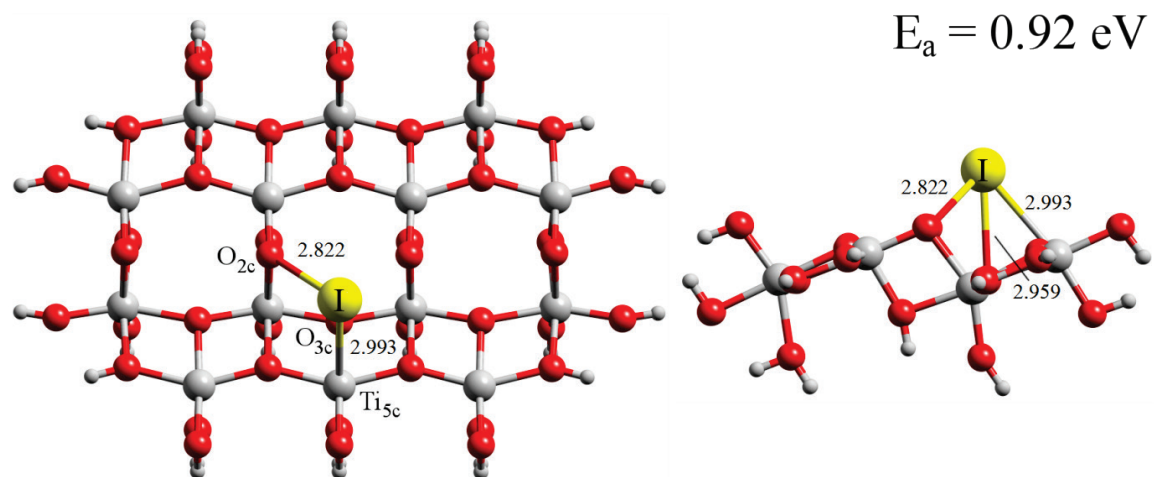


Figure 7.3: Top and side view of the optimised geometry for Au<sub>1</sub> on the stoichiometric anatase(101) surface.

For the Au<sub>2</sub> cluster, the calculations predict two geometrically unique isomers that differ by 0.34 eV, identified in Table 7.2 as Au<sub>2</sub>-A and Au<sub>2</sub>-B, respectively. Both of these isomers have a Au atom that resides close to the O<sub>2c</sub> atom (2.244 Å and 2.320 Å) while having Au-Ti<sub>5c</sub> bond lengths of 2.886 Å and 2.848 Å respectively. Au<sub>2</sub>-A has a Au-Au bond length of 2.613 Å, with a binding energy of 1.63 eV, while Au<sub>2</sub>-B has a Au-Au bond length of 2.657 Å, with a binding energy of 1.23 eV.

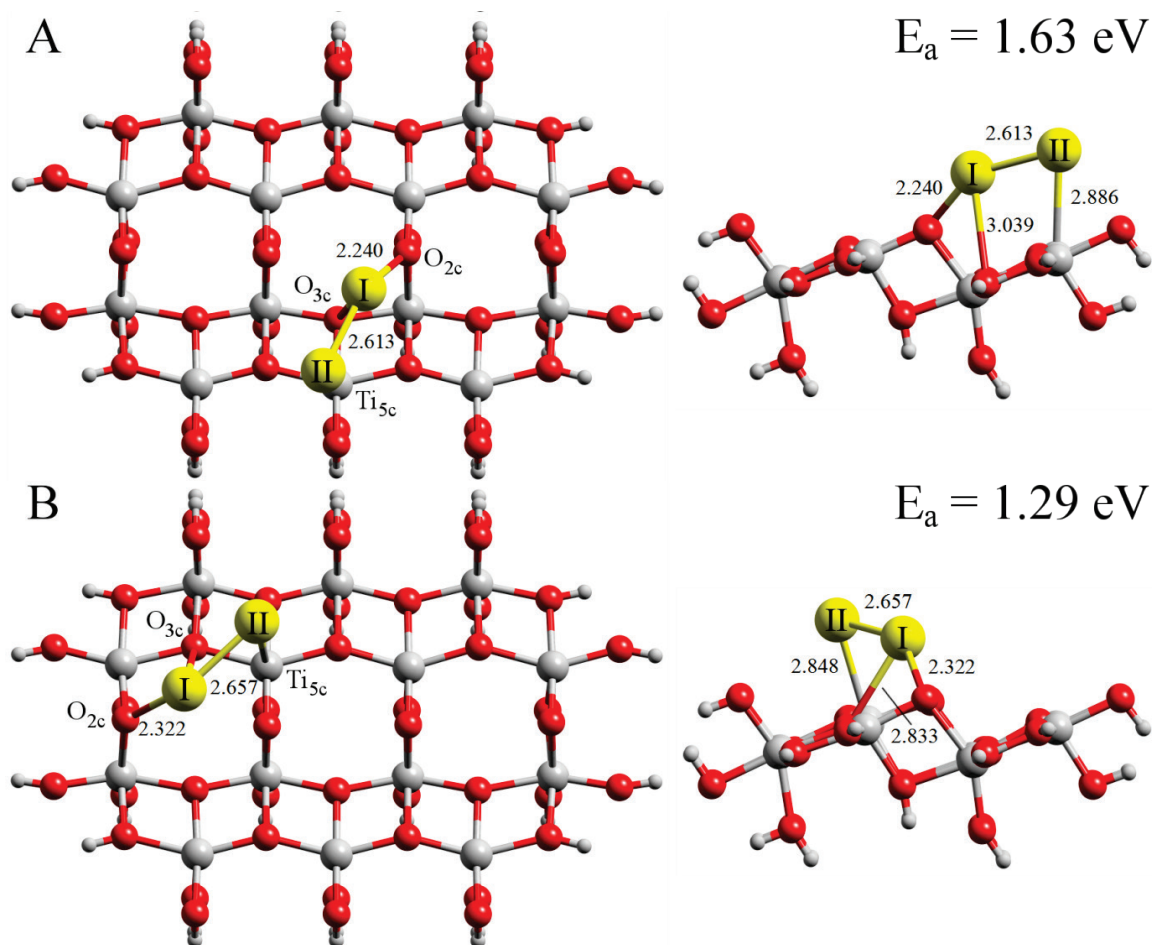


Figure 7.4: Top and side view of the optimised geometries for Au<sub>2</sub>-A and Au<sub>2</sub>-B on the stoichiometric anatase(101) surface.

The lowest energy isomer for the Au<sub>3</sub> cluster stands orthogonal to the surface, with the Au I atom bound to O<sub>2c</sub> with a bond length of 2.175 Å, and the Au II atom bound to Ti<sub>5c</sub> and O<sub>3c</sub> with bond lengths of 3.212 and 2.809 Å respectively, with a binding energy of 2.30 eV. The Au<sub>3</sub>-B isomer lies flat along the surface, with a Au-O<sub>2c</sub> bond length of 2.193 Å and Au-Ti<sub>5c</sub> bond length of 2.902 Å, and is only 0.016 eV higher in energy than the Au<sub>3</sub>-A isomer. Its Au-O<sub>3c</sub> bond length has decreased by 0.145 Å compared to Au<sub>3</sub>-A. The Au<sub>3</sub>-C isomer geometry is almost identical to that of Au<sub>3</sub>-A in terms of bond lengths and orientation, but is shifted one unit cell over into the centre of the of the model. It is also only 0.067 eV higher in energy than Au<sub>3</sub>-A. The Au<sub>3</sub>-D isomer also stands orthogonal to the surface, with Au I bound to the O<sub>2c</sub> atom with a bond length of 2.197 Å, and Au II bound to the Ti<sub>5c</sub> and O<sub>3c</sub> atoms with bond lengths of 2.813 and 3.047 Å respectively, with a binding energy of 1.87 eV.

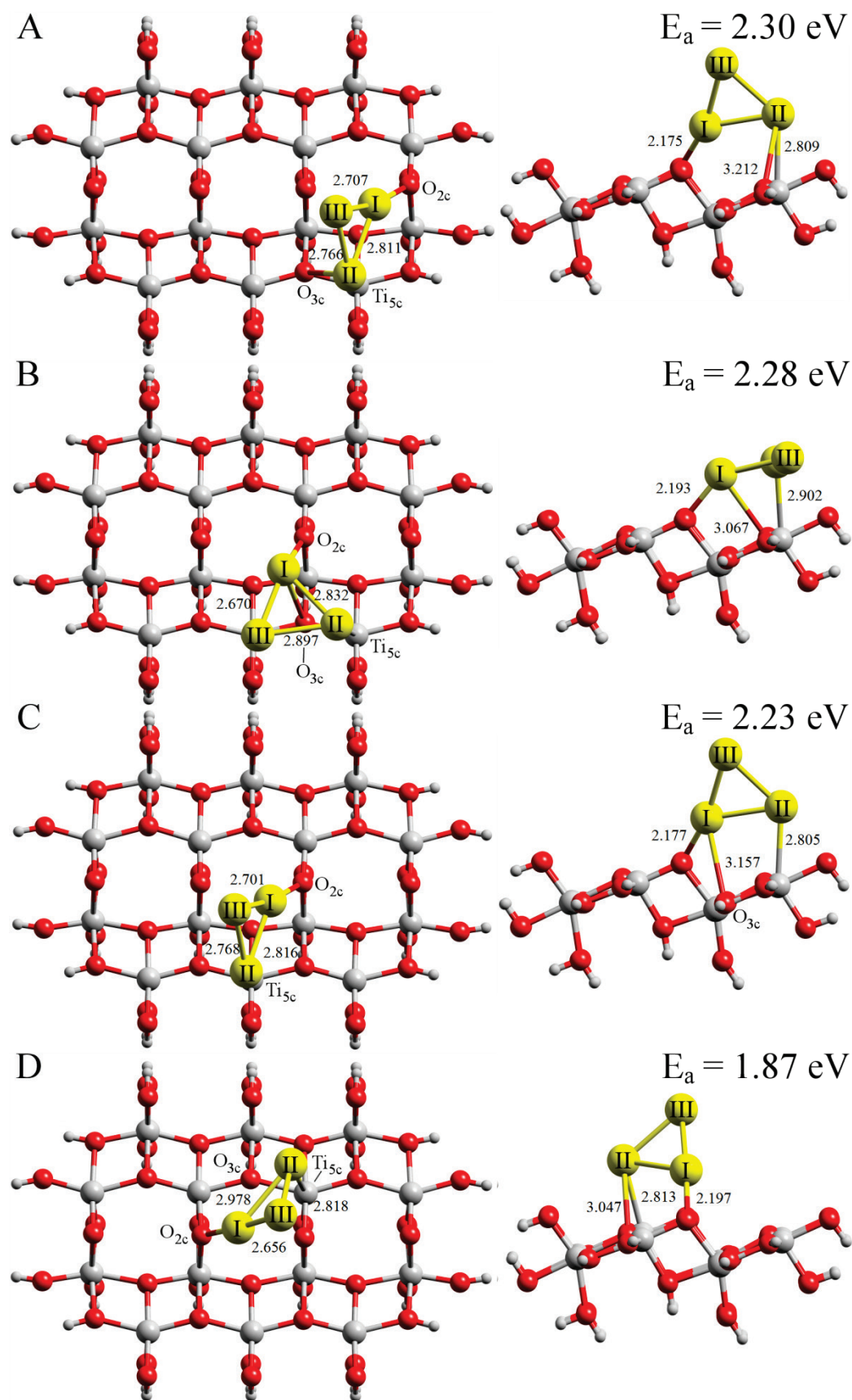


Figure 7.5: Top and side view of the optimised geometries for Au<sub>3</sub>-A, Au<sub>3</sub>-B, Au<sub>3</sub>-C, and Au<sub>3</sub>-D on the stoichiometric anatase(101) surface.

For the Au<sub>4</sub> cluster, all of the low energy isomers within 0.5 eV lie flat along the surface, with binding energies of 2.59, 2.54, 2.38, and 2.11 eV for Au<sub>4</sub>-A, B, C, and D, respectively, with various bond lengths between the Au atoms as shown in Figure 7.6. Au<sub>4</sub>-A adopts a distorted diamond configuration with bond lengths of 2.231, 3.018, and 2.883 Å to the O<sub>2c</sub>, O<sub>3c</sub> and Ti<sub>5c</sub> atoms. Au<sub>4</sub>-B adopts a similar distorted geometry to that of Au<sub>4</sub>-A, with bond lengths of 2.242, 3.033, and 2.862 Å to the O<sub>2c</sub>, O<sub>3c</sub> and Ti<sub>5c</sub> atoms respectively. Au<sub>4</sub>-C adopts a trimer configuration with the Au IV atom residing above the Ti<sub>5c</sub> atom over the next terrace with a bond length of 2.779 Å to the Ti<sub>5c</sub> atom and 2.689 Å to the Au III atom. The Au I atom has a bond length of 2.183 Å to the O<sub>2c</sub> atom, while the Au II atom has bond lengths of 3.411 and 3.602 Å to O<sub>2c</sub> and the Ti<sub>5c</sub> atom directly beneath it. Au<sub>4</sub>-D adopts an almost symmetrical diamond configuration, with a bond length of 2.304 Å between the Au II and O<sub>2c</sub> atoms, 3.005 Å between the Au III and O<sub>3c</sub> atoms, and 2.939 Å between the Au I and Ti<sub>5c</sub> atoms.

It appears that for Au<sub>4</sub>, configurations that maximise the number of bonds to O<sub>3c</sub> and Ti<sub>5c</sub> along the [010] direction, such as isomers A and B, are preferred. Conversely, the Au<sub>4</sub>-C isomer which ‘bridges’ across the O<sub>2c</sub> atoms to the next terrace results in a decrease in binding energy by 0.211 eV, while the undistorted diamond shape of the Au<sub>4</sub>-D isomers results in a decreased binding energy compared to Au<sub>4</sub>-A of 0.48 eV. Other than Au<sub>4</sub>-C, which has a unique structure compared with the other isomers, it is found that the binding energy increases with decreasing Au-O<sub>2c</sub> bond length.

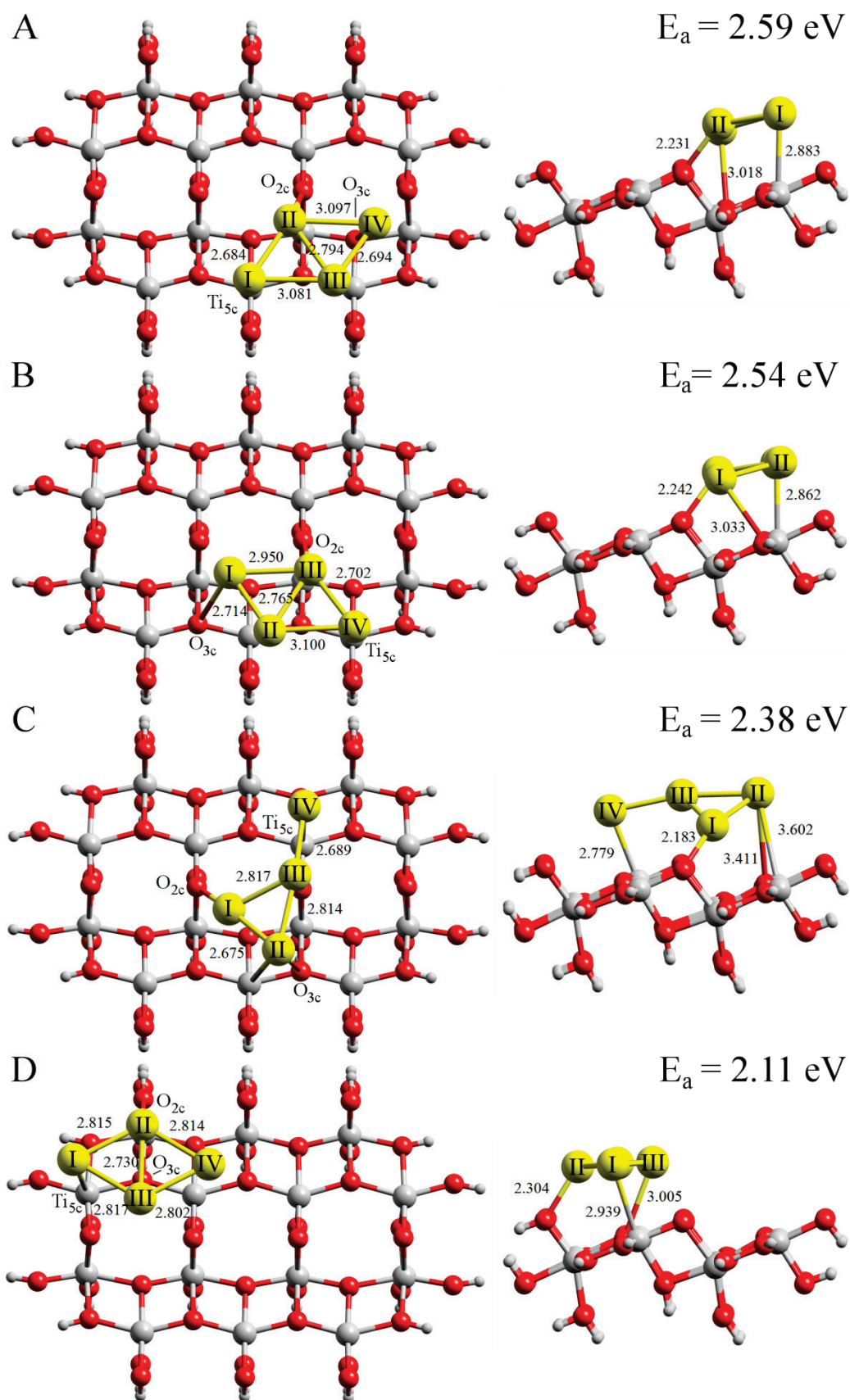


Figure 7.6: Top and side view of the optimised geometries for Au<sub>4</sub>-A, Au<sub>4</sub>-B, Au<sub>4</sub>-C, and Au<sub>4</sub>-D on the stoichiometric anatase(101) surface.

### 7.2.1.1 Discussion

For the Au<sub>1</sub> system, the binding energy of the single Au atom to the surface is only 0.92 eV, the smallest of all clusters presented in this study, while the bond length of the Au<sub>1</sub> cluster to the Ti<sub>5c</sub> atom beneath is 2.993 Å, which is longer than other clusters in this study. The general binding configuration of the Au<sub>1</sub> cluster on the surface is consistent with previous studies by both Vittadini and Selloni, and Gong,<sup>337,342</sup> however, the bond lengths presented here are longer than those predicted by either study. This is because the structure predicted here is equidistant from both O<sub>2c</sub> atoms, while the studies by Gong and Vittadini predict a bond length of 2.358 and 2.41 Å respectively, which also results in a shorter Ti<sub>5c</sub> bond length of 2.747 and 2.70 Å. The calculated binding energy of the Au<sub>1</sub> cluster of this study is also much higher than that calculated by both Gong (0.25 eV) and Vittadini (0.39 eV). However, both studies predict Au<sub>1</sub> to have the smallest binding energy of all the Au clusters calculated on the anatase(101) surface within their own studies, which is also the case for Au<sub>1</sub> within this study. Au<sub>1</sub> was also shown to have the smallest binding energy for a selection in a similar study of Au<sub>1-7</sub> clusters on the rutile(110) surface.<sup>341</sup>

For the Au<sub>2</sub> system, the position of the Au I atom near the O<sub>2c</sub> for Au<sub>2</sub>-A resides in a comparable position to that of the Au<sub>1</sub> species, bound almost directly above the O<sub>3c</sub> atom, albeit with a larger bond length of 3.039 Å. However, the second Au atom of the cluster is positioned over the Ti<sub>5c</sub> atom, and not over the adjacent O<sub>3c</sub> atom, consistent with the structure determined by Gong *et al.*<sup>337</sup> for Au<sub>2</sub> on anatase(101). In comparison, Vittadini and Selloni<sup>127</sup> predict the lowest energy structure of Au<sub>2</sub> to have the cluster standing orthogonal from the surface, with the lower Au atom at a distance of only 2.11 Å from the surface O<sub>2c</sub>. The structure they predict with Au<sub>2</sub> lying flat across the surface, similar to the geometry presented here, has a smaller binding energy of 0.25 eV, with the two Au atoms bound to the Ti<sub>5c</sub> atoms. For the Au<sub>2</sub>-B isomer, the position of both atoms has changed significantly and neither atom resembles the binding configuration of the Au<sub>1</sub> species. The Au-O<sub>3c</sub> and Au-Ti<sub>5c</sub> bond lengths are actually the shortest (2.833 Å and 2.848 Å respectively) compared to Au<sub>2</sub>-A when in this configuration. This type of geometric configuration has not been reported in the literature, yet the 1.29 eV binding energy of this isomer is greater than any configuration predicted by Gong or Vittadini.

Compared to Au<sub>1</sub>, both of the Au<sub>2</sub> isomers have a Au atom that resides much closer to the O<sub>2c</sub> atom, with shorter Au-Ti<sub>5c</sub> bond lengths, despite the two structures having different positions on the anatase surface. This results in a significantly greater binding energy for Au<sub>2</sub>-A and Au<sub>2</sub>-B (1.63 and 1.23 eV) compared with the Au<sub>1</sub> cluster (0.92 eV).

For the Au<sub>3</sub> system, there is the possibility that the Au<sub>3</sub>-A and C isomers could be equal when considering that the true surface would extend near infinitely in all directions. The slightly higher binding energy of the Au<sub>3</sub>-A isomer may be due to the finite nature of the model, since the Au<sub>3</sub>-C isomer resides close to the edge of the anatase(101) surface model and this may have a small unintended influence upon its binding energy. As discussed earlier, the use of a larger anatase(101) surface model found that edge effects were of no concern in the tested scenarios, and that the use of an extended model resulted in excessively long computational times, plagued by convergence issues.

The lowest energy Au<sub>3</sub> isomer in this study, Au<sub>3</sub>-A, has a binding energy of 2.30 eV, which is larger than the binding energies reported by both Vittadini and Selloni, and Gong *et al.*, of 1.87 and 1.63 eV respectively. This could be attributed to the different geometry that is predicted for the lowest energy isomer; Vittadini and Selloni, and Gong *et al.* both predict a Au<sub>3</sub> cluster geometry that is similar to the Au<sub>3</sub>-D isomer (1.87 eV binding energy), except that the plane of their Au<sub>3</sub> cluster is aligned along the [010] direction, with the lower gold atoms both bound to O<sub>2c</sub> atoms. Given that the calculations in this study predict a similar geometry in terms of bond lengths and positions, with comparable energy (Au<sub>3</sub>-D), it is likely the approach used in this thesis was able to find the additional geometric minima of Au<sub>3</sub>-A, B, and C.

In comparison to the Au<sub>2</sub> system, the Au<sub>3</sub>-A and C isomers are geometrically similar to the Au<sub>2</sub>-A isomer, but with an additional Au atom residing above the two Au atoms bound along the [10 $\bar{1}$ ] axis. This is also observed for Au<sub>3</sub>-D, which is equivalent to Au<sub>2</sub>-B, with an additional Au atom above the structure. It can be seen that generally, the greatest binding energy for these clusters correspond to those isomers with the shortest bond lengths between the Au I atoms and the O<sub>2c</sub> atoms, which are the lowest coordinated atoms on the surface available for binding. All of the Au-Au bond lengths calculated for Au<sub>3</sub> on the stoichiometric surface are larger than those of Au<sub>2</sub>, implying less electron density between the cluster and a greater amount being transferred to the surface. This will be discussed in further detail in the charge transfer section.

Comparison between Au<sub>4</sub> isomers and the smaller Au clusters shows that Au<sub>4</sub>-C adopts a geometric configuration similar to that of Au<sub>3</sub>-B lying flat on the surface, but with an additional Au atom bridging from the Ti<sub>5c</sub> over the next terrace site along the [10 $\bar{1}$ ] axis. The calculations also show the geometric configuration of Au<sub>4</sub>-A and B to be similar to that of Au<sub>3</sub>-B, with an additional Au atom added along the [010] axis. For the Au<sub>4</sub> cluster series, the binding energy of the lowest energy isomer (2.59 eV) is the greatest of all the calculated clusters on the stoichiometric anatase(101) surface investigated in this study. There are no studies available of Au<sub>4</sub> on either a stoichiometric or oxygen-deficient surfaces available in the literature for further comparison.

Comparison between the structures of Au<sub>1-4</sub> on the stoichiometric anatase(101) surface to Au<sub>1-4</sub> in the gas-phase calculated at the same level of theory shows a number of changes. The structures of the gas-phase clusters optimised at the same level of theory are available in Appendix B. For the Au<sub>2</sub> system, the bond lengths for both Au<sub>2</sub> isomers on the stoichiometric surface are slightly elongated compared to that calculated for gas-phase Au<sub>2</sub> (2.592 Å). Gas-phase Au<sub>3</sub> is a C<sub>2v</sub> trimer that has two equal Au-Au bonds of 2.690 Å, with the third bond length being 3.085 Å, similar to the geometries found for Au<sub>3</sub>-A, B, and C, which match that of an approximate isosceles triangle. For the Au<sub>3</sub>-D isomer, the geometry is that of a scalene triangle, with each bond length significantly different to the other (2.978, 2.818, and 2.656 Å). Calculations of the Au<sub>4</sub> cluster in the gas-phase results in a diamond shaped cluster with D<sub>2h</sub> symmetry, similar to the structure of Au<sub>4</sub>-D on the stoichiometric anatase(101) surface. However, Au<sub>4</sub> in the gas phase contains shorter bond lengths of 2.790 Å for the outer bonds, and 2.691 Å for the inner Au-Au bond, compared with those of Au<sub>4</sub>-D (2.812 Å on average, and 2.730 Å respectively). The only cluster that contains a shorter bond length is that of Au<sub>4</sub>-C, with its significant change in geometry from that of the gas-phase, which has a bond length between Au I and Au II of 2.675 Å.

As the number of Au atoms on the stoichiometric surface is increased, there is a general trend of increasing binding energy. This is shown in Figure 7.7, along with a comparison to other studies of Au<sub>1-3</sub> on the stoichiometric anatase(101) surface. There is also an increase in the average Au-Au bond length within the cluster as the number of Au atoms is increased, from 2.635 Å for Au<sub>2</sub>, to 2.785 Å for Au<sub>3</sub>, and 2.815 Å for Au<sub>4</sub>. From the calculations presented in this study, it is shown that there is a steady rise in binding energy as up until Au<sub>3</sub>, followed by a smaller increase as a fourth Au atom is added to the system. This same trend for Au<sub>1</sub> to Au<sub>3</sub> is predicted by the two studies by Vittadini and

Selloni,<sup>342</sup> and Gong *et al.*,<sup>337</sup> although the magnitude of the binding energy is approximately 0.63 eV lower in these studies. This discrepancy can be attributed to the PBC approach using the PBE functional that is employed by these studies, which is significantly different from the approach taken in this thesis.

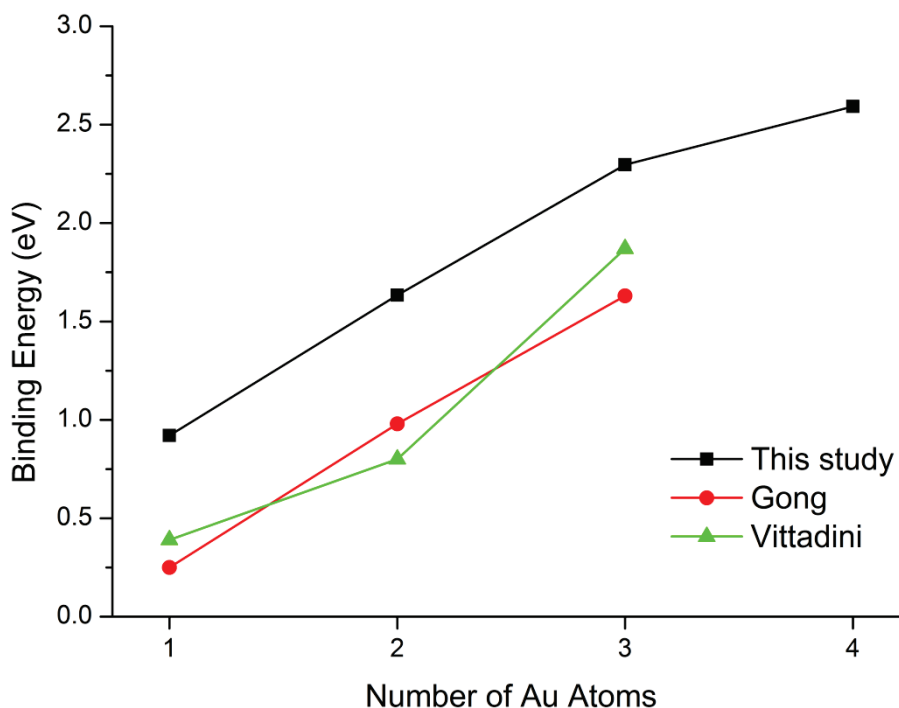


Figure 7.7: Binding energy comparisons between this work and that of Vittadini and Selloni,<sup>342</sup> and Gong *et al.*<sup>337</sup>

Zapol and co-workers<sup>134</sup> have suggested that the GGA PBE functional has a tendency to underestimate the binding energies of small molecules on anatase(101) surfaces. This was discovered when comparing their cluster models using atomic centred basis sets with the B3LYP functional to their periodic slab models using PBE, and to other studies<sup>525,526</sup> that made use of cluster models with symmetry-adapted cluster-configuration interaction. They discovered that their PBE based approach greatly underestimated the binding energies of CO<sub>2</sub>. It may be due to these reasons that the calculated binding energies presented in this thesis for Au clusters on the stoichiometric anatase(101) surface are higher than those of in the literature, which make use of periodic boundary conditions with the PBE functional.

### 7.2.2 Oxygen-Deficient TiO<sub>2</sub> Anatase(101)

The calculated parameters for the lowest energy optimised geometries of Au<sub>1-4</sub> on the oxygen-deficient TiO<sub>2</sub> anatase(101) surface are summarised in Table 7.3. For clusters that have multiple isomers within 0.5 eV, the isomers are labelled alphabetically, with the A isomer being the lowest in energy. Although the lowest energy structure of the oxygen-deficient anatase(101) surface is a triplet as discussed previously, after adsorption of Au<sub>1</sub> and Au<sub>3</sub>, the doublet state is favoured, while for Au<sub>2</sub>-And Au<sub>4</sub>, the singlet state is favoured. The lowest energy optimised geometries of the Au<sub>1-4</sub> clusters adsorbed to the oxygen-deficient TiO<sub>2</sub> anatase(101) surface are displayed in Figure 7.8-7.10.

Table 7.3: Calculated structural parameters and binding energies of Au<sub>1-4</sub> on the oxygen-deficient anatase(101) surface. *S* denotes the number of unpaired electrons.

Cluster	Vittadini & Selloni <sup>342</sup>	E <sub>a</sub> (eV)		Bond Lengths (Å)		
		Gong <sup>337</sup>	This work	Au-O <sub>2c</sub>	Au-Ti <sub>4c</sub>	Au-Ti <sub>5c</sub>
<b>Au<sub>1</sub></b>	3.15	3.16	2.78	3.951	2.630	2.884
<b>Au<sub>2</sub> (S=0)</b>	2.60	2.41	2.68	3.902	2.684	2.793
<b>Au<sub>2</sub> (S=1)</b>	N/A	N/A	2.25	3.980	2.791	2.945
<b>Au<sub>3</sub>-A</b>	3.58	2.77	3.69	2.250	2.652	2.898
<b>Au<sub>3</sub>-B</b>			3.29	3.702	2.619	2.873
<b>Au<sub>4</sub>-A</b>	N/A	N/A	3.71	2.449	2.641	2.858
<b>Au<sub>4</sub>-B</b>			3.53	2.604	2.775	2.836
<b>Au<sub>4</sub>-C</b>			3.51	2.486	2.721	3.050
<b>Au<sub>4</sub> (S=1)</b>			3.24	2.321	2.809	2.992

The Au<sub>1</sub> cluster adsorbs in the position of the oxygen vacancy, albeit higher than the row of adjacent oxygen atoms. It has a bond length of 2.884 Å to the 5 coordinated Ti atom (Ti<sub>5c</sub>), and 2.630 Å to the 4 coordinated Ti atom (Ti<sub>4c</sub>). These are the two exposed Ti atoms that become under-coordinated after removal of the bridging oxygen. Given the under-coordinated nature of these Ti atoms, it is reasonable that the binding energy of Au<sub>1</sub> in the oxygen vacancy (2.78 eV) is much greater compared with that of Au<sub>1</sub> on the stoichiometric anatase surface (0.92 eV).

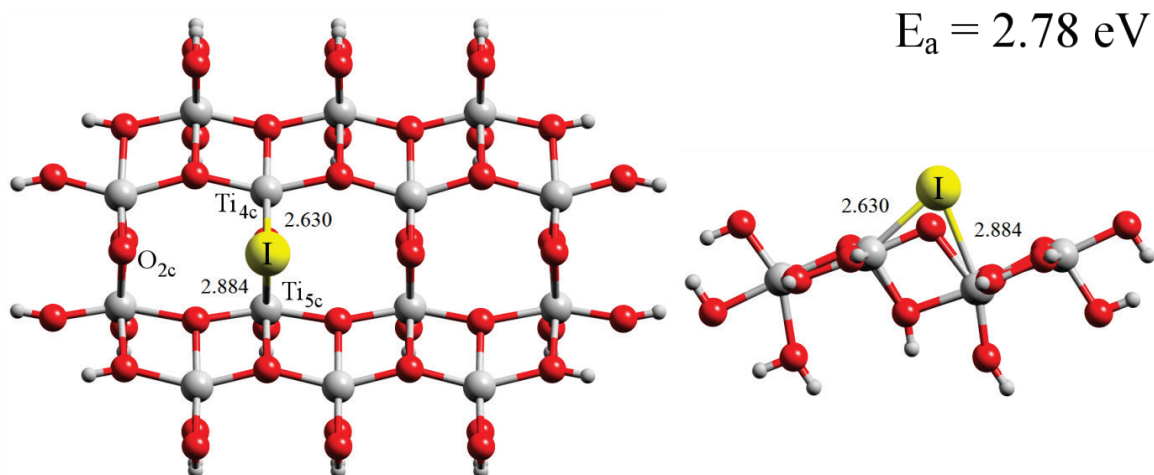


Figure 7.8: Top and side view of the optimised singlet geometry for Au<sub>1</sub> on the oxygen-deficient anatase(101) surface.

For the Au<sub>2</sub> cluster, the Au I atom has bond lengths of 2.793 and 2.684 Å to Ti<sub>5c</sub> and Ti<sub>4c</sub> respectively, with an Au-Au bond length of 2.818 Å, as shown in Figure 7.9. The Au II atom resides above the Ti<sub>5c</sub> atom in a position similar to that of other clusters on the stoichiometric anatase(101) surface. The position of the Au I atom closest to the under-coordinated Ti atoms is similar to that of the Au<sub>1</sub> cluster on oxygen-deficient anatase. Compared with Au<sub>2</sub> on the stoichiometric anatase(101) surface, the Au-Au bond length is significantly longer (2.818 Å vs 2.613 for Au<sub>2</sub>-A and 2.657 Å for Au<sub>2</sub>-B) and it is also greater than that calculated for gas-phase Au<sub>2</sub> (2.592 Å).

For the Au<sub>2</sub> cluster on the oxygen-deficient surface, there is a triplet state that is 0.43 eV higher in energy. The geometry of this structure is different from the singlet species, with the first Au atom shifting 0.103 Å away from the surface along the [101] direction, while both atoms move across the surface along the [010] direction by 0.052 Å for the first, and -0.039 Å for the second atom. The Au-Au bond length of the Au<sub>2</sub> cluster in the triplet state also shortens to 2.727 Å. For further details of this triplet state, see Appendix B.

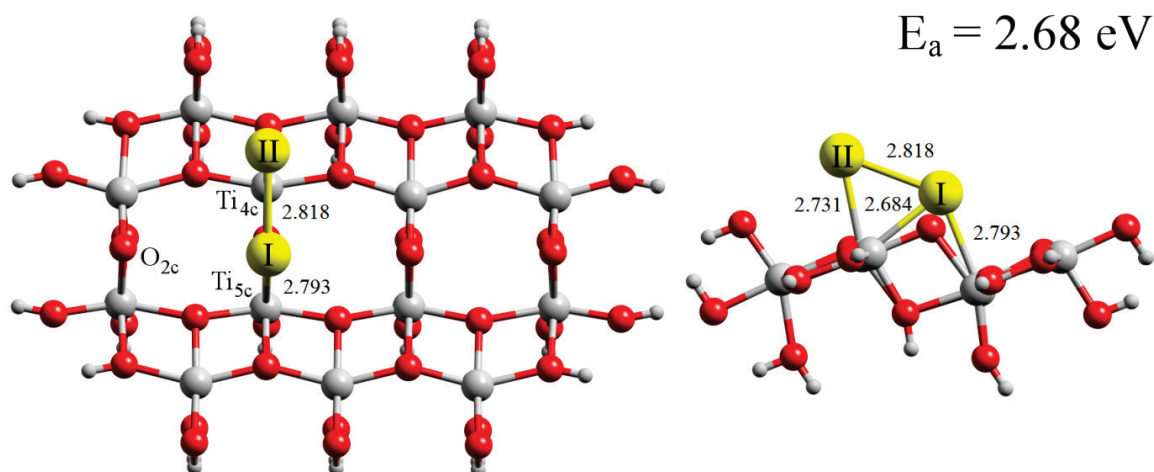


Figure 7.9: Top and side view of the optimised singlet geometry for Au<sub>2</sub> on the oxygen-deficient anatase(101) surface.

For the Au<sub>3</sub> clusters on the oxygen-deficient surface, the calculations predict two geometrically unique isomers. The Au<sub>3</sub>-A isomer lies flat across the surface, with the Au I atom bound to Ti<sub>4c</sub> and Ti<sub>5c</sub> with bond lengths of 2.652 and 2.898 Å respectively. Au II is bound to the nearby O<sub>2c</sub> atom with a bond length of 2.250 Å and Au III has a bond length of 2.884 Å to the Ti<sub>5c</sub> atom beneath it. The Au<sub>3</sub>-B isomer stands orthogonal to the surface, with the Au I atom bound to Ti<sub>4c</sub> and Ti<sub>5c</sub> with bond lengths of 2.619 and 2.876 Å respectively. The Au II atom has a bond length of 2.842 Å to the Ti<sub>5c</sub> beneath it, while the Au III atom resides furthest from the surface, with bond lengths of 2.821 and 2.700 Å to Au I and Au II respectively.

The Au<sub>3</sub> clusters adsorb to the oxygen-deficient surface with a similar configuration to that on the stoichiometric surface, with the Au I atom residing in the oxygen vacancy. Au<sub>3</sub>-A on the oxygen-deficient surface adsorbs flat on the surface with a similar geometry to that of Au<sub>3</sub>-B on stoichiometric anatase, although it has a significantly increased bond length between Au I and Au III of 3.738 Å, which is an increase of 1.068 Å. Au<sub>3</sub>-B on oxygen-deficient anatase adopts a configuration similar to that of Au<sub>3</sub>-A on stoichiometric anatase, with an increased bond length between Au I and Au II of 3.131 Å, an increase of 0.320 Å. These clusters maintain approximately the same bond lengths between the Au I atoms and the Ti<sub>4c</sub> and Ti<sub>5c</sub> atoms as for Au<sub>1</sub> and Au<sub>2</sub> on the oxygen-deficient surface.

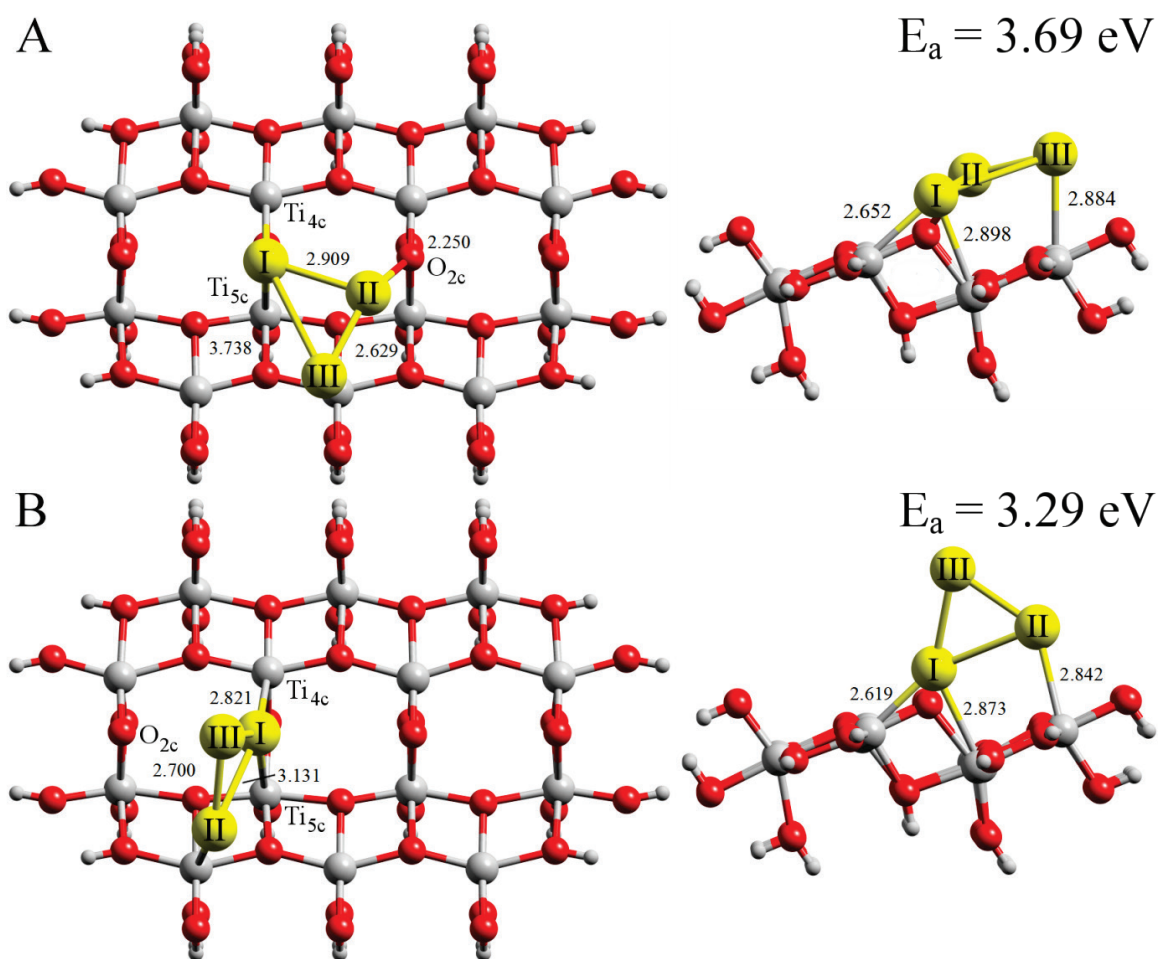


Figure 7.10: Top and side view of the optimised singlet geometries for Au<sub>3</sub>-A and Au<sub>3</sub>-B on the oxygen-deficient anatase(101) surface.

For the Au<sub>4</sub> system on the oxygen-deficient surface, the lowest energy isomer displays a heavily distorted diamond geometry with a large binding energy of 3.71 eV. It has Au-Ti<sub>4c</sub> and Au-Ti<sub>5c</sub> bond lengths of 2.641 and 2.858 Å respectively for the Au II atom, along with a Au-Ti<sub>5c</sub> bond length of 2.775 for Au I. The Au IV atom is close to the nearby O<sub>2c</sub> atom with a bond length of 2.449 Å. It also has three large internal Au-Au bond lengths of 3.322, 3.051 and 3.008 Å. Au<sub>4</sub>-B adopts a trimer configuration with the Au IV atom above the nearby Ti<sub>5c</sub> atom with a bond length of 2.753 Å, and a binding energy of 3.53 eV. The Au III atom bound in the position of the oxygen vacancy results in Au-Ti<sub>4c</sub> and Au-Ti<sub>5c</sub> bond lengths of 2.836 and 2.775 Å respectively, with the Au I atom 2.604 Å away from the edge O<sub>2c</sub> atom.

Au<sub>4</sub>-C also adopts a similar trimer configuration, with Au IV above a nearby Ti<sub>5c</sub> atom with a bond length of 2.761 Å, and a binding energy of 3.51 eV. The Au I atom is bound

in a position between the O<sub>2c</sub> and Ti<sub>5c</sub> with bond lengths of 2.486 and 3.050 Å respectively, while Au II resides above the Ti<sub>4c</sub> atom with a bond length of 2.721 Å. The Au<sub>4</sub>-A isomer has three rather large (3.322, 3.051, and 3.008 Å) internal Au-Au bond lengths relative to gas phase Au<sub>4</sub> (2.790 Å for the outer bonds and 2.691 Å for the inner Au-Au bonds) with a distorted diamond shape. Compared with the gas-phase Au<sub>4</sub> cluster, the Au<sub>4</sub>-B and C isomers involve significant rearrangement of atomic positions, and are 0.19 and 0.20 eV higher in energy than Au<sub>4</sub>-A. The internal Au-Au bond lengths for Au<sub>4</sub>-B and C isomers are shorter than those for Au<sub>4</sub>-A presented above, while the closest Au-Ti<sub>4c</sub> and Au-Ti<sub>5c</sub> are longer, indicating less interaction with the surface, as reflected in the decreased binding energy. There is also a triplet state of Au<sub>4</sub> bound to the oxygen-deficient surface which is 0.47 eV higher in energy, with very similar geometry to that of Au<sub>4</sub>-A on the oxygen-deficient surface. Details about this isomer are available in Appendix B.

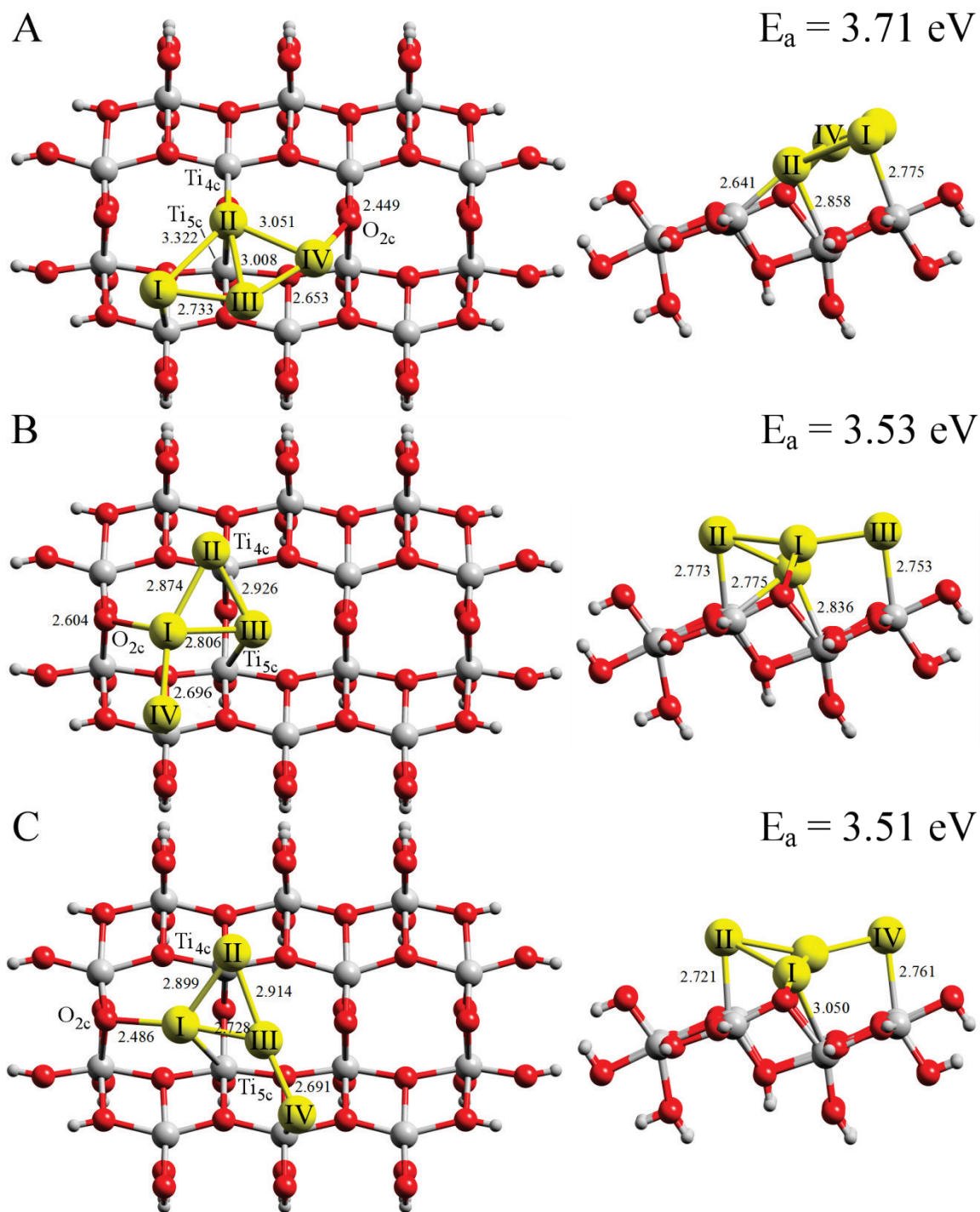


Figure 7.11: Top and side view of the optimised singlet geometries for Au<sub>4</sub>-A, Au<sub>4</sub>-B, and Au<sub>4</sub>-C on the oxygen-deficient anatase(101) surface.

### 7.2.2.1 Discussion

Comparison of the binding energies for Au<sub>1-4</sub> bound to the oxygen-deficient surface is presented in Figure 7.12. There is no clear trend of increasing binding energy as the number of Au atoms is increased. Compared with Au<sub>1-4</sub> on the stoichiometric surface, all of the binding energies calculated for the Au clusters on the oxygen-deficient surface are much greater. For the Au<sub>3</sub> system, for example, the binding energies have increased substantially, with Au<sub>3</sub>-A and B, which have binding energies of 3.69 and 3.29 eV resulting in a binding energy increase of 1.41 and 0.99 eV compared with their respective geometries on the stoichiometric surface. Au<sub>4</sub>-A has also has the greatest binding energy of all clusters in this study at 3.71 eV, an increase of 1.12 eV compared with the stoichiometric surface.

There is also no clear trend for the average Au-Au bond lengths with additional Au atoms, with the averages ranging from 2.828 Å for Au<sub>2</sub>, to 2.988 Å for Au<sub>3</sub>, to 2.863 Å for Au<sub>4</sub>. For the oxygen-deficient surface, the binding energy decreases by 0.10 eV upon addition of a 2<sup>nd</sup> Au atom to the surface, followed by a large increase of 1.01 eV upon addition of a 3<sup>rd</sup> Au atom, followed by a marginal increase of 0.02 eV for the addition of the 4<sup>th</sup> Au atom. This could be explained by the closed shell nature of Au<sub>2</sub> and Au<sub>4</sub> in the gas-phase, which are not stabilised to as great of an extent as Au<sub>1</sub> and Au<sub>3</sub> upon binding to the oxygen-deficient surface, since Au<sub>1</sub> and Au<sub>3</sub> both have an unpaired electron in the gas-phase. This unpaired electron of the Au cluster can possibly pair with one of the two unpaired electrons from the triplet state oxygen-deficient surface, stabilising the adsorbate, leaving an unpaired electron delocalised over the anatase(101) surface.

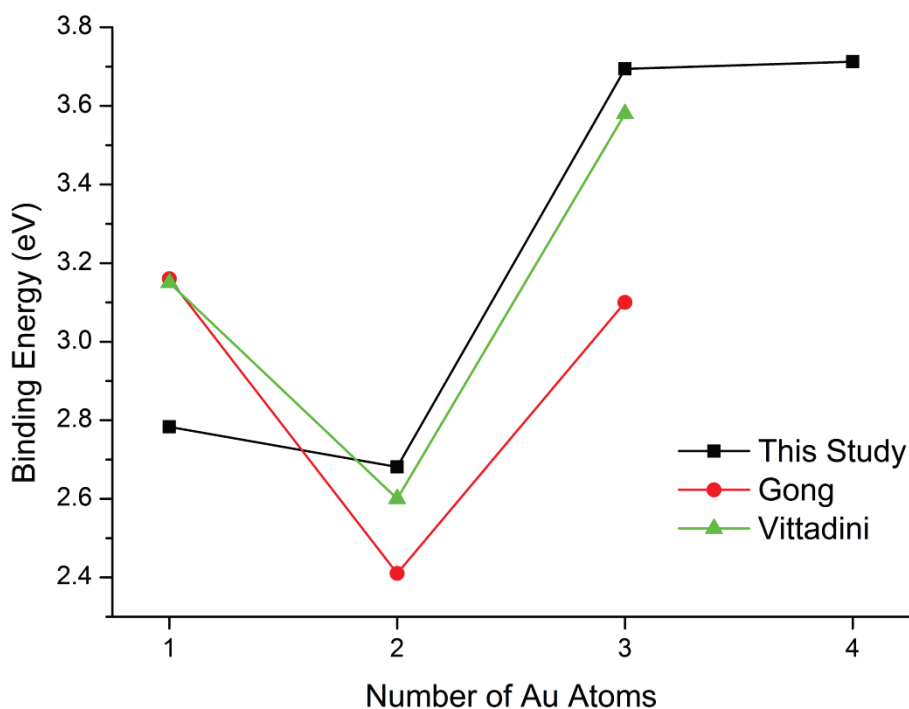


Figure 7.12: Binding energy comparisons between this work and that of Vittadini and Selloni,<sup>342</sup> and Gong *et al.*<sup>337</sup>

The position of the Au<sub>1</sub> and Au<sub>2</sub> clusters on the oxygen-deficient surface agree with the previous theoretical studies by Vittadini and Selloni,<sup>342</sup> and Gong *et al.*, although the binding energy of the Au<sub>1</sub> cluster in these calculations (2.78 eV) is lower than their results of 3.16 and 3.15 eV respectively. For the Au<sub>3</sub> system, there are significant differences in geometry compared with those in the literature, although the calculations in this thesis predict binding energies that closely match their numbers. Vittadini and Selloni report two structures for Au<sub>3</sub> adsorbed on the oxygen-deficient surface, with a binding energy of 2.97 and 3.54 eV that are geometrically similar to Au<sub>3</sub>-B in terms of them standing orthogonal to the surface, with one aligned along the  $[10\bar{1}]$  axis and the other aligned along the  $[101]$  axis. They do not report a structure for Au<sub>3</sub> lying flat along the oxygen-deficient surface, however, instead reporting a bent linear Au<sub>3</sub> cluster bound along the  $[10\bar{1}]$  direction, with the 3<sup>rd</sup> Au atom skewed along the  $[010]$  direction. This bent linear structure is also reported by Gong *et al.*<sup>337</sup> in their study, however, this structure was not found to be stable in the present study, and hence has not been reported. There are no studies of Au<sub>4</sub> on the oxygen-deficient surface available for comparison in the literature.

## Chapter 7. DFT Studies of Au<sub>1-4</sub> on the TiO<sub>2</sub> Anatase(101) Surface

The calculated binding energies presented here are consistent with the idea that Au clusters prefer to bind over oxygen vacancies in preference to the stoichiometric surface, which has more coordinated surface atoms that are difficult for Au atoms to access due to their stability. This idea is supported by scanning tunnelling microscopy work and previous DFT studies on both the anatase(101)<sup>337,344</sup> and rutile(110) surfaces.<sup>330,332,333,335</sup>

### 7.3 Predicted Vibrational Spectra

Vibrations that have greater than 20% non-mass-weighted Au motion are deemed significant and are included in all data presented herein. The full predicted infrared and Raman spectra of gas-phase Au<sub>1-4</sub> clusters and the bare stoichiometric anatase(101) surface are available in Appendix B. To the best of this authors knowledge, these are the first predicted IR and Raman spectra of small Au clusters on the anatase(101) surface to be reported.

#### 7.3.1 Au<sub>1</sub> on the Stoichiometric and Oxygen-Deficient Anatase(101) Surfaces

Figure 7.13 displays the convoluted IR and Raman spectra between 0 and 175 cm<sup>-1</sup> for the Au<sub>1</sub> cluster adsorbed to the stoichiometric (blue line) and oxygen-deficient (red line) anatase(101) surface. The vibrational modes that contribute to the convoluted peaks are summarised in Table 7.4.

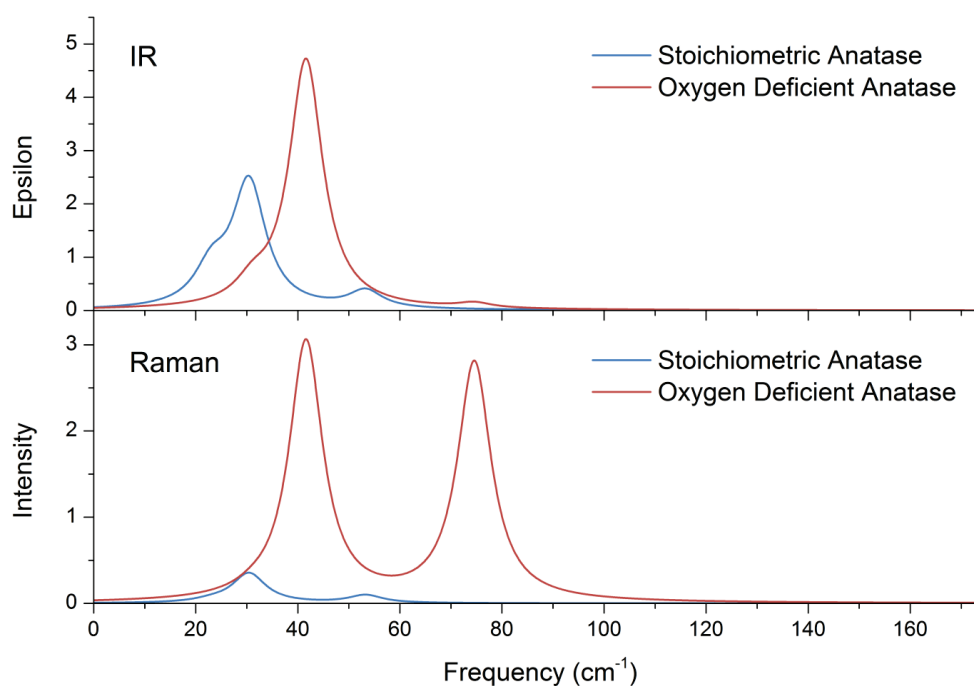
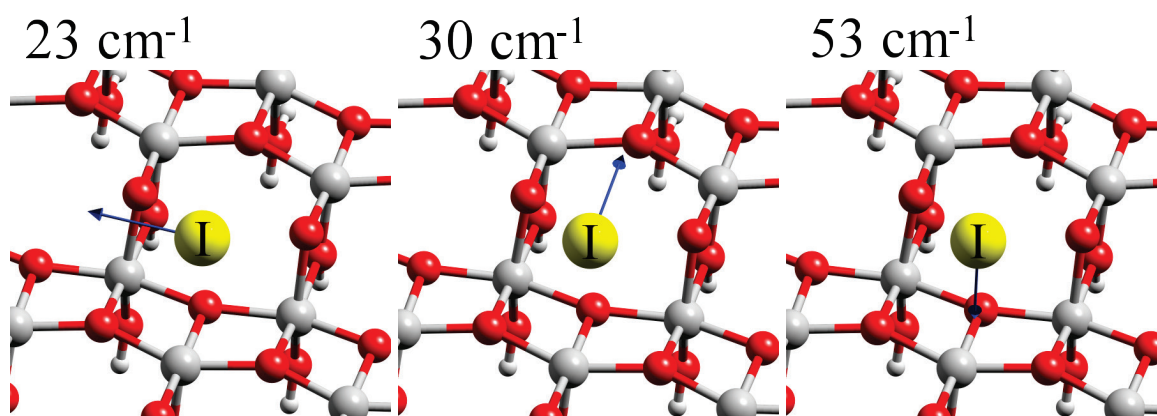


Figure 7.13: Predicted IR and Raman spectra of Au<sub>1</sub> on stoichiometric anatase(101) and oxygen-deficient anatase(101) surfaces.

Table 7.4: Calculated vibrational modes of Au<sub>1</sub> on stoichiometric and oxygen-deficient anatase(101).

	Frequency (cm <sup>-1</sup> )	IR Intensity (km mol <sup>-1</sup> )	Raman Intensity (A <sup>4</sup> amu <sup>-1</sup> )	%Au Motion of Mode	Direction of Motion
<b>Au<sub>1</sub> on stoichiometric anatase(101)</b>	23.07	0.194	0.327	90.1%	[010]
	30.42	0.684	4.378	91.3%	[10 $\bar{1}$ ]
	53.27	0.095	1.153	86.0%	[101]
<b>Au<sub>1</sub> on oxygen- deficient anatase(101)</b>	31.12	0.100	0.562	85.2%	[010]
	41.59	1.355	38.058	62.3%	[10 $\bar{1}$ ]
	74.58	0.027	35.209	56.9%	[101]

The Au<sub>1</sub> cluster on the stoichiometric surface displays 2 convoluted peaks: the first being made up of two vibrations at 23 and 30 cm<sup>-1</sup>, while the second peak is at 53 cm<sup>-1</sup> and has very low IR intensity. These peaks correspond to vibrations of the Au atoms along the approximate [010], [10 $\bar{1}$ ], and [101] directions, which are displayed in the vector diagrams of Figure 7.14. For the oxygen-deficient surface, the same three vibrations have shifted to higher frequencies, now residing at 31, 42, and 75 cm<sup>-1</sup>; however, the intensity of the 42 cm<sup>-1</sup> vibration along the [10 $\bar{1}$ ] axis dwarfs the surrounding vibrations after convolution.

Figure 7.14: Vector displacement diagrams for the three vibrational modes of the Au<sub>1</sub> cluster on the stoichiometric anatase(101) surface.

The Raman spectrum provides a stark contrast to the IR, with the 42 and 75 cm<sup>-1</sup> vibrational modes having a large degree of polarisability, resulting in two high intensity peaks. The Raman intensity of the oxygen-deficient surface vibrations are also larger than those on the stoichiometric surface. It should be noted that the magnitude of these

vibrational motions are rather small ( $<1 \text{ km}\cdot\text{mol}^{-1}$ ) compared with some of the TiO<sub>2</sub> vibrations present nearby at  $155 \text{ cm}^{-1}$  and beyond that often have infrared activities greater than  $20 \text{ km}\cdot\text{mol}^{-1}$ , as shown in Appendix B.

### 7.3.2 Au<sub>2</sub> on the Stoichiometric and Oxygen-Deficient Anatase(101) Surfaces

Figure 7.15 displays the convoluted IR and Raman spectra between 0 and  $175 \text{ cm}^{-1}$  for the Au<sub>2</sub> cluster adsorbed to the stoichiometric and oxygen-deficient anatase(101) surface. The vibrational modes that contribute to the convoluted peaks are summarised in Table 7.5.

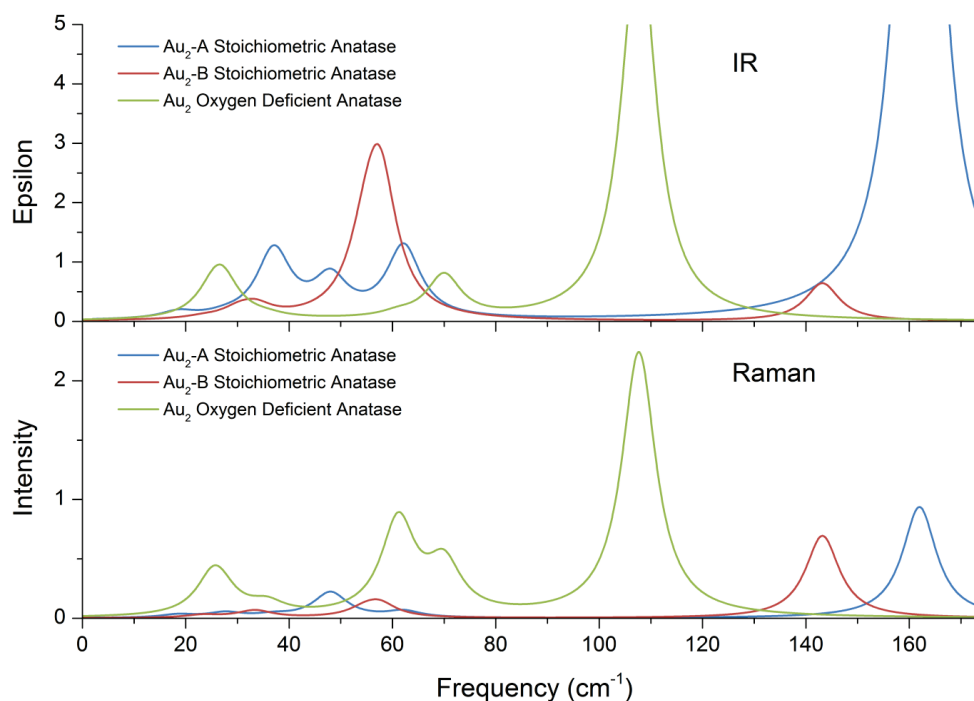


Figure 7.15: Predicted IR and Raman spectra of Au<sub>2</sub> adsorbed to the stoichiometric and oxygen-deficient anatase(101) surfaces.

Table 7.5: Calculated vibrational modes of Au<sub>2</sub> on stoichiometric and oxygen-deficient anatase(101) surfaces.

	Frequency (cm <sup>-1</sup> )	IR Intensity (km mol <sup>-1</sup> )	Raman Intensity (A <sup>4</sup> amu <sup>-1</sup> )	%Au Motion of Mode	Direction of Motion
<b>Au<sub>2</sub>-A on stoichiometric anatase(101)</b>	18.51	0.032	0.328	90.68%	[010] Cluster
	27.65	0.012	0.523	89.62%	[010] Cluster wag
	37.05	0.332	0.273	82.92%	[10 $\bar{1}$ ] Cluster
	48.00	0.185	2.717	81.66%	[101] Au II
	62.16	0.351	0.676	74.39%	[101] Au I
	161.98	4.502	12.134	44.16%	Au I/II stretch
<b>Au<sub>2</sub>-B on stoichiometric anatase(101)</b>	23.28	0.008	0.291	92.69%	[10 $\bar{1}$ ]/[010] Cluster
	30.25	0.040	0.047	87.94%	[010] Cluster
	33.49	0.056	0.746	90.72%	Cluster twist
	54.74	0.244	0.797	76.53%	[101] Cluster
	57.50	0.686	1.388	78.12%	[101] Cluster wag
	143.20	0.184	8.946	51.20%	Au I/II stretch
<b>Au<sub>2</sub> on oxygen- deficient anatase(101)</b>	25.43	0.091	4.252	88.83%	[010] AuI/AuII wag
	26.99	0.185	1.083	88.04%	[010] Cluster
	35.72	0.011	1.178	82.28%	[10 $\bar{1}$ ] Cluster
	61.13	0.020	10.122	79.22%	[101] Au II Primary
	69.98	0.209	5.245	69.11%	[101] Au I
	107.68	1.896	28.531	68.06%	Au I/II stretch +Ti <sub>4c</sub>

For the Au<sub>2</sub>-A isomer, there are 3 major peaks predicted at ~39, 48.00 and 62.16 cm<sup>-1</sup>, with a high intensity peak at 162 cm<sup>-1</sup>. An illustration of the cluster wag mode, and the two most intense vibrations, are shown in Figure 7.16. The peak at 39 cm<sup>-1</sup> consists of the two vibrational modes at 27.65 and 37 cm<sup>-1</sup>, which correspond to a cluster wag along the [010] direction and cluster displacement along the [10 $\bar{1}$ ] directions, respectively. The modes at 48.00 and 62.16 cm<sup>-1</sup> correspond to vibrations of the Au atoms above the O<sub>2c</sub> atom and Ti<sub>5c</sub> atom, along the [101] direction, while the large 161.98 cm<sup>-1</sup> vibration is a Au-Au stretching mode which is predicted to appear due to the addition of a second Au atom to the cluster, and is the most intense vibration.

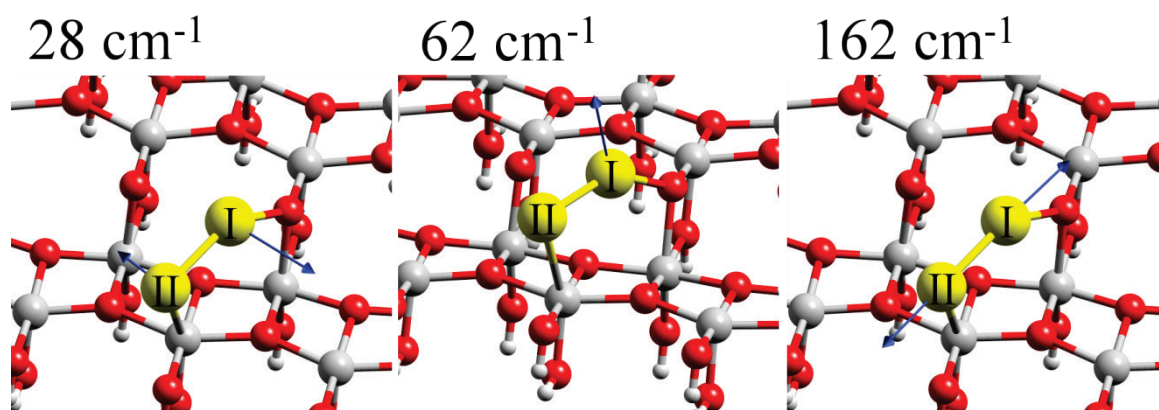


Figure 7.16: Vector displacement diagrams for the cluster wag at  $28\text{ cm}^{-1}$ , and the two most significant vibrational modes of the Au<sub>2</sub>-A isomer on the stoichiometric anatase(101) surface.

For the Au<sub>2</sub>-B isomer there are three major peaks predicted at  $\sim 33$ ,  $58$ , and  $143\text{ cm}^{-1}$ . The two peak at  $33\text{ cm}^{-1}$  consists of two vibrational modes at  $30.25$  and  $33.49\text{ cm}^{-1}$ , which correspond to vibrational motion of the cluster along the  $[010]$  direction and a cluster twisting motion respectively. The second major peak consists of two vibrational modes at  $54.74$  and  $58\text{ cm}^{-1}$  that correspond to cluster motion along the  $[101]$  direction and a cluster wag with displacement along the  $[101]$  direction respectively. As for the Au<sub>2</sub>-A cluster, the mode near  $143.20\text{ cm}^{-1}$  corresponds to a Au-Au stretching mode. The modes at  $18$  and  $143\text{ cm}^{-1}$  are both very active in the Raman spectra. This is similar to that predicted for the Au<sub>2</sub>-A isomer, where the vibrational mode along the  $[101]$  direction, and the Au-Au stretching mode, are both the most active mode in the Raman spectra. In general, there are only small changes in the vibrational modes and frequencies between the two isomers, due to the relatively small change in binding geometry. There is, however, a major decrease in the intensity for the Au-Au stretching mode for Au<sub>2</sub>-B.

Comparing Au<sub>2</sub>-A and Au<sub>2</sub>-B on the stoichiometric anatase surface to Au<sub>2</sub> adsorbed to the oxygen-deficient surface, there is a major shift predicted for the intense Au-Au stretching mode at  $161.98$  and  $143.20\text{ cm}^{-1}$ , to  $107.68\text{ cm}^{-1}$ . The vector displacements for the most significant vibrational modes are displayed in Figure 7.17. The peak at  $27\text{ cm}^{-1}$  consists of two vibrational modes at  $25.43$  and  $26.99\text{ cm}^{-1}$ , which correspond to wag and displacement modes along the  $[010]$  direction, respectively. The peak convoluted peak at  $70\text{ cm}^{-1}$  consists of the two vibrational modes at  $61.13$  and  $69.98\text{ cm}^{-1}$ , which correspond to displacements of Au II and Au I along the  $[101]$  direction, respectively. The large Au-

Au stretching mode has decreased in frequency to 107.68 cm<sup>-1</sup> compared with the isomers on the stoichiometric surface, and consists of a notable localised component from the nearby Ti<sub>4c</sub> atom. As shown for Au<sub>2</sub> on the stoichiometric surface, the most active Raman modes are those along the [101] direction and the Au-Au stretching modes.

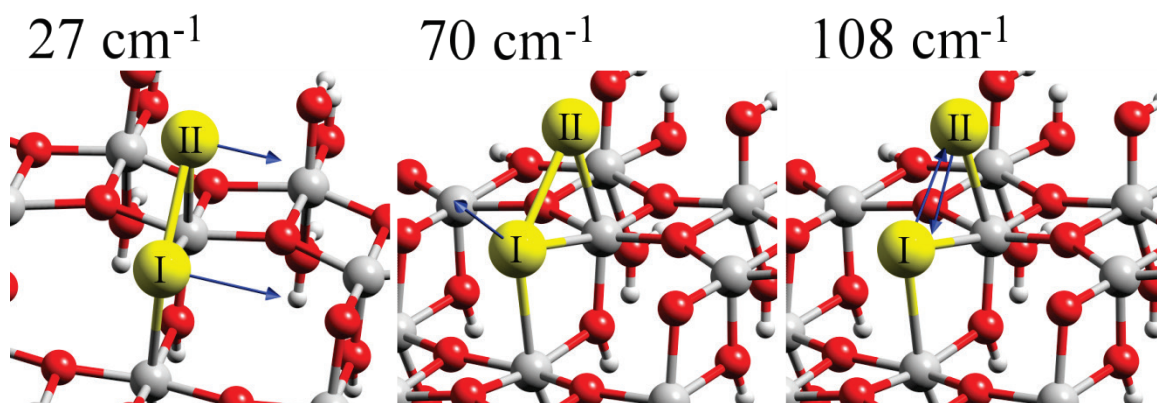


Figure 7.17: Vector displacement diagrams for the significant vibrational modes of the Au<sub>2</sub> cluster on the oxygen-deficient anatase(101) surface.

For gas-phase Au<sub>2</sub>, there is no IR activity predicted due to the lack of dipole moment for the Au-Au stretching mode, but a Raman active mode is predicted at 163 cm<sup>-1</sup> with 31.7 A<sup>4</sup>amu<sup>-1</sup> scattering activity. Comparing the gas-phase Au<sub>2</sub> mode to that of the Au<sub>2</sub> cluster on the stoichiometric surface, the frequency remains virtually unchanged for the Au<sub>2</sub>-A isomer, but is shifted 20 cm<sup>-1</sup> lower for Au<sub>2</sub>-B, with both modes having decreased Raman intensity. However, for the Au<sub>2</sub> cluster bound to the oxygen-deficient surface, an even greater shift of 55 cm<sup>-1</sup> to lower frequencies is predicted, with similar intensity to that of the gas-phase mode (28.5 vs 31.7 A<sup>4</sup>amu<sup>-1</sup>).

The vibrational modes for the triplet state of Au<sub>2</sub> on the oxygen-deficient surface, which is higher in binding energy by 0.42 eV, is compared with the singlet state Au<sub>2</sub> in Figure 7.18 and summarised in Table 7.6. Due to the small geometry changes between the singlet and triplet state discussed in the previous section, there are only small changes in the majority of the vibrational modes; however, the [10 $\bar{1}$ ] vibration has shifted from 35.72 to 25.96 cm<sup>-1</sup>, now involving mainly Au I, and the Au-Au stretching mode has shifted significantly from 107.68 to 128.44 cm<sup>-1</sup>. The intensity of the Au-Au vibration has increased by a factor of 3 for the IR, and a factor of 18 for the Raman intensity.

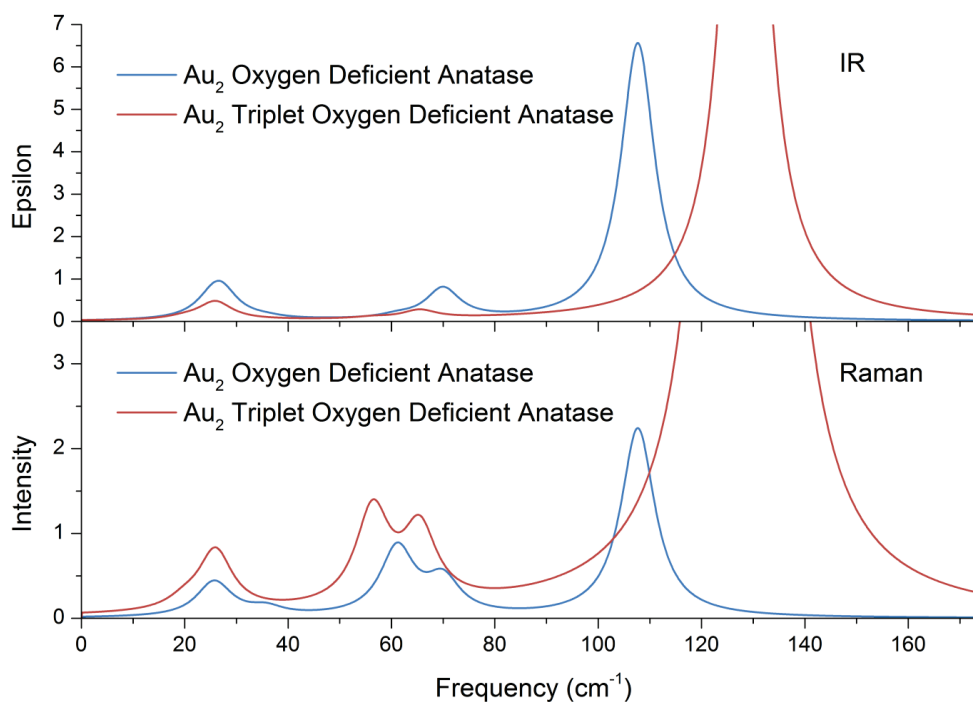


Figure 7.18: Predicted IR and Raman spectra of triplet Au<sub>2</sub> on stoichiometric and oxygen-deficient anatase(101) surfaces.

Table 7.6: Calculated vibrational modes of triplet Au<sub>2</sub> on oxygen-deficient anatase(101).

	Frequency (cm <sup>-1</sup> )	IR Intensity (km mol <sup>-1</sup> )	Raman Intensity (A <sup>4</sup> amu <sup>-1</sup> )	%Au Motion of Mode	Direction of Motion
<b>Au<sub>2</sub> triplet on oxygen- deficient anatase(101)</b>	19.93	0.015	1.293	93.53%	[010] AuI/AuII wag
	25.60	0.020	0.599	87.07%	[10T] Cluster
	25.96	0.105	8.444	88.12%	[10T] Au I
	56.37	0.011	14.277	80.48%	[101] Au II Primary
	65.45	0.056	11.050	75.38%	[101] Au I
	128.44	5.744	491.978	48.39%	Au I/II stretch + Ti <sub>4c</sub>

### 7.3.3 Au<sub>3</sub> on the Stoichiometric and Oxygen-Deficient Anatase(101) Surfaces

The predicted infrared spectra for the Au<sub>3</sub> cluster series on the stoichiometric and oxygen-deficient surface are presented in Figure 7.19, with a summary of the calculated transitions presented in Table 7.7 and Table 7.8 respectively. For the predicted Raman spectra, see Appendix B. In the following text, generally only those modes that make a significant contribution to the convoluted spectrum will be discussed.

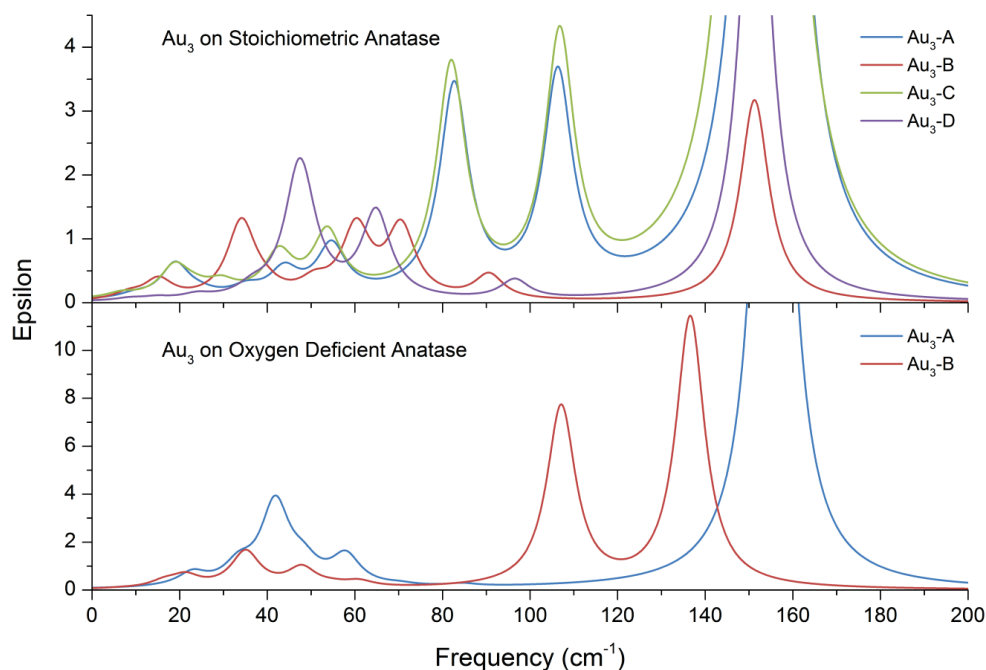


Figure 7.19: Predicted IR spectra of various Au<sub>3</sub> isomers on the stoichiometric and oxygen-deficient anatase(101) surfaces.

For the Au<sub>3</sub>-A cluster, the modes at 19.03 and 24.77 cm<sup>-1</sup> correspond to general twisting motions of the entire cluster along the [10 $\bar{1}$ ] direction, and make up the first peak. For the remaining peaks, each one is convoluted over a single mode. Vector displacement diagrams for one of the twisting modes and the three most intense vibrations are shown in Figure 7.20. The mode at 35.27 cm<sup>-1</sup> corresponds to a strong stretch of the Au I atom along the [010] direction; 43.90 cm<sup>-1</sup> corresponds to a vibration of the Au I atom between the [010] and [10 $\bar{1}$ ] direction; 54.66 cm<sup>-1</sup> results in a overall cluster motion along the [101] direction away from the surface; 82.65 cm<sup>-1</sup> corresponds to a stretching vibration between the Au I and Au II along the [10 $\bar{1}$ ] direction, while the Au III atom moves into the surface along the [101] direction; 106.37 cm<sup>-1</sup> is a stretching mode between Au II and Au III, while Au I moves towards the O<sub>2c</sub>; and the intense vibration at 154.81 cm<sup>-1</sup> involves a breathing mode of the Au<sub>3</sub> cluster, coupled with the surface O<sub>2c</sub> and nearby Ti<sub>5c</sub> atoms moving along the [010] direction. The last three vibrations are the most intense as they involve large motion of all three Au atoms.

Table 7.7: Calculated vibrational modes of Au<sub>3</sub> on the stoichiometric anatase(101) surface.

	Frequency (cm <sup>-1</sup> )	IR Intensity (km mol <sup>-1</sup> )	Raman Intensity (A <sup>4</sup> amu <sup>-1</sup> )	%Au Motion of Mode	Direction of Motion
<b>Au<sub>3</sub>-A on stoichiometric anatase(101)</b>	9.60	0.017	4.499	98.54%	[010] Au III
	19.03	0.157	1.064	96.69%	[10 $\bar{1}$ ] twist
	24.77	0.015	1.148	94.24%	[10 $\bar{1}$ ] twist
	35.27	0.039	0.664	89.58%	[010] Au I
	43.90	0.116	1.797	91.32%	[010]/ [10 $\bar{1}$ ]Au I
	54.66	0.225	11.551	85.07%	[101] cluster
	82.65	0.941	5.445	90.74%	Au I/Au II stretch
	106.37	0.977	2.844	77.75%	Au II/Au III stretch
	154.81	9.555	5.011	40.27%	Breathing + O <sub>2c</sub>
<b>Au<sub>3</sub>-B on stoichiometric anatase(101)</b>	8.25	0.027	2.120	97.59%	[010] twist
	15.16	0.090	0.611	95.92%	Cluster twist
	34.12	0.352	0.376	87.62%	[10 $\bar{1}$ ] cluster
	39.50	0.029	2.538	87.21%	[101] Au III
	50.77	0.063	7.620	87.07%	[101] Au II
	60.30	0.318	2.769	79.27%	[101] Au I
	70.54	0.320	0.968	83.86%	Au II/Au III stretch
	90.63	0.112	2.644	86.58%	Au II/Au I stretch
	151.26	0.916	6.342	38.39%	Au I/Au III stretch
<b>Au<sub>3</sub>-C on stoichiometric anatase(101)</b>	6.70	0.021	3.569	98.02%	[010] Au III
	18.86	0.137	1.829	95.02%	[10 $\bar{1}$ ]twist
	23.25	0.027	2.198	92.35%	[10 $\bar{1}$ ]twist
	29.50	0.054	0.440	89.81%	[010] Au I
	42.66	0.184	1.331	88.42%	[10 $\bar{1}$ ]Au I
	53.71	0.275	15.569	81.68%	[101] cluster
	82.01	1.025	6.811	87.79%	Au I/Au II stretch
	106.80	1.134	3.925	75.68%	Au II/Au III stretch
	153.03	12.265	5.379	21.85%	Cluster breathing
<b>Au<sub>3</sub>-D on stoichiometric anatase(101)</b>	8.68	0.010	1.673	98.22%	[010]/[10 $\bar{1}$ ] Au III
	14.71	0.012	1.155	95.38%	[010]/[10 $\bar{1}$ ] cluster
	23.91	0.020	0.104	91.52%	[010] Au I/Au II
	36.64	0.041	1.666	87.39%	Cluster twist
	47.18	0.517	1.183	83.43%	[101] Au I
	48.88	0.125	9.042	88.45%	Au I/Au II stretch
	64.84	0.391	2.511	79.74%	[10 $\bar{1}$ ]Au II
	96.51	0.086	6.315	82.68%	Au II/Au III stretch
	151.51	2.413	16.568	34.62%	Au I/Au III stretch + O <sub>2c</sub>

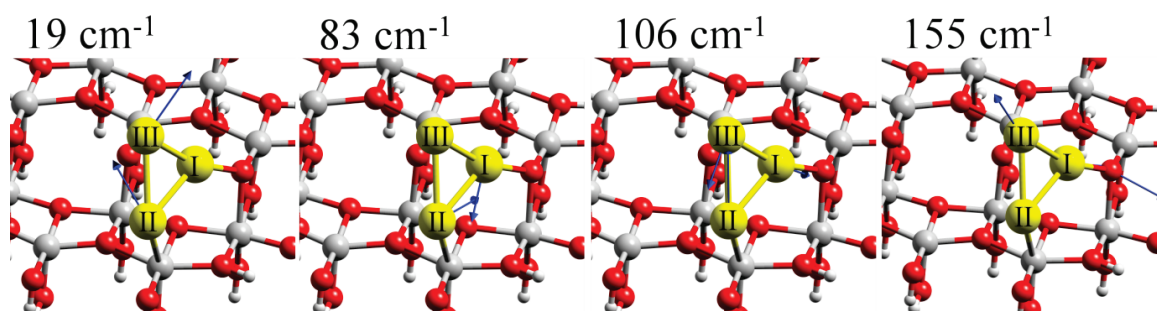


Figure 7.20: Vector displacement diagrams for the significant vibrational modes of the Au<sub>3</sub>-A isomer on the stoichiometric anatase(101) surface.

For the Au<sub>3</sub>-B isomer, the frequency and magnitude of vibrations have changed significantly due to the altered binding geometry. The vibrational motion for one of the twisting modes and the three most intense vibrations are shown in Figure 7.21. The mode at 15.16 cm<sup>-1</sup> involves Au I displacing along the [010] direction, as Au II moves along the [10 $\bar{1}$ ] axis, so the entire cluster pivots anti-clockwise around Au III when viewed from above the surface; 34.12 cm<sup>-1</sup> involves an overall movement of the entire cluster along [10 $\bar{1}$ ], while the mode at 39.50 cm<sup>-1</sup> involves Au III moving away from the surface along the [101] direction, together making up the peak at 35 cm<sup>-1</sup> in the convoluted spectrum; the mode at 50.77 cm<sup>-1</sup> involves the same movement, but of the Au II atom; the mode at 60.30 cm<sup>-1</sup> corresponds to displacement of Au I along the [101] direction; 70.54 cm<sup>-1</sup> is a stretching mode between Au II and Au III; 90.63 cm<sup>-1</sup> is a stretching mode involving Au II and Au I; and the mode at 151.26 cm<sup>-1</sup> involves the breathing mode discussed previously, although with more emphasis on a stretch between Au I and Au III, along with a general clockwise twisting motion of the Ti and O surface atoms about their centre of mass when viewed from above the surface.

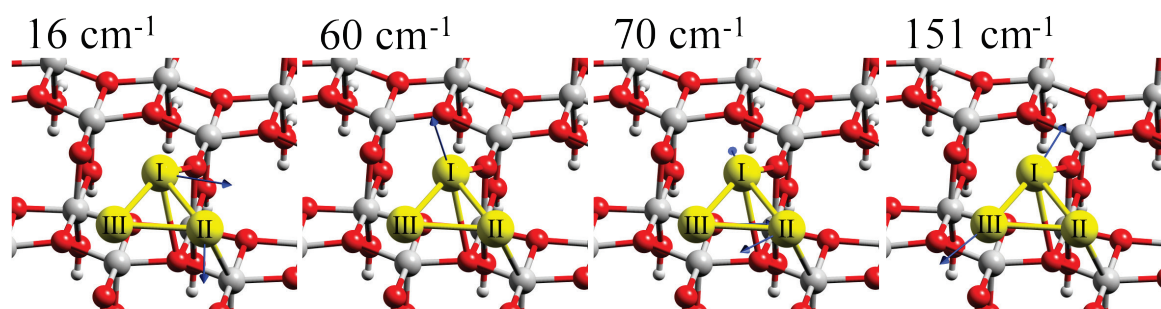


Figure 7.21: Vector displacement diagrams for the significant vibrational modes of the Au<sub>3</sub>-B isomer on the stoichiometric anatase(101) surface.

The pattern of vibrational motion for the Au<sub>3</sub>-C isomer is the same as those for Au<sub>3</sub>-A isomer due to the similar geometry, except for the vibration at 42.66 cm<sup>-1</sup>, which is instead directly along the [10 $\bar{1}$ ] direction, as opposed to Au<sub>3</sub>-A in which it is between [010] and [10 $\bar{1}$ ] axes. The similarities between the predicted modes are most readily observed in the convoluted IR spectra of Figure 7.19, whereby the peaks and intensities are almost identical for both isomers.

For the final Au<sub>3</sub> isomer, Au<sub>3</sub>-D, the calculations predict a spectrum that is distinctive amongst the Au<sub>3</sub> series, with three main peaks at 44, 64.84, and 151.51 cm<sup>-1</sup>. The vibrational motion for one of the twisting modes and the three most intense vibrations are shown in Figure 7.22. The first peak is made up of the mode at 36.64 cm<sup>-1</sup> that involves twisting motion of Au I between the [010] and [10 $\bar{1}$ ] axis, while Au III moves outwards from the surface along the [101] axis, the mode at 47.18 cm<sup>-1</sup>, which involves the movement of Au I away from the surface along the [101] axis, and the mode at 48.88 cm<sup>-1</sup>, which involves a distorted stretching mode between Au and Au II. The peak at 64.84 cm<sup>-1</sup> is due to a single mode at 64.84 cm<sup>-1</sup> involving the displacement of the Au II atom along the [10 $\bar{1}$ ] axis, while the intense peak at 151.51 cm<sup>-1</sup> is an intense stretching mode between Au I and Au II, along with some motion of the nearby O<sub>2c</sub> atom along the [010] direction.

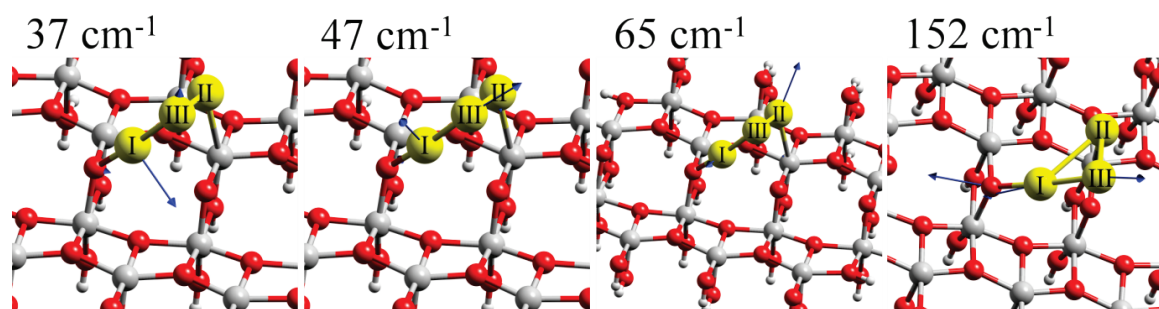


Figure 7.22: Vector displacement diagrams for the significant vibrational modes of the Au<sub>3</sub>-D isomer on the stoichiometric anatase(101) surface.

Table 7.8: Calculated vibrational modes of Au<sub>3</sub> on the oxygen-deficient anatase(101) surface.

	Frequency (cm <sup>-1</sup> )	IR Intensity (km mol <sup>-1</sup> )	Raman Intensity (A <sup>4</sup> amu <sup>-1</sup> )	%Au Motion of Mode	Direction of Motion
<b>Au<sub>3</sub>-A on oxygen- deficient anatase(101)</b>	16.27	0.003	0.657	91.76%	[010] Au III
	22.93	0.157	0.754	89.83%	[010] Au I/Au II
	33.48	0.228	0.390	87.00%	[10 $\bar{1}$ ] Au II/Au III
	41.82	0.994	34.695	68.60%	[10 $\bar{1}$ ] Au I
	48.25	0.224	2.570	84.67%	[101] Au III
	57.93	0.357	4.387	77.90%	[101] Au II + O <sub>2c</sub>
	70.25	0.021	11.887	66.40%	[101] Au I
	84.44	0.030	8.140	77.57%	Au I/Au II stretching
155.42	10.959	8.730	42.39%	Au II/Au III stretching + O <sub>2c</sub>	
<b>Au<sub>3</sub>-B on oxygen- deficient anatase(101)</b>	6.58	0.004	4.250	99.46%	[010] Au III
	16.46	0.071	3.179	96.19%	Cluster pivot Au I
	21.31	0.139	2.250	92.91%	[010] Au II
	35.06	0.434	1.726	85.75%	[010] Au I
	47.89	0.233	2.942	90.06%	Cluster distortion
	54.94	0.024	20.535	81.47%	[101] Au II
	60.90	0.068	1.336	70.72%	[10 $\bar{1}$ ] Au I
	107.13	2.179	1.733	67.50%	[101] Au I
136.59	3.272	10.425	77.91%	Au II/Au III stretch	

For Au<sub>3</sub>-A on the oxygen-deficient surface, the modes between 22.93 and 48.25 cm<sup>-1</sup> contribute to the wide convoluted peak with its maximum at ~42 cm<sup>-1</sup>. The vibrational motion for the three most intense vibrations are shown in Figure 7.23. These consist of the mode at 22.93 cm<sup>-1</sup>, which involves the movement of the Au I and Au II atoms along [010] direction; 33.48 cm<sup>-1</sup>, which involves the movement of both Au III and Au II primarily along the [10 $\bar{1}$ ] axis; 41.82 cm<sup>-1</sup>, which involves the movement of Au I along the same direction, while also moving along the [101] axis; and 48.25 cm<sup>-1</sup>, which

corresponds to a strong displacement of Au III along the [101] axis, with alternating movement of the Au II atom along the [101] axis. There is a small peak at 57.93 cm<sup>-1</sup> that corresponds to a single mode with a large displacement of Au II primarily along the [101] axis, coupled with movement of the nearby O<sub>2c</sub> atom towards the Au cluster. The large peak at 155.42 cm<sup>-1</sup> corresponds to a single mode that consists of an intense stretching mode between Au II and Au III, with a large displacement by the nearby O<sub>2c</sub> atom along the [010] axis, and to a lesser extent, other nearby Ti and O atoms along the same [010] direction.

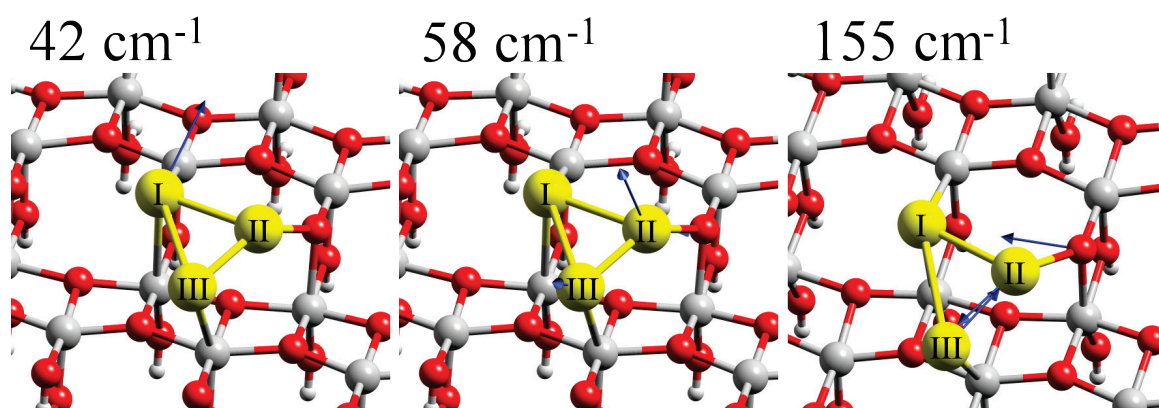


Figure 7.23: Vector displacement diagrams for the significant vibrational modes of the Au<sub>3</sub>-A isomer on the oxygen-deficient anatase(101) surface.

For the Au<sub>3</sub>-B isomer on the oxygen-deficient surface, there is a broad, low intensity feature centred at ~37 cm<sup>-1</sup> that consists of 7 modes ranging from 16.46 to 60.90 cm<sup>-1</sup>. The vibrational motion for the three most intense modes are shown in Figure 7.24. The 16.46 cm<sup>-1</sup> mode involves a general twisting motion of the cluster around the Au I atom, with Au II moving along the [010] direction; 21.31 cm<sup>-1</sup> involves the motion of Au II along the [010] direction; 35.06 cm<sup>-1</sup> primarily involves the movement of the Au I atom along the [010] direction; 47.89 cm<sup>-1</sup> involves a distorted rotation of the Au cluster about its C<sub>3</sub> axis, with Au I and Au III moving up and away from the surface; 54.94 cm<sup>-1</sup> involves the movement of Au II along the [101] direction; and 60.90 cm<sup>-1</sup> involves the movement of Au I along the [10 $\bar{1}$ ] direction. The two large peaks at 107.13 and 136.59 cm<sup>-1</sup> correspond to two discrete vibrational modes; the first mode at 107.13 cm<sup>-1</sup> consists primarily of movement of the Au I atom outwards and away from the vacant oxygen site, towards the Au II atom, with some movement of Au III along the [10 $\bar{1}$ ] direction, along with some movement of Au II along the [101] direction; the second mode at 136.59 cm<sup>-1</sup>

is a breathing mode. The large geometric change for the Au<sub>3</sub>-B isomer on the oxygen-deficient surface compared with Au<sub>3</sub>-A results in a large shift in the predicted spectrum for the high frequency modes. This results in two separate high frequency peaks at 107.13 and 136.59 cm<sup>-1</sup>.

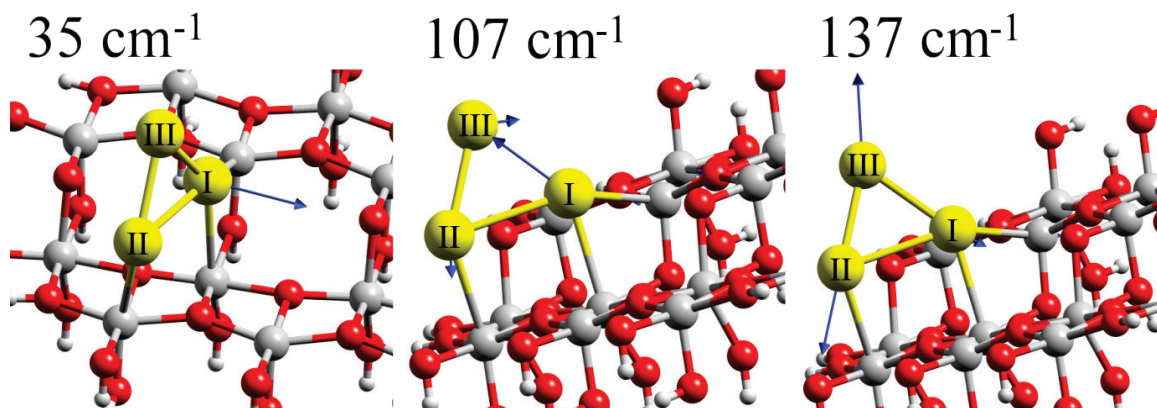


Figure 7.24: Vector displacement diagrams for the significant vibrational modes of the Au<sub>3</sub>-B isomer on the oxygen-deficient anatase(101) surface.

In general, the Au<sub>3</sub> isomers on the stoichiometric and oxygen-deficient surface predict a similar set of low frequency modes involving lateral motion across the surface, along with more intense modes at higher frequencies that involve strong Au-Au stretching and trimer breathing modes. There are significant shifts in the higher frequency modes beyond 80 cm<sup>-1</sup> when comparing Au<sub>3</sub> adsorbed to the stoichiometric versus the oxygen-deficient surface. Between the various isomers are distinct sets of peaks (except between Au<sub>3</sub>-A and C on the stoichiometric surface) that are clearly identifiable in the convoluted spectra of Figure 7.19.

The gas-phase Au<sub>3</sub> cluster calculated at the same level of theory predicts three vibrational modes at 39.75, 90.58, and 148.67 cm<sup>-1</sup> that correspond to a bending mode, asymmetric stretching mode, and symmetric breathing mode respectively. The mode at 90.58 cm<sup>-1</sup> has moderate IR and Raman intensity, while the symmetric breathing mode at 148.67 cm<sup>-1</sup> has low IR but a high Raman intensity. Compared to Au<sub>3</sub> on the stoichiometric surface, isomers A and C develop two peaks at 82 and 106 cm<sup>-1</sup> that correspond to the splitting of the asymmetric stretching mode for the C<sub>s</sub> symmetric gas-phase Au<sub>3</sub> cluster into two separate modes. This can be attributed to the orthogonal binding geometry of these isomers, which maintain the approximate shape of the gas-phase Au<sub>3</sub> trimer. The breathing mode at 148 cm<sup>-1</sup> in the gas-phase appears to have split into the multiple Au-

Au stretching modes predicted for all isomers on the stoichiometric surface. For the Au<sub>3</sub> cluster on the oxygen-deficient surface, there are large shifts in the frequency and motion of all vibrational modes, such that they are difficult to compare with the symmetric gas-phase Au<sub>3</sub> cluster, other than the strong Au-Au stretching modes at higher frequencies that are preserved throughout all isomers.

### 7.3.4 Au<sub>4</sub> on the Stoichiometric and Oxygen-Deficient Anatase(101) Surfaces

The predicted infrared spectra for the Au<sub>4</sub> cluster series on the stoichiometric and oxygen-deficient surface are presented in Figure 7.25, with a summary of the calculated transitions presented in Table 7.9 and Table 7.10 respectively. For the predicted Raman spectra, see Appendix B. In the following text, generally only those modes that make a significant contribution to the convoluted spectrum will be discussed.

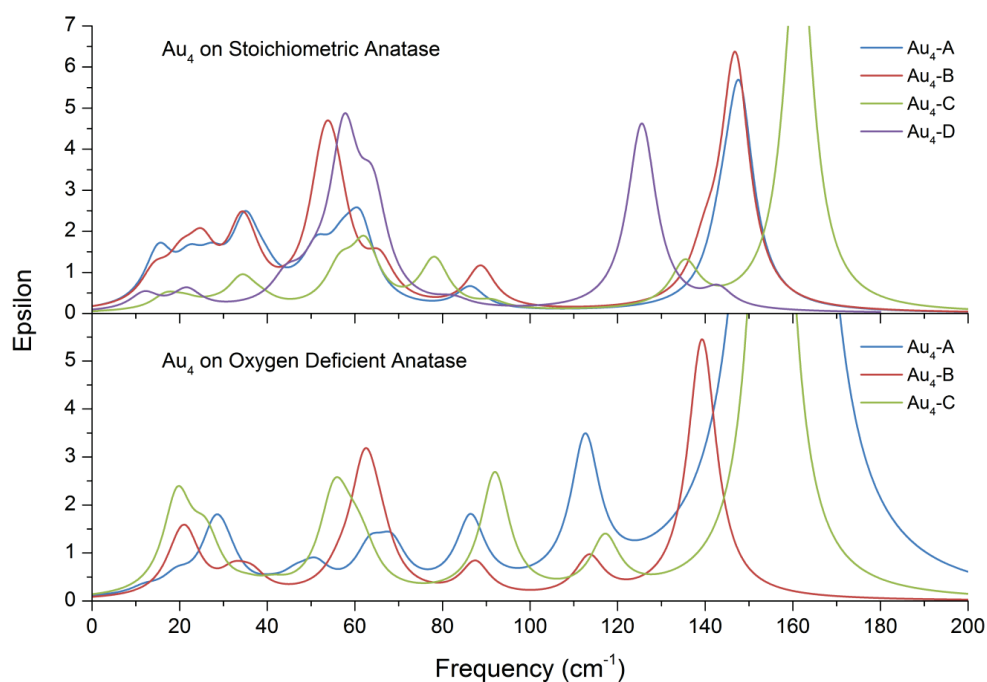


Figure 7.25: Predicted IR spectra of various Au<sub>4</sub> isomers on the stoichiometric and oxygen-deficient anatase(101) surfaces.

Table 7.9: Calculated vibrational modes of Au<sub>4</sub> on the stoichiometric anatase(101) surface.

	Frequency (cm <sup>-1</sup> )	IR Intensity (km mol <sup>-1</sup> )	Raman Intensity (A <sup>4</sup> amu <sup>-1</sup> )	%Au Motion of Mode	Direction of Motion
<b>Au<sub>4</sub>-A on stoichiometric anatase(101)</b>	15.22	0.378	0.440	93.90%	Cluster distortion[010]
	22.27	0.238	0.951	92.16%	Cluster twist
	27.40	0.218	0.493	91.64%	[10 $\bar{1}$ ] Cluster
	34.99	0.531	0.736	89.14%	[10 $\bar{1}$ ]/[101] Cluster
	39.46	0.139	1.964	91.84%	[101] Au III + distortion
	46.06	0.029	0.904	89.95%	[101] distortion
	51.20	0.314	3.313	87.17%	[101] Au I
	57.01	0.263	2.751	87.83%	[101] Au IV
	61.19	0.528	1.108	77.03%	[101] Au II
	86.37	0.156	8.241	87.57%	Au II/Au III dist. stretch
	143.76	0.282	4.245	74.81%	Au III/Au IV stretch
147.76	1.497	13.210	56.45%	Cluster breathing	
<b>Au<sub>4</sub>-B on stoichiometric anatase(101)</b>	14.30	0.209	0.693	93.22%	[010] Cluster
	20.30	0.238	1.227	92.90%	Cluster twist (clock)
	25.00	0.351	0.969	92.30%	[10 $\bar{1}$ ]/[010] Au IV
	34.18	0.496	0.965	89.08%	[010]/[101] Au II (III+IV)
	36.55	0.100	1.592	90.52%	[101] Au II +Au III rock
	52.33	0.515	0.220	84.92%	[101] Au III + distortion
	54.21	0.637	3.580	86.76%	Au I + Au IV rock
	56.24	0.279	3.220	81.64%	[101] Cluster
	65.70	0.265	0.779	85.11%	Au I/III distorted stretch
	88.72	0.296	11.229	86.41%	Au II/III distorted stretch
	139.89	0.278	1.964	64.78%	Alternating cluster stretch
146.85	1.768	17.927	65.39%	Cluster breathing	
<b>Au<sub>4</sub>-C on stoichiometric anatase(101)</b>	8.47	0.001	0.560	96.50%	[101] Au II
	16.96	0.100	0.592	94.77%	[010] Cluster
	21.35	0.055	0.783	93.54%	[010] Cluster
	27.46	0.022	0.768	94.25%	[010] Au IV
	34.25	0.216	0.257	85.83%	[101]/[10 $\bar{1}$ ] Au I
	38.69	0.047	0.193	90.41%	[101] Au III
	56.59	0.262	0.701	83.93%	[101]/[010] Au I
	62.33	0.424	2.196	78.67%	[101] Au IV
	78.16	0.351	4.061	83.93%	Au II to Au III/IV stretch
	91.25	0.047	0.804	89.47%	Au I/III distorted stretch
	135.42	0.313	5.912	70.46%	Au I/II, Au III/IV stretch
161.32	2.742	3.915	37.24%	Cluster breathing + O <sub>2c</sub>	

Table 7.9 continued

	Frequency (cm <sup>-1</sup> )	IR Intensity (km mol <sup>-1</sup> )	Raman Intensity (A <sup>4</sup> amu <sup>-1</sup> )	%Au Motion of Mode	Direction of Motion
<b>Au<sub>4</sub>-D on stoichiometric anatase(101)</b>	10.25	0.001	1.172	97.50%	Cluster twist
	11.95	0.117	0.641	95.22%	[010] Cluster
	21.52	0.092	0.225	96.94%	[10 $\bar{1}$ ] Cluster
	21.88	0.044	1.171	89.25%	[101] Au III
	44.36	0.174	5.553	94.13%	[101] Au I
	50.51	0.128	4.901	86.80%	[101] Au IV
	57.56	1.165	0.245	90.96%	[101] Au II + Au I/II wag
	64.09	0.685	0.124	90.26%	[10 $\bar{1}$ ]/[101]AuII/III
	80.82	0.022	0.785	95.19%	Alternating cluster dist.
	83.29	0.034	9.054	96.05%	Au I/IV stretch
	125.55	1.323	0.388	77.54%	[010]AuII/III vs Au I/IV
	143.00	0.130	11.740	81.00%	Cluster breathing

For the Au<sub>4</sub>-A isomer on the stoichiometric surface, there are numerous modes that are convoluted under the broad peak between  $\sim 10$  and  $70$  cm<sup>-1</sup>; Of these, the modes between  $15.22$  to  $46.06$  cm<sup>-1</sup> involve general cluster distortions and displacements primarily along the  $[10\bar{1}]$  and  $[101]$  directions, followed by three modes at  $51.20$ ,  $57.01$ , and  $61.19$  cm<sup>-1</sup> that correspond to individual Au atom displacements along the  $[101]$  direction. There are two stretching modes at  $86.37$  and  $143.76$  cm<sup>-1</sup>, the latter of which is dwarfed by the intense cluster breathing mode at  $147.76$  cm<sup>-1</sup>. Vector displacement diagrams for the three most intense vibrations are shown in Figure 7.26.

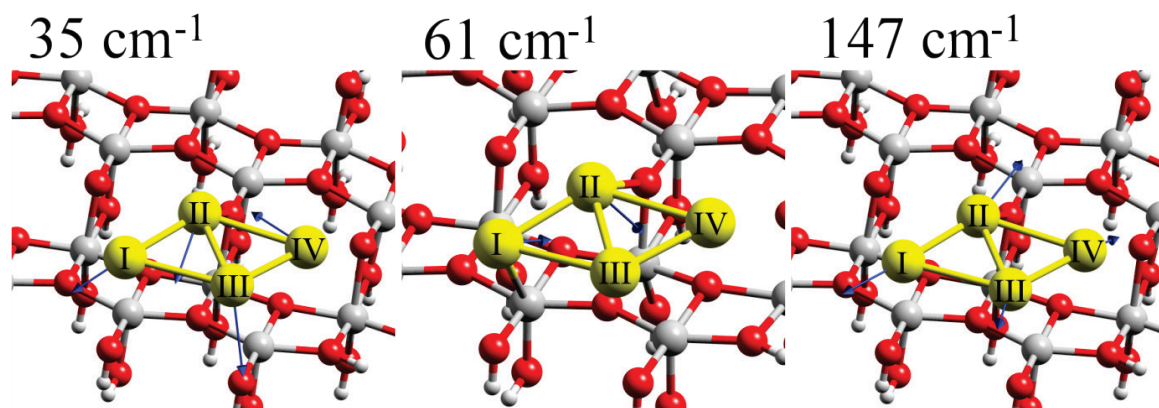


Figure 7.26: Vector displacement diagrams for the significant vibrational modes of the Au<sub>4</sub>-A isomer on the stoichiometric anatase(101) surface.

The Au<sub>4</sub>-B isomer has an almost identical predicted spectrum to that of the Au<sub>4</sub>-A isomer, except for some discrepancy near  $54$  cm<sup>-1</sup>; however, the types of vibrational motion for each mode have changed substantially between  $25.00$  and  $56.24$  cm<sup>-1</sup>. There is now a

cluster displacement mode along the [101] axis at 56.24 cm<sup>-1</sup> and an additional stretching mode at 65.70 cm<sup>-1</sup>. The cluster breathing mode at 146.85 cm<sup>-1</sup> remains virtually unchanged, however. Vector displacement diagrams for the three most intense vibrations are shown in Figure 7.27.

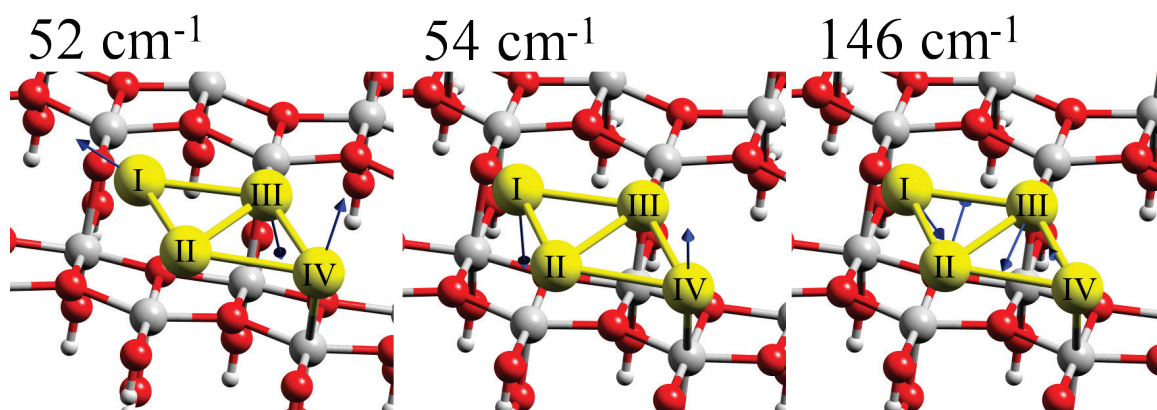


Figure 7.27: Vector displacement diagrams for the significant vibrational modes of the Au<sub>4</sub>-B isomer on the stoichiometric anatase(101) surface.

The predicted IR spectrum of the Au<sub>4</sub>-C isomer displays a broad series of peaks between 10 and 70 cm<sup>-1</sup> made up of a number of modes involving cluster and atom displacement primarily along the [010] and [101] directions. Vector displacement diagrams for the three most intense vibrations are shown in Figure 7.28. The modes at 78.16 and 135.42 cm<sup>-1</sup> are strong stretching modes, with a weaker distorted stretching mode between them at 91.25 cm<sup>-1</sup>. The intense peak at 161.32 cm<sup>-1</sup> consists of the same cluster breathing mode as seen for other clusters in this series, but with a larger component from the nearby surface O<sub>2c</sub> atom, reflected in the decreased %Au contribution to this mode. The predicted spectrum and vibrational modes of this isomer are the most unique amongst the Au<sub>4</sub> series on the stoichiometric surface due to the substantial change in geometry for this isomer. This isomer also lacks the cluster twisting motion usually seen below 20 cm<sup>-1</sup> for the Au<sub>4</sub> series.

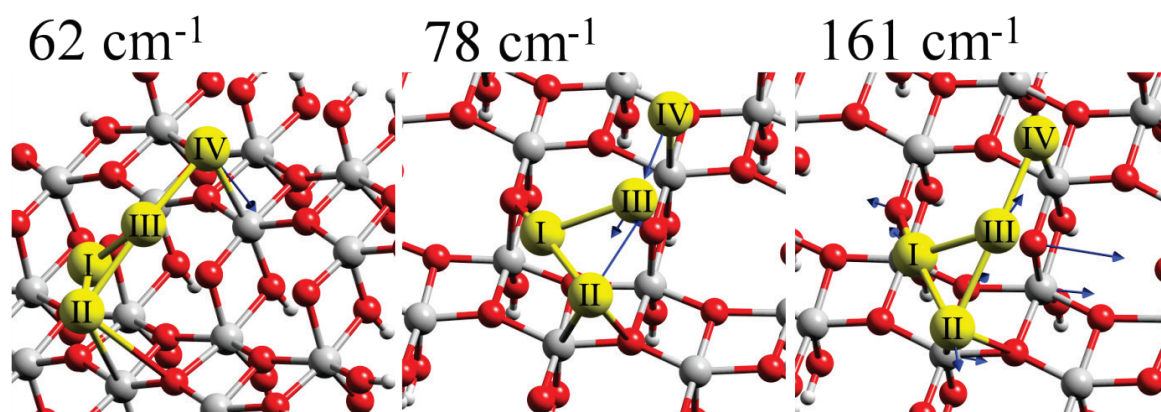


Figure 7.28: Vector displacement diagrams for the significant vibrational modes of the Au<sub>4</sub>-C isomer on the stoichiometric anatase(101) surface.

The predicted IR spectrum of the Au<sub>4</sub>-D isomer displays two main peaks near 60 and 125.55 cm<sup>-1</sup>, the former of which is made up of multiple Au atom displacements along the [101] direction, including a strong Au I/Au II wag motion at 57.56 cm<sup>-1</sup>. The latter intense peak at 125.55 cm<sup>-1</sup> is due to a strong bending mode between three Au atoms, and these are shown in the vector displacement diagrams for the three most intense vibrations in Figure 7.29. The cluster breathing mode at 143.00 cm<sup>-1</sup> is of much lower intensity than the Au<sub>4</sub> isomer on the stoichiometric surface, although it remains at the same frequency as the Au<sub>4</sub>-A and Au<sub>4</sub>-B isomers.

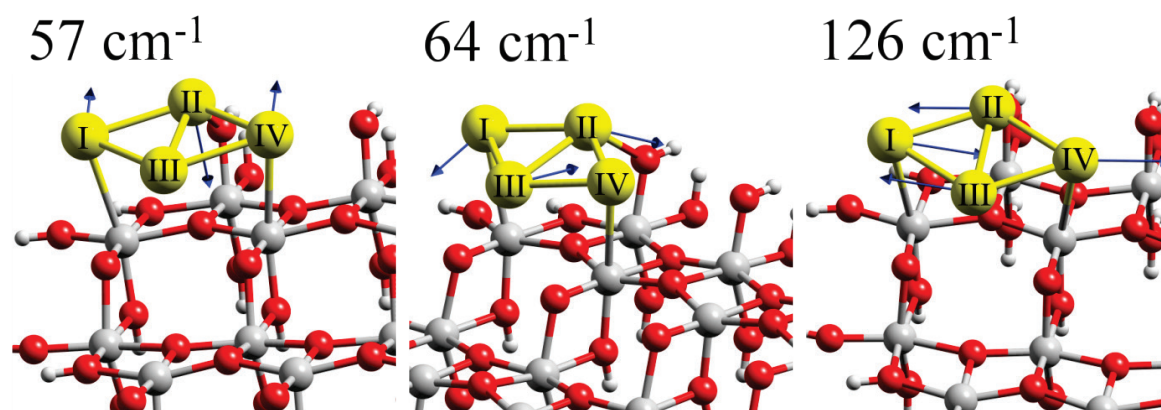


Figure 7.29: Vector displacement diagrams for the significant vibrational modes of the Au<sub>4</sub>-D isomer on the stoichiometric anatase(101) surface.

Table 7.10: Calculated vibrational modes of Au<sub>4</sub> on the oxygen-deficient anatase(101) surface.

	Frequency (cm <sup>-1</sup> )	IR Intensity (km mol <sup>-1</sup> )	Raman Intensity (A <sup>4</sup> amu <sup>-1</sup> )	%Au Motion of Mode	Direction of Motion
<b>Au<sub>4</sub>-A on oxygen- deficient anatase(101)</b>	11.99	0.038	1.077	92.45%	[010]/[10 $\bar{1}$ ] Au I + Au <sub>4</sub> twist
	19.30	0.093	0.701	92.66%	[10 $\bar{1}$ ] Au I
	28.14	0.368	1.692	90.06%	Cluster twist
	30.61	0.130	1.252	89.98%	[101] Au III + Au <sub>4</sub> twist
	40.75	0.024	1.989	83.48%	[101] Au III
	46.51	0.075	2.331	87.10%	[101] Au IV
	50.95	0.138	1.405	84.92%	[101] Au IV + [010] Au II
	63.43	0.225	4.895	88.12%	[101] Au I
	68.42	0.240	0.808	79.20%	[101]/[10 $\bar{1}$ ] Au II
	86.43	0.422	8.254	68.03%	[101]/[10 $\bar{1}$ ] Au II
	112.62	0.846	6.891	80.11%	Cluster breathing
157.97	19.344	21.624	34.90%	Au III/IV stretch + O <sub>2c</sub>	
<b>Au<sub>4</sub>-B on oxygen- deficient anatase(101)</b>	19.47	0.136	1.553	93.64%	Cluster distortion
	21.42	0.265	0.724	93.80%	[010]/[10 $\bar{1}$ ] Au I/II/IV
	21.69	0.047	1.331	93.40%	[010] Au IV [101] Au I
	32.43	0.115	0.576	90.36%	[101]/[010] Au I
	36.49	0.106	0.905	85.93%	[010]/[10 $\bar{1}$ ] Au II
	56.48	0.077	3.208	82.00%	[101]/[10 $\bar{1}$ ] Au II
	61.86	0.479	1.271	82.40%	[101]/[10 $\bar{1}$ ] Au III
	63.13	0.332	4.754	83.96%	[101] Au IV
	66.07	0.156	3.922	80.78%	[101] Au III
	87.49	0.200	5.879	79.15%	Au <sub>3</sub> trimer breathing
	113.56	0.232	2.602	82.53%	Overall cluster breathing
139.30	1.567	7.826	71.18%	Au I/IV stretching	
<b>Au<sub>4</sub>-C on oxygen- deficient anatase(101)</b>	19.49	0.576	1.464	90.46%	[010] Au I/II
	23.37	0.026	1.078	92.24%	[010] Au IV
	26.03	0.292	0.784	90.19%	[010]/[10 $\bar{1}$ ] Au III+twist
	35.58	0.031	0.854	86.99%	[010] Au II
	41.32	0.040	0.472	85.89%	[010]/[101] Au III
	54.98	0.432	1.946	78.26%	[101]Au I+Au II/III dist.
	56.78	0.190	2.125	81.93%	[101] Au I/II wag
	59.99	0.169	2.413	81.44%	[101] Au IV
	62.28	0.131	4.336	83.97%	[101]Au IV + clust. dist.
	91.98	0.733	16.360	73.22%	[101]/[10 $\bar{1}$ ] Au II
	117.18	0.326	5.844	83.37%	Au <sub>3</sub> trimer breathing
155.22	5.158	5.784	51.27%	Cluster breathing + O <sub>2c</sub> and surface [010]	

For the Au<sub>4</sub>-A isomers on the oxygen-deficient surface, there are a number of convoluted peaks spread over 30–115 cm<sup>-1</sup>, with a major peak at 157.97 cm<sup>-1</sup>. Vector displacements for the significant vibrational modes are displayed in Figure 7.30. The modes at 11.99, 28.14, and 30.61 cm<sup>-1</sup> consist of general cluster twisting modes in different directions,

with a mode at 19.30 involving displacement of Au I along the  $[10\bar{1}]$  direction. The modes from 30.61 to 63.43  $\text{cm}^{-1}$  are all predicted to involve displacement of various Au atoms along the  $[101]$  direction away from the surface, followed by two intense modes at 68.42 and 86.43 that involve Au II displacing along the  $[101]$  and  $[10\bar{1}]$  directions. The large peak at 112.62  $\text{cm}^{-1}$  consists of a cluster breathing mode while the large peak at 157.97  $\text{cm}^{-1}$  is an intense Au III to Au IV stretching mode that involves significant motion of the nearby O<sub>2c</sub> atom and surrounding surface atoms.

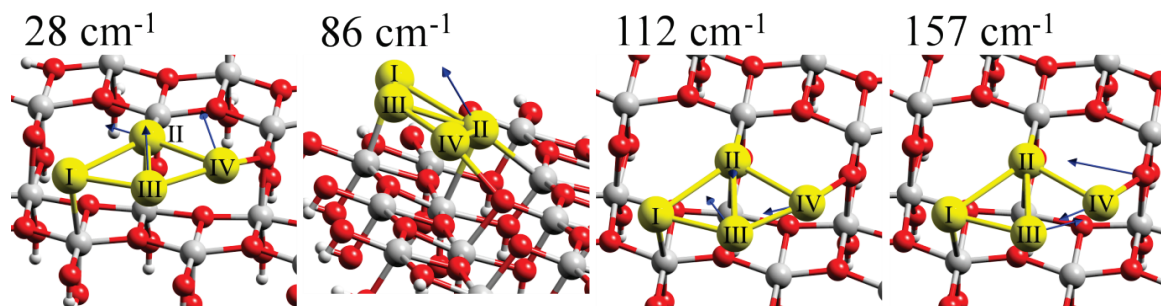


Figure 7.30: Vector displacement diagrams for the significant vibrational modes of the Au<sub>4</sub>-A isomer on the oxygen-deficient anatase(101) surface.

For the Au<sub>4</sub>-B isomer on the oxygen-deficient surface, there is a large change in the binding geometry compared with Au<sub>4</sub>-A, primarily resulting in a change in the intensity of multiple low frequency peaks, as well as a large shift in the high intensity peak at 139.30  $\text{cm}^{-1}$ . The vector displacements for the significant vibrational modes for this isomer are displayed in Figure 7.31. The vibrational motion of all modes between 19.47 and 61.86  $\text{cm}^{-1}$  have changed significantly, while the relatively intense mode at 87.49  $\text{cm}^{-1}$  is now a breathing mode involving the Au<sub>3</sub> trimer core that does not include the lone Au IV atom. The large overall cluster breathing mode at 113.56  $\text{cm}^{-1}$  is also present, although at a much lower intensity than the Au<sub>4</sub>-A isomer. The final Au-Au stretching mode at 139.30  $\text{cm}^{-1}$  has shifted significantly from 157.97  $\text{cm}^{-1}$  for Au<sub>4</sub>-A, and undergoes a large decrease in intensity. This vibrational mode now has a large %Au motion of 71.18%, which is much greater than both Au<sub>4</sub>-A and C isomers on the oxygen-deficient surface.

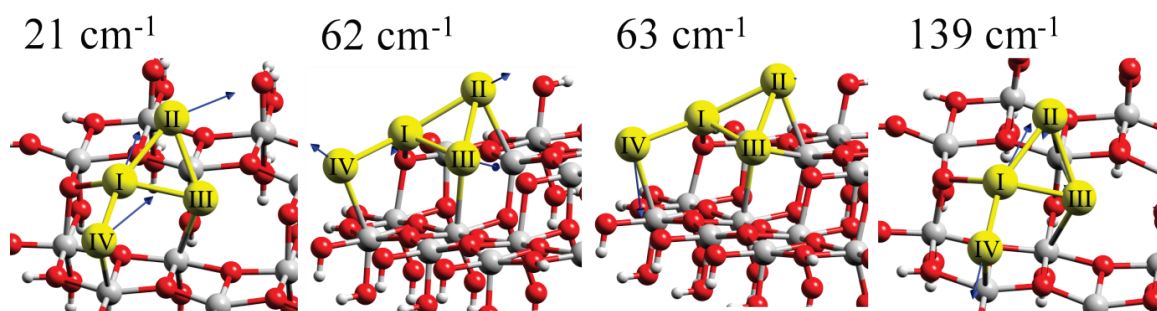


Figure 7.31: Vector displacement diagrams for the significant vibrational modes of the Au<sub>4</sub>-B isomer on the oxygen-deficient anatase(101) surface.

The Au<sub>4</sub>-C isomer on the oxygen-deficient surface predicts notable shifts in the frequency and intensity for all modes from 54.98 cm<sup>-1</sup> onwards. Vector displacements for the significant vibrational modes are displayed in Figure 7.32. The vibrational motion of modes between 19.49 and 41.32 cm<sup>-1</sup> primarily involve displacement of Au atoms along the [010] direction, which do not resemble those of Au<sub>4</sub>-A or B on the same surface. Those modes between 54.98 and 91.98 cm<sup>-1</sup> involve displacements along the [101] direction, alternating wags, and general distortions. The mode at 19.49 cm<sup>-1</sup> also involves alternating displacement of the Au III and Au IV atoms as shown in Figure 7.32. The mode at 117.18 cm<sup>-1</sup> is the same Au<sub>3</sub> trimer breathing mode seen for Au<sub>4</sub>-B on the same surface, shifted 29.69 cm<sup>-1</sup> higher in frequency to a position similar to that of Au<sub>4</sub>-A on the same surface. The large peak at 155.22 cm<sup>-1</sup> corresponds to a general cluster breathing mode with significant contribution from the nearby O<sub>2c</sub> and surface displacement along the [010] direction. The position of this mode is similar to that of Au<sub>4</sub>-A on the same surface, but with dramatically different Au atom motion.

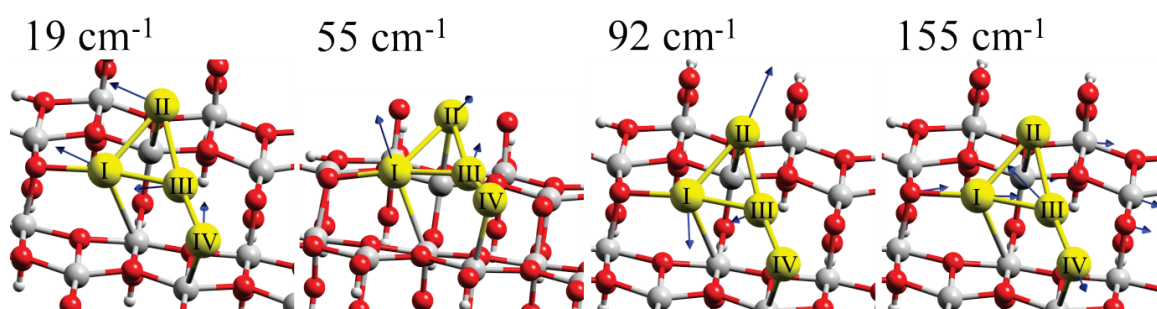


Figure 7.32: Vector displacement diagrams for the significant vibrational modes of the Au<sub>4</sub>-D isomer on the oxygen-deficient anatase(101) surface.

In general, for the Au<sub>4</sub> isomers on the stoichiometric surface, the calculations predict a similar set of low frequency lateral modes across the surface, along with more intense modes at higher frequencies that involve large stretching modes of the Au atoms and cluster breathing modes, as predicted for the Au<sub>3</sub> cluster series. There is generally a large change in the predicted IR spectrum and vibrational modes when comparing the clusters with distorted diamond geometries to those that consist of the Au<sub>3</sub> trimer with the fourth Au atom bound further along the surface.

The gas-phase Au<sub>4</sub> cluster calculation predicts six vibrational modes, two of which have large IR intensity at 65.79 and 136.23 cm<sup>-1</sup>, and two with large Raman intensities at 84.50 and 154.05 cm<sup>-1</sup>. The two intense IR modes can be characterised as an asymmetric wag and asymmetric stretches of the outer Au atoms, while the two intense Raman modes can be characterised as a symmetric stretching and a cluster breathing mode. In comparison, the cluster breathing mode of Au<sub>4</sub> adsorbed to the stoichiometric and oxygen-deficient surface has shifted by ~10 and ~40 cm<sup>-1</sup> respectively, whereas the asymmetric and symmetric stretching modes have split into multiple stretching modes due to the loss of D<sub>2h</sub> cluster symmetry upon adsorption to the surface. The intensity of some of these stretching modes when adsorbed to the surface have increased considerably compared with the gas-phase Au<sub>4</sub> cluster.

### 7.3.5 Discussion

The addition of Au atoms to a cluster results in large changes to the predicted IR and Raman modes as would be expected for large geometry changes. Between the different isomers of the same cluster, however, the changes to the predicted spectra are often quite subtle, even if there are significant changes to the motion of the vibrational modes.

Figure 7.33 shows the correlation between the frequencies of the averaged stretching modes against the averaged Au-Au bond lengths for the Au<sub>2-4</sub> clusters on the stoichiometric surface. While there is also an increase in the average frequencies of the stretching modes for the Au<sub>2-4</sub> clusters on the oxygen-deficient anatase surface, there is no correlation between the average Au-Au bond lengths due to their irregularity. This trend could be expected to continue for large clusters as the reduced mass of the cluster increases, decreasing the force constant of these key vibrations. These modes are typically

some of the most intense vibrations that are predicted to occur, and could provide a useful indicator as to the approximate size or stoichiometry of a cluster on the anatase surface during experimental studies.

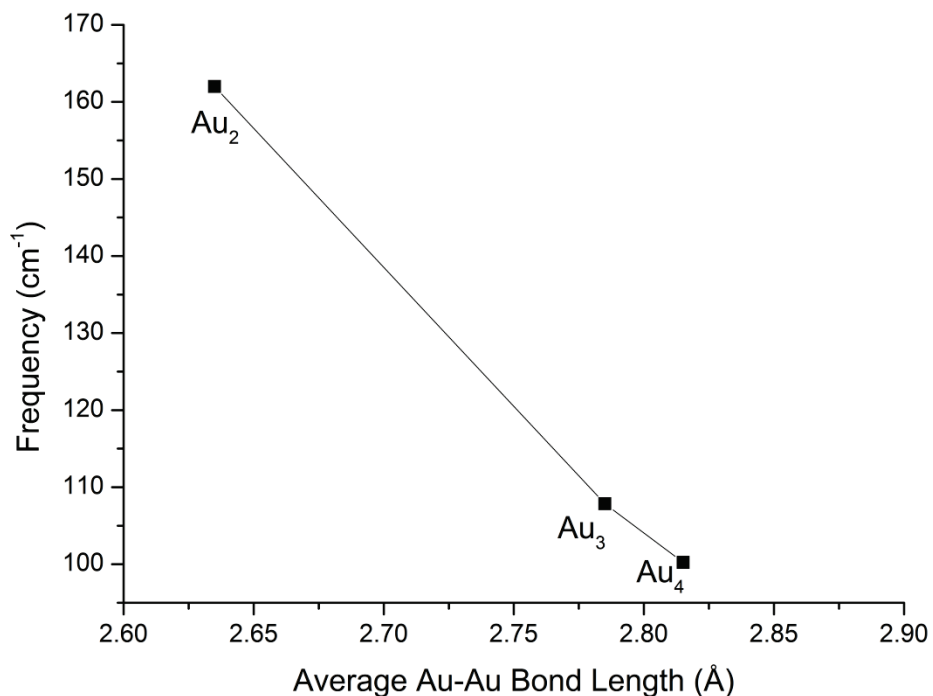


Figure 7.33: The correlation between the frequencies of the stretching modes of Au<sub>2-4</sub> with their respective Au-Au bond lengths. The frequencies and bond lengths have been averaged for all isomers.

#### 7.4 Charge Analysis of Au<sub>1-4</sub> on Anatase(101) Surfaces

This section contains a summary of the calculated charge distribution over key surface and cluster atoms using natural bond orbital (NBO), Löwdin, and Hirshfeld charge analysis methods. Although the NBO method is one of the most popular in the literature, multiple analysis methods are included for comparison to the wide range of methods used in other studies in the literature.

In the following discussion, Hirshfeld and Löwdin analysis methods predict similar signs and magnitudes, while NBO analysis predicts charge magnitudes almost twice as large. Due to the similar trends predicted between the analysis methods, discussion will focus on the NBO method, and deviations from trends in the other methods will be presented and discussed where applicable. It should be noted that while the predicted charges may not be quantitatively useful, relative trends in their values can provide insightful qualitative information.

##### 7.4.1 Stoichiometric and Oxygen-Deficient Anatase(101) Surfaces

The charge analysis for key atoms on the stoichiometric and oxygen-deficient surfaces is shown in Table 7.11 and Table 7.12. For the stoichiometric anatase(101) surface, NBO analysis predicts the O<sub>3c</sub> and O<sub>2c</sub> atoms to have charges of -0.583 and -0.706 respectively, while the Ti<sub>5c</sub> atom has a +1.462 charge. Löwdin and Hirshfeld calculations provide a similar story of charge transfer, albeit with smaller charge magnitude, especially for Ti<sub>5c</sub>.

For the oxygen-deficient surface, NBO analysis predicts the O<sub>3c</sub> atom to develop a -0.757 charge, while the undercoordinated Ti<sub>5c</sub> and Ti<sub>4c</sub> atoms that result from the removal of O<sub>2c</sub> attain charges of +1.168 and +1.385 respectively. Compared with the stoichiometric surface, the charge on the O<sub>3c</sub> atom near the oxygen defect site has a small increase in negative charge (-0.051), while the Ti<sub>5c</sub> atom has gained 0.294 of electron charge, becoming less positive. Again, Löwdin and Hirshfeld calculations provide a similar story of charge transfer. This charge transfer could be attributed to the two unpaired electrons between the under-coordinated Ti<sub>5c</sub> and Ti<sub>4c</sub> sites, which no longer have an O<sub>2c</sub> atom to pair with to draw away electron density.

Figure 7.34 shows the electrostatic potential mapped to the isosurface of the electron density for both the stoichiometric and oxygen-deficient surfaces. This figure illustrates general areas of charge across the surface map, with the bridging O<sub>2c</sub> oxygens, and to a lesser degree, the recessed O<sub>3c</sub> atoms contributing to the negative charge across the surface. Comparison between the stoichiometric surface and the oxygen-deficient surface shows that upon loss of the bridging O<sub>2c</sub> atom, there is a localised region of roughly neutral charge in the vacancy site, with the charge over the remainder of the surface remaining virtually unchanged.

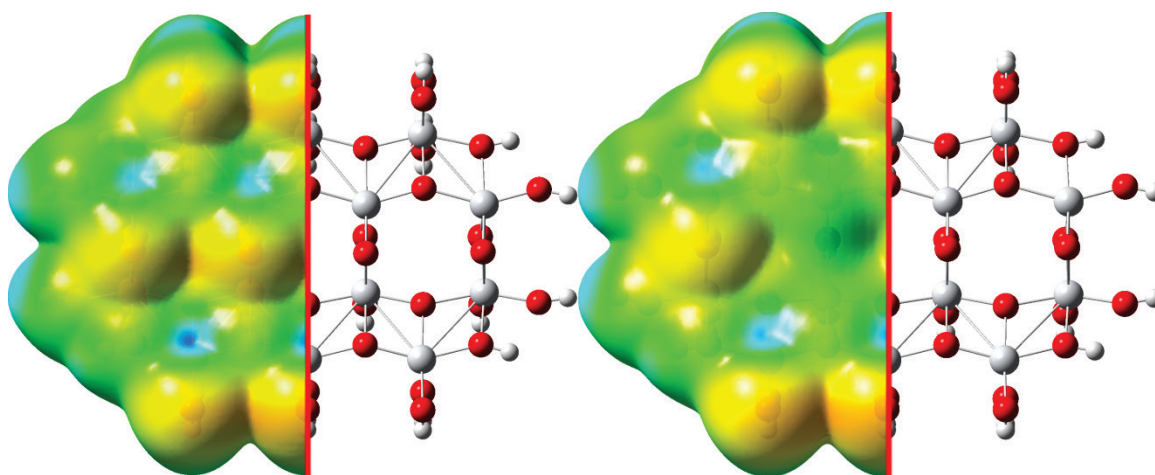


Figure 7.34: (101) view of the electrostatic potential mapped to the isosurface of the electron density for the stoichiometric (left) and oxygen-deficient (right) anatase(101) surfaces. The red gradient highlights areas of negative charge, while the blue gradient highlights areas of positive charge.

#### 7.4.2 Au<sub>1-4</sub> on the Stoichiometric Anatase(101) Surface

The charge distribution for the Au<sub>1-4</sub> clusters on the stoichiometric anatase(101) surface are summarised Table 7.11. Upon adsorption of Au<sub>1</sub> to the stoichiometric anatase(101) surface charge flows from the Au atom to the O<sub>2c</sub> and Ti<sub>5c</sub> atoms of the surface, resulting in charges of -0.622 and +1.135 respectively, with the Au atom being left with a +0.319 charge.

Chapter 7. DFT Studies of Au<sub>1-4</sub> on the TiO<sub>2</sub> Anatase(101) Surface

Table 7.11: Charge distribution of Au<sub>1-4</sub> on the stoichiometric anatase(101) surface. Negatively charged atoms are highlighted in a green gradient, while positively charged atoms are highlighted with a red gradient.

Cluster	Surface Atoms			Cluster Atoms				Total Cluster Charge
	O <sub>3c</sub>	O <sub>2c</sub>	Ti <sub>5c</sub>	Au I	Au II	Au III	Au IV	
<b>NBO Charge Analysis</b>								
Bare Surface	-0.706	-0.583	1.462	-	-	-	-	-
Au <sub>1</sub>	-0.700	-0.622	1.135	0.319	-	-	-	0.319
Au <sub>2</sub> -A	-0.690	-0.712	0.930	0.175	0.314	-	-	0.489
Au <sub>2</sub> -B	-0.754	-0.722	0.909	0.124	0.391	-	-	0.515
Au <sub>3</sub> -A	-0.704	-0.750	0.961	0.280	0.275	0.026	-	0.581
Au <sub>3</sub> -B	-0.691	-0.727	1.051	0.310	0.220	0.244	-	0.774
Au <sub>3</sub> -C	-0.693	-0.732	0.945	0.294	0.295	0.015	-	0.604
Au <sub>3</sub> -D	-0.745	-0.735	0.975	0.178	0.284	0.004	-	0.466
Au <sub>4</sub> -A	-0.685	-0.706	1.035	0.141	0.200	0.168	0.286	0.795
Au <sub>4</sub> -B	-0.687	-0.701	0.996	0.286	0.217	0.157	0.115	0.775
Au <sub>4</sub> -C	-0.697	-0.741	0.935	0.319	0.089	0.028	0.138	0.574
Au <sub>4</sub> -D	-0.734	-0.605	0.943	0.046	0.215	0.251	0.159	0.671
<b>Löwdin Charge Analysis</b>								
Bare Surface	-0.415	-0.312	0.663	-	-	-	-	-
Au <sub>1</sub>	-0.395	-0.305	0.452	0.202	-	-	-	0.202
Au <sub>2</sub> -A	-0.397	-0.315	0.342	0.105	0.176	-	-	0.281
Au <sub>2</sub> -B	-0.421	-0.283	0.442	0.108	0.213	-	-	0.321
Au <sub>3</sub> -A	-0.405	-0.337	0.333	0.047	0.106	0.152	-	0.305
Au <sub>3</sub> -B	-0.399	-0.316	0.401	0.123	0.132	0.186	-	0.441
Au <sub>3</sub> -C	-0.401	-0.324	0.328	0.074	0.117	0.156	-	0.347
Au <sub>3</sub> -D	-0.399	-0.329	0.473	0.064	0.088	0.153	-	0.305
Au <sub>4</sub> -A	-0.403	-0.298	0.384	0.160	0.011	0.071	0.116	0.358
Au <sub>4</sub> -B	-0.395	-0.298	0.391	-0.005	0.096	-0.005	0.139	0.225
Au <sub>4</sub> -C	-0.399	-0.333	0.432	0.092	0.224	-0.044	0.196	0.468
Au <sub>4</sub> -D	-0.395	-0.312	0.446	0.144	-0.016	0.081	0.209	0.418
<b>Hirshfeld Charge Analysis</b>								
Bare Surface	-0.400	-0.332	0.713	-	-	-	-	-
Au <sub>1</sub>	-0.397	-0.334	0.605	0.196	-	-	-	0.196
Au <sub>2</sub> -A	-0.398	-0.300	0.574	0.052	0.140	-	-	0.192
Au <sub>2</sub> -B	-0.411	-0.349	0.611	0.057	0.155	-	-	0.212
Au <sub>3</sub> -A	-0.407	-0.324	0.534	0.169	0.111	-0.003	-	0.277
Au <sub>3</sub> -B	-0.402	-0.295	0.574	0.192	0.089	0.117	-	0.398
Au <sub>3</sub> -C	-0.402	-0.295	0.521	0.190	0.130	-0.007	-	0.313
Au <sub>3</sub> -D	-0.410	-0.304	0.596	0.169	0.078	0.001	-	0.248
Au <sub>4</sub> -A	-0.400	-0.294	0.568	0.019	0.149	0.075	0.086	0.329
Au <sub>4</sub> -B	-0.400	-0.295	0.570	0.148	0.106	0.148	-0.022	0.380
Au <sub>4</sub> -C	-0.400	-0.302	0.598	0.176	0.091	0.068	0.028	0.363
Au <sub>4</sub> -D	-0.407	-0.374	0.590	-0.047	0.138	0.196	0.061	0.348



For the adsorption of Au<sub>2</sub>-A, the total charge of the gold cluster sums to +0.489 due to charge flowing from the cluster to the O<sub>2c</sub> and Ti<sub>5c</sub> atoms, resulting in charges of -0.712 and +0.930 respectively. The majority of the charge on the Au<sub>2</sub>-A cluster is localised on the second Au atom, furthest from the surface. The O<sub>3c</sub> atom loses some electron charge, resulting in a charge of -0.690. The Au<sub>2</sub>-B cluster shows a similar effect, with an increased charge on the second Au atom, resulting in an overall cluster charge of +0.515, with O<sub>2c</sub> and Ti<sub>5c</sub> charges of -0.722 and +0.909 respectively. The nearby O<sub>3c</sub> atom gains -0.048 more charge than the bare surface. It should be noted that this O<sub>3c</sub> atom forms part of the next ridge along the [10 $\bar{1}$ ] direction of the stoichiometric surface.

The increased positive charge on the Au II atom for Au<sub>2</sub>-B may be due to the increased electron withdrawal effects from the O<sub>3c</sub> atom when in this configuration, compared with Au<sub>2</sub>-A or Au<sub>1</sub> that show little effect from the O<sub>3c</sub> atom. For both Au<sub>2</sub>-A and B, the O<sub>2c</sub> and Ti<sub>5c</sub> atoms gain electron charge relative to the bare surface, whereas the O<sub>3c</sub> sees little change, losing some charge for Au<sub>2</sub>, but gaining some charge for Au<sub>2</sub>-B.

Adsorption of the Au<sub>3</sub> isomers to the stoichiometric anatase(101) surface predicts an increase in positive charge over the clusters, however, the positive charge is distributed mainly between the Au I and Au II atoms for isomers A, C, and D, with the Au III remaining almost neutral. This results in a overall cluster charge of +0.581 for Au<sub>3</sub>-A, +0.604 for Au<sub>3</sub>-C, and +0.466 for Au<sub>3</sub>-D. For these three isomers, there is a significant flow of charge from the cluster to the surface atoms, manifesting as an increase in negative charge for the O<sub>2c</sub> atom, from -0.583 to -0.736 on average, and a decrease in positive charge for the Ti<sub>5c</sub> atom from +1.462 to +0.983 on average. For Au<sub>3</sub>-B, the charge on the cluster is more evenly distributed (+0.310 for Au I, +0.220 for Au II, and +0.244 for Au III), while having less charge flow to the surface atoms, resulting in O<sub>3c</sub>, O<sub>2c</sub>, and Ti<sub>5c</sub> atom charges of -0.691, -0.727, and +1.051 respectively. The O<sub>3c</sub> atom remains virtually unchanged for Au<sub>3</sub>-A at -0.704, while for Au<sub>3</sub>-C the O<sub>3c</sub> atom loses some charge to become -0.693, and for Au<sub>3</sub>-D, it gains charge to become -0.745.

The lack of charging for the Au III atom of isomers A, C, and D, could be due to its distant proximity and lack of interaction with the anatase surface owing to the orthogonal binding configuration. Au<sub>3</sub>-B on the other hand, which lies flat across the surface, has all three Au atoms in close proximity to the surface, resulting in charge flowing from each Au atom to the surface.

For the adsorption of the Au<sub>4</sub>-A and B isomers, the calculations predict all four Au atoms to develop positive charge, transferring charge to the surface, with the Au atoms residing between the O<sub>2c</sub> and O<sub>3c</sub> surface atoms developing the greatest positive, resulting in total cluster charges of +0.795 and +0.775, respectively. Binding of the Au<sub>4</sub>-A isomer results in the TiO<sub>2</sub> surface atoms developing similar charges to those of the Au<sub>4</sub>-B isomer. The O<sub>3c</sub> charges for these isomers are less than the bare surface, while the O<sub>2c</sub> and Ti<sub>5c</sub> atoms have gained charge from the clusters, due to the greater amount of interaction between these geometries and the O<sub>2c</sub> and Ti<sub>5c</sub> surface atoms. These two isomers produce similar charge transfer predictions due to their almost identical, but mirrored geometries; however, the Au<sub>4</sub>-A isomer still has the largest loss of charge of the Au<sub>4</sub> series.

The Au<sub>4</sub>-C isomer has the Au I atom develop a large positive charge of +0.319, with the Au II and Au III atoms remaining fairly neutral (+0.089 and +0.028), resulting in an overall cluster charge of +0.574. This cluster transfers charge to the surface O<sub>2c</sub> and Ti<sub>5c</sub> atoms, resulting in charges of -0.741 and +0.935 respectively, while the O<sub>3c</sub> atom remains virtually unchanged relative to the bare surface, with a charge of -0.697. The overall cluster charge of this isomer is the least of all the Au<sub>4</sub> clusters, although it has the greatest charge for the Au I atom, due to its unique geometric structure of a Au<sub>3</sub> trimer with an additional Au atom attached over the terrace as presented previously. It also has the greatest negative charge for the O<sub>2c</sub> atom of the Au<sub>4</sub> series on the stoichiometric surface.

For Au<sub>4</sub>-D, there is only a small positive charge of +0.046 for the Au I atom, with a distribution of charges for the Au II, Au III, and Au IV atoms of +0.215, +0.251, and +0.159, respectively, resulting in an overall cluster charge of +0.671. Charge transferred from the cluster to the surface O<sub>3c</sub> and Ti<sub>5c</sub> atoms results in charges of -0.734 and +0.943 respectively. This is the only isomer that produces an O<sub>3c</sub> atom whose charge is greater than that of the bare surface.

### 7.4.3 Au<sub>1-4</sub> on the Oxygen-Deficient Anatase(101) Surface

The charge distribution for the Au<sub>1-4</sub> clusters on the oxygen-deficient surface are summarised in Table 7.12. Upon adsorption of Au<sub>1</sub>, there is only a small transfer in charge, resulting in Au<sub>1</sub> having a charge of +0.096, while the undercoordinated Ti<sub>5c</sub> and

Ti<sub>4c</sub> atoms show a gain in charge to become +0.964 and +1.014 respectively, while a small amount of charge is also transferred to the O<sub>3c</sub> atom to become -0.721.

Table 7.12: Charge distribution of Au<sub>1-4</sub> on the oxygen-deficient anatase(101) surface. The Ti<sub>5c</sub> refers to the under-coordinated Ti site after oxygen removal. Negatively charged atoms are highlighted in a green gradient, while positively charged atoms are highlighted with a red gradient.

Cluster	Surface Atoms			Cluster Atoms				Total Cluster Charge
	O <sub>3c</sub>	Ti <sub>5c</sub>	Ti <sub>4c</sub>	Au I	Au II	Au III	Au IV	
<b>NBO Charge Analysis</b>								
Bare Surface	-0.757	1.168	1.385	-	-	-	-	-
Au <sub>1</sub>	-0.721	0.964	1.014	0.096	-	-	-	0.096
Au <sub>2</sub>	-0.710	0.933	0.563	0.166	0.148	-	-	0.314
Au <sub>3</sub> -A	-0.707	0.991	1.030	0.085	0.213	0.200	-	0.498
Au <sub>3</sub> -B	-0.701	0.927	1.078	0.069	0.119	-0.017	-	0.171
Au <sub>4</sub> -A	-0.703	0.974	1.086	0.051	0.119	0.013	0.176	0.359
Au <sub>4</sub> -B	-0.713	0.974	0.652	0.006	0.198	0.186	0.158	0.548
Au <sub>4</sub> -C	-0.704	1.003	0.611	0.293	0.256	-0.059	0.185	0.675
<b>Löwdin Charge Analysis</b>								
Bare Surface	-0.431	0.543	0.648	-	-	-	-	-
Au <sub>1</sub>	-0.411	0.436	0.472	0.178	-	-	-	0.178
Au <sub>2</sub>	-0.402	0.447	0.292	0.070	0.159	-	-	0.229
Au <sub>3</sub> -A	-0.398	0.454	0.498	0.097	0.033	0.183	-	0.313
Au <sub>3</sub> -B	-0.389	0.439	0.548	-0.024	0.075	0.111	-	0.162
Au <sub>4</sub> -A	-0.394	0.465	0.562	0.125	0.009	-0.014	0.084	0.204
Au <sub>4</sub> -B	-0.391	0.460	0.365	-0.075	0.187	0.043	0.172	0.327
Au <sub>4</sub> -C	-0.396	0.476	0.353	0.041	0.191	-0.059	0.183	0.356
<b>Hirshfeld Charge Analysis</b>								
Bare Surface	-0.414	0.575	0.602	-	-	-	-	-
Au <sub>1</sub>	-0.405	0.588	0.580	-0.029	-	-	-	-0.029
Au <sub>2</sub>	-0.401	0.585	0.558	-0.010	-0.018	-	-	-0.028
Au <sub>3</sub> -A	-0.403	0.580	0.570	-0.042	0.123	0.047	-	0.128
Au <sub>3</sub> -B	-0.399	0.575	0.615	-0.032	0.051	-0.020	-	-0.001
Au <sub>4</sub> -A	-0.403	0.588	0.614	-0.041	-0.017	0.036	0.051	0.029
Au <sub>4</sub> -B	-0.398	0.575	0.562	0.098	0.015	0.046	-0.012	0.147
Au <sub>4</sub> -C	-0.400	0.567	0.544	0.087	0.021	0.080	0.009	0.197



Adsorption of Au<sub>2</sub> shows a large transfer of charge from the Au<sub>2</sub> cluster to the surface, resulting in a total charge on the cluster of +0.314, while the charge gained by the surface Ti<sub>4c</sub> atom increases from +1.395 on the bare surface to +0.563. The O<sub>3c</sub> and Ti<sub>5c</sub> atoms gain a small amount of charge from the Au<sub>2</sub> cluster, developing charges of -0.710 and +0.933 respectively.

For both Au<sub>3</sub>-A and B isomers, the Au I atom bound in the position of the oxygen vacancy develops a very small positive charge of +0.085 and +0.069, respectively. The overall cluster charge transfer to the surface results in total cluster charges of +0.498 and +0.171 respectively. Adsorption of these clusters results in moderate charge transfer to the surface Ti<sub>5c</sub> and Ti<sub>4c</sub> atoms, while the nearby O<sub>3c</sub> atom loses some charge. The large difference in overall cluster charge of the two Au<sub>3</sub> isomers is due to the Au III atom of Au<sub>3</sub>-B withdrawing electron charge from the surface, most likely due to the orthogonal binding geometry of this isomer, with Au III being distant from the surface, while the Au<sub>3</sub>-A isomer lies flat across the surface. It is therefore surprising that the O<sub>3c</sub>, Ti<sub>5c</sub>, and Ti<sub>4c</sub> charges do not change much between the two isomers, perhaps indicating how well the electron charge can be delocalised throughout the surface. Note that Löwdin charge analysis does not predict the Au III atom to withdraw electron charge from the surface, instead predicting the Au III atom to donate charge to the surface and develop a positive charge of +0.111. However, Hirshfeld charge analysis predicts the same electron withdrawal effects as for the NBO charge analysis.

The Au<sub>4</sub>-A isomer, while having the greatest binding energy of all clusters in the study, has the least amount of charge transfer for the Au<sub>4</sub> series, with an overall cluster charge of only +0.359, due to poor charge transfer to the surface as shown by the very small positive charges on the Au I and Au III atoms (+0.051 and +0.013), which could be due to their distant proximity to the Ti<sub>4c</sub> and Ti<sub>5c</sub> atoms. The surface atoms for this configuration gain some charge for Ti<sub>5c</sub> and Ti<sub>4c</sub>, while the O<sub>3c</sub> atom loses some charge, resulting in less charge than the bare surface O<sub>3c</sub>. There are a number of discrepancies here between the different charge analysis methods, with Löwdin predicting a small negative charge on the Au III atom, and Hirshfeld predicting negative charges for Au I and Au II, with a barely charged Au<sub>4</sub> cluster of +0.029. Hirshfeld also predicts some charge transfer from the surface Ti<sub>5c</sub> and Ti<sub>4c</sub> atoms to the cluster as a result. The Hirshfeld method disagrees with the general trends predicted by both NBO and Löwdin.

Conversely, there is an increased amount of charge transfer to the surface for the Au<sub>4</sub>-B isomer and this results in the positive charge being shared between Au II, III, and IV (+0.198, +0.186, and +0.158). The surface Ti<sub>5c</sub> atom gains charge to become +0.974, while the Ti<sub>4c</sub> atom gains significantly more from the charge transfer, to become +0.652. The O<sub>3c</sub> atom loses some charge to become -0.713, similar to that of Au<sub>4</sub>-A. The Au<sub>4</sub>-C isomer has the greatest overall positive charge of +0.675, due to the significant levels charge transfer from the Au I and Au II atoms to the surface, despite the charge withdrawal of the Au III atom (-0.059). This results in a large amount of charge flow to Ti<sub>4c</sub>, developing a charge of +0.611, some charge flow to the Ti<sub>5c</sub> atom, developing a charge of +1.003, and charge is lost from the O<sub>3c</sub> atom to become -0.704. Löwdin predicts a similar transfer of charge for these two isomers, although Au I atom of Au<sub>4</sub>-A is slightly negative for this method. The large amount of charge flow to the Ti<sub>4c</sub> atom is due to the geometric configuration of Au<sub>4</sub>-B and C, which consists of a trimer with an additional Au atom over the nearby Ti<sub>5c</sub> (away from the oxygen defect site). This binding geometry results in Au II having exclusive binding to Ti<sub>4c</sub>, while Au III has exclusive binding to Ti<sub>5c</sub>, allowing for greater charge transfer. For the Au<sub>4</sub>-A isomer, the Au II atom is almost directly in the position of the oxygen vacancy, resulting in this atom being involved in shared binding between the Ti<sub>4c</sub> and Ti<sub>5c</sub> atoms.

#### 7.4.4 Discussion

Figure 7.35 shows the clear trends of increasing cluster positive charge and decreasing positive charge per Au atom within a cluster as the number of Au atoms bound to the stoichiometric surface is increased. The rate of decrease of positive charge per Au atom decreases as the number of Au atoms is increased, with NBO analysis actually predicting a small rise for the Au<sub>4</sub> cluster. For the oxygen-deficient surface, Figure 7.36 shows an increase in cluster positive charge as the number of Au atoms is increased up to three, after which there is a decline for the fourth Au atom. This trend is also reflected in the plot of per Au atom charge against the number of Au atoms. This is a significant variation from the trend observed for the Au clusters on the stoichiometric surface. Comparison between the different methods also shows that while the magnitude of the charges can vary substantially, the overall trend is the same. However, for some isomers on the

oxygen-deficient surface, Hirshfeld charge analysis predicts a small amount of charge flowing from the surface to the cluster, as opposed to donating charge.

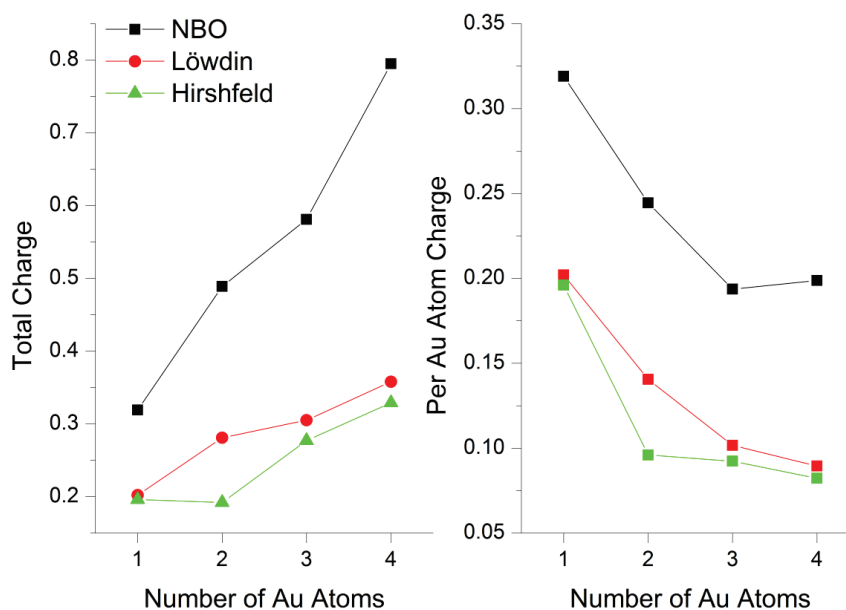


Figure 7.35: The change in the total cluster charge and per Au atom charge for the lowest energy isomer as the number of Au atoms bound to the stoichiometric surface are increased.

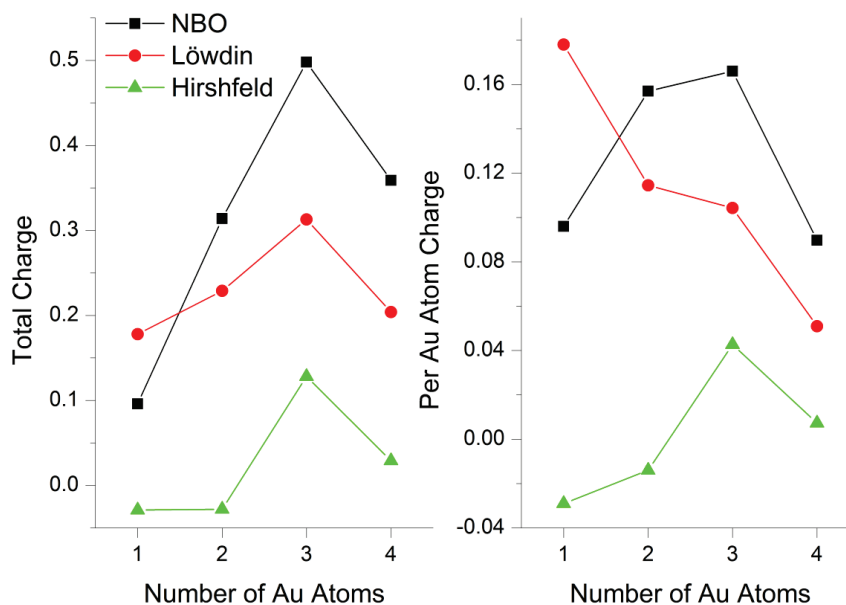


Figure 7.36: The change in the total cluster charge and per Au atom charge for the lowest energy isomer as the number of Au atoms bound to the oxygen-deficient surface are increased.

Comparing the overall levels of charge transfer from the clusters to the surface, Au<sub>4</sub>-A on the stoichiometric model has the greatest charge transfer of +0.795, followed closely by Au<sub>4</sub>-B at +0.775, and Au<sub>3</sub>-B at +0.774. Conversely for the oxygen-deficient surface, the Au<sub>4</sub>-C isomer has the greatest charge transfer of +0.675, followed by Au<sub>4</sub>-B at +0.548, and Au<sub>3</sub>-A at +0.498. The amount of charge transferred to the surface, and the degree to which the Au clusters lose charge, tends to increase as the number of Au atoms in the cluster increase, for both the stoichiometric and oxygen-deficient surface; however, the effect is more pronounced for the stoichiometric surface. The levels of charge transfer do not appear to correlate with the binding energies of the clusters to the surface.

Charge transfer to the stoichiometric surface typically results in the surface O<sub>2c</sub> and Ti<sub>5c</sub> atoms increasing in charge, with the Ti<sub>5c</sub> atoms gaining the most charge. However, the trend of increased charge transfer from the Au cluster as the number of Au atoms is increased does not appear to be reflected as prominently in the increase in charge for the surface atoms. Hirshfeld charge analysis predicts the charge to be somewhat distributed over the surface, so that nearby surface atoms further away from the binding site may also increase in charge. However, this is not predicted by NBO or Löwdin. The O<sub>3c</sub> atom is less predictable than that of O<sub>2c</sub> and Ti<sub>5c</sub>, tending to oscillate between charge gained and charge lost, and appears to be more sensitive to the binding geometry of the cluster.

These trends are also evident for Au<sub>1-4</sub> bound to the oxygen-deficient surface; albeit with smaller differences between the surface atom charges of the bare surface compared to when the Au clusters are adsorbed to the surface. There is also a small loss of charge for the O<sub>3c</sub> surface atoms, in contrast to increases in electron charge for Ti<sub>5c</sub> and Ti<sub>4c</sub> from their bare surface values. Of note is the large amount of charge transfer to the Ti<sub>4c</sub> atom for the Au<sub>2</sub>, Au<sub>4</sub>-B, and Au<sub>4</sub>-C structures, due the similar geometric arrangement of these clusters around the oxygen defect site.

## 7.5 Predicted Molecular Orbital Properties of Au<sub>1-4</sub> on Anatase(101) Surfaces

### 7.5.1 Stoichiometric and Oxygen-Deficient Anatase(101)

The calculations predict a HOMO-LUMO gap of 4.63 eV for the stoichiometric surface and 4.74 eV for the oxygen-deficient surface. These predictions are higher than the experimentally accepted value for the anatase band gap of 3.2 eV.<sup>60</sup> This may be related to the effect of increasing band gap energy with decreasing nanoparticle size,<sup>60</sup> given the small size of the model relative to that of bulk TiO<sub>2</sub>. This effect is illustrated when comparing the predicted HOMO-LUMO gap of the different model anatase surfaces, as shown in Figure 7.37. The Ti<sub>7</sub>O<sub>26</sub>H<sub>26</sub> and Ti<sub>18</sub>O<sub>57</sub>H<sub>42</sub> models are the same size as the regular and deep models created by Zapol and co-workers<sup>134</sup> that have been re-optimised at the same level of theory as this study. The Ti<sub>14</sub>O<sub>45</sub>H<sub>34</sub> is the model that has been used throughout this Chapter, while the Ti<sub>28</sub>O<sub>86</sub>H<sub>60</sub> is the extended model discussed previously that was used to investigate if larger models had an effect on the binding energy of the Au clusters. Lundqvist *et al.*<sup>527</sup> have found strong variations in the electronic properties, including HOMO-LUMO gaps, for TiO<sub>2</sub> cluster models smaller than ~1.2 nm in size, as well as band gap broadening as they decreased the size of their models from 2 to 1 nm. Their work also showed that band gaps predicted by hybrid functionals tend to be larger than what would be expected experimentally. Labat *et al.*<sup>528</sup> showed that there is a strong basis set and Hamiltonian dependency on the accuracy of the predicted band gap. They also suggested that hybrid functionals have the best compromise between accurate band gap energies and structural properties.

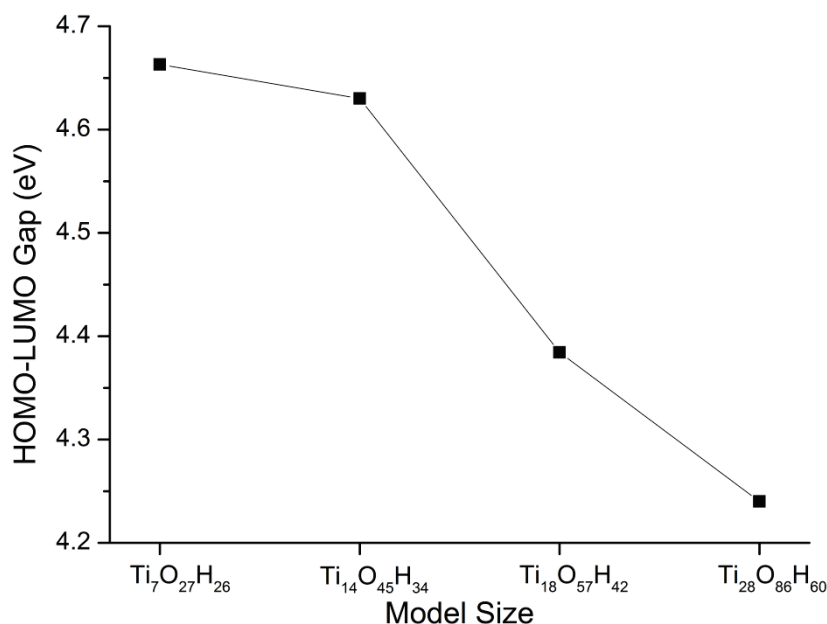


Figure 7.37: The decrease in the HOMO-LUMO gap as the size of the model anatase(101) surface is increased.

The density of states (DOS) for the stoichiometric and oxygen-deficient surfaces is presented in Figure 7.38. For the stoichiometric surface, the calculations predict the valence and conduction band edges to be at -7.72 eV and -3.09 eV relative to vacuum, respectively, while for the oxygen-deficient surface, the calculations predict the valence and conduction band edges to be -7.86 eV and -3.12 eV, respectively. There are multiple states at the valence and conduction bands predicted using this model, typically with ~20 states within 1 eV of a band edge. The calculations of the stoichiometric surface predict the valence and conduction bands to have strong O *p* and Ti *d* orbital character, as shown in the DOS of Figure 7.38, and the molecular orbital (MO) diagrams in Figure 7.39. These predictions agree with the widely accepted notion that the valence and conduction bands of stoichiometric TiO<sub>2</sub> are dominated by O<sub>2p</sub> and Ti<sub>3d</sub> electrons respectively.<sup>60</sup>

For the oxygen-deficient surface, there are two new occupied states within the band gap, which are attributed to the two unpaired electrons that arise from the two under-coordinated Ti atoms after the removal of the bridging O<sub>2c</sub> oxygen. These two states are clearly visible in the DOS of Figure 7.48. These new states are at -4.76 and -4.68 eV, and result in a SOMO-LUMO gap of only 1.56 eV. Note that for spin unrestricted calculations such as doublet or triplet states, the MOs consist of two sets of predicted states to account for opposing spins; one set for the spin-up electrons (alpha) and one set for the spin-down

electrons (beta). The SOMO at -4.68 eV consists primarily of Ti *d* character, with minor *s* and *p* character, and hybridisation with oxygen 2*p* orbitals, while the SOMO-1 state at -4.76 eV consists mainly of Ti 3*d*<sub>z<sup>2</sup></sub> character and oxygen 2*p* character. These two states are attributed to the well-known Ti 3*d* defect states that appear below the conduction band edge for TiO<sub>2</sub> surfaces with oxygen vacancies, and are localised around the neighbouring Ti atoms (See Chapter 1).

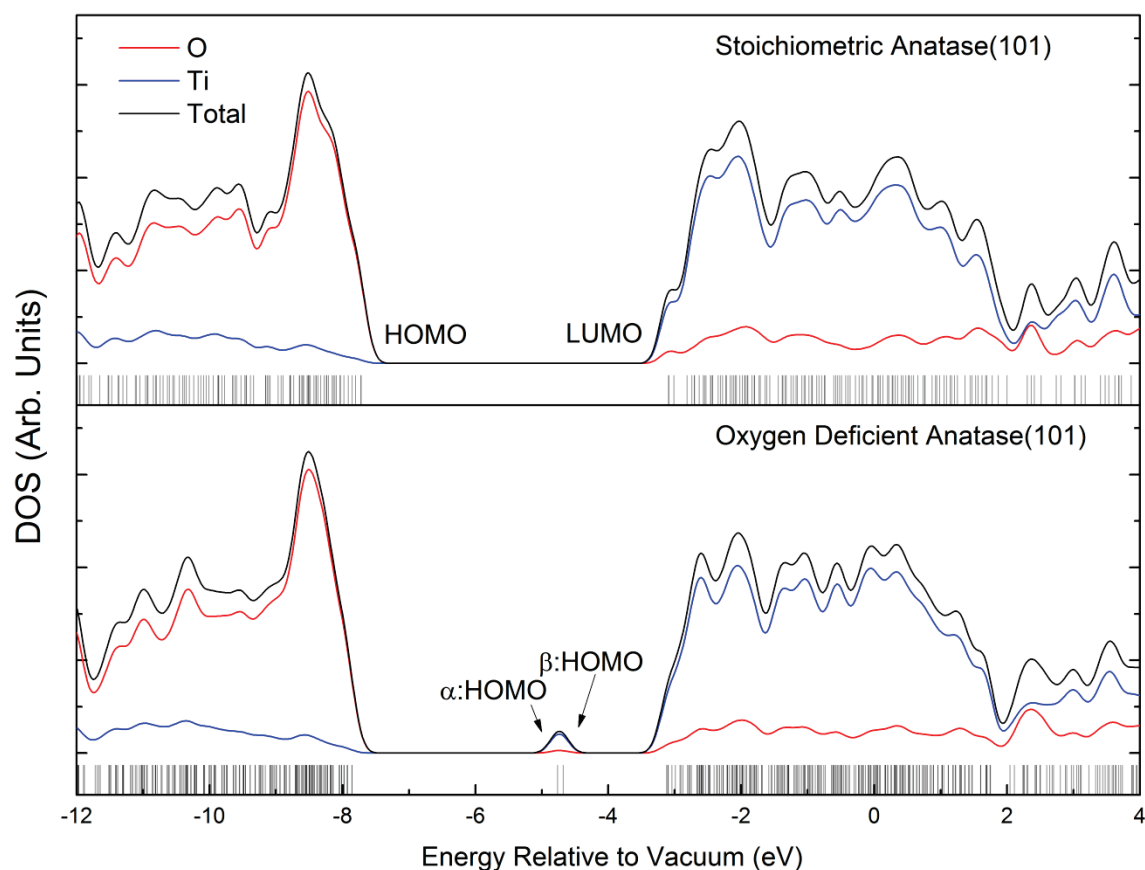


Figure 7.38: The density of states for the stoichiometric and oxygen-deficient surfaces. The oxygen-deficient surface shows two new occupied states in the band gap at -4.76 and -4.68 eV.

It should be noted that the calculation of the partial density of state contributions is based on the overlap matrix and Mulliken population analysis, which is known to be very basis set dependent and does not take into account differences in electronegativity between different atoms.<sup>472</sup> Nevertheless, it still provides a reasonable prediction of which atoms are contributing to each molecular orbital in a qualitative way. The PDOS analysis employed here also sums the contributions from hydrogens into the oxygen contribution.

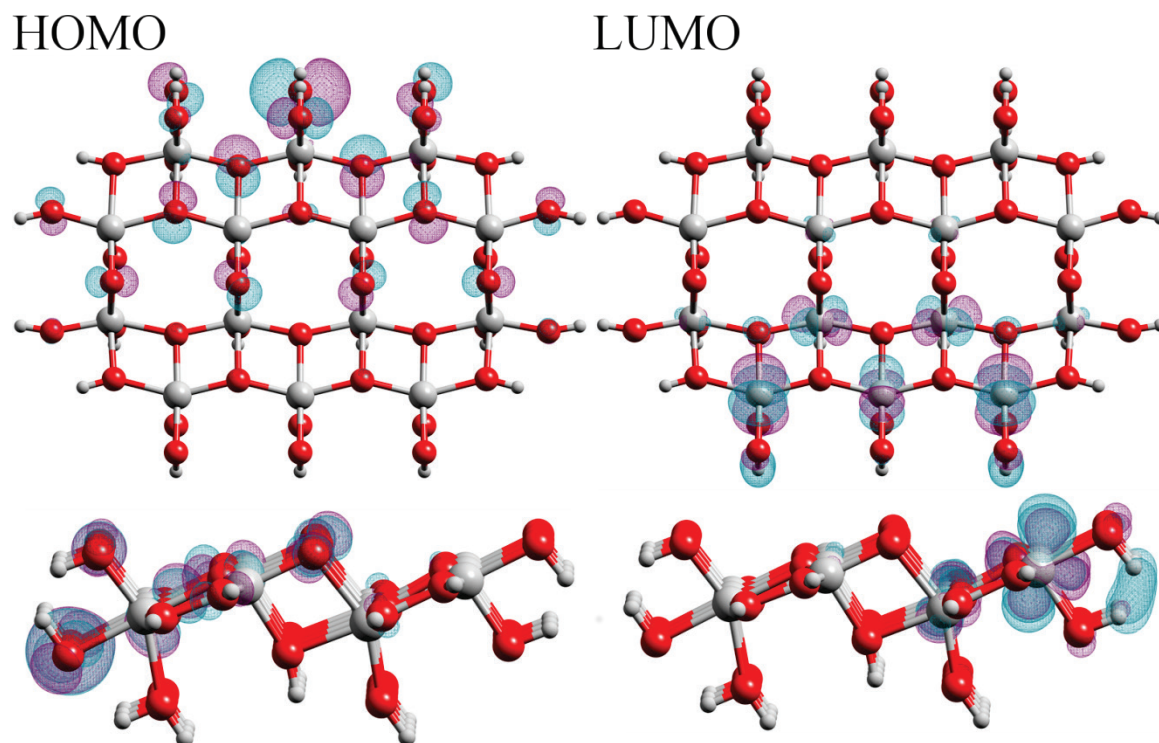


Figure 7.39: Top and side wireframe view of the HOMO and LUMO of the stoichiometric surface.

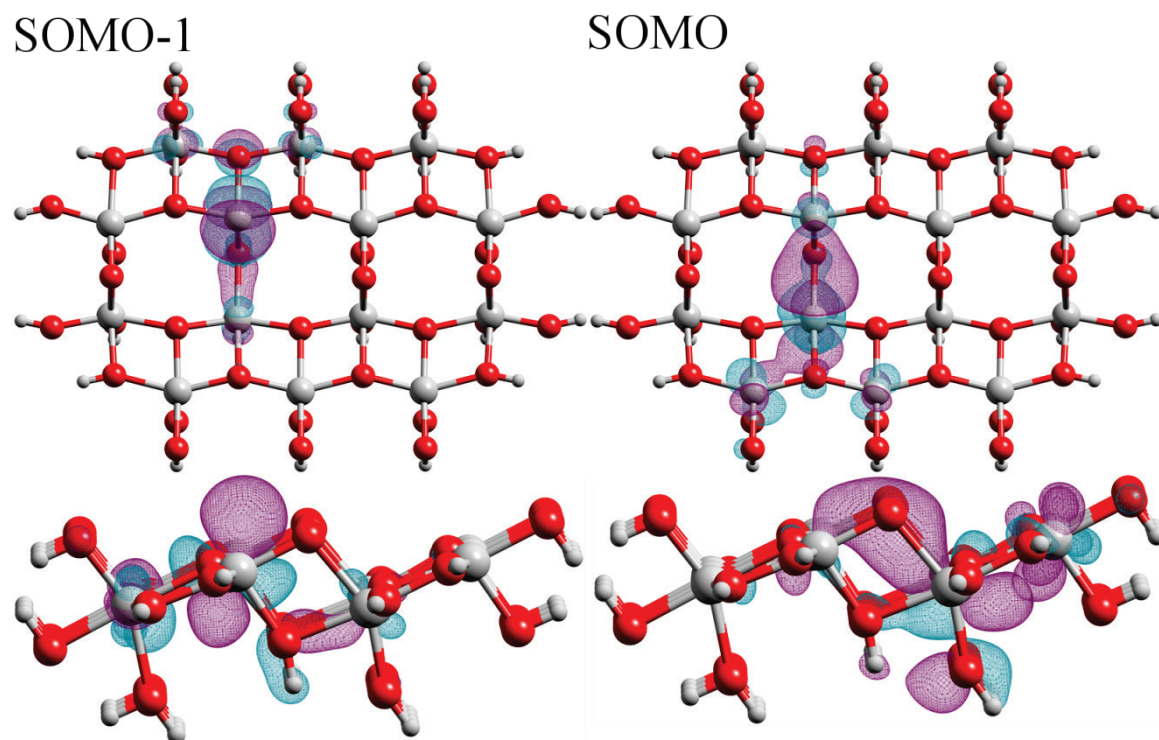


Figure 7.40: Top and side wireframe view of the alpha SOMO-1 and SOMO of oxygen-deficient anatase(101).

7.5.2 Au<sub>1-4</sub> on the Stoichiometric Anatase(101) Surface

Table 7.13 summarises the % contributions and orbital character for the HOMOs and LUMOs of the Au<sub>1-4</sub> isomers on the stoichiometric surface discussed in the following sections. Many of these parameters are also visualised in the DOS plots and isosurface illustrations in Figures presented in the following sub-sections.

Table 7.13: Summary of the key predicted orbital parameters of the HOMO and LUMO states for Au<sub>1-4</sub> on the stoichiometric surface.

Isomer	HOMO-LUMO gap (eV)	MO	Contributions (%)			Orbital Character
			Au	Ti	O	
<b>Au<sub>1</sub></b>	2.02	$\beta$ :LUMO	63	29	7	Au <i>s</i> , Ti <i>d</i> , and Ti <i>p</i>
		$\alpha$ :HOMO	77	14	9	Au <i>s</i> and Ti <i>d</i>
		$\beta$ :HOMO	77	3	21	Au <i>d</i> and O <i>p</i>
<b>Au<sub>2</sub>-A</b>	2.81	LUMO	0	83	17	Ti <i>p</i> , <i>d</i> and O <i>p</i>
		HOMO	77	13	10	Au <i>s</i> , Ti <i>p</i> , minor Au <i>p</i> and Ti <i>s</i>
		HOMO-1	84	3	13	Au <i>d</i> , minor Au <i>s</i> and Ti <i>p</i>
<b>Au<sub>2</sub>-B</b>	2.98	LUMO	0	84	16	Ti <i>p</i> , <i>d</i> , and O <i>p</i>
		HOMO	81	9	10	Au <i>s</i> , Ti <i>p</i> , minor Au <i>p</i> and Ti <i>s</i>
		HOMO-1	78	4	18	Au <i>d</i> , minor Au <i>s</i> and Ti <i>p</i>
<b>Au<sub>3</sub>-A</b>	1.54	$\beta$ :LUMO	0	84	16	Ti <i>p</i> , <i>d</i> , and O <i>p</i>
		$\alpha$ :HOMO	44	45	11	Ti <i>p</i> , <i>d</i> , and Au <i>s</i>
<b>Au<sub>3</sub>-B</b>	1.61	$\beta$ :LUMO	49	43	9	Ti <i>p</i> , <i>d</i> , and O <i>p</i>
		$\alpha$ :HOMO	46	45	9	Ti <i>p</i> , <i>d</i> , and Au <i>s</i>
<b>Au<sub>3</sub>-C</b>	1.39	$\beta$ :LUMO	0	84	16	Ti <i>p</i> , <i>d</i> , and O <i>p</i>
		$\alpha$ :HOMO	42	46	12	Ti <i>p</i> , <i>d</i> , and Au <i>s</i>
<b>Au<sub>3</sub>-D</b>	1.60	$\beta$ :LUMO	92	1	7	Ti <i>s</i> , <i>p</i> , Au <i>s</i> , minor Ti <i>d</i> and Au <i>p</i>
		$\alpha$ :HOMO	64	32	4	Au <i>s</i> , <i>d</i> , and minor Ti <i>p</i>
<b>Au<sub>4</sub>-A</b>	2.05	LUMO	0	84	17	Ti <i>p</i> , <i>d</i> , and minor O <i>s</i> , <i>p</i>
		HOMO	66	27	7	Au <i>s</i> , Ti <i>p</i> , and minor Au <i>d</i>
<b>Au<sub>4</sub>-B</b>	2.00	LUMO	0	83	17	Ti <i>p</i> , <i>d</i> , and minor O <i>s</i> , <i>p</i>
		HOMO	66	26	8	Au <i>s</i> , Ti <i>p</i> , and minor Au <i>d</i>
<b>Au<sub>4</sub>-C</b>	2.60	LUMO	0	84	16	Ti <i>p</i> , <i>d</i>
		HOMO	63	31	6	Au <i>s</i> , <i>p</i> , Ti <i>s</i> , minor Ti <i>p</i> and Au <i>d</i>
<b>Au<sub>4</sub>-D</b>	2.54	LUMO	0	84	16	Ti <i>d</i> , <i>p</i>
		HOMO	64	30	6	Au <i>s</i> , Ti <i>p</i> , and Au <i>d</i>

### 7.5.2.1 Au<sub>1</sub> and Au<sub>2</sub>

Upon adsorption of Au<sub>1</sub> to the stoichiometric surface there are numerous states introduced at the edge of the valence and conduction band. Most significantly, the appearance of an occupied orbital in the middle of the band gap, at -5.25 eV, as shown in Figure 7.41. This new alpha HOMO results in a HOMO-LUMO gap of only 2.02 eV. The proportional contributions of the partial DOS displayed in Figure 7.41 show that this alpha HOMO consists primarily of Au contributions (77%) while the new beta LUMO, which resides at -3.23 eV, consists of 63% Au contribution. In contrast, the alpha LUMO has no Au character whatsoever.

There are many states deeper in the valence band that also contain significant amounts of Au character, ranging from 20% up to 91%, starting from the alpha HOMO at -5.25 eV, down to -7.96 eV. These states have large contributions from Au *d* orbitals, with minor O *p* orbital character. The isosurface of four important MOs near the band gap are presented in Figure 7.42, showing the Au *s* and Ti *d* character of the alpha HOMO, as well as the large contribution to the beta LUMO from the Au cluster, with some small contribution from Ti *d* and less so Ti *p* orbitals. Determination of the atomic orbitals involved in a state is achieved by using Chemcraft's MO analysis of eigenvalue coefficients and visual inspection of the MO isosurface.

The alpha HOMO for Au<sub>1</sub>/anatase is 2.47 eV higher in energy than the valence band edge for the bare surface, while the beta LUMO is 0.11 eV lower in energy than the conduction band edge of the bare surface. These shifts can be easily visualised by comparing the positions of the dashed lines in Figure 7.41, which represent the positions of the valence and conduction bands of the bare stoichiometric surface, to the positions of the new states introduced by the addition of the Au atom to the surface.

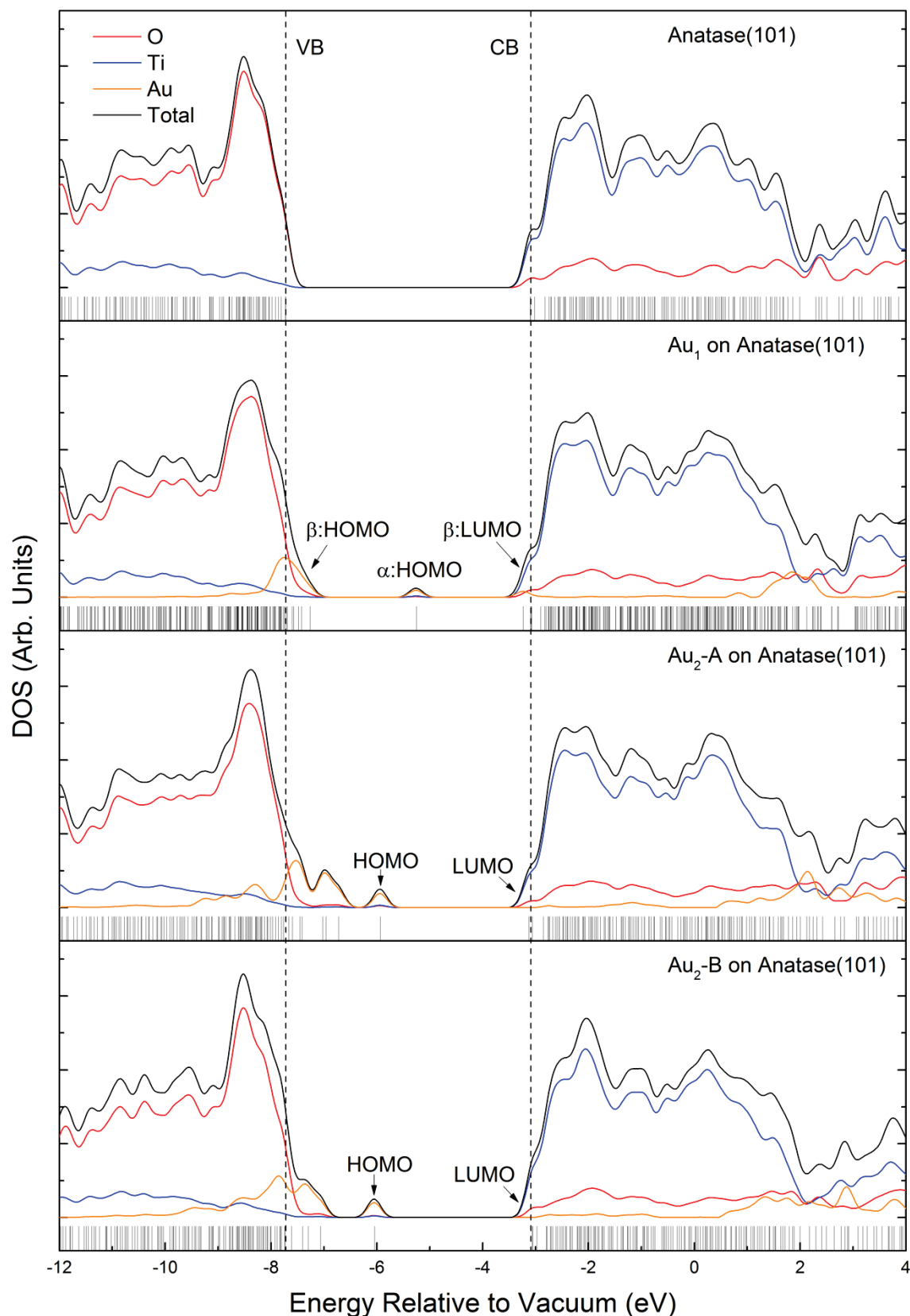


Figure 7.41: The density of states for the stoichiometric surface before and after adsorption of Au<sub>1</sub> and Au<sub>2</sub> clusters. VB and CB indicate the calculated position of the valence and conduction band edges of the bare stoichiometric surface.

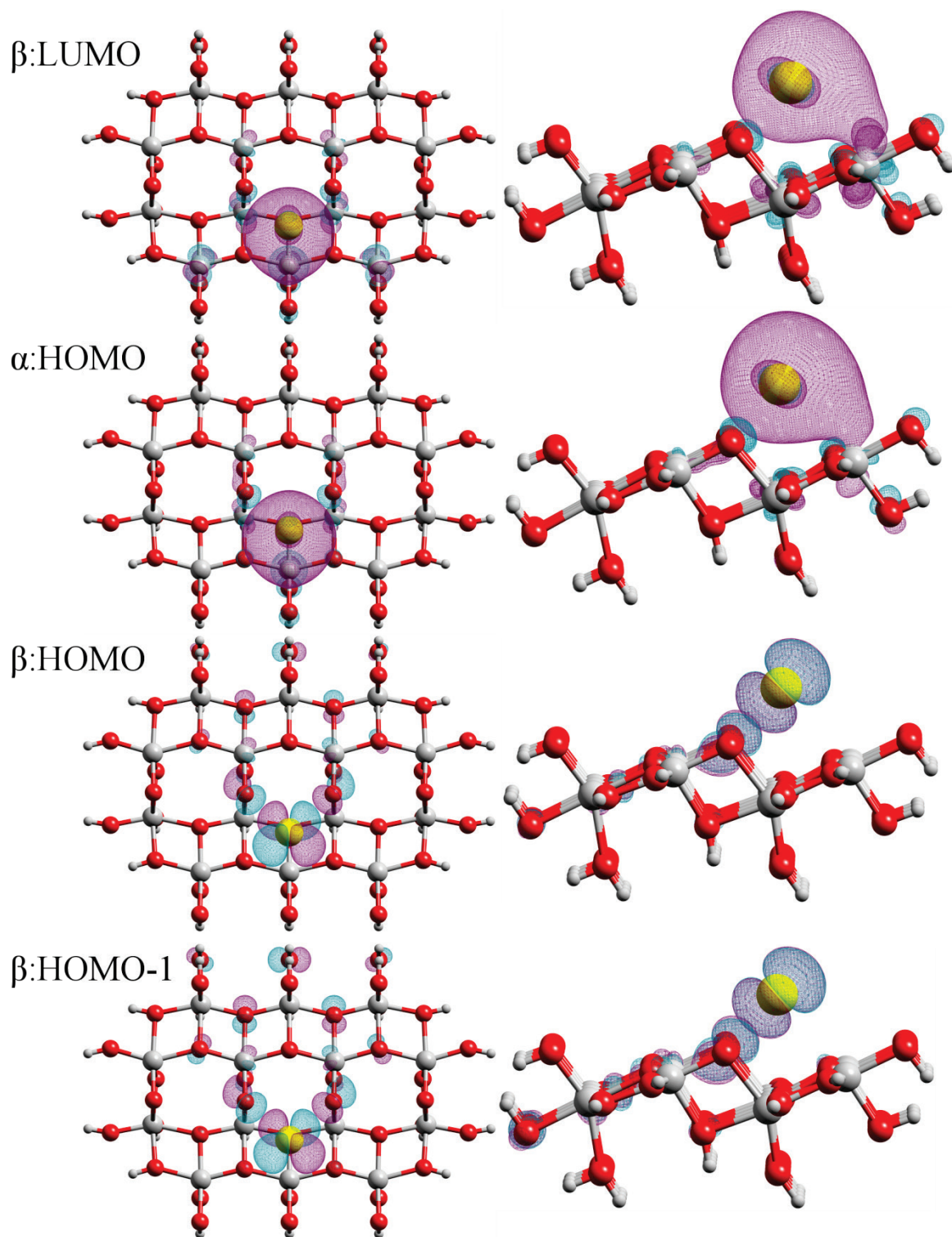


Figure 7.42: Top and side wireframe view of the beta LUMO, alpha HOMO, beta HOMO, and beta HOMO-1 of Au<sub>1</sub> on the stoichiometric surface.

For the Au<sub>2</sub>-A and Au<sub>2</sub>-B isomers adsorbed to stoichiometric anatase(101), multiple new occupied states are predicted within and above the valence band edge of anatase, as shown in Figure 7.41. The new HOMO and LUMO for Au<sub>2</sub>-A resides at -5.93 and -3.12 eV respectively, while for Au<sub>2</sub>-B it resides at -6.04 and -3.06 eV. This results in a HOMO-LUMO gap of 2.81 eV for Au<sub>2</sub>-A and 2.98 eV for Au<sub>2</sub>-B. For both isomers, there are multiple states within the valence band, ranging from  $\sim$ -7.66 eV up to the HOMOs. The LUMO of these isomers contain no Au contribution, consisting entirely of TiO<sub>2</sub> orbitals. For both Au<sub>2</sub>-A and Au<sub>2</sub>-B, the HOMO is predicted to have a large proportion of Au *s* and Ti *p* orbital character, with total Au contributions of 77% for Au<sub>2</sub>-A and 81% for Au<sub>2</sub>-B. An example of these molecular orbitals are shown in Figure 7.43 for Au<sub>2</sub>-A. Compared with the HOMO, the HOMO-1 state contains markedly different orbital contributions, with Au *d* orbitals forming the primary component of this MO, with minor contributions from Au *s* and Ti *p* orbitals.

The HOMO state introduced by both Au<sub>2</sub> clusters is  $\sim$ 0.75 eV lower in energy compared with those introduced for the Au<sub>1</sub> cluster, placing them closer to the original valence band of unmodified stoichiometric anatase(101). The large number of states that reside at the edge of the band gap for the Au<sub>2</sub> isomers extends to higher energies and therefore further into the band gap than for Au<sub>1</sub>, as shown in Figure 7.41. There are also many more unoccupied and virtual states with high Au contributions predicted to be further into the conduction band than for the Au<sub>1</sub> cluster. Compared with Au<sub>1</sub>, there are no significant contributions from the Au<sub>2</sub> clusters to the edge of the conduction band, leaving the edge of the conduction band almost completely unmodified compared with that of the bare surface. Also of note are the significant differences between atomic orbital compositions of the frontier orbitals for Au<sub>2</sub>, compared with those of Au<sub>1</sub>.

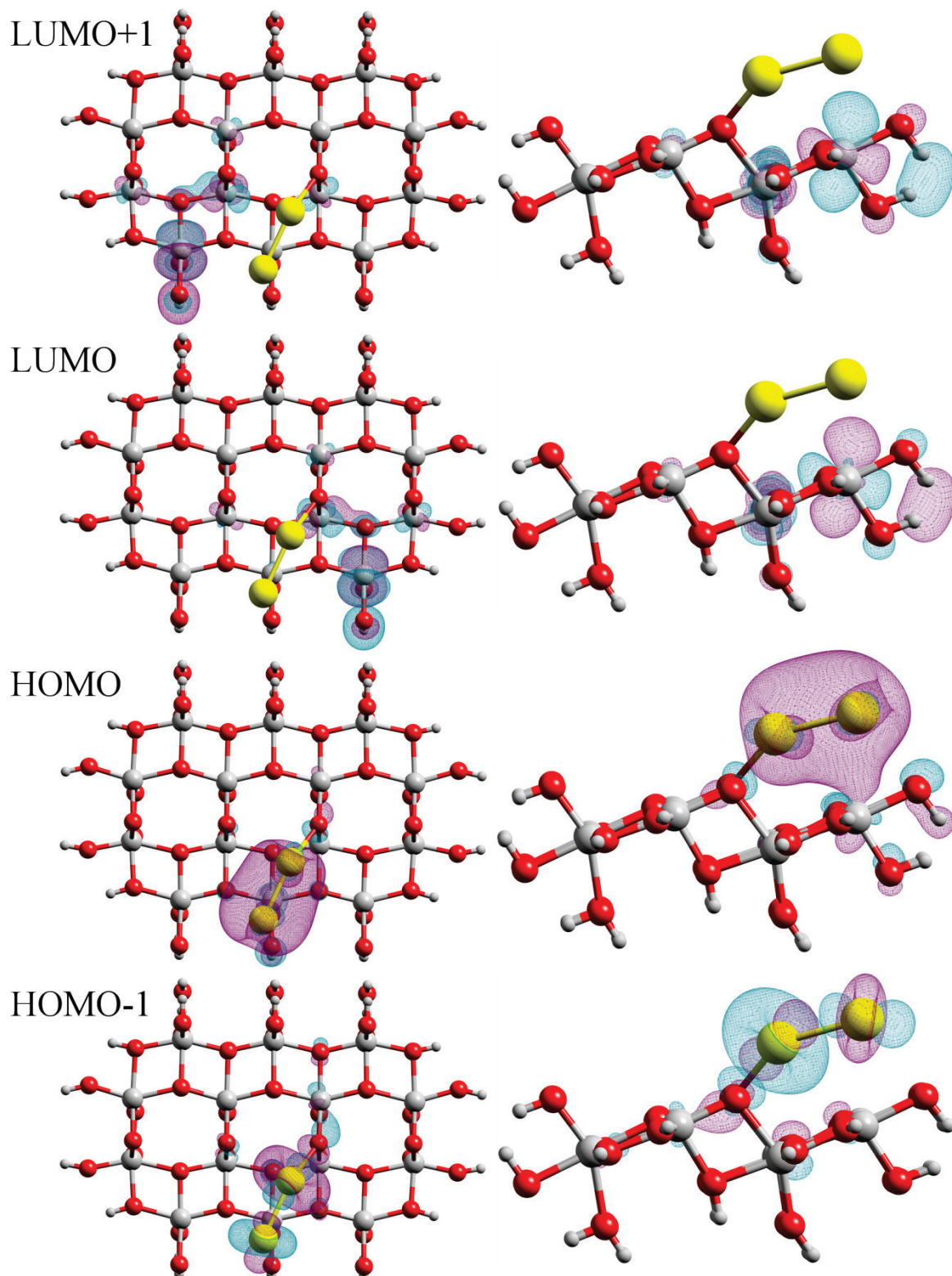


Figure 7.43: Top and side wireframe view of the LUMO+1, LUMO, HOMO, and HOMO-1 of Au<sub>2</sub>-A on the stoichiometric surface.

### 7.5.2.2 Au<sub>3</sub>

Adsorption of Au<sub>3</sub>-A to the stoichiometric surface results in the introduction of a multitude of new states at the edge of the valence band and a single state within the band gap, as shown in Figure 7.44. The alpha HOMO within the band gap at -4.56 eV consists primarily of Au and Ti contributions, with Ti *p*, *d*, and Au *s* orbital character, as shown in Figure 7.45. The beta LUMO resides at -3.02 eV, consisting of 84% Ti contribution and 16% O, with Ti *p*, *d*, and O *p* character, and results in a HOMO-LUMO gap of 1.54 eV.

The first few MOs going deeper into the valence band from -6.89 down to -7.67 eV contain Au contributions >71%, followed by multiple states deeper into the valence band with contributions from Au ranging from less than 5% to 50 %, and these are clearly visible in the DOS of Figure 7.44. There is a single state in the conduction band with significant Au contribution at -2.86 eV, consisting of a large contribution from the Au *s* orbitals, mixed with Ti *p* and *d* orbitals.

For Au<sub>3</sub>-B, the HOMO-LUMO gap increases to 1.61 eV due to the shift in the alpha HOMO from -4.56 to -4.91 eV and the shift in the beta LUMO from -3.02 to -3.30 eV. The alpha HOMO of this isomer is similar to that of Au<sub>3</sub>-A, albeit with added Au *p* and *d* orbital character that is not as strongly predicted for Au<sub>3</sub>-A. There is a similar array of MOs ranging from the alpha HOMO down to -7.60 eV containing large contributions of Au, although the majority of these states have shifted deeper in the valence band, and are easily visible in the DOS plots for this isomer in Figure 7.44. Comparison between the beta LUMO of Au<sub>3</sub>-B vs Au<sub>3</sub>-A, there are significant changes due to the variation in geometry, with contributions of 49% Au, 9% O, and 43% Ti. A similar state is seen higher in the conduction band for Au<sub>3</sub>-A, but is actually the LUMO for Au<sub>3</sub>-B. There are no other states at the edge of the conduction band with significant levels of Au contributions for this isomer.

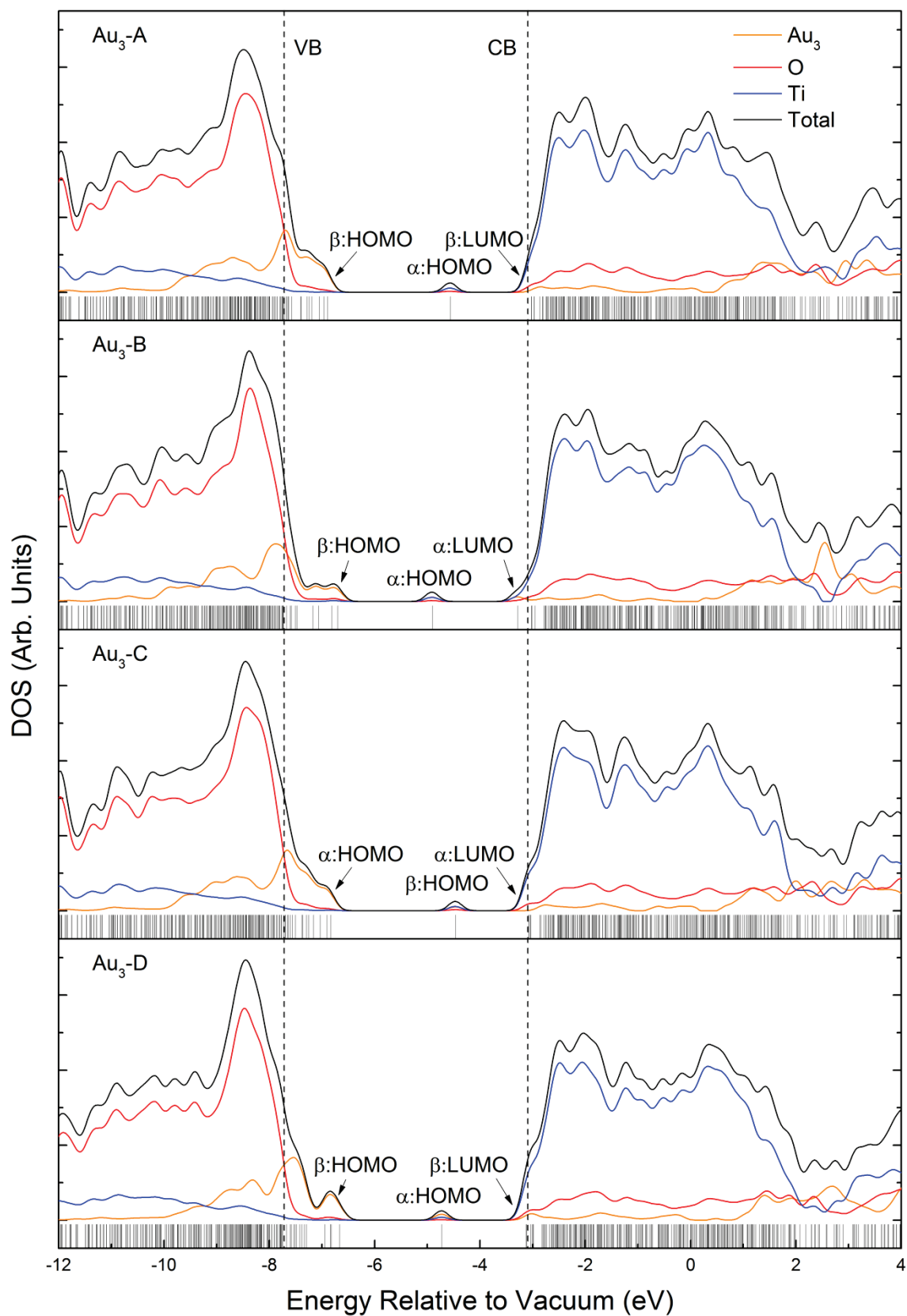


Figure 7.44: The density of states for the stoichiometric surface after adsorption of Au<sub>3</sub> clusters. VB and CB indicate the calculated position of the valence and conduction band edges of the bare stoichiometric surface.

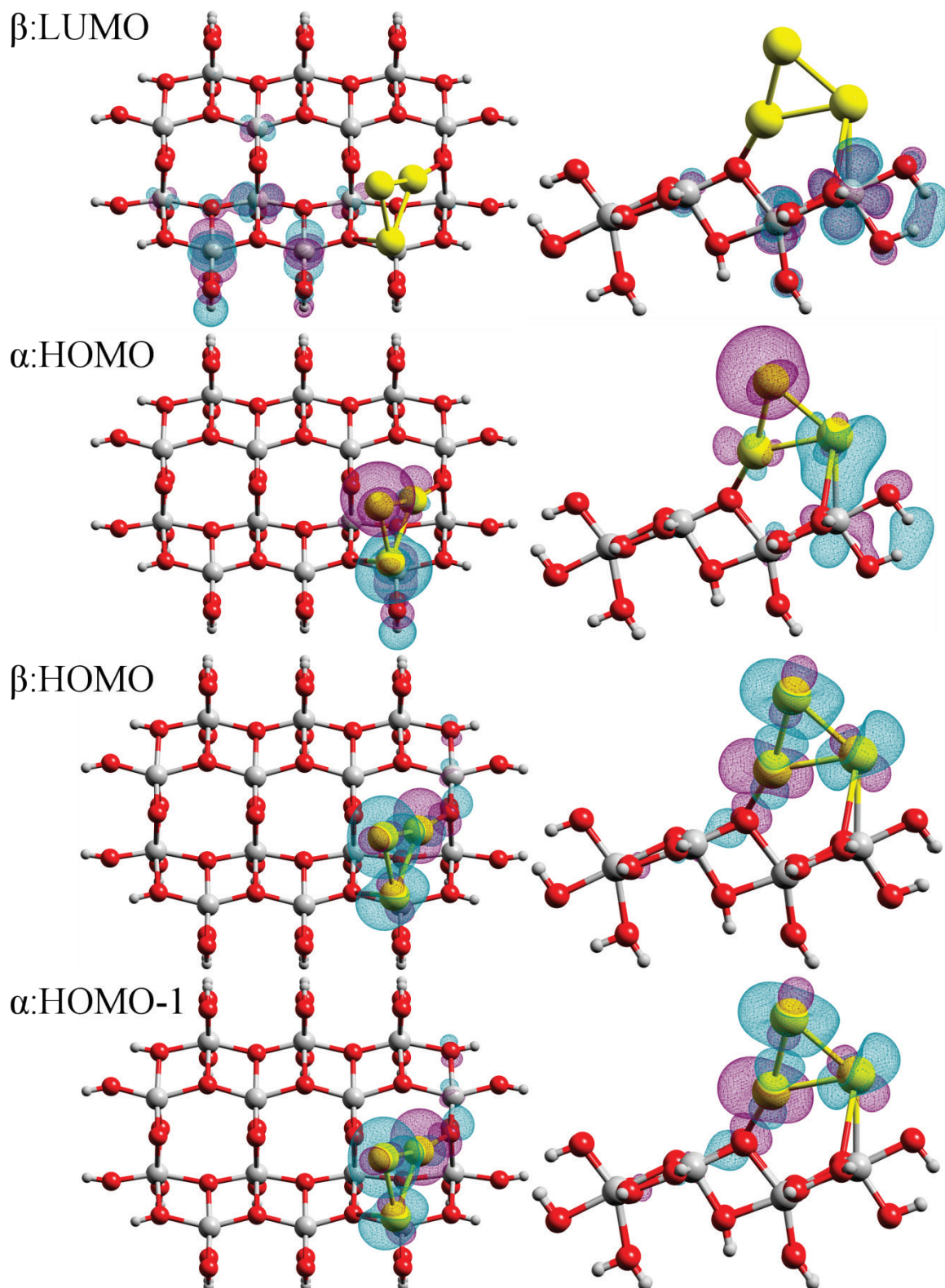


Figure 7.45: Top and side wireframe view of the beta LUMO, alpha HOMO, beta HOMO, and alpha HOMO-1 for Au<sub>3</sub>-A on the stoichiometric surface.

For Au<sub>3</sub>-C, the HOMO-LUMO gap is calculated to be 1.39 eV, the lowest of all the Au<sub>3</sub> isomers, due to the shift in the alpha HOMO to -4.46 eV and a shift in the LUMO to -3.07

eV. The alpha HOMO and LUMO have almost identical contribution and orbital makeup as for the Au<sub>3</sub>-A isomer; this is to be expected, given the almost identical geometry of the two isomers, as it is merely shifted along the [010] direction. However, the Au<sub>3</sub>-C isomer also has a state at the edge of the conduction band with large contributions from Au of 38%, along with an array of MOs stretching through the edge of the valence band with significant levels of Au contribution. This is a very similar DOS to that discussed previously for Au<sub>3</sub>-A. All other states around the band gap, including the beta HOMO and alpha HOMO-1, show identical DOS contribution and orbital characteristics to that of the Au<sub>3</sub>-A isomer.

For Au<sub>3</sub>-D, the HOMO-LUMO gap increases to 1.60 eV, due to the shift in the alpha HOMO to -4.72 and a shift in the beta LUMO to -3.12 eV. The alpha HOMO has a 20% greater contribution from Au compared with the same orbital for Au<sub>3</sub>-A. This MO contains large contributions of Ti *s*, *p*, and Au *s* atomic orbitals, with minor contributions from Ti *d* and Au *p* atomic orbitals. The MO visualisations of this isomer are available in Appendix B and show decreased hybridisation between the Au cluster and orbitals from the surface, with greater orbital overlap between the two Au atoms above the O<sub>2c</sub> atoms. This geometric configuration decreases the amount of contact between the Au atom and the Ti<sub>5c</sub> atom, which results in a significant effect on the amount of hybridisation with the cluster. There is a similar effect predicted for the beta HOMO, which has a 48% increase in Au contributions, displaying Au *s*, *d*, and minor Ti *p* orbital character.

Close inspection of the Au states around the edge of the valence band reveals that there is a small decrease in the density of states at -7.2 eV, before increasing again as energy decreases, and following a pattern similar to that of Au<sub>3</sub>-A and C. These states between the alpha HOMO and -7.2 eV show very high contributions (> 80%) of Au. There is also a state closer to the edge of the conduction band for this isomer than that observed for the others, with 44% Au contribution, which is the beta LUMO+1 state. In addition, the beta LUMO+3 state also has a high Au contribution of 21%, while other Au<sub>3</sub> isomers have only one state in the conduction band which feature good overlap between the Au orbitals and those of the surface.

The Au<sub>3</sub> isomer series also show a large shift in HOMO-LUMO gap, from 1.54 eV for A, 1.61 eV for B, 1.39 eV for C, and 1.60 eV for D. The orthogonal binding geometries of isomers A and C appear to lead to the smallest band gap when bound across the O<sub>3c</sub> and

Ti<sub>5c</sub>, in contact with the O<sub>2c</sub>. This is accompanied by a small shift in the HOMO state residing in the band gap between the different isomers. The small number of states with Au contribution within the conduction band also shifts significantly between the different isomers.

### 7.5.2.3 Au<sub>4</sub>

The DOS for the Au<sub>4</sub> series adsorbed to the stoichiometric surface are presented in Figure 7.46. For Au<sub>4</sub>-A, the HOMO is calculated to be in the middle of the band gap at -5.07 eV, with the LUMO at the edge of the conduction band at -3.03 eV, resulting in a HOMO-LUMO gap of 2.05 eV. The HOMO has a 66% contribution from Au, with atomic orbital character consisting primarily of Au *s* and Ti *p*. As shown in the HOMO isosurface visualisation in Figure 7.47, there is a notable level of orbital overlap between that of the Au atoms and the surface Ti<sub>5c</sub> atom. The HOMO-1 also shows the large amount of overlap with the O<sub>2c</sub> atom, with 80% Au and 14% O contribution. The LUMO contains no contribution from Au, consisting mainly of Ti *p*, *d*, and O *s* orbitals. There are no states at the conduction band edge with significant levels of Au contribution, until approaching the region near -1.77 eV. There are a number of states at the edge of the valence band containing large Au percentage, which decreases in contribution at -7.45 eV, yet still maintaining notable levels of Au contribution deeper in the valence band until reaching -10 eV.

For the Au<sub>4</sub>-B isomer the HOMO-LUMO gap is calculated to be 2.00 eV due to a small shift in the HOMO to -5.11 eV and a small shift in the LUMO to -3.11 eV. The atomic contributions to the HOMO and LUMO of this isomer are almost identical to that of Au<sub>4</sub>-A, along with a similar DOS throughout the valence band and the conduction band. This is unsurprising given the similar, but inverted binding geometry of this isomer along the [010] direction, and the similar binding energies which are only 0.05 eV apart.

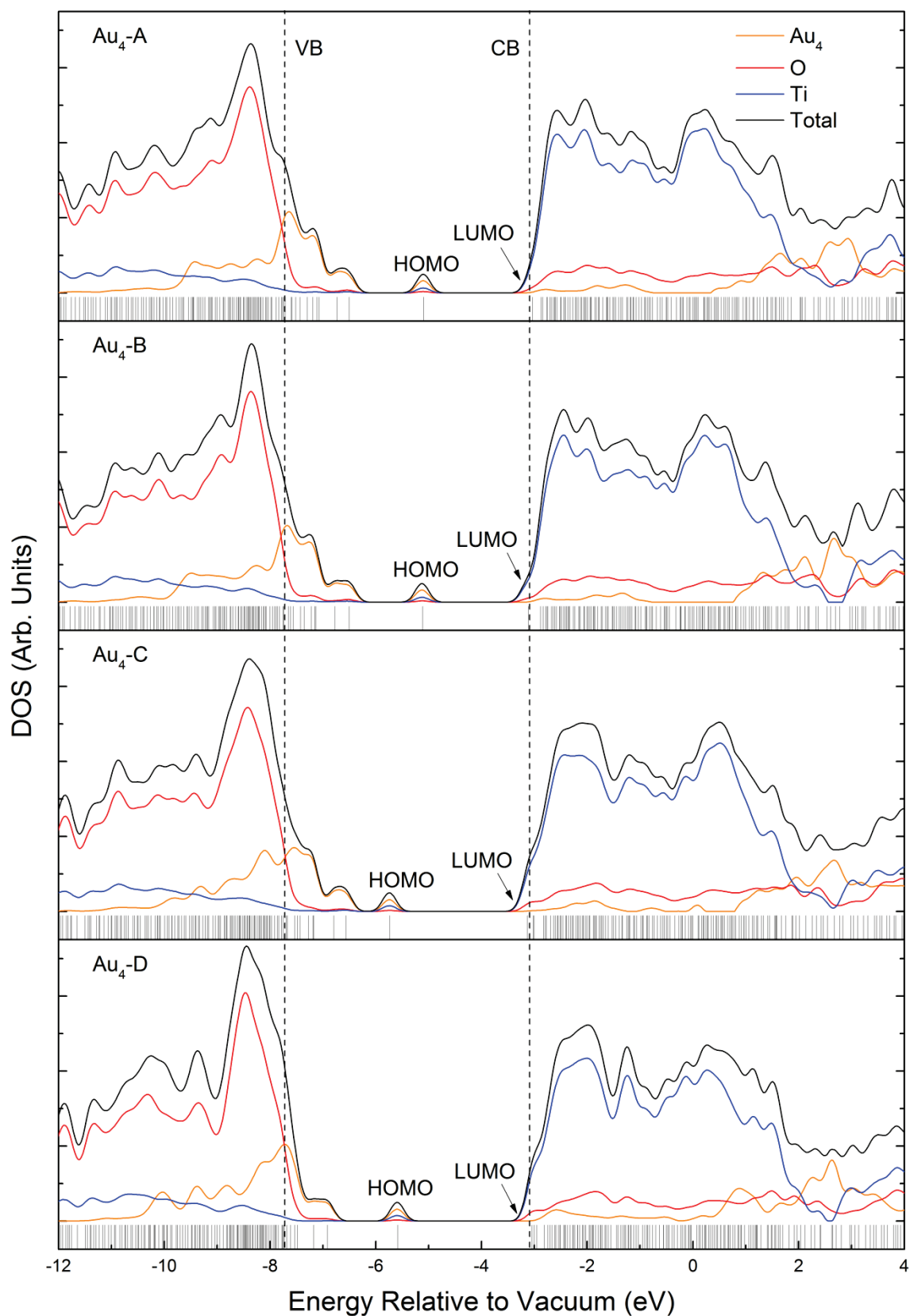


Figure 7.46: The density of states for the stoichiometric surface after adsorption of Au<sub>4</sub> clusters. VB and CB indicate the calculated position of the valence and conduction band edges of the bare stoichiometric surface.

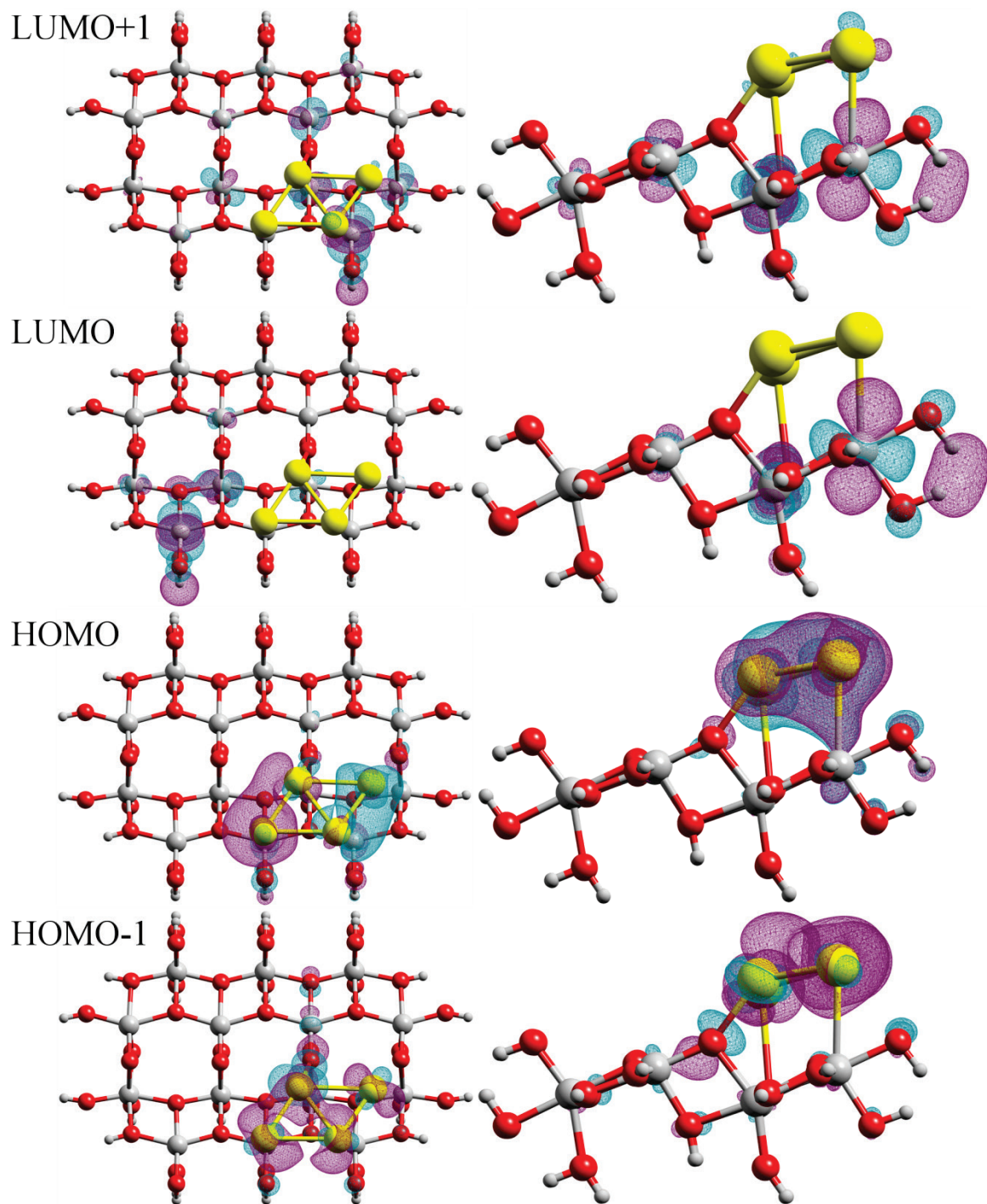


Figure 7.47: Top and side wireframe view of the LUMO+1, LUMO, HOMO, and HOMO-1 for Au<sub>4</sub>-A on the stoichiometric surface.

For the Au<sub>4</sub>-C isomer, the HOMO-LUMO gap is calculated to be much larger than that of Au<sub>4</sub>-A and B, at 2.60 eV, due to the large shift in the HOMO towards the valence band to -5.73 eV, and a smaller shift in the LUMO to -3.13 eV. The shifted HOMO and LUMO has a similar % contribution to that of the other Au<sub>4</sub> isomers. Analysis of the AOs that contribute to the HOMO shows subtle changes, with this MO consisting primarily of Au *s*, *p*, and Ti *s* character, while the LUMO consists primarily of Ti *p* and *d* states as expected.

For the Au<sub>4</sub>-D isomer, the HOMO-LUMO gap is calculated to be 2.54 eV, comparable to that of Au<sub>4</sub>-C, with the HOMO shifted to -5.58 eV, and the LUMO shifted to -3.04 eV. The HOMO and LUMO states have similar proportions and AO contributions as those of the Au<sub>4</sub>-A and Au<sub>4</sub>-B isomers. However, the calculations predict some states near the edge of the conduction band edge with % Au contributions between 10–20%, containing some Au *s* and Ti *s* character, uncharacteristic of the Au<sub>4</sub> series. In addition to this, the HOMO-1 state contains a large Au contribution of 86%, comprising of large Au *d* orbital contributions, more so than other isomers of the Au<sub>4</sub> series. Close inspection of the DOS reveals that the total set of Au states around the valence band edge to have shifted deeper into the valence band, resulting in more overlap between the orbitals of the Au<sub>4</sub>-D cluster and the surface.

There are few changes in the overall DOS between the Au<sub>4</sub> isomers, other than the shift of some of the deeper states within the valence band, which are spread out relatively evenly for Au<sub>4</sub>-A and B. These states shift to higher energies, near the -8 eV region, with greater overlap with oxygen orbitals compared with the large amount of Ti contributions deeper in the valence band.

7.5.3 Au<sub>1-4</sub> on the Oxygen-Deficient Anatase(101) Surface

Table 7.14 summarises the % contributions and orbital character for the HOMOs and LUMOs of the Au<sub>1-4</sub> isomers on the oxygen-deficient surface discussed in the following sections. Many of these parameters are also visualised in the DOS plots and isosurface illustrations in Figures presented in the following sub-sections.

Table 7.14: Summary of the key predicted orbital parameters of the HOMO and LUMO states for Au<sub>1-4</sub> on the oxygen-deficient surface.

Isomer	HOMO-LUMO gap (eV)	MO	Contributions (%)			Orbital Character
			Au	Ti	O	
<b>Au<sub>1</sub></b>	1.42	$\alpha$ :LUMO	0	87	13	Ti <i>d, p</i>
		$\alpha$ :HOMO	7	81	12	Ti <i>d</i> , and minor Au <i>d</i>
		$\beta$ :HOMO	58	32	10	Au <i>s, d</i> , and Ti <i>s, p</i>
		$\alpha$ :HOMO-1	52	38	11	Au <i>s, d</i> , and Ti <i>s, p</i>
<b>Au<sub>2</sub></b>	1.50	LUMO	0	87	13	Ti <i>d, p</i>
		HOMO	31	61	8	Ti <i>p, d</i> , and Au <i>s, p</i>
<b>Au<sub>2</sub> Triplet</b>	1.05	$\beta$ :LUMO	42	51	7	Ti <i>d, p</i> , and Au <i>s, p</i>
		$\alpha$ :LUMO	1	87	12	Ti <i>d, p</i>
		$\alpha$ :HOMO	1	84	14	Ti <i>d, p</i>
		$\beta$ :HOMO	71	19	10	Au <i>s, d</i> , and Ti <i>p</i>
<b>Au<sub>3</sub>-A</b>	1.44	$\alpha$ :LUMO	0	87	13	Ti <i>d, p</i>
		$\alpha$ :HOMO	6	82	12	Ti <i>d, p</i> , and Au <i>s</i>
		$\beta$ :HOMO	58	35	7	Au <i>s, d</i> , Ti <i>p</i> and minor Au <i>d</i>
<b>Au<sub>3</sub>-B</b>	1.43	$\alpha$ :LUMO	9	81	11	Ti <i>d, p</i> , and Au <i>s</i>
		$\alpha$ :HOMO	34	57	8	Au <i>s, p</i> , and Ti <i>d, p</i>
<b>Au<sub>4</sub>-A</b>	1.87	LUMO	0	87	13	Ti <i>p, d</i>
		HOMO	59	35	6	Au <i>s, p</i> , and Ti <i>p</i>
<b>Au<sub>4</sub>-B</b>	1.62	LUMO	0	87	13	Ti <i>p, d</i>
		HOMO	38	53	9	Ti <i>p, d</i> , and Au <i>s</i>
<b>Au<sub>4</sub>-C</b>	1.46	LUMO	0	87	13	Ti <i>p, d</i>
		HOMO	30	60	10	Ti <i>d, p</i> , and Au <i>s</i>

### 7.5.3.1 Au<sub>1</sub> and Au<sub>2</sub>

The DOS for Au<sub>1</sub> and Au<sub>2</sub> adsorbed to the oxygen-deficient surface are presented in Figure 7.48. Upon Au<sub>1</sub> adsorption, the calculations predict the introduction of additional occupied states at the top of the valence band, two new states within the band gap and some unoccupied states in the conduction band. The alpha HOMO in the middle of the band gap at -4.57 eV has only 7% Au contribution, while the beta HOMO and alpha HOMO-1 have significant contributions of 58% and 52%, respectively. The LUMO has shifted by -0.03 eV relative to the bare oxygen-deficient surface, but otherwise remains unchanged. The alpha HOMO is predicted to have primarily Ti *d* and minor Au *d* character, whereas the beta HOMO with significant Au contribution has Au *s*, *d*, and Ti *s* and *p* character, as shown in Figure 7.49.

There are many states just below the HOMO but above the typical valence band edge that contain significant Au contribution, ranging from -6.03 down to -7.81 eV. In addition, there are also a few states below this valence band edge that have 10–40% Au contribution that are spread out within the valence band, with two states at -7.91 and 7.92 eV that have 48% Au contribution. There are no unoccupied states at the edge of the conduction band edge with Au contribution and such states are instead predicted to be much further into the conduction band, at -2 eV and beyond.

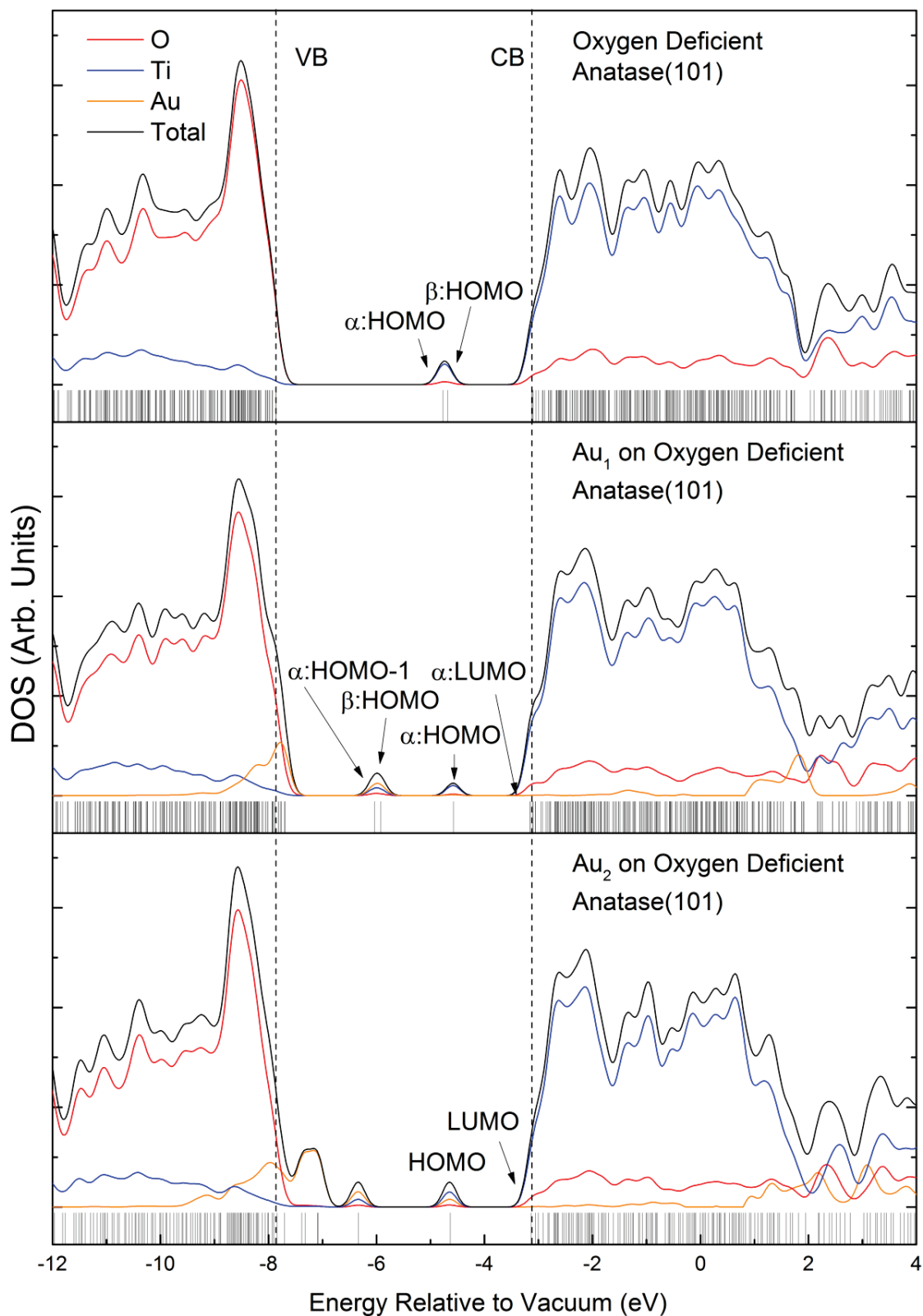


Figure 7.48: The density of states for the oxygen-deficient surface before and after adsorption of Au<sub>1</sub> and Au<sub>2</sub> clusters. VB and CB indicate the calculated position of the valence and conduction band edges of the bare oxygen-deficient surface.

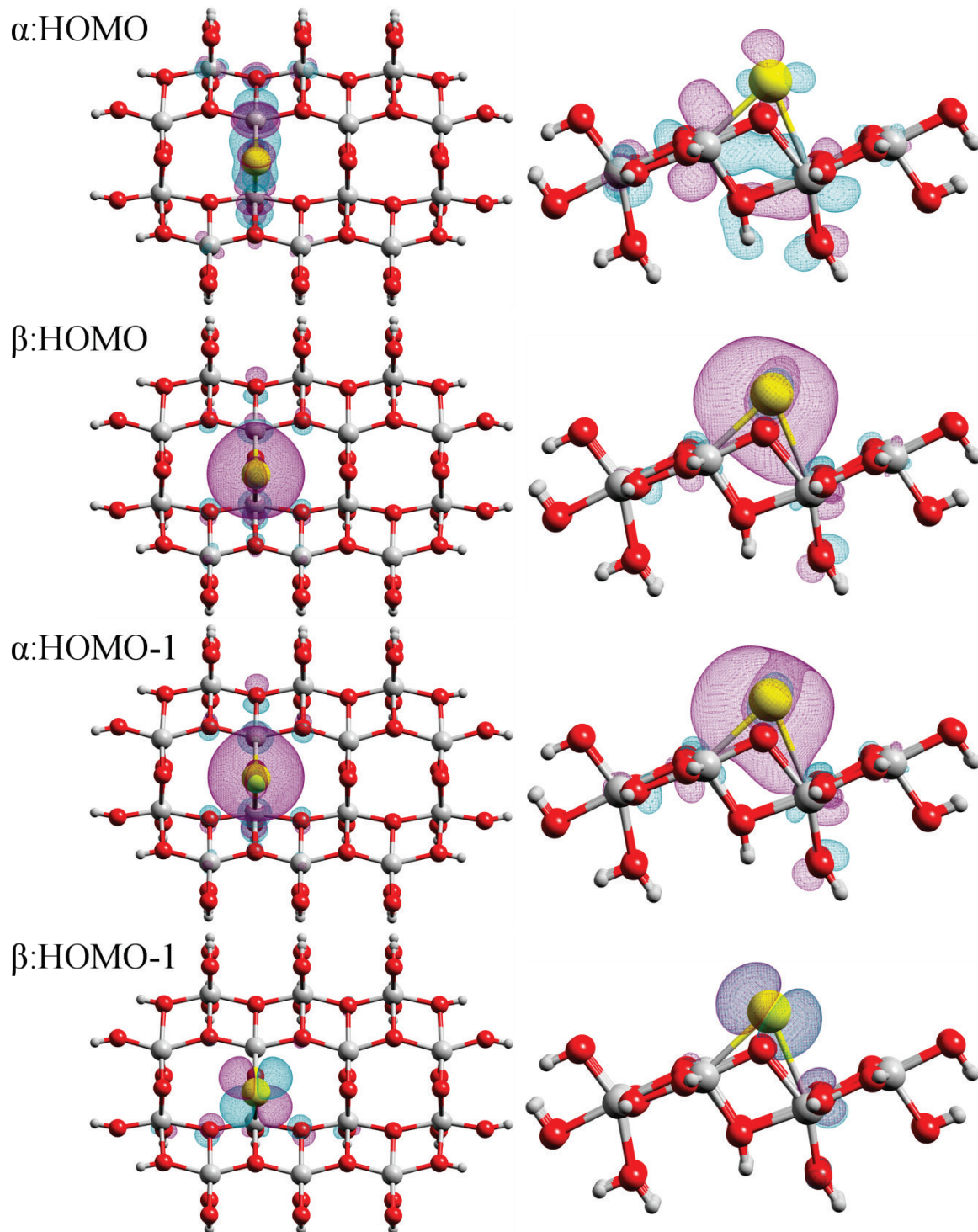


Figure 7.49: Top and side wireframe view of the alpha HOMO, beta HOMO, alpha HOMO-1, and beta HOMO-1 of Au<sub>1</sub> on the oxygen-deficient surface.

The calculations predict a similar outcome for the adsorption of Au<sub>2</sub>, with multiple states introduced at the edge of the valence band, two states in the band gap, and unoccupied states in the conduction band. The LUMO remains virtually unchanged from that of the bare oxygen-deficient surface, while the new HOMO at -4.63 eV with 31% Au contribution results in a HOMO-LUMO gap of only 1.50 eV. This new HOMO consists primarily of Au *s*, *p*, Ti *p*, and *d* orbital character, as shown in Figure 7.50. There are eight states between -6.33 eV and -7.90 eV just below the HOMO that have very large Au contributions (up to 98%), followed by more states that have between 10 and 40% Au contribution. There are no unoccupied states at the edge of the conduction band edge with Au contribution and are instead predicted to be much further into the conduction band, at -2 eV and beyond.

For Au<sub>2</sub>, there is an energetically competitive triplet isomer that is 0.42 eV higher in binding energy, with a virtually identical binding geometry. This triplet isomer predicts an additional state within the band gap at -5.08 eV as shown in the spin up-down PDOS plot of Figure 7.51. This is an alpha HOMO-1 state with 33% Au contribution, while the alpha HOMO at -4.35 eV has only 1% Au contribution. Compared with Au<sub>1</sub> or the singlet Au<sub>2</sub> isomer, the frontier HOMOs have much less Au contribution, although there are still numerous states in the valence band with significant Au contributions.

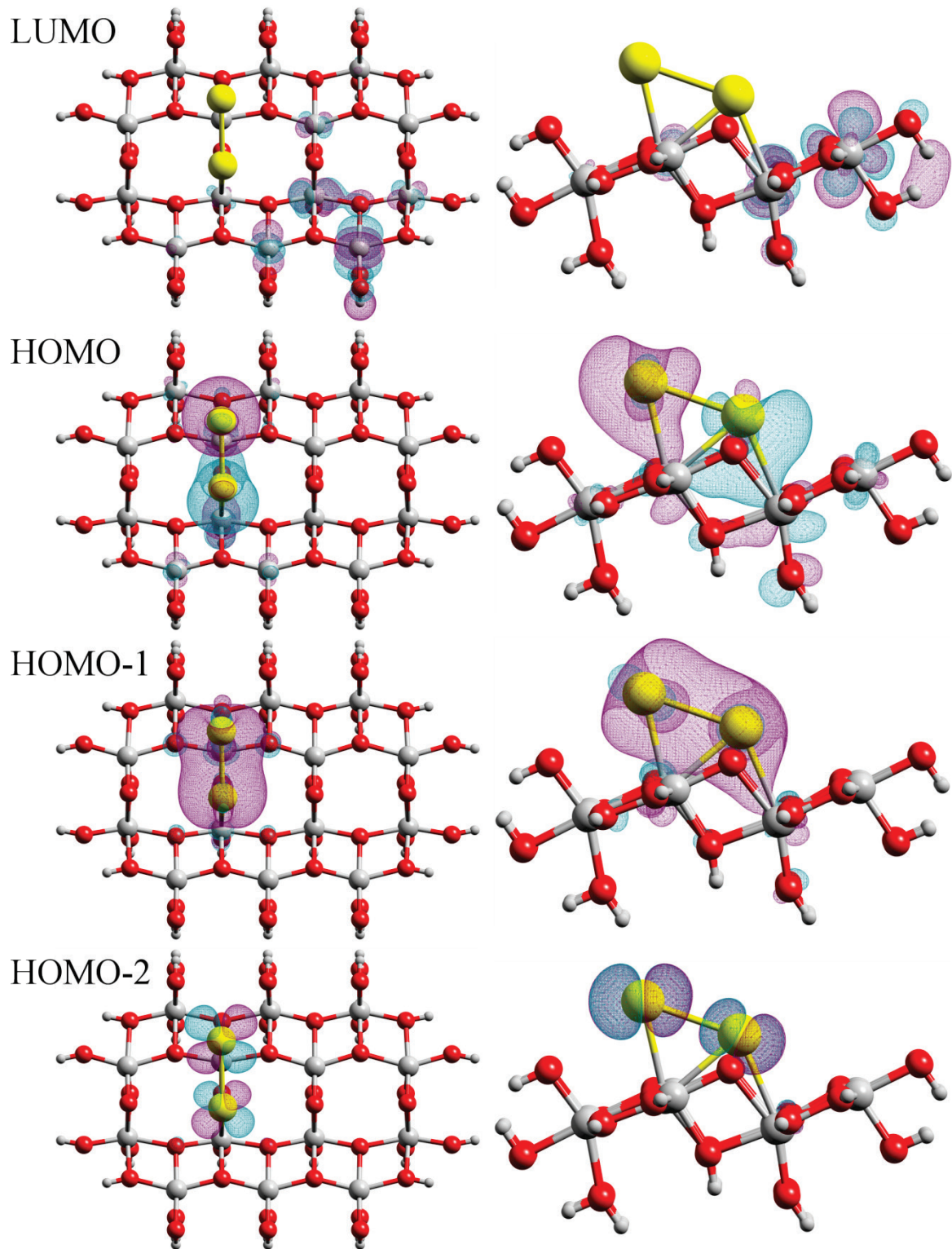


Figure 7.50: Top and side wireframe view of the LUMO, HOMO, HOMO-1, and HOMO-2 of Au<sub>2</sub> on the oxygen-deficient surface.

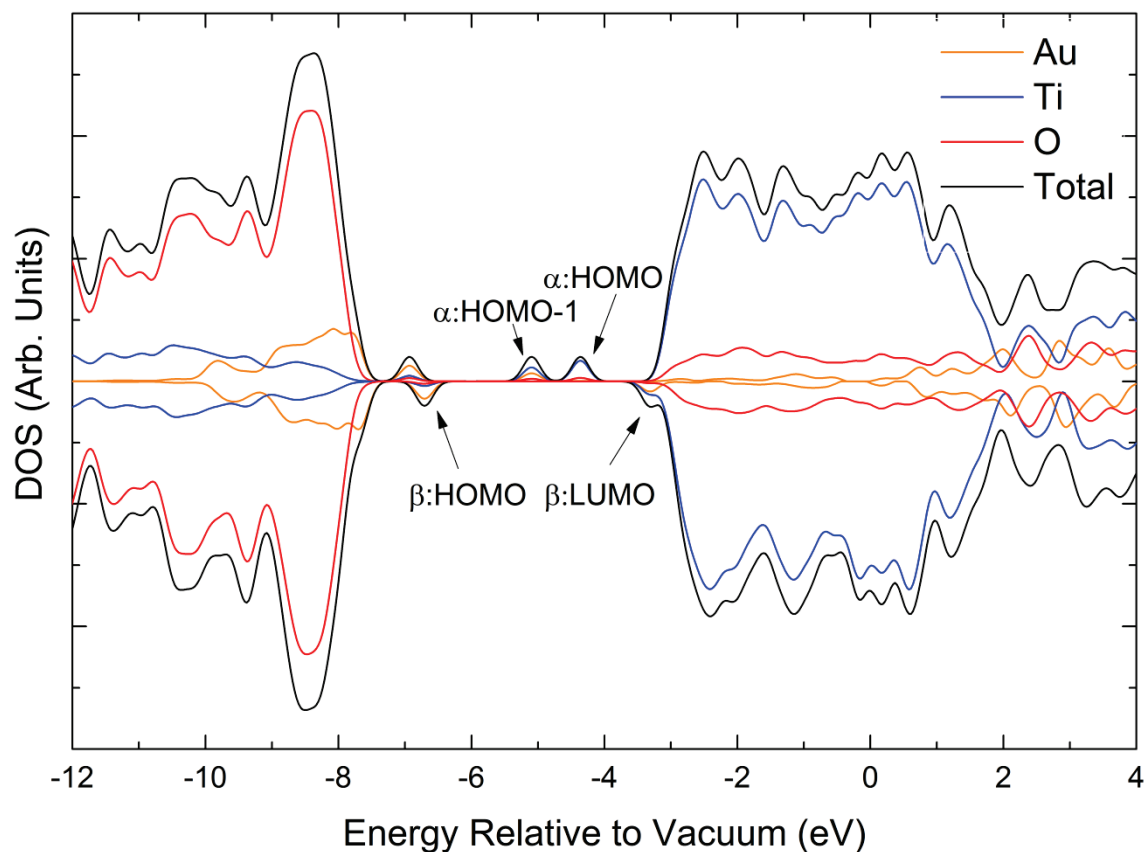


Figure 7.51: The alpha/beta split DOS for the triplet Au<sub>2</sub> cluster bound to oxygen-deficient surface.

### 7.5.3.2 Au<sub>3</sub>

For the Au<sub>3</sub> cluster on the oxygen-deficient surface, there are two states predicted within the band gap and a greater number of states around the valence band edge, extending deeper into the band gap as shown in Figure 7.52. For the Au<sub>3</sub>-A isomer, the alpha HOMO resides at -4.60 eV with only 6% Au contribution, while the alpha LUMO resides at -3.15 eV, consisting of 13% O and 87% Ti, resulting in a HOMO-LUMO gap of 1.44 eV. The HOMO has Ti *d*, *p*, and Au *s* character, while the LUMO has the expected Ti *d* and *p* character. Of greater interest is the beta HOMO state at -5.26 eV, which contains 58% Au contribution, with primarily Au *s*, *d*, and Ti *p* character. This state shows a large degree of orbital overlap between the Au cluster and the surface as shown in Figure 7.53, involving all three Au atoms, compared with the alpha HOMO, which only involves a single Au atom. The edge of valence band states beginning at -5.37 eV down to -7.85 eV contain >68% Au contributions, followed by more states deeper into the valence band

with decreasing Au contributions. The conduction band edge does not contain any states with significant levels of Au contribution, until approaching 0 eV.

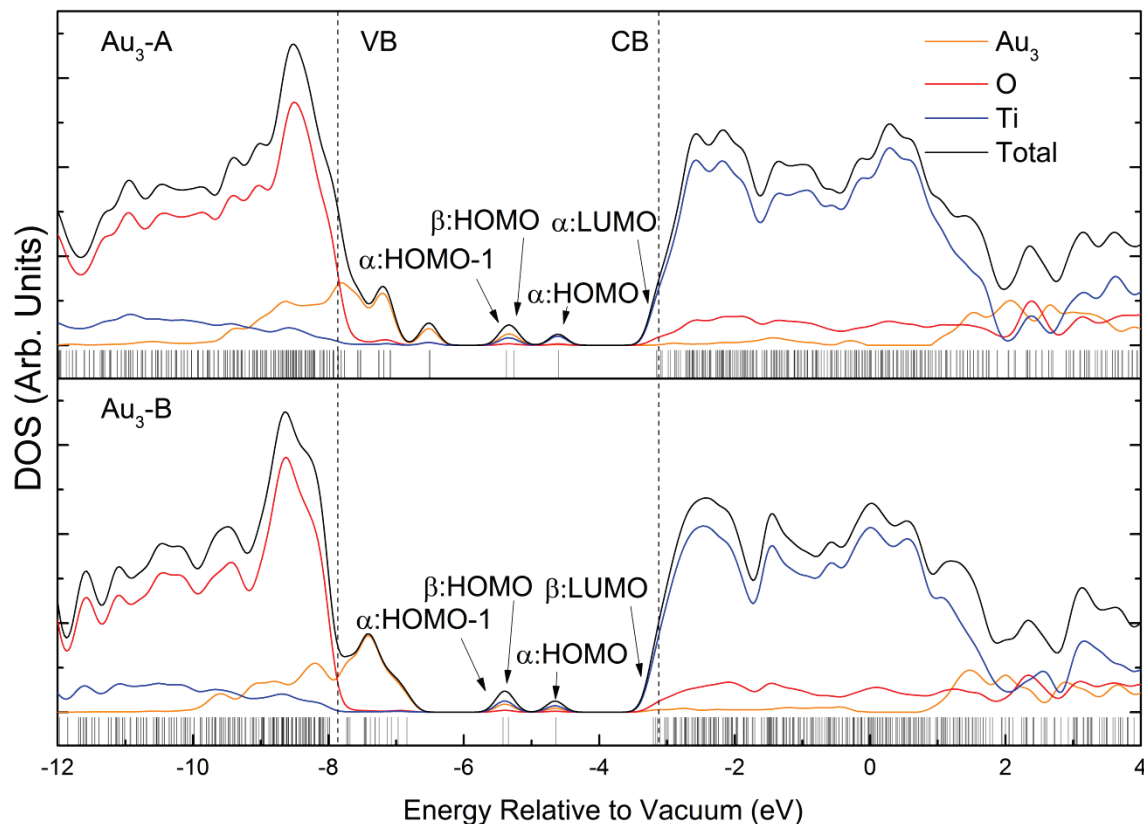


Figure 7.52: The density of states for the oxygen-deficient surface after adsorption of Au<sub>3</sub> clusters. VB and CB indicate the calculated position of the valence and conduction band edges of the bare oxygen-deficient surface.

For the Au<sub>3</sub>-B isomer the alpha HOMO resides at -4.64 eV, with a large Au contribution of 34%, a 28% increase compared with the Au<sub>3</sub>-A isomer, and a shift of -0.04 eV of the state, with Au *s*, *p*, Ti *d*, and *p* character. The beta LUMO at -3.20 eV is shifted by -0.05 eV, resulting in an HOMO-LUMO gap of 1.43 eV, and consists of 9% Au contribution with primarily Ti *d* and *p* orbitals, and minor Au *s* character. The calculations clearly predict the orthogonal binding geometry of the Au<sub>3</sub>-B isomer to result in a greater amount of hybridisation of the Au orbitals with those of the surface for the HOMO and LUMO states, compared with Au<sub>3</sub>-A. At the valence band edge the contribution from Au increases, similar to Au<sub>3</sub>-A, although there is a greater density of states for Au<sub>3</sub>-B in the region centred around -7.30 eV, followed by more states deeper into the valence band with decreasing Au contributions.

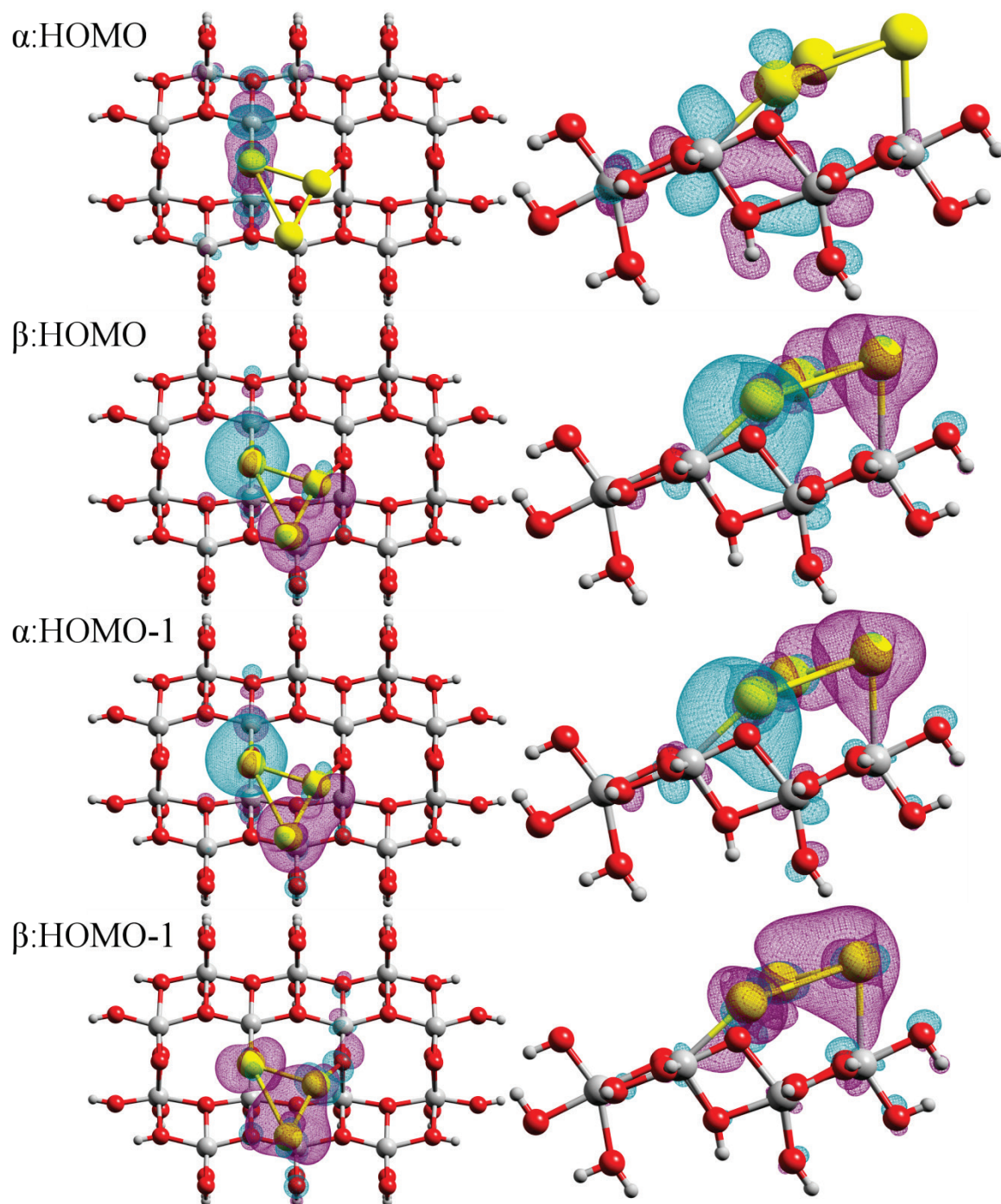


Figure 7.53: Top and side wireframe view of the alpha HOMO, beta HOMO, alpha HOMO-1, and beta HOMO-1 of Au<sub>3</sub>-A on the oxygen-deficient surface.

### 7.5.3.3 Au<sub>4</sub>

The addition of a fourth Au atom to the oxygen-deficient surface affords further states around the valence band edge as shown in Figure 7.54. For the Au<sub>4</sub>-A isomer, there are two states predicted within the band gap that are close together, which are the HOMO-1 at -5.36 eV and the HOMO at -5.01 eV, with Au contributions of 43% and 59%, respectively. The LUMO resides at -3.14 eV with no Au contribution, resulting in a HOMO-LUMO gap of 1.87 eV. The LUMO has the expected Ti *p* and *d* character of all other LUMOs without Au contribution. The HOMO contains primarily Au *s*, *p*, and Ti *p* character, while the HOMO-1 contains primarily Au *s*, *p*, and Ti *d* character, as shown in Figure 7.55.

For Au<sub>4</sub>-B, the two states in the band gap shift away from each other, with the HOMO-1 decreasing in energy to -5.60 eV and the HOMO increasing to -4.71 eV. These two states have contributions of 60% and 38% Au respectively. The LUMO has also increased to -3.10 eV, resulting in a HOMO-LUMO gap of 1.62 eV. The HOMO state has contributions from Ti *p*, *d*, and Au *s* type orbitals, while the HOMO-1 has contributions from Au *s*, *p*, Ti *p*, and *d* type orbitals.

The DOS for the Au<sub>4</sub>-C isomer is similar to that of the Au<sub>4</sub>-B isomer, which is expected given the similarity of the binding geometry. The HOMO-1 state has decreased by 0.02 eV to -5.62 eV, and the HOMO has increased by 0.17 eV to -4.54 eV. These two states have Au contributions of 30% and 56% Au respectively, with similar AO contributions as that of Au<sub>4</sub>-B. The LUMO has increased to -3.07 eV, resulting in a HOMO-LUMO gap of 1.46 eV, the smallest of the Au<sub>4</sub> series on an oxygen-deficient surface.

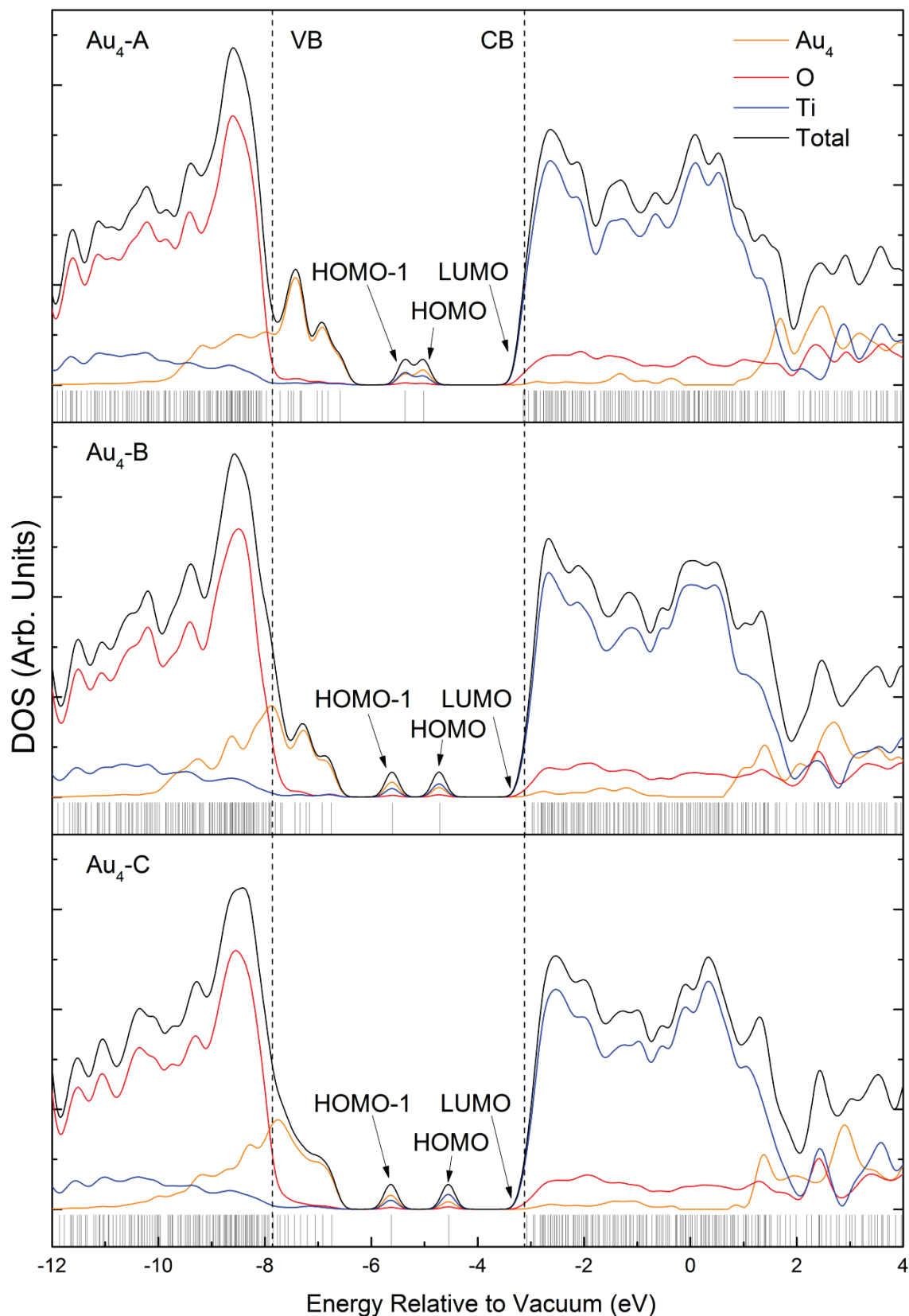


Figure 7.54: The density of states for the oxygen-deficient surface after adsorption of Au<sub>4</sub> clusters. VB and CB indicate the calculated position of the valence and conduction band edges of the bare oxygen-deficient surface.

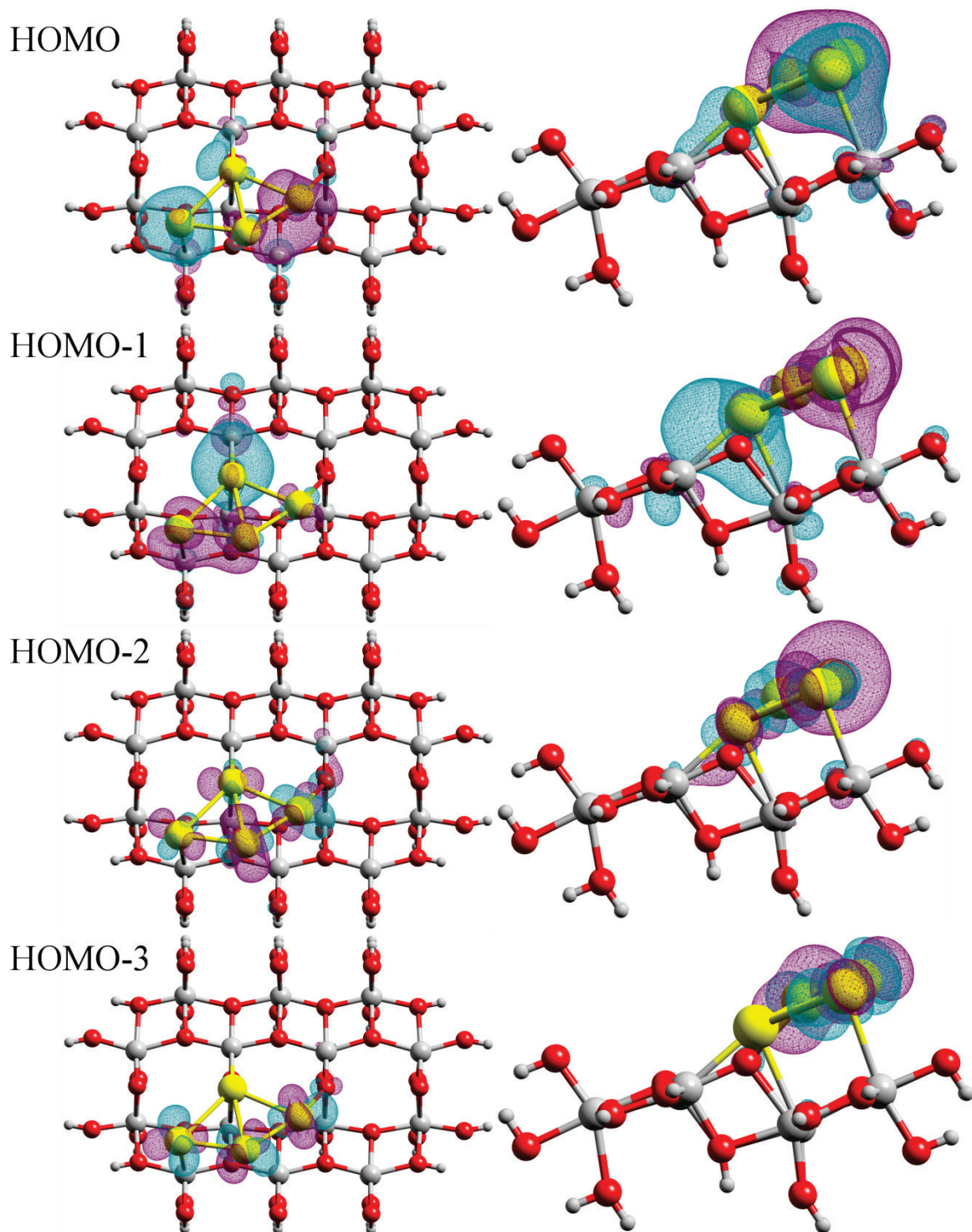


Figure 7.55: Top and side wireframe view of the HOMO, HOMO-1, HOMO-2, and HOMO-3 of Au<sub>4</sub>-A on the oxygen-deficient surface.

The large shift in MO energies and contributions between Au<sub>4</sub>-A and Au<sub>4</sub>-B can clearly be attributed to the significant change in binding geometry, adopting the Au<sub>3</sub> trimer motif with an additional Au atom attached to the side, bound over the Ti<sub>5c</sub> atom. Close inspection of the MO visualisation for the HOMO available in Appendix B shows that this 4<sup>th</sup> Au atom is not involved in the bonding, unlike for Au<sub>4</sub>-A, which has all four Au atoms involved in the HOMO. However, the HOMO-1 does involve large contributions from the 4<sup>th</sup> Au atom for the Au<sub>4</sub>-B isomer.

#### 7.5.4 Discussion

Overall comparisons between the Au<sub>1-4</sub> clusters on the stoichiometric surface shows that the edge of the conduction band rarely changes between isomers, with the most significant changes focused around the valence band edge due to the greater number of Au states. As the number of Au atoms in a cluster is increased, there is a large increase in the number of states with high Au contribution at both the valence band edge, and deeper into the valence band, while the conduction band has only marginal increases to the number of states. The isomers of Au<sub>1</sub>, Au<sub>3</sub>-B, and Au<sub>3</sub>-D also predict a LUMO with significant contributions from Au.

For the Au<sub>1-4</sub> clusters on the oxygen-deficient surface, the calculations predict a similar introduction of states with significant Au contribution centred around the valence band edge, although there are some key differences. The overall DOS for the Au<sub>1</sub> and Au<sub>2</sub> series on the oxygen-deficient surface compared with the stoichiometric surface shows small differences in the valence band structure, but the major difference is the presence of an extra state in the band gap for the cluster bound to the oxygen-deficient surface. This state is due to the oxygen defect site and remains at the same approximate energy, despite the large amount of interaction between the Au cluster and the oxygen vacancy.

The Au<sub>3</sub> clusters on the oxygen-deficient surface show a larger number of states above the typical valence band edge, which extend further into the band gap compared with Au<sub>3</sub> on the stoichiometric anatase surface. There are also two isolated states in the band gap compared to a single state for the stoichiometric surface, although this still results in a similar HOMO-LUMO gap for Au<sub>3</sub> on the oxygen-deficient surface (1.44 eV) compared with Au<sub>3</sub> on the stoichiometric surface (1.54 eV).

Similar to that of Au<sub>4</sub>-A on the stoichiometric surface, for Au<sub>4</sub>-A on the oxygen-deficient surface, there is a spike in the DOS for %Au at the valence band edge, followed by a stable level of %Au contribution upon moving deeper into the valence band, until sharply falling off. This differs from Au<sub>4</sub>-B and C on the oxygen-deficient surface, as relative Au contribution tends to decline erratically as energy decreases.

The HOMO-LUMO gap of the various isomers show no clear trend, except for those on the stoichiometric surface, whereby the singlet systems of Au<sub>2</sub> and Au<sub>4</sub> result in larger gaps than the doublet systems of Au<sub>1</sub> and Au<sub>3</sub>. For the oxygen-deficient surface, the HOMO-LUMO gaps of Au<sub>1</sub>, Au<sub>2</sub> and Au<sub>4</sub> are also smaller than those on the stoichiometric surface.

The DOS attributed to the Au<sub>1-4</sub> clusters bound to the anatase(101) surfaces have changed substantially from the DOS of the gas-phase Au<sub>1-4</sub> clusters. There is a general shift in the Au states towards the valence band region, which have become less localised. The states of the Au atoms are well overlapped with the valence band edge of the TiO<sub>2</sub> support, which indicates a strong interaction between the cluster and its support.<sup>344</sup>

In the wider context of the thesis, the consequence of the new states introduced by the Au clusters could be useful for photocatalysis. For example, those isomers that have a LUMO with a large Au contribution at the edge of the conduction band may be able to promote electron transfer away from the TiO<sub>2</sub> and into the Au cluster, spatially separating a photo-excited electron from its hole, which can reduce the chance of recombination; analogous to what occurs when Pt nanoparticles are present on the TiO<sub>2</sub> surface.<sup>173,529</sup> Alternatively, the presence of a large number of states at the edge of the valence band with significant overlap with Au could allow charge separation by enabling the photo-excited hole to transfer from the anatase surface into the Au cluster, where it would become a site for oxidation. If the Au clusters themselves were photo-active due to appropriately spaced HOMO-LUMO gaps, they may also be able to donate electrons into the conduction band of TiO<sub>2</sub>, although the benefit of such an effect may be minimal, due to the low (<1%) loadings used for most photocatalytic systems. The presence of occupied states between the valence and conduction band may help to reduce the effective band gap and enable the absorption of longer wavelength light.

## 7.6 Conclusions

The calculations predict a number of unique geometric isomers within 0.5 eV of the lowest energy isomer for the Au<sub>1-4</sub> clusters bound to stoichiometric and oxygen-deficient anatase(101). These clusters have changed substantially from their gas-phase optimised structures. The binding geometries of the Au<sub>1-3</sub> clusters generally agree with previous studies in the literature by both Vittadini and Selloni, and Gong *et al.*,<sup>337,342</sup> although for Au<sub>3</sub> there are some differences. There is a clear trend of increasing binding energy as the number of Au atoms on the surface is increased on the stoichiometric surface, in contrast to the oxygen-deficient surface, where there are low binding energies predicted for Au<sub>1</sub> and Au<sub>2</sub> compared with the high binding energies of Au<sub>3</sub> and Au<sub>4</sub>. It was suggested that the increased binding energy of Au<sub>1</sub> and Au<sub>3</sub> on the oxygen-deficient surface could be due to stabilisation of the unpaired Au cluster electrons upon binding to the surface. Interaction between Au clusters and the oxygen-deficient surface is typically stronger, and involves a greater perturbation of the cluster geometry upon adsorption. The predicted binding energy trends are also consistent with the previous studies by Vittadini and Selloni, and Gong *et al.*

There are a number of vibrational modes predicted below 200 cm<sup>-1</sup> for the Au<sub>1-4</sub> clusters when adsorbed to the anatase surface that have changed substantially from their gas-phase counterparts. The increase in the number of Au atoms on the anatase surfaces resulted in a large number of changes to the predicted IR and Raman spectra, as would be expected for large geometry changes. Between the different isomers of the same cluster, however, the changes to the predicted spectra were less dramatic, even if there are significant changes to the type of vibrational modes. For all clusters, there are a number of low frequency vibrations involving cluster twisting and displacements along the anatase surface, while for the Au<sub>2-4</sub> clusters, there are a number of relatively intense, higher frequency modes near 80–140 cm<sup>-1</sup> that involve Au-Au stretching and cluster breathing modes. Of these higher frequency modes, a correlation was found between the frequency of the Au-Au stretching modes on the stoichiometric surface and the average Au-Au bond lengths for Au<sub>2-4</sub>. These shifts between clusters and between the two surfaces for the high intensity modes could provide a useful experimental diagnostic of the chemical form of small Au clusters in future experimental studies.

Charge analysis of these systems showed that increasing the number of Au atoms bound to the anatase surface leads to increased charge transfer from the Au cluster to the TiO<sub>2</sub> surface atoms. This is also reflected by the increased average Au-Au bond lengths within the Au clusters upon binding. The exception to this is for Au<sub>4</sub> on the oxygen-deficient surface, whereby the cluster charge has decreased compared to Au<sub>3</sub>. The charge per Au atom was found to steadily decrease as the number of Au atoms was increased on the stoichiometric surface; however, for the oxygen-deficient surface, there was no clear trend. In general, the changes in charge of the surface atoms of TiO<sub>2</sub> are small but noteworthy upon Au cluster adsorption, with Hirshfeld charge analysis showing that the cluster charge was distributed over more of the surface atoms than other charge analysis methods.

Inspection of the DOS revealed the introduction of numerous states at the valence band edge with large contributions from Au orbitals that are well overlapped with the TiO<sub>2</sub> support. The position of these states has changed significantly from those of the gas-phase Au<sub>1-4</sub> clusters. In addition, there is typically a new HOMO predicted near the middle of the TiO<sub>2</sub> band gap consisting primarily of Au orbitals. It was found that as the number of atoms in a Au cluster increases, so too does the number of states near the valence band edge, with more states also appearing deeper into the valence band. For the bare oxygen-deficient surface, there is already a HOMO near the middle of the band gap, which becomes well hybridised with Au orbitals after the adsorption of any Au cluster. For Au<sub>3</sub> and Au<sub>4</sub>, additional isolated states within the band gap are also predicted when they bind to the oxygen-deficient surface. For some clusters, there are new LUMO states predicted at, or just below the conduction band edge, with sizable contributions from Au orbitals. The position of these new states predicted by DFT calculation could indicate advantageous energetic levels for anatase-supported Au clusters during photocatalytic reactions that could be used in the design of heterogeneous catalytic systems.

This work has provided the foundation for future studies that will use these anatase models to investigate the reactive properties of small Au clusters with photocatalytically relevant molecules and their reaction pathways. These calculations will also form the basis of future theoretical investigations of chemically synthesised, ligand-protected Au clusters bound to the TiO<sub>2</sub> anatase(101) surface. The predicted DOS will also help to characterise the features of future experimental studies using metastable impact electron spectroscopy and ultraviolet photoelectron spectroscopy conducted by our collaborators.

# **Chapter Eight**

Conclusions and Future Work

## 8 Conclusions and Future Work

The four result chapters presented in this thesis brought together a variety of techniques to investigate the Au cluster/TiO<sub>2</sub> system. Correlations between the data reveal a series of trends that would otherwise have been difficult to understand on their own.

In Chapter four, synchrotron-based far-IR spectroscopy was used to elucidate the solid-phase vibrational characteristics of Au<sub>6</sub>, Au<sub>8</sub>, Au<sub>9</sub>, Au<sub>11</sub>, Au<sub>6</sub>Pd, and Au<sub>7</sub>Pt clusters in the far-IR region between 50 and 450 cm<sup>-1</sup>. Gas-phase DFT calculations were used to provide verification and detailed analysis of the vibrational modes of each cluster. Characteristic metal-core distortion modes were observed for all clusters between 80 and 185 cm<sup>-1</sup> that shift depending upon the cluster geometry and composition. The most significant of such shifts was observed for Au<sub>6</sub>Pd, which was attributed to the addition of a metal atom of significantly different mass compared to a Au atom. Conversely, the addition of a Pt atom to Au<sub>7</sub>Pt had only marginal affect upon its vibrational spectrum, which was closely related to that of the Au<sub>8</sub> cluster, due to their similar geometry. The Au<sub>6</sub> cluster also has a metal core transition resolved at 90 cm<sup>-1</sup> that was the lowest in energy of all clusters studied in this Chapter. Additionally, strong absorptions in all spectra from 400 cm<sup>-1</sup> and higher were attributed to PPh<sub>3</sub> ligand modes. Au-P stretches were only observed experimentally for Au<sub>6</sub> and Au<sub>6</sub>Pd, near 420 and 180 cm<sup>-1</sup> respectively. The positions of metal core vibrations were observed at similar energies to those reported for gas-phase Au<sub>7</sub> and Au<sub>6</sub>Y clusters reported in FELIX IR studies in the literature.

Charge population analysis showed a general negative to neutral charge for the majority of cluster metal atoms, with the P atoms of the ligands developing a strong positive charge. The central atoms of Au<sub>8</sub>, Au<sub>9</sub>, and Au<sub>11</sub>, as well as the heteroatoms of Au<sub>6</sub>Pd and Au<sub>7</sub>Pt were also predicted to have a larger negative charge than their surrounding metal atoms. While all methods presented agreed on the strong positive charges of the P atoms, there was some discrepancy between the methods for the core metal atoms.

Chapter five continued the characterisation with the use of synchrotron X-ray and TEM techniques to investigate the full effect of treatments that are undertaken to remove the organic protective ligands after the gold clusters are supported upon titanium dioxide. For the Au<sub>8</sub>, Au<sub>9</sub>, and Au<sub>11</sub> clusters supported upon acid-washed P25 nanoparticles, the untreated samples remain intact according to XPS, and are too small to be seen under

HRTEM. Subsequent washing at 100 °C in toluene results in the removal of some ligands for a portion of the clusters, in addition to the formation of Au-O bonds. Another portion of the clusters remain intact upon the surface, while a significant fraction of the clusters have clearly been removed from the surface during treatment when comparing the total signal intensity to those of the untreated samples. Further treatment by heating to 200 °C under vacuum results in the agglomeration of a portion of the clusters, while still being protected by ligands (these remain smaller than Au<sub>101</sub>), while another portion of the clusters lose ligands to form Au-O bonds and agglomerate into larger particles. Of the portion that loses ligands to form Au-O bonds, some clusters may remain intact. The removal of ligands is also less effective for the Au<sub>9</sub> cluster. The agglomeration of a portion of the clusters is supported by HRTEM as the particles become large enough to be resolvable. Calcination under an O<sub>2</sub> atmosphere at 200 °C results in a further increase in particle size as observed by HRTEM for all clusters, but it is unknown as to the state of the ligands without further complementary experimental studies.

For the Au<sub>8</sub> and Au<sub>9</sub> clusters supported upon pure anatase nanoparticles, the untreated samples undergo partial ligand removal, with approximately half of the clusters remaining intact, while the other half undergo agglomeration, according to XPS. This effect of immediate agglomeration upon being supported on anatase is supported by XANES analysis, which showed that 38% of the Au<sub>9</sub> clusters had agglomerated. Interestingly, untreated Au<sub>9</sub> samples supported on anatase that were kept in the dark showed no agglomeration according to XANES, and is an observation that will have to be explored further in future studies. Treatment of Au<sub>8</sub> by calcination under O<sub>2</sub> at 200 °C results in further removal of ligands and increased agglomeration for half of the clusters, while the remaining portion of clusters maintain their size. In comparison, Au<sub>9</sub> calcined under O<sub>2</sub> at 200 °C also results in further removal of ligands and increased agglomeration for the entire sample, with no Au<sub>9</sub> clusters remaining intact. EXAFS analysis showed that these supported Au<sub>9</sub> clusters had agglomerated to such an extent that they could be modelled using a FCC bulk gold structure, and exhibited lattice contraction and small Debye temperatures indicative of nanoparticulate gold. Further calcination of Au<sub>8</sub> and Au<sub>9</sub> under O<sub>2</sub> + H<sub>2</sub> at 200 °C results in complete ligand removal and further progression of agglomeration, with no evidence of either cluster remaining intact upon the anatase surface. An increase in Debye temperature is calculated by EXAFS modelling for Au<sub>9</sub>, indicating a further increase in particle size.

In comparison, untreated Au<sub>9</sub> samples supported on fumed silica showed no signs of agglomeration. XANES indicated that calcination under O<sub>2</sub> at 200 °C leaves 15.5% intact Au<sub>9</sub> clusters, although EXAFS analysis showed that the remaining portion of agglomerated clusters could still be fit well with a bulk gold lattice model, showing similar lattice contraction and small Debye temperatures, similar to that calculated for the same treatment on anatase. Further treatment under O<sub>2</sub> + H<sub>2</sub> at 200 °C for silica-supported Au<sub>9</sub> results in negligible intact cluster remaining according to XANES, while EXAFS analysis calculated an increase in Debye temperature indicative of increased agglomeration.

For the Au<sub>101</sub> series, the untreated sample supported upon acid-washed P25 nanoparticles showed a small increase in particle size according to HRTEM. During HRTEM studies it was also observed that Au<sub>101</sub> is prone to agglomeration under ambient light, and this should be investigated further in future studies. Washing at 100 °C in toluene results in a loss of a significant amount of clusters from the surface according to XPS, however, there is no indication of Au-O bond formation or an increase in particle size. Samples heated at 200 °C under vacuum result in further agglomeration of the particles according to HRTEM, the removal of some ligands, and the formation of Au-O bonds. By comparison, Au<sub>101</sub> supported on pure anatase nanoparticles show a similar progression of ligand removal, but to a far greater extent, with complete ligand removal for those samples calcined under O<sub>2</sub> + H<sub>2</sub> at 200 °C. It is unknown, however, if these anatase-supported Au<sub>101</sub> particles undergo agglomeration.

In Chapter six, benchmark photocatalytic water-splitting experiments were undertaken using Pt-P25 and Pt-Anatase nanoparticles to ensure the newly designed experimental apparatus was performing adequately. During these studies, it was discovered that there is a decrease in the photocatalytic performance of samples when repeating experiments using the same catalyst material. Further preliminary studies of Au/TiO<sub>2</sub> found a similar effect of performance degradation. This degradation in the performance of samples was accompanied by a colour change in the samples. The degradation and colour change of samples was attributed to accumulation of carbon deposits during the oxidation of organic compounds, and may be related to the known photo-induced agglomeration effects of ambient light on the Au<sub>9</sub> and Au<sub>101</sub> clusters evidenced by XANES and HRTEM data from Chapter 5. Improved performance was also observed for all samples prepared in the

reaction cell with 12 hours of exposure to vacuum, compared to relatively short vacuum exposure times of 10 minutes.

The production of H<sub>2</sub> from photocatalytic water-splitting experiments was accompanied by the production of CO<sub>2</sub> and consumption of O<sub>2</sub>. The CO<sub>2</sub> by-product arises from the well-known capacity for TiO<sub>2</sub> to photo-oxidise organic contaminants, and consumes the stoichiometrically evolved O<sub>2</sub> from the water-splitting reaction throughout the experiment. The source of carbon in the reaction cell is most likely from unavoidable adventitious carbon that is present in all vacuum systems and samples exposed to atmosphere, in addition to the possible contribution from oil backstreaming from the rotary pump. Various carbon based sealant material used in the reaction cell and adsorbed CO that is difficult to evacuate during sample preparation may also contribute to the source of carbon.

O<sub>2</sub> present in the reaction cell at the beginning of the experiment due to low vacuum is likely rapidly consumed by quenching defect states within the TiO<sub>2</sub> nanoparticles and by photo-adsorption of O<sub>2</sub> to the TiO<sub>2</sub> surface over the initial hour of experiments. This initial O<sub>2</sub> presence could also include O<sub>2</sub> molecules adsorbed to the TiO<sub>2</sub> surface at ambient temperature, or those adsorbed to the walls of the reaction cell. The formation of surface O<sub>2</sub><sup>-</sup> and O<sub>3</sub><sup>-</sup> species during this period by molecular O<sub>2</sub> likely behaves as electron traps or hole scavengers after photo-excitation, increasing electron-hole separation, which could explain the decrease in both H<sub>2</sub> and CO<sub>2</sub> production after the excess O<sub>2</sub> in the reaction cell is consumed.

Following this work, photocatalytic water-splitting experiments were successfully undertaken with a wide range of chemically synthesised Au<sub>8</sub>, Au<sub>9</sub>, and Au<sub>101</sub> clusters supported on P25 or pure anatase nanoparticles with various pre- and post-treatments. All samples were found to be active towards photocatalytic water-splitting. For the anatase-supported samples, successively harsher treatments led to higher catalytic performance for all clusters, with calcination under an O<sub>2</sub> and H<sub>2</sub> atmosphere resulting in the highest performance. It was found that it is the unligated, large Au particles that have lost their atomically precise nature, which are the most effective photocatalysts on the unwashed anatase nanoparticles. The overall performance also increased as the initial size of the cluster increased, providing further evidence that it is the largest Au particles that are the most effective photocatalysts on this support. Changes in Au particle size are known to

have a dramatic effect on their catalytic capacity due to a number of reasons outlined in detail in the introduction Chapter. Au<sub>101</sub>/anatase calcined under O<sub>2</sub> and H<sub>2</sub> at 200 °C was found to be the most effective photocatalyst, with a H<sub>2</sub> production rate of  $190.4 \pm 29.6 \mu\text{mol hr}^{-1} \text{g}^{-1} \text{cm}^{-2}$ . It is also known that anatase is more active towards the photo-reduction of O<sub>2</sub> that contributes to the unwanted backward reaction between H<sub>2</sub> and O<sub>2</sub>, which may contribute to the overall lower performance of the anatase-supported samples compared to the P25 supported samples.<sup>103,120,524</sup>

For the acid-washed P25 supported samples, heat treatment under vacuum at 200 °C was found to be the most effective for Au<sub>101</sub> and Au<sub>9</sub> for maximum H<sub>2</sub> production, while further treatment via calcination under an O<sub>2</sub> atmosphere resulted in decreased performance. The H<sub>2</sub> production rate for these heat treated samples was found to be  $511.4 \pm 51.1$  and  $437.5 \pm 43.7 \mu\text{mol hr}^{-1} \text{g}^{-1} \text{cm}^{-2}$  for Au<sub>9</sub> and Au<sub>101</sub> respectively. The comparable production rate was attributed to the heat treatment yielding Au particles of similar size after agglomeration. Untreated Au<sub>101</sub> on acid-washed anatase nanoparticles were also found to be very effective, with a production rate of  $534.8 \pm 53.5 \mu\text{mol hr}^{-1} \text{g}^{-1} \text{cm}^{-2}$ . These clusters may be of similar size and with a comparable number of ligands to the heat-treated samples on acid-washed P25, hence the similar production rates. These results suggest that for the acid-washed nanoparticle supports, there may be an ideal Au particle size and ligand coverage that provides the most performance, compared to the unwashed anatase supports, which favour increasingly larger particles and major ligand removal. When weighted by grams of precious metal present in the catalyst, it was also shown that small Au particles supported on TiO<sub>2</sub> vastly outperform platinised TiO<sub>2</sub>.

In Chapter seven, density functional theory investigations of Au<sub>1</sub>, Au<sub>2</sub>, Au<sub>3</sub>, and Au<sub>4</sub> clusters bound to the stoichiometric and oxygen-deficient titanium dioxide anatase(101) surface were undertaken using an atomic centred basis set approach. The calculations predict a number of unique isomers within 0.5 eV of the lowest energy isomer for the Au<sub>1-4</sub> clusters bound to stoichiometric and oxygen-deficient anatase(101). These clusters have changed substantially from their gas-phase optimised structures. The binding geometries of the Au<sub>1-3</sub> clusters generally agree with previous studies in the literature by both Vittadini and Selloni, and Gong *et al.*,<sup>337,342</sup> although for Au<sub>3</sub> there are some differences. There is a clear trend of increasing binding energy as the number of Au atoms on the surface is increased on the stoichiometric surface, in contrast to the oxygen-deficient surface, where there are low binding energies predicted for Au<sub>1</sub> and Au<sub>2</sub>

compared with the high binding energies of Au<sub>3</sub> and Au<sub>4</sub>. It was suggested that the increased binding energy of Au<sub>1</sub> and Au<sub>3</sub> on the oxygen-deficient surface could be due to stabilisation of the unpaired Au cluster electrons upon binding to the surface. Interaction between Au clusters and the oxygen-deficient surface is typically stronger, and involves a greater perturbation of the cluster geometry upon adsorption. The predicted binding energy trends are also consistent with the previous studies by Vittadini and Selloni, and Gong *et al.*

There are a number of vibrational modes predicted below 200 cm<sup>-1</sup> for the Au<sub>1-4</sub> clusters when adsorbed to the anatase surface that have changed substantially from their gas-phase counterparts. The increase in the number of Au atoms on the anatase surfaces resulted in a large number of changes to the predicted IR and Raman spectra, as would be expected for large geometry changes. Between the different isomers of the same cluster, however, the changes to the predicted spectra were less dramatic, even if there are significant changes to the type of vibrational modes. For all clusters, there are a number of low frequency vibrations involving cluster twisting and displacements along the anatase surface, while for the Au<sub>2-4</sub> clusters, there are a number of relatively intense, higher frequency modes near 80–140 cm<sup>-1</sup> that involve Au-Au stretching and cluster breathing modes. Of these higher frequency modes, a correlation was found between the frequency of the Au-Au stretching modes on the stoichiometric surface and the average Au-Au bond lengths for Au<sub>2-4</sub>. These shifts between clusters and between the two surfaces for the high intensity modes could provide a useful experimental diagnostic of the chemical form of small Au clusters in future experimental studies.

Charge analysis of these systems showed that increasing the number of Au atoms bound to the anatase surface leads to increased charge transfer from the Au cluster to the TiO<sub>2</sub> surface atoms. This is also reflected by the increased average Au-Au bond lengths within the Au clusters upon binding. The exception to this is for Au<sub>4</sub> on the oxygen-deficient surface, whereby the cluster charge has decreased compared to Au<sub>3</sub>. The charge per Au atom was found to steadily decrease as the number of Au atoms was increased on the stoichiometric surface; however, for the oxygen-deficient surface, there was no clear trend. In general, the changes in charge of the surface atoms of TiO<sub>2</sub> are small but noteworthy upon Au cluster adsorption, with Hirshfeld charge analysis showing that the cluster charge was distributed over more of the surface atoms than other charge analysis methods.

Inspection of the DOS revealed the introduction of numerous states at the valence band edge with large contributions from Au orbitals that are well overlapped with the TiO<sub>2</sub> support. The position of these states has changed significantly from those of the gas-phase Au<sub>1-4</sub> clusters. In addition, there is typically a new HOMO predicted near the middle of the TiO<sub>2</sub> band gap consisting primarily of Au orbitals. It was found that as the number of atoms in a Au cluster increases, so too does the number of states near the valence band edge, with more states also appearing deeper into the valence band. For the bare oxygen-deficient surface, there is already a HOMO near the middle of the band gap, which becomes well hybridised with Au orbitals after the adsorption of any Au cluster. For Au<sub>3</sub> and Au<sub>4</sub>, additional isolated states within the band gap are also predicted when they bind to the oxygen-deficient surface. For some clusters, there are new LUMO states predicted at, or just below the conduction band edge, with sizable contributions from Au orbitals. The position of these new states predicted by DFT calculation could indicate advantageous energetic levels for anatase-supported Au clusters during photocatalytic reactions that could be used in the design of heterogeneous catalytic systems.

In terms of future work, the far-IR characterisation studies contained in Chapter four provided valuable information about the metal core structure of ligated gold clusters when correlated with theoretical models of the ligated gold clusters. This work showed that it is possible to characterise ligated clusters using far-IR spectroscopy, providing a foundation for future experimental and computational studies of their TiO<sub>2</sub>-supported counterparts.

Following this work, the characterisation studies of Chapter five showed that harsher treatments result in the removal of a greater number of ligands and increased agglomeration of the clusters. The effect of acidic pre-treatment of the surface, and the strong influence of supports, are also remarkably clear, with ligand loss and agglomeration more severe on untreated anatase nanoparticles. EXAFS analysis and ADF-STEM images confirmed the atomically precise nature of the clusters before being supported upon TiO<sub>2</sub> nanoparticles.

The photocatalytic studies of Chapter six demonstrated the capability of TiO<sub>2</sub>-supported gold clusters for photocatalytic water-splitting. Future directions will look at the possibility of supporting samples on silicon wafer chips, so that after samples undergo photocatalytic experiments, they may then be investigated via XPS, MIES, or UPS techniques to determine if any significant changes have occurred. Further characterisation experiments

on acid-washed anatase will be necessary to understand the probable differences between the anatase and P25 nanoparticle support, in addition to the full effects of acidic pre-treatment. Future studies will also begin to explore alternative photocatalytic reactions that can be driven by these catalysts, as well as investigating the effects of various irradiation wavelengths, irradiation intensity, pressure, and temperature.

Finally, the computational study of Chapter seven provided the foundation for future studies that will use these anatase models to investigate the reactive properties of small Au clusters with photocatalytically relevant molecules and their reaction pathways. These calculations will also form the basis of future theoretical investigations of chemically synthesised, ligand-protected Au clusters bound to the  $\text{TiO}_2$  anatase(101) surface. The predicted DOS will also help to characterise the features of future experimental studies using metastable impact electron spectroscopy and ultraviolet photoelectron spectroscopy conducted by our collaborators.

## References

1. N. Oreskes, *Science*, 2004, **306**, 1686.
2. B. S. R. o. W. E. J. 2014, BP Statistical Review of World Energy June 2014.
3. F. Krausmann, S. Gingrich, N. Eisenmenger, K.-H. Erb, H. Haberl and M. Fischer-Kowalski, *Ecological Economics*, 2009, **68**, 2696-2705.
4. B. E. Smith, *Science*, 2002, **297**, 1654-1655.
5. M. Kitano, Y. Inoue, Y. Yamazaki, F. Hayashi, S. Kanbara, S. Matsuishi, T. Yokoyama, S.-W. Kim, M. Hara and H. Hosono, *Nat Chem*, 2012, **4**, 934-940.
6. M. Gratzel, *Nature*, 2001, **414**, 338-344.
7. M. G. Walter, E. L. Warren, J. R. McKone, S. W. Boettcher, Q. Mi, E. A. Santori and N. S. Lewis, *Chemical Reviews*, 2010, **110**, 6446-6473.
8. A. Fujishima and K. Honda, *Nature*, 1972, **238**, 37-38.
9. A. Kudo and Y. Miseki, *Chemical Society Reviews*, 2009, **38**, 253-278.
10. K. Maeda and K. Domen, *The Journal of Physical Chemistry Letters*, 2010, **1**, 2655-2661.
11. B. Probst, C. Kolano, P. Hamm and R. Alberto, *Inorganic Chemistry*, 2009, **48**, 1836-1843.
12. A. Kubacka, M. Fernández-García and G. Colón, *Chemical Reviews*, 2011, **112**, 1555-1614.
13. C.-C. Lo, C.-W. Huang, C.-H. Liao and J. C. S. Wu, *International Journal of Hydrogen Energy*, 2010, **35**, 1523-1529.
14. D. Jing, L. Guo, L. Zhao, X. Zhang, H. Liu, M. Li, S. Shen, G. Liu, X. Hu, X. Zhang, K. Zhang, L. Ma and P. Guo, *International Journal of Hydrogen Energy*, 2010, **35**, 7087-7097.
15. H. Yoneyama, *Critical Reviews in Solid State and Materials Sciences*, 1993, **18**, 69-111.
16. A. Kudo, *Catalysis Surveys from Asia*, 2003, **7**, 31-38.
17. Z. Zou and H. Arakawa, *Journal of Photochemistry and Photobiology A: Chemistry*, 2003, **158**, 145-162.
18. H. Arakawa and K. Sayama, *Catalysis Surveys from Japan*, 2000, **4**, 75-80.
19. M. Anpo, S. Dohshi, M. Kitano, Y. Hu, M. Takeuchi and M. Matsuoka, *Annual Review of Materials Research*, 2005, **35**, 1-27.
20. J. Lee, *Catalysis Surveys from Asia*, 2005, **9**, 217-227.
21. A. Kudo, *International Journal of Hydrogen Energy*, 2006, **31**, 197-202.
22. W. Shangguan, *Science and technology of advanced materials*, 2007, **8**, 76-81.
23. A. Kudo, *International Journal of Hydrogen Energy*, 2007, **32**, 2673-2678.
24. K. Maeda, K. Teramura and K. Domen, *Catalysis Surveys from Asia*, 2007, **11**, 145-157.
25. S. Ekambaram, *Journal of Alloys and Compounds*, 2008, **448**, 238-245.
26. F. E. Osterloh, *Chemistry of Materials*, 2007, **20**, 35-54.
27. K. Maeda, K. Teramura, N. Saito, Y. Inoue, H. Kobayashi and K. Domen, *Pure and Applied Chemistry*, 2006, **78**, 2267-2276.
28. K. Domen, J. N. Kondo, M. Hara and T. Takata, *Bulletin of the Chemical Society of Japan*, 2000, **73**, 1307-1331.
29. J. A. Turner, *Science*, 1999, **285**, 687-689.
30. O. Khaselev and J. A. Turner, *Science*, 1998, **280**, 425-427.
31. B. Marsen, B. Cole and E. L. Miller, *Solar Energy Materials and Solar Cells*, 2008, **92**, 1054-1058.

## References

32. A. M. Fernández, N. Dheree, J. A. Turner, A. M. Martínez, L. G. Arriaga and U. Cano, *Solar Energy Materials and Solar Cells*, 2005, **85**, 251-259.
33. E. Aharon-Shalom and A. Heller, *Journal of The Electrochemical Society*, 1982, **129**, 2865-2866.
34. S. Trasatti, *Pure and applied chemistry*, 1986, **58**, 955-966.
35. N. S. Lewis, *Nature*, 2001, **414**, 589-590.
36. B. Ohtani, *Journal of Photochemistry and Photobiology C: Photochemistry Reviews*, 2010, **11**, 157-178.
37. R. Schloegl, *Nat Mater*, 2008, **7**, 772-774.
38. T. F. Jaramillo, K. P. Jørgensen, J. Bonde, J. H. Nielsen, S. Horch and I. Chorkendorff, *Science*, 2007, **317**, 100-102.
39. R. S. Loewe, R. K. Lammi, J. R. Diers, C. Kirmaier, D. F. Bocian, D. Holten and J. S. Lindsey, *Journal of Materials Chemistry*, 2002, **12**, 1530-1552.
40. M. Grätzel, *Inorganic Chemistry*, 2005, **44**, 6841-6851.
41. Y.-L. Lee, B.-M. Huang and H.-T. Chien, *Chemistry of Materials*, 2008, **20**, 6903-6905.
42. Y. Tamaki, A. Furube, M. Murai, K. Hara, R. Katoh and M. Tachiya, *Physical Chemistry Chemical Physics*, 2007, **9**, 1453-1460.
43. Y. Tamaki, K. Hara, R. Katoh, M. Tachiya and A. Furube, *The Journal of Physical Chemistry C*, 2009, **113**, 11741-11746.
44. M. F. Weber and M. J. Dignam, *International Journal of Hydrogen Energy*, 1986, **11**, 225-232.
45. M. A. Henderson, *Surface Science Reports*, 2011, **66**, 185-297.
46. K. Rajeshwar, *J Appl Electrochem*, 2007, **37**, 765-787.
47. K. Maeda, *Journal of Photochemistry and Photobiology C: Photochemistry Reviews*, 2011, **12**, 237-268.
48. J.-M. Herrmann, *Journal of Photochemistry and Photobiology A: Chemistry*, 2010, **216**, 85-93.
49. H. Zhang, G. Chen and D. W. Bahnemann, *Journal of Materials Chemistry*, 2009, **19**, 5089-5121.
50. A. J. Bard, *The Journal of Physical Chemistry*, 1982, **86**, 172-177.
51. A. Fujishima, X. Zhang and D. A. Tryk, *International Journal of Hydrogen Energy*, 2007, **32**, 2664-2672.
52. M. Higashi, R. Abe, T. Takata and K. Domen, *Chemistry of Materials*, 2009, **21**, 1543-1549.
53. R. Abe, K. Shinmei, K. Hara and B. Ohtani, *Chemical Communications*, 2009, 3577-3579.
54. A. Kudo, H. Kato and I. Tsuji, *Chemistry Letters*, 2004, **33**, 1534-1539.
55. K. Sayama, K. Mukasa, R. Abe, Y. Abe and H. Arakawa, *Journal of Photochemistry and Photobiology A: Chemistry*, 2002, **148**, 71-77.
56. G. Liu, L. Wang, H. G. Yang, H.-M. Cheng and G. Q. Lu, *Journal of Materials Chemistry*, 2010, **20**, 831-843.
57. P. Qin, A. L. Domanski, A. K. Chandiran, R. Berger, H.-J. Butt, M. I. Dar, T. Moehl, N. Tetreault, P. Gao and S. Ahmad, *Nanoscale*, 2014, **6**, 1508-1514.
58. I. M. Arabatzis, T. Stergiopoulos, D. Andreeva, S. Kitova, S. G. Neophytides and P. Falaras, *Journal of Catalysis*, 2003, **220**, 127-135.
59. Y. Inoue, M. Okamura and K. Sato, *The Journal of Physical Chemistry*, 1985, **89**, 5184-5187.
60. X. Chen and S. S. Mao, *Chemical Reviews*, 2007, **107**, 2891-2959.
61. A. L. Linsebigler, G. Lu and J. T. Yates Jr, *Chemical Reviews*, 1995, **95**, 735-758.

## References

62. Y. Y. Gurkan, E. Kasapbasi and Z. Cinar, *Chemical Engineering Journal*, 2013, **214**, 34-44.
63. O. K. Varghese, M. Paulose, T. J. LaTempa and C. A. Grimes, *Nano Letters*, 2009, **9**, 731-737.
64. T. L. Thompson and J. T. Yates, *Chemical Reviews*, 2006, **106**, 4428-4453.
65. Y. Shimizu, K. Fakuda, Y. Takao and M. Egashira, *Sensors and Actuators B: Chemical*, 1993, **14**, 623-624.
66. S. N. Frank and A. J. Bard, *Journal of the American Chemical Society*, 1977, **99**, 303-304.
67. Y. Ohko, K. Hashimoto and A. Fujishima, *Journal of Physical Chemistry A*, 1997, **101**, 8057-8062.
68. H. Einaga, S. Futamura and T. Ibusuki, *Physical Chemistry Chemical Physics*, 1999, **1**, 4903-4908.
69. T. Minabe, D. A. Tryk, P. Sawunyama, Y. Kikuchi, K. Hashimoto and A. Fujishima, *Journal of Photochemistry and Photobiology A: Chemistry*, 2000, **137**, 53-62.
70. R. Wang, K. Hashimoto, A. Fujishima, M. Chikuni, E. Kojima, A. Kitamura, M. Shimohigoshi and T. Watanabe, *Advanced Materials*, 1998, **10**, 135-138.
71. K. Kobayakawa, C. Sato, Y. Sato and A. Fujishima, *Journal of Photochemistry and Photobiology A: Chemistry*, 1998, **118**, 65-69.
72. R. W. Matthews, *The Journal of Physical Chemistry*, 1987, **91**, 3328-3333.
73. I. Sopyan, M. Watanabe, S. Murasawa, K. Hashimoto and A. Fujishima, *Journal of Photochemistry and Photobiology A: Chemistry*, 1996, **98**, 79-86.
74. Y. Kikuchi, K. Sunada, T. Iyoda, K. Hashimoto and A. Fujishima, *Journal of Photochemistry and Photobiology A: Chemistry*, 1997, **106**, 51-56.
75. K. Sunada, T. Watanabe and K. Hashimoto, *Journal of Photochemistry and Photobiology A: Chemistry*, 2003, **156**, 227-233.
76. K. Sunada, T. Watanabe and K. Hashimoto, *Environmental Science & Technology*, 2003, **37**, 4785-4789.
77. K. Sunada, Y. Kikuchi, K. Hashimoto and A. Fujishima, *Environmental Science & Technology*, 1998, **32**, 726-728.
78. H. Honda, A. Ishizaki, R. Soma, K. Hashimoto and A. Fujishima, *Journal of the Illuminating Engineering Society*, 1998, **27**, 42-49.
79. I. A. Shkrob, T. W. Marin, H. He and P. Zapol, *The Journal of Physical Chemistry C*, 2012, **116**, 9450-9460.
80. J. Wu and C.-W. Huang, *Frontiers of Chemical Engineering in China*, 2010, **4**, 120-126.
81. A. Kudo, K. Domen, K.-i. Maruya and T. Onishi, *Journal of Catalysis*, 1992, **135**, 300-303.
82. A. Kudo, K. Domen, K.-i. Maruya and T. Onishi, *Chemistry Letters*, 1987, **6**, 1019-1022.
83. A. Fujishima, T. N. Rao and D. A. Tryk, *Journal of Photochemistry and Photobiology C: Photochemistry Reviews*, 2000, **1**, 1-21.
84. S. N. Frank and A. J. Bard, *Journal of the American Chemical Society*, 1977, **99**, 303-304.
85. S. N. Frank and A. J. Bard, *The Journal of Physical Chemistry*, 1977, **81**, 1484-1488.
86. D. F. Ollis, *Comptes Rendus de l'Académie des Sciences - Series IIC - Chemistry*, 2000, **3**, 405-411.

## References

87. C. Anderson and A. J. Bard, *The Journal of Physical Chemistry*, 1995, **99**, 9882-9885.
88. A. Heller, *Accounts of Chemical Research*, 1995, **28**, 503-508.
89. I. Sopyan, M. Watanabe, S. Murasawa, K. Hashimoto and A. Fujishima, *Journal of Electroanalytical Chemistry*, 1996, **415**, 183-186.
90. S. I. Matsushita, T. Miwa, D. A. Tryk and A. Fujishima, *Langmuir*, 1998, **14**, 6441-6447.
91. N. Negishi, T. Iyoda, K. Hashimoto and A. Fujishima, *Chemistry Letters*, 1995, 841-842.
92. Y. Cui, H. Du and L. Wen, 2008, **24**.
93. A. J. Bard, *Journal of Photochemistry*, 1979, **10**, 59-75.
94. A. J. Bard, *Science*, 1980, **207**, 139-144.
95. A. Kudo, K. Domen, K.-i. Maruya and T. Onishi, *Bulletin of the Chemical Society of Japan*, 1988, **61**, 1535-1538.
96. K. Sayama and H. Arakawa, *J Chem Soc Faraday T*, 1997, **93**, 1647-1654.
97. V. M. Daskalaki, P. Panagiotopoulou and D. I. Kondarides, *Chemical Engineering Journal*, 2011, **170**, 433-439.
98. R. Baba, S. Nakabayashi, A. Fujishima and K. Honda, *The Journal of Physical Chemistry*, 1985, **89**, 1902-1905.
99. S. Sato and J. M. White, *Chemical Physics Letters*, 1980, **72**, 83-86.
100. T. Ohno, D. Haga, K. Fujihara, K. Kaizaki and M. Matsumura, *The Journal of Physical Chemistry B*, 1997, **101**, 6415-6419.
101. K. Fujihara, T. Ohno and M. Matsumura, *Journal of the Chemical Society, Faraday Transactions*, 1998, **94**, 3705-3709.
102. T. Abe, E. Suzuki, K. Nagoshi, K. Miyashita and M. Kaneko, *The Journal of Physical Chemistry B*, 1999, **103**, 1119-1123.
103. K. Maeda, *Chemical Communications*, 2013, **49**, 8404-8406.
104. S.-C. Moon, H. Mametsuka, S. Tabata and E. Suzuki, *Catalysis Today*, 2000, **58**, 125-132.
105. K. Nakata and A. Fujishima, *Journal of Photochemistry and Photobiology C: Photochemistry Reviews*, 2012, **13**, 169-189.
106. D. O. Scanlon, C. W. Dunnill, J. Buckeridge, S. A. Shevlin, A. J. Logsdail, S. M. Woodley, C. R. A. Catlow, M. J. Powell, R. G. Palgrave and I. P. Parkin, *Nature materials*, 2013, **12**, 798-801.
107. H. Tang, K. Prasad, R. Sanjinès, P. E. Schmid and F. Lévy, *Journal of Applied Physics*, 1994, **75**, 2042-2047.
108. Y. Pleskov and Y. Gurevich, in *Semiconductor photoelectrochemistry*, 1986.
109. K. Rajeshwar, P. Singh and J. DuBow, *Electrochimica Acta*, 1978, **23**, 1117-1144.
110. C. T. Campbell and J. Sauer, *Chemical Reviews*, 2013, **113**, 3859-3862.
111. W. M. C. Sameera and F. Maseras, *Wiley Interdisciplinary Reviews: Computational Molecular Science*, 2012, n/a-n/a.
112. M. Ni, M. K. H. Leung, D. Y. C. Leung and K. Sumathy, *Renewable and Sustainable Energy Reviews*, 2007, **11**, 401-425.
113. K. Nakata, T. Ochiai, T. Murakami and A. Fujishima, *Electrochimica Acta*, 2012, **84**, 103-111.
114. U. Diebold, *Surface Science Reports*, 2003, **48**, 53-229.
115. R. W. G. Wyckoff, *Crystal structures*, Interscience Publishers, New York, 1948.
116. M. A. Henderson, *Langmuir*, 1996, **12**, 5093-5098.
117. M. A. Henderson, *Surface Science*, 1999, **419**, 174-187.

## References

118. M. A. Henderson, J. M. White, H. Uetsuka and H. Onishi, *Journal of the American Chemical Society*, 2003, **125**, 14974-14975.
119. A. Sclafani and J. M. Herrmann, *The Journal of Physical Chemistry*, 1996, **100**, 13655-13661.
120. T. Ohno, K. Tokieda, S. Higashida and M. Matsumura, *Applied Catalysis A: General*, 2003, **244**, 383-391.
121. O.-O. Prieto-Mahaney, N. Murakami, R. Abe and B. Ohtani, *Chemistry Letters*, 2009, **38**, 238-239.
122. A. Mills and G. Porter, *Journal of the Chemical Society, Faraday Transactions 1: Physical Chemistry in Condensed Phases*, 1982, **78**, 3659-3669.
123. B. Ohtani, *Chemistry Letters*, 2008, **37**, 216-229.
124. J. Yan, G. Wu, N. Guan, L. Li, Z. Li and X. Cao, *Physical Chemistry Chemical Physics*, 2013, **15**, 10978-10988.
125. W. Yan, B. Chen, S. M. Mahurin, V. Schwartz, D. R. Mullins, A. R. Lupini, S. J. Pennycook, S. Dai and S. H. Overbury, *The Journal of Physical Chemistry B*, 2005, **109**, 10676-10685.
126. C. Sousa, S. Tosoni and F. Illas, *Chemical Reviews*, 2012, **113**, 4456-4495.
127. A. Vittadini, M. Casarin and A. Selloni, *Theor Chem Account*, 2007, **117**, 663-671.
128. X.-Q. Gong and A. Selloni, *Journal of Catalysis*, 2007, **249**, 134-139.
129. N. A. Deskins, R. Rousseau and M. Dupuis, *The Journal of Physical Chemistry C*, 2010, **114**, 5891-5897.
130. M. Jonas, E. Stephan, T. Ralf and G. Stefan, *Journal of Physics: Condensed Matter*, 2012, **24**, 424206.
131. R. Sánchez-de-Armas, M. San-Miguel, J. Oviedo, A. Márquez and J. Sanz, *Physical Chemistry Chemical Physics*, 2011, **13**, 1506-1514.
132. M. Lazzeri, A. Vittadini and A. Selloni, *Physical Review B*, 2001, **63**, 155409.
133. E. Berardo, H.-S. Hu, K. Kowalski and M. A. Zwijnenburg, *The Journal of Chemical Physics*, 2013, **139**, 064313.
134. H. He, P. Zapol and L. A. Curtiss, *The Journal of Physical Chemistry C*, 2010, **114**, 21474-21481.
135. P. Zapol and L. Curtiss, *Journal of Computational and Theoretical Nanoscience*, 2007, **4**, 222-230.
136. R. Erdogan, M. F. Fellah and I. Onal, *International Journal of Quantum Chemistry*, 2011, **111**, 174-181.
137. A. V. Bandura, D. G. Sykes, V. Shapovalov, T. N. Troung, J. D. Kubicki and R. A. Evarestov, *The Journal of Physical Chemistry B*, 2004, **108**, 7844-7853.
138. Y.-G. Wang, Y. Yoon, V.-A. Glezakou, J. Li and R. Rousseau, *Journal of the American Chemical Society*, 2013, **135**, 10673-10683.
139. A. Valdés and G. J. Kroes, *The Journal of Physical Chemistry C*, 2010, **114**, 1701-1708.
140. W.-K. Li, X.-Q. Gong, G. Lu and A. Selloni, *The Journal of Physical Chemistry C*, 2008, **112**, 6594-6596.
141. C. L. Muhich, Y. Zhou, A. M. Holder, A. W. Weimer and C. B. Musgrave, *The Journal of Physical Chemistry C*, 2012, **116**, 10138-10149.
142. K. Kaur and C. V. Singh, *Energy Procedia*, 2012, **29**, 291-299.
143. D. M. Tobaldi, R. C. Pullar, M. P. Seabra and J. A. Labrincha, *Materials Letters*, 2014, **122**, 345-347.

## References

144. R. Su, R. Bechstein, L. Sør, R. T. Vang, M. Sillassen, B. Esbjörnsson, A. Palmqvist and F. Besenbacher, *The Journal of Physical Chemistry C*, 2011, **115**, 24287-24292.
145. X. Yan, T. Ohno, K. Nishijima, R. Abe and B. Ohtani, *Chemical Physics Letters*, 2006, **429**, 606-610.
146. B. Ohtani, O. O. Prieto-Mahaney, D. Li and R. Abe, *Journal of Photochemistry and Photobiology A: Chemistry*, 2010, **216**, 179-182.
147. W. Göpel, G. Rocker and R. Feierabend, *Physical Review B*, 1983, **28**, 3427-3438.
148. R. L. Kurtz, R. Stock-Bauer, T. E. Msdey, E. Román and J. De Segovia, *Surface Science*, 1989, **218**, 178-200.
149. T. L. Thompson, O. Diwald and J. T. Yates Jr, *Chemical Physics Letters*, 2004, **393**, 28-30.
150. M. A. Henderson, W. S. Epling, C. L. Perkins, C. H. F. Peden and U. Diebold, *The Journal of Physical Chemistry B*, 1999, **103**, 5328-5337.
151. U. Diebold, *Applied Physics A Materials Science & Processing*, 2003, **76**, 681-687.
152. R. Schaub, E. Wahlström, A. Rønnau, E. Lægsgaard, I. Stensgaard and F. Besenbacher, *Science*, 2003, **299**, 377-379.
153. S. Wendt, R. Schaub, J. Matthiesen, E. K. Vestergaard, E. Wahlström, M. D. Rasmussen, P. Thostrup, L. M. Molina, E. Lægsgaard, I. Stensgaard, B. Hammer and F. Besenbacher, *Surface Science*, 2005, **598**, 226-245.
154. O. Bikondoa, C. L. Pang, R. Ithnin, C. A. Muryn, H. Onishi and G. Thornton, *Nature Materials*, 2006, **5**, 189-192.
155. S. Wendt, J. Matthiesen, R. Schaub, E. K. Vestergaard, E. Lægsgaard, F. Besenbacher and B. Hammer, *Physical Review Letters*, 2006, **96**, 066107.
156. Z. Zhang, O. Bondarchuk, B. D. Kay, J. M. White and Z. Dohnálek, *The Journal of Physical Chemistry B*, 2006, **110**, 21840-21845.
157. J. V. Lauritsen, A. S. Foster, G. H. Olesen, M. C. Christensen, A. Kühnle, S. Helveg, J. R. Rostrup-Nielsen, B. S. Clausen, M. Reichling and F. Besenbacher, *Nanotechnology*, 2006, **17**, 3436.
158. V. E. Henrich and P. A. Cox, *The Surface Science of Metal Oxides*, by Victor E. Henrich and PA Cox, pp. 480. ISBN 0521566878. Cambridge, UK: Cambridge University Press, April 1996., 1996, **1**.
159. V. E. Henrich, G. Dresselhaus and H. J. Zeiger, *Physical Review Letters*, 1976, **36**, 1335-1339.
160. C. Di Valentin, G. Pacchioni and A. Selloni, *Physical Review Letters*, 2006, **97**, 166803.
161. M. V. Ganduglia-Pirovano, A. Hofmann and J. Sauer, *Surface Science Reports*, 2007, **62**, 219-270.
162. W. S. Epling, C. H. F. Peden, M. A. Henderson and U. Diebold, *Surface Science*, 1998, **412-413**, 333-343.
163. C. M. Yim, C. L. Pang and G. Thornton, *Physical Review Letters*, 2010, **104**, 036806.
164. S. Wendt, P. T. Sprunger, E. Lira, G. K. H. Madsen, Z. Li, J. Ø. Hansen, J. Matthiesen, A. Blekinge-Rasmussen, E. Lægsgaard, B. Hammer and F. Besenbacher, *Science*, 2008, **320**, 1755-1759.
165. E. Cho, S. Han, H.-S. Ahn, K.-R. Lee, S. K. Kim and C. S. Hwang, *Physical Review B*, 2006, **73**, 193202.
166. K. Mitsuhashi, H. Okumura, A. Visikovskiy, M. Takizawa and Y. Kido, *The Journal of Chemical Physics*, 2012, **136**, 124707.

## References

167. M. Murdoch, G. Waterhouse, M. Nadeem, J. Metson, M. Keane, R. Howe, J. Llorca and H. Idriss, *Nature Chemistry*, 2011, **3**, 489-492.
168. H. Van Damme and W. K. Hall, *Journal of the American Chemical Society*, 1979, **101**, 4373-4374.
169. S. Sato and J. M. White, *Journal of Catalysis*, 1981, **69**, 128-139.
170. K. Sayama and H. Arakawa, *Journal of Photochemistry and Photobiology A: Chemistry*, 1994, **77**, 243-247.
171. Y. Yoshida, M. Matsuoka, S. C. Moon, H. Mametsuka, E. Suzuki and M. Anpo, *Research on Chemical Intermediates*, 2000, **26**, 567-574.
172. C. M. Y. Yeung, K. M. K. Yu, Q. J. Fu, D. Thompsett, M. I. Petch and S. C. Tsang, *Journal of the American Chemical Society*, 2005, **127**, 18010-18011.
173. G. R. Bamwenda, S. Tsubota, T. Nakamura and M. Haruta, *Journal of Photochemistry and Photobiology A: Chemistry*, 1995, **89**, 177-189.
174. K. Domen, Y. Sakata, A. Kudo, K.-i. Maruya and T. Onishi, *Bull. Chem. Soc. Jpn*, 1988, **61**, 359-362.
175. R. Abe, H. Takami, N. Murakami and B. Ohtani, *Journal of the American Chemical Society*, 2008, **130**, 7780-7781.
176. S. Tabata, H. Nishida, Y. Masaki and K. Tabata, *Catalysis Letters*, 1995, **34**, 245-249.
177. K. Yamaguti and S. Sato, *Journal of the Chemical Society, Faraday Transactions 1: Physical Chemistry in Condensed Phases*, 1985, **81**, 1237-1246.
178. H. Yi, T. Peng, D. Ke, D. Ke, L. Zan and C. Yan, *International Journal of Hydrogen Energy*, 2008, **33**, 672-678.
179. A. Iwase, H. Kato and A. Kudo, *Catalysis Letters*, 2006, **108**, 7-10.
180. A. Kudo, K. Domen, K.-i. Maruya and T. Onishi, *Chemical Physics Letters*, 1987, **133**, 517-519.
181. K. Sayama and H. Arakawa, *Journal of the Chemical Society, Faraday Transactions*, 1997, **93**, 1647-1654.
182. J. Yu, H. Yu, C. Ao, S. Lee, J. C. Yu and W. Ho, *Thin Solid Films*, 2006, **496**, 273-280.
183. N. Serpone, D. Lawless, J. Disdier and J.-M. Herrmann, *Langmuir*, 1994, **10**, 643-652.
184. P. Qin, A. L. Domanski, A. K. Chandiran, R. Berger, H.-J. Butt, M. I. Dar, T. Moehl, N. Tetreault, P. Gao, S. Ahmad, M. K. Nazeeruddin and M. Gratzel, *Nanoscale*, 2014.
185. R. Asahi, T. Morikawa, T. Ohwaki, K. Aoki and Y. Taga, *Science*, 2001, **293**, 269-271.
186. S. J. Stewart, M. Fernández-García, C. Bolver, B. S. Mun and F. G. Requejo, *The Journal of Physical Chemistry B*, 2006, **110**, 16482-16486.
187. S. Sato, R. Nakamura and S. Abe, *Applied Catalysis A: General*, 2005, **284**, 131-137.
188. S. Sakthivel, M. Janczarek and H. Kisch, *The Journal of Physical Chemistry B*, 2004, **108**, 19384-19387.
189. T. Matsumoto, N. Iyi, Y. Kaneko, K. Kitamura, Y. Takasu and Y. Murakami, *Chemistry Letters*, 2004, **33**, 1508-1509.
190. H. Irie, S. Washizuka, Y. Watanabe, T. Kako and K. Hashimoto, *Journal of The Electrochemical Society*, 2005, **152**, E351-E356.
191. Y. Nosaka, M. Matsushita, J. Nishino and A. Y. Nosaka, *Science and Technology of Advanced Materials*, 2005, **6**, 143-148.
192. T. Ohno, T. Mitsui and M. Matsumura, *Chemistry Letters*, 2003, **32**, 364-365.

## References

193. T. Umebayashi, T. Yamaki, S. Tanaka and K. Asai, *Chemistry Letters*, 2003, **32**, 330-331.
194. W. Ho, J. C. Yu and S. Lee, *Journal of Solid State Chemistry*, 2006, **179**, 1171-1176.
195. W. Ho, J. C. Yu and S. Lee, *Chemical Communications*, 2006, 1115-1117.
196. S. U. M. Khan, M. Al-Shahry and W. B. Ingler, *Science*, 2002, **297**, 2243-2245.
197. S. Sakthivel and H. Kisch, *Angewandte Chemie International Edition*, 2003, **42**, 4908-4911.
198. W. Zhao, W. Ma, C. Chen, J. Zhao and Z. Shuai, *Journal of the American Chemical Society*, 2004, **126**, 4782-4783.
199. T. Peng, K. Dai, H. Yi, D. Ke, P. Cai and L. Zan, *Chemical Physics Letters*, 2008, **460**, 216-219.
200. R. Abe, *Journal of Photochemistry and Photobiology C: Photochemistry Reviews*, 2010, **11**, 179-209.
201. K. Rajeshwar, *J Appl Electrochem*, 1985, **15**, 1-22.
202. H. P. Maruska and A. K. Ghosh, *Solar Energy*, 1978, **20**, 443-458.
203. M. R. Hoffmann, S. T. Martin, W. Choi and D. W. Bahnemann, *Chemical Reviews*, 1995, **95**, 69-96.
204. M. Haruta, T. Kobayashi, H. Sano and N. Yamada, *Chemistry Letters*, 1987, 405-408.
205. M. Haruta, N. Yamada, T. Kobayashi and S. Iijima, *Journal of Catalysis*, 1989, **115**, 301-309.
206. M. Haruta, *Catalysis Today*, 1997, **36**, 153-166.
207. T. Hayashi, K. Tanaka and M. Haruta, *Journal of Catalysis*, 1998, **178**, 566-575.
208. M. Haruta and M. Daté, *Applied Catalysis A: General*, 2001, **222**, 427-437.
209. M. Haruta, *CATTECH*, 2002, **6**, 102-115.
210. M. Haruta, *Journal of New Materials for Electrochemical Systems*, 2004, **7**, 163-172.
211. M. Haruta, *Nature*, 2005, **437**, 1098-1099.
212. J. Huang, T. Akita, J. Faye, T. Fujitani, T. Takei and M. Haruta, *Angewandte Chemie International Edition*, 2009, **48**, 7862-7866.
213. G. Schmid, *Chemical Reviews*, 1992, **92**, 1709-1727.
214. G. Schmid and L. F. Chi, *Advanced Materials*, 1998, **10**, 515-526.
215. M. Brust and C. J. Kiely, *Colloids and Surfaces A: Physicochemical and Engineering Aspects*, 2002, **202**, 175-186.
216. J. H. Fendler, *Nanoparticles and Nanostructured Films: Preparation, Characterization, and Applications*, John Wiley & Sons, 2008.
217. D. L. Fedlheim and C. A. Foss, *Metal nanoparticles: synthesis, characterization, and applications*, CRC Press, 2001.
218. U. Kreibitz and M. Vollmer, 1995.
219. L. Guzzi, D. Horváth, Z. Pászti, L. Tóth, Z. E. Horváth, A. Karacs and G. Pető, *The Journal of Physical Chemistry B*, 2000, **104**, 3183-3193.
220. T. Kawasaki, Y. Takai and R. Shimizu, *Applied Physics Letters*, 2001, **79**, 3509-3511.
221. L. Guzzi, G. Pető, A. Beck, K. Frey, O. Geszti, G. Molnár and C. Daróczi, *Journal of the American Chemical Society*, 2003, **125**, 4332-4337.
222. S. Schimpf, M. Lucas, C. Mohr, U. Rodemerck, A. Brückner, J. Radnik, H. Hofmeister and P. Claus, *Catalysis Today*, 2002, **72**, 63-78.

## References

223. R. M. Finch, N. A. Hodge, G. J. Hutchings, A. Meagher, Q. A. Pankhurst, M. Rafiq H. Siddiqui, F. E. Wagner and R. Whyman, *Physical Chemistry Chemical Physics*, 1999, **1**, 485-489.
224. Y. Yuan, K. Asakura, H. Wan, K. Tsai and Y. Iwasawa, *Chemistry Letters*, 1996, **25**, 755-756.
225. A. Ueda, T. Oshima and M. Haruta, *Applied Catalysis B: Environmental*, 1997, **12**, 81-93.
226. T. M. Salama, R. Ohnishi, T. Shido and M. Ichikawa, *Journal of Catalysis*, 1996, **162**, 169-178.
227. H. Sakurai and M. Haruta, *Catalysis Today*, 1996, **29**, 361-365.
228. D. Andreeva, T. Tabakova, V. Idakiev, P. Christov and R. Giovanoli, *Applied Catalysis A: General*, 1998, **169**, 9-14.
229. D. Andreeva, V. Idakiev, T. Tabakova and A. Andreev, *Journal of Catalysis*, 1996, **158**, 354-355.
230. F. Boccuzzi, A. Chiorino, M. Manzoli, D. Andreeva and T. Tabakova, *Journal of Catalysis*, 1999, **188**, 176-185.
231. H. Sakurai, T. Akita, S. Tsubota, M. Kiuchi and M. Haruta, *Applied Catalysis A: General*, 2005, **291**, 179-187.
232. F. Boccuzzi, A. Chiorino, M. Manzoli, D. Andreeva, T. Tabakova, L. Ilieva and V. Iadakiev, *Catalysis Today*, 2002, **75**, 169-175.
233. D. Andreeva, *Gold Bulletin*, 2002, **35**, 82-88.
234. A. Venugopal and M. S. Scurrrell, *Applied Catalysis A: General*, 2004, **258**, 241-249.
235. A. Venugopal, J. Aluha, D. Mogano and M. S. Scurrrell, *Applied Catalysis A: General*, 2003, **245**, 149-158.
236. H. Sakurai, A. Ueda, T. Kobayashi and M. Haruta, *Chemical Communications*, 1997, 271-272.
237. V. Idakiev, T. Tabakova, Z. Y. Yuan and B. L. Su, *Applied Catalysis A: General*, 2004, **270**, 135-141.
238. N. Yi, R. Si, H. Saltsburg and M. Flytzani-Stephanopoulos, *Energy & Environmental Science*, 2010, **3**, 831-837.
239. M. Haruta, A. Ueda, S. Tsubota and R. Torres Sanchez, *Catalysis Today*, 1996, **29**, 443-447.
240. W. Zhu, R. Michalsky, Ö. Metin, H. Lv, S. Guo, C. J. Wright, X. Sun, A. A. Peterson and S. Sun, *Journal of the American Chemical Society*, 2013, **135**, 16833-16836.
241. A. Corma and P. Serna, *Science*, 2006, **313**, 332-334.
242. C. Della Pina, E. Falletta, L. Prati and M. Rossi, *Chemical Society Reviews*, 2008, **37**, 2077-2095.
243. M. Turner, V. B. Golovko, O. P. Vaughan, P. Abdulkin, A. Berenguer-Murcia, M. S. Tikhov, B. F. Johnson and R. M. Lambert, *Nature*, 2008, **454**, 981-983.
244. P. Landon, J. Ferguson, B. E. Solsona, T. Garcia, S. Al-Sayari, A. F. Carley, A. A. Herzing, C. J. Kiely, M. Makkee, J. A. Moulijn, A. Overweg, S. E. Golunski and G. J. Hutchings, *Journal of Materials Chemistry*, 2006, **16**, 199-208.
245. P. Landon, J. Ferguson, B. E. Solsona, T. Garcia, A. F. Carley, A. A. Herzing, C. J. Kiely, S. E. Golunski and G. J. Hutchings, *Chemical Communications*, 2005, 3385-3387.
246. H. Kominami, A. Furusho, S.-y. Murakami, H. Inoue, Y. Kera and B. Ohtani, *Catalysis Letters*, 2001, **76**, 31-34.

## References

247. R. Meyer, C. Lemire, S. K. Shaikhutdinov and H. J. Freund, *Gold Bulletin*, 2004, **37**, 72-124.
248. M. D. Hughes, Y.-J. Xu, P. Jenkins, P. McMorn, P. Landon, D. I. Enache, A. F. Carley, G. A. Attard, G. J. Hutchings and F. King, *Nature*, 2005, **437**, 1132-1135.
249. L. Prati and M. Rossi, *Journal of Catalysis*, 1998, **176**, 552-560.
250. G. Hutchings, in *Nanotechnology in Catalysis*, eds. B. Zhou, S. Han, R. Raja and G. Somorjai, Springer New York, 2007, ch. 4, pp. 39-54.
251. J. Cai, H. Ma, J. Zhang, Q. Song, Z. Du, Y. Huang and J. Xu, *Chemistry – A European Journal*, 2013, 14215-14223.
252. S. Galvagno and G. Parravano, *Journal of Catalysis*, 1978, **55**, 178-190.
253. E. Bae and W. Choi, *Environmental Science & Technology*, 2002, **37**, 147-152.
254. N. Dimitratos, J. A. Lopez-Sanchez and G. J. Hutchings, *Chemical Science*, 2012, **3**, 20-44.
255. A. S. K. Hashmi and G. J. Hutchings, *Angewandte Chemie International Edition*, 2006, **45**, 7896-7936.
256. G. J. Hutchings, *Catalysis today*, 2002, **72**, 11-17.
257. A. S. Hashmi, *Gold Bulletin*, 2003, **36**, 3-9.
258. J. H. Teles, S. Brode and M. Chabanas, *Angewandte Chemie International Edition*, 1998, **37**, 1415-1418.
259. M. J. Kahlich, H. A. Gasteiger and R. J. Behm, *Journal of Catalysis*, 1999, **182**, 430-440.
260. B. Qiao and Y. Deng, *Chemical Communications*, 2003, 2192-2193.
261. G. Avgouropoulos, T. Ioannides, C. Papadopoulou, J. Batista, S. Hocevar and H. K. Matralis, *Catalysis Today*, 2002, **75**, 157-167.
262. S. Minicò, S. Scirè, C. Crisafulli, A. M. Visco and S. Galvagno, *Catalysis Letters*, 1997, **47**, 273-276.
263. L. Guczi, D. Horváth, Z. Pászti and G. Pető, *Catalysis Today*, 2002, **72**, 101-105.
264. M. Haruta, S. Tsubota, T. Kobayashi, H. Kageyama, M. J. Genet and B. Delmon, *Journal of Catalysis*, 1993, **144**, 175-192.
265. S. D. Gardner, G. B. Hoflund, B. T. Upchurch, D. R. Schryer, E. J. Kielin and J. Schryer, *Journal of Catalysis*, 1991, **129**, 114-120.
266. W. S. Epling, G. B. Hoflund, J. F. Weaver, S. Tsubota and M. Haruta, *The Journal of Physical Chemistry*, 1996, **100**, 9929-9934.
267. A. A. Herzing, C. J. Kiely, A. F. Carley, P. Landon and G. J. Hutchings, *Science*, 2008, **321**, 1331-1335.
268. M. M. Schubert, S. Hackenberg, A. C. van Veen, M. Muhler, V. Plzak and R. J. Behm, *Journal of Catalysis*, 2001, **197**, 113-122.
269. J. Guzman, S. Carrettin and A. Corma, *Journal of the American Chemical Society*, 2005, **127**, 3286-3287.
270. A. Luengnaruemitchai, S. Osuwan and E. Gulari, *International Journal of Hydrogen Energy*, 2004, **29**, 429-435.
271. R. D. Waters, J. J. Weimer and J. E. Smith, *Catalysis Letters*, 1994, **30**, 181-188.
272. F. Boccuzzi, A. Chiorino, S. Tsubota and M. Haruta, *Catalysis Letters*, 1994, **29**, 225-234.
273. F. Boccuzzi, A. Chiorino, S. Tsubota and M. Haruta, *Sensors and Actuators B: Chemical*, 1995, **25**, 540-543.
274. M. Haruta, H. Kageyama, N. Kamijo, T. Kobayashi and F. Delannay, in *Studies in Surface Science and Catalysis*, ed. T. Inui, Elsevier, 1989, vol. Volume 44, pp. 33-42.

## References

275. F. Moreau, G. C. Bond and A. O. Taylor, *Journal of Catalysis*, 2005, **231**, 105-114.
276. R. Zanella and C. Louis, *Catalysis Today*, 2005, **107–108**, 768-777.
277. W.-C. Li, M. Comotti and F. Schüth, *Journal of Catalysis*, 2006, **237**, 190-196.
278. M. Comotti, W.-C. Li, B. Spliethoff and F. Schüth, *Journal of the American Chemical Society*, 2005, **128**, 917-924.
279. G. Bond and D. Thompson, *Gold Bulletin*, 2000, **33**, 41-50.
280. M. Okumura, S. Nakamura, S. Tsubota, T. Nakamura, M. Azuma and M. Haruta, *Catalysis Letters*, 1998, **51**, 53-58.
281. S. Tsubota, T. Nakamura, K. Tanaka and M. Haruta, *Catalysis Letters*, 1998, **56**, 131-135.
282. G. R. Bamwenda, S. Tsubota, T. Nakamura and M. Haruta, *Catalysis Letters*, 1997, **44**, 83-87.
283. M. A. Bollinger and M. A. Vannice, *Applied Catalysis B: Environmental*, 1996, **8**, 417-443.
284. V. Bondzie, S. Parker and C. Campbell, *Catalysis Letters*, 1999, **63**, 143-151.
285. M. Valden, S. Pak, X. Lai and D. W. Goodman, *Catalysis Letters*, 1998, **56**, 7-10.
286. M. Valden, X. Lai and D. W. Goodman, *Science*, 1998, **281**, 1647-1650.
287. J. Schwank, *Gold Bulletin*, 1983, **16**, 103-110.
288. Y. Iizuka, H. Fujiki, N. Yamauchi, T. Chijiwa, S. Arai, S. Tsubota and M. Haruta, *Catalysis Today*, 1997, **36**, 115-123.
289. S. D. Lin, M. Bollinger and M. A. Vannice, *Catalysis Letters*, 1993, **17**, 245-262.
290. J.-D. Grunwaldt and A. Baiker, *The Journal of Physical Chemistry B*, 1999, **103**, 1002-1012.
291. H. Liu, A. I. Kozlov, A. P. Kozlova, T. Shido, K. Asakura and Y. Iwasawa, *Journal of Catalysis*, 1999, **185**, 252-264.
292. J.-D. Grunwaldt, C. Kiener, C. Wögerbauer and A. Baiker, *Journal of Catalysis*, 1999, **181**, 223-232.
293. F. Boccuzzi, A. Chiorino, M. Manzoli, P. Lu, T. Akita, S. Ichikawa and M. Haruta, *Journal of Catalysis*, 2001, **202**, 256-267.
294. K. Sayo, S. Deki and S. Hayashi, *Journal of Colloid and Interface Science*, 1999, **212**, 597-599.
295. B. Schumacher, V. Plzak, M. Kinne and R. J. Behm, *Catalysis Letters*, 2003, **89**, 109-114.
296. L. Fan, N. Ichikuni, S. Shimazu and T. Uematsu, *Applied Catalysis A: General*, 2003, **246**, 87-95.
297. Y. Iizuka, T. Tode, T. Takao, K.-i. Yatsu, T. Takeuchi, S. Tsubota and M. Haruta, *Journal of Catalysis*, 1999, **187**, 50-58.
298. S. Tsubota, D. A. H. Cunningham, Y. Bando and M. Haruta, in *Studies in Surface Science and Catalysis*, eds. J. M. B. D. P. A. J. G. Poncelet and P. Grange, Elsevier, 1995, vol. Volume 91, pp. 227-235.
299. G. C. Bond and D. T. Thompson, *Catalysis Reviews*, 1999, **41**, 319-388.
300. A. I. Kozlov, A. P. Kozlova, H. Liu and Y. Iwasawa, *Applied Catalysis A: General*, 1999, **182**, 9-28.
301. N. Lopez, J. K. Nørskov, T. V. W. Janssens, A. Carlsson, A. Puig-Molina, B. S. Clausen and J. D. Grunwaldt, *Journal of Catalysis*, 2004, **225**, 86-94.
302. M. Mavrikakis, P. Stoltze and J. K. Nørskov, *Catalysis Letters*, 2000, **64**, 101-106.
303. Y.-W. Tai, J.-S. Chen, C.-C. Yang and B.-Z. Wan, *Catalysis Today*, 2004, **97**, 95-101.

## References

304. K. Qian, B. C. Sweeny, A. C. Johnston-Peck, W. Niu, J. O. Graham, J. S. DuChene, J. Qiu, Y.-C. Wang, M. H. Engelhard, D. Su, E. A. Stach and W. D. Wei, *Journal of the American Chemical Society*, 2014, **136**, 9842-9845.
305. C. Gomes Silva, R. Juárez, T. Marino, R. Molinari and H. García, *Journal of the American Chemical Society*, 2010, **133**, 595-602.
306. Z. W. Seh, S. Liu, M. Low, S.-Y. Zhang, Z. Liu, A. Mlayah and M.-Y. Han, *Advanced Materials*, 2012, **24**, 2310-2314.
307. J. B. Priebe, M. Karnahl, H. Junge, M. Beller, D. Hollmann and A. Brückner, *Angewandte Chemie International Edition*, 2013, **52**, 11420-11424.
308. S. Linic, P. Christopher and D. B. Ingram, *Nature Materials*, 2011, **10**, 911-921.
309. A. Primo, A. Corma and H. Garcia, *Physical Chemistry Chemical Physics*, 2011, **13**, 886-910.
310. E. Thimsen, F. Le Formal, M. Grätzel and S. C. Warren, *Nano Letters*, 2010, **11**, 35-43.
311. A. Primo, T. Marino, A. Corma, R. Molinari and H. García, *Journal of the American Chemical Society*, 2011, **133**, 6930-6933.
312. A. Tanaka, K. Hashimoto and H. Kominami, *Journal of the American Chemical Society*, 2013, **136**, 586-589.
313. C. R. Henry, *Surface Science Reports*, 1998, **31**, 231-325.
314. C. R. Henry, *Crystal Research and Technology*, 1998, **33**, 1119-1140.
315. M.-C. Daniel and D. Astruc, *Chemical Reviews*, 2003, **104**, 293-346.
316. F. Sastre, M. Oteri, A. Corma and H. Garcia, *Energy & Environmental Science*, 2013, **6**, 2211-2215.
317. S. Lin and M. A. Vannice, *Catalysis Letters*, 1991, **10**, 47-61.
318. G. H. Takaoka, T. Hamano, K. Fukushima, J. Matsuo and I. Yamada, *Nuclear Instruments and Methods in Physics Research Section B: Beam Interactions with Materials and Atoms*, 1997, **121**, 503-506.
319. Z.-P. Liu, P. Hu and A. Alavi, *Journal of the American Chemical Society*, 2002, **124**, 14770-14779.
320. M. Haruta, B. S. Uphade, S. Tsubota and A. Miyamoto, *Research on Chemical Intermediates*, 1998, **24**, 329-336.
321. C. Bianchi, F. Porta, L. Prati and M. Rossi, *Topics in Catalysis*, 2000, **13**, 231-236.
322. G. Liu, G. Li and H. Song, *Catalysis Letters*, 2009, **128**, 493-501.
323. G. Wu, T. Chen, W. Su, G. Zhou, X. Zong, Z. Lei and C. Li, *International Journal of Hydrogen Energy*, 2008, **33**, 1243-1251.
324. F. Cosandey and T. E. Madey, *Surface Review & Letters*, 2001, **8**, 73.
325. R. Zanella, S. Giorgio, C. R. Henry and C. Louis, *The Journal of Physical Chemistry B*, 2002, **106**, 7634-7642.
326. R. Zanella, L. Delannoy and C. Louis, *Applied Catalysis A: General*, 2005, **291**, 62-72.
327. M. S. Chen and D. W. Goodman, *Catalysis Today*, 2006, **111**, 22-33.
328. Y. Chen, B. Zhu, M. Yao, S. Wang and S. Zhang, *Catalysis Communications*, 2010, **11**, 1003-1007.
329. D. A. H. Cunningham, W. Vogel, H. Kageyama, S. Tsubota and M. Haruta, *Journal of Catalysis*, 1998, **177**, 1-10.
330. E. Wahlström, N. Lopez, R. Schaub, P. Thstrup, A. Rønnau, C. Africh, E. Lægsgaard, J. K. Nørskov and F. Besenbacher, *Physical Review Letters*, 2003, **90**, 026101.

## References

331. N. Lopez and J. K. Nørskov, *Journal of the American Chemical Society*, 2002, **124**, 11262-11263.
332. J. A. Rodriguez, G. Liu, T. Jirsak, J. Hrbek, Z. Chang, J. Dvorak and A. Maiti, *Journal of the American Chemical Society*, 2002, **124**, 5242-5250.
333. Y. Wang and G. S. Hwang, *Surface Science*, 2003, **542**, 72-80.
334. A. K. Santra, A. Kolmakov, F. Yang and D. W. Goodman, *Japanese Journal of Applied Physics*, 2003, **42**, 4795.
335. N. Lopez and J. K. Nørskov, *Surface Science*, 2002, **515**, 175-186.
336. B. K. Min, W. T. Wallace and D. W. Goodman, *Surface Science*, 2006, **600**, L7-L11.
337. X.-Q. Gong, A. Selloni, O. Dulub, P. Jacobson and U. Diebold, *Journal of the American Chemical Society*, 2007, **130**, 370-381.
338. A. Vijay, G. Mills and H. Metiu, *The Journal of Chemical Physics*, 2003, **118**, 6536-6551.
339. Z. Yang, R. Wu and D. W. Goodman, *Physical Review B*, 2000, **61**, 14066-14071.
340. L. Giordano, G. Pacchioni, T. Bredow and J. F. Sanz, *Surface Science*, 2001, **471**, 21-31.
341. S. Chretien and H. Metiu, *The Journal of Chemical Physics*, 2007, **127**, 084704.
342. A. Vittadini and A. Selloni, *The Journal of Chemical Physics*, 2002, **117**, 353-361.
343. M. Boronat, F. Illas and A. Corma, *The Journal of Physical Chemistry A*, 2009, **113**, 3750-3757.
344. C. Sun and S. C. Smith, *The Journal of Physical Chemistry C*, 2012, **116**, 3524-3531.
345. J. R. Kitchin, M. A. Barteau and J. G. Chen, *Surface Science*, 2003, **526**, 323-331.
346. C. E. J. Mitchell, A. Howard, M. Carney and R. G. Egdell, *Surface Science*, 2001, **490**, 196-210.
347. L. Zhang, F. Cosandey, R. Persaud and T. E. Madey, *Surface Science*, 1999, **439**, 73-85.
348. P. Buffat and J. P. Borel, *Physical Review A*, 1976, **13**, 2287-2298.
349. M. Okumura, K. Tanaka, A. Ueda and M. Haruta, *Solid State Ionics*, 1997, **95**, 143-149.
350. C. Xu, W. S. Oh, G. Liu, D. Y. Kim and D. W. Goodman, *Journal of Vacuum Science & Technology A*, 1997, **15**, 1261-1268.
351. P. Wynblatt and N. A. Gjostein, *Acta Metallurgica*, 1976, **24**, 1165-1174.
352. P. Wynblatt, *Acta Metallurgica*, 1976, **24**, 1175-1182.
353. M. J. J. Jak, C. Konstapel, A. van Kreuningen, J. Verhoeven and J. W. M. Frenken, *Surface Science*, 2000, **457**, 295-310.
354. E. C. H. Sykes, F. J. Williams, M. S. Tikhov and R. M. Lambert, *The Journal of Physical Chemistry B*, 2002, **106**, 5390-5394.
355. A. Kolmakov and D. W. Goodman, *Catalysis Letters*, 2000, **70**, 93-97.
356. A. Kolmakov and D. W. Goodman, *Surface Science*, 2001, **490**, L597-L601.
357. K.-i. Fukui, S. Sugiyama and Y. Iwasawa, *Physical Chemistry Chemical Physics*, 2001, **3**, 3871-3877.
358. J. A. Schwarz, C. Contescu and A. Contescu, *Chemical Reviews*, 1995, **95**, 477-510.
359. A. I. Kozlov, A. P. Kozlova, K. Asakura, Y. Matsui, T. Kogure, T. Shido and Y. Iwasawa, *Journal of Catalysis*, 2000, **196**, 56-65.
360. J. K. Edwards, E. Ntainjua N, A. F. Carley, A. A. Herzing, C. J. Kiely and G. J. Hutchings, *Angewandte Chemie International Edition*, 2009, **48**, 8512-8515.

## References

361. L. Zhang, R. Persaud and T. E. Madey, *Physical Review B*, 1997, **56**, 10549-10557.
362. X. Lai, T. P. S. Clair, M. Valden and D. W. Goodman, *Progress in Surface Science*, 1998, **59**, 25-52.
363. Q. Guo, K. Luo, K. A. Davis and D. W. Goodman, *Surface and Interface Analysis*, 2001, **32**, 161-165.
364. N. Spiridis, J. Haber and J. Korecki, *Vacuum*, 2001, **63**, 99-105.
365. S. C. Parker, A. W. Grant, V. A. Bondzie and C. T. Campbell, *Surface Science*, 1999, **441**, 10-20.
366. L. D. Menard, F. Xu, R. G. Nuzzo and J. C. Yang, *Journal of Catalysis*, 2006, **243**, 64-73.
367. J. A. Lopez-Sanchez, N. Dimitratos, C. Hammond, G. L. Brett, L. Kesavan, S. White, P. Miedziak, R. Tiruvalam, R. L. Jenkins and A. F. Carley, *Nature Chemistry*, 2011, **3**, 551-556.
368. D. P. Anderson, J. F. Alvino, A. Gentleman, H. Al Qahtani, L. Thomsen, M. I. Polson, G. F. Metha, V. B. Golovko and G. G. Andersson, *Physical Chemistry Chemical Physics*, 2013, **15**, 3917-3929.
369. D. P. Anderson, R. H. Adnan, J. F. Alvino, O. Shipper, B. Donoeva, J.-Y. Ruzicka, H. Al Qahtani, H. H. Harris, B. Cowie, J. B. Aitken, V. B. Golovko, G. F. Metha and G. G. Andersson, *Physical Chemistry Chemical Physics*, 2013, **15**, 14806-14813.
370. T. H. Lee and K. M. Ervin, *The Journal of Physical Chemistry*, 1994, **98**, 10023-10031.
371. D. M. Cox, R. Brickman, K. Creegan and A. Kaldor, *Z Phys D - Atoms, Molecules and Clusters*, 1991, **19**, 353-355.
372. A. Sanchez, S. Abbet, U. Heiz, W. D. Schneider, H. Häkkinen, R. N. Barnett and U. Landman, *The Journal of Physical Chemistry A*, 1999, **103**, 9573-9578.
373. S. Chrétien and H. Metiu, *The Journal of Chemical Physics*, 2007, **126**, -.
374. W. E. Kaden, T. Wu, W. A. Kunkel and S. L. Anderson, *Science*, 2009, **326**, 826-829.
375. M. D. Morse, M. E. Geusic, J. R. Heath and R. E. Smalley, *The Journal of Chemical Physics*, 1985, **83**, 2293-2304.
376. U. Heiz, A. Sanchez, S. Abbet and W. D. Schneider, *Journal of the American Chemical Society*, 1999, **121**, 3214-3217.
377. G. Schmid and D. Fenske, *Philosophical Transactions of the Royal Society A: Mathematical, Physical and Engineering Sciences*, 2010, **368**, 1207-1210.
378. K. Okazaki, S. Ichikawa, Y. Maeda, M. Haruta and M. Kohyama, *Applied Catalysis A: General*, 2005, **291**, 45-54.
379. C. Wang and D. Astruc, *Chemical Society Reviews*, 2014.
380. P. Wang, B. Huang, Y. Dai and M.-H. Whangbo, *Physical Chemistry Chemical Physics*, 2012, **14**, 9813-9825.
381. K. M. Mayer and J. H. Hafner, *Chemical Reviews*, 2011, **111**, 3828-3857.
382. K. Nakayama, K. Tanabe and H. A. Atwater, *Applied Physics Letters*, 2008, **93**, -.
383. P. K. Jain, I. H. El-Sayed and M. A. El-Sayed, *Nano Today*, 2007, **2**, 18-29.
384. C. J. Murphy, A. M. Gole, J. W. Stone, P. N. Sisco, A. M. Alkilany, E. C. Goldsmith and S. C. Baxter, *Accounts of Chemical Research*, 2008, **41**, 1721-1730.
385. R. Bardhan, S. Lal, A. Joshi and N. J. Halas, *Accounts of Chemical Research*, 2011, **44**, 936-946.

## References

386. R. Mout, D. F. Moyano, S. Rana and V. M. Rotello, *Chemical Society Reviews*, 2012, **41**, 2539-2544.
387. S. S. Rayalu, D. Jose, M. V. Joshi, P. A. Mangrulkar, K. Shrestha and K. Klabunde, *Applied Catalysis B: Environmental*, 2013, **142–143**, 684-693.
388. S. C. Warren and E. Thimsen, *Energy & Environmental Science*, 2012, **5**, 5133-5146.
389. J. Yan, G. Wu, N. Guan and L. Li, *Chemical Communications*, 2013, **49**, 11767-11769.
390. X. Zhang, Y. L. Chen, R.-S. Liu and D. P. Tsai, *Reports on Progress in Physics*, 2013, **76**, 046401.
391. V. D. Borman, M. A. Pushkin, V. N. Tronin and V. I. Troyan, *J. Exp. Theor. Phys.*, 2010, **110**, 1005-1025.
392. C. C. Chusuei, X. Lai, K. Luo and D. W. Goodman, *Topics in Catalysis*, 2000, **14**, 71-83.
393. Z. Yang and R. Wu, *Physical Review B*, 2003, **67**, 081403.
394. A. Howard, D. N. S. Clark, C. E. J. Mitchell, R. G. Egdell and V. R. Dhanak, *Surface Science*, 2002, **518**, 210-224.
395. R. S. Cataliotti, G. Compagnini, C. Crisafulli, S. Minicò, B. Pignataro, P. Sassi and S. Scirè, *Surface Science*, 2001, **494**, 75-82.
396. S. Link, M. A. El-Sayed, T. Gregory Schaaff and R. L. Whetten, *Chemical Physics Letters*, 2002, **356**, 240-246.
397. M. Haruta, in *Studies in Surface Science and Catalysis*, eds. S. T. O. A. M. G. R.K. Grasselli and J. E. Lyons, Elsevier, 1997, vol. Volume 110, pp. 123-134.
398. V. Subramanian, E. E. Wolf and P. V. Kamat, *Journal of the American Chemical Society*, 2004, **126**, 4943-4950.
399. H. Huber, D. McIntosh and G. A. Ozin, *Inorganic Chemistry*, 1977, **16**, 975-979.
400. J. Li, X. Li, H.-J. Zhai and L.-S. Wang, *Science*, 2003, **299**, 864-867.
401. K. J. Taylor, C. L. Pettiette-Hall, O. Cheshnovsky and R. E. Smalley, *The Journal of Chemical Physics*, 1992, **96**, 3319-3329.
402. I. Balteanu, O. P. Balaj, B. S. Fox, M. K. Beyer, Z. Bastl and V. E. Bondybey, *Physical Chemistry Chemical Physics*, 2003, **5**, 1213-1218.
403. G. Schmid, *Chemical Society Reviews*, 2008, **37**, 1909-1930.
404. M. Büttner and P. Oelhafen, *Surface Science*, 2006, **600**, 1170-1177.
405. Y. Kitsudo, A. Iwamoto, H. Matsumoto, K. Mitsuhara, T. Nishimura, M. Takizawa, T. Akita, Y. Maeda and Y. Kido, *Surface Science*, 2009, **603**, 2108-2114.
406. S. Kunz, K. Hartl, M. Nesselberger, F. F. Schweinberger, G. Kwon, M. Hanzlik, K. J. J. Mayrhofer, U. Heiz and M. Arenz, *Physical Chemistry Chemical Physics*, 2010, **12**, 10288-10291.
407. B. Yoon, H. Häkkinen, U. Landman, A. S. Wörz, J.-M. Antonietti, S. Abbet, K. Judai and U. Heiz, *Science*, 2005, **307**, 403-407.
408. U. Heiz and W.-D. Schneider, *Critical Reviews in Solid State and Materials Sciences*, 2001, **26**, 251-290.
409. M. Chen and D. W. Goodman, *Chemical Society Reviews*, 2008, **37**, 1860-1870.
410. R. M. Crooks, M. Zhao, L. Sun, V. Chechik and L. K. Yeung, *Accounts of Chemical Research*, 2000, **34**, 181-190.
411. H. Sakurai, S. Tsubota and M. Haruta, *Applied Catalysis A: General*, 1993, **102**, 125-136.
412. J.-D. Grunwaldt, M. Maciejewski, O. S. Becker, P. Fabrizioli and A. Baiker, *Journal of Catalysis*, 1999, **186**, 458-469.

## References

413. A. Beck, A. Horváth, Z. Schay, G. Stefler, Z. Koppány, I. Sajó, O. Geszti and L. Guzzi, *Topics in Catalysis*, 2007, **44**, 115-121.
414. P. Maity, S. Xie, M. Yamauchi and T. Tsukuda, *Nanoscale*, 2012, **4**, 4027-4037.
415. Y. Liu, H. Tsunoyama, T. Akita and T. Tsukuda, *The Journal of Physical Chemistry C*, 2009, **113**, 13457-13461.
416. H.-G. Boyen, G. Kästle, F. Weigl, B. Koslowski, C. Dietrich, P. Ziemann, J. P. Spatz, S. Riethmüller, C. Hartmann, M. Möller, G. Schmid, M. G. Garnier and P. Oelhafen, *Science*, 2002, **297**, 1533-1536.
417. A. P. Kozlova, A. I. Kozlov, S. Sugiyama, Y. Matsui, K. Asakura and Y. Iwasawa, *Journal of Catalysis*, 1999, **181**, 37-48.
418. D. Guillemot, V. Y. Borovkov, V. B. Kazansky, M. Polisset-Thfoin and J. Fraissard, *Journal of the Chemical Society, Faraday Transactions*, 1997, **93**, 3587-3591.
419. R. Raja, V. B. Golovko, J. M. Thomas, A. Berenguer-Murcia, W. Zhou, S. Xie and B. F. G. Johnson, *Chemical Communications*, 2005, 2026-2028.
420. Y. Liu, H. Tsunoyama, T. Akita, S. Xie and T. Tsukuda, *Acs Catal*, 2010, **1**, 2-6.
421. J. A. Lopez-Sanchez, N. Dimitratos, C. Hammond, G. L. Brett, L. Kesavan, S. White, P. Miedziak, R. Tiruvalam, R. L. Jenkins, A. F. Carley, D. Knight, C. J. Kiely and G. J. Hutchings, *Nature Chemistry*, 2011, **3**, 551-556.
422. Y. Liu, H. Tsunoyama, T. Akita and T. Tsukuda, *Chemical Communications*, 2010, **46**, 550-552.
423. T. Tsukuda, *Bulletin of the Chemical Society of Japan*, 2012, **85**, 151-168.
424. A. Simon, *Philosophical Transactions of the Royal Society A: Mathematical, Physical and Engineering Sciences*, 2010, **368**, 1285-1299.
425. C. C. Chusuei, X. Lai, K. A. Davis, E. K. Bowers, J. P. Fackler and D. W. Goodman, *Langmuir*, 2001, **17**, 4113-4117.
426. J. F. Alvino, T. Bennett, D. P. Anderson, B. Donoeva, D. Ovoshchnikov, R. Adnan, D. R. Appadoo, V. Golovko, G. G. Andersson and G. F. Metha, *RSC Advances*, 2013, **3**, 22140-22149.
427. T. Bennett, R. H. Adnan, J. F. Alvino, V. Golovko, G. G. Andersson and G. F. Metha, *Inorganic Chemistry*, 2014, **53**, 4340-4349.
428. F. Allen, *Acta Crystallographica Section B*, 2002, **58**, 380-388.
429. J. W. A. Van der Velden, J. J. Bour, J. J. Steggerda, P. T. Beurskens, M. Roseboom and J. H. Noordik, *Inorganic Chemistry*, 1982, **21**, 4321-4324.
430. J. W. A. Van der Velden, J. J. Bour, W. P. Bosman and J. H. Noordik, *Inorganic Chemistry*, 1983, **22**, 1913-1918.
431. F. Wen, U. Englert, B. Gutrath and U. Simon, *European Journal of Inorganic Chemistry*, 2008, **2008**, 106-111.
432. L. C. McKenzie, P. M. Haben, S. D. Kevan and J. E. Hutchison, *The Journal of Physical Chemistry C*, 2010, **114**, 22055-22063.
433. W. W. Weare, S. M. Reed, M. G. Warner and J. E. Hutchison, *Journal of the American Chemical Society*, 2000, **122**, 12890-12891.
434. T. G. Schaaff, M. N. Shafigullin, J. T. Khoury, I. Vezmar, R. L. Whetten, W. G. Cullen, P. N. First, C. Gutiérrez-Wing, J. Ascensio and M. J. Jose-Yacamán, *The Journal of Physical Chemistry B*, 1997, **101**, 7885-7891.
435. N. H. Takata, A. M. P. Felicissimo and V. G. Young Jr, *Inorganica Chimica Acta*, 2001, **325**, 79-84.
436. R. P. F. Kanters, J. J. Bour, P. P. J. Schlebos, W. P. Bosman, H. Behm, J. J. Steggerda, L. N. Ito and L. H. Pignolet, *Inorganic Chemistry*, 1989, **28**, 2591-2594.

## References

437. L. Malatesta, L. Naldini, G. Simonetta and F. Cariati, *Coordination Chemistry Reviews*, 1966, **1**, 255-262.
438. Y. Zhu, H. Qian and R. Jin, *Chemistry – A European Journal*, 2010, **16**, 11455-11462.
439. P. Gruene, D. M. Rayner, B. Redlich, A. F. G. van der Meer, J. T. Lyon, G. Meijer and A. Fielicke, *Science*, 2008, **321**, 674-676.
440. Techniques for Surface Chemical Composition, <http://www.cem.msu.edu/~cem924sg/Topic09.pdf>, Accessed 21st October, 2014.
441. Example of a "Wide Scan Survey Spectrum" using XPS., <http://upload.wikimedia.org/wikipedia/commons/3/36/Wide.jpg>, Accessed 21st October, 2014.
442. Y.-Y. Fong, B. R. Visser, J. R. Gascooke, B. C. Cowie, L. Thomsen, G. F. Metha, M. A. Buntine and H. H. Harris, *Langmuir*, 2011, **27**, 8099-8104.
443. B. C. C. Cowie, A. Tadich and L. Thomsen, *AIP Conference Proceedings*, 2010, **1234**, 307-310.
444. D. A. Shirley, *Physical Review B*, 1972, **5**, 4709-4714.
445. J. Végh, *Journal of Electron Spectroscopy and Related Phenomena*, 2006, **151**, 159-164.
446. H. Hughes and J. Scarfe, *Journal of Physics: Condensed Matter*, 1996, **8**, 1421.
447. J. F. Moulder, W. F. Stickle, P. E. Sobol and K. D. Bomben, *Handbook of X-ray photoelectron spectroscopy*, Perkin Elmer Eden Prairie, MN, 1992.
448. M. Newville, *Reviews in Mineralogy and Geochemistry*, 2014, **78**, 33-74.
449. P. J. Ellis and H. C. Freeman, *Journal of synchrotron radiation*, 1995, **2**, 190-195.
450. B. Ravel and M. Newville, *Journal of Synchrotron Radiation*, 2005, **12**, 537-541.
451. J. Mustre de Leon, J. J. Rehr, S. I. Zabinsky and R. C. Albers, *Physical Review B*, 1991, **44**, 4146-4156.
452. J. J. Rehr, *Japanese Journal of Applied Physics*, 1993, **32**, 8-12.
453. J. J. Rehr and R. C. Albers, *Physical Review B*, 1990, **41**, 8139-8149.
454. A. Maeland and T. B. Flanagan, *Canadian Journal of Physics*, 1964, **42**, 2364-2366.
455. E. Sevillano, H. Meuth and J. J. Rehr, *Physical Review B*, 1979, **20**, 4908-4911.
456. S. R. Systems, *SRS Residual Gas Analyzer*, Stanford Research Systems, Inc., 1996.
457. R. E. Ellefson, D. Cain and C. N. Lindsay, *Journal of Vacuum Science & Technology A: Vacuum, Surfaces, and Films*, 1987, **5**, 134-139.
458. C. J. Cramer and D. G. Truhlar, *Physical Chemistry Chemical Physics*, 2009, **11**, 10757-10816.
459. W. Koch and M. C. Holthausen, *A chemist's guide to density functional theory*, Wiley-Vch Weinheim, 2001.
460. P. Hohenberg and W. Kohn, *Physical Review*, 1964, **136**, B864-B871.
461. W. Kohn and L. J. Sham, *Physical Review*, 1965, **140**, A1133-A1138.
462. Y. Zhao and D. Truhlar, *Theor Chem Account*, 2008, **120**, 215-241.
463. C. J. Cramer and F. Bickelhaupt, *Angewandte Chemie-International Edition in English*, 2003, **42**, 381-381.
464. T. H. Dunning, Jr. and P. J. Hay, in *Methods of Electronic Structure Theory*, ed. H. Schaefer, III, Springer US, 1977, vol. 3, ch. 1, pp. 1-27.
465. P. J. Hay and W. R. Wadt, *The Journal of Chemical Physics*, 1985, **82**, 270-283.
466. W. R. Wadt and P. J. Hay, *The Journal of Chemical Physics*, 1985, **82**, 284-298.
467. P. J. Hay and W. R. Wadt, *The Journal of Chemical Physics*, 1985, **82**, 299-310.

## References

468. Gaussian 09, Revision C.01, M. J. Frisch, G. W. Trucks, H. B. Schlegel, G. E. Scuseria, M. A. Robb, J. R. Cheeseman, G. Scalmani, V. Barone, B. Mennucci, G. A. Petersson, H. Nakatsuji, M. Caricato, X. Li, H. P. Hratchian, A. F. Izmaylov, J. Bloino, G. Zheng, J. L. Sonnenberg, M. Hada, M. Ehara, K. Toyota, R. Fukuda, J. Hasegawa, M. Ishida, T. Nakajima, Y. Honda, O. Kitao, H. Nakai, T. Vreven, J. A. Montgomery, J. E. Peralta, F. Ogliaro, M. Bearpark, J. J. Heyd, E. Brothers, K. N. Kudin, V. N. Staroverov, R. Kobayashi, J. Normand, K. Raghavachari, A. Rendell, J. C. Burant, S. S. Iyengar, J. Tomasi, M. Cossi, N. Rega, J. M. Millam, M. Klene, J. E. Knox, J. B. Cross, V. Bakken, C. Adamo, J. Jaramillo, R. Gomperts, R. E. Stratmann, O. Yazyev, A. J. Austin, R. Cammi, C. Pomelli, J. W. Ochterski, R. L. Martin, K. Morokuma, V. G. Zakrzewski, G. A. Voth, P. Salvador, J. J. Dannenberg, S. Dapprich, A. D. Daniels, Farkas, J. B. Foresman, J. V. Ortiz, J. Cioslowski and D. J. Fox, Wallingford CT, 2009.
469. GaussView, version 5, R. Dennington, T. Keith and J. Millam, Semichem Inc., Shawnee Mission KS, 2009.
470. Chemcraft, G. A. Zhurko and D. A. Zhurko, <http://www.chemcraftprog.com>.
471. S. Saha, R. K. Roy and P. W. Ayers, *International Journal of Quantum Chemistry*, 2009, **109**, 1790-1806.
472. C. Fonseca Guerra, J.-W. Handgraaf, E. J. Baerends and F. M. Bickelhaupt, *Journal of Computational Chemistry*, 2004, **25**, 189-210.
473. Ł. M. Mentel and E. J. Baerends, *Journal of Chemical Theory and Computation*, 2014, **10**, 252-267.
474. N. M. O'Boyle, A. L. Tenderholt and K. M. Langner, *Journal of Computational Chemistry*, 2008, **29**, 839-845.
475. A. G. Jones and D. B. Powell, *Spectrochimica Acta Part A: Molecular Spectroscopy*, 1974, **30**, 563-570.
476. G. B. Deacon and J. H. S. Green, *Spectrochimica Acta Part A: Molecular Spectroscopy*, 1968, **24**, 845-852.
477. K. P. Hall and D. M. P. Mingos, in *Progress in Inorganic Chemistry*, John Wiley & Sons, Inc., 2007, pp. 237-325.
478. K. Konishi, in *Gold Clusters, Colloids and Nanoparticles I*, ed. D. M. P. Mingos, Springer International Publishing, 2014, vol. 161, ch. 143, pp. 49-86.
479. G. H. Woehrle, M. G. Warner and J. E. Hutchison, *The Journal of Physical Chemistry B*, 2002, **106**, 9979-9981.
480. L. Lin, P. Claes, P. Gruene, G. Meijer, A. Fielicke, M. T. Nguyen and P. Lievens, *ChemPhysChem*, 2010, **11**, 1932-1943.
481. L. Lin, T. Höltzl, P. Gruene, P. Claes, G. Meijer, A. Fielicke, P. Lievens and M. T. Nguyen, *ChemPhysChem*, 2008, **9**, 2471-2474.
482. L. Lin, P. Claes, T. Holtzl, E. Janssens, T. Wende, R. Bergmann, G. Santambrogio, G. Meijer, K. R. Asmis, M. T. Nguyen and P. Lievens, *Physical Chemistry Chemical Physics*, 2010, **12**, 13907-13913.
483. R. S. Mulliken, *The Journal of Chemical Physics*, 1955, **23**, 1833-1840.
484. NBO Version 3.1., E. D. Glendening, A. E. Reed, J. E. Carpenter and F. Weinhold.
485. P.-O. Löwdin, *Advances in Quantum Chemistry*, 1970, **5**, 185-199.
486. F. L. Hirshfeld, *Theoret. Chim. Acta*, 1977, **44**, 129-138.
487. D. Briggs and P. Seah, *Practical Surface Analysis: Auger and X-ray photoelectron spectroscopy*, Wiley, 1990.
488. T. L. Barr and S. Seal, *Journal of Vacuum Science & Technology A*, 1995, **13**, 1239-1246.

## References

489. T. Darrah Thomas and P. Weightman, *Physical Review B*, 1986, **33**, 5406-5413.
490. K. Asami, *Journal of Electron Spectroscopy and Related Phenomena*, 1976, **9**, 469-478.
491. K. Dücker and H. P. Bonzel, *Surface Science*, 1989, **213**, 25-48.
492. M. P. Seah, G. C. Smith and M. T. Anthony, *Surface and Interface Analysis*, 1990, **15**, 293-308.
493. P. M. T. M. Van Attekum, J. W. A. Van der Velden and J. M. Trooster, *Inorganic Chemistry*, 1980, **19**, 701-704.
494. H. G. Boyen, A. Ethirajan, G. Kästle, F. Weigl, P. Ziemann, G. Schmid, M. G. Garnier, M. Büttner and P. Oelhafen, *Physical Review Letters*, 2005, **94**, 016804.
495. D. C. Lim, R. Dietsche, G. Ganteför and Y. D. Kim, *Chemical Physics Letters*, 2008, **457**, 391-395.
496. L. K. Ono and B. Roldan Cuenya, *The Journal of Physical Chemistry C*, 2008, **112**, 4676-4686.
497. B. Koslowski, H. G. Boyen, C. Wilderotter, G. Kästle, P. Ziemann, R. Wahrenberg and P. Oelhafen, *Surface Science*, 2001, **475**, 1-10.
498. D.-C. Lim, C.-C. Hwang, G. Gantefor and Y. D. Kim, *Physical Chemistry Chemical Physics*, 2010, **12**, 15172-15180.
499. K. Juodkazis, J. Juodkazyt, V. Jasulaitien, A. Lukinskas and B. Šebeka, *Electrochemistry Communications*, 2000, **2**, 503-507.
500. T. Comaschi, A. Balerna and S. Mobilio, *Physical Review B*, 2008, **77**, 075432.
501. Y. Yuan, K. Asakura, H. Wan, K. Tsai and Y. Iwasawa, *Catalysis Letters*, 1996, **42**, 15-20.
502. A. Balerna, E. Bernieri, P. Picozzi, A. Reale, S. Santucci, E. Burattini and S. Mobilio, *Physical Review B*, 1985, **31**, 5058-5065.
503. P. Kluth, B. Johannessen, V. Giraud, A. Cheung, C. J. Glover, G. d. M. Azevedo, G. J. Foran and M. C. Ridgway, *Applied Physics Letters*, 2004, **85**, 3561-3563.
504. A. Pinto, A. R. Pennisi, G. Faraci, G. D'Agostino, S. Mobilio and F. Boscherini, *Physical Review B*, 1995, **51**, 5315-5321.
505. W. Vogel, J. Bradley, O. Vollmer and I. Abraham, *The Journal of Physical Chemistry B*, 1998, **102**, 10853-10859.
506. D. Zanchet, H. Tolentino, M. C. Martins Alves, O. L. Alves and D. Ugarte, *Chemical Physics Letters*, 2000, **323**, 167-172.
507. C. C. Yang and S. Li, *Physica Status Solidi (B)*, 2011, **248**, 1375-1378.
508. M. Ni, M. K. H. Leung, D. Y. C. Leung and K. Sumathy, *Renewable and Sustainable Energy Reviews*, 2007, **11**, 401-425.
509. K. Yamaguti and S. Sato, *Nippon Kagaku Kaishi*, 1984, 258-263.
510. Y. Ide, H. Hattori and T. Sano, *Physical Chemistry Chemical Physics*, 2014, **16**, 7913-7918.
511. N. Van Hieu and D. Lichtman, *Surface Science*, 1981, **103**, 535-541.
512. T. Inoue, A. Fujishima, S. Konishi and K. Honda, *Nature*, 1979, **277**, 637-638.
513. R. I. Bickley and F. S. Stone, *Journal of Catalysis*, 1973, **31**, 389-397.
514. G. Munuera, V. Rives-Arnau and A. Saucedo, *Journal of the Chemical Society, Faraday Transactions 1: Physical Chemistry in Condensed Phases*, 1979, **75**, 736-747.
515. A. R. Gonzalez-Elipse, G. Munuera and J. Soria, *Journal of the Chemical Society, Faraday Transactions 1: Physical Chemistry in Condensed Phases*, 1979, **75**, 748-761.
516. C. M. Wang, A. Heller and H. Gerischer, *Journal of the American Chemical Society*, 1992, **114**, 5230-5234.

## References

517. M. A. Fox and M. T. Dulay, *Chemical Reviews*, 1993, **93**, 341-357.
518. T. Berger, M. Sterrer, O. Diwald and E. Knözinger, *ChemPhysChem*, 2005, **6**, 2104-2112.
519. G. Lu, A. Linsebigler and J. T. Yates, *The Journal of Physical Chemistry*, 1994, **98**, 11733-11738.
520. W. Göpel, G. Rocker and R. Feierabend, *Physical Review B*, 1983, **28**, 3427-3438.
521. S. Ikeda, N. Sugiyama, S.-y. Murakami, H. Kominami, Y. Kera, H. Noguchi, K. Uosaki, T. Torimoto and B. Ohtani, *Physical Chemistry Chemical Physics*, 2003, **5**, 778-783.
522. M. Anpo, Y. Kubokawa, T. Fujii and S. Suzuki, *The Journal of Physical Chemistry*, 1984, **88**, 2572-2575.
523. J. D. Stiehl, T. S. Kim, S. M. McClure and C. B. Mullins, *Journal of the American Chemical Society*, 2004, **126**, 13574-13575.
524. T. Ohno, K. Sarukawa and M. Matsumura, *The Journal of Physical Chemistry B*, 2001, **105**, 2417-2420.
525. V. P. Indrakanti, J. D. Kubicki and H. H. Schobert, *Energy & Fuels*, 2008, **22**, 2611-2618.
526. V. P. Indrakanti, H. H. Schobert and J. D. Kubicki, *Energy & Fuels*, 2009, **23**, 5247-5256.
527. M. J. Lundqvist, M. Nilsing, P. Persson and S. Lunell, *International Journal of Quantum Chemistry*, 2006, **106**, 3214-3234.
528. F. Labat, P. Baranek, C. Domain, C. Minot and C. Adamo, *The Journal of Chemical Physics*, 2007, **126**, 154703.
529. M. Matsuoka, M. Kitano, M. Takeuchi, K. Tsujimaru, M. Anpo and J. M. Thomas, *Catalysis Today*, 2007, **122**, 51-61.

## Appendix A

### Appendix A. Cartesian Coordinates and Additional Information of the Refined EXAFS Models

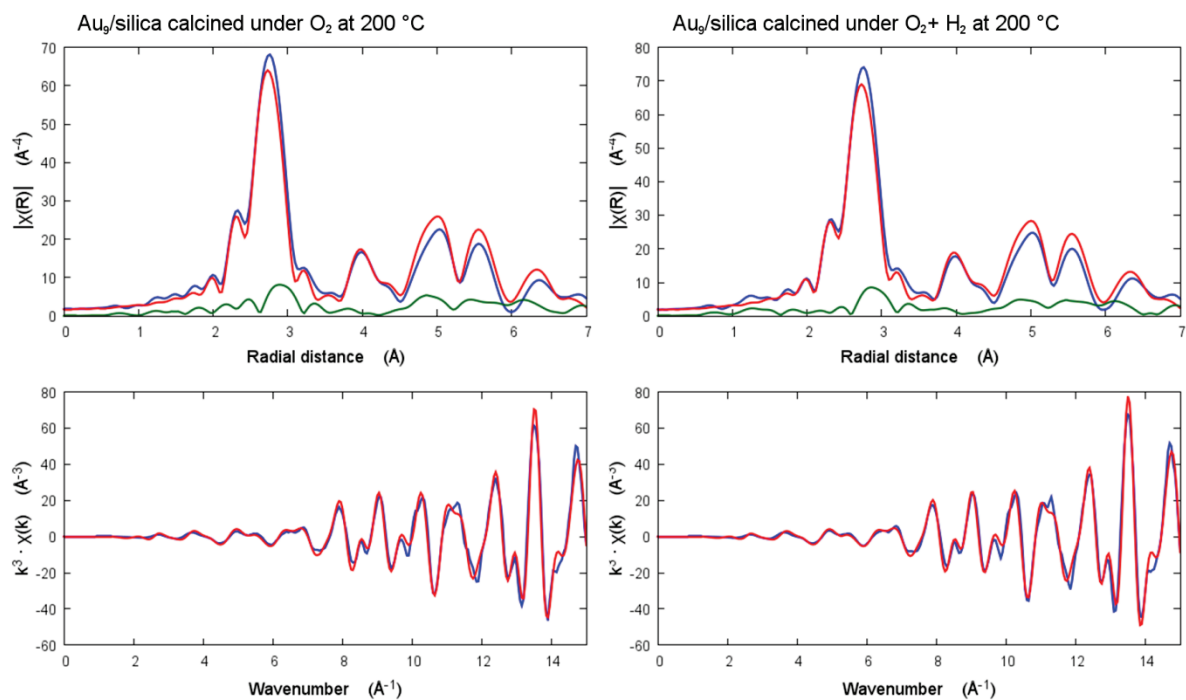
Refined Au<sub>8</sub> EXAFS model:

79	0.00000000	0.00000000	0.00000000
79	0.12634600	2.63149400	-0.14983000
79	2.43130600	0.99575500	-0.64471100
79	-1.50000000	1.10000000	-1.50000000
79	-0.34695700	1.17021900	2.20933200
79	1.71445700	-0.34662200	1.75052200
79	0.70294100	-0.13237900	-2.62063600
79	-2.35258500	-0.25962800	1.08025700
16	-0.00061600	-2.43987700	0.01217800
16	-0.29887700	4.80238800	-0.46012500
16	4.49712700	0.50952200	-1.42793700
16	-3.72690300	1.44053300	-1.96569300
16	0.18940700	1.83489800	4.31831900
16	3.18272100	-0.88349400	3.42414300
16	1.11918300	-0.95556300	-4.75279600
16	-4.60072800	-0.56490200	0.90274200

Refined Au<sub>9</sub> EXAFS model:

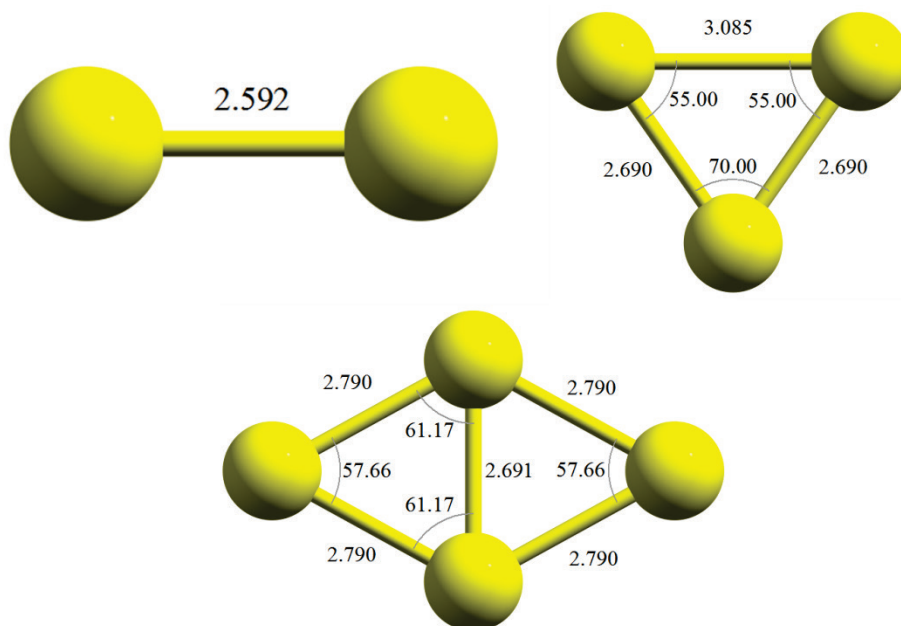
79	0.00000000	0.00000000	0.00000000
79	-1.37750100	2.37127900	-0.65157400
79	1.41085000	-2.46261400	-0.63316100
79	-2.43954800	-0.26288700	-1.37637400
79	2.46411900	0.15111900	-1.34498300
79	1.61930600	2.53087900	0.36458200
79	-1.34823400	-2.60026000	0.39675100
79	2.55423000	-0.83227000	1.46425900
79	-2.39184300	0.57890900	1.54774900
16	3.09772200	3.70864700	-0.43233900
16	-2.45697400	-3.99223000	-0.49366200
16	3.14407400	-1.26724500	3.55597500
16	-2.86112000	0.91390800	3.65990100
16	-2.86541700	3.57049100	0.09637800
16	2.01745200	-4.49817500	-1.16136200
16	-2.89595700	-0.34266200	-3.51620000
16	2.98833900	0.04504800	-3.46783200

## Appendix A

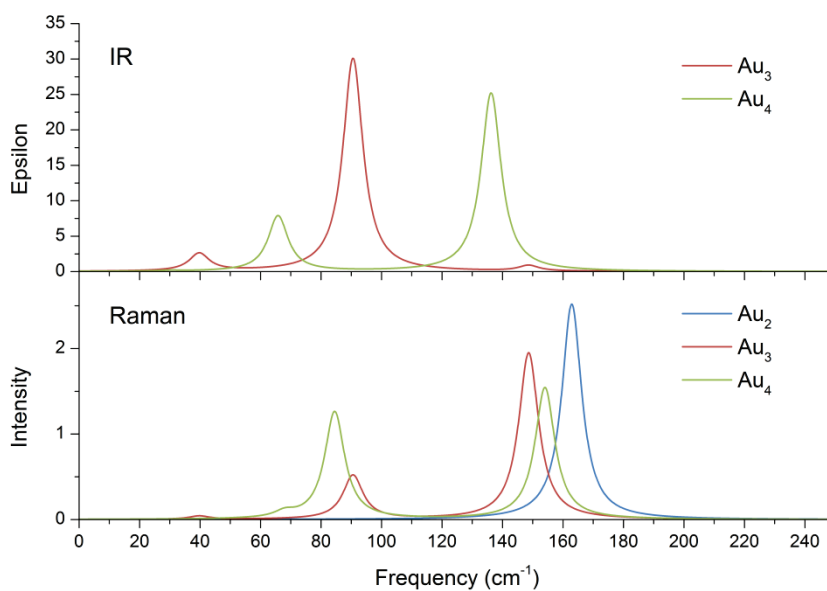


Appendix A.1: Multiple scattering bulk Au EXAFS fits in  $k^3$  weighted  $k$  space (bottom) and the associated Fourier transform (top) for Au<sub>9</sub>/silica calcined under O<sub>2</sub> at 200 °C and Au<sub>9</sub>/silica calcined under O<sub>2</sub> + H<sub>2</sub> 200 °C. The experimental EXAFS data is represented as the blue line, the calculated EXAFS is the red line, and the residual is the green line. The data is fit between 1 and 7 Å in  $R$  space, with all 53 multiple scattering paths up to 7 Å included in the model.

**Appendix B. Additional Calculated Parameters of Gas-phase Au<sub>1-4</sub> Clusters, and the Anatase(101) Surface Model**

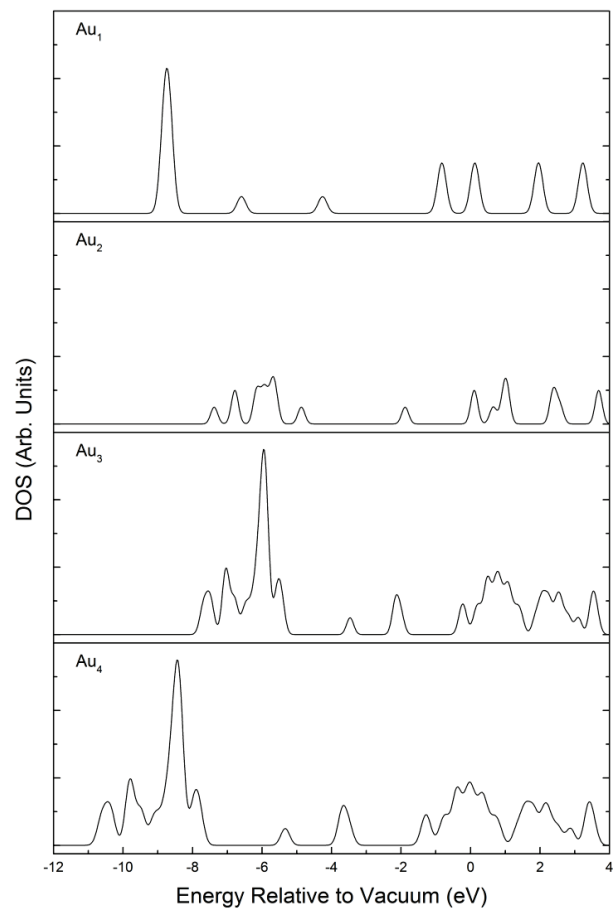


Appendix B.1: Gas-phase optimised geometries of Au<sub>2</sub>, Au<sub>3</sub>, and Au<sub>4</sub> with  $D_h$ ,  $C_{2v}$ , and  $D_{2h}$  symmetry respectively.

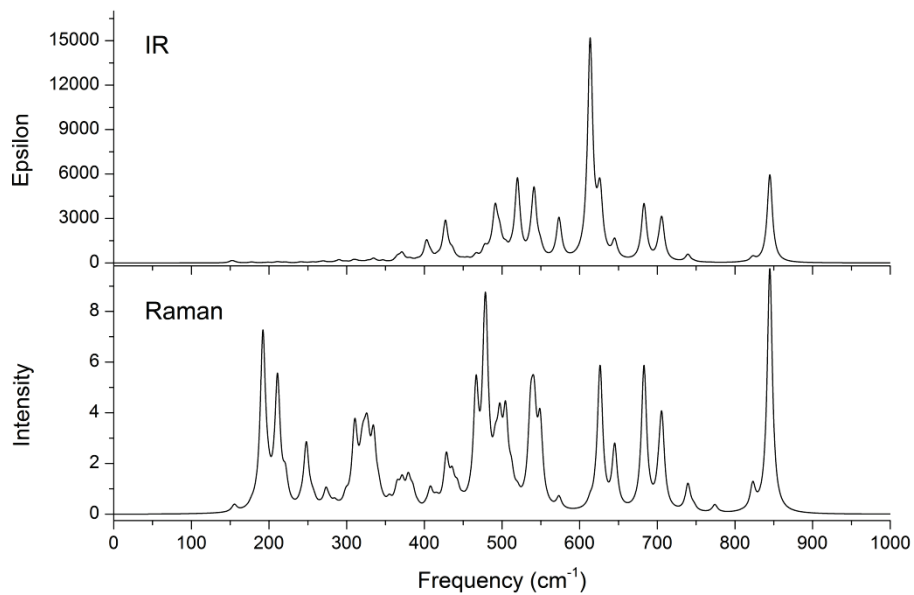


Appendix B.2: Predicted IR and Raman spectra of gas-phase Au<sub>1-4</sub> clusters.

## Appendix B

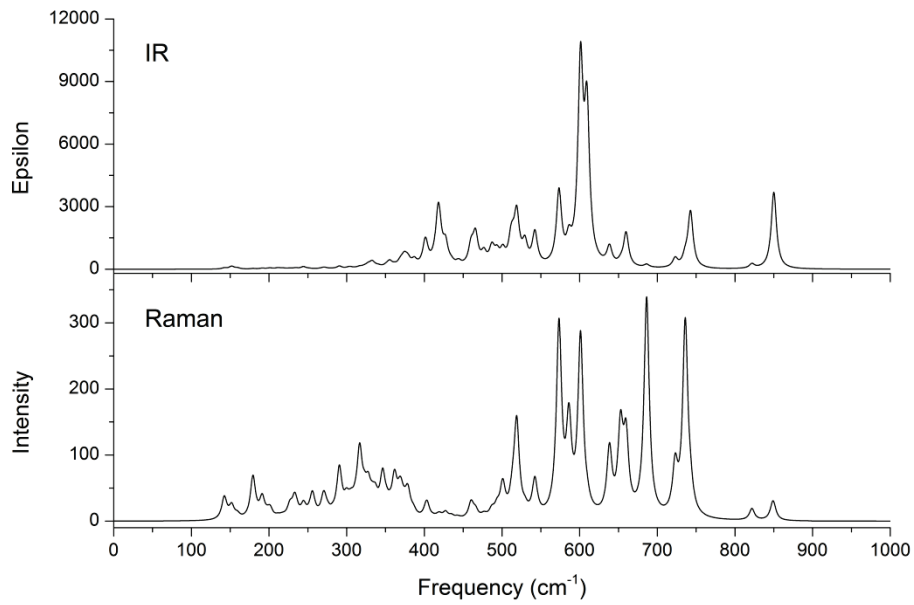


Appendix B.3: The density of states for gas-phase Au<sub>1-4</sub>.

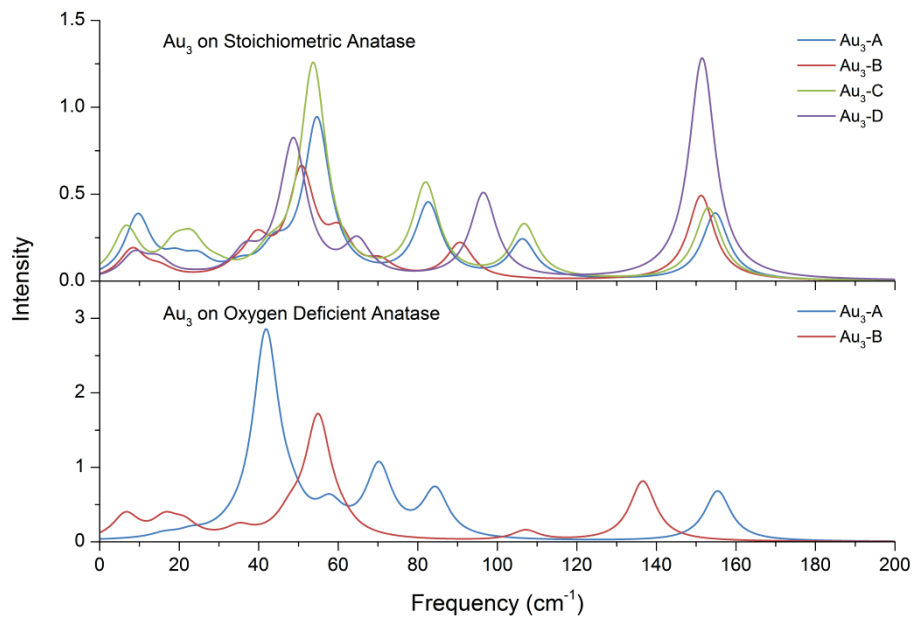


Appendix B.4: Predicted IR and Raman spectra of the bare stoichiometric anatase(101) model.

## Appendix B

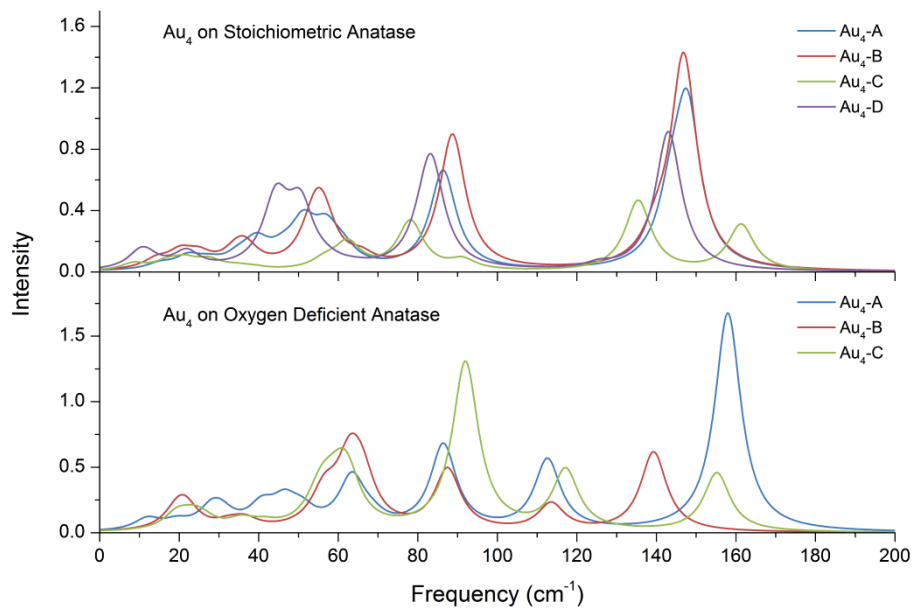


Appendix B.5: Predicted IR and Raman spectra of the bare oxygen-deficient anatase(101) model.

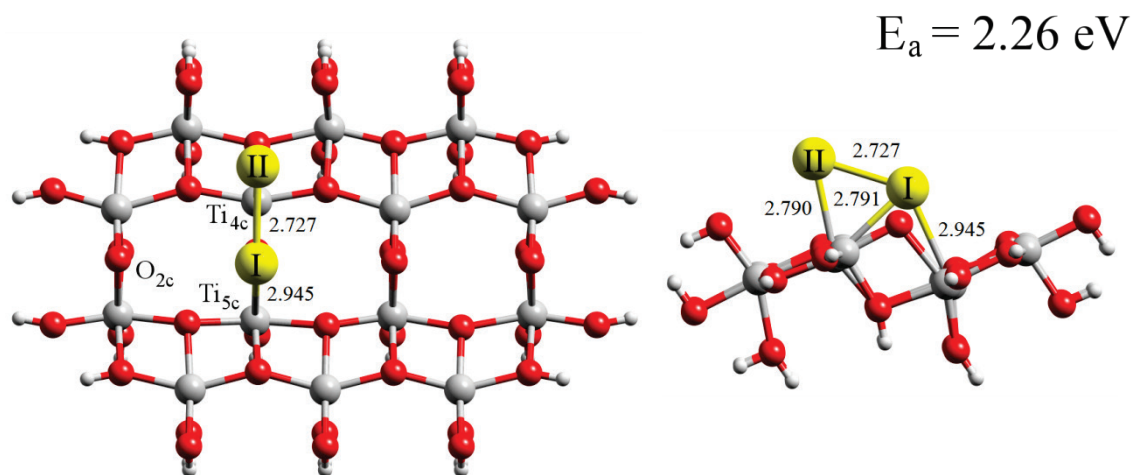


Appendix B.6: Predicted Raman spectra of Au<sub>3</sub> on the stoichiometric and oxygen-deficient anatase(101) models.

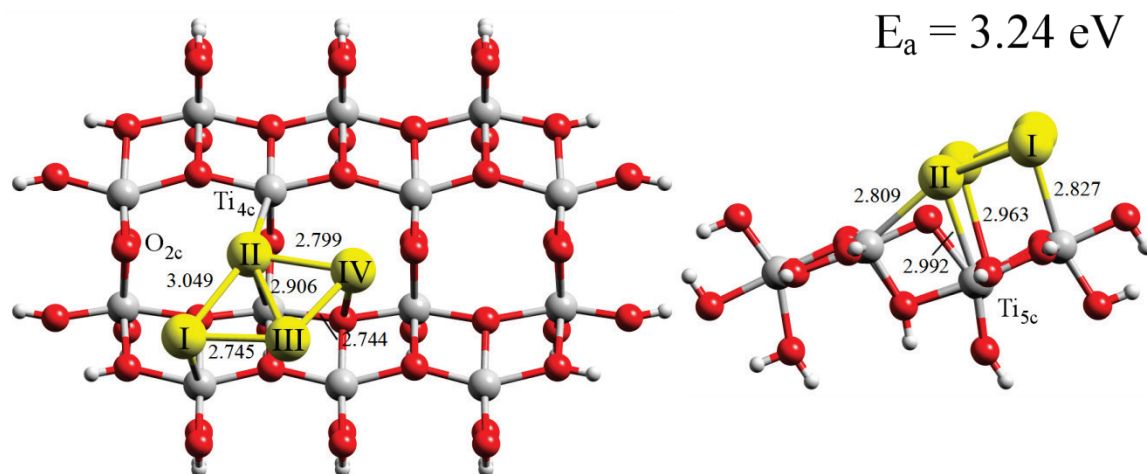
## Appendix B



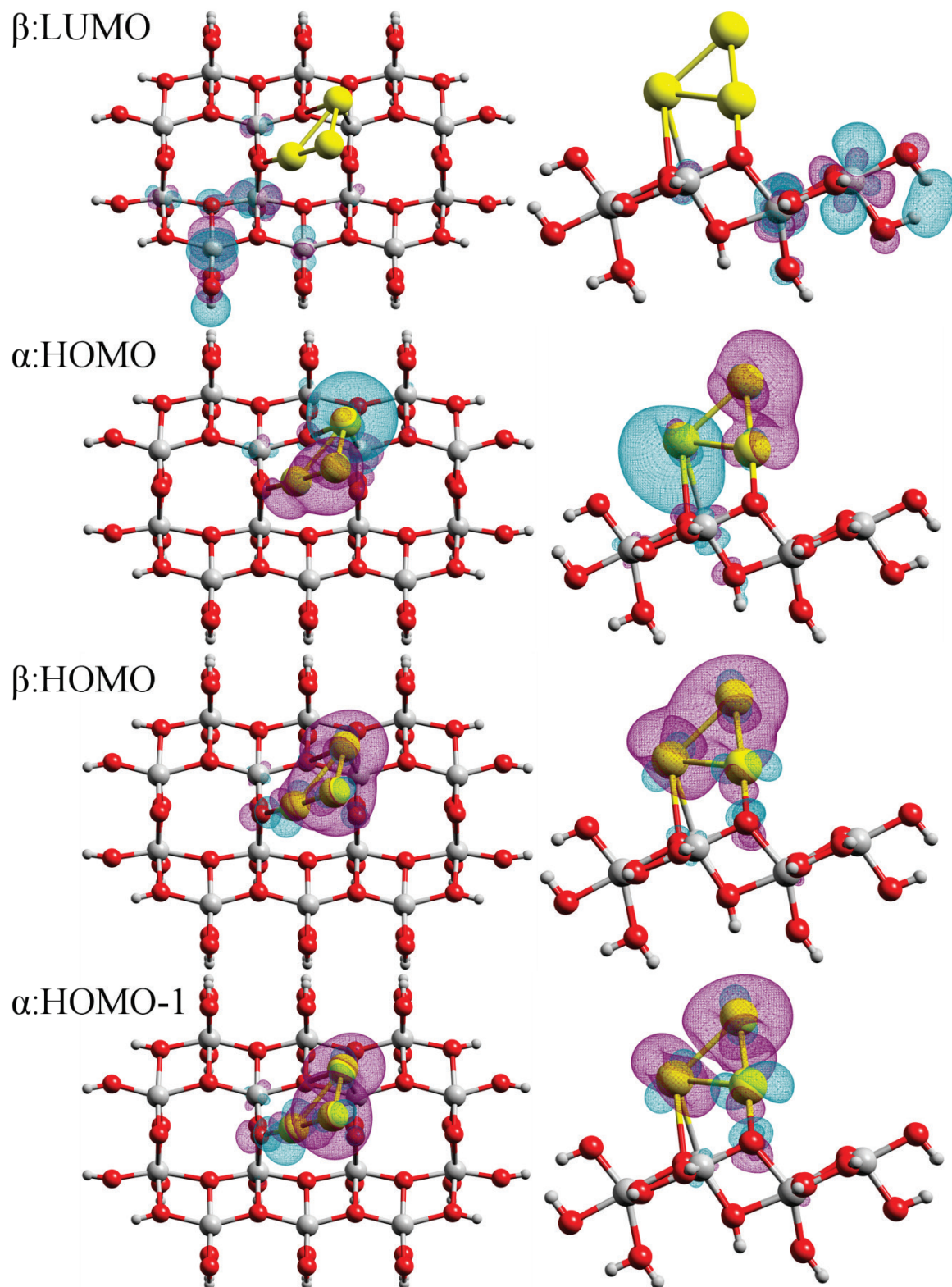
Appendix B.7: Predicted Raman spectra of Au<sub>4</sub> on the stoichiometric and oxygen-deficient anatase(101) models.



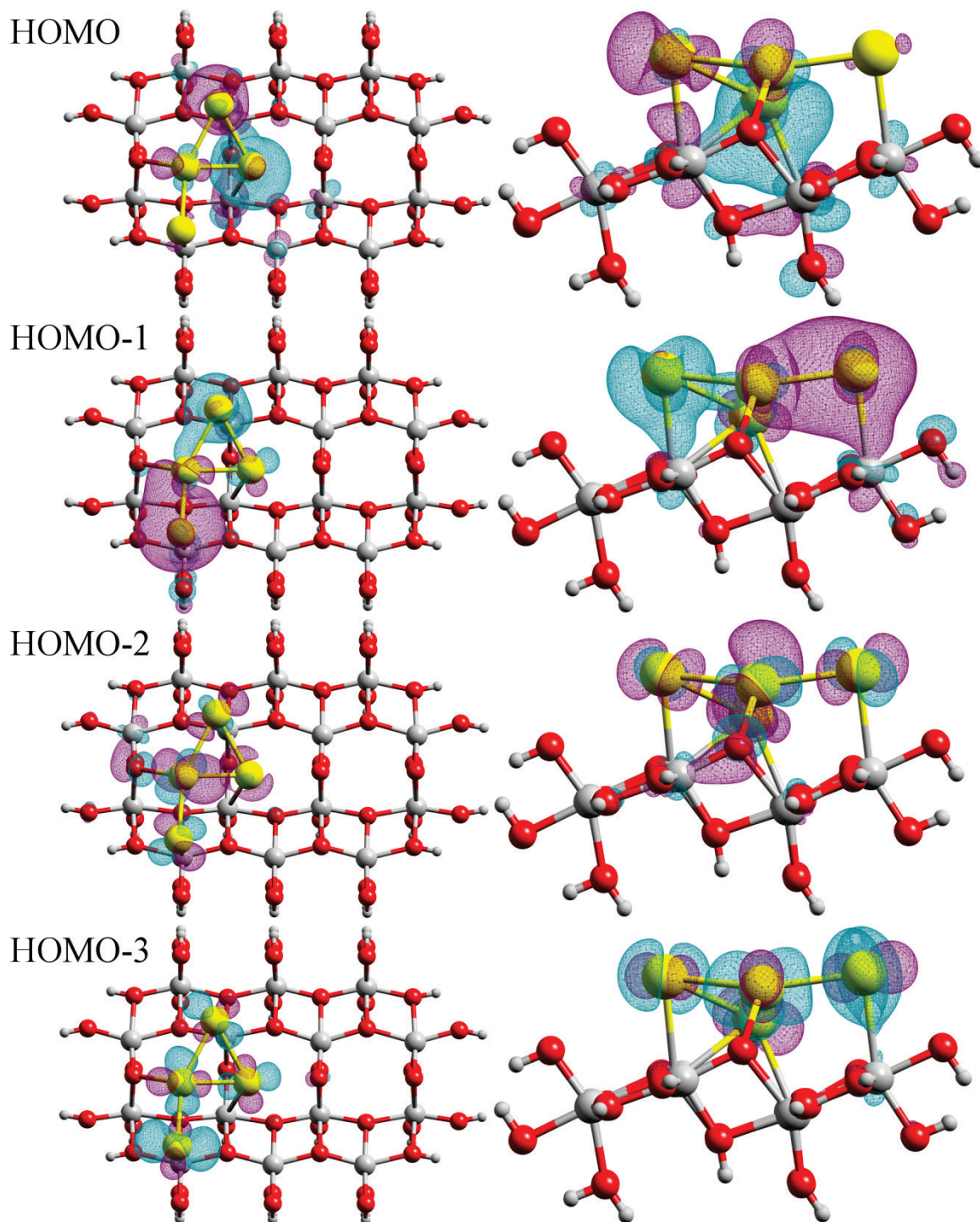
Appendix B.8: Top and side view of the optimised geometry for triplet Au<sub>2</sub> on the oxygen-deficient anatase(101) surface.



Appendix B.9: Top and side view of the optimised geometry for triplet Au<sub>4</sub> on the oxygen-deficient anatase(101) surface.



Appendix B.10: Top and side wireframe view of the beta LUMO, alpha HOMO, beta HOMO, and alpha HOMO-1 for Au<sub>3</sub>-D on the stoichiometric anatase(101) surface.



Appendix B.11: Top and side wireframe view of the HOMO, HOMO-1, HOMO-2, and HOMO-3 for Au<sub>4</sub>-B on the oxygen-deficient anatase(101) surface.

## Appendix C

### Appendix C. Cartesian Coordinates and Electronic Parameters of Ligated Gas-phase Gold Clusters

Element	Cartesian Coordinates						
#	X	Y	Z				
<b>Au<sub>6</sub></b>							
Energy = -5038.82862397 a.u.							
79	3.584322	-0.048737	-0.012753	6	7.488881	-0.889627	0.852136
79	1.055703	1.005914	0.931901	6	7.007306	-3.193005	0.244307
15	4.359098	1.373978	-2.014725	6	8.789491	-1.027876	0.356838
15	0.300943	2.969769	2.345746	1	7.169780	0.061546	1.277491
6	3.030823	1.543904	-3.353771	6	8.312329	-3.327799	-0.256587
6	1.725576	2.175165	-2.851517	1	6.333858	-4.045175	0.196873
6	-1.574369	3.096648	2.553164	6	9.204818	-2.249612	-0.197841
79	1.039597	-0.928156	-0.994064	1	9.476325	-0.188952	0.401242
15	4.859132	-1.699255	1.444636	1	8.630803	-4.276042	-0.678767
79	-1.192661	-1.094663	1.112145	1	10.215720	-2.358037	-0.577537
79	-1.432011	0.777119	-0.859784	6	4.891481	3.125311	-1.636292
6	0.557416	1.828402	-3.787169	6	5.417543	3.384692	-0.357923
6	-2.147827	1.862208	3.262910	6	4.847762	4.157825	-3.589967
15	0.528791	-2.443700	-2.905997	6	5.918874	4.655111	-0.043867
6	4.193626	-3.469101	1.671005	1	5.438695	2.589473	0.388297
79	-3.886387	-0.176637	0.339740	6	5.349252	5.428613	-2.275080
15	0.069957	-2.731179	2.604778	1	4.426636	3.984212	-3.578821
15	-1.121562	2.114452	-2.966896	6	5.893031	5.675883	-1.005294
6	-3.668114	1.896969	3.471104	1	6.329589	4.847120	0.942034
6	-1.209693	-2.185159	-3.606361	1	5.325940	6.218296	-3.019690
6	2.907227	-3.544864	2.513554	1	6.291437	6.656941	-0.766859
15	-4.690179	1.609636	1.903860	6	5.775257	0.642865	-3.001212
15	-4.714175	-1.871737	-1.318047	6	6.317415	-0.586179	-2.593006
6	1.715908	-3.011660	1.718860	6	6.286879	1.285471	-4.141990
6	-2.258951	-2.471817	-2.527034	6	7.359516	-1.175256	-3.324739
6	-3.650775	-1.937747	-2.884623	1	5.933227	-1.080008	-1.699352
1	2.851547	0.506045	-3.675743	6	7.323222	0.694500	-4.875976
1	3.443312	2.076459	-4.222222	1	5.895392	2.251265	-4.456353
1	1.509352	1.776810	-1.844233	6	7.859678	-0.537978	-4.468835
1	1.826161	3.266602	-2.752040	1	7.781350	-2.119817	-2.992523
1	-1.977806	3.192618	1.535050	1	7.719628	1.196176	-5.753187
1	-1.832100	4.021837	3.089991	1	8.669403	-0.989592	-5.033502
1	0.602355	0.758541	-4.046128	6	-4.748460	3.281966	1.066241
1	0.596919	2.412535	-4.718082	6	-4.198133	3.441196	-0.214905
1	-1.679343	1.750456	4.252590	6	-5.359781	4.374198	1.705543
1	-1.885891	0.958587	2.686173	6	-4.253344	4.686507	-0.855858
1	4.024018	-3.896174	0.672107	1	-3.715181	2.589656	-0.702711
1	4.999772	-4.032838	2.160867	6	-5.406223	5.620995	1.067989
1	-3.950306	1.089672	4.159129	1	-5.821445	4.251326	2.684404
1	-3.985320	2.851778	3.916233	6	-4.853690	5.777611	-0.212901
1	-1.273686	-1.135399	-3.932599	1	-3.829237	4.804020	-1.850753
1	-1.343846	-2.834265	-4.482866	1	-5.883393	6.462242	1.560936
1	3.036923	-2.971061	3.443440	1	-4.897363	6.741950	-0.710059
1	2.748336	-4.590011	2.813558	6	-6.435532	1.415066	2.540134
1	1.952709	-2.013323	1.322628	6	-6.796152	1.629986	3.879848
1	1.506816	-3.639373	0.836494	6	-7.419369	1.057632	1.600724
1	-1.934235	-1.995668	-1.584588	6	-8.133702	1.485337	4.276912
1	-2.317035	-3.552807	-2.335985	1	-6.053875	1.908847	4.623760
1	-3.590616	-0.914191	-3.285379	6	-8.754853	0.926532	1.997714
1	-4.149593	-2.577329	-3.626230	1	-7.141952	0.882609	0.560384
6	5.119233	-1.196335	3.221542	6	-9.113589	1.137102	3.338105
6	4.181094	-0.354517	3.840469	1	-8.408819	1.648912	5.314130
6	6.188999	-1.726924	3.964121	1	-9.512210	0.662212	1.266126
6	4.314700	-0.046879	5.202194	1	-10.148381	1.030770	3.647601
1	3.344149	0.049843	3.266237	6	-4.581551	-3.629240	-0.705467
6	6.321966	-1.410060	5.321594	6	-3.820583	-3.910270	0.440545
1	6.920774	-2.374994	3.484861	6	-5.167722	-4.677784	-1.435992
6	5.382642	-0.572139	5.941802	6	-3.636427	-5.239082	0.848694
1	3.576181	0.591436	5.680387	1	-3.372083	-3.095502	1.015182
1	7.151169	-1.816027	5.892340	6	-4.982564	-6.004203	-1.025202
1	5.484503	-0.332078	6.995749	1	-5.773654	-4.460874	-2.314599
6	6.593453	-1.975533	0.808743	6	-4.213059	-6.284942	0.114935
				1	-3.057992	-5.452363	1.744464
				1	-5.438872	-6.812923	-1.587310
				1	-4.073652	-7.313097	0.436432
				6	-6.465558	-1.722050	-1.932461
				6	-7.507977	-1.934913	-1.011318
				6	-6.766263	-1.371958	-3.258453
				6	-8.840597	-1.813653	-1.420306
				1	-7.277903	-2.202005	0.019783
				6	-8.103760	-1.243378	-3.662399
				1	-5.972533	-1.203229	-3.983620
				6	-9.140934	-1.465516	-2.747261
				1	-9.641621	-1.994667	-0.710235
				1	-8.334492	-0.978915	-4.689980
				1	-10.174792	-1.372617	-3.064087
				6	-0.581618	-4.428020	3.017570
				6	-1.656904	-4.530709	3.920993
				6	-0.058273	-5.592721	2.429105
				6	-2.183805	-5.785218	4.249731
				1	-2.072804	-3.633083	4.375929
				6	-0.591879	-6.847058	2.755666
				1	0.769745	-5.532921	1.724712
				6	-1.650405	-6.947696	3.668858
				1	-3.004924	-5.857413	4.955548
				1	-0.171237	-7.743420	2.309181
				1	-2.053569	-7.920519	3.931103
				6	0.538201	-2.018287	4.267812
				6	0.923155	-2.840882	5.341457
				6	0.507144	-0.623951	4.436444
				6	1.254590	-2.270325	6.577503
				1	0.950637	-3.922323	5.221380
				6	0.838691	-0.054755	5.673571
				1	0.221677	0.016232	3.598398
				6	1.203970	-0.878600	6.747256
				1	1.545188	-2.909833	7.404923
				1	0.803175	1.026387	5.797831
				1	1.448966	-0.439677	7.709953
				6	-1.266649	3.968201	-2.878525
				6	-1.640200	4.729849	-4.000299
				6	-0.958153	4.603831	-1.665885
				6	-1.706495	6.126098	-3.900166
				1	-1.888273	4.239926	-4.940337
				6	-1.014697	6.000742	-1.571761
				1	-0.679335	4.012337	-0.793223
				6	-1.391965	6.761450	-2.687359
				1	-1.999995	6.715820	-4.762934
				1	-0.774099	6.482950	-0.627878
				1	-1.443135	7.834410	-2.615342
				6	-2.369139	1.608909	-4.257763
				6	-2.003428	1.057816	-5.496906
				6	-3.733437	1.760155	-3.941028
				6	-2.992863	0.650402	-6.405986
				1	-0.956088	0.953768	-5.772278
				6	-4.718392	1.370592	-4.856076
				1	-4.029411	2.186705	-2.982391
				6	-4.349061	0.806422	-6.085478
				1	-2.704704	0.230094	-7.364611
				1	-5.766819	1.511220	-4.610022
				1	-5.111453	0.505751	-6.800335
				6	0.590952	-4.283762	-2.605250
				6	1.164477	-5.164818	-3.536352
				6	-0.013255	-4.789552	-1.438099
				6	1.128561	-6.547170	-3.303182
				1	1.634663	-4.779960	-4.438941
				6	-0.065872	-6.172668	-1.221624
				1	-0.461560	-4.112566	-0.707944
				6	0.507931	-7.052306	-2.151972
				1	1.573250	-7.226579	-4.023439
				1	-0.568124	-6.555947	-0.336601
				1	0.468543	-8.124025	-1.983965
				6	1.695596	-2.098320	-4.312266
				6	1.248813	-1.741807	-5.595845
				6	3.077300	-2.126314	-4.038695
				6	2.176851	-1.400888	-6.592608

## Appendix C

1	5.065994	-1.819649	-4.818077	6	-2.248037	1.975367	4.565384	6	6.655282	2.161530	-2.171257
1	4.267675	-1.165415	-7.086872	6	-2.987967	3.003572	5.163199	6	5.889243	1.091339	-1.692664
6	1.000371	3.193485	4.067046	6	-2.469883	3.685927	6.274892	6	-3.027805	5.134314	-2.243703
6	2.388002	3.022411	4.218563	6	-1.208696	3.340523	6.782040	6	-4.012141	4.357018	-1.609239
6	0.227113	3.606305	5.164099	6	-0.463582	2.313723	6.182895	6	-5.339979	4.403161	-2.053877
6	2.996762	3.269479	5.455391	6	5.126003	2.767406	1.521048	6	-5.685670	5.219524	-3.141947
1	2.995333	2.714175	3.365674	6	5.220577	1.401986	1.852715	6	-4.702191	5.991013	-3.779998
6	0.836238	4.538877	6.406302	6	6.472581	0.821941	2.088123	6	-3.373440	5.951710	-3.331501
1	-0.845345	3.761285	5.064308	6	7.635393	1.600082	1.978494	6	-0.218965	5.651883	-2.989354
6	2.220928	3.673318	6.553203	6	7.544107	2.957786	1.636562	6	0.200087	4.720954	-3.955882
1	4.071912	3.156250	5.558539	6	6.289668	3.544937	1.409735	6	0.977065	5.142205	-5.043380
1	0.234446	4.160996	7.250335	6	6.587628	4.961657	0.164035	6	1.333033	6.494309	-5.170138
1	2.692918	3.869814	7.510544	6	3.332241	4.827969	-1.212763	6	0.914585	7.422904	-4.204650
6	0.838291	4.576411	1.553798	6	3.399733	5.946962	-2.051960	6	0.141675	7.003556	-3.111838
6	0.394461	5.815829	2.048253	6	3.723792	7.202684	-1.516739	6	-1.170757	6.363498	-0.292275
6	1.791964	4.534932	0.523726	6	3.979143	7.338951	-0.143801	6	0.005559	6.422277	0.478311
6	0.902331	7.005600	1.510109	6	3.908670	6.220633	0.699240	6	0.139125	7.392230	1.479222
1	-0.321273	5.861205	2.867193	6	2.829269	4.087905	2.870725	6	-0.900040	8.307348	1.713287
6	2.299434	5.726302	-0.013346	6	3.711361	4.459179	3.897322	6	-2.069221	8.252777	0.940602
1	2.150753	3.572970	0.150881	6	3.202944	4.953377	5.107758	6	-2.208059	7.280533	-0.062060
6	1.857013	6.960998	0.480744	6	1.817632	5.078678	5.289361	6	-2.921491	-5.244848	-2.312058
1	0.569340	7.961575	1.902143	6	0.935757	4.705559	4.262998	6	-1.871951	-5.826521	-1.578022
1	3.043283	5.683429	-0.805834	6	1.438802	4.206606	3.056008	6	-1.278943	-7.015018	-2.022497
1	2.256959	7.884379	0.073451	6	-6.113729	0.546061	0.129589	6	-1.727334	-7.623051	-3.206011
				6	-7.360641	0.170213	0.657431	6	-2.770357	-7.039741	-3.940990
				6	-8.354581	-0.333941	-0.193662	6	-3.368248	-5.850853	-3.496182
				6	-8.103127	-0.468795	-1.567515	6	-4.930114	-4.200858	-0.405654
				6	-6.859038	-0.093088	-2.095943	6	-5.525412	-3.201803	0.386838
				6	-5.865976	0.414056	-1.249287	6	-6.468759	-3.550513	1.361323
				6	-4.974527	2.959228	1.519346	6	-6.821015	-4.897032	1.547540
				6	-3.837202	3.713136	1.867828	6	-6.231873	-5.891845	0.753248
				6	-3.950591	5.088483	2.100491	6	-5.284792	-5.546575	-0.223228
				6	-5.199048	5.717827	1.975877	6	-4.660765	-2.976902	-3.078681
				6	-6.332500	4.969299	1.624155	6	-5.985515	-3.376768	-3.321569
				6	-6.223508	3.588643	1.397351	6	-6.677560	-2.861606	-4.426911
				6	-4.957144	0.298453	2.837846	6	-6.051140	-1.945088	-5.286713
				6	-5.783747	0.830760	3.840738	6	-4.731037	-1.537937	-5.037527
				6	-5.943637	0.140169	5.050960	6	-4.036565	-2.053530	-3.934688
				6	-5.277981	-1.077425	5.258200	1	4.226200	8.311908	0.269374
				6	-4.445642	-1.605097	4.259339	1	6.221489	4.596505	1.135690
				6	-4.283218	-0.918983	3.049894	1	8.444678	3.557216	1.546053
				6	2.475166	-5.554783	0.591414	1	8.607639	1.147177	2.149956
				6	2.564947	-5.348767	-0.797157	1	6.539098	-0.233697	2.340814
				6	3.524761	-6.037625	-1.548414	1	4.320622	0.785095	1.900340
				6	4.398406	-6.933489	-0.914554	1	4.084481	6.333034	1.767989
				6	4.311744	-7.140254	0.470521	1	3.767935	8.072121	-2.165968
				6	3.352668	-6.450531	1.226013	1	3.183568	5.842916	-3.112851
				6	1.944884	-4.341920	3.229005	1	3.055763	3.853775	-1.619142
				6	1.737593	-5.265095	4.265737	1	4.787056	4.356829	3.760472
				6	2.312282	-5.039253	5.525160	1	3.884622	5.238867	5.902980
				6	3.094375	-3.896095	5.745551	1	1.424941	5.460575	6.227300
				6	3.304395	-2.975001	4.707486	1	-0.139101	4.794764	4.402767
				6	2.727720	-3.193476	3.450997	1	0.750132	3.894929	2.268099
				6	-0.288871	-5.636602	1.753572	1	5.196785	1.246633	-0.863671
				6	-1.522229	-4.983781	1.944940	1	6.562135	3.139308	-1.704034
				6	-2.695106	-5.730423	2.109994	1	8.133161	2.793903	-3.618059
				6	-2.641724	-7.132321	2.071722	1	8.324941	0.548520	-4.675433
				6	-1.416030	-7.784866	1.869787	1	6.970132	-1.352431	-3.829386
				6	-0.237465	-7.039296	1.712390	1	7.864214	-1.130981	-0.679588
				6	6.067579	-2.222951	-0.154932	1	9.206592	-2.097113	1.175787
				6	7.409887	-1.844450	0.005616	1	8.166994	-3.704734	2.767502
				6	8.165250	-2.382237	1.059239	1	5.778710	-4.369892	2.483478
				6	7.579776	-3.289396	1.954184	1	4.438774	-3.440461	0.612120
				6	6.236275	-3.665520	1.794322	1	6.939587	-3.738463	-2.275412
				6	5.480223	-3.135289	0.741225	1	6.900085	-5.466765	-4.061381
				6	5.001193	-2.926365	-2.803720	1	4.942308	-5.643422	-5.589902
				6	6.084139	-3.810119	-2.945070	1	2.999326	-4.095374	-5.310389
				6	6.058532	-4.790465	-3.947134	1	3.040514	-2.364594	-3.529922
				6	4.953225	-4.890633	-4.807649	1	1.904748	-4.628782	-1.283747
				6	3.863258	-4.019477	-4.654484	1	3.601443	-5.861254	-2.618857
				6	3.886386	-3.042165	-3.650165	1	5.149832	-7.458582	-1.496710
				6	6.009556	-0.180372	-2.279998	1	4.991660	-7.829817	0.961092
				6	6.883644	-0.374209	-3.360608	1	3.302975	-6.595767	2.303946
				6	7.644556	0.701084	-3.843142	1	2.870271	-2.461367	2.653168
				6	7.535450	1.966820	-3.246996	1	3.902733	-2.083339	4.878543

### Au<sub>8</sub>:

Energy = -6690.07907619 a.u.

79	0.014263	-0.004707	-0.867408
79	-0.066956	0.137928	1.845076
79	1.870095	1.763770	0.260903
79	-2.488486	0.654669	0.219516
79	0.633161	-2.413974	0.430288
79	2.733329	-0.816383	-0.816433
79	-0.688720	2.741576	-0.788038
79	-1.978256	-2.027920	-0.823827
15	0.105180	-0.029005	-3.428683
15	-0.106289	0.173854	4.305000
15	3.416784	3.442943	1.225443
15	-4.711772	1.143948	1.197030
15	1.214765	-4.559248	1.530745
15	5.004446	-1.560510	-1.536202
15	-1.285709	5.034145	-1.591324
15	-3.664478	-3.664809	-1.662815
6	-0.242565	-1.686641	-4.236414
6	0.110233	-2.856764	-3.539417
6	-0.107682	-4.115389	-4.116190
6	-0.692394	-4.213626	-5.388030
6	-1.052170	-3.049999	-6.083010
6	-0.822848	-1.789329	-5.511916
6	-1.046968	1.138081	-4.338823
6	-0.720278	1.640697	-5.611259
6	-1.608022	2.496570	-6.278683
6	-2.824164	2.854749	-5.678100
6	-3.151493	2.357711	-4.407657
6	-2.264862	1.501649	-3.738977
6	1.770268	0.450543	-4.142922
6	2.411802	-0.301037	-5.138884
6	3.658623	0.109735	-5.636306
6	4.255471	1.283707	-5.158436
6	3.607976	2.045145	-4.171522
6	2.376756	1.624192	-3.657055
6	-0.940800	-1.288229	5.110574
6	-1.661201	-1.156986	6.309202
6	-2.195446	-2.294847	6.930202
6	-2.014483	-3.562185	6.356061
6	-1.304417	-3.690726	5.153128
6	-0.770372	-2.554686	4.529930
6	1.579684	0.209061	5.101700
6	2.607269	0.921467	4.462644
6	3.860329	1.048515	5.078719
6	4.089048	0.460537	6.331607
6	3.066326	-0.263292	6.963319
6	1.812329	-0.391472	6.349602
6	-0.986724	1.626507	5.076769

## Appendix C

1 3.534151 -3.718517 6.722699	1 -5.285385 6.787230 2.144667	6 -6.849155 -1.892868 3.494975
1 2.148159 -5.749973 6.329258	1 -7.296781 5.457567 1.523423	1 -7.136175 -2.893252 3.183753
1 1.122104 -6.148095 4.098773	1 -7.102191 3.012155 1.111811	6 -7.823728 -0.984824 3.940304
1 0.710781 -7.547586 1.544554	1 -6.290959 1.782026 3.685073	1 -8.866906 -1.282046 3.976689
1 -1.377019 -8.869072 1.833196	1 -6.582197 0.550293 5.827138	6 -7.447400 0.302339 4.346982
1 -3.553205 -7.710967 2.188467	1 -5.400161 -1.610317 6.196656	1 -8.197265 1.000359 4.706873
1 -3.645405 -5.219997 2.252300	1 -3.916036 -2.541159 4.424612	6 -6.100525 0.692873 4.297771
1 -1.571982 -3.892877 1.934483	1 -3.619033 -1.318660 2.280646	1 -5.816577 1.698672 4.602128
1 -1.514184 -5.351136 -0.663553		6 2.398500 0.906294 4.775545
1 -0.469913 -7.458599 -1.447611		6 -2.398500 -0.906294 4.775545
1 -1.270049 -8.545441 -3.550837		6 2.899680 1.302285 6.028215
1 -3.121879 -7.510116 -4.854193		6 -2.899680 -1.302285 6.028215
1 -4.170306 -5.398172 -4.075483		1 3.897519 0.999179 6.341509
1 -4.824180 -6.322618 -0.831645		1 -3.897519 -0.999179 6.341509
1 -6.512292 -6.932324 0.887237		6 2.121335 2.115807 6.861951
1 -7.553056 -5.167689 2.302205		6 -2.121335 -2.115807 6.861951
1 -6.922799 -2.773751 1.971228		1 2.503255 2.412680 7.833689
1 -5.260671 -2.151868 0.239782		1 -2.503255 -2.412680 7.833689
1 -6.474952 -4.082072 -2.652209		6 0.852515 2.546514 6.441427
1 -7.697726 -3.179482 -4.620174		6 -0.852515 -2.546514 6.441427
1 -6.588136 -1.554057 -6.145568		1 0.245885 3.170729 7.091229
1 -4.239376 -0.825283 -5.694976		1 -0.245885 -3.170729 7.091229
1 -3.007529 -1.740801 -3.748019		6 0.368314 2.179503 5.177500
1 0.536865 -2.776056 -2.536496		6 -0.368314 -2.179503 5.177500
1 0.162577 -5.205426 -3.570610		1 -0.605490 2.526413 4.838371
1 -0.871178 -5.190332 -5.827540		1 0.605490 -2.526413 4.838371
1 -1.511665 -3.120987 -7.064183		6 1.139855 1.357259 4.345960
1 -1.110573 -0.893655 -6.058558		6 -1.139855 -1.357259 4.345960
1 1.948141 -1.205426 -5.531287		1 0.762189 1.073874 3.360484
1 4.155986 -0.486964 -6.395684		1 -0.762189 -1.073874 3.360484
1 5.217110 1.604731 -5.547534		6 3.195193 -1.960256 4.439807
1 4.069811 2.957100 -3.800051		6 -3.195193 1.960256 4.439807
1 1.885409 2.197067 -2.866671		6 -3.250021 2.155553 5.831057
1 0.229306 1.376535 -6.074808		1 -3.357035 1.308747 6.504876
1 -1.349341 2.883597 -7.259812		6 -3.154962 3.450733 6.357872
1 -3.508718 3.524413 -6.189879		1 -3.203195 3.599840 7.431855
1 -4.086431 2.647586 -3.933231		6 3.010712 -4.552550 5.498676
1 -2.504273 1.127455 -2.740521		6 -3.010712 4.552550 5.498676
1 -0.090156 3.671684 -3.871882		1 2.944625 -5.554831 5.909995
1 1.295862 4.417717 -5.788144		1 -2.944625 5.554831 5.909995
1 1.925985 6.822916 -6.018287		6 2.958168 -4.357948 4.111373
1 1.181528 8.470601 -4.304914		6 -2.958168 4.357948 4.111373
1 -0.175429 7.725332 -2.361386		1 2.854491 -5.208750 3.442633
1 -2.613331 6.546737 -3.833800		1 -2.854491 5.208750 3.442633
1 -4.968558 6.625056 -4.620018		6 3.047576 -3.062692 3.581199
1 -6.713670 5.256309 -3.489263		6 -3.047576 3.062692 3.581199
1 -6.095829 3.802865 -1.552419		1 3.002975 -2.910333 2.501100
1 -3.741518 3.713926 -0.770619		1 -3.002975 2.910333 2.501100
1 -3.120406 7.236545 -0.653835		79 -1.415645 2.425059 -0.314187
1 -2.868740 8.967474 1.111755		79 1.415645 -2.425059 0.314187
1 -0.795859 9.060850 2.487917		79 -2.435941 -0.204913 -1.411833
1 1.049261 7.430651 2.072068		79 2.435941 0.204913 -1.411833
1 0.822047 5.720266 0.291226		79 0.000000 0.000000 0.000000
1 -1.810516 -0.176110 6.756297		15 -3.003552 4.312920 -0.572756
1 -2.744151 -2.191349 7.861491		15 3.003552 -4.312920 -0.572756
1 -2.421319 -4.442848 6.843607		15 -3.344791 -0.265864 -3.685543
1 -1.161851 -4.669084 4.699666		15 3.344791 0.265864 -3.685543
1 -0.212737 -2.650621 3.595979		6 -3.615223 4.665544 -2.291154
1 2.424142 1.382635 3.489574		6 3.615223 -4.665544 -2.291154
1 4.649320 1.608366 4.581925		6 -2.705043 4.557036 -3.357856
1 5.056689 0.566115 6.812463		6 2.705043 -4.557036 -3.357856
1 3.240678 -0.722055 7.931975		1 -1.679937 4.228758 -3.178411
1 1.025831 -0.962444 6.839237		1 1.679937 -4.228758 3.178411
1 -2.659199 1.431386 3.712667		6 -3.121177 4.860867 -4.660564
1 -3.964963 3.264456 4.763215		6 3.121177 -4.860867 -4.660564
1 -3.046344 4.477091 6.744376		1 -2.416443 4.780428 -5.482433
1 -0.806554 3.862805 7.645095		1 2.416443 -4.780428 5.482433
1 0.517756 2.057678 6.577499		6 -4.444108 5.262092 -4.901226
1 -7.550136 0.249549 1.726788		6 4.444108 -5.262092 -4.901226
1 -9.316420 -0.628280 0.214552		1 -4.765019 5.496398 -5.911112
1 -8.868717 -0.873849 -2.222582		1 4.765019 -5.496398 5.911112
1 -6.655020 -0.211597 -3.157310		6 -5.352606 5.364071 -3.837215
1 -4.889314 0.682521 -1.654506		6 5.352606 -5.364071 -3.837215
1 -2.858420 3.233124 1.929442		1 -6.373625 5.682641 -4.023173
1 -3.066524 5.665548 2.363009		1 -6.373625 -5.682641 4.023173
		6 -4.940721 5.067705 -2.530156
		6 4.940721 -5.067705 2.530156
		1 -5.646558 -5.150542 1.705278
		1 5.646558 5.150542 -1.705278
		6 -4.529336 3.913538 0.418407
		6 4.529336 -3.913538 -0.418407
		6 -5.054717 -2.610065 -0.313694
		6 5.054717 2.610065 0.313694
		1 4.585800 1.879351 0.350353
		1 -4.585800 -1.879351 -0.350353
		6 -6.181688 2.247625 1.060614
		6 6.181688 -2.247625 -1.060614
		1 -6.583775 1.239809 0.986058
		1 6.583775 -1.239809 -0.986058
		6 -6.796127 3.190374 1.901627
		6 6.796127 -3.190374 -1.901627
		1 -7.678558 2.912879 2.470039
		1 7.678558 -2.912879 -2.470039
		6 -6.277578 4.488341 2.001285
		6 6.277578 -4.488341 -2.001285
		1 -6.754450 5.217036 2.648955
		1 6.754450 -5.217036 -2.648955
		6 -5.140555 4.852098 1.262448
		6 5.140555 -4.852098 -1.262448
		6 5.140555 -4.852098 1.262448
		6 -5.140555 4.852098 -1.262448
		1 -4.735868 5.858996 1.349053
		1 4.735868 -5.858996 -1.349053
		6 -2.366341 5.927225 0.091092
		6 2.366341 -5.927225 -0.091092
		6 -1.363024 5.887268 1.075747
		6 1.363024 -5.887268 -1.075747
		1 -0.959879 4.927338 1.407192
		1 0.959879 -4.927338 -1.407192
		6 -0.866000 7.080310 1.615741
		6 0.866000 -7.080310 -1.615741
		1 -0.093848 7.048944 2.379205
		1 0.093848 -7.048944 -2.379205
		1 0.093848 -7.048944 2.379205
		1 -0.093848 7.048944 -2.379205
		6 1.364031 -8.313064 1.167937
		6 -1.364031 8.313064 -1.167937
		1 0.974426 -9.237786 1.582220
		1 -0.974426 9.237786 -1.582220
		6 2.361262 -8.353363 0.181120
		6 -2.361262 8.353363 -0.181120
		1 2.746557 -9.307215 -0.164662
		1 -2.746557 9.307215 0.164662
		6 -2.864717 -7.161671 0.358701
		6 2.864717 7.161671 -0.358701
		1 -3.632631 -7.198947 1.129145
		1 3.632631 7.198947 -1.129145
		6 -5.130733 -0.216614 3.851107
		6 5.130733 0.216614 -3.851107
		6 -5.502826 -1.513785 3.452422
		6 5.502826 1.513785 -3.452422
		1 4.748383 2.232682 3.122628
		1 -4.748383 -2.232682 -3.122628

**Au<sub>9</sub>:**

Energy = -6825.29299611 a.u.





## Appendix C

6	3.412788	-2.183264	3.753716	6	-5.782792	-4.959947	-0.584150	6	6.836980	-1.275747	1.625848
6	3.748380	-2.832487	4.953165	1	-5.426383	-5.802137	-1.173849	1	6.541396	-1.870496	2.487345
1	3.444301	-3.864215	5.121518	6	-2.332879	-4.818296	-1.032379	6	5.919187	-1.052949	0.590540
6	4.461558	-2.140820	5.943747	6	-2.514135	-6.167914	-1.381982	1	4.919453	-1.487033	0.644817
1	4.723660	-2.643914	6.869266	1	-3.323725	-6.459079	-2.048433	6	5.303412	-1.483215	-3.034696
6	4.837919	-0.803913	5.738831	6	-1.630201	-7.140256	-0.896117	6	6.469332	-2.263902	-2.996930
1	5.392456	-0.273632	6.506745	1	-1.772007	-8.181493	-1.168191	1	7.250793	-2.050795	-2.270107
6	4.495053	-0.151882	4.543447	6	-0.565212	-6.244298	-0.060201	6	6.621071	-3.331526	-3.894242
1	4.783019	0.883464	4.374805	1	0.115210	-7.524019	0.322409	1	7.526309	-3.930579	-3.870676
6	3.781570	-0.839682	3.553036	6	-0.371715	-5.421103	0.272547	6	5.612110	-3.618833	-4.826419
1	3.508553	-0.324572	2.629858	1	0.457305	-5.130783	0.915744	1	5.735742	-4.443307	-5.521747
6	1.566512	-4.442155	3.207215	6	-1.251271	-4.445304	-0.216028	6	4.445866	-2.838090	-4.862169
6	0.380689	-4.118204	3.892302	1	-1.087266	-3.391414	0.025122	1	3.657415	-3.056596	-5.577858
1	0.048443	-3.080354	3.960501	6	-3.951242	-3.925528	-3.337081	6	4.290402	-1.772893	-3.965909
6	-0.378576	-5.131236	4.489735	6	-2.902002	-4.207336	-4.232176	1	3.381408	-1.169936	-3.990607
1	-1.297432	-4.877010	5.010876	1	-1.868872	-6.244298	-3.880592	6	-5.334924	3.423456	-3.696028
6	0.042565	-6.467814	4.404864	6	-3.182784	-4.442267	-5.583262	6	-5.912154	2.236802	-1.183956
1	-0.548174	-7.253242	4.865517	1	-2.369810	-4.662790	-6.268649	1	-5.286585	1.483397	-1.664148
6	1.227177	-6.788817	3.726743	6	-4.506458	-4.393098	-6.048019	6	-7.290740	2.023958	-1.047763
1	1.556837	-7.821381	3.666277	1	-4.722578	-4.579160	-7.095218	1	-7.736253	1.109755	-1.427441
6	1.992174	-5.777599	3.125924	6	-5.549629	-4.105162	-5.156866	6	-8.092676	2.992006	-0.423865
1	2.902998	-6.033771	2.588547	1	-6.574654	-4.069433	-5.512210	1	-9.160619	2.827508	-0.320182
6	3.810823	-3.845736	1.330005	6	-5.274773	-3.865302	-3.802730	6	-7.515966	4.174321	0.065162
6	4.988565	-4.374673	1.884512	1	-6.089093	-3.639579	-3.117521	1	-8.136820	4.924499	0.546676
1	5.148190	-4.348081	2.961616	6	3.659781	3.376908	2.402105	6	-6.137055	4.391498	-0.068697
6	5.968963	-4.923311	1.045925	6	4.467525	2.494210	1.662581	1	-5.690493	5.304291	0.321298
1	6.879570	-5.330097	1.474285	1	4.028706	1.892978	0.861072	6	-3.268194	4.634132	-2.471736
6	5.778101	-4.937086	-0.344275	6	5.831909	2.375589	1.958141	6	-4.335896	5.232030	-3.157106
1	6.543977	-5.351277	-0.993080	1	6.453893	1.704153	1.371138	1	-5.353830	5.128412	-2.787157
6	4.602263	-4.411862	-0.900119	6	6.388887	3.123892	3.006137	6	-4.087369	5.962427	-4.329990
1	4.457288	-4.412044	-1.978073	1	7.445982	3.029791	3.235378	1	-4.912896	6.425477	-4.861119
6	3.617486	-3.871200	-0.063219	6	5.580231	3.989795	3.757981	6	-2.777415	6.099279	-4.812512
1	2.711912	-3.442412	-0.495274	1	6.008795	4.566090	4.571840	1	-2.590138	6.668026	-5.717888
6	-1.345849	-0.835005	4.950501	6	4.217057	4.122046	3.454430	6	-1.709492	5.497889	-4.125847
6	-1.785643	-1.360351	6.178345	1	3.595910	4.796834	4.039461	1	-0.692758	5.593681	-4.497642
1	-2.826484	-1.651796	6.308981	6	1.021074	4.199614	3.431473	6	-1.955993	4.760903	-2.961474
6	-0.875920	-1.524393	7.232128	6	0.979053	5.568169	3.741043	1	-1.129729	4.276351	-2.439216
1	-1.214369	-1.934042	8.178596	1	1.392565	6.299502	3.048558	6	-3.009167	4.834076	0.454276
6	0.470986	-1.163461	7.063423	6	0.395497	5.990340	4.944371	6	-2.693259	4.294531	1.715342
1	1.174862	-1.296666	7.879455	1	0.372307	7.047621	5.190335	1	-2.708137	3.214293	1.872926
6	0.911356	-0.641483	5.839008	6	-0.143128	5.049321	5.835607	6	-2.352204	5.149303	2.771074
1	1.955781	-0.369738	5.699266	1	-0.582036	3.579814	6.771901	1	-2.104768	4.732002	3.744768
6	0.004177	-0.481693	4.782304	6	-0.107071	3.681766	5.520190	6	-2.321307	6.537817	2.569724
1	0.352404	-0.116315	3.812342	1	-0.513663	2.947600	6.210168	1	-2.054128	7.195944	3.391462
6	-3.530658	-2.191044	3.483233	6	0.470557	3.257435	4.316555	6	-2.629559	7.074664	1.311825
6	-4.724963	-2.304365	4.214248	1	0.495577	2.196191	4.068777	1	-2.606095	8.148686	1.155847
1	-5.096236	-1.458981	4.791640	6	1.855793	4.961839	0.679364	6	-2.975772	6.223833	0.251896
6	-5.444254	-3.507274	4.185180	6	0.620152	5.309580	0.102307	1	-3.220413	6.641811	-0.723604
1	-6.366583	-3.597933	4.750853	1	-0.291757	4.783137	0.394988	6	0.465520	-1.759226	-4.215196
6	-4.976752	-4.592236	3.426601	6	0.556431	6.345367	-0.837738	6	0.334838	-2.042448	-1.587292
1	-5.542806	-5.518688	3.400648	1	-0.403927	6.621304	-1.267318	1	0.015837	-1.263054	-6.277182
6	-3.788508	-4.476227	2.690358	6	1.724678	7.027888	-1.213024	6	0.568568	-3.341691	-6.059835
1	-3.423266	-5.308254	2.091505	1	1.673300	7.834506	-1.937881	1	0.468853	-3.555815	-7.119815
6	-3.066494	-3.276111	2.719715	6	2.956004	6.674325	-0.643531	6	0.917165	-4.366714	-5.163868
1	-2.144644	-3.184465	2.142586	1	3.858347	7.209515	-0.923370	1	1.088703	-5.373793	-5.532121
6	-3.655220	0.755585	3.875427	6	3.025246	5.641715	0.304741	6	1.030197	-4.091845	-3.792166
6	-3.565223	1.530563	5.040454	1	3.982380	5.378339	0.751283	1	1.279276	-4.885342	-3.092497
1	-2.839223	1.280366	5.811609	6	5.667256	1.448009	-2.811095	6	0.807524	-2.789478	-3.321504
6	-4.414669	2.636223	5.208918	6	5.403980	2.718934	-2.270145	1	0.877739	-2.563642	-2.255195
1	-4.346120	3.234847	6.112257	1	4.792420	2.817514	-1.371953	6	-1.494098	0.414632	-4.341657
6	-5.348398	2.966893	4.217444	6	5.921124	3.862822	-2.889728	6	-2.518889	-0.540287	-4.471620
1	-5.998915	3.825775	4.348884	1	5.724636	4.842167	-2.463253	1	-2.336173	-1.584908	-4.216824
6	-5.440046	2.189125	3.051121	6	6.689991	3.742435	-4.057817	6	-3.783954	-0.158947	-4.933758
1	-6.156911	2.446462	2.275339	1	7.095864	4.628864	-4.535610	1	-4.563044	-0.910711	-5.035937
6	-4.593830	1.088913	2.878374	6	6.935181	2.476073	-4.608139	6	-4.036887	1.182345	-5.265269
1	-4.649444	0.501149	1.961082	1	7.527893	2.380841	-5.512507	1	-5.018347	1.480956	-5.620865
6	-5.087584	-3.738262	-0.591396	6	6.427309	1.326526	-3.984772	6	-3.012108	2.131962	-5.151010
6	-5.562298	-2.657191	0.169735	1	6.626186	0.345411	-4.411215	1	-3.193553	3.170390	-5.418493
1	-5.014917	-1.713443	0.167073	6	6.286677	-0.277462	-0.522199	6	-1.742429	1.749538	-4.693118
6	-6.733607	-2.791051	0.927000	6	7.577862	0.272906	-0.598899	1	-0.956186	2.498946	-4.612501
1	-7.094663	-1.953043	1.516376	1	7.866604	0.878300	-1.455971	6	1.347493	1.145618	-4.179332
6	-7.430551	-4.007174	0.926928	6	8.495566	0.045216	0.437163	6	2.083014	0.942881	-5.355927
1	-8.340904	-4.111684	1.509328	1	9.494016	0.466162	0.373414	1	1.965094	0.027349	-5.932414
6	-6.953528	-5.091606	0.173391	6	8.126073	-0.727453	1.549557	6	2.989739	1.921677	-5.792859
1	-7.495231	-6.032255	0.170309	1	8.838984	-0.901263	2.349478	1	3.568152	1.755307	-6.696574

## Appendix C

6 3.146041 3.112576 -5.070770  
 1 3.845971 3.868559 -5.414738  
 6 2.409138 3.320491 -3.894026  
 1 2.538410 4.234286 -3.318390  
 6 1.522900 2.334967 -3.443059  
 1 0.977930 2.475236 -2.506480

### Au<sub>7</sub>Pt:

Energy = -6674.38107063 a.u.

78 -0.037422 -0.067214 -0.808996  
 79 2.471654 0.607952 0.268216  
 79 2.058243 -1.975950 -1.056735  
 79 -1.071408 -2.362655 0.427120  
 79 -2.789623 -0.502373 -1.058629  
 79 0.706953 2.586706 -0.915676  
 79 0.140966 -0.110799 1.925449  
 79 -1.713367 1.702223 0.491323  
 15 -0.165753 0.214521 -3.275797  
 15 4.663227 1.232606 1.262993  
 15 3.789289 -3.530176 -1.839039  
 15 -1.376961 -4.635818 1.271231  
 15 -5.128250 -1.034292 -1.714016  
 15 1.323886 4.892781 -1.557165  
 15 0.211286 -0.250255 4.416481  
 15 -3.271057 3.236571 1.627439  
 6 -1.139386 -2.400657 -3.818086  
 6 -1.958196 -3.358632 -4.426793  
 6 -2.947549 -2.963226 -5.340935  
 6 -3.098097 -1.606935 -5.655607  
 6 -2.265868 -0.646835 -5.058735  
 6 -1.292835 -1.035616 -4.124496  
 6 -1.878570 2.466374 -3.307757  
 6 -2.440678 3.640793 -3.822605  
 6 -1.921707 4.210938 -4.995415  
 6 -0.844251 3.597648 -5.649851  
 6 -0.295813 2.408011 -5.146397  
 6 -0.809249 1.837503 -3.970341  
 6 2.666260 0.231026 -3.642257  
 6 3.860809 0.034003 -4.351272  
 6 3.824533 -0.455602 -5.665149  
 6 2.591132 -0.745750 -6.268692  
 6 1.397239 -0.549271 -5.559668  
 6 1.428674 -0.059872 -4.240472  
 6 5.526049 1.790636 3.942297  
 6 5.370602 2.365809 5.211852  
 6 4.210866 3.093967 5.515369  
 6 3.199603 3.242214 4.553652  
 6 3.348593 2.665009 3.286923  
 6 4.516859 1.943748 2.977888  
 6 5.274902 -1.462840 1.718357  
 6 6.098084 -2.589622 1.832799  
 6 7.484339 -2.465354 1.650231  
 6 8.045659 -1.213872 1.357231  
 6 7.224035 -0.081502 1.247019  
 6 5.837366 -0.204634 1.428024  
 6 5.263489 2.624752 -1.096833  
 6 5.865749 3.615523 -1.881949  
 6 6.756815 4.526191 -1.295003  
 6 7.045527 4.444795 0.075787  
 6 6.441139 3.455449 0.864751  
 6 5.549449 2.541634 0.278085  
 6 3.438194 -5.302501 0.311290  
 6 3.840622 -6.237783 1.273579  
 6 5.183395 -6.642746 1.340747  
 6 6.122612 -6.113292 0.442950  
 6 5.724297 -5.175348 -0.521302  
 6 4.381968 -4.770155 -0.586496  
 6 5.815868 -1.578579 -1.832578  
 6 6.961947 -0.926350 -2.305135  
 6 7.602369 -1.387652 -3.465814  
 6 7.096666 -2.504132 -4.148995  
 6 5.953042 -3.162881 -3.674028

6 5.313207 -2.700390 -2.512963  
 6 3.436066 -5.895476 -3.425919  
 6 2.937620 -6.592243 -4.537726  
 6 2.146401 -5.930437 -5.488697  
 6 1.854685 -4.565561 -5.331295  
 6 2.351605 -3.866898 -4.223996  
 6 3.141995 -4.532622 -3.269664  
 6 -3.568130 -6.486293 1.301894  
 6 -4.926476 -6.809102 1.433254  
 6 -5.866661 -5.802492 1.702551  
 6 -5.452965 -4.468352 1.836656  
 6 -4.098577 -4.140938 1.697356  
 6 -3.154246 -5.150625 1.435806  
 6 0.004862 -7.055350 0.609844  
 6 0.655107 -7.925869 -0.276549  
 6 0.761014 -7.595472 -1.635345  
 6 0.213494 -6.395584 -2.114070  
 6 -0.442241 -5.526626 -1.232493  
 6 -0.546107 -5.854332 0.131821  
 6 -1.172531 -5.709150 3.926386  
 6 -0.501874 -5.905643 5.143816  
 6 0.770714 -5.353074 5.342470  
 6 1.378256 -4.597716 4.325939  
 6 0.708382 -4.389353 3.115629  
 6 -0.567426 -4.949808 2.915611  
 6 -5.140560 0.844449 -3.805155  
 6 -5.715029 1.691858 -4.761986  
 6 -7.111107 1.813224 -4.839941  
 6 -7.928078 1.091382 -3.954896  
 6 -7.353592 0.237688 -3.002107  
 6 -5.956803 0.106662 -2.932585  
 6 -6.157703 -0.144548 0.750229  
 6 -7.032139 -0.145776 1.845211  
 6 -8.061506 -1.096944 1.920586  
 6 -8.212635 -2.049905 0.901748  
 6 -7.331841 -2.058803 -0.189818  
 6 -6.305498 -1.102932 -0.268312  
 6 -6.028110 -3.052158 -3.564019  
 6 -6.071559 -4.370782 -4.043033  
 6 -5.318318 -5.375329 -3.417244  
 6 -4.509094 -5.061130 -2.313730  
 6 -4.457899 -3.744951 -3.142927  
 6 -5.225456 -2.740453 -2.457024  
 6 3.026202 5.279989 0.639194  
 6 3.656814 6.002910 1.659581  
 6 3.355757 7.361936 1.843391  
 6 2.424156 7.993835 1.005715  
 6 1.789229 7.271055 -0.015789  
 6 2.092988 5.913307 -0.200279  
 6 2.640781 3.857018 -3.817425  
 6 3.538482 3.872304 -4.893700  
 6 4.382464 4.977461 -5.083658  
 6 4.334038 6.059887 -4.189853  
 6 3.435100 6.045429 -3.114059  
 6 2.579931 4.945769 -2.932739  
 6 -0.043601 6.714949 -3.307215  
 6 -1.155640 7.478615 -3.693698  
 6 -2.334194 7.444008 -2.934088  
 6 -2.404631 6.637998 -1.786624  
 6 -1.298567 5.870920 -1.401516  
 6 -0.113353 5.914414 -2.157293  
 6 0.926186 1.609753 6.488273  
 6 0.841511 2.848227 7.140735  
 6 0.062220 3.880396 6.596777  
 6 -0.630526 3.674690 5.394091  
 6 -0.550872 2.436430 4.743236  
 6 0.221679 1.399839 5.291975  
 6 1.633391 -1.908100 6.287843  
 6 2.802620 -2.468149 6.823230  
 6 4.040409 -2.245363 6.201400  
 6 4.107946 -1.465379 5.037113  
 6 2.940972 -0.902858 4.502447  
 6 1.702492 -1.116651 5.130710  
 6 -1.683023 -0.840800 6.486153  
 6 -2.744717 -1.563706 7.047387

6 -3.377772 -2.574352 6.306940  
 6 -2.952523 -2.855526 5.000415  
 6 -1.888482 -2.135289 4.439053  
 6 -1.246354 -1.132067 5.182719  
 6 -4.883171 3.268526 -0.673375  
 6 -6.078534 3.368354 -1.396607  
 6 -7.279674 3.644394 -0.726529  
 6 -7.284665 3.821655 0.665043  
 6 -6.089738 3.719106 1.391723  
 6 -4.885528 3.443437 0.722155  
 6 -3.333649 6.107496 1.804984  
 6 -2.726515 7.358353 1.997041  
 6 -1.352645 7.440542 2.268042  
 6 -0.578241 6.271990 2.341671  
 6 -1.178404 5.023518 2.139869  
 6 -2.559563 4.938768 1.878320  
 6 -4.035974 3.548230 4.375609  
 6 -4.410003 3.052816 5.633331  
 6 -4.516197 1.669704 5.839627  
 6 -4.246363 0.778419 4.789732  
 6 -3.866666 1.268196 3.534440  
 6 -3.763858 2.656100 3.326585  
 1 -2.840489 -7.266217 1.083758  
 1 -5.249273 -7.839827 1.325742  
 1 -6.917367 -6.057016 1.801191  
 1 -6.177826 -3.682235 2.032123  
 1 -3.781676 -3.098221 1.766292  
 1 -0.058908 -7.303725 1.668254  
 1 1.080224 -8.853962 0.092849  
 1 1.273228 -8.265254 -2.319664  
 1 0.311855 -6.134904 -3.165869  
 1 -0.857614 -4.585029 -1.596025  
 1 -2.161412 -6.138563 3.775146  
 1 -0.971693 -6.488025 5.930247  
 1 1.288690 -5.504841 6.285014  
 1 2.363735 -4.164549 4.478867  
 1 1.170767 -3.778887 2.336262  
 1 -4.057104 0.757639 -3.734308  
 1 -5.074404 2.252099 -5.438384  
 1 -7.560181 2.465654 -5.582452  
 1 -9.007916 1.187501 -4.011072  
 1 -7.991030 -3.125151 -2.312494  
 1 -5.368935 0.608296 0.683308  
 1 -6.910247 0.596070 2.630136  
 1 -8.744094 -1.092873 2.764955  
 1 -9.013447 -2.781410 0.954115  
 1 -7.439689 -2.811285 -0.969334  
 1 -6.612718 -2.276385 -4.054904  
 1 -6.697558 -4.612745 -4.896565  
 1 -5.363544 -6.395734 -3.575739  
 1 -3.920395 -5.832439 -1.821748  
 1 -3.818823 -3.498252 -0.989625  
 1 3.265780 4.225391 0.488813  
 1 4.378915 5.505529 2.302612  
 1 3.846733 7.925637 2.630768  
 1 2.196357 9.046817 1.141893  
 1 1.058896 7.761777 -0.656829  
 1 1.985162 2.998983 -3.666987  
 1 3.572975 3.025042 -5.574732  
 1 5.073467 4.996897 -5.920926  
 1 4.988461 6.914006 -4.334321  
 1 3.405470 6.882237 -2.418433  
 1 0.865936 6.741904 -3.903712  
 1 -1.097590 8.102650 -4.580299  
 1 -3.189534 8.043072 -3.231814  
 1 -3.313530 6.603536 -1.190396  
 1 -1.358786 5.241367 -0.512032  
 1 1.546256 0.818799 6.906010  
 1 1.379124 3.003641 8.071386  
 1 -0.006100 4.836418 7.106849  
 1 -1.235851 4.469459 4.963913  
 1 -1.096990 2.270222 3.812891  
 1 0.675038 -2.100875 6.765486  
 1 2.746088 -3.071837 7.724229  
 1 4.944786 -2.675019 6.621207

## Appendix C

1	5.062457	-1.289836	4.546116
1	2.991720	-0.290451	3.600057
1	-1.208631	-0.045096	7.057540
1	-3.073511	-1.340820	8.057927
1	-4.196437	-3.137016	6.745084
1	-3.440511	-3.636565	4.420970
1	-1.557257	-2.350669	3.420546
1	-3.949328	3.028484	-1.185263
1	-6.075960	3.214935	-2.473862
1	-8.207359	3.709874	-1.287066
1	-8.215108	4.030693	1.183571
1	-6.100967	3.835330	2.474167
1	-4.399338	6.045547	1.590215
1	-3.323638	8.262847	1.935345
1	-0.885120	8.409845	2.413883
1	0.489064	6.332031	2.541701
1	-0.566795	4.119160	2.157401
1	-3.947780	4.622437	4.218474
1	-4.615514	3.742638	6.446031
1	-4.800207	1.285035	6.814879
1	-4.320546	-0.294750	4.949994
1	-3.629867	0.571391	2.727304
1	-0.381288	-2.713855	-3.098594
1	-1.831436	-4.412132	-4.188544
1	-3.588874	-3.706693	-5.804727
1	-3.857930	-1.290865	-6.365064
1	-2.377543	0.401544	-5.333510
1	-2.254662	2.034925	-2.376083
1	-3.269608	4.120342	-3.306278
1	-2.348387	5.129518	-5.387538
1	-0.431202	4.038898	-6.551877
1	0.532397	1.936313	-5.672102
1	2.687532	0.592853	-2.611364
1	4.815151	0.252855	-3.876961
1	4.749364	-0.613961	-6.211475
1	2.557582	-1.124627	-7.285781
1	0.444802	-0.786018	-6.031206
1	6.423160	1.218107	3.710619
1	6.149603	2.245801	5.958379
1	4.089745	3.538011	6.499166
1	2.294131	3.796170	4.791614
1	2.548586	2.758779	2.549354
1	4.193504	-1.569416	1.826167
1	5.659158	-3.560089	2.052216
1	8.121391	-3.341317	1.729777
1	9.117265	-1.118799	1.212184
1	7.661105	0.886994	1.008811
1	4.547908	1.933653	-1.545276
1	5.626133	3.686017	-2.940698
1	7.215210	5.301482	-1.901706
1	7.731507	5.152964	0.530093
1	6.650056	3.409597	1.932468
1	2.391936	-4.993021	0.256761
1	3.108779	-6.645472	1.965752
1	5.495141	-7.368408	2.085690
1	7.159482	-6.431961	0.488967
1	6.457224	-4.756910	-1.208609
1	5.312161	-1.212535	-0.937182
1	7.347071	-0.062842	-1.767964
1	8.490118	-0.882797	-3.834267
1	7.591973	-2.863973	-5.045452
1	5.560814	-4.023924	-4.211495
1	4.043971	-6.413795	-2.686420
1	3.174113	-7.644509	-4.664589
1	1.766849	-6.471831	-6.349789
1	1.247273	-4.043066	-6.065342
1	2.129767	-2.803215	-4.113342
1	0.115159	-1.765621	-1.157437

## Appendix D

### Appendix D. Cartesian Coordinates and Electronic Parameters of Au<sub>1</sub>-4 on the Stoichiometric and Oxygen-deficient Anatase(101) Surface

Cartesian Coordinates											
Element #	X	Y	Z								
<b>Anatase(101) Model (Ti<sub>14</sub>O<sub>45</sub>H<sub>34</sub>)</b>				1	5.580066	1.261026	0.000000	8	0.029099	4.672589	-1.574174
Energy = -4220.07088456 a.u.				1	5.578552	1.260612	3.787800	8	3.814065	4.664887	-1.579893
22	1.289643	0.680945	5.766831	1	6.000847	0.097106	0.000000	8	-7.545233	1.809972	-0.585162
22	1.260003	0.717221	1.909688	1	6.010426	0.094098	3.786686	8	-3.772621	1.815618	-0.825424
22	1.260003	0.717221	-1.909688	1	4.302485	-2.312230	-3.787965	8	0.031963	1.754272	-0.955578
22	1.289643	0.680945	-5.766831	1	4.302485	-2.312230	3.787965	8	3.807279	1.792582	-0.906558
22	-1.505039	-0.319153	5.783562	1	4.316550	-2.314321	0.000000	8	7.594668	1.779152	-0.607985
22	-1.537354	-0.298451	1.907842	1	2.895413	-2.810124	3.786176	8	-3.771041	-4.731057	1.085424
22	-1.537354	-0.298451	-1.907842	1	2.893916	-2.810477	0.000000	8	0.013948	-4.738753	1.079715
22	-1.505039	-0.319153	-5.783562	1	2.895413	-2.810124	-3.786176	8	3.798944	-4.746470	1.073996
22	-3.778470	0.461067	3.737181	1	0.249047	-1.875033	5.690255	8	-3.750739	5.502279	0.737337
22	-3.790113	0.483673	0.000000	1	0.250112	-1.874470	1.895577	8	0.034251	5.494576	0.731621
22	-3.778470	0.461067	-3.737181	1	0.250112	-1.874470	-1.895577	8	3.819236	5.486873	5.725503
22	3.636844	0.068620	3.744168	1	0.249047	-1.875033	-5.690255	8	-5.648995	3.267527	-0.063512
22	3.630926	0.069061	0.000000	1	-2.235943	-2.998155	1.894363	8	-1.849756	3.198007	-0.050901
22	3.636844	0.068620	-3.744168	1	-2.235943	-2.998155	-1.894363	8	1.912539	3.157382	0.029165
8	-1.697940	-2.167425	5.677787	1	-2.241029	-3.002771	-5.670237	8	5.705953	3.244405	-0.080591
8	-1.699441	-2.169277	1.886486	1	-2.241029	-3.002771	5.670237	8	-5.653611	0.389433	0.914238
8	-1.699441	-2.169277	-1.886486	1	1.598013	0.663942	8.510581	8	-1.868407	0.381759	0.908528
8	-1.697940	-2.167425	-5.677787	1	-1.676616	-0.185092	8.511921	8	1.916571	0.374057	0.902807
8	-0.328556	1.332679	5.729798	1	1.598013	0.663942	-8.510581	8	5.701734	0.366335	0.897082
8	-0.394755	1.308083	1.898898	1	-1.676616	-0.185092	-8.511921	8	-7.551634	-1.845319	0.113518
8	-0.394755	1.308083	-1.898898	1	3.445201	0.004688	-6.618744	8	-3.766491	-1.943327	0.080560
8	-0.328556	1.332679	-5.729798	1	-3.538205	0.472120	-6.615299	8	0.019477	-1.900932	-0.001891
8	-3.286324	0.401957	5.673446	1	3.445201	0.004688	6.618744	8	3.806665	-1.901561	-0.034160
8	-3.329952	0.614382	1.887823	1	-3.538205	0.472120	-6.615299	8	7.588294	-1.876122	0.090637
8	-3.329952	0.614382	-1.887823	1	-6.098873	0.381813	-3.781654	1	3.819044	5.997666	-0.089819
8	-3.286324	0.401957	-5.673446	1	-6.097373	0.382175	0.000000	1	3.816423	5.570742	-1.254728
8	3.386231	-1.993147	3.775325	1	-6.098873	0.381813	3.781654	1	0.031426	5.578444	-1.249012
8	-5.515169	1.196962	3.778379	1	-5.664097	-0.784069	3.787930	1	-3.753568	5.586146	-1.243294
8	3.384870	-1.994850	0.000000	1	-5.665547	-0.784371	0.000000	1	0.034054	6.005369	-0.084102
8	-5.516330	1.195243	0.000000	1	-5.664097	-0.784069	-3.787930	1	-3.750932	6.013070	-0.078385
8	3.386231	-1.993147	-3.775325	<b>Triplet Oxygen-deficient</b>				1	3.819195	4.291950	2.307702
8	-5.515169	1.196962	-3.778379	<b>Anatase(101) Model (Ti<sub>14</sub>O<sub>44</sub>H<sub>34</sub>)</b>				1	-3.750785	4.307355	2.319136
8	4.655288	1.548122	3.771319	Energy = -4144.75750776 a.u.				1	0.034207	4.299652	2.313420
8	4.654001	1.546390	0.000000	22	-5.758246	1.291756	-0.688027	1	-3.752908	2.890707	2.809688
8	4.655288	1.548122	-3.771319	22	-1.905783	1.252136	-0.731942	1	0.032076	2.883004	2.803970
8	1.797225	0.575193	7.559915	22	1.925089	1.375643	-0.702046	1	3.817022	2.875303	2.798254
8	1.797667	0.829122	3.792450	22	5.809515	1.264586	-0.710809	1	-5.652031	0.264886	1.868584
8	1.766203	0.881016	0.000000	22	-5.759775	-1.519984	0.327086	1	-1.867193	0.257167	1.862865
8	1.797667	0.829122	-3.792450	22	-1.879370	-1.561475	0.294875	1	1.917796	0.249465	1.857148
8	1.797225	0.575193	-7.559915	22	1.936087	-1.523554	0.319090	1	5.702659	0.241776	1.851433
8	-4.696782	-1.093879	3.779326	22	5.794048	-1.546921	0.306969	1	-1.870583	-2.229804	2.980868
8	-4.698078	-1.095850	0.000000	22	-3.723916	-3.801880	-0.467227	1	1.914405	-2.237505	2.975152
8	-4.696782	-1.093879	-3.779326	22	0.044820	-3.817552	-0.499393	1	5.699360	-2.245213	2.969431
8	5.473309	-0.742999	3.775013	22	3.741822	-3.813440	-0.484698	1	-5.655562	-2.222103	2.986584
8	5.472092	-0.744806	0.000000	22	-3.731899	-3.657639	-0.081371	1	-8.486086	1.618773	-0.652985
8	5.473309	-0.742999	-3.775013	22	-0.001029	3.649708	-0.080138	1	-8.491473	-1.650295	0.184222
8	3.247275	0.055047	5.677727	22	3.807292	3.643484	-0.084567	1	8.534517	1.584146	-0.678724
8	3.180333	0.040383	1.882602	8	-5.655775	-1.711305	2.170871	1	8.529129	-1.684937	0.158525
8	3.247275	0.055047	-5.677727	8	-1.870765	-1.719011	2.165158	1	6.646785	3.435564	-0.012621
8	3.180333	0.040383	-1.882602	8	1.914221	-1.726716	2.159443	1	6.631880	-3.528718	-0.501590
8	0.391136	-0.919391	5.646389	8	5.699268	-1.734407	2.153727	1	-6.588828	3.462486	0.007433
8	0.387391	-0.919710	1.881961	8	-5.711375	-0.318755	-1.338119	1	-6.603745	-3.501760	-0.481694
8	0.387391	-0.919710	-1.881961	8	-1.916307	-0.380866	-1.334221	1	3.793979	-6.079231	-0.416102
8	0.391136	-0.919391	-5.646389	8	5.774703	-0.329850	-1.376645	1	0.008985	-6.071529	-0.410385
8	-1.835807	-0.120365	7.563913	8	-5.662901	-3.310495	-0.414130	1	-3.776004	-6.063825	-0.404667
8	-1.928366	-0.093548	3.776554	8	-1.874613	-3.348883	-0.593131	1	-3.773372	-5.636897	0.760242
8	-1.938652	-0.115628	0.000000	8	1.905662	-3.367347	-0.678232	1	0.011617	-5.644599	0.754524
8	-1.928366	-0.093548	-3.776554	8	5.692024	-3.333568	-0.431396	1	3.796603	-5.652302	0.748808
8	-1.835807	-0.120365	-7.563913	8	-3.753130	3.401504	1.993977	<b>Au<sub>1</sub> on Stoichiometric Anatase</b>			
1	6.010426	0.094098	-3.786686	8	-3.776189	-5.553024	-1.220381	Energy = -4355.514487 a.u.			
1	5.578552	1.260612	-3.787800	8	0.031858	3.393800	1.988257	22	-5.768314	1.449809	-0.495122
				8	0.008798	-5.560721	-1.226089	22	-1.909206	1.418649	-0.525695
				8	3.816899	3.386097	1.982538	22	1.909207	1.418650	-0.525706
				8	3.793779	-5.568427	-1.231814	22	5.768317	1.449810	-0.495118
				8	-3.755878	4.680287	-1.568457	22	-5.782658	-1.269996	0.692576

## Appendix D

22 -1.914338 -1.312067 0.687963  
 22 1.914339 -1.312070 0.687947  
 22 5.782659 -1.269996 0.692573  
 22 -3.739747 -3.591760 0.067070  
 22 -0.000006 -3.596216 0.025743  
 22 3.739751 -3.591765 0.067064  
 22 -3.745997 3.833372 -0.042097  
 22 0.000001 3.828304 -0.042039  
 22 3.745999 3.833370 -0.042090  
 8 -5.677781 -1.337307 2.548764  
 8 -1.886470 -1.338691 2.550724  
 8 1.886469 -1.338695 2.550703  
 8 5.677777 -1.337309 2.548765  
 8 -5.732084 -0.205152 -1.039185  
 8 -1.860463 -0.272128 -1.027247  
 8 1.860463 -0.272128 -1.027259  
 8 5.732088 -0.205150 -1.039184  
 8 -5.673428 -3.095324 0.092261  
 8 -1.902398 -3.142227 -0.087953  
 8 1.902395 -3.142236 -0.087941  
 8 5.673439 -3.095323 0.092262  
 8 -3.775325 3.723548 2.032118  
 8 -3.778361 -5.372656 -0.550630  
 8 -0.000001 3.722304 2.033909  
 8 0.000027 -5.373598 -0.548795  
 8 3.775323 3.723547 2.032125  
 8 3.778370 -5.372668 -0.550629  
 8 -3.771316 4.750986 -1.586648  
 8 0.000003 4.749818 -1.584832  
 8 3.771321 4.750984 -1.586641  
 8 -7.559913 1.965015 -0.423257  
 8 -3.789875 1.947080 -0.677884  
 8 0.000000 1.916905 -0.736074  
 8 3.789877 1.947081 -0.677888  
 8 7.559915 1.965012 -0.423243  
 8 -3.779331 -4.401703 1.679826  
 8 -0.000051 -4.402830 1.681936  
 8 3.779324 -4.401700 1.679824  
 8 -3.775013 5.721599 0.644114  
 8 0.000001 5.720506 0.646000  
 8 3.775014 5.721598 0.644120  
 8 -5.677723 3.446829 -0.002049  
 8 -1.881625 3.376815 0.017147  
 8 1.881626 3.376813 0.017148  
 8 5.677725 3.446827 -0.002039  
 8 -5.646383 0.662879 1.162734  
 8 -1.881936 0.659139 1.163303  
 8 1.881938 0.659138 1.163287  
 8 5.646382 0.662879 1.162736  
 8 -7.563911 -1.612862 0.515655  
 8 -3.783687 -1.692862 0.490953  
 8 -0.000001 -1.701480 0.533486  
 8 3.783690 -1.692868 0.490935  
 8 7.563910 -1.612862 0.515659  
 1 3.786687 6.201064 -0.227279  
 1 3.787804 5.691531 -1.362025  
 1 0.000002 5.693014 -1.362543  
 1 -3.787801 5.691532 -1.362031  
 1 0.000001 6.191306 -0.229638  
 1 -3.786685 6.201066 -0.227285  
 1 3.787964 4.659229 2.288713  
 1 -3.787966 4.659231 2.288707  
 1 -0.000002 4.673404 2.289848  
 1 -3.786179 3.288925 2.880326  
 1 -0.000002 3.287454 2.880782  
 1 3.786175 3.288923 2.880333  
 1 -5.690262 0.585548 2.125766  
 1 -1.895599 0.586568 2.125135  
 1 1.895592 0.586566 2.125138  
 1 5.690254 0.585544 2.125775  
 1 -1.894379 -1.818081 3.413861  
 1 1.894369 -1.818080 3.413865  
 1 5.670232 -1.822841 3.418818  
 1 -5.670241 -1.822838 3.418809  
 1 -8.510581 1.760278 -0.498377

1 -8.511921 -1.449661 0.569479  
 1 8.510582 1.760273 -0.498361  
 1 8.511919 -1.449669 0.569501  
 1 6.618744 3.647702 0.034861  
 1 6.615298 -3.351316 0.039218  
 1 -6.618743 3.647706 0.034849  
 1 -6.615300 -3.351311 0.039190  
 1 3.781665 -5.900085 0.302005  
 1 -0.000007 -5.898636 0.301524  
 1 -3.781678 -5.900084 0.301998  
 1 -3.787927 -5.387698 1.435920  
 1 0.000001 -5.389119 1.436296  
 1 3.787923 -5.387700 1.435926  
 79 -0.000002 -1.871622 -2.420577

### Au<sub>2</sub>-A on Stoichiometric Anatase

Energy = -4491.026798 a.u.

22 5.756028 1.693891 0.417505  
 22 1.898860 1.731434 0.446441  
 22 -1.930605 1.717322 0.485976  
 22 -5.781720 1.785550 0.477543  
 22 5.740523 -0.862681 -1.085981  
 22 1.866313 -0.881231 -1.089736  
 22 -1.957858 -0.840684 -1.043071  
 22 -5.823401 -0.769209 -1.029837  
 22 3.681181 -3.227162 -0.739430  
 22 -0.068792 -3.193539 -0.661670  
 22 -3.801657 -3.161609 -0.704361  
 22 3.757441 4.136116 0.263814  
 22 -0.018767 4.158725 0.282983  
 22 -3.746960 4.192815 0.302370  
 8 5.627844 -0.706450 -2.938646  
 8 1.836846 -0.676921 -2.921469  
 8 -1.937527 -0.646377 -2.902223  
 8 -5.727469 -0.614633 -2.880860  
 8 5.710340 -0.012142 0.761998  
 8 1.832455 -0.003014 0.821102  
 8 -1.923885 -0.007220 0.770918  
 8 -5.759297 0.079386 0.819501  
 8 5.618126 -2.746944 -0.711322  
 8 1.855328 -2.774879 -0.574745  
 8 -1.960421 -2.743273 -0.542635  
 8 -5.728145 -2.655202 -0.653595  
 8 3.771097 4.270778 -1.807745  
 8 3.706174 -5.069731 -0.337147  
 8 -0.003976 4.300282 -1.790476  
 8 -0.072051 -5.039994 -0.319834  
 8 -3.779042 4.331820 -1.769336  
 8 -3.850271 -5.008623 -0.298702  
 8 3.790768 4.855640 1.908254  
 8 0.019632 4.885185 1.925489  
 8 -3.751515 4.916622 1.946626  
 8 7.550370 2.199207 0.399131  
 8 3.786264 2.188752 0.659931  
 8 -0.011877 2.183920 0.734037  
 8 -3.800960 2.246814 0.708696  
 8 -7.568765 2.321450 0.475994  
 8 3.706400 -3.837652 -2.434695  
 8 -0.072772 -3.807998 -2.417652  
 8 -3.851914 -3.776528 -2.396239  
 8 3.793744 6.087372 -0.189663  
 8 0.018902 6.117039 -0.172457  
 8 -3.755941 6.148416 -0.151249  
 8 5.679356 3.736101 0.168693  
 8 1.883961 3.701392 0.162945  
 8 -1.884889 3.744780 0.174970  
 8 -5.675600 3.827926 0.226331  
 8 5.619246 1.112734 -1.322084  
 8 1.854844 1.139574 -1.303994  
 8 -1.908291 1.169997 -1.284785  
 8 -5.673023 1.204063 -1.264615  
 8 7.519622 -1.239695 -0.962932  
 8 3.738640 -1.277196 -0.912882

8 -0.035871 -1.234761 -0.931235  
 8 -3.836108 -1.226444 -0.888846  
 8 -7.607479 -1.117407 -0.886071  
 1 -3.759910 6.519704 0.771514  
 1 -3.760821 5.877452 1.836777  
 1 0.026812 5.848236 1.818198  
 1 3.814458 5.816199 1.798232  
 1 0.026514 6.479114 0.753415  
 1 3.813118 6.458469 0.732985  
 1 -3.784775 5.291642 -1.911527  
 1 3.790817 5.230386 -1.950077  
 1 0.003134 5.275223 -1.930224  
 1 3.774798 3.941217 -2.702097  
 1 -0.011285 3.970425 -2.683461  
 1 -3.797321 4.002446 -2.663572  
 1 5.658458 1.151420 -2.287660  
 1 1.864051 1.183032 -2.267601  
 1 -1.927262 1.213672 -2.248309  
 1 -5.721495 1.243432 -2.229760  
 1 1.836551 -1.049127 -3.835999  
 1 -1.950882 -1.018522 -3.816725  
 1 -5.727487 -0.992095 -3.803000  
 1 5.612290 -1.083787 -3.860693  
 1 8.499540 1.979261 0.444289  
 1 8.468794 -1.078915 -1.001734  
 1 -8.520846 2.116889 0.530928  
 1 -8.554270 -0.941254 -0.915057  
 1 -6.614968 4.039366 0.218877  
 1 -6.672001 -2.908143 -0.626921  
 1 6.621918 3.932338 0.151439  
 1 6.557994 -3.015123 -0.694238  
 1 -3.861570 -5.429646 -1.208535  
 1 -0.080096 -5.458821 -1.227136  
 1 3.701375 -5.490799 -1.247013  
 1 3.707463 -4.845859 -2.311140  
 1 -0.080312 -4.816599 -2.292433  
 1 -3.868053 -4.784604 -2.272595  
 79 0.676596 -1.508545 2.009867  
 79 -0.418123 -3.878546 2.120044

### Au<sub>2</sub>-B on Stoichiometric Anatase

Energy = -4491.01423 a.u.

22 -6.205443 -1.525863 0.680118  
 22 -2.390984 -1.223853 0.295107  
 22 1.385613 -0.982018 -0.044747  
 22 5.224397 -0.764110 -0.651840  
 22 -6.504061 1.336550 -0.047405  
 22 -2.661906 1.641387 -0.455978  
 22 1.107022 1.883320 -0.893668  
 22 4.941553 2.160020 -1.335010  
 22 -4.519474 3.670362 0.712466  
 22 -0.811376 3.941268 0.321268  
 22 2.866957 4.192522 -0.115051  
 22 -4.135192 -3.666138 -0.371828  
 22 -0.436513 -3.399337 -0.786417  
 22 3.246725 -3.148954 -1.206756  
 8 -6.627006 1.693923 -1.869046  
 8 -2.868437 1.960936 -2.291254  
 8 0.872774 2.224990 -2.709767  
 8 4.630502 2.488628 -3.128362  
 8 -6.187006 0.028267 1.471350  
 8 -2.404700 0.369248 1.030000  
 8 1.327243 0.675574 0.583475  
 8 5.100597 0.782806 0.262531  
 8 -6.417528 3.050666 0.821771  
 8 -2.642577 3.339642 0.619678  
 8 1.100533 3.612682 0.205967  
 8 4.831212 3.844803 -0.436999  
 8 -4.417365 -3.240653 -2.384768  
 8 -4.578887 5.329606 1.607285  
 8 -0.674422 -2.974907 -2.805082  
 8 -0.833324 5.595358 1.186653  
 8 3.068408 -2.712163 -3.222144  
 8 2.912657 5.858464 0.769253



## Appendix D

8	-7.442188	-2.988721	-0.727183	8	0.194414	4.824085	2.174818	22	-3.369937	4.057609	-0.521386
1	-5.836017	5.323125	1.324869	8	-3.572354	4.984852	2.124619	22	0.326223	3.911245	-0.258469
1	-5.578371	4.645734	2.335792	8	7.670003	2.082895	0.479157	22	4.072965	3.735938	-0.042635
1	-1.951528	5.719424	2.126706	8	3.899425	2.169605	0.659676	22	-3.653681	-3.313529	-1.378928
1	1.675742	6.790415	1.916123	8	0.106695	2.297854	0.657728	22	0.056679	-3.464259	-1.142600
1	-2.207384	6.385466	1.115553	8	-3.678473	2.491147	0.563791	22	3.839061	-3.642997	-0.898335
1	1.415693	7.467142	0.905428	8	-7.435012	2.724951	0.270002	8	-5.213832	2.224102	-3.394706
1	-5.695976	4.303941	-1.440818	8	3.701943	-3.423220	-3.152688	8	-1.433759	2.062906	-3.152961
1	1.558596	6.448753	-1.860568	8	-0.073738	-3.263303	-3.207189	8	2.328010	1.900891	-2.910626
1	-2.072575	5.389925	-1.649077	8	-3.849476	-3.102224	-3.257251	8	6.107824	1.736475	-2.665374
1	1.858838	5.257619	-2.708406	8	4.056194	6.142906	0.299166	8	-5.556018	0.656408	0.005275
1	-1.765841	4.184570	-2.499453	8	0.286424	6.302329	0.244643	8	-1.733058	0.595462	0.207884
1	-5.391445	3.114139	-2.289083	8	-3.486049	6.463415	0.194681	8	1.964736	0.378194	0.493226
1	4.487162	3.116019	-2.605888	8	5.855590	3.700787	0.402652	8	5.874857	0.159632	0.741712
1	0.854175	2.042157	-2.395031	8	2.064665	3.795730	0.319092	8	-5.319118	3.654540	-0.736233
1	-2.777124	0.969172	-2.184940	8	-1.702880	3.979308	0.264012	8	-1.558475	3.530556	-0.266968
1	-6.410063	-0.105779	-1.975623	8	-5.488646	4.182894	0.245623	8	2.201255	3.349778	-0.025695
1	1.352486	-0.004358	-4.128244	8	5.746669	1.283534	-1.400816	8	5.993852	3.167301	-0.007479
1	-2.272062	-1.075659	-3.918652	8	1.985746	1.440129	-1.453778	8	-3.526592	-2.938399	-3.416246
1	-5.886204	-2.148114	-3.715342	8	-1.774611	1.600232	-1.505389	8	-3.395995	5.748488	0.316396
1	4.972281	1.062105	-4.343333	8	-5.535282	1.762977	-1.556919	8	0.237583	-3.099059	-3.175382
1	7.155841	4.568049	0.037363	8	7.560823	-1.160343	-1.296758	8	0.371248	5.587503	0.557428
1	7.900852	1.725479	-1.637127	8	3.787785	-1.070543	-1.328960	8	4.001444	-3.262633	-2.931297
1	-9.141876	-0.250133	0.980243	8	0.012845	-0.845452	-1.383519	8	4.138173	5.423991	0.801742
1	-8.399442	-3.093726	-0.695365	8	-3.791354	-0.751326	-1.445182	8	-3.808360	-4.415691	0.031844
1	-7.892885	2.158145	0.723685	8	-7.552313	-0.517916	-1.505997	8	-0.048141	-4.576250	0.272419
1	-6.017434	-4.442662	-0.654585	1	-3.500423	6.719089	1.156016	8	3.711725	-4.739581	0.516281
1	4.781985	5.905351	-0.009741	1	-3.547382	5.951639	2.133806	8	-7.409431	-1.344569	-1.002142
1	6.650730	-0.696789	-1.387371	1	0.236591	5.792102	2.187032	8	-3.692609	-1.516659	-0.500230
1	-2.651015	-5.999335	-1.568985	1	4.020369	5.629946	2.238618	8	0.150179	-1.668270	-0.280560
1	0.969659	-4.927092	-1.777817	1	0.282151	6.548267	1.208326	8	3.897514	-1.849363	-0.025405
1	4.590695	-3.858063	-1.987928	1	4.065581	6.397486	1.260788	8	7.665199	-1.993844	-0.031019
1	4.337359	-3.176882	-2.997732	1	-3.500233	5.830429	-1.657790	8	-3.275925	5.069180	-2.016378
1	0.708502	-4.251130	-2.788802	1	4.067906	5.508722	-1.552993	8	0.492284	4.908303	-1.775528
1	-2.916482	-5.321499	-2.578253	1	0.284650	5.683581	-1.603066	8	4.260126	4.744600	-1.530910
79	1.029625	-3.778451	1.649429	1	4.028344	4.322856	-2.458350	8	-3.690998	-5.094500	-2.301363
79	3.645646	-2.546575	1.466097	1	0.245581	4.482436	-2.511553	8	0.072901	-5.255284	-2.060630
79	1.219890	-1.118482	1.778380	1	-3.536601	4.644457	-2.563117	8	3.836464	-5.418708	-1.816451
				1	5.810226	1.438865	-2.353350	8	-5.554608	-2.840440	-1.489832
				1	2.019787	1.600925	-2.404954	8	-1.778717	-2.930691	-1.254479
				1	-1.768120	1.762014	-2.457403	8	2.004143	-3.099669	-1.022279
				1	-5.558828	1.922164	-2.510791	8	5.766895	-3.328079	-0.760456
				1	1.957159	-0.420241	-4.236656	8	-5.347105	0.064789	-2.280052
				1	-1.826941	-0.259467	-4.289037	8	-1.593860	-0.093092	-2.038354
				1	-5.599455	-0.102404	-4.347261	8	2.159051	-0.254727	-1.796607
				1	5.729579	-0.583961	-4.190380	8	5.911900	-0.420122	-1.554750
				1	8.610066	1.825692	0.515477	8	-7.225555	2.320327	-1.468402
				1	8.515143	-1.029395	-1.296259	8	-3.453679	2.254976	-1.202388
				1	-8.394108	2.548538	0.279963	8	0.323737	2.100824	-0.976808
				1	-8.491717	-0.306460	-1.531836	8	4.074715	1.915998	-0.694560
				1	-6.420035	4.426845	0.245160	8	7.857050	1.670714	-0.496791
				1	-6.681548	-2.358603	-1.451116	1	3.771327	-6.004867	-1.015489
				1	6.804214	3.864680	0.428307	1	3.711414	-5.643880	0.173363
				1	6.535849	-2.920437	-1.268067	1	-0.065161	-5.482761	-0.069597
				1	-3.940957	-4.886956	-2.282664	1	-3.841549	-5.318573	-0.313192
				1	-0.163134	-5.046188	-2.229557	1	-0.003867	-5.832888	-1.255101
				1	3.614632	-5.208104	-2.178042	1	-3.779408	-5.679655	-1.501901
				1	3.667144	-4.438311	-3.154267	1	3.999686	-4.157891	-3.305470
				1	-0.116964	-4.278745	-3.207425	1	-3.553611	-3.832569	-3.792047
				1	-3.900974	-4.116607	-3.259062	1	0.222629	-4.009132	-3.551720
				79	0.588772	-1.288581	1.688229	1	-3.463836	-2.399649	-4.200009
				79	-0.369739	-3.883790	1.165060	1	0.311125	-2.560719	-3.957092
				79	-0.798359	-2.616866	3.588036	1	4.085903	-2.724818	-3.713661
								1	-5.321599	0.265469	-3.225802
								1	-1.538290	0.101422	-2.981587
								1	2.241372	-0.061380	-2.738107
								1	6.024903	-0.223236	-2.494873
								1	-1.365269	2.647798	-3.945517
								1	2.412078	2.485103	-3.702185
								1	6.177150	2.328313	-3.463953
								1	-5.129409	2.815287	-4.192313
								1	-8.355422	-1.110383	-0.962350
								1	-8.172608	2.206146	-1.603697
								1	8.614865	-1.841289	0.130843
								1	8.800350	1.475117	-0.510311

### Au<sub>3</sub>-C on Stoichiometric Anatase

Energy = -4626.497092 a.u.

22	5.863822	1.636964	0.399109
22	2.012532	1.821205	0.349420
22	-1.822044	1.927413	0.318160
22	-5.667406	2.128375	0.240529
22	5.793011	-0.711018	-1.411880
22	1.907380	-0.589722	-1.485886
22	-1.892544	-0.418573	-1.513583
22	-5.753562	-0.218665	-1.571423
22	3.655842	-3.017656	-1.397117
22	-0.089763	-2.847258	-1.426353
22	-3.818421	-2.698999	-1.502121
22	3.951804	4.153725	0.508368
22	0.166790	4.306356	0.455354
22	-3.554964	4.468744	0.404225
8	5.735054	-0.323135	-3.228862
8	1.947428	-0.162899	-3.283714
8	-1.821572	-0.002549	-3.335757
8	-5.609387	0.159090	-3.385893
8	5.753915	-0.090573	0.536877
8	1.850038	0.044608	0.516941
8	-1.869640	0.185131	0.406940
8	-5.709418	0.395217	0.373875
8	5.606386	-2.619439	-1.270547
8	1.841630	-2.514924	-1.173215
8	-1.973996	-2.354641	-1.233925
8	-5.730099	-2.137538	-1.427486
8	4.013706	4.540012	-1.530476
8	3.611322	-4.901969	-1.223245
8	0.241596	4.699362	-1.584682
8	-0.163309	-4.720202	-1.277370
8	-3.529447	4.860546	-1.634911
8	-3.938039	-4.581065	-1.327793
8	3.962887	4.664564	2.228937

### Au<sub>3</sub>-D on Stoichiometric Anatase

Energy = -4626.483858 a.u.

22	-5.615554	-0.913580	-0.746570
22	-1.823449	-1.074177	-0.380996
22	2.046274	-1.280643	-0.273809
22	5.892356	-1.413199	-0.007471
22	-5.448440	1.929940	-1.575304
22	-1.601668	1.764961	-1.318752
22	2.194886	1.640829	-1.062267
22	6.080458	1.431978	-0.829756

## Appendix D

1 6.700760 -3.562860 -0.762558  
 1 6.938016 3.373846 0.138648  
 1 -6.497164 -2.994434 -1.612720  
 1 -6.253036 3.941995 -0.711126  
 1 4.218564 6.054658 0.026508  
 1 0.448130 6.215531 -0.216108  
 1 -3.322141 6.379438 -0.459258  
 1 -3.267524 6.015741 -1.647993  
 1 0.509163 5.854546 -1.404917  
 1 4.285698 5.690422 -1.161420  
 79 0.539454 0.331733 2.165088  
 79 -1.466347 -1.866261 2.294727  
 79 -1.120642 0.151707 4.230615

### Au<sub>4</sub>-A on Stoichiometric Anatase

Energy = -4762.006787 a.u.

22 -4.208414 3.590225 0.171332  
 22 -0.536069 2.441777 -0.204345  
 22 3.076302 1.256427 -0.588705  
 22 6.746961 0.159308 -0.925244  
 22 -4.778897 1.214795 1.930760  
 22 -1.105574 0.040382 1.563102  
 22 2.515635 -1.076042 1.169682  
 22 6.203911 -2.182167 0.813485  
 22 -3.567932 -1.646535 1.572502  
 22 -0.010623 -2.766324 1.201049  
 22 3.543433 -3.866113 0.896976  
 22 -1.569195 5.296146 -0.099291  
 22 2.012639 4.174632 -0.453436  
 22 5.549200 3.077814 -0.805213  
 8 -4.427057 1.468393 3.710354  
 8 -0.822273 0.348524 3.355313  
 8 2.764990 -0.765003 2.999881  
 8 6.369837 -1.882986 2.640511  
 8 -4.674920 1.909510 -0.107277  
 8 -1.065214 0.770185 -0.415557  
 8 2.545800 -0.395998 -0.712382  
 8 6.182583 -1.476648 -1.098423  
 8 -5.270407 -0.620993 1.698396  
 8 -1.689926 -1.771446 1.280565  
 8 1.898954 -2.921176 0.839076  
 8 5.518235 -3.969825 0.629393  
 8 -1.329441 5.565311 1.944435  
 8 -4.181290 -3.432628 1.382780  
 8 2.260069 4.450252 1.590775  
 8 -0.588801 -4.548421 1.028767  
 8 5.849729 3.336892 1.233072  
 8 3.003692 -5.662876 0.670835  
 8 -1.596968 5.883398 -1.794332  
 8 1.988748 4.769585 -2.147608  
 8 5.574591 3.657348 -2.504938  
 8 -5.775286 4.593818 0.290653  
 8 -2.234001 3.443073 -0.291815  
 8 1.364043 2.275492 -0.698412  
 8 4.979966 1.186098 -1.023988  
 8 8.600662 0.131499 -1.133845  
 8 -3.581588 -2.123282 3.343295  
 8 0.011792 -3.239401 2.989472  
 8 3.605183 -4.354082 2.631186  
 8 -0.999937 7.193285 0.166829  
 8 2.589364 6.078463 -0.186758  
 8 6.178659 4.965052 -0.544475  
 8 -3.521528 5.504360 0.205298  
 8 0.077948 4.335939 -0.120700  
 8 3.664663 3.229504 -0.473222  
 8 7.275254 2.153034 -0.864519  
 8 -4.067110 3.089561 1.931317  
 8 -0.488812 1.975170 1.578088  
 8 3.089945 0.864316 1.223403  
 8 6.670080 -0.243292 0.867365  
 8 -6.603190 1.403916 1.970472  
 8 -3.032724 0.256502 1.604951  
 8 0.578450 -0.864875 1.239026  
 8 4.168218 -2.026277 0.895266

8 7.780360 -3.060762 0.545233  
 1 6.187100 5.256317 -1.495502  
 1 5.878411 4.575396 -2.489652  
 1 2.277295 5.694589 -2.133604  
 1 -1.324472 6.811183 -1.775918  
 1 2.583722 6.364308 -1.138942  
 1 -1.013649 7.491451 -0.781988  
 1 6.153426 4.252706 1.280847  
 1 -1.049755 6.493085 1.994604  
 1 2.555830 5.388655 1.635790  
 1 -1.328517 5.311763 2.863237  
 1 2.271068 4.193047 2.507283  
 1 5.871292 3.076929 2.149818  
 1 -3.983622 3.201580 2.888290  
 1 -0.375469 2.082523 2.529943  
 1 3.229160 0.963630 2.172767  
 1 6.836966 -0.157145 1.816093  
 1 -0.828422 0.054707 4.298000  
 1 2.773890 -1.063440 3.941058  
 1 6.363464 -2.181408 3.591150  
 1 -4.419060 1.165501 4.659572  
 1 -6.745879 4.668813 0.351038  
 1 -7.452303 1.846485 2.077180  
 1 9.437854 -0.354646 -1.252581  
 1 8.733978 -3.177761 0.473295  
 1 8.229832 2.070440 -0.960352  
 1 6.336544 -4.497583 0.543977  
 1 -4.356381 5.977225 0.286790  
 1 -6.243118 -0.592845 1.790480  
 1 2.993652 -6.006903 1.612498  
 1 -0.601622 -4.889520 1.968017  
 1 -4.197535 -3.774750 2.325061  
 1 -3.893110 -3.089777 3.318288  
 1 -0.291871 -4.208976 2.962111  
 1 3.310021 -5.325640 2.604538  
 79 -4.166526 -0.134876 -1.164138  
 79 -1.254684 -1.040761 -1.704648  
 79 -0.492773 -3.607370 -1.514320  
 79 -3.430572 -2.725444 -1.223143

### Au<sub>4</sub>-B on Stoichiometric Anatase

Energy = -4762.004825 a.u.

22 -4.328217 3.767079 0.024330  
 22 -0.679614 2.534313 -0.237362  
 22 2.920519 1.263442 -0.506967  
 22 6.564390 0.030104 -0.748463  
 22 -5.002695 1.478705 1.785766  
 22 -1.396466 0.197929 1.555004  
 22 2.240233 -1.048974 1.294170  
 22 5.912094 -2.265392 1.011787  
 22 -3.874944 -1.437891 1.527050  
 22 -0.332200 -2.649604 1.278617  
 22 3.205561 -3.873484 1.063265  
 22 -1.649482 5.423215 -0.201552  
 22 1.905033 4.197179 -0.453015  
 22 5.446498 2.983870 -0.705199  
 8 -4.671529 1.738362 3.599454  
 8 -1.092603 0.508107 3.347866  
 8 2.464398 -0.713027 3.095612  
 8 6.043821 -1.941151 2.839563  
 8 -4.867436 2.127462 -0.149063  
 8 -1.277605 0.885125 -0.428991  
 8 2.300857 -0.387628 0.684783  
 8 5.957665 -1.592525 -0.910938  
 8 -5.529103 -0.359645 1.602371  
 8 -1.972419 -1.620628 1.280479  
 8 1.595407 -2.884237 0.973805  
 8 5.178234 -4.036265 0.843158  
 8 -1.415523 5.713689 1.840839  
 8 -4.515838 -3.206380 1.358414  
 8 2.147077 4.489484 1.590270  
 8 -0.950456 -4.431230 1.107530  
 8 5.709823 3.266929 1.335472  
 8 2.614950 -5.654962 0.852705

8 -1.586961 5.975984 -1.907868  
 8 1.971765 4.753117 -2.158150  
 8 5.530705 3.531884 -2.412694  
 8 -5.848604 4.843256 0.098633  
 8 -2.326609 3.575644 -0.389130  
 8 1.240514 2.302314 -0.684389  
 8 4.827453 1.101724 -0.899034  
 8 8.419676 -0.056306 -0.913433  
 8 -3.923506 -1.881832 3.310969  
 8 -0.357289 -3.107103 3.060362  
 8 3.209031 -4.331064 2.805142  
 8 -0.997459 7.301120 0.045306  
 8 2.564865 6.077180 -0.205231  
 8 6.127299 4.854566 -0.459978  
 8 -3.567681 5.686747 0.051734  
 8 0.001425 4.410256 -0.170710  
 8 3.554578 3.176006 -0.425521  
 8 7.148182 2.006952 -0.708523  
 8 -4.223281 3.318179 1.803293  
 8 -0.669837 2.094695 1.552895  
 8 2.877847 0.876293 1.301147  
 8 6.432957 -0.341079 1.047574  
 8 -6.808195 1.707570 1.810110  
 8 -3.251756 0.455059 1.527186  
 8 0.334033 -0.792385 1.297049  
 8 3.877792 -2.041257 1.030881  
 8 7.467596 -3.194589 0.797658  
 1 6.166234 5.129331 -1.415148  
 1 5.860870 4.440845 -2.405087  
 1 2.286729 5.669572 -2.152460  
 1 -1.288170 6.895743 -1.898107  
 1 2.589571 6.346871 -1.161848  
 1 -0.980497 7.583433 -0.980309  
 1 6.039137 4.178773 1.375538  
 1 -1.110128 6.633750 1.882526  
 1 2.468921 5.419623 1.626936  
 1 -1.443266 5.475803 2.763423  
 1 2.129183 4.247631 2.510802  
 1 5.702460 3.022050 2.256656  
 1 -4.159206 3.444082 2.760103  
 1 -0.579564 2.215567 2.505415  
 1 3.001157 0.986076 2.251468  
 1 6.580626 -0.243869 1.998449  
 1 -1.132344 0.232351 4.295061  
 1 2.446005 -0.996557 4.041248  
 1 6.007130 -2.223186 3.794522  
 1 -4.694975 1.451824 4.553516  
 1 -6.817621 4.947335 0.134786  
 1 -7.646163 2.176209 1.889474  
 1 9.244793 -0.568313 -1.004190  
 1 8.418747 -3.340293 0.750153  
 1 8.101868 1.895275 -0.780112  
 1 5.982686 -4.588859 0.785558  
 1 -4.389989 6.184793 0.105620  
 1 -6.502641 -0.301455 1.671160  
 1 2.573318 -5.982659 1.799316  
 1 -0.995126 -4.755890 2.051636  
 1 -4.564265 -3.531669 2.305516  
 1 -4.262955 -2.839073 3.294386  
 1 -0.688631 -4.067831 3.041532  
 1 2.886466 -5.294103 2.787344  
 79 -4.392989 -2.221317 -1.175954  
 79 -2.198244 -0.729041 -1.683846  
 79 0.582719 -1.713146 -1.633875  
 79 -1.531487 -3.395854 -1.382561

### Au<sub>4</sub>-C on Stoichiometric Anatase

Energy = -4761.999031 a.u.

22 -5.431089 1.464717 0.756235  
 22 -1.636347 1.489504 0.230060  
 22 2.202284 1.597975 -0.012397  
 22 6.045448 1.639099 -0.396688  
 22 -5.269217 -1.166360 2.109322  
 22 -1.432547 -1.115170 1.728917

## Appendix D

22 2.380126 -1.103896 1.353175	1 8.768263 1.989232 -0.693715	8 5.536193 1.347482 -0.339562
22 6.236198 -0.997531 0.951152	1 8.942428 -1.144796 0.567886	8 1.963687 2.334453 0.378647
22 -3.249167 -3.488137 1.430854	1 6.899252 3.879267 -0.093471	8 -1.619247 3.303314 1.063919
22 0.435110 -3.447657 1.018885	1 7.042973 -3.104215 0.350339	8 -5.234388 4.186299 1.796185
22 4.187413 -3.384731 0.679438	1 -6.270462 3.685804 1.230232	1 -3.396022 -4.288913 2.611117
22 -3.434227 3.906172 0.861048	1 -6.119918 -3.297584 1.673063	1 -3.574050 -4.073305 1.398848
22 0.271982 3.952156 0.485101	1 4.303207 -5.671855 1.054312	1 0.018745 -5.050536 0.701643
22 4.040178 4.023631 0.105753	1 0.540872 -5.725681 1.431833	1 3.612060 -6.024792 0.004392
8 -4.981462 -1.112428 3.944892	1 -3.221356 -5.782391 1.810458	1 0.197343 -5.255814 1.908999
8 -1.210491 -1.058269 3.568008	1 -3.126287 -5.198091 2.904949	1 3.787826 -6.239903 1.216867
8 2.544231 -1.003129 3.190712	1 0.642340 -5.144129 2.526734	1 -2.471158 -2.259870 4.543778
8 6.316051 -0.946460 2.809636	1 4.410797 -5.087372 2.147544	1 4.715031 -4.211510 3.149069
8 -5.403840 -0.221851 0.315577	79 -1.961993 2.071295 -2.467985	1 1.119423 -3.248734 3.851497
8 -1.603535 -0.265165 0.011876	79 0.891712 -1.460819 -1.656088	1 5.132504 -2.788608 3.318825
8 2.165957 -0.158487 -0.453432	79 -0.934564 -3.303324 -2.308900	1 1.541545 -1.811776 4.015845
8 5.987965 -0.049833 -0.827385	79 -1.605021 -0.588645 -2.627565	1 -2.050131 -0.837959 4.712848
8 -5.182993 -3.024895 1.615337		1 7.293731 -0.917639 1.493519
8 -1.440632 -3.046583 1.054098		1 3.693802 0.058869 2.191805
8 2.331541 -2.975477 0.658941		1 0.096335 1.035864 2.889971
8 6.105817 -2.859073 0.480945		1 -3.501192 2.014149 3.588568
8 -3.245812 3.931842 2.924313		1 4.489859 2.613232 2.725175
8 -3.313503 -5.311070 0.930378		1 0.895737 3.589308 3.422735
8 0.510538 3.985886 2.548692		1 -2.682911 4.567487 4.120930
8 0.445743 -5.256795 0.554475		1 8.073682 1.646136 2.033357
8 4.266222 4.042196 2.169403		1 9.089798 -3.353527 -1.163711
8 4.204630 -5.200622 0.174875		1 9.994917 -0.095430 -1.066477
8 -3.620681 4.723701 -0.734045		1 -7.055599 1.031315 1.969940
8 0.131279 4.777769 -1.109194		1 -6.153029 4.290146 2.067562
8 3.883019 4.833950 -1.488108		1 -5.507402 -1.103243 2.657455
8 -7.216919 1.963494 0.974633		1 -4.103984 5.462901 0.681627
8 -3.513710 1.983142 0.384659		1 7.048935 -4.513419 0.220221
8 0.310080 2.000597 -0.054859		1 8.445814 2.054447 -1.754191
8 4.059443 2.103002 -0.404828		1 -0.842233 7.184636 -0.313577
8 7.825600 2.184467 -0.536834		1 2.744435 6.208972 -1.009781
8 -3.114309 -4.198398 3.084440		1 6.331954 5.236270 -1.705950
8 0.645899 -4.144198 2.708714		1 6.513914 5.016400 -0.494795
8 4.405676 -4.087933 2.328762		1 2.921238 5.993635 0.202516
8 -3.424694 5.835998 1.420661		1 -0.672160 6.968010 0.899896
8 0.331342 5.890201 1.045187		79 -1.030613 -1.621187 -2.008916
8 4.086841 5.946356 0.665824		79 -3.623273 -2.349083 -1.192756
8 -5.333838 3.496749 1.111646		79 -5.719428 -0.473379 -1.076477
8 -1.556437 3.477471 0.746769		79 -3.108744 0.251070 -1.846345
8 2.199739 3.532613 0.380492		
8 5.963605 3.662700 -0.023310		
8 -5.128605 0.794707 2.439978		
8 -1.384099 0.846005 2.064465		
8 2.360939 0.900807 1.688125		
8 6.105918 0.959511 1.310981		
8 -7.053007 -1.546202 2.132231		
8 -3.294858 -1.586805 1.751989		
8 0.489535 -1.532744 1.395486		
8 4.230339 -1.467422 0.984737		
8 7.997378 -1.324969 0.619463		
1 4.002254 6.368746 -0.230722		
1 3.901873 5.787163 -1.325691		
1 0.133292 5.733250 -0.947594		
1 -3.635181 5.676440 -0.568288		
1 0.234928 6.303513 0.146128		
1 -3.532223 6.258064 0.526418		
1 4.284527 4.992564 2.364259		
1 -3.252727 4.881843 3.121676		
1 0.515714 4.951420 2.743213		
1 -3.163534 3.552725 3.794909		
1 0.603168 3.606623 3.416942		
1 4.369945 3.663388 3.037864		
1 -5.076247 0.778617 3.405557		
1 -1.300005 0.835184 3.025407		
1 2.470981 0.890611 2.646451		
1 6.246371 0.945084 2.267761		
1 -1.121002 -1.481068 4.455798		
1 2.647736 -1.425670 4.077087		
1 6.404762 -1.374930 3.704812		
1 -4.877631 -1.540673 4.838580		
1 -8.165787 1.740478 1.008101		
1 -7.994315 -1.393493 2.269614		
	<b>Au<sub>4</sub>-D on Stoichiometric Anatase</b>	
	Energy = -4761.989028 a.u.	
	22 6.551949 -2.354757 -0.743182	
	22 2.904763 -1.337882 -0.073146	
	22 -0.733385 -0.366461 0.560695	
	22 -4.418864 0.606630 1.327533	
	22 7.399357 0.469377 -0.398062	
	22 3.719896 1.500172 0.289748	
	22 0.101078 2.474836 1.010996	
	22 -3.569564 3.440155 1.742858	
	22 5.766564 3.026414 -1.265096	
	22 2.211078 3.998554 -0.599868	
	22 -1.324026 4.952775 0.113167	
	22 4.270090 -3.968148 0.731285	
	22 0.729929 -2.997259 1.420385	
	22 -2.807620 -2.006015 2.143031	
	8 7.770159 0.987331 1.350238	
	8 4.174740 1.965740 2.049640	
	8 0.596406 2.937583 2.744150	
	8 -3.001532 3.912657 3.440943	
	8 6.712350 -0.916501 -1.715598	
	8 3.095562 0.133766 -1.005941	
	8 -0.516956 1.150199 -0.301589	
	8 -4.096436 2.058215 0.384096	
	8 7.514241 2.069149 -1.458480	
	8 3.881450 3.047744 -0.974328	
	8 0.300753 4.024136 -0.286864	
	8 -3.248927 4.992037 0.630425	
	8 4.827099 -3.389858 2.645244	
	8 6.014049 4.544987 -2.358839	
	8 1.246635 -2.415731 3.341598	
	8 2.430739 5.519698 -1.661872	
	8 -2.335258 -1.444747 4.035268	
	8 -1.153893 6.491697 -0.967729	
	8 3.729318 -5.190187 -0.470008	
	8 0.152635 -4.217131 0.225638	
	8 -3.425016 -3.247226 0.919165	
	8 8.165517 -3.283336 -0.860168	
	8 4.536233 -2.360742 -0.411037	
	8 0.956396 -1.365437 0.240895	
	8 -2.643701 -0.392373 1.051647	
	8 -6.176088 0.611639 1.923085	
	8 6.368553 4.150071 0.015205	
	8 2.784430 5.125213 0.712565	
	8 -0.801212 6.097266 1.406661	
	8 4.086542 -5.585410 1.903728	
	8 0.506432 -4.611482 2.600146	
	8 -3.074886 -3.640519 3.293551	
	8 6.187398 -4.091094 0.301915	
	8 2.610547 -3.058578 1.007232	
	8 -0.968774 -2.087705 1.700139	
	8 -4.583410 -1.165864 2.391775	
	8 7.000201 -1.201769 0.616877	
	8 3.430463 -0.228560 1.309410	
	8 -0.138227 0.740841 2.001790	
	8 -3.712547 1.707323 2.696134	
	8 9.115077 0.289435 -0.988776	
		<b>Au<sub>1</sub> on Oxygen-deficient Anatase</b>
		Energy = -4280.269598 a.u.
		22 -5.951786 1.247899 -0.645252
		22 -2.099681 1.281963 -0.566751
		22 1.727966 1.487030 -0.404827
		22 5.597316 1.420212 -0.325926
		22 -5.945820 -1.544615 0.414994
		22 -2.074616 -1.515371 0.494113
		22 1.746234 -1.486665 0.646503
		22 5.614969 -1.373339 0.726744
		22 -3.855070 -3.811318 -0.281634
		22 -0.109024 -3.767525 -0.202570
		22 3.633144 -3.702547 -0.078930
		22 -3.989601 3.658255 -0.018947
		22 -0.269885 3.716687 0.083989
		22 3.543868 3.777265 0.191604
		8 -5.888033 -1.709308 2.266015
		8 -2.104869 -1.654402 2.369373
		8 1.678310 -1.599412 2.472743
		8 5.461406 -1.544391 2.576317
		8 -5.863365 -0.380587 -1.258445
		8 -2.054574 -0.378440 -1.131943
		8 5.596579 -0.207318 -0.948668
		8 -5.794278 -3.350480 -0.290775
		8 -2.005566 -3.332288 -0.378241
		8 1.776464 -3.296006 -0.273806
		8 5.555180 -3.185545 0.019339
		8 -4.063674 3.430762 2.057689
		8 -3.849182 -5.574418 -1.004369
		8 -0.280495 3.485717 2.161113
		8 -0.065906 -5.519312 -0.900760



## Appendix D

1	3.629411	-5.702724	-1.014703
1	3.690414	-5.344714	0.171657
1	-0.084022	-5.495992	0.413738
1	-3.857879	-5.647223	0.655723
1	-0.144868	-5.853933	-0.772632
1	-3.919662	-6.005228	-0.530575
1	3.408584	-3.861605	-3.299267
1	-4.139964	-4.164129	-2.815174
1	-0.365650	-4.012862	-3.057230
1	-4.223501	-2.722437	-3.217785
1	-0.449162	-2.571188	-3.459831
1	3.325726	-2.419901	-3.701903
1	-6.142758	-0.229917	-1.996802
1	-2.367812	-0.078795	-2.238910
1	1.406906	0.071663	-2.481121
1	5.180553	0.223808	-2.722953
1	-2.530871	2.467263	-3.201547
1	1.257836	2.617649	-3.444816
1	5.017614	2.769583	-3.685752
1	-6.306645	2.315977	-2.959400
1	-8.751828	-1.834990	0.618420
1	-8.925223	1.474727	-0.017057
1	8.220446	-1.155260	-0.468596
1	8.047072	2.154090	-1.103953
1	6.356113	-3.035005	-1.120841
1	6.137141	3.883501	-0.211605
1	-6.841989	-3.563518	-0.276257
1	-7.060924	3.354897	0.634060
1	3.208758	6.326821	0.045737
1	-0.559282	6.173728	0.285754
1	-4.333557	6.022534	0.527835
1	-4.395293	5.664506	-0.658447
1	-0.619418	5.815812	-0.900571
1	3.154866	5.967128	-1.142744
79	1.792795	-1.911795	2.586958
79	1.673146	0.693946	1.793118
8	7.722784	2.120918	0.447236
8	3.955532	2.175686	0.607080
8	0.173723	2.237923	0.561397
8	-3.658193	2.355596	0.460808
8	-7.411382	2.451523	0.188757
8	3.856039	-3.880274	-2.528424
8	0.072402	-3.797605	-2.592986
8	-3.711059	-3.714963	-2.657588
8	4.034146	6.089784	-0.202701
8	0.250576	6.172440	-0.267284
8	-3.533059	6.255096	-0.331846
8	5.868531	3.697186	0.183820
8	2.095968	3.732957	0.089271
8	-1.689819	3.858382	0.032821
8	-5.482125	3.945126	-0.009936
8	5.837060	1.063398	-1.333281
8	2.052884	1.146117	-1.397875
8	-1.730370	1.228750	-1.462425
8	-5.513607	1.311434	-1.526977
8	7.671223	-1.329183	-0.946865
8	3.889124	-1.321164	-0.992215
8	0.112288	-1.209307	-1.060794
8	-3.690299	-1.149621	-1.100931
8	-7.462968	-0.998558	-1.205123
8	-3.540696	6.598247	0.567311
1	-3.572938	5.954060	1.627155
1	0.210604	5.871403	1.691728
1	3.994174	5.788746	1.756302
1	0.242773	6.515593	0.631884
1	4.026303	6.432938	0.696456
1	-3.521402	5.389166	-2.115097
1	4.045675	5.223854	-1.985952
1	0.262104	5.306510	-2.050528
1	4.030298	3.929261	-2.741816
1	0.246673	4.011917	-2.806389
1	-3.536774	4.094574	-2.870962
1	5.854480	1.125928	-2.293530
1	2.071395	1.208544	-2.358098
1	-1.712361	1.291220	-2.422674
1	-5.496146	1.373861	-2.487253
1	2.049635	-1.014436	-3.936953
1	-1.734108	-0.931773	-4.001531
1	-5.517810	-0.849095	-4.066114
1	5.833006	-1.097088	-3.872383
1	8.657823	1.897564	0.493736
1	8.616145	-1.146900	-0.961343
1	-8.356299	2.269268	0.203490
1	-8.397975	-0.775214	-1.251753
1	-6.417142	4.168487	-0.056637
1	-6.553586	-2.757100	-0.927476
1	6.813430	3.879444	0.169123
1	6.676996	-3.046124	-0.701465
1	-3.766458	-5.310579	-1.454416
1	0.017131	-5.393246	-1.389838
1	3.800662	-5.475892	-1.325269
1	3.832803	-4.831700	-2.385114
1	0.049330	-4.749046	-2.449690
1	-3.734294	-4.666388	-2.514259
79	-0.379792	-3.813128	1.954401
79	0.832978	-1.480994	1.930849
79	-1.841273	-0.393436	1.575117
22	0.158363	-3.390383	-0.858114
22	-3.504487	-2.593495	-1.421937
22	5.209286	3.135638	0.634194
22	1.635854	3.906203	0.069756
22	-2.123016	4.704769	-0.525193
8	6.499433	-2.138950	-2.210051
8	2.840436	-1.361731	-2.788625
8	-0.819219	-0.584289	-3.367336
8	-4.477315	0.192722	-3.945740
8	6.152769	-1.306487	1.456971
8	2.469731	-0.566311	0.860036
8	-4.934368	1.058408	-0.281333
8	5.739050	-4.056923	0.022163
8	2.049462	-3.341782	-0.377628
8	-1.578344	-2.552499	-1.015895
8	-5.237574	-1.725256	-1.713377
8	5.547832	3.178665	-1.429341
8	3.363574	-5.950663	0.120062
8	1.888862	3.955899	-2.007901
8	-0.295312	-5.173457	-0.458498
8	-1.770036	4.733109	-2.586449
8	-3.954196	-4.396222	-1.037034
8	5.119196	3.907360	2.260037
8	1.460299	4.684566	1.681487
8	-2.198504	5.461786	1.102948
8	8.446311	0.483469	1.381301
8	4.765952	1.233037	1.028747
8	1.098118	1.987556	0.420912
8	-2.557780	2.816030	-0.207060
8	-6.189179	3.592315	-0.932943
8	3.934339	-4.825113	-1.977498
8	0.275419	-4.047899	-2.556056
8	-3.383443	-3.270689	-3.134615
8	5.689982	5.032921	0.162492
8	2.031093	5.810140	-0.416048
8	-1.627805	6.587356	-0.994627
8	6.973346	2.361990	0.839244
8	3.324510	3.108381	0.243650
8	-0.335100	3.898189	-0.305813
8	-4.003310	4.693651	-0.896568
8	6.641805	-0.284779	-0.618198
8	2.982660	0.492513	-1.196797
8	-0.675224	1.269535	-1.775147
8	-4.335159	2.046949	-2.353902
8	7.924983	-2.955645	0.058373
8	4.249948	-2.272145	-0.509602
8	0.619126	-1.479650	-1.071339
8	-3.057868	-0.630275	-1.640622
8	-6.710540	0.153218	-2.255806
1	-1.687146	6.965239	-0.111444
1	-1.977619	6.385330	0.946200
1	1.681311	5.608105	1.524756
1	5.340195	4.830892	2.103310
1	1.971727	6.188031	0.467106
1	5.630606	5.410818	1.045657
1	-1.548989	5.656628	-2.743178
1	5.768774	4.102202	-1.586073
1	2.109904	4.879411	-2.164629
1	5.607163	2.800771	-2.312501
1	1.948315	3.577973	-2.891046
1	-1.710542	4.355187	-3.469596
1	6.795037	-0.268814	-1.568228
1	3.136337	0.508342	-2.146752
1	-0.523209	1.285695	-2.725408
1	-4.181395	2.062768	-3.303851
1	2.900001	-1.739650	-3.671754
1	-0.758313	-0.962600	-4.250197
1	-4.417794	-0.185230	-4.828857
1	6.558808	-2.516853	-3.093211
1	9.308243	0.093506	1.558374
1	8.881082	-2.951850	0.168756
1	-7.145296	3.588540	-1.043281
1	-7.572450	0.543171	-2.432949
1	-4.865192	5.083572	-1.073657
1	-6.193650	-1.729100	-1.824212

### Au<sub>3</sub>-A on Oxygen-deficient

#### Anatase

Energy = -4551.23756 a.u.

22	5.922320	1.638516	0.416039
22	2.070021	1.740576	0.351217
22	-1.771143	1.925224	0.289161
22	-5.632224	1.894014	0.217572
22	5.894123	-0.920583	-1.122689
22	2.023356	-0.879935	-1.202290
22	-1.806067	-0.797785	-1.293930
22	-5.665004	-0.665628	-1.317279
22	3.802717	-3.270507	-0.827763
22	0.042630	-3.186065	-0.828336
22	-3.691265	-3.102143	-0.957022
22	3.969426	4.131659	0.241162
22	0.214384	4.214610	0.177260
22	-3.576136	4.301863	0.110169
8	5.825151	-0.753935	-2.973224
8	2.041367	-0.671271	-3.037806
8	-1.741915	-0.588626	-3.102379
8	-5.525264	-0.505997	-3.166934
8	5.831642	-0.067716	0.738553
8	2.006125	0.002007	0.711186
8	-5.634033	0.185690	0.545277
8	5.741976	-2.822777	-0.747824
8	1.973617	-2.785694	-0.698275
8	-1.844757	-2.720048	-0.761476
8	-5.608655	-2.574779	-0.941284
8	4.022413	4.272417	-1.842661
8	3.792771	-5.132733	-0.426110
8	0.239008	4.355070	-1.907227
8	0.009200	-5.050049	-0.490720
8	-3.544724	4.437725	-1.971809
8	-3.774294	-4.967418	-0.555246
8	3.970872	4.837305	1.899596
8	0.187351	4.919963	1.835025
8	-3.596203	5.002619	1.770448

### Au<sub>3</sub>-B on Oxygen-deficient

#### Anatase

Energy = -4551.222864 a.u.

22	6.608098	0.332204	1.116911
22	2.884342	1.086758	0.551368
22	-0.755723	2.078331	-0.153790
22	-4.575130	2.703372	-0.655258
22	6.291191	-2.238186	-0.369999
22	2.527982	-1.476542	-0.947684
22	-1.204564	-0.776226	-1.599442
22	-4.882214	0.131353	-2.136237
22	3.780629	-4.141324	-0.307429

## Appendix D

1 7.929477 2.365755 0.949344  
 1 6.600995 -4.446602 0.199018  
 1 -3.894816 -4.774143 -1.1920198  
 1 -0.235928 -5.551350 -1.341648  
 1 3.422956 -6.328567 -0.763095  
 1 3.713380 -5.748641 -1.820745  
 1 0.054524 -4.971433 -2.399296  
 1 -3.604385 -4.194214 -2.977848  
 79 -3.452213 -2.574694 1.419207  
 79 -1.681610 -0.008806 1.128234  
 79 -3.166673 -0.766487 3.403842

**Au<sub>4</sub>-A on Oxygen-deficient  
 Anatase**

Energy = -4686.734384 a.u.

22 6.518286 0.496227 0.714198  
 22 2.777498 1.340518 0.447152  
 22 -0.907963 2.397364 0.081051  
 22 -4.727231 3.092351 -0.120209  
 22 6.068974 -1.939760 -0.951673  
 22 2.290738 -1.114499 -1.244577  
 22 -1.469898 -0.339070 -1.586347  
 22 -5.162571 0.653474 -1.784271  
 22 3.550555 -3.826130 -0.879209  
 22 -0.092563 -3.000656 -1.074521  
 22 -3.783537 -2.145566 -1.353838  
 22 5.133053 3.342103 0.552855  
 22 1.532962 4.182621 0.289836  
 22 -2.243994 5.059573 0.009785  
 8 6.159824 -1.693558 -2.786739  
 8 2.481763 -0.842674 -3.058254  
 8 -1.196243 0.008357 -3.329730  
 8 -4.874495 0.859307 -3.601235  
 8 6.063608 -1.157804 0.955200  
 8 2.365182 -0.339505 0.702621  
 8 -5.089679 1.425822 0.141776  
 8 5.520791 -3.780426 -0.670983  
 8 1.846912 -2.993401 -0.829666  
 8 -1.846285 -2.125676 -1.187526  
 8 -5.513406 -1.227575 -1.485387  
 8 5.331995 3.550494 -1.519074  
 8 3.131729 -5.656791 -0.569583  
 8 1.653909 4.401429 -1.790585  
 8 -0.546362 -4.805817 -0.841079  
 8 -2.024204 5.252335 -2.062098  
 8 -4.224451 -3.954862 -1.112553  
 8 5.154092 3.980309 2.237233  
 8 1.475985 4.831281 1.965717  
 8 -2.201985 5.682223 1.694209  
 8 8.371067 0.612641 0.868009  
 8 4.686563 1.422464 0.816599  
 8 1.002487 2.255678 0.508778  
 8 -2.688999 3.146541 0.202128  
 8 -6.341279 4.016428 -0.218004  
 8 3.579709 -4.369099 -2.602712  
 8 -0.098335 -3.518179 -2.874213  
 8 -3.776420 -2.667187 -3.145732  
 8 5.602133 5.268061 0.204208  
 8 1.924070 6.118986 -0.067341  
 8 -1.754072 6.969893 -0.338978  
 8 6.891120 2.540741 0.577374  
 8 3.221986 3.358774 0.288463  
 8 -0.463473 4.218013 0.058070  
 8 -4.143184 5.093590 -0.237140  
 8 6.430177 0.023911 -1.063560  
 8 2.751648 0.875014 -1.335123  
 8 -0.926419 1.725915 -1.606573  
 8 -4.604444 2.576861 -1.878032  
 8 7.718955 -2.703289 -0.690398  
 8 4.035244 -1.935316 -0.951957  
 8 0.382340 -1.060679 -1.249961  
 8 -3.327280 -0.172300 -1.500548  
 8 -6.993404 0.700500 -1.776413  
 1 -1.750788 7.275259 0.573851

1 -1.979502 6.613660 1.598198  
 1 1.698672 5.762691 1.869688  
 1 5.376775 4.911740 2.141163  
 1 1.927290 6.424319 0.845348  
 1 5.605400 5.573375 1.116845  
 1 -1.801672 6.183799 -2.158102  
 1 5.554553 4.481891 -1.615142  
 1 1.876448 5.332843 -1.886624  
 1 5.328666 3.245135 -2.431798  
 1 1.650562 4.096085 -2.703298  
 1 -2.027509 4.947045 -2.974801  
 1 6.521465 0.115802 -2.017219  
 1 2.843667 0.966627 -2.288701  
 1 -0.834276 1.817590 -2.560184  
 1 -4.512600 2.668580 -2.831701  
 1 2.478436 -1.147929 -3.970963  
 1 -1.199792 -0.296969 -4.242466  
 1 -4.877745 0.553936 -4.513951  
 1 6.156539 -1.998897 -3.699457  
 1 9.237426 0.202686 0.955834  
 1 8.680186 -2.716150 -0.643436  
 1 -7.302507 4.029288 -0.265048  
 1 -7.859745 1.110449 -1.864338  
 1 -5.009486 5.503536 -0.325214  
 1 -6.474656 -1.214753 -1.532907  
 1 7.852351 2.527885 0.624100  
 1 6.387185 -4.190396 -0.583461  
 1 -4.227735 -4.260238 -2.025305  
 1 -0.549629 -5.111180 -1.753808  
 1 3.128465 -5.962121 -1.482311  
 1 3.357159 -5.300512 -2.506637  
 1 -0.321003 -4.449550 -2.778144  
 1 -3.999103 -3.598601 -3.049638  
 79 -4.190807 -1.841761 1.374757  
 79 -1.680457 -2.866999 1.718099  
 79 0.776536 -1.866331 1.771475  
 79 -1.497414 0.097162 1.237705

**Au<sub>4</sub>-B on Oxygen-deficient Surface**  
 Energy = -4686.727508 a.u.

22 -6.732156 0.469092 -0.949829  
 22 -2.978387 1.069926 -0.361944  
 22 0.742597 1.901471 0.295496  
 22 4.533943 2.345764 0.904211  
 22 -6.477543 -2.247605 0.265391  
 22 -2.698963 -1.657424 0.870344  
 22 1.032228 -1.089749 1.524992  
 22 4.777373 -0.399211 2.098476  
 22 -4.020061 -4.204707 -0.030154  
 22 -0.373460 -3.612644 0.545158  
 22 3.291595 -2.979102 1.107422  
 22 -5.255095 3.169170 -0.204966  
 22 -1.668601 3.766765 0.378131  
 22 2.133365 4.410109 1.007189  
 8 -6.659699 -2.329480 2.108803  
 8 -2.972564 -1.719114 2.707860  
 8 0.714550 -1.108750 3.306911  
 8 4.401723 -0.498368 3.905968  
 8 -6.333110 -1.140130 -1.460143  
 8 -2.549448 -0.550454 -0.840575  
 8 4.804578 0.734868 0.304162  
 8 -5.983743 -4.031522 -0.317269  
 8 -2.272089 -3.461026 0.073543  
 8 1.392833 -2.840484 0.760444  
 8 5.077576 -2.200404 1.479758  
 8 -5.559913 3.010812 1.855985  
 8 -3.667001 -5.972108 -0.642061  
 8 -1.872795 3.621176 2.455033  
 8 0.020112 -5.361735 -0.043007  
 8 1.814371 4.231549 3.054087  
 8 3.707288 -4.751409 0.556038  
 8 -5.154532 4.098102 -1.746750  
 8 -1.467425 4.708471 -1.147702  
 8 2.219667 5.318832 -0.548658

8 -8.571079 0.698370 -1.168989  
 8 -4.863858 1.304318 -0.808085  
 8 -1.215022 1.936664 -0.209603  
 8 2.535121 2.539621 0.542448  
 8 6.177326 3.139816 1.227250  
 8 -4.178601 -5.049759 1.566995  
 8 -0.491489 -4.439388 2.166050  
 8 3.195643 -3.829034 2.765102  
 8 -5.666143 5.020474 0.462293  
 8 -1.979026 5.630840 1.061343  
 8 1.708087 6.241203 1.660392  
 8 -7.036454 2.469585 -0.461861  
 8 -3.385687 3.058311 0.173054  
 8 0.328099 3.637348 0.756125  
 8 4.024865 4.300670 1.335357  
 8 -6.766146 -0.319891 0.715084  
 8 -3.078827 0.290539 1.314172  
 8 0.608276 0.900903 1.913223  
 8 4.295567 1.511278 2.512285  
 8 -8.136253 -2.870736 -0.208906  
 8 -4.438662 -2.348686 0.368842  
 8 -0.796675 -1.763644 1.026467  
 8 2.933836 -1.052827 1.523070  
 8 6.612187 -0.429271 2.187267  
 1 1.767974 6.705033 0.819209  
 1 2.028203 6.227563 -0.295953  
 1 -1.658922 5.617196 -0.895005  
 1 -5.346043 5.006830 -1.494054  
 1 -1.919144 6.094669 0.220160  
 1 -5.606257 5.484303 -0.378889  
 1 1.622848 5.140268 3.306782  
 1 -5.751387 3.919537 2.108683  
 1 -2.064270 4.529902 2.707734  
 1 -5.619767 2.546982 2.697161  
 1 -1.932654 3.157346 3.296209  
 1 1.754420 3.767705 3.895252  
 1 -6.907294 -0.396188 1.664056  
 1 -3.220321 0.214137 2.263080  
 1 0.466797 0.824503 2.862130  
 1 4.153789 1.434859 3.461161  
 1 -3.032456 -2.182947 3.549029  
 1 0.654657 -1.572582 4.148078  
 1 4.341746 -0.962226 4.747120  
 1 -6.719562 -2.793312 2.949980  
 1 -9.446309 0.353007 -1.371615  
 1 -9.093089 -2.828653 -0.303896  
 1 7.134177 3.097748 1.322200  
 1 7.487391 -0.083925 2.389964  
 1 4.900058 4.645992 1.538127  
 1 6.034366 -2.242584 1.575259  
 1 -7.993316 2.511616 -0.556609  
 1 -6.858999 -4.376936 -0.519634  
 1 3.647290 -5.215203 1.397215  
 1 -0.039774 -5.825584 0.798161  
 1 -3.726890 -6.435948 0.199112  
 1 -3.987110 -5.958472 1.314276  
 1 -0.299992 -5.348106 1.913325  
 1 3.387120 -4.737742 2.512374  
 79 1.641005 1.993268 -2.326530  
 79 3.256581 -0.251167 -1.543214  
 79 3.878724 -2.873654 -1.580395  
 79 0.480509 -0.434572 -1.178630

**Au<sub>4</sub>-C on Oxygen-deficient  
 Anatase**

Energy = -4686.726991 a.u.

22 -6.106310 -1.767791 0.395796  
 22 -2.292154 -1.615830 0.151742  
 22 1.516002 -1.722505 -0.128003  
 22 5.423810 -1.447581 -0.422236  
 22 -6.273413 0.901998 -0.926168  
 22 -2.420939 1.064739 -1.181989  
 22 1.382478 1.191455 -1.489060  
 22 5.237634 1.276309 -1.737798

## Appendix D

22 -4.284886 3.317013 -0.535453  
 22 -0.536707 3.426632 -0.720372  
 22 3.176747 3.555684 -1.040379  
 22 -4.062551 -4.143570 -0.087397  
 22 -0.386281 -4.039289 -0.345896  
 22 3.482033 -3.916712 -0.608614  
 8 -6.298655 0.887609 -2.780948  
 8 -2.524339 1.005831 -3.039713  
 8 1.249990 1.124024 -3.298484  
 8 5.024326 1.242255 -3.557239  
 8 -6.081075 -0.099957 0.862831  
 8 -2.265193 0.059026 0.596158  
 8 5.238305 0.213236 0.137559  
 8 -6.193881 2.767338 -0.394453  
 8 -2.435038 2.911953 -0.569874  
 8 1.381378 3.035450 -0.788885  
 8 5.128972 3.121967 -1.170618  
 8 -4.202385 -4.115175 -2.172689  
 8 -4.341558 5.140351 0.025516  
 8 -0.428074 -3.996946 -2.431441  
 8 -0.567252 5.258566 -0.233270  
 8 3.346254 -3.878719 -2.690196  
 8 3.206994 5.376788 -0.492017  
 8 -3.923308 -4.983420 1.500796  
 8 -0.149014 -4.865168 1.242054  
 8 3.625238 -4.746995 0.983289  
 8 -7.871913 -2.353634 0.472408  
 8 -4.110277 -2.220224 0.442070  
 8 -0.355875 -2.080727 0.138065  
 8 3.500234 -2.039085 -0.154884  
 8 7.225208 -1.880769 -0.562687  
 8 -4.458378 4.063994 -2.169982  
 8 -0.684093 4.182206 -2.428755  
 8 3.090241 4.300440 -2.687516  
 8 -4.040136 -6.059804 -0.694687  
 8 -0.265835 -5.941574 -0.953415  
 8 3.508445 -5.823349 -1.212224  
 8 -5.962065 -3.805047 -0.015645  
 8 -2.216341 -3.667811 -0.295465  
 8 1.560985 -3.525086 -0.560235  
 8 5.360795 -3.450384 -0.791943  
 8 -6.136627 -1.056994 -1.302942  
 8 -2.362143 -0.938801 -1.561724  
 8 1.412468 -0.821330 -1.820570  
 8 5.186630 -0.702345 -2.079240  
 8 -8.058335 1.197756 -0.624028  
 8 -4.301743 1.384164 -0.856702  
 8 -0.503608 1.456660 -1.102146  
 8 3.295999 1.631681 -1.408912  
 8 7.038817 1.670608 -1.659036  
 1 3.580777 -6.238666 -0.346982  
 1 3.639341 -5.683302 0.760906  
 1 -0.134976 -5.801518 1.019668  
 1 -3.909262 -5.919734 1.278432  
 1 -0.193519 -6.356885 -0.088223  
 1 -3.967811 -6.475097 0.170539  
 1 3.360284 -4.815043 -2.912573  
 1 -4.188299 -5.051475 -2.395051  
 1 -0.414007 -4.933259 -2.653812  
 1 -4.274687 -3.699877 -3.037903  
 1 -0.500390 -3.581664 -3.296665  
 1 3.273863 -3.463452 -3.555424  
 1 -6.202564 -1.040913 -2.262985  
 1 -2.428400 -0.922683 -2.521736  
 1 1.345547 -0.803917 -2.780463  
 1 5.120044 -0.686265 -3.039248  
 1 -2.596674 1.421123 -3.904925  
 1 1.177604 1.539350 -4.163680  
 1 4.951863 1.657558 -4.422441  
 1 -6.370961 1.302908 -3.646165  
 1 -8.812616 -2.183411 0.584035  
 1 -8.993011 0.968793 -0.607124  
 1 8.159898 -1.651814 -0.579545  
 1 7.979499 1.500406 -1.770768  
 1 6.301469 -3.620597 -0.903749

1 6.063622 3.351002 -1.188052  
 1 -6.896753 -4.033977 0.001036  
 1 -7.134599 2.937600 -0.283113  
 1 3.134725 5.792089 -1.357225  
 1 -0.639619 5.673872 -1.098461  
 1 -4.413899 5.555651 -0.839704  
 1 -4.472452 5.000284 -1.947598  
 1 -0.698150 5.118499 -2.206357  
 1 3.076122 5.236715 -2.465118  
 79 1.500857 -1.482029 2.582541  
 79 2.941761 0.507107 1.041843  
 79 -0.731297 3.506625 2.032893  
 79 0.365954 1.067121 1.743016

### Triplet Au<sub>4</sub> on Oxygen-deficient

#### Anatase

Energy = -4686.716934 a.u.

22 -6.614063 0.271959 -0.794183  
 22 -2.910468 1.244313 -0.452081  
 22 0.756579 2.310850 -0.121637  
 22 4.531206 3.174979 0.253406  
 22 -6.124896 -2.182026 0.839356  
 22 -2.381065 -1.250887 1.192268  
 22 1.326038 -0.292774 1.599609  
 22 5.018524 0.714496 1.883122  
 22 -3.535326 -3.990799 0.779401  
 22 0.099402 -3.052513 1.085462  
 22 3.701623 -2.114556 1.410050  
 22 -5.295514 3.153130 -0.566063  
 22 -1.677122 4.095700 -0.226860  
 22 1.984603 5.045823 0.116063  
 8 -6.246807 -1.965800 2.678479  
 8 -2.598592 -1.017123 3.020418  
 8 1.048882 -0.069341 3.362584  
 8 4.697623 0.880433 3.704379  
 8 -6.108079 -1.370077 -1.046874  
 8 -2.403517 -0.440953 -0.712675  
 8 4.932121 1.509267 -0.028778  
 8 -5.517097 -4.001797 0.542475  
 8 -1.849556 -3.105522 0.718533  
 8 1.792039 -2.154840 1.153846  
 8 5.427073 -1.155473 1.568563  
 8 -5.547041 3.317850 1.501364  
 8 -3.075070 -5.809219 0.451220  
 8 -1.898855 4.266579 1.843337  
 8 0.572877 -4.860643 0.793355  
 8 1.749228 5.215292 2.185324  
 8 4.221209 -3.911508 1.134928  
 8 -5.323565 3.809402 -2.244920  
 8 -1.675387 4.758120 -1.902945  
 8 1.972642 5.706810 -1.560980  
 8 -8.465535 0.333103 -0.976361  
 8 -4.805578 1.242545 -0.863222  
 8 -1.145709 2.149613 -0.570609  
 8 2.522323 3.166415 -0.166236  
 8 6.127138 4.128057 0.391565  
 8 -3.590149 -4.565421 2.495768  
 8 0.057983 -3.616385 2.837895  
 8 3.705906 -2.667924 3.179751  
 8 -5.838820 5.053149 -0.200392  
 8 -2.190666 6.001866 0.141513  
 8 1.457526 6.950580 0.483515  
 8 -7.044861 2.297010 -0.634108  
 8 -3.392478 3.191294 -0.258454  
 8 0.236016 4.174298 0.074968  
 8 3.899679 5.143254 0.391926  
 8 -6.538759 -0.230601 0.976689  
 8 -2.889773 0.718461 1.318558  
 8 0.757821 1.667131 1.660910  
 8 4.406004 2.615751 2.002656  
 8 -7.744642 -2.986631 0.543139  
 8 -4.079136 -2.122526 0.878646  
 8 -0.450786 -1.143820 2.129542  
 8 3.208402 -0.168906 1.526678

8 6.847988 0.808313 1.911075  
 1 1.459705 7.269554 -0.424520  
 1 1.722591 6.630157 -1.454746  
 1 -1.925681 5.681388 -1.796727  
 1 -5.573882 4.732636 -2.138687  
 1 -2.188448 6.320810 -0.766493  
 1 -5.836653 5.372056 -1.108468  
 1 1.499248 6.138637 2.291540  
 1 -5.797170 4.241130 1.607616  
 1 -2.148985 5.189877 1.949577  
 1 -5.549197 2.998919 2.409446  
 1 -1.901008 3.947653 2.751415  
 1 1.747151 4.896395 3.093386  
 1 -6.647236 -0.155762 1.930080  
 1 -2.999585 0.792771 2.272009  
 1 0.648123 1.741503 2.613928  
 1 4.297123 2.690407 2.955983  
 1 -2.601058 -1.336035 3.928508  
 1 1.048913 -0.386683 4.270695  
 1 4.695574 0.561504 4.612471  
 1 -6.248987 -2.284735 3.586551  
 1 -9.318599 -0.099422 -1.083791  
 1 -8.704306 -3.025543 0.480940  
 1 7.086778 4.166956 0.453922  
 1 7.701065 1.240838 2.018692  
 1 4.752642 5.575740 0.499670  
 1 6.387011 -1.116737 1.631224  
 1 -8.004557 2.258117 -0.696091  
 1 -6.370199 -4.434324 0.435425  
 1 4.219138 -4.230639 2.043276  
 1 0.570947 -5.179357 1.701313  
 1 -3.077205 -6.128107 1.359338  
 1 -3.340091 -5.488725 2.389553  
 1 0.308365 -4.539907 2.731536  
 1 3.956398 -3.591203 3.073512  
 79 4.335676 -1.896452 -1.335895  
 79 1.772920 -2.757812 -1.810696  
 79 -0.446953 -1.146275 -1.743277  
 79 2.022185 0.089402 -1.284721

### Zapol's Anatase(101) Model

#### (Ti<sub>7</sub>O<sub>7</sub>H<sub>2</sub>)

Energy = -2453.72023445 a.u.

8 -0.025371 -0.227109 -0.960611  
 22 -0.046817 -2.056165 -0.095508  
 8 1.849893 -1.639484 -0.094345  
 8 -0.083747 -3.885991 0.802559  
 8 -0.033384 -1.728458 1.974352  
 8 3.707374 -3.185641 -1.534880  
 22 1.836151 0.208336 -0.747463  
 8 1.984797 1.802872 -1.483407  
 8 -0.071857 -3.116095 -1.535070  
 22 -1.876722 0.291064 -0.758878  
 8 -1.884437 1.882782 -1.488094  
 8 -3.851086 -3.046550 -1.535260  
 8 3.773432 -0.290086 -0.657001  
 22 3.850348 -2.145705 -0.064056  
 8 5.631921 -1.788573 -0.073988  
 8 3.695483 -3.955537 0.802749  
 8 3.745847 -1.798003 1.904541  
 22 1.967605 3.007812 0.113684  
 8 3.855184 3.343490 -0.073038  
 8 1.918748 1.176527 0.803700  
 8 1.969109 3.334061 1.975492  
 8 1.996696 4.841978 -0.656052  
 22 -1.823005 3.081606 0.116428  
 8 0.077625 3.386663 -0.118594  
 8 -1.860483 1.246072 0.803510  
 8 -1.810122 3.403606 1.975301  
 8 -1.782588 4.908984 -0.652893  
 8 -3.786379 -0.152234 -0.671467  
 22 -3.899418 -2.021869 -0.054639  
 8 -1.931613 -1.584970 -0.086330  
 8 -3.862978 -3.816445 0.802369

## Appendix D

8 -3.812615	-1.658912	1.974162	8 -3.154969	0.785076	5.650665	1 -3.319223	0.666827	10.402830
8 -5.705662	-1.574289	-0.071329	8 -3.133527	0.794122	1.883971	1 -5.876344	0.716719	7.569995
1 3.693833	-4.120380	-1.215128	8 -3.133527	0.794122	-1.883971	1 -6.626951	-0.001550	6.617830
1 -0.081861	-4.039130	-1.198468	8 -3.154969	0.785076	-5.650665	1 -5.509742	-0.468564	7.570011
1 -3.872205	-3.965644	-1.187325	8 -3.129867	0.587877	-9.462498	1 -8.438058	0.755603	4.725329
8 -3.698343	3.483234	-0.078784	8 7.107811	0.410393	5.677484	1 -8.438059	0.755603	2.844671
1 1.062272	5.068848	-0.767868	8 7.036538	0.698329	1.895981	1 -8.438061	0.755600	0.940329
1 -2.730349	-5.147580	-0.756332	8 7.036538	0.698329	-1.895981	1 -8.438059	0.755603	-2.844671
1 -4.663388	3.343883	-0.033426	8 7.107811	0.410393	-5.677484	1 -8.438058	0.755603	-4.725329
1 -4.731588	0.055120	-0.739854	8 -6.784243	-1.986980	3.785016	1 -6.626951	-0.001550	-6.617830
1 -6.660858	-1.745224	0.002751	8 -6.784244	-1.986978	0.000000	1 -5.876344	0.716719	-7.569995
1 6.585338	-2.020239	-0.037536	8 -6.784243	-1.986980	-3.785016	1 -5.509742	-0.468564	-7.570011
1 1.979499	3.897542	2.756530	8 3.453458	-2.164358	7.570077	1 -3.319223	0.666827	-10.402830
1 -1.807572	3.970503	2.764396	8 -5.324365	1.505156	7.570005	1 -1.508053	-0.090182	-12.295328
1 3.698018	-4.524807	-0.017343	8 3.453466	-2.164384	3.785032	1 1.799716	0.578350	12.295327
1 -0.090429	-4.446152	-0.005820	8 -5.225882	1.471839	3.751322	1 3.610743	-0.179007	-10.402830
1 -3.878874	-4.367498	0.005703	8 3.453480	-2.164370	0.000000	1 5.801328	0.956539	-7.569990
1 2.935586	5.041978	-0.760529	8 -5.227147	1.463935	0.000000	1 6.167939	-0.228740	-7.569971
1 -0.848925	5.107336	-0.765728	8 3.453466	-2.164384	-3.785032	1 3.610743	-0.179007	10.402830
1 1.926481	1.346787	1.727498	8 -5.225882	1.471839	-3.751322	1 6.167939	-0.228740	7.569971
1 -1.861966	1.425442	1.739020	8 3.453458	-2.164358	-7.570077	1 5.801328	0.956539	7.569990
1 3.769219	-1.279288	2.757828	8 -5.324365	1.505156	-7.570005	1 6.918045	0.489700	6.617716
1 -0.019227	-1.200632	2.769350	8 4.913359	1.327783	7.570002	1 6.918045	0.489700	-6.617716
1 -3.815549	-1.130447	2.795260	8 4.946386	1.264027	3.835248	1 8.729652	-0.267623	4.725329
1 3.739161	-2.706892	2.314461	8 4.897066	1.263205	0.000000	1 8.729645	-0.267629	-2.844671
1 -0.049285	-2.628237	2.325985	8 4.946386	1.264027	-3.835248	1 8.729652	-0.267611	-4.725329
1 -3.837732	-2.549582	2.337507	8 4.913359	1.327783	-7.570002	1 8.729648	-0.267623	-0.940329
1 4.796565	3.150904	-0.042491	8 -8.248767	0.676476	3.785000	1 8.729648	-0.267623	0.940329
1 4.541193	0.241345	-0.919671	8 -8.248767	0.676476	-3.785000	1 -7.336210	-2.775418	3.784988
			8 1.988873	0.498883	11.355002	1 -7.336210	-2.775418	0.000000
			8 2.005335	0.731789	7.596054	1 -7.336210	-2.775418	-3.785018
			8 1.958537	0.706503	3.802903	1 -4.795154	-1.786479	-3.785018
			8 1.951989	0.693437	0.000000	1 -4.795159	-1.786478	0.000000
			8 1.958537	0.706503	-3.802903	1 -4.795154	-1.786479	3.785018
			8 2.005335	0.731789	-7.596054	1 -2.217349	-2.864118	-5.677512
			8 1.988873	0.498883	-11.355002	1 -2.217349	-2.864118	-1.892496
			8 -4.621765	-0.839775	7.569989	1 -2.217349	-2.864118	1.892496
			8 -4.621767	-0.839777	3.784976	1 -2.217349	-2.864118	5.677512
			8 -4.621756	-0.839785	0.000000	1 -2.217344	-2.864121	9.462557
			8 -4.621767	-0.839777	-3.784976	1 -2.217344	-2.864121	-9.462557
			8 -4.621765	-0.839775	-7.569989	1 0.323703	-1.875178	-9.462496
			8 5.615944	-1.017157	7.570037	1 0.323699	-1.875177	-5.677492
			8 5.615955	-1.017196	3.785080	1 0.323700	-1.875177	-1.892479
			8 5.615966	-1.017159	0.000000	1 0.323700	-1.875177	1.892479
			8 5.615955	-1.017196	-3.785080	1 0.323699	-1.875178	9.462496
			8 5.615944	-1.017157	-7.570037	1 2.901522	-2.952824	7.569952
			8 -6.816205	0.077639	5.677498	1 2.901515	-2.952819	3.784975
			8 -6.824489	0.066704	1.897202	1 2.901512	-2.952817	0.000000
			8 -6.824489	0.066704	-1.897202	1 2.901515	-2.952819	-3.784975
			8 -6.816205	0.077639	-5.677498	1 2.901522	-2.952824	-7.569952
			8 3.421572	-0.099703	9.462476	1 4.341462	-2.535590	-7.569986
			8 3.363268	-0.100724	5.682648	1 5.442568	-1.963878	-3.784940
			8 3.355246	-0.079802	1.903416	1 5.442566	-1.963877	0.000000
			8 3.355246	-0.079802	-1.903416	1 5.442568	-1.963878	3.784940
			8 3.363268	-0.100724	-5.682648			
			8 3.421572	-0.099703	-9.462476			
			8 0.497121	-0.928452	9.462521			
			8 0.497120	-0.928478	5.677507			
			8 0.497111	-0.928484	1.892527			
			8 0.497111	-0.928484	-1.892527			
			8 0.497120	-0.928478	-5.677507			
			8 0.497121	-0.928452	-9.462521			
			8 -1.697401	-0.011158	11.355004			
			8 -1.803036	0.026015	7.562768			
			8 -1.716219	0.000470	3.783608			
			8 -1.720121	-0.004025	0.000000			
			8 -1.716219	0.000470	-3.783608			
			8 -1.803036	0.026015	-7.562768			
			8 -1.697401	-0.011158	-11.355004			
			8 8.540357	-0.188500	3.785000			
			8 8.540356	-0.188490	0.000000			
			8 8.540357	-0.188500	-3.785000			
			1 1.799716	0.578350	12.295327			
			1 -1.508053	-0.090182	12.295328			

**Extended Anatase(101) Surface**  
**Model (Ti<sub>28</sub>O<sub>66</sub>H<sub>60</sub>)**  
 Energy = -6500.66799117 a.u.

22 1.483414	0.622590	9.564869
22 1.449206	0.649940	5.728804
22 1.442071	0.647314	1.908956
22 1.442071	0.647314	-1.908956
22 1.449206	0.649940	-5.728804
22 1.483414	0.622590	-9.564869
22 -1.376931	-0.239364	9.559582
22 -1.404159	-0.206297	5.635904
22 -1.404392	-0.196014	1.880035
22 -1.404392	-0.196014	-1.880035
22 -1.404159	-0.206297	-5.635904
22 -1.376931	-0.239364	-9.559582
22 -3.601367	0.661191	7.520890
22 -3.664599	0.759104	3.767680
22 -3.654691	0.758182	0.000000
22 -3.664599	0.759104	-3.767680
22 -3.601367	0.661191	-7.520890
22 6.541646	0.558225	3.792037
22 6.513734	0.601367	0.000000
22 6.541646	0.558225	-3.792037
22 -6.462014	-0.173122	3.773971
22 -6.451474	-0.170225	0.000000
22 -6.462014	-0.173122	-3.773971
22 3.812861	-0.106561	7.534920
22 3.698365	-0.285122	3.784229
22 3.685698	-0.285801	0.000000
22 3.698365	-0.285122	-3.784229
22 3.812861	-0.106561	-7.534920
8 -1.665389	-2.075664	9.462427
8 -1.665382	-2.075669	5.677486
8 -1.665386	-2.075681	1.892506
8 -1.665386	-2.075681	-1.892506
8 -1.665382	-2.075669	-5.677486
8 -1.665389	-2.075664	-9.462427
8 -0.099478	1.351581	9.514528
8 -0.156038	1.345960	5.698356
8 -0.160386	1.354689	1.893698
8 -0.160386	1.354689	-1.893698
8 -0.156038	1.345960	-5.698356
8 -0.099478	1.351581	-9.514528
8 -3.129867	0.587877	9.462498